ASME
SETTING THE STANDARD

Transactions of the ASME, Journal of Turbomachinery (ISSN 0889-504X) is published quarterly (Jan., Apr., July, Oct.) by The American Society of Mechanical Engineers, Three Park Avenue, New York, NY 10016. Periodicals postage paid at New York, NY and additional mailing offices.
POSTMASTER: Send address changes to Transactions of the ASME, Journal of Turbomachinery, c/o THE AMERICAN SOCIETY OF MECHANICAL ENGINEERS, 22 Law Drive, Box 2300, Fairfield, NJ 07007-2300.
CHANGES OF ADDRESS must be received at Society headquarters seven weeks before they are to be effective. Please send old label and new address.
STATEMENT from By-Laws. The Society shall not be responsible for statements or opinions advanced in papers or ... printed in its publications (B7.1, Par. 3).

Journal of Turbomachinery

Published Quarterly by ASME

VOLUME 129 • NUMBER 4 • OCTOBER 2007

RESEARCH PAPERS

(Contents continued on inside back cover)

This journal is printed on acid-free paper, which exceeds the ANSI Z39.48-1992 specification for permanence of paper and library materials. ♾™
♻ 85% recycled content, including 10% post-consumer fibers.

Journal of Turbomachinery Volume 129, Number 4 OCTOBER 2007

The ASME Journal of Turbomachinery is abstracted and indexed in the following:

Aluminum Industry Abstracts, Aquatic Science and Fisheries Abstracts, Ceramics Abstracts, Chemical Abstracts, Civil Engineering Abstracts, Compendex (The electronic equivalent of Engineering Index), Corrosion Abstracts, Current Contents, Ei EncompassLit, Electronics & Communications Abstracts, Energy Information Abstracts, Engineered Materials Abstracts, Engineering Index, Environmental Science and Pollution Management, Excerpta Medica, Fluidex, Fuel and Energy Abstracts, INSPEC, Index to Scientific Reviews, Materials Science Citation Index, Mechanical & Transportation Engineering Abstracts, Mechanical Engineering Abstracts, METADEX (The electronic equivalent of Metals Abstracts and Alloys Index), Metals Abstracts, Oceanic Abstracts, Pollution Abstracts, Referativnyi Zhurnal, Shock & Vibration Digest, Steels Alert

Effects of Bleed Rate and Endwall Location on the Aerodynamic Behavior of a Circular Hole Bleed Off-Take

B. A. Leishman

N. A. Cumpsty[1]

Rolls-Royce plc.,
Derby DE24 8BJ, UK

J. D. Denton
Whittle Laboratory,
University of Cambridge,
Cambridge CB3 0DY, UK

In a jet engine bleed off-takes on the hub and casing endwalls, part way through the compressor, supply high-pressure air for cooling, sealing, de-icing, and aircraft cabin air applications; bleed also assists compressor operation at part-speed conditions. Two separate issues are of interest: the bleed off-take air pressure and the interaction of the bleed off-take with the primary flow through the blade passage. In this paper, the aerodynamic behavior is presented for a circular-hole bleed off-take at three endwall locations within a stationary cascade blade passage: at midpassage; near the blade pressure surface; and near the blade suction surface. Results from low-speed cascade experiments are complemented by three-dimensional numerical calculations using an unstructured mesh-based solver, in which the blade passage and bleed off-take geometry are fully modeled. The bleed off-take location and the magnitude of bleed rate influence the off-take air pressure and the interaction with the primary passage flow. For optimum design at zero and low bleed rates, off-takes near the blade pressure surface give the highest bleed air pressures and minimum loss in the blade passage. For minimum blade passage loss at higher bleed rates, however, it is necessary to take bleed near the blade suction surface. The paper discusses the causes for this pattern of behavior.
[DOI: 10.1115/1.2752191]

Introduction

Part way through a jet engine compressor air is bled from the primary (core) flow through bleed off-takes on the hub and casing endwalls. The bleed air is used to cool high-temperature engine components, pressurize drum cavities to control leakage flows, pressurize bearing chambers, and allow compressor axial stage matching at off-design conditions (i.e., handling bleed). Bleed air also supplies warm air for engine de-icing applications and supplies the aircraft cabin air system (cabin bleed). Typical bleed rates vary throughout the flight cycle for each application. At low- and part-speed conditions handling bleed rates can be as high as 20% of the primary (core) flow, but at the design point, handling bleed is zero. Cabin and cooling air bleed rates are typically about 3% of the primary flow but can be as high as 15% during certain emergency conditions. Since the bleed off-take must be sized to allow for this high bleed rate condition, the off-take area is sometimes much larger than that required for lower, normal, bleed rates.

Two aspects of bleed off-take performance are of interest. First, maximizing bleed off-take air pressure, at both low and high bleed rates, is beneficial to the engine cycle efficiency and is also necessary for certain applications. High off-take pressure demands that the drop in static pressure should be small as air passes through the off-take. Second, the bleed off-take will affect the primary flow in the blade passage, so the presence of a bleed off-take can increase blade passage loss and reduce the pressure rise across the blade row.

Bleed off-takes are a significant feature of the compressor geometry but have not normally been modeled explicitly in the computational fluid dynamics (CFD) used for its aerodynamic design. Instead, the hub and casing endwalls are assumed to be solid. CFD codes with topologically structured grids makes it difficult, and sometimes impossible, to model geometric features other than the blade passages. Moreover, minimizing solution times during design iteration restricts mesh size and therefore limits the resolution of geometric features modeled.

The aerodynamic effects of endwall features, such as bleed off-takes, are sometimes accounted for with endwall boundary condition models that attempt to represent the physics governing the flow into and around them. Rhie et al. [1] and LeJambre et al. [2], Conan and Savarese [3], and Gallimore et al. [4] reported the modeling of bleed off-take flows in CFD design codes with cell boundary condition models. These models account for the removal of mass flow from the blade passage, but without modeling the actual geometry of the bleed off-take. Instead, on the mesh for a solid-walled blade passage, boundary conditions are applied to surface cells that approximately trace the shape of the bleed off-take on the endwall. Typical boundary conditions are: constant bleed mass flow across the off-take; constant static pressure across the off-take (in which the imposed pressure is iteratively updated to achieve the prescribed bleed flow rate); and a specified bleed mass flow (with local velocities across the off-take determined by the static pressure field).

Wellborn and Koiro [5] compared the predictive accuracy of simple boundary condition models (i.e., constant mass flux or constant static pressure across the off-take) against full three-dimensional modeling of the bleed off-take geometry. They investigated numerically axisymmetric bleed slot configurations on the rotor and stator casing and concluded that simple boundary condition models were incapable of resolving the complex flow structures within the bleed slot and the interaction with the primary flow. Instead, full discretization of the primary flow and off-take geometry was shown by Wellborn and Koiro [5] to be necessary for accurate modeling, and the results presented in this present paper support this conclusion. Using CFD, Wellborn and Koiro [5] predicted an efficiency increase by bleeding through axisym-

[1]Now at the Department of Mechanical Engineering, Imperial College, London SW7 2AZ, UK.

Contributed by the International Gas Turbine Institute of ASME for publication in the JOURNAL OF TURBOMACHINERY. Manuscript received December 7, 2006; final manuscript received December 21, 2006. Review conducted by David Wisler. Paper presented at the ASME Power 2004 (PWR2004), Baltimore, MD, USA, March 30–April 1, 2004. Paper No. GT2004-54197.

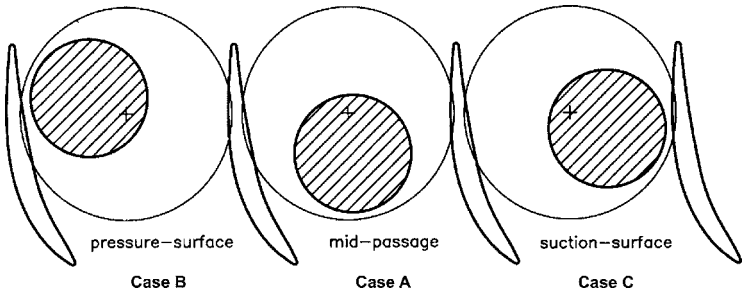

Fig. 1 Circular bleed hole rotated to three different endwall locations

metric casing slots located outside of the blade passage (i.e., near the leading or trailing edge of the blades), while a compressor efficiency decrease was predicted for off-takes located within the blade passage. That is, the presence of bleed off-takes at the endwall caused increased loss in the primary flow through the blade passages.

A number of bleed off-take investigations were carried out in the Whittle Laboratory, University of Cambridge, notably by Dr. I. J. Day, in support of a number of Rolls-Royce engine programs. The major objective of these tests, using low-speed cascades, was to develop off-take configurations giving high bleed off-take pressure, but the strong effect of a bleed off-take on the primary flow through the blade passage was also demonstrated. Flow recirculation between low- and high-pressure regions within the off-take caused spillage of flow into the blade passage and increased loss. These studies prompted a detailed investigation of bleed off-take configurations at the Whittle Laboratory [6], in which experiments and CFD were used to understand bleed off-take aerodynamic behavior and optimize their design.

This paper presents results from an investigation of the effect of endwall location and bleed flow rate on the aerodynamic behavior of a simple off-take configuration—a circular hole. (Alternative off-take configurations are considered in a companion paper by the same authors.) As shown in Fig. 1, the circular hole was located at three endwall locations within a stationary cascade blade passage:

(1) Case A: circular hole at midpassage;
(2) Case B: circular hole near the blade pressure surface; and
(3) Case C: circular hole near the blade suction surface.

The circular bleed hole, with diameter 80 mm and radial depth 35 mm, had an area 14.5% of the blade passage area (i.e., pitch $\times$ span; blade pitch 152 mm, blade span 228 mm). The large hole size represents engine bleed off-takes designed with sufficient area to pass, under certain conditions, large bleed flows up to 15% of the primary (core) mass flow, but which normally operate at smaller bleed rates (e.g., 3% of the primary mass flow). In the cascade rig the circular hole was machined eccentric to a larger plug that fitted into the cascade sidewall. When the larger plug was rotated, the circular bleed hole was located at different endwall locations within the blade row, as shown in Fig. 1, which is a composite picture showing three blade passages with three different rotations of the plug and eccentric bleed hole (the bleed hole is shown shaded).

The simple low-speed cascade approach allowed detailed mea-

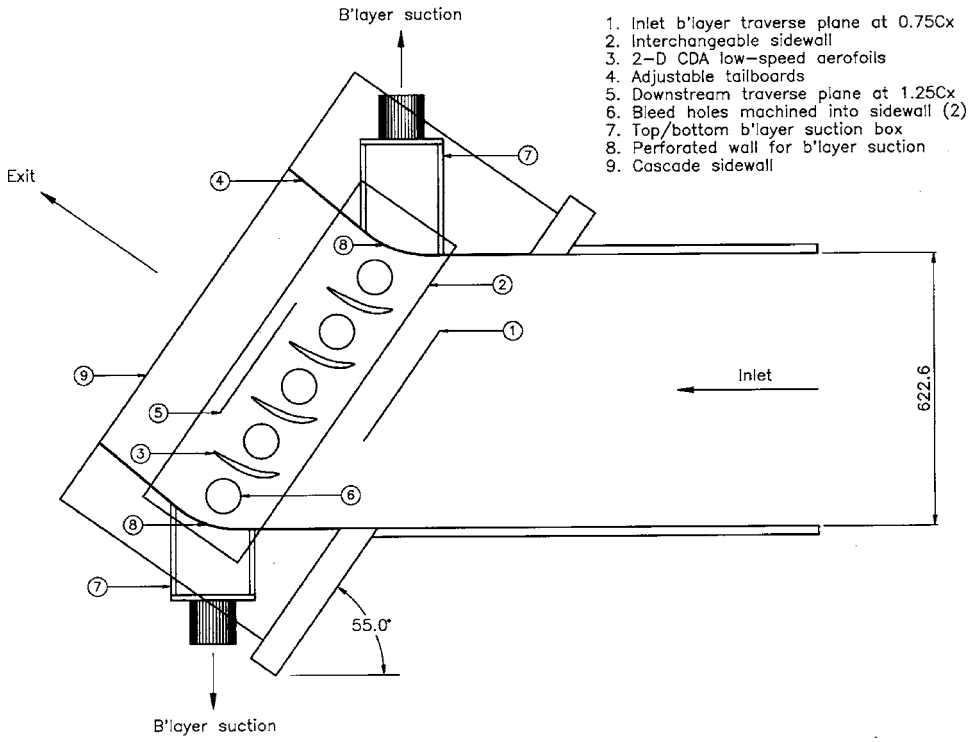

Fig. 2 Linear cascade rig

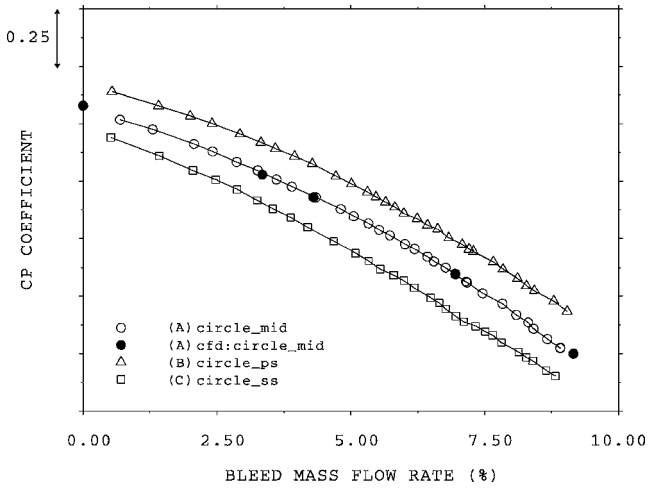

Fig. 3 Bleed characteristics for circular hole off-take at three endwall locations

surements and the identification of the mechanisms controlling bleed flows; moreover, the cascade was easily adapted to test different off-take configurations. The cascade flow, however, ignores a number of the complexities associated with the real flow in multistage axial compressors. The linear cascade restricted research to the effects of bleed on an isolated row of stationary blades (i.e., modeling a stator blade row), so the effect of bleed on compressor stalling characteristics and the effect of endwall bleed on the downstream rotor performance were not investigated. Similarly, the effects of unsteadiness from upstream blade wakes and the blade potential field of downstream rotors are ignored. The relatively thin, collateral inlet boundary layer to the cascade differed from the generally thick, skewed boundary layer that would occur in a real compressor. Since the effect of bleed on the primary passage flow is so strong, however, the effect of the inlet boundary layer is shown to be small for the circular hole off-take configuration. The low-speed cascade approach assumes that the effects of compressibility are small. Bleed off-takes in an aeroengine compressor are sufficiently sized to prevent choking of flow through them, thereby minimizing compressibility effects, and the assumption of incompressible flow becomes even more valid at the low bleed rates typical of normal engine operation (e.g., about 3% of the primary flow).

The objectives of this paper are therefore: to understand the processes associated with bleed off-take flows, including the interaction of the bleed off-take with the primary flow through the blade passage; to identify the importance of bleed off-take geometry and flow in calculating the blade passage aerodynamics; to demonstrate that CFD modeling of the off-take geometry can predict bleed flows; and to establish design guidelines for the endwall location of a bleed off-take.

Experimental Method

Experiments were made on a large-scale, low-speed linear compressor cascade, shown in Fig. 2, attached to an open-circuit wind tunnel supplied by a centrifugal fan nearly 10 m upstream of the cascade. Downstream of the fan the flow passed through a series of honeycomb and wire mesh screens to promote flow uniformity into the cascade. No turbulence generating screens were used upstream of the cascade, and experiments were performed with the background level of tunnel turbulence, expected to be less than 1%. The mechanisms associated with bleed flows are largely inviscid, pressure-driven phenomena, so that the use of low freestream turbulence is unlikely to have affected the results or conclusions.

The cascade blades are a low-speed design of an HP compressor stator, with a controlled-diffusion pressure distribution. The two-dimensional cascade blades, with 152 mm chord and 228 mm span, were configured for passage solidity 1.0, set at a stagger angle of 15.6 deg, with inlet flow direction 35.0 deg and design exit flow direction 5.6 deg. Inlet flow angles to the cascade were held constant for all testing at the design incidence of the aerofoil; off-design incidence conditions (i.e., more positive and negative incidences) were therefore not tested. Results and conclusions from the design-point incidences are, however, believed to extrapolate to off-design incidences. This is because, although a change of incidence will modify the blade loading distribution and flow field near the leading edge, the magnitude of the static pressure gradients within the blade passage (i.e., the blade-to-blade static pressure field) are largely unchanged, and this has the dominant influence on bleed off-take flows.

Cascade periodicity was achieved using adjustable tailboards and endwall suction of the boundary layers that developed along the top and bottom surfaces of the cascade tunnel. An interchangeable cascade sidewall, with bleed off-takes machined into the sidewall, allowed different off-take configurations to be installed without modification to the remainder of the rig. Bleed off-takes were included in each of the five blade passages of the cascade.

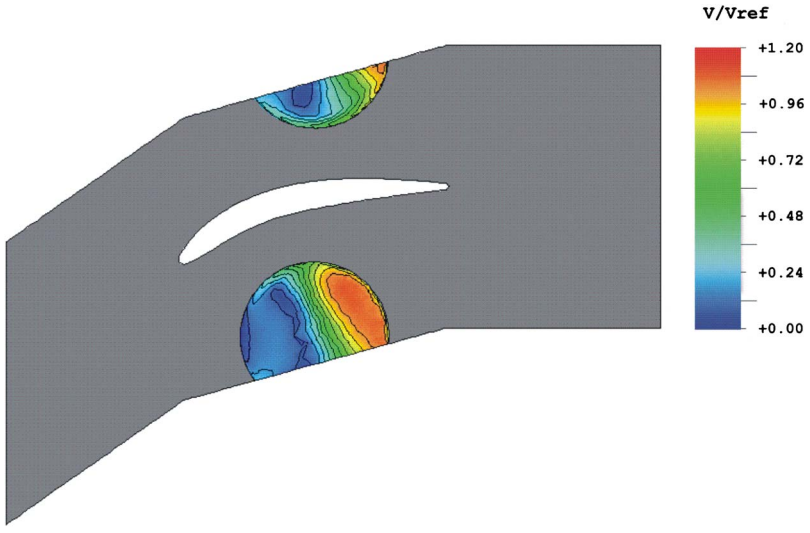

Fig. 4 Case A: calculated contours of velocity—6.9% bleed rate

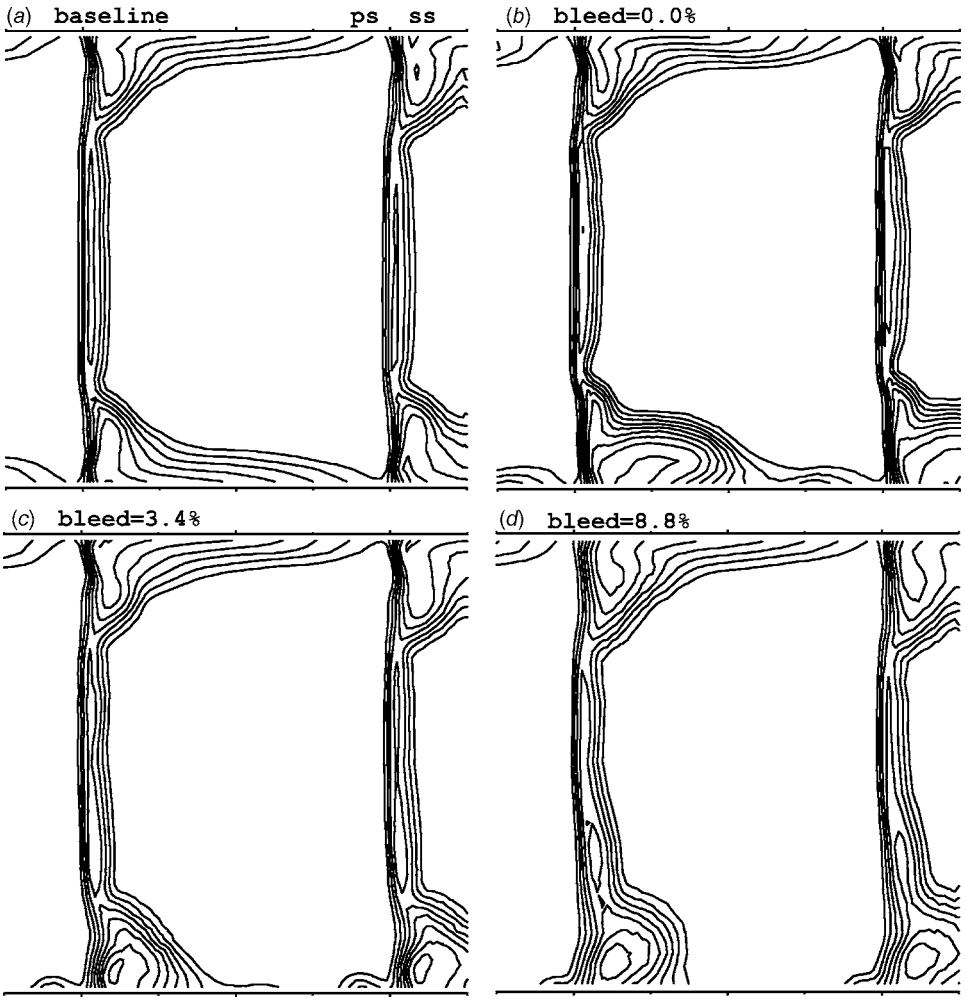

Fig. 5 Case A: circular hole at midpassage—measured contours of stagnation pressure loss, Y_p (minimun contour 0.1, increment 0.1)

Inlet freestream flow conditions were measured five blade chords upstream of the cascade with a total-static pressure probe in the middle of the parallel inlet section to the cascade. Experiments were performed with inlet freestream velocity 22 m/s and Reynolds number based on blade chord of 230,000. At inlet to the cascade the overall thickness of the boundary layer measured 0.75 axial chord lengths upstream of the blade leading edge was δ_{99} =17.0 mm (δ_{99}/C=0.112), and the displacement and momentum thicknesses were given by δ^*/C=0.018 and θ/C=0.013 respectively. Experiments were also performed with a thinner (δ^*/C =0.005) and thicker (δ^*/C=0.035) inlet boundary layer to the cascade to test the sensitivity of the flow behavior to inlet boundary layer thickness. Experimental results presented in this paper are, unless otherwise stated, for the inlet boundary layer with displacement thickness δ^*/C=0.018.

Air bled from the primary cascade flow (i.e., the bleed air) was collected in a large plenum box attached to the cascade sidewall. A centrifugal fan drew air from the plenum box. Bleed mass flow rates were measured using a square-edged orifice plate in accordance with BS1042. The cascade was operated for a range of bleed mass flow rates between 0% and 10% of the primary flow through the cascade. Bleed air pressures were calculated from the average of measured static pressure from 12 wall tappings distributed around the plenum box. The variation of the bleed off-take static pressure with bleed mass flow rate defined the bleed characteristic.

Area traverse measurements across the blade pitch and span were performed 0.25 axial chord lengths downstream of the blade trailing edge using a calibrated five-hole pneumatic probe. Traverses were made across 1.5 blade pitches between 1.8% and 98.2% blade span, on a measurement grid of 2277 points, with 46 points across the blade pitch and 33 points across the blade span. The uncertainty in measured pressure was ±1.7% of the inlet dynamic pressure and the uncertainty in measured flow angle was ±0.3 deg. For each bleed off-take configuration tested, area traverse measurements were made at three bleed mass flow rates to assess the effect of bleed rate on the blade passage (primary flow) aerodynamics: zero bleed; about 3.5% of the inlet mass flow to the cascade—a normal bleed rate; and about 9% of the inlet mass flow to the cascade—a high bleed rate. Further details of the test facility and experimental method are given in Ref. [6].

Numerical Method

The NEWT unstructured tetrahedral flow solver of Dawes [7] was used for three-dimensional numerical calculations of the cascade geometry. NEWT solves the full three-dimensional Reynolds averaged Navier-Stokes equations on an unstructured mesh of tetrahedral cells, using a finite-volume discretization. Turbulence is modeled via the standard two-equation k-ε model.

Use of an unstructured mesh-based solver allowed modeling of the real cascade geometry, including the blade passage, bleed off-take, and bleed collection plenum. The bleed collection plenum was modeled as a rectangular box with a depth of one blade chord to locate the exit boundary, at plenum exit, a sufficient distance

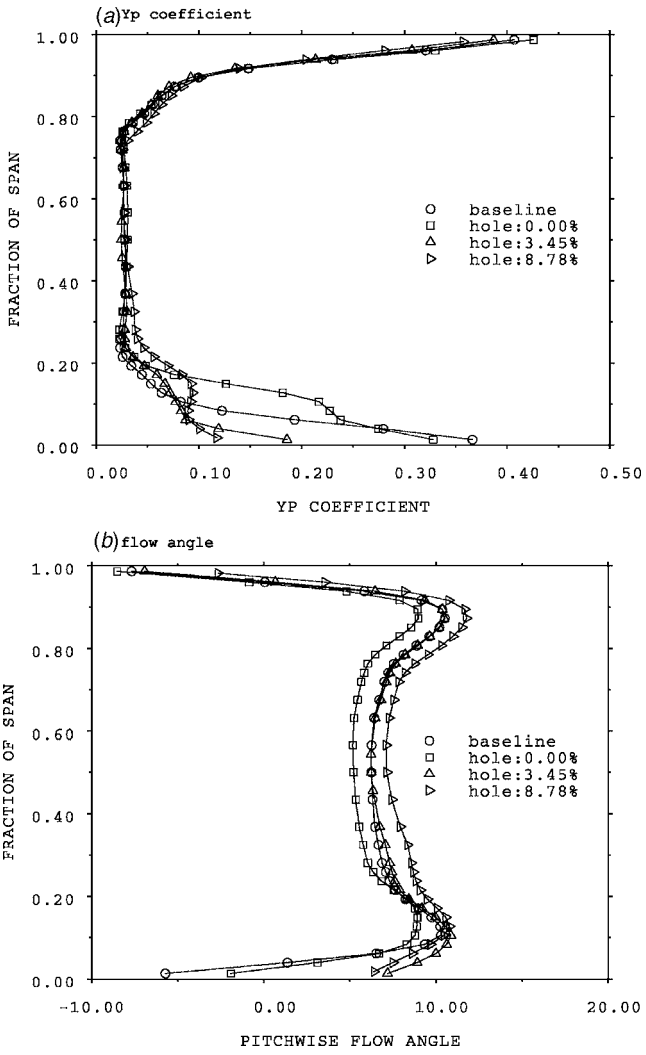

Fig. 6 Case A: measured exit profiles (*a*) stagnation pressure loss; and (*b*) pitchwise flow angle

(i.e., one blade chord) from the bleed off-take. Flow within the plenum was highly nonuniform close to the bleed off-take where the high velocity bleed flow enters the relatively stagnant flow within the plenum, but at one blade chord distance from the off-take, the flow within the plenum was more uniform and the imposed plenum exit boundary condition had little influence on the flow through the off-take. At the plenum exit, a uniform static pressure boundary condition was applied, and the bleed mass flow rate was calculated for the prescribed exit pressure. Achieving a target bleed rate was therefore an iterative process, in which the plenum exit pressure was changed between calculations. For the calculations, as for the measurements, exit pressure was altered until the bleed rate was near enough to the target. This is why the bleed rates quoted in this paper rarely hit the targets of 3.5% and 9% exactly for calculations and measurements.

A typical calculation mesh contained about 2,800,000 tetrahedral cells and 500,000 nodes. Further details of mesh generation and the numerical calculations are given in Ref. [6]. Only the baseline (i.e., solid wall with no bleed hole) and circular hole at midpassage configurations were modeled with CFD.

Bleed Off-Take Pressure

Bleed characteristics, showing the variation of bleed off-take static pressure (expressed as a static pressure coefficient, C_p) with bleed rate, are shown in Fig. 3 for the circular hole geometry at the three endwall locations. In Fig. 3 only the increment in C_p is shown on the axis. Numerical calculations were also performed on the circular hole for the midpassage configuration (Case A) at five bleed rates (plotted as solid symbols in Fig. 3) and were in excellent agreement with the measured data.

For the circular hole configuration, Fig. 3 shows the absolute value of bleed off-take static pressure is a function of the off-take endwall location. Bleeding near the pressure surface of the blade (Case B) gave the highest off-take pressure, as flow was taken from a region of the blade passage where the static pressures were highest, while bleeding near the suction surface of the blade (Case C) gave the lowest off-take pressures.

The rate of fall of bleed pressure with increasing bleed rate is, however, virtually independent of endwall location. For all configurations, the bleed off-take static pressure dropped by about one inlet freestream dynamic pressure (i.e., $\Delta C_p = -1.0$) as the bleed rate was increased from 0% to about 10%. The cause of the bleed off-take pressure falling with increasing bleed rate is that the flow accelerates to a high velocity (and low static pressure) at the sharp inlet edge to the hole, and then separates, causing blockage within the hole and leaving flow over part of the hole with high velocity and low static pressure.

For the circular hole at midpassage configuration (Case A), Fig. 4 shows calculated velocity contours (normalized by the inlet freestream velocity to the cascade) on a radial plane within the bleed hole (a depth from the endwall equal to 95% of the radial depth of the hole) for 6.9% bleed rate. CFD plots, such as Fig. 4, show exactly one blade pitch. In the computational domain, the aerofoil was positioned in the middle of the passage with periodic boundaries at the top and bottom surfaces, thereby making possible the generation of a high-quality unstructured mesh around the leading edge of the aerofoil. From Fig. 4, the flow through the hole is highly nonuniform; bleed flow is concentrated towards the rear of the hole (red contours), while there is virtually no flow through the forward regions of the hole. The highly nonuniform flow through the hole, with regions of separated flow, makes a diffuser downstream of the hole ineffective for decelerating the flow and increasing the static pressure.

Blade Passage Aerodynamics

Case A: Circular Hole at Midpassage. Measured contours of stagnation pressure loss coefficient (Y_p) are shown in Fig. 5 for the configuration with the circular hole at midpassage (Case A) for three bleed rates: zero, about 3.5% and 9% of the primary flow. The bleed hole is located on the endwall at the bottom of each figure (i.e., at zero span in each figure). Also shown at the top left is the baseline configuration with no bleed hole. The measurements were made with the inlet boundary layer to the cascade having displacement thickness $\delta^*/C = 0.018$.

At zero bleed rate, Fig. 5(*b*), the region of low stagnation pressure at the endwall, near the suction surface of the blade, is larger than the baseline case, extending across about 50% of the blade pitch. With increasing bleed rate, endwall boundary layer fluid is removed from the blade passage, leaving a region of high stagnation pressure downstream of the bleed hole, towards the pressure surface of the blade. Near the suction surface of the blade, however, a loss core of increased size is found with increasing bleed rate between about 0% and 20% span (Figs. 5(*c*) and 5(*d*)) but the peak stagnation pressure loss contour is lower than the peak loss for zero bleed rate. A thickening of the blade wake, relative to the baseline case, between 20% and 50% of blade span is also evident at the high bleed rates near 3.5% and 9%. Mass removal (or bleed) from the blade passage causes an additional static pressure rise (i.e., streamtube expansion) and the higher static pressure, downstream of the bleed hole, is imposed on the blades. Measured blade-surface static pressure distributions (not shown for brevity) show the suction-surface boundary layer exposed to a stronger adverse pressure gradient. This causes the suction-surface boundary layer to thicken, thereby increasing the thickness and depth of

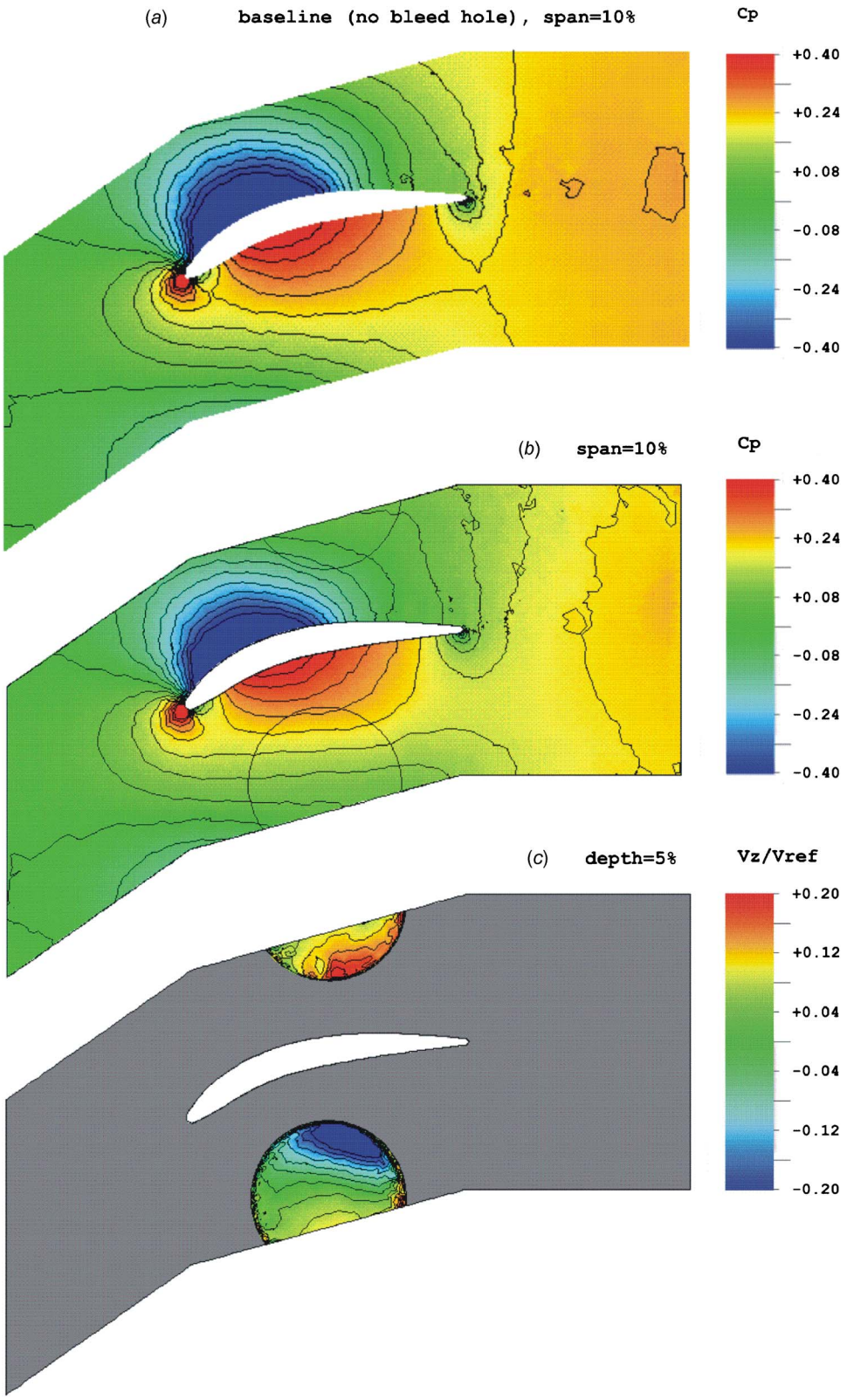

Fig. 7 Calculated contours: (*a*) baseline: static pressure at 10% span; Case A: (*b*) static pressure at 10% span; and (*c*) radial velocity inside the hole (5% depth) for zero bleed rate

the blade wake at high bleed rates.

The spanwise variations of measured stagnation pressure loss coefficient (Y_p) and pitchwise flow angle, both mass-averaged across the pitch, are plotted in Fig. 6 for the circular hole at midpassage (Case A) as well as the baseline (no bleed hole). At zero bleed rate, Fig. 6(*a*) shows increased loss above the baseline configuration up to about 20% span away from the bleed endwall. With increasing bleed rate, particularly at the highest bleed rate of 9%, losses very near the endwall decreased, but then increased relative to the baseline level further from the endwall between

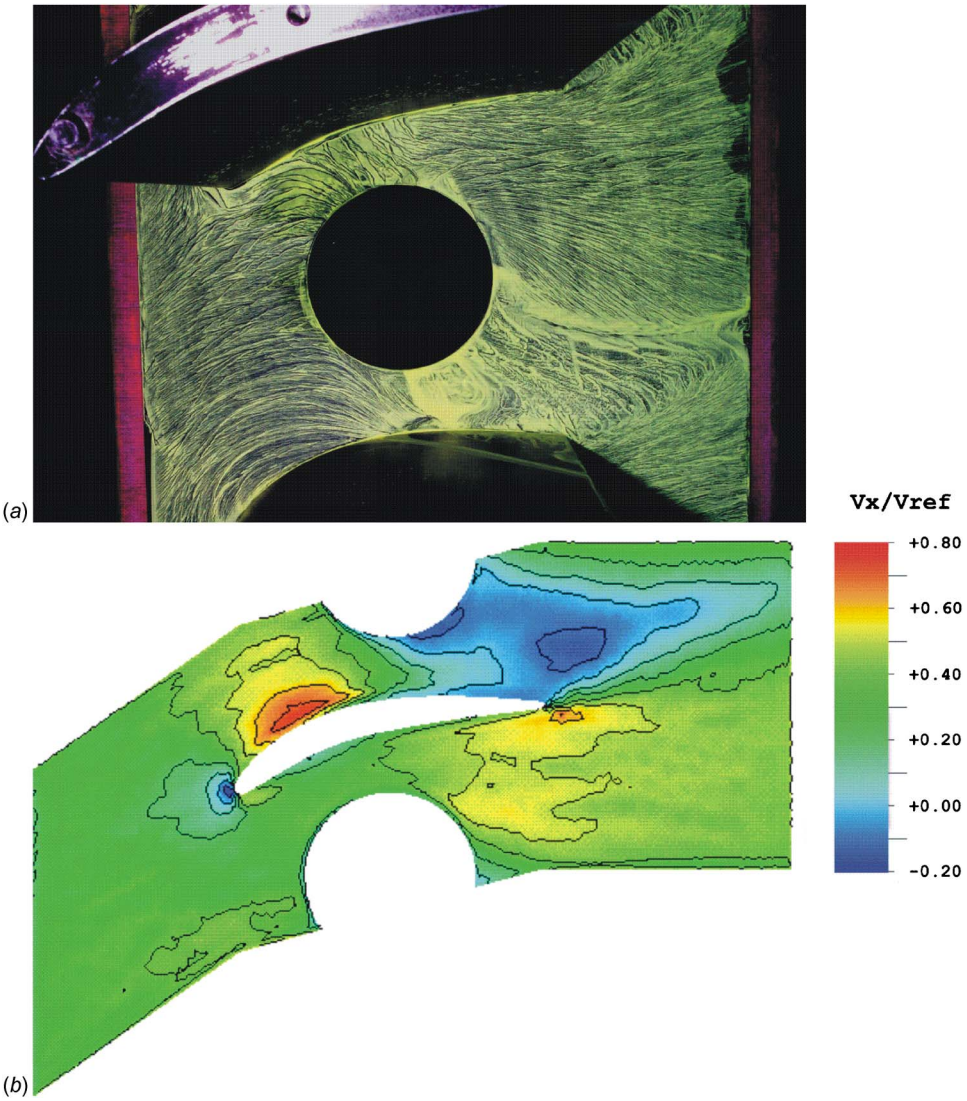

Fig. 8 Case A: endwall flow pattern at zero bleed rate: (*a*) surface flow visualization; and (*b*) calculated contours of axial velocity

about 10% and 40% span. The pitchwise flow angles generally varied across the whole span. At zero bleed rate the bulk of the flow was overturned relative to the baseline configuration by about 1 deg. At the highest rate of about 9%, flow at midspan was underturned by about 1 deg, and close to the endwall the amount of underturning was about 12 deg.

The increased loss at the suction-surface endwall corner of the blade passage at zero bleed rate is caused by fluid spilling into the primary flow from regions of the bleed hole near the suction surface of the blade. Spillage into the primary flow occurs because the hole is exposed to static pressure gradients within the blade passage, causing regions of inflow and outflow within the hole. Figures 7(*a*) and 7(*b*) plot calculated contours of static pressure on a radial plane at 10% blade span away from the endwall for the baseline (no bleed hole) configuration and for the circular hole at zero bleed rate configuration, respectively. (For clarity, the position of the circular bleed hole is outlined in Fig. 7(*b*)). Despite the presence of the hole at the endwall, the blade-to-blade pressure field is only slightly modified relative to the baseline configuration (i.e., the pressure field at midspan is imposed onto the endwalls).

The static pressure gradients in the primary flow above the hole in Fig. 7(*b*) cause nonuniform radial flow into and from the hole, and Fig. 7(*c*) shows calculated contours of radial velocity on a radial plane, just below the endwall, for zero bleed rate. In Fig. 7(*c*), blue contours represent radial flow into the hole, while red contours represent radial flow from the hole into the blade passage. Regions of high static pressure in the primary flow near the pressure surface of the blade cause positive inflow to the hole (blue contours), while regions of low static pressure in the primary flow near the suction surface of the blade cause outflow from the hole (red contours). At zero bleed rate, the highest radial velocity for flow entering and spilling from the hole is about 20% of the inlet freestream velocity to the cascade.

Flow spilling from the hole with a large radial component of velocity causes severe disruption to the primary flow through the blade passage. Figure 8 compares endwall surface flow visualization in Fig. 8(*a*) with calculated contours of axial velocity, at zero bleed rate, in Fig. 8(*b*). In Fig. 8(*a*), the endwall flow visualization, at 0% span, is viewed looking radially along the blade span; the aerofoil surfaces are painted black and the top of the aerofoil at 100% span is visible at the top of the figure. The blade pressure surface is above the circular hole and the blade suction surface is below the circular hole. The flow direction is from left to right.

The general flow pattern is well predicted by the numerical calculation. Flow spilling from the hole causes a region of separated flow on the endwall surface, downstream of the bleed hole

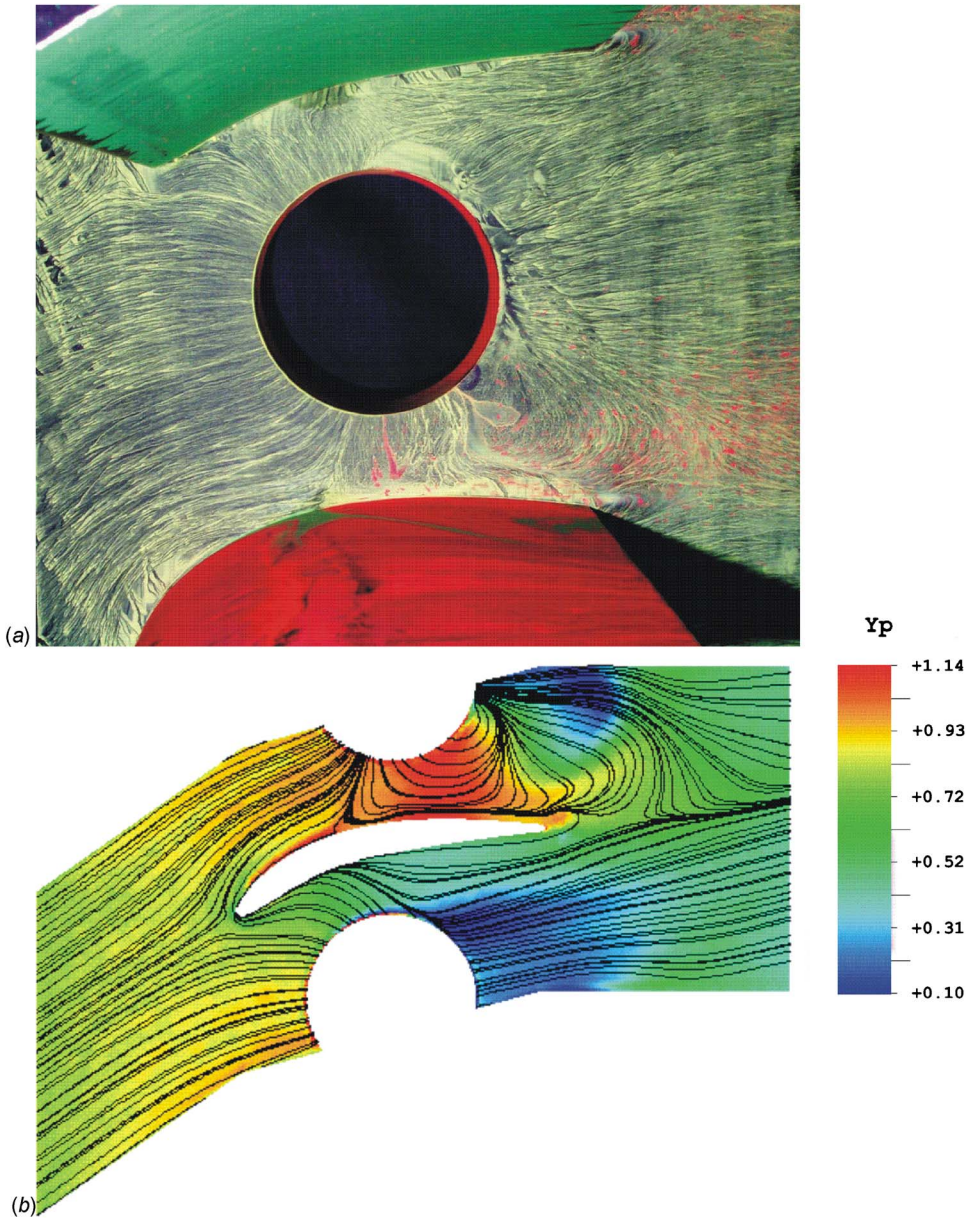

Fig. 9 Case A: endwall flow pattern at high bleed rate: (*a*) surface flow visualization; and (*b*) calculated streamlines colored with Y_p contours

and between the hole and the suction surface of the blade. The mixing of the spillage flow with the primary flow generates loss within the blade passage and causes the region of low stagnation pressure measured at zero bleed rate at the suction-surface endwall corner of the blade passage, downstream of the blade row, in Fig. 5(*b*).

At high bleed rates the endwall flow pattern is quite different. Figure 9(*a*) shows enwall surface flow visualization for the circular hole at midpassage configuration, for a high bleed rate near 9%. The endwall is again viewed looking radially along the blade span, but in this figure, the aerofoil pressure surface is painted green and the suction surface is painted red. The flow direction is again from left to right. The calculated endwall streamline pattern, colored with stagnation pressure loss coefficient (blue is low loss; red is high loss), is shown in Fig. 9(*b*). (In the steady cascade flow, the fluid streamlines, streaklines, and pathlines are the same, and will henceforth be referred to as streamlines).

The predicted flow pattern is similar to that observed experimentally. The near-endwall flow at inlet to the blade passage is drawn into the hole from across the whole passage. Flow near the forward part of the blade suction surface is drawn across the passage and into the hole (i.e., in the opposite direction to the conventional cross-passage secondary flow from the blade pressure surface to the blade suction surface that is normally associated with a solid-walled blade passage). A stagnation point is evident on the suction surface of the blade close to the endwall at about 0.4 axial chord. This is a limiting streamline which separates the upstream flow that is drawn into the hole from the region of separated, recirculating flow, near the endwall between the bleed hole and the suction surface of the blade.

At high bleed rates, discrete bleed holes at midpitch draw primary flow from across the whole passage into the hole, causing separated flow and increased losses in the endwall region of the blade passage between the bleed hole and the suction surface of the blade. The tendency to make the primary flow through the blade passage worse at high bleed rates is clearly undesirable.

The measured stagnation pressure contours of Fig. 5 showed a loss core at the suction-surface endwall corner of the blade pas-

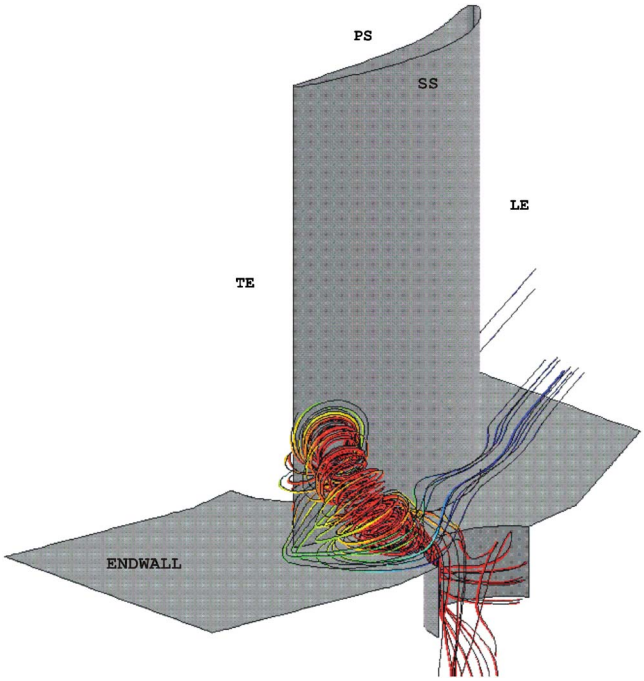

Fig. 10 Case A: calculated streamlines showing vortex flow structure—9.3% bleed rate

sage at high bleed rates and the flow visualization of Fig. 9 showed a recirculating flow pattern on the endwall at the suction-surface trailing edge region of the blade passage behind the bleed hole. Calculations show that the loss core and the swirling flow pattern on the endwall are associated with a vortex that extends from the blade suction surface to the endwall. The calculated vortex is shown in Fig. 10 for a bleed rate of about 9%, with the calculated streamlines colored to indicate stagnation pressure loss (blue is low loss and red is high loss). Primary flow is entrained into and around the vortex before entering the hole near the suction surface of the blade. The vortex generates loss, but most of the loss generated within the vortex does not convect downstream with the primary flow, but is instead drawn into the hole. The loss contours in Fig. 5 showed blockage (caused by the vortex) at the suction-surface endwall corner of the blade passage increasing with bleed rate, but the peak loss contour decreased as the bleed rate increased (i.e., more high loss fluid, generated by the vortex, was drawn into the bleed hole at high bleed rates instead of convecting through the blade passage with the primary flow). Numerical calculations at low bleed rates predicted a similar vortex structure at the suction-surface endwall corner of the blade passage.

In the primary flow, the same general flow structures downstream of the blade row were observed when measurements were repeated with a thinner ($\delta^*/C=0.005$) and thicker ($\delta^*/C=0.035$) inlet boundary layer to the cascade. The case for the thicker inlet boundary layer is of more interest, as the boundary layers in a real

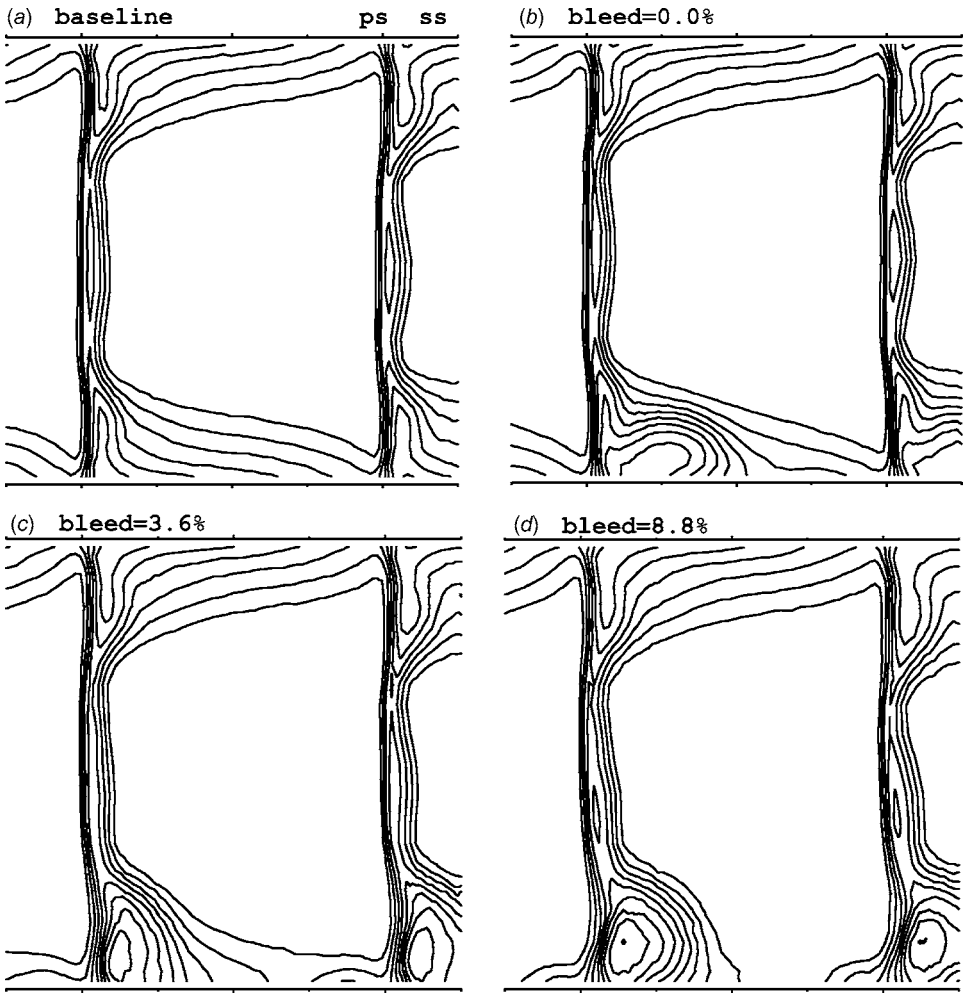

Fig. 11 Case A: thick inlet boundary layer—measured contours of stagnation pressure loss, Y_p (minimum contour 0.1, increment 0.1)

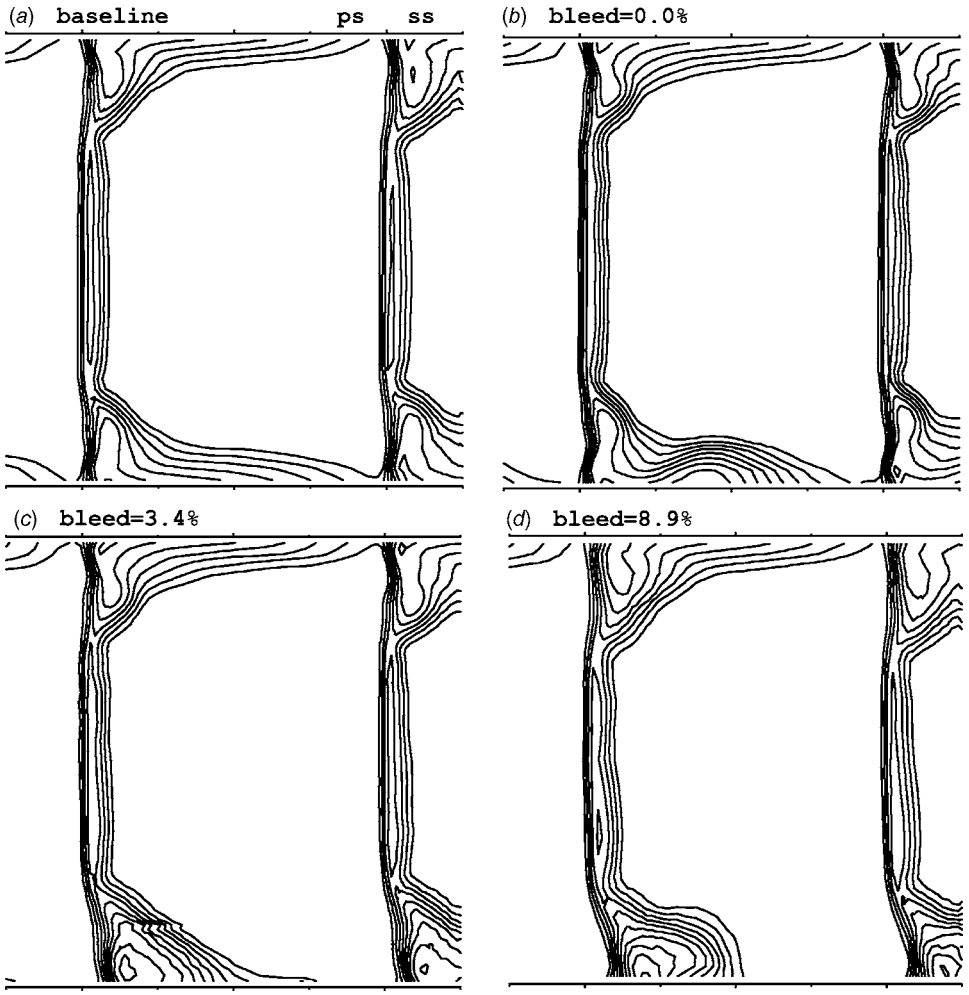

Fig. 12 Case B: circular hole near the pressure surface: measured contours of stagnation pressure loss, Y_p (minimum contour 0.1, increment 0.1)

compressor are generally thicker than the basic case, $\delta^*/C = 0.018$ used in this cascade. Figure 11 shows measured contours of stagnation pressure loss coefficient (Y_p) with the thicker inlet boundary layer for comparison with Fig. 5. The primary flow structure downstream of the blade row is generally unchanged by the increase in inlet boundary layer thickness.

At zero bleed rate there is a loss core at the endwall, near the suction surface of the blade, which is associated with spillage from the hole, but the peak loss contour is less deep (i.e., lower loss) for the thicker inlet boundary layer compared to the thinner inlet boundary layer condition in Fig. 5. At about 3.5% and 9% bleed rates the loss core at the suction-surface endwall corner of the blade passage, associated with the vortex extending from the blade suction surface to the endwall, is increased in size and the level of blade passage loss increases similarly to the thin inlet boundary layer shown in Fig. 5. For the thicker inlet boundary layer conditions, however, the peak loss contour increased as the bleed rate was increased, whereas for the thin inlet boundary layer conditions (Fig. 5) the peak loss contour decreased at higher bleed rates. The explanation for this effect is uncertain.

Case B: Circular Hole Near the Blade Pressure Surface. Measured contours of stagnation pressure loss coefficient (Y_p) are shown in Fig. 12 for the circular hole near the blade pressure surface configuration (Case B) for three bleed rates: 0%, and about 3.5% and 9% of the primary flow. The measurements were made with the inlet boundary layer to the cascade having thickness $\delta^*/C = 0.018$.

The hole near the pressure surface is located in a region where the static pressure in the blade passage above the hole is relatively uniform. Flows within the hole that are driven by pressure gradients in the primary flow are therefore weaker than for the hole at midpassage configuration. There is consequently less fluid spilling from the hole into the primary flow at zero bleed rate, as is evident by comparing Fig. 12(*b*) with Fig. 5(*b*). Moreover, the location of the hole relative to the blade passage means that flow spilling into the passage is not washed onto the suction surface of the blade, and the size of the blade corner separation is not increased by the interaction with the spillage flow. At bleed rates of about 3.5% and 9%, Figs. 12(*c*) and 12(*d*), the flow removal from blade passage leaves a region of high stagnation pressure on the endwall near the pressure surface of the blade, but a loss core develops at the suction-surface endwall corner of the blade passage, behind the bleed hole. The near-endwall flow is drawn into the hole from across the blade passage, and this results in the loss core associated with the region of separated flow at the suction-surface endwall corner of the blade passage, similar to that shown in Fig. 9(*a*). This pattern of behavior at high bleed rate is similar to that observed for the circular hole at midpassage configuration (Case A).

Measured spanwise profiles of mass-averaged stagnation pressure loss coefficient and pitchwise flow angle are shown in Fig. 13. Spillage at zero bleed rate caused a small increase in loss near

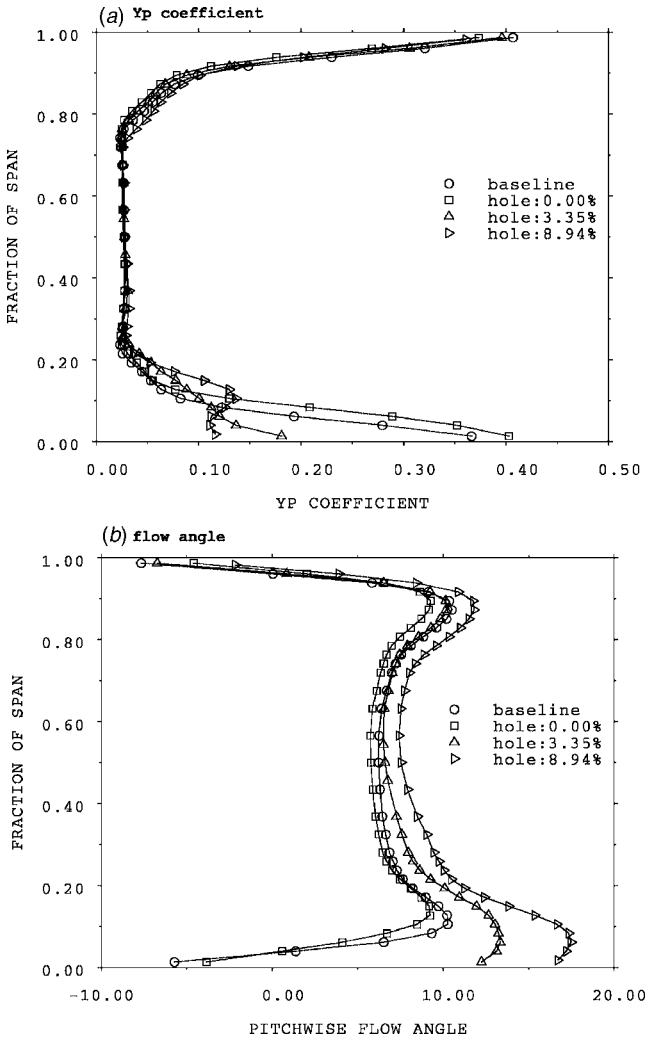

Fig. 13 Case B: measured exit profiles (*a*) stagnation pressure loss; and (*b*) pitchwise flow angle

the endwall relative to the baseline configuration data. With increasing bleed rate, losses over about the first 10% of span from the endwall decreased relative to the baseline data, but were slightly higher between about 10% and 20% span.

Pitchwise flow angles varied with bleed rate across the whole span, and in general Fig. 13(*b*) shows the bulk of the flow was underturned relative to the baseline flow for all bleed rates. At zero bleed rate, changes to the flow angle were small, and the passage flow was only slightly affected by the presence of the hole near the pressure surface of the blade. At the highest bleed rate near about 9%, however, flow near the endwall was underturned by about 22.4 deg relative to the baseline flow, and even at midspan the flow was underturned by 1.3 deg. The underturned flow is the result of increased blockage at the suction-surface endwall corner of the blade passage, as well as the influence of the bleed hole near the pressure surface of the blade which, by drawing primary flow into the hole near the pressure surface, opposes the turning of the primary flow by the blades.

Case C: Circular Hole Near the Blade Suction Surface. Measured contours of stagnation pressure loss are shown in Fig. 14 for the circular hole near the blade suction-surface configuration (Case C) for three bleed rates: 0%, and about 3.5% and 9% of the primary flow. The measurements were made with the inlet boundary layer to the cascade having thickness $\delta^*/C=0.018$.

For this configuration, the hole is located in a region of large pressure gradients in the primary flow above the hole. Moreover, this is a region where cross-passage endwall secondary flow is directed towards the suction surface of the blade, so flow spilling from the hole is washed onto the blade suction surface. At zero bleed rate Fig. 14(*b*) shows a large increase in stagnation pressure loss and blockage at the suction-surface endwall corner of the blade passage (i.e., downstream of the bleed hole). Fluid is spilled from the hole, mixed with the primary flow, and is subsequently swept onto the blade suction surface by the cross-passage secondary flow, thereby increasing the size of the corner separation. With bleed rates near about 3.5% and 9%, however, Figs. 14(*c*) and 14(*d*) show the progressive removal of high-loss boundary layer flow from the endwall as it is drawn into the bleed hole. Blockage and loss in the primary flow through the blade passage is then reduced by removing high-loss endwall boundary layer fluid from the blade passage, thereby preventing the cross-passage secondary flows from washing onto the suction surface of the blade and eliminating the blade corner separation.

Measured spanwise profiles of mass-averaged stagnation pressure loss and pitchwise flow angle for three bleed rates are shown in Fig. 15, together with the baseline configuration data for comparison. At zero bleed rate the increased loss above the baseline data at the bleed endwall is evident between about 10% and 25% of the span. With increasing bleed rate, however, losses at the endwall decreased to levels below the baseline data, as progressively more of the high-loss endwall fluid is removed from the passage. At zero bleed rate, Fig. 15(*b*) shows underturning of the flow relative to the baseline data over about 50% span from the endwall caused by the increased blockage at the suction-surface endwall corner of the blade passage. With increasing bleed rate, however, reduced blockage in the passage, and the tendency for the primary flow to be drawn towards the bleed hole in the suction-surface region of the blade passage, enhances the turning of the flow by the blades. At high bleed rates the flow is consequently overturned relative to the baseline data across the lower 50% span.

Blade Static Pressure Distributions

Figures 16(*a*)–16(*c*) show measured blade surface static pressure distributions at 10% span for the three circular hole bleed configurations investigated. (The baseline configuration data are also shown on each for comparison.) For each bleed hole configuration, data are presented for bleed rates of 0%, and about 3.5% and 9%.

For the circular hole at midpassage (Fig. 16(*a*)), there is a progressive decrease in static pressure over the forward region of the blade pressure surface and a progressive increase in static pressure over the rear region of the blade pressure surface with increasing bleed rate. This effect is explained using calculated static pressure contours near the endwall in Fig. 17 at 9% bleed rate. Static pressure over the forward part of the blade surface decreases as fluid ahead of the bleed hole is accelerated and drawn into the hole, thereby lowering static pressure in the endwall region, and causing the progressive decrease in pressure over the forward region of the blade in Fig. 16(*a*). From about 0.25 axial chord, static pressure increases in the blade passage, particularly along the blade pressure surface behind the bleed hole. This is caused by streamtube expansion in the primary flow behind the flow that is drawn into the hole. For the highest rate, near about 9%, the static pressure over the rear part of the blade suction surface is decreased relative to the baseline data, and this effect extended to 30% of the blade span (not shown for brevity). The low static pressure is associated with the foot of the vortex that extends from the blade suction surface to the endwall (Fig. 8).

Measured blade surface static pressure distributions for the circular hole near the pressure surface configuration, Fig. 16(*b*), show a similar effect of decreasing static pressure over the forward part of the blade pressure surface. With bleed rates of 3.5%

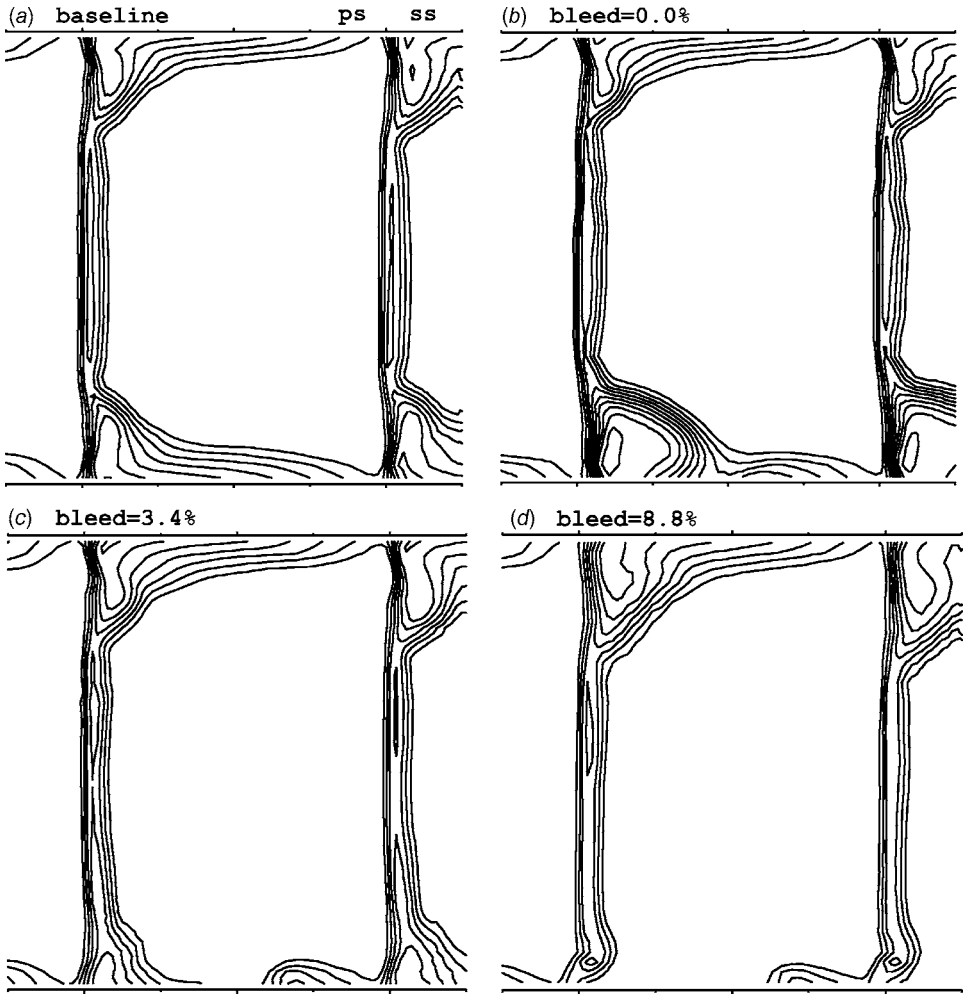

Fig. 14 Case C: circular hole near the suction surface—measured contours of stagnation pressure loss, Y_p (minimum contour 0.1, increment 0.1)

and 9%, near-endwall fluid ahead of the bleed hole is accelerated as it is drawn into the hole, thereby creating a local decrease in static pressure in this region of the endwall. The hole is located close to the trailing edge of the blade row, but the decrease in static pressure extends over about the forward 75% of the blade chord.

Blade surface static pressure distributions for the circular hole near the suction-surface configuration are shown in Fig. 16(*c*). At zero bleed rate, the reduced blade force and increase suction-surface corner separation, relative to the baseline data, are evident by the nearly constant pressure over the rear half of the blade suction surface. With bleed rates of about 3.5% and 9%, reduced blockage within the blade passage, and mass removal from the constant area annulus, causes a strong reduction in the minimum pressure on the suction surface followed by an increase in the static pressure rise across the blade row, as reflected by the increase in the blade exit static pressure at the trailing edge. With high bleed near the suction surface of the blade, the elimination of the blade corner separation is reflected by the continuous increase in static pressure (deceleration of flow) over the blade suction surface to higher exit static pressure without evidence of flow separation (i.e., flattening of the pressure distribution).

Conclusions

It should be reiterated that this research has been concerned with bleed off-takes which were large enough in area to pass, under certain conditions, large bleed flows up to 15% of the primary (core) mass flow. The conclusions below therefore pertain to large bleed off-takes and do not all apply to small orifices which operate continually with a constant rate of flow removal.

1. An interaction, sometimes deleterious, between the bleed off-take and the primary flow in the blade passage has been demonstrated for different bleed locations and bleed rates. The interaction affects the blade passage loss, blockage, and flow turning. Blade-passage loss is strongly dependent on bleed rate and bleed off-take location.
2. The interaction of bleed off-takes with the primary passage flow primarily involves inviscid, pressure-driven phenomena. The nonuniform static pressure imposed by the primary flow on the bleed hole causes radial velocities within the hole, even when there is zero net flow drawn from the blade passage. The resultant flow within the hole is highly nonuniform; primary flow enters the hole where the static pressure in the blade passage is high and flow spills out of the hole into regions of the blade passage where the static pressure is low. The radial velocities within the hole can be a significant fraction (i.e., more than 20%) of the inlet velocity to the blade row.
3. To be accurate, CFD calculations of the blade passage flow with a bleed off-take must model the off-take geometry to reproduce the interaction correctly. Bleed off-take models that impose uniform boundary conditions of static pressure or radial velocity will be inaccurate.
4. Bleed off-take pressure is influenced by the off-take location

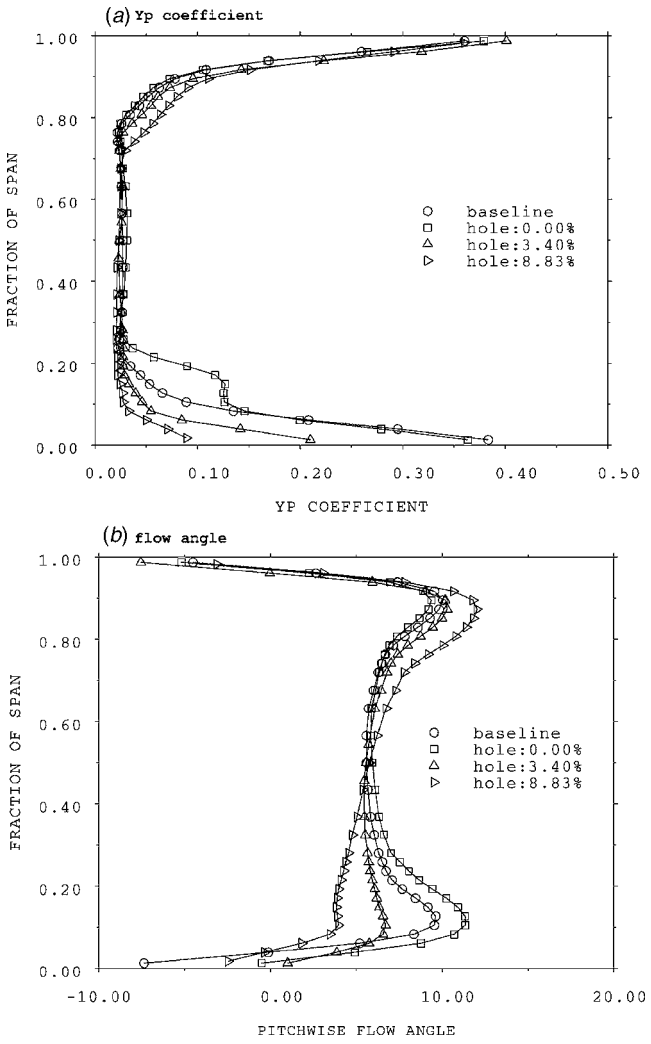

Fig. 15 Case C: measured exit profiles (*a*) stagnation pressure loss; and (*b*) pitchwise flow angle

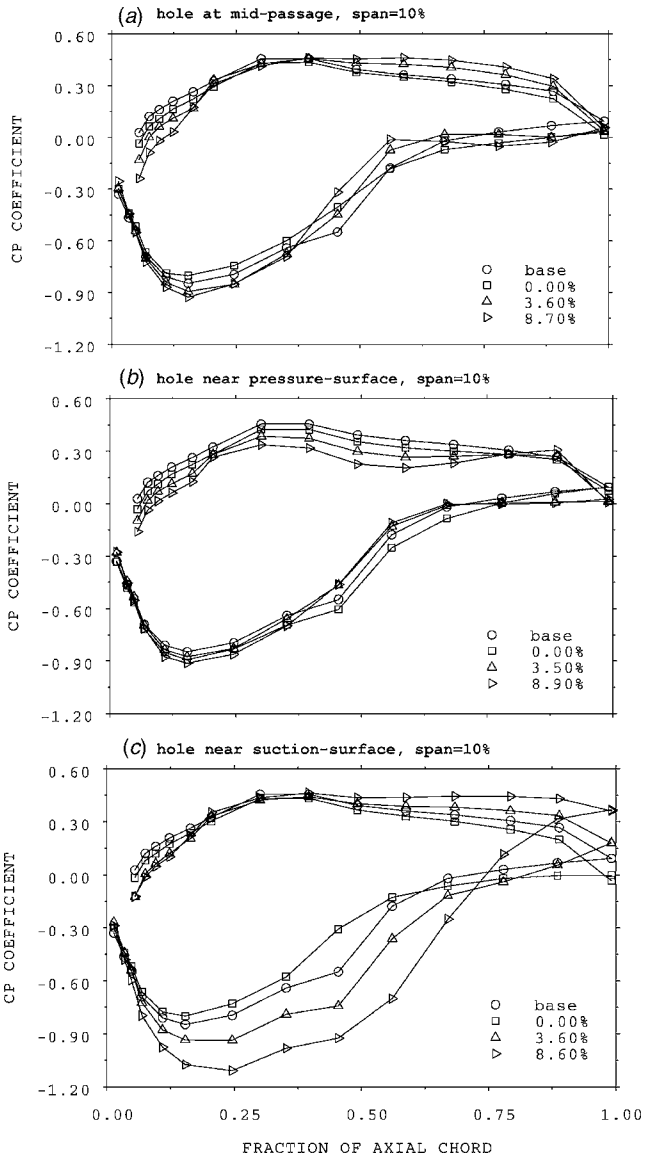

Fig. 16 Measured blade pressure distributions at 10% span: (*a*) Case A: hole at midpassage; (*b*) Case B: hole near the pressure surface; and (*c*) Case C: hole near the suction surface

on the endwall, following the static pressure field within the blade passage. Holes near the blade pressure surface therefore give higher bleed off-take pressure than holes near the blade suction surface.

5. Bleed off-take pressure decreases with increasing bleed rate. The static pressure drops as the flow is accelerated past the sharp inlet edge to the hole, producing high velocity over part of the inlet leading to separation and blockage within the hole. The measured variation of bleed off-take static pressure with bleed rate was accurately calculated by the CFD for the sharp-edge circular hole configuration (Case A).
6. With a discrete-hole type of bleed off-take, large enough to cope with high off-take requirements, placement near the pressure surface of the blade is optimal for low bleed-rate applications because this minimizes spillage into the primary flow and the bleed off-take pressure is highest. At high bleed rates, however, drawing endwall flow into the hole near the blade pressure surface from across the whole blade passage causes a large region of separated flow at the suction-surface endwall corner of the blade passage, thereby increasing loss in the primary flow.
7. Benefits to the primary flow result from the removal of flow from regions of the blade passage with high loss such as a large bleed near the blade suction surface. However the tendency for flow to spill from the off-take and mix with the primary flow means that small or zero bleed through large holes near the blade suction surface gives increased primary flow loss and blockage.
8. Endwall bleed influences the exit flow angles from a blade row. Bleeding primary flow near the blade pressure surface opposes the turning of the primary flow by the blades and causes the bulk flow to be underturned, particularly near the endwall. Bleeding primary flow near the blade suction surface enhances the turning of the primary flow by the blades and causes the bulk flow to be overturned near the endwall.

Acknowledgment

The work, which was carried out at the Whittle Laboratory, was supported by Rolls-Royce plc., the Applied Research Programme of the Ministry of Defence, and the Department of Trade and Industry Aeronautical Research Programme. The authors wish to thank the sponsors for permission to publish this paper. However, the opinions expressed here are those of the authors and not necessarily those of any of the sponsoring organisations. The experimental program was greatly assisted by all members of the Whittle Laboratory Workshop. The authors acknowledge J. J.

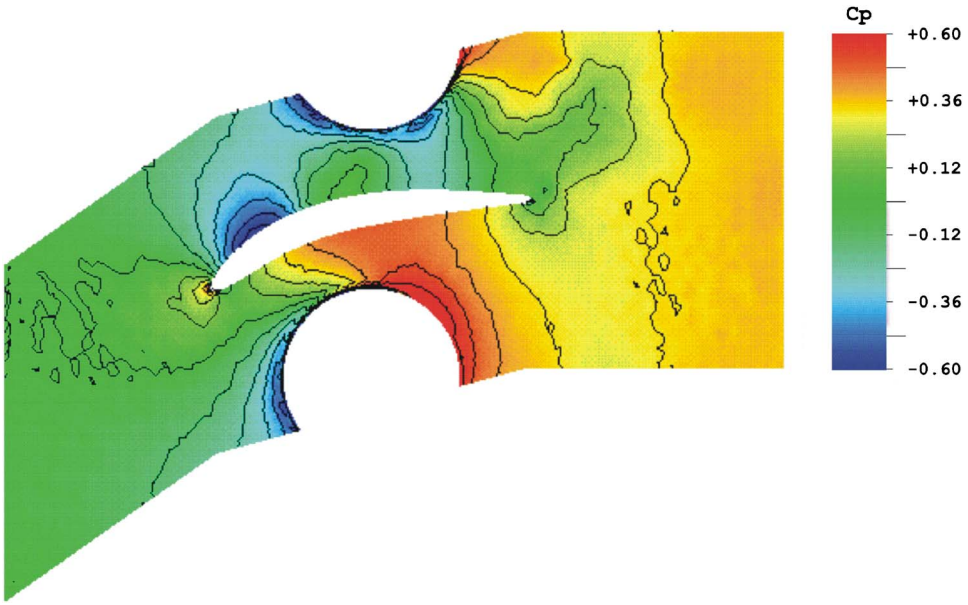

Fig. 17 Case A: calculated contours of static pressure at endwall for circular hole at midpassage configuration—9% bleed rate

Bolger and S. J. Gallimore, from Rolls-Royce, for their enthusiastic support of this research, and would like to thank W. N. Dawes for the use of his CFD code NEWT, and A. A. J. Demargne for his assistance with unstructured mesh generation.

Nomenclature

C = blade chord
C_p = $(P_S - P_{S1})/\frac{1}{2}\rho V_{\text{ref}}^2$, static pressure coefficient
P_0 = stagnation pressure
P_{01} = inlet freestream stagnation pressure
P_S = static pressure
P_{S1} = inlet freestream static pressure
V = total velocity
V_{ref} = cascade inlet total velocity
V_x = axial velocity
V_z = radial velocity
Y_p = $(P_0 - P_{01})/\frac{1}{2}\rho V_{\text{ref}}^2$, stagnation pressure coefficient
δ_{99} = boundary layer thickness
δ^* = boundary layer displacement thickness
θ = boundary layer momentum thickness
ρ = density

References

[1] Rhie, C. M., Gleixner, A. J., Spear, D. A., Fischberg, C. J., and Zacharias, R. M., 1998, "Development and Application of a Multistage Navier-Stokes Flow Solver–Part 1: Multistage Modeling using Bodyforces and Deterministic Stresses," ASME J. Turbomach., **120**, pp. 205–214.
[2] LeJambre, C. R., Zacharias, R. M., Biederman, B. P., Gleixner, A. J., and Yetka, C. J., 1998, "Development and Application of a Multistage Navier-Stokes Flow Solver—Part II: Application to a High Pressure Compressor Design," ASME J. Turbomach., **120**, pp. 215–223.
[3] Conan, F., and Savarese, S., 2001, "Bleed Airflow CFD Modeling in Aerodynamics Simulation of Jet Engine Compressors," ASME Paper No. 2001-GT-544.
[4] Gallimore, S. J., Bolger, J. J., Cumpsty, N. A., Taylor, M. J., Wright, P. I., and Place, J. M. M., 2002, "The Use of Sweep and Dihedral in Multistage Axial Flow Compressor Blading—Part I: University Research and Methods Development," ASME J. Turbomach., **124**, pp. 521–532.
[5] Wellborn, S. R., and Koiro, M. L., 2002, "Bleed Flow Interactions With an Axial-Flow Compressor Powerstream," AIAA Paper No. 2002–4057.
[6] Leishman, B. A., 2003, "The Aerodynamic Behaviour and Design of Compressor Bleed Slots," Ph.D. dissertation, University of Cambridge, Cambridge, UK.
[7] Dawes, W. N., 1993, "The Practical Application of Solution-Adaption to the Numerical Simulation of Complex Turbomachinery Problems," Prog. Aerosp. Sci., **29**, pp. 221–269.

Effects of Inlet Ramp Surfaces on the Aerodynamic Behavior of Bleed Hole and Bleed Slot Off-Take Configurations

B. A. Leishman

N. A. Cumpsty[1]

Rolls-Royce plc.,
Derby DE24 8BJ, UK

J. D. Denton
Whittle Laboratory,
University of Cambridge,
Cambridge CB3 0DY, UK

*Bleed off-take air pressure and the interaction of the off-take with the primary flow through the blade passage is determined by: (1) the location of the bleed off-take at the endwall relative to the blade passage; (2) the bleed flow rate; and (3) the off-take geometry. In the companion paper (Leishman et al., 2007, ASME J. Turbomach., **129**, pp. 645–658) the effect of bleed rate and endwall location was investigated using a circular hole bleed off-take configuration; the circular hole was tested at three endwall locations and for bleed flow rates between 0% and 9% of the primary (core) flow through the blade passage. The effects of bleed off-take geometry are presented in this paper by comparing the aerodynamic behavior of a number of generic bleed off-take configurations. Using results from low-speed cascade experiments and three-dimensional numerical calculations, the off-take configurations are compared with respect to the requirement to maximize bleed off-take air pressure and minimize loss generated within the blade passage. The off-take geometry, and especially the introduction of contoured inlet ramp surfaces to guide flow into the off-take for high bleed pressure, has a strong effect on its aerodynamic behavior because it determines the extent to which flow within the off-take is coupled to the primary flow through the blade passage. In this paper, the off-take configurations that give the highest bleed pressure generally cause the highest levels of loss in the blade passage.* [DOI: 10.1115/1.2752192]

Introduction

An objective of bleed off-take design is to maximize bleed off-take air pressure. The bleed air pressure required for each application (e.g., cooling, sealing, de-icing, or cabin air) determines the axial location of the bleed off-take through the compressor. But bleeding high-pressure air from the compressor, without extracting work from it through the turbine, penalizes the engine cycle efficiency. So it is therefore desirable to take bleed as far forward in the compressor as possible, but this necessitates minimizing the static pressure drop of the flow removed from the blade passage. There are therefore two aspects of bleed off-take design to be optimized. First, it is beneficial to minimize the drop in static pressure through the off-take both for design conditions, when it might be a small bleed rate, and for the maximum bleed flow rate required. Second, the bleed off-take should ideally cause no significant degradation to the primary (core) flow through the blade passage at zero, small, and high-bleed flow rates (i.e., should cause no increase in loss).

An investigation of circular hole bleed off-take configurations was reported in Leishman et al. [1]. The circular holes investigated had sharp inlet edges, which caused separation of flow at entry to the hole and a large drop in static pressure through the hole. As expected, the bleed off-take pressure was higher if the hole was located near the pressure surface of the blade. While the circular hole off-take is simple to manufacture, the large drop of bleed air pressure at high bleed rates makes it less than optimal for use in a jet engine compressor.

Minimizing the static pressure drop is also a design requirement of auxiliary air and engine inlets located on the external fuselage of aircraft. Mossman and Randall [2] and Dennard [3] investigated the pressure recovery of submerged duct entrances under National Advisory Committee for Aeronautics (NASA) sponsored research programs. The NACA intake duct, optimized experimentally using low-speed wind tunnel testing [2], maximizes the pressure recovery of the submerged intake with minimal disruption of the primary flow (i.e., the flow over the fuselage), and finds wide application on aircraft. Design features of the NACA intake duct provide lessons for bleed off-take design. First, gently sloping inlet ramp surfaces minimize flow separation at the inlet to the duct and increase the pressure recovery. Second, lowering the proportion of boundary layer fluid to free-stream fluid entering the NACA intake duct increases the pressure recovery. This was achieved using narrow slots, in which the major axis is aligned with the freestream direction, as well as shaping the intake to divert boundary layer flow around the sides of the intake. Optimizing compressor bleed off-take designs for jet engine applications is, however, complicated by the space constraints within the blade passages and between the blade rows, as well as the constraints associated with blade fixings and mechanical hardware outside of the compressor casing. Additionally, while a compressor bleed off-take for jet engine applications might have a typical bleed rate of about 3%, it may sometimes be required to bleed up to 20% of the primary flow, thereby making necessary a bleed off-take area greater than that required for more normal levels of bleed. Moreover, off-takes within compressor blade rows are exposed to strong pressure gradients from the blades, and the endwall boundary layers are highly three dimensional, which contrasts with the relatively uniform flow over external fuselage intakes such as NACA ducts.

Off-take performance is sensitive to details of the geometry, and Computational Fluid Dynamics (CFD) is a modern tool that can be applied to understanding the flow through the off-take and

[1]Now at Department of Mechanical Engineering, Imperial College, London SW7 2AZ, UK

Contributed by the International Gas Turbine Institute of ASME for publication in the JOURNAL OF TURBOMACHINERY. Manuscript received December 7, 2006; final manuscript received December 21, 2006. Review conducted by David Wisler. Paper presented at the ASME Turbo Expo 2004: Land, Sea and Air (GT2004), Vienna, Austria, June 14–17, 2004. Paper No. GT2004-54331.

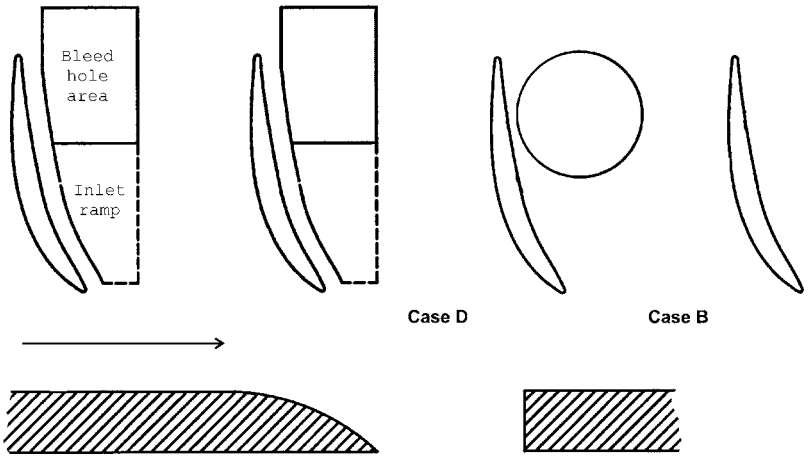

Fig. 1 Near pressure-surface bleed hole with ramped inlet surface (Case D), circular hole off-take (Case B)

to ultimately aid design optimization. Young and Snowsill [4], for example, used CFD to investigate flow details associated with circular hole off-takes on a rotating hub at the bottom of a shrouded stator well. The swirl velocity of the bleed air is increased as it passes through the rotating holes, and as the air flows inward towards the engine center line, a free vortex flow is established which causes a drop in static pressure. Instead of circular hole off-takes on the hub, rectangular and elliptic holes, elongated in the circumferential direction (i.e., direction of hub rotation), reduced the level of swirl imparted to the bleed air flowing through the holes, and caused the bleed off-take pressures to be higher.

Off-take geometries for jet engine compressor applications are considered in this paper. The objective is to increase bleed off-take pressure and understand the trade between high-bleed off-take pressure and the effect on the primary flow through the blade passage. To raise bleed off-take pressures, the off-take geometries considered use inlet ramp surfaces to turn the flow gently into the off-take with minimum acceleration and cause minimum separation. Such off-take geometries find applications in modern aero-engine compressors, and are used in preference to the sharp-edged circular hole configurations (Cases A, B, and C) presented in the companion paper [1]. Three bleed off-take configurations are presented here:

(1) Case D: a discrete bleed hole located within the blade passage, near the pressure surface of the blade, and with a large inlet ramp surface (i.e., large radius of curvature). To provide a comparison with earlier tests the bleed pressure is compared with Case B, a sharp-edge circular hole, from the companion paper [1];
(2) Case E: an axisymmetric slot located downstream of the blade row (i.e., outside of the blade passage). Results are presented for a number of radius sizes on the inlet edge to the slot; and
(3) Case F: an axisymmetric slot with a large inlet ramp surface that extends into the blade passage.

All the off-take configurations had area equal to 14.5% of the blade-passage area (i.e., pitch $\times$ span), that is, the same area as the circular hole off-takes (Cases A, B, and C). Because the results of these tests have a competitive significance, absolute values of loss and pressure recovery cannot be given, but relative levels, which illustrate the effects, are shown.

Method

Experiments were made using a large-scale, low-speed linear compressor cascade rig at the Whittle Laboratory, University of Cambridge, as described in Ref. [1]. All measurements presented in this paper were performed with inlet freestream velocity 22 m/s and Reynolds number based on blade chord of 230,000. The inlet boundary layer to the cascade had overall thickness $\delta_{99}=17.0$ mm ($\delta_{99}/C=0.112$) with displacement and momentum thicknesses given by $\delta^*/C=0.018$ and $\theta/C=0.013$, respectively.

Area traverse measurements of the primary flow were performed 0.25 axial chord lengths downstream of the blade trailing edge using a calibrated five-hole pneumatic probe. Area traverse measurements were made at three bleed rates to assess the effect of bleed rate on the blade passage aerodynamics: zero bleed; about 3.5% (a normal bleed rate); and about 9% (a high bleed rate). Bleed air off-take pressures were calculated from the average of measured static pressure from 12 wall tappings distributed around the plenum box in which the bleed air collected.

Numerical calculations were made using the NEWT unstructured tetrahedral flow solver of Dawes [5]. The numerical calculations modeled the blade passage and the real geometry of the bleed off-take and plenum. Further details of the experimental and computational approach are described in Leishman [6].

Case D: Near Pressure-Surface Hole With Inlet Ramp Surface

Whereas the body of this paper is concerned with bleed off-takes typical of modern engines, one set of results is shown with a sharp-edged circular hole near the pressure surface. This is shown on the right hand passage of Fig. 1 (Case B) and provides a link back to the test cases of the companion paper [1]. This was the configuration found in that paper to give the highest bleed off-take pressure of the three circular hole configurations tested.

To raise bleed off-take pressure levels, a discrete bleed hole with a ramped inlet surface to turn the flow gently into the off-take with minimum acceleration and flow separation, was investigated. The intent was to design a bleed off-take that gives high-bleed off-take pressure and minimizes disruption to the primary flow through the blade passages.

The bleed off-take configuration with a large, curved, inlet ramp surface is shown in the two leftmost blade passages in Fig. 1 with a drawing of the blade and bleed hole geometry; the ramped inlet surface guides flow into the bleed hole, which is located near the pressure surface region of the blade passage. A section of the off-take geometry, showing the inlet ramp surface curvature, is shown at the bottom of Fig. 1.

Measured bleed off-take characteristics are shown in Fig. 2 for the ramped-inlet hole (Case D) and the circular hole configuration (Case B). The bleed characteristics show the variation of bleed

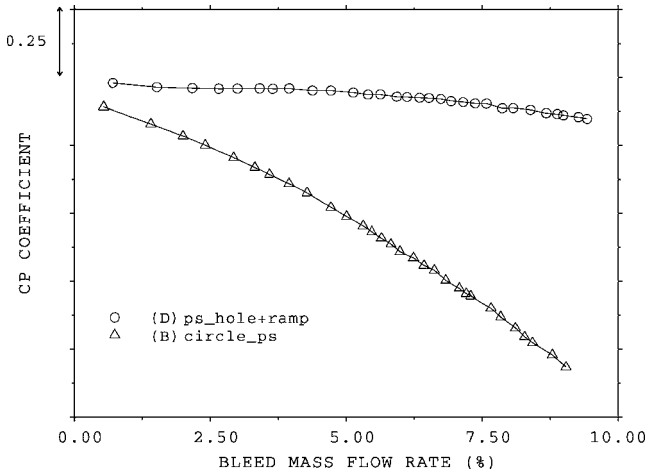

Fig. 2 Measured bleed characteristics—Case D and circular hole (Case B)

off-take static pressure with bleed rate, with bleed off-take static pressure expressed as a static pressure coefficient, C_p, based on inlet freestream values to the cascade.

The near pressure-surface hole with large inlet ramp surface gave increased bleed off-take pressures at all bleed rates relative to the sharp-edged circular hole configuration. The bleed off-take pressure at low bleed rates is high, in part, as a result of locating the hole near the pressure surface of the blade. While for the circular hole configuration the off-take static pressure fell by about one freestream dynamic pressure (i.e., $\Delta C_p = -1.0$) as the bleed flow was increased from 0% to 10% bleed rate, the equivalent drop in bleed pressure for the ramped-inlet hole was only about $\Delta C_p = -0.13$. The lower pressure drop is because the ramped inlet surface turns the primary flow more gently into the hole than is the case for a sharp inlet edge. When the flow is turned more gradually over the inlet ramp surface and into the hole, the streamline curvature is less, and the static pressure is therefore higher at inlet to the off-take. The inlet ramp surface, with large radius of curvature, also reduces the area occupied by separated flow within the hole, thereby lowering blockage within the hole and reducing the velocity of the bleed flow through the hole.

Measured contours of stagnation pressure loss coefficient (Y_p), in the primary flow 0.25 axial chord lengths downstream of the blade trailing edge, are shown in Fig. 3 for the configuration of near pressure-surface hole with inlet ramp (Case D) for three bleed rates: 0%, and about 3.5% and 9% of the primary flow. Also shown at the top left is the baseline configuration with no bleed hole.

The downstream primary flow is similar to that for the circular hole located near the blade pressure surface (Case B) that was reported in the companion paper [1]. At zero bleed rate there is an increase in loss near the endwall at about midpitch that is associated with flow spilling from the hole into the blade passage. At higher bleed rates, flow removed from the pressure-surface region of the blade passage leaves high stagnation pressure on the endwall near the blade pressure surface, but near the suction surface of the blade a region of high stagnation pressure loss occurs.

Figure 4 shows endwall surface flow visualization for the ramped pressure-surface hole for a high bleed rate of about 9%. The flow pattern shows inlet flow on the endwall drawn into the hole from across the whole blade passage. Even primary flow from near the suction surface of the blade is drawn across the passage and into the hole. Between the bleed hole and the blade suction surface is a region of separated flow on the endwall that corresponds to the high loss regions measured in the primary flow downstream of the blade row (Figs. 3(*c*) and 3(*d*)). (A similar flow pattern, with endwall flow drawn across the blade passage causing

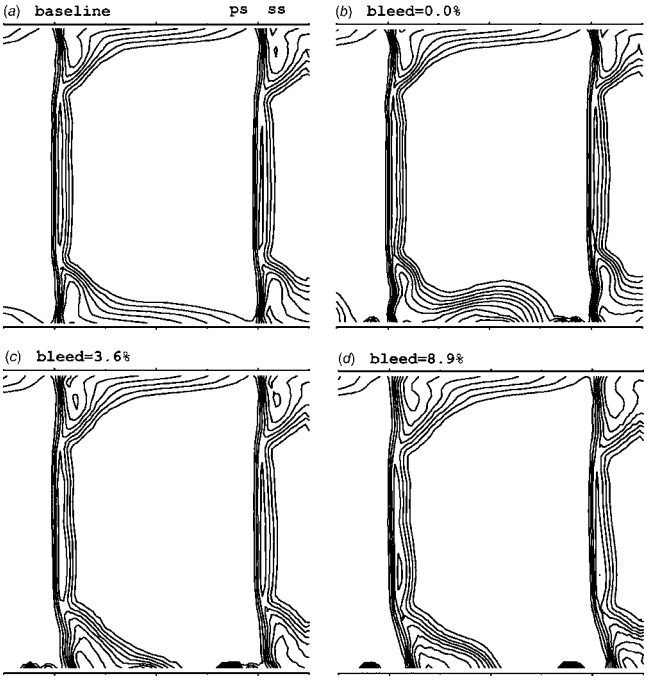

Fig. 3 Case D: near pressure-surface hole with inlet ramp surface—measured contours of stagnation pressure loss (minimum contour 0.1, increment 0.1)

a separated region on the endwall, was reported in Ref. [1] for circular hole off-takes located at midpassage and near the blade pressure surface). This behavior causes a progressive worsening of the primary flow with increasing bleed rate so that losses within the blade passage increase as the bleed flow is increased from low (i.e., 3.6%) to higher values (i.e., 8.9%).

Measured spanwise profiles of mass-averged stagnation pressure loss coefficient and pitchwise flow angle are shown in Fig. 5. The baseline (no bleed hole) configuration data are also included for comparison. At zero bleed rate the loss increased relative to the baseline level over about the lower 20% of span due to fluid spilling out of the hole into the blade passage. With increasing bleed rate the loss decreased very near to the endwall relative to the baseline data, but increased between about 10% and 50% span away from the endwall. Figure 5(*b*) shows that for bleed rates above zero the flow across the whole blade span was underturned

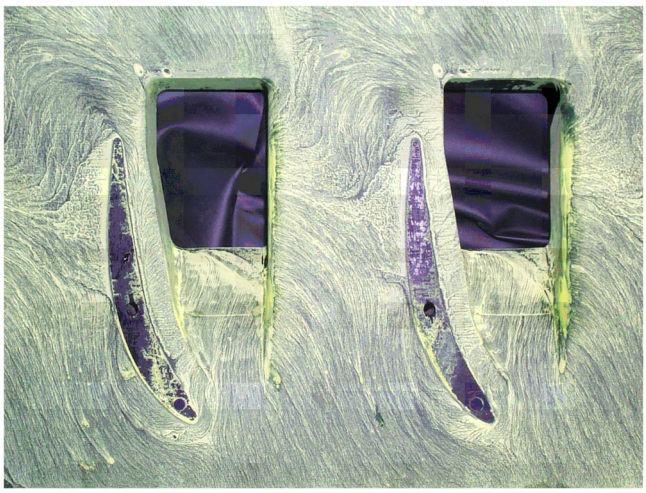

Fig. 4 Case D: endwall flow pattern at high bleed rate

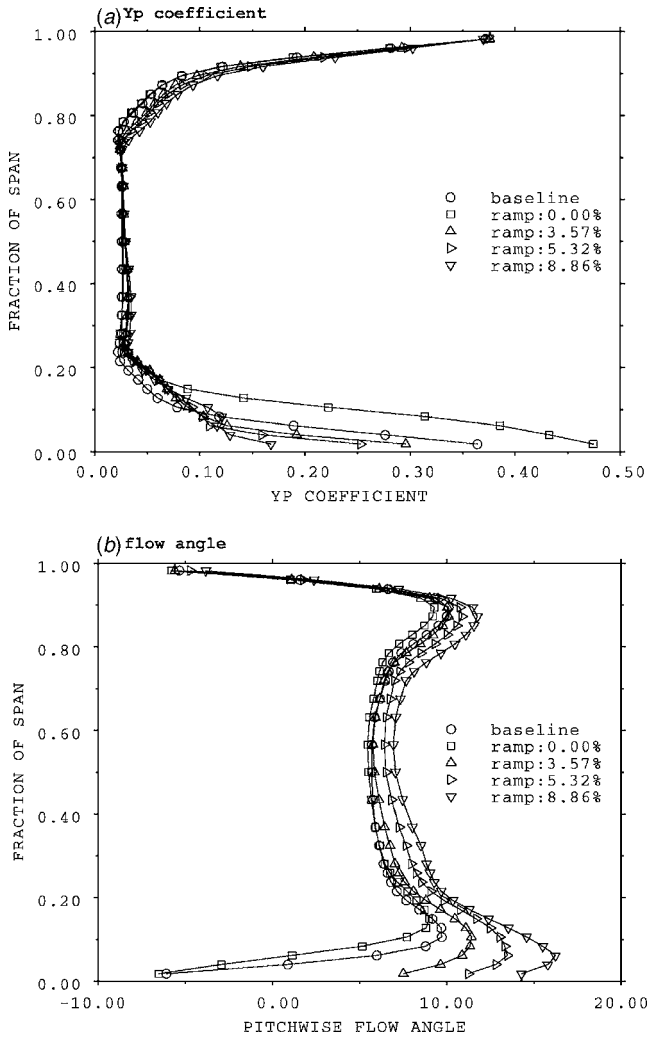

Fig. 5 Case D: measured exit profiles (*a*) stagnation pressure loss; and (*b*) pitchwise flow angle

Fig. 6 Case E: downstream axisymmetric slot

relative to the baseline data; at a bleed rate of about 9%, the flow was underturned by 1.3 deg at midspan relative to the baseline flow. The largest changes in exit flow angle occurred nearer to the bleed off-take endwall so that very near the endwall, the flow was underturned by 13.6 deg at about 3.5% bleed rate, and by 20.4 deg at about 9% bleed rate. The bleed hole near the pressure surface of the blade draws primary flow into the pressure-surface region of the blade passage, thereby opposing the action of the blades in turning the flow, and causing bulk underturning of the flow.

Case E: Axisymmetric Slot Downstream of Blade Row

A circumferential, axisymmetric slot (Case E), located downstream of the blade row and shown in Fig. 6, was investigated. The slot configuration differed from previous off-take configurations tested because it was located outside of the blade passage, and therefore outside almost all of the blade-to-blade static pressure field, in a region where the static pressure in the primary flow is nearly uniform. (This is only true for the cascade; in a multistage compressor, the potential pressure field of the downstream rotor causes the static pressure downstream of the stator blade row to be unsteady circumferentially nonuniform.) In its original configuration, the axisymmetric slot off-take had a sharp inlet edge as shown in Fig. 6.

Measured contours of stagnation pressure loss coefficient (Y_p) downstream of the blade row are shown in Fig. 7 for the sharp-

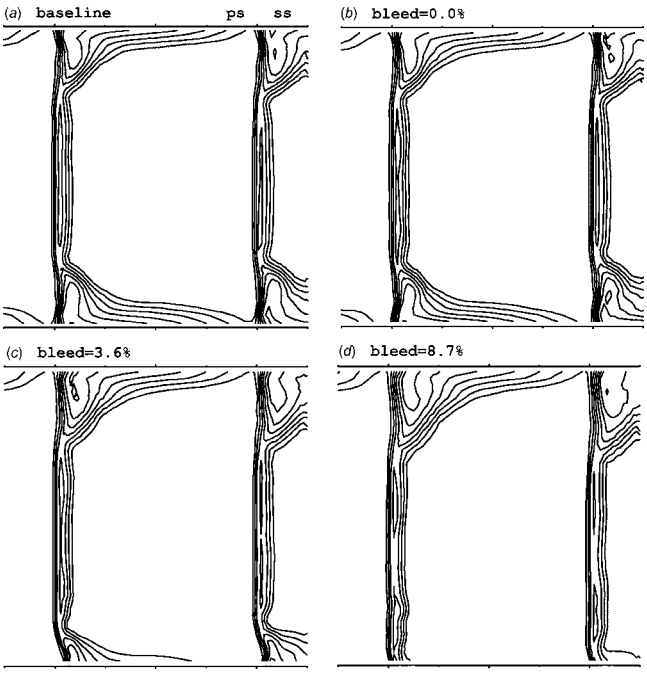

Fig. 7 Case E: axisymmetric slot—measured contours of stagnation pressure loss (minimum Y_p contour 0.1; contour increment 0.1)

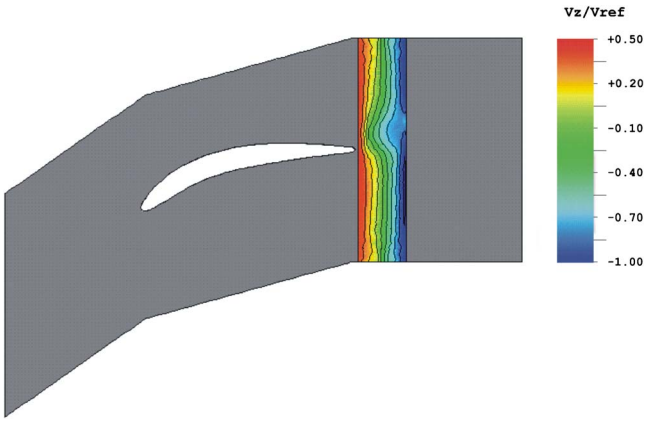

Fig. 8 Case E: calculated contours of radial velocity inside the slot—8% bleed rate

edged axisymmetric slot configuration for three bleed rates: 0%, about 3.5%, and 9% of the primary flow. In the region of nearly uniform static pressure downstream of the blade row, pressure driven flows within the slot were small and there was no significant spillage of fluid from the slot into the primary flow. At zero bleed rate there was no measurable increase in primary flow passage loss and, compared to the baseline configuration, the flow downstream of the blade row was nearly unchanged by the presence of the slot. (This contrasts with the strong interaction generally associated with off-take configurations located within the blade passage.) At higher bleed rates, the removal of high-loss endwall boundary layer fluid from across the whole endwall left a region of high stagnation pressure near the endwall, and gave lower passage loss compared to discrete off-take configurations, which can cause flow disruption to regions of the blade passage near the suction surface of the blade (as shown in Fig. 3). Also evident in Fig. 7 is the increased size of the blade suction-surface corner separation at the endwall opposite the bleed slot at high bleed rates, which is caused by the additional static pressure rise across the blade row with increasing bleed rate.

In the nearly uniform static pressure field downstream of the blade row, primary flow enters the slot almost uniformly (in the pitchwise direction) across the blade passage. Calculated contours of radial velocity are shown in Fig. 8 on a radial plane within the slot for 8% bleed rate. The radial plane on which the contours are shown is at 50% of the radial depth of the slot. In the figure blue contours represent radial velocity into the slot (i.e., from the blade passage to the slot) while red contours represent radial velocity out of the slot (i.e., from the slot to the blade passage). At entry to the slot, flow separation across the sharp inlet edge causes a recirculating flow across the forward regions of the slot, similar to a trapped vortex with the axis of rotation in the pitchwise direction. The vortical motion causes a radial component of flow in the direction out from the slot (red contours) near the forward surface of the slot. The inward flowing bleed air (blue contours) passes through the slot near the rear surface. The bleed flow enters the slot nearly uniformly across the blade passage (i.e., in a pitchwise direction), which contrasts with the nonuniform radial flows associated with discrete bleed off-takes located within the blade passage that are exposed to the blade passage static pressure field [1].

Measured spanwise exit profiles of mass-averaged stagnation pressure loss coefficient (Y_p) and pitchwise flow angle are shown in Fig. 9 for the downstream axisymmetric slot configuration (Case E). The baseline (no bleed slot) configuration data are also shown for comparison. At zero bleed rate there was no measurable increase in loss relative to the baseline levels, and losses near the endwall decreased with increasing bleed rate because of the removal of the endwall boundary layer from the blade passage.

Figure 9(*b*) shows virtually no variation to the exit flow angle,

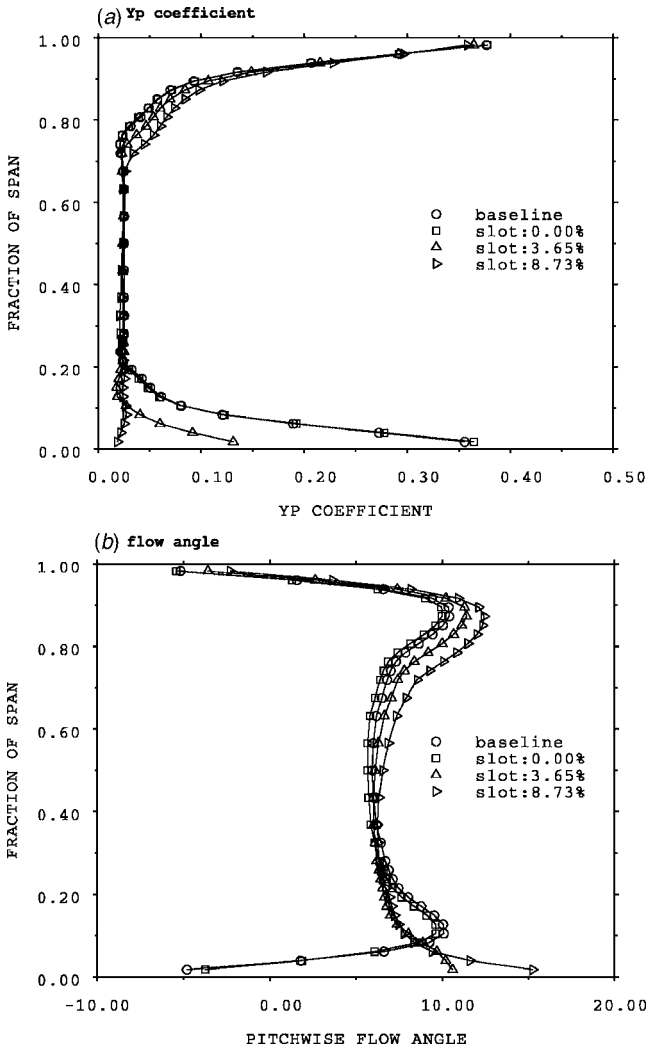

Fig. 9 Case E: measured exit profiles: (*a*) stagnation pressure loss; and (*b*) pitchwise flow angle

relative to the baseline data, across the whole span at zero bleed rate. With increasing bleed rate, the general trend was that the flow was underturned relative to the baseline data out to about 10% span and by as much as 20 deg at about 9% bleed rate near the endwall. Across the outer 50% of span the amount of flow underturning relative to the baseline data also increased with increasing bleed rate as the size of the corner separation at the endwall increased.

Measured and calculated bleed characteristics are shown in Fig. 10 for the downstream axisymmetric slot configuration, with the circles corresponding to the slot configuration with a sharp inlet edge (i.e., $R=0$), while the other three sets of data correspond to data for the slot with a finite radius on the inlet (upstream) edge of the slot. Also shown in Fig. 10, for comparison, is data for the near pressure-surface hole with inlet ramp (Case D: ps_hole +ramp). The data in Fig. 10 are plotted over the same range as in Fig. 2.

At zero and small bleed rates, the radius on the inlet edge of the slot had only a small effect on bleed pressure, but with increasing bleed rate, the drop in bleed off-take pressure was strongly dependent on the radius of the upstream edge of the slot. The bleed off-take static pressure increased with radius size because allowing flow to be turned into the slot on a larger radius of curvature lowers the acceleration over the inlet edge and reduces the flow separation and therefore blockage within the slot.

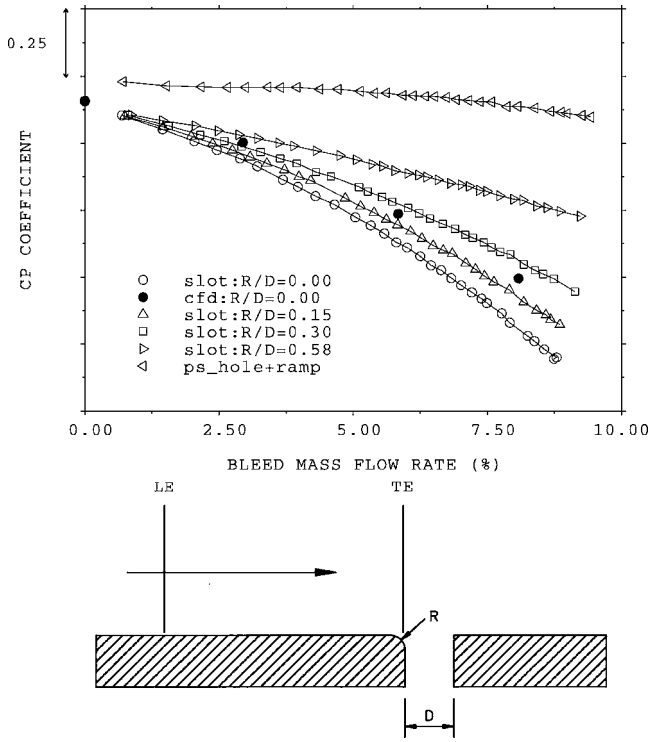

Fig. 10 Case E: bleed characteristic for downstream axisymmetric slots with inlet-edge fillet radius (*R*)

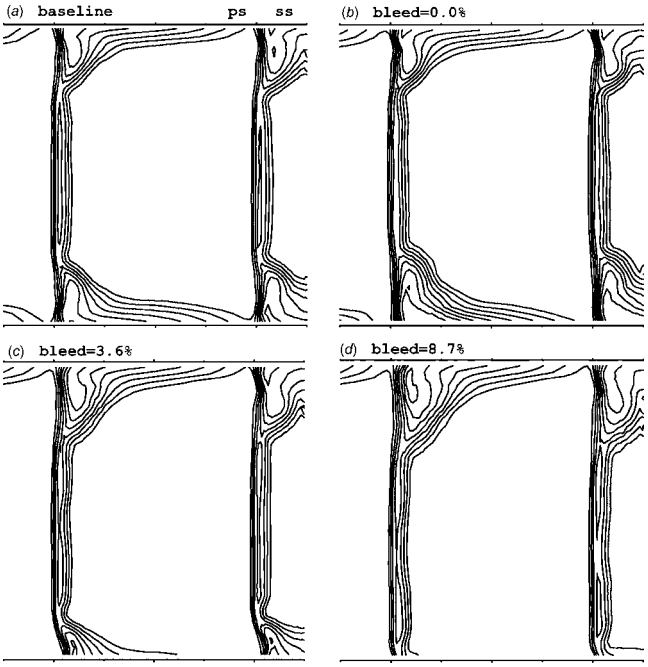

Fig. 11 Case E: axisymmetric slot (R/D=0.58)—measured contours of stagnation pressure loss, Y_p (minimum contour 0.1, increment 0.1)

Numerical calculations were performed at four bleed rates on the sharp-edged configuration (i.e., R/D=0) and are plotted as solid symbols in Fig. 10. Compared with the measured data, the calculated bleed off-take pressure was higher than the measured pressure, the discrepancy being larger at high bleed rates. The errors in calculated bleed off-take pressure are believed to be associated with the incorrect prediction of blockage within the slot caused by errors in prediction of the separation of flow at the inlet to the slot.

For high bleed air pressure, contoured (or ramped) inlet surfaces to the off-take are necessary to reduce the amount of acceleration and static pressure drop. High bleed pressure with contoured inlet surfaces to the off-take was demonstrated in Figs. 2 and 10 for two different bleed off-take configurations: a discrete hole (Case D) and an axisymmetric slot (Case E), respectively. For the sharp-edge axisymmetric slot configuration shown in Fig. 6, the slot is located entirely outside of the blade passage and downstream of the blade trailing edge. As the radius across the inlet edge of the slot is increased, however, the contoured inlet surface extends forward into the blade passage and flow over the inlet ramp surface and into the slot becomes influenced by the blade passage static pressure field, thereby coupling flow within the slot to the primary flow through the blade passage.

Figure 11 plots measured contours of stagnation pressure loss for the downstream axisymmetric slot configuration with inlet edge radius R/D=0.58, the configuration that gave the highest bleed off-take pressures (Fig. 10). Figure 11 should be compared with Fig. 7, which shows contours for the sharp inlet edge (i.e., R/D=0). At zero bleed rate, the larger inlet-edge radius caused increased loss at the endwall near the suction surface of the blade; the boundary layer near the endwall was thicker and the blade corner separation was larger than when the inlet edge was sharp. (Mass-averaged loss, integrated over the blade passage, is tabulated at the end of the paper.) Thus, the inlet edge radius gave raised bleed off-take pressure but at small bleed rates caused increased loss in the blade passage; at higher bleed rates the inlet edge radius caused virtually no difference in the flow downstream of the blade row while giving higher bleed off-take pressure.

Case F: Full-Pitch Ramped Slot

As noted in Fig. 10, a radius on the inlet edge to the downstream axisymmetric slot configuration (i.e., R/D=0.58) increased bleed off-take pressures by reducing the drop in pressure with increasing bleed rate. To raise bleed off-take pressures further, a bleed off-take configuration with a larger inlet ramp surface radius of curvature (i.e., R/D=3.94) was investigated. Figure 12 shows two views of the bleed slot geometry with a gently sloping inlet ramp surface beginning within the blade passage at about 0.35 axial chord from the leading edge and extending across the whole pitch of the blade passage to both blade surfaces.

Measured bleed characteristics are shown in Fig. 13 for the full-pitch ramped slot configuration (Case F: slot+ramp) with R/D=3.94. Again shown in Fig. 13, for comparison, are bleed characteristics for the near pressure-surface hole with inlet ramp (Case D: ps_hole+ramp) as well as the downstream axisymmetric slot configurations (Case E). Numerical calculations were performed at three bleed rates for the full-pitch ramped slot configuration (Case F) and are plotted as solid symbols in Fig. 13. The CFD predicted bleed off-take pressures slightly higher than the measured data, but the predicted rate of drop of bleed off-take pressure with bleed flow rate is in reasonably good agreement with the measured data.

For the full-pitch ramped slot configuration with R/D=3.94, the rate of static pressure drop with bleed rate was virtually the same as for the downstream axisymmetric slot configuration with R/D=0.58, shown in Fig. 10, but the absolute level of pressure was increased by about ΔC_p=0.15. Figure 13 shows that bleed pressures for the full-pitch ramped slot configuration were, however, lower than for the pressure-surface hole with inlet ramp, confirming that the highest bleed off-take pressures are always achieved bleeding the primary flow from near the pressure surface of the blade.

Measured contours of stagnation pressure loss coefficient (Y_p) downstream of the blade row for the full-pitch ramped slot con-

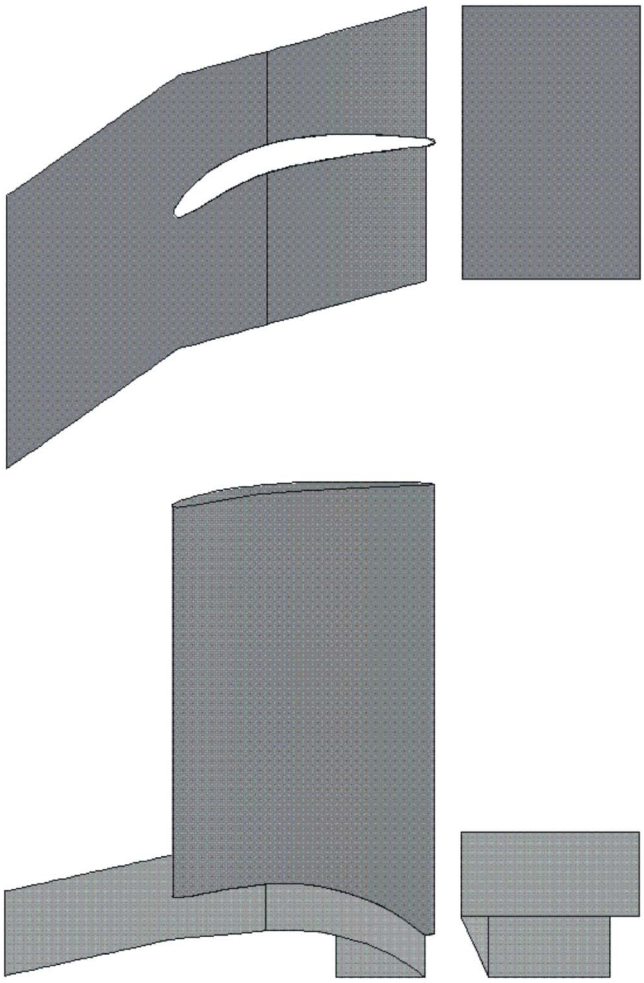

Fig. 12 Case F: full-pitch ramped bleed slot

figuration (Case F) are shown in Fig. 14 for three bleed rates: 0%, and about 3.5% and 9% of the primary flow. The full-pitch inlet ramp surface caused a strong and deleterious interaction with the primary flow, with a large increase of loss and blockage at the suction-surface endwall corner of the blade passage at 0% and about 3.5% bleed rates. At these bleed rates, the region of high loss extended nearly 40% blade span away from the endwall, and

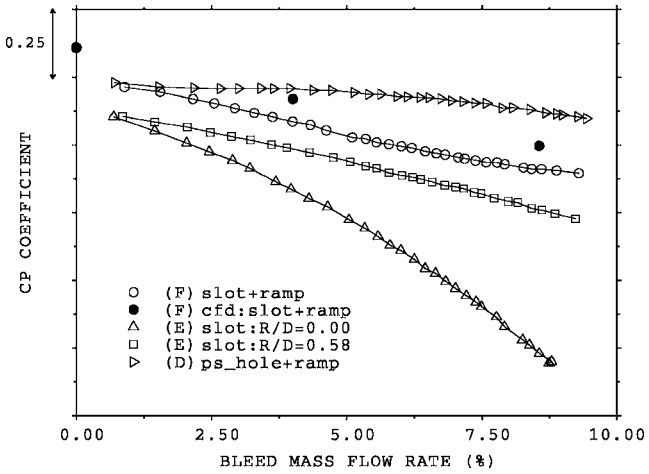

Fig. 13 Bleed characteristics

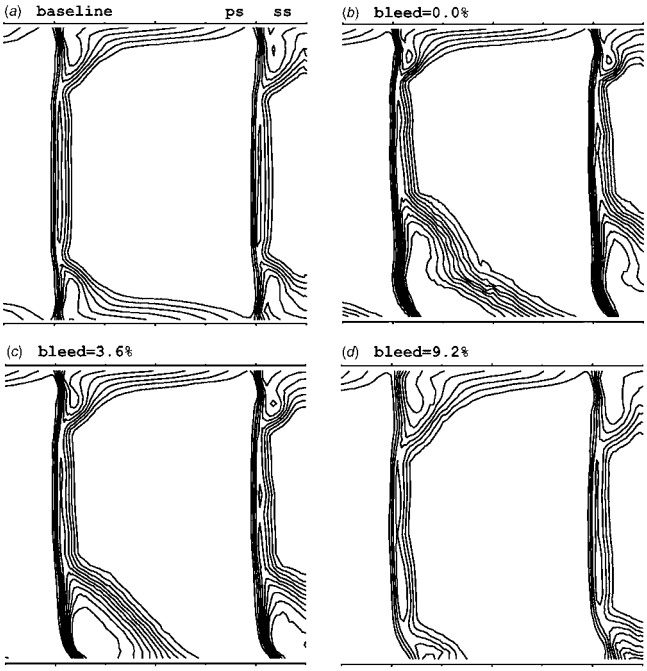

Fig. 14 Case F: full-pitch ramped bleed slot—measured contours of stagnation pressure loss (minimum contour 0.1, increment 0.1)

more than 50% across the blade pitch. At the highest bleed rate of about 9%, however, the bleed was sufficient to draw high loss endwall boundary layer fluid into the slot, leaving a region of high stagnation pressure near the endwall.

The measured spanwise variation of mass-averaged stagnation pressure loss (Y_p) and pitchwise flow angle are shown in Fig. 15 for the full-pitch ramped slot configuration. At the low bleed rates (0% and about 3.5%) the large increase in loss over the lower half of the blade span is evident. At the highest bleed rate of about 9% the loss at the bleed slot endwall was reduced because all the endwall boundary layer was drawn off from the blade passage, but losses at the opposite endwall increased. The large increase in blockage within the blade passage at small bleed rates caused bulk underturning of the flow relative to the baseline configuration. As Fig. 15(*b*) shows, near the endwall the flow was underturned by more than 20 deg at all bleed rates. Large underturning of the flow extended across much of the span.

Measured and calculated pitchwsise-averaged profiles of stagnation pressure loss (Y_p) and exit flow angle are compared in Figs. 16(*a*) and 16(*b*) for two bleed rates near about 3.5% and 9%. The calculated loss profiles show reasonable agreement with the measured data, accurately predicting the high passage loss at low bleed rates (circle symbols) between about 0% and 40% span. Figure 16(*b*) shows that the bulk underturning of the flow over the lower 50% of blade span was well captured by the numerical calculations; however, there is a discrepancy between measured and calculated data of about 2 deg across almost the whole span, the calculation overpredicting flow deviation relative to the measured data. Much of this discrepancy is attributed to the CFD mesh and modeling of the flow at the trailing edge of the blade. Without sufficient mesh resolution around the trailing edge circle, or a trailing-edge cusp model, the separation point is incorrectly predicted and the calculated deviation is too high.

Calculated contours of radial velocity within the full-pitch slot (on a radial plane at 90% of the depth of the slot) are shown in Fig. 17 for three bleed rates. Static pressure gradients in the primary flow above the slot (i.e., the blade-to-blade static pressure field) causes nonuniform radial inflow to the slot. Primary flow enters the slot (blue contours) near the blade pressure surface,

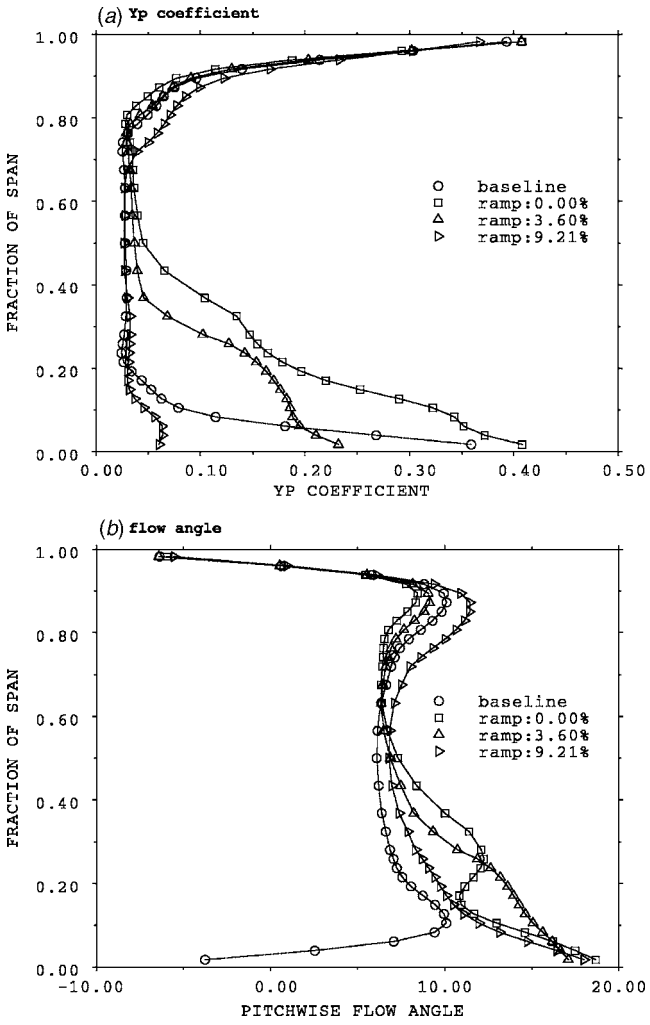

Fig. 15 Case F—measured exit profiles: (*a*) stagnation pressure loss; and (*b*) pitchwise flow angle

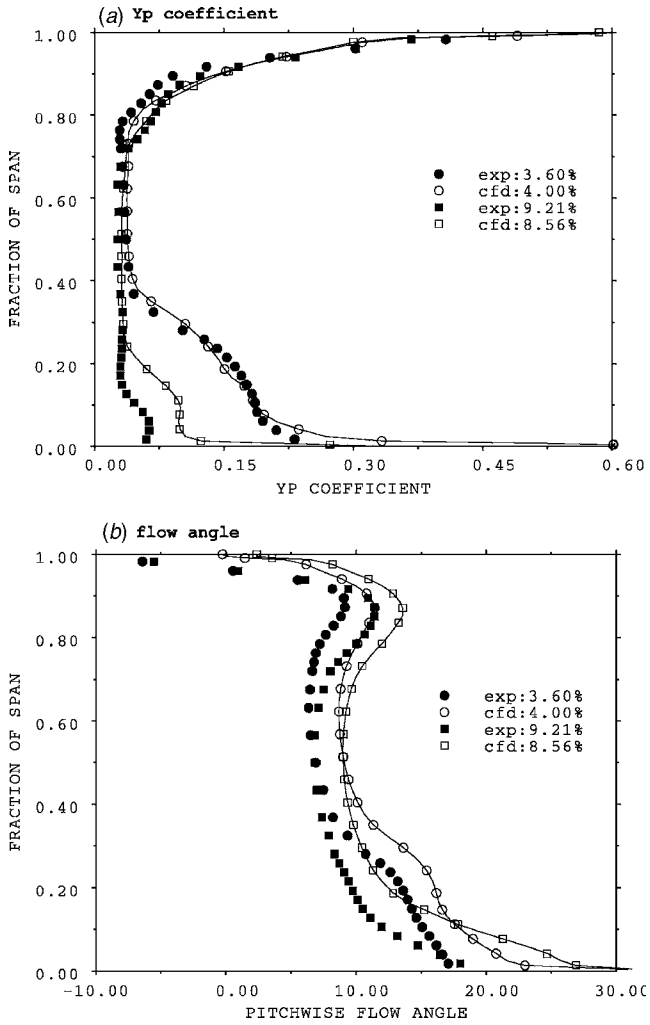

Fig. 16 Case F: measured (exp) and calculated (CFD) exit profiles—(*a*) stagnation pressure loss; and (*b*) pitchwise flow angle

primarily near the downstream surface of the slot. In regions of the slot near the suction surface of the blade there is no radial inflow, even for the highest bleed rate 8.6%. At 0% and 4% bleed rate there is radial outward flow (red contours) from the slot near the blade suction surface. The outward flow has a radial component of velocity more than 20% of the inlet freestream velocity to the blade row. Flow spilling from the slot washes onto the blade suction surface, causing the large measured increase in the suction-surface corner separation shown in Fig. 14.

Regions of the bleed slot near the suction surface of the blade are therefore ineffective for bleed, but instead create a spillage path between the bleed slot and the primary flow. The nonuniform flow within the ramped bleed slot in Fig. 17 contrasts the nearly pitchwise-uniform flow within the axisymmetric slot shown in Fig. 8; the influence of the blade passage static pressure field causes highly nonuniform flow within the full-pitch ramped slot and a strong interaction between the bleed slot and the primary flow.

Comparison of Configurations

The bleed off-take configurations described in this paper have been evaluated based on their respective bleed off-take pressure characteristics and their effect on the primary flow downstream of the blade row. In Table 1, the blade passage mass-averaged stagnation pressure loss coefficients, relative to the baseline (no bleed off-take) level of loss, are presented for each configuration at three bleed rates. In the right-hand column of the table, using the data in Fig. 13, the off-take configurations are ranked in order of highest bleed off-take pressure (1 being best).

Comparing the four configurations in Table 1 shows that the configurations that give high bleed off-take pressure generally cause high levels of loss in the primary flow. The full-pitch ramped slot configuration (Case F), for example, gives high-bleed off-take pressure levels but causes the largest increase in passage loss at low bleed rates. The downstream axisymmetric slot configurations ($R/D=0.00$ and 0.58) give the lowest bleed off-take pressure, but cause less loss in the blade passage. At zero bleed rate, the increased loss for the axisymmetric slot configuration with $R/D=0.58$, relative to the sharp-edged configuration ($R/D=0.00$), is consistent with the measured contours in Fig. 11. At the highest bleed rate, 9%, the three configurations with slots extend-

Table 1 Passage loss and bleed pressure

Off-take case	ΔY_p 0%	ΔY_p 3.5%	ΔY_p 9%	C_p
(D) ps_hole+ramp	+0.017	+0.003	+0.005	1
(E) slot: $R/D=0.00$	0	−0.012	−0.011	4
(E) slot: $R/D=0.58$	+0.005	−0.010	−0.010	3
(F) slot+ramp	+0.053	+0.026	−0.007	2

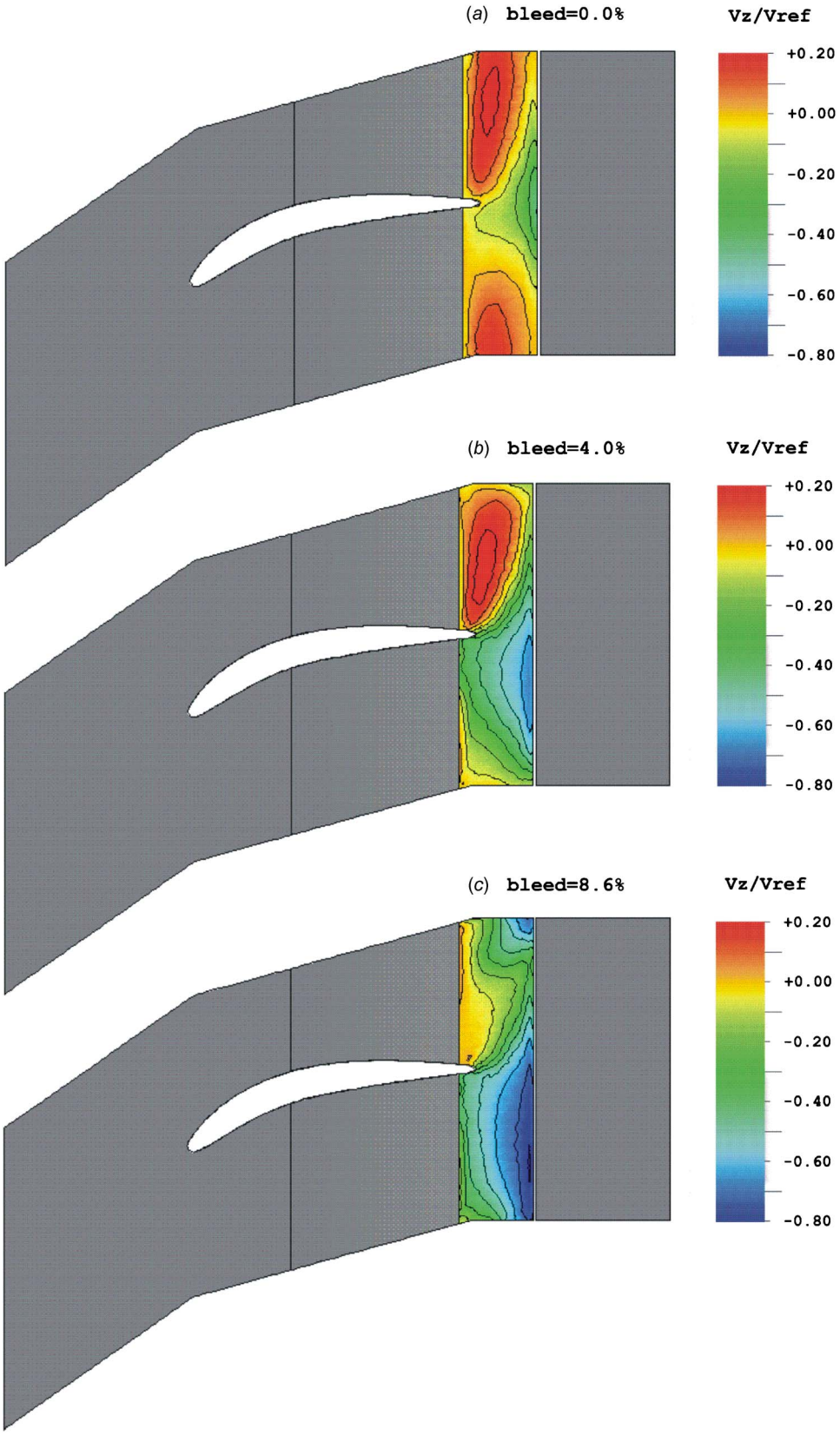

Fig. 17 Case F: calculated contours of radial velocity within slot—(*a*) zero bleed; (*b*) 4.0% bleed, and (*c*) 8.6% bleed

ing across the full pitch of the blade passage gave levels of loss below the baseline level; the discrete hole off-take (Case D), however, still caused an increase in loss relative to the baseline level.

Conclusions

It should be reiterated that this research has been concerned with bleed off-takes which were large enough in area to pass, under certain conditions, large bleed flows up to 15% of the primary (core) mass flow. The conclusions below therefore pertain to large bleed off-takes and do not all apply to small orifices which operate continually with a constant rate of flow removal.

1. Results show that maximizing bleed off-take pressure and minimizing loss within the blade passage are sometimes conflicting objectives. In this paper, the configurations that give the highest bleed off-take pressures cause the highest loss to the primary flow within the blade passage; configurations that give the lowest bleed off-take pressures cause the lowest loss within the blade passage.
2. As one would expect, the pressure of the bleed off-take air for configurations with contoured (i.e., large radius of curvature) inlet edges is larger than for configurations with sharp inlet edges.
3. A discrete bleed hole with a large inlet ramp surface located near the pressure surface of the blade has an interaction with the primary passage flow similar to a circular hole bleed configuration without the inlet ramp surface. Off-takes near the blade pressure surface cause a small amount of spillage into the primary flow at zero bleed rate, but at high bleed rates the endwall flow is drawn into the hole from across the blade passage, causing separated flow at the endwall, and increasing loss in the blade passage near the blade suction surface.
4. Axisymmetric slots located downstream of the blade row, in a region of nearly uniform static pressure, cause no measurable increase in loss within the blade passage at all bleed rates. The primary flow enters the slot virtually uniformly across the blade pitch, with no evidence of flow spilling from the slot into the blade passage; the endwall boundary layer is bled from the blade passage and overall passage loss is reduced.
5. An axisymmetric slot configuration, with an inlet ramp surface of large radius of curvature that extends into the blade passage, gives increased bleed off-take pressure relative to configurations with smaller inlet ramp radius of curvature. However this geometry causes large loss and blockage in the primary flow at small bleed rates because the inlet ramp surface, which extends into the blade passage, couples the flow within the off-take to the primary passage flow. Static pressure gradients within the blade passage (i.e., the blade-to-blade static pressure field) cause flow within the slot to be highly nonuniform leading to large regions of flow spilling from the slot into the blade passage and increasing loss.
6. The variation of bleed off-take pressure and the effect on the primary passage flow with bleed flow rate for various geometries is complicated and cannot be assessed intuitively. However, the behavior was calculated by CFD with accuracy sufficient for evaluating bleed off-take designs, both in terms of bleed off-take pressure levels and the effects on the primary flow.

Acknowledgment

The work, which was carried out at the Whittle Laboratory, was supported by Rolls-Royce plc., the Applied Research Programme of the Ministry of Defence, and the Department of Trade and Industry Aeronautical Research Programme. The authors wish to thank the sponsors for permission to publish this paper. However, the opinions expressed here are those of the authors and not necessarily those of any of the sponsoring organizations. The experimental program was greatly assisted by all members of the Whittle Laboratory Workshop. The authors acknowledge J. J. Bolger and S. J. Gallimore, from Rolls-Royce, for their enthusiastic support of this research, and would like to thank W. N. Dawes for the use of his CFD code NEWT.

Nomenclature

C = blade chord
C_p = $(P_S - P_{S1})/1/2\rho V_{\text{ref}}^2$, static pressure coefficient
D = slot axial length
P_0 = stagnation pressure
P_{01} = inlet freestream stagnation pressure
P_S = static pressure
P_{S1} = inlet freestream static pressure
R = radius
V_{ref} = cascade inlet velocity
V_z = radial velocity
Y_p = $(P_0 - P_{01})/1/2\rho V_{\text{ref}}^2$, stagnation pressure coefficient
δ_{99} = boundary layer thickness
δ^* = boundary layer displacement thickness
θ = boundary layer momentum thickness
ρ = density
ΔY_p = $(Y_p)_{\text{BLEED}} - (Y_p)_{\text{BASELINE}}$, increment in loss

References

[1] Leishman, B. A., Cumpsty, N. A., and Denton, J. D., 2007, "Effects of Bleed Rate and Endwall Location on the Aerodynamic Behavior of a Circular Hole Bleed Off-Take," ASME J. Turbomach. **129**, pp. 645–658.
[2] Mossman, E. A., and Randall, L. M., 1948, "An Experimental Investigation of the Design Variables for NACA Submerged Duct Entrances," NACA Research Memorandum, No. RM A7130.
[3] Dennard, J. S., 1957, "A Transonic Investigation of the Mass-Flow and Pressure Recovery Characteristics of Several Types of Auxiliary Air Inlets," NACA Research Memorandum, No. RM L57B07.
[4] Young, C. and Snowsill, G. D., 2002, "CFD Optimization of Cooling Air Off-Take Passages Within Rotor Cavities," ASME Paper No. GT-2002–30480.
[5] Dawes, W. N., 1993, "The Practical Application of Solution-Adaption to the Numerical Simulation of Complex Turbomachinery Problems," Prog. Aerosp. Sci. **29**, pp. 221–269.
[6] Leishman, B. A., 2003, "The Aerodynamic Behaviour and Design of Compressor Bleed Slots," Ph.D. dissertation, University of Cambridge, Cambridge, UK.

Mechanism of the Interaction of a Ramped Bleed Slot With the Primary Flow

B. A. Leishman

N. A. Cumpsty[1]

Rolls-Royce plc.,
Derby DE24 8BJ, UK

*An experimental and computational study of the ramped bleed slot in a compressor cascade is presented. The geometry is a circumferential slot downstream of the stator blade trailing edge, with endwall ramps inside the blade passage, and the paper builds on work previously reported for different bleed off-take geometries (Leishman et al., 2007, ASME J. Turbomach., **129**, pp. 645–658; Leishman et al., 2007, ASME J. Turbomach., **129**, pp. 659–668). The strong interaction between any bleed slot and the primary flow through the cascade can be strong, thereby causing the levels of loss and blockage in the primary flow leaving the blade passage to be increased at some bleed flow rates. Radial flow into the bleed slot is highly nonuniform because the blade-to-blade pressure field causes flow to enter the bleed slot preferentially where the static pressure is high, and to spill out into the primary flow where the static pressure is low. The mechanism for the ramped bleed slot is different from that described in the earlier papers for other geometries. For the ramped bleed slot a static pressure field, with large variations of static pressure in the circumferential direction, is set up in the slot because the endwall flow entering the slot has higher stagnation pressure downstream of the pressure surface than downstream of the suction surface of the upstream blades. The flow entering the slot with high stagnation pressure is brought to rest in a stagnation point on the downstream surface of the slot, and the consequent variation in static pressure on the rear surface sets tangential and radial components of velocity which are a large fraction of the freestream velocity. As well as demonstrating the mechanism for the flow behavior, the paper presents results of experiments and calculations to demonstrate the behavior and gives guidance for the design of bleed slots by stressing the fundamental features of the flow.* [DOI: 10.1115/1.2752193]

Introduction

Bleed off-takes on the hub and casing endwalls, part way through a jet engine compressor, remove air from the primary (core) air stream to supply the internal air system with cooling and sealing air, to supply cabin air to the aircraft, and for compressor handling at part-speed conditions. The two aspects of bleed off-take performance of interest are the bleed off-take air pressure and the effect of the bleed off-take on the primary flow through the blade passages.

Leishman et al. [1,2] reported on both aspects of bleed performance for a combination of bleed off-take geometries and different bleed rates. It was concluded that achieving high-bleed air pressure and minimizing loss in the blade passage are generally conflicting objectives, because configurations which give high off-take air pressure generally have a strong deleterious effect on the primary flow. This deleterious interaction between the bleed off-take and primary flow results in a large increase in passage loss and blockage, particularly at low bleed rates, as well as altering the deviation from the blade row. As a generalization it was also shown that certain bleed off-take configurations good for low-bleed flow rates would be unsatisfactory at high-bleed flow rates; conversely, certain off-take configurations good for high-bleed flow rates can be deleterious to the primary flow at low-bleed flow rates.

The objectives of this paper are different and more specific than Refs. [1,2]. A ramped off-take configuration was chosen as the subject of investigation: this gives high-bleed air pressure but causes a strong interaction with the primary flow aerodynamics so that the levels of loss and blockage in the primary flow are increased. The ramped bleed slot geometry is shown in Fig. 1 in both plan and side view (the flow in this case would be from left to right). It includes a gently sloping ramp surface beginning at about 35% axial chord within the blade row and extending across most of the blade pitch, with the blade supported on a platform at the endwall. The contoured ramped surface, which forms a smooth inlet to a circumferential slot downstream of the blade row, is exposed to the nonuniform blade-to-blade static pressure field within the blade passage, whereas the circumferential slot downstream of the trailing edge of the blade is located in a region where the static pressure in the primary flow is nearly uniform. Flow is drawn into the bleed slot and collects in a large plenum outside of the blade passage (not shown). Through experimental and numerical investigation, a fluid dynamic explanation was sought to explain the mechanism for the strong and sometimes deleterious interaction between the bleed slot and the primary flow. Using numerical computations the effect of inlet boundary layer thickness on the flow mechanisms was also investigated.

Method

Experiments were made on a large-scale, low-speed linear compressor cascade rig attached to an open-circuit wind tunnel in the Whittle Laboratory, University of Cambridge. Details of the experimental facility and technique are given by Leishman [3] and Leishman et al. [1,2].

The cascade blades are a low-speed design of a HP compressor stator, with a controlled-diffusion pressure distribution. The two-dimensional cascade blades, with 152 mm chord and 228 mm

[1]Now at Department of Mechanical Engineering, Imperial College, London SW7 2AZ, UK.

Contributed by the International Gas Turbine Institute of ASME for publication in the JOURNAL OF TURBOMACHINERY. Manuscript received December 7, 2006; final manuscript received December 21, 2006. Review conducted by David Wisler. Paper presented at the ASME Turbo Expo 2005: Land, Sea and Air (GT2005), Reno, NV, USA, June 6–9 2005. Paper No. GT2005-68483.

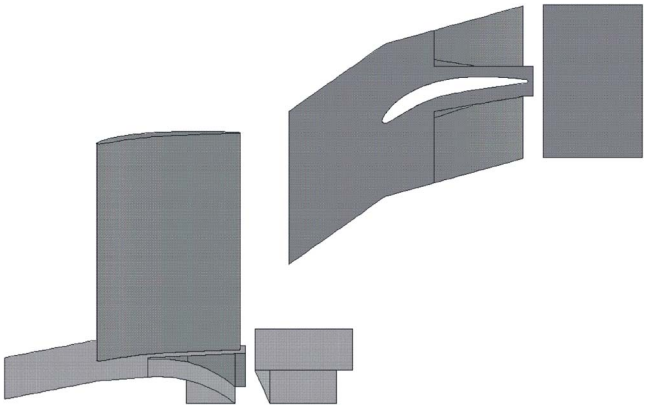

Fig. 1 Ramped bleed slot geometry

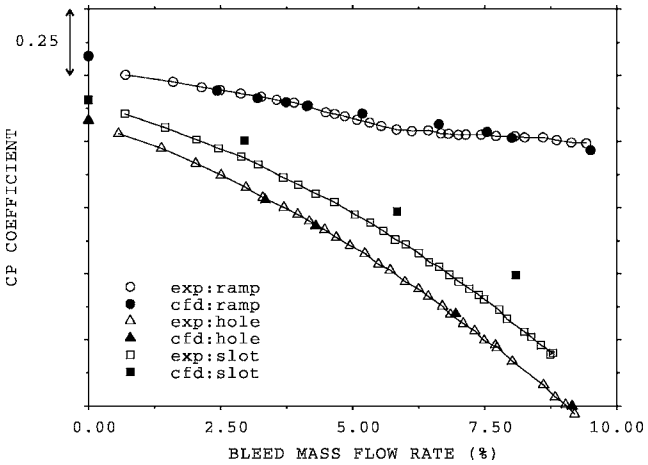

Fig. 2 Measured (exp) and calculated (CFD) bleed characteristics

span, were configured for passage solidity 1.0, with inlet flow direction 35.0 deg and design exit flow direction 5.6 deg. An interchangeable cascade sidewall was used with bleed off-takes machined into each of the five blade passages of the cascade.

Experiments were performed with inlet freestream velocity 22 m/s and Reynolds number based on blade chord of 230,000 (representative of an embedded HP compressor stage). At inlet to the cascade, the overall thickness of the natural endwall boundary layer, was $\delta_{99}=17.0$ mm ($\delta_{99}/C=0.112$), measured 0.75 axial chord lengths upstream of the blade leading edge, and the displacement and momentum thicknesses were given by $\delta^*/C=0.018$ and $\theta/C=0.013$, respectively. Numerical results are also presented in this paper with five different inlet boundary layer profiles, having displacement thickness $\delta^*/C=0.007$, 0.018, 0.034, 0.066, and 0.088 respectively, to test the sensitivity of the flow behavior to inlet boundary layer thickness. Experimental and numerical results presented in this paper are, unless otherwise stated, for the inlet boundary layer with displacement thickness $\delta^*/C=0.018$.

Air bled from the primary cascade flow was collected in a large plenum box attached to the side of the cascade. The cascade was operated for a range of bleed mass flow rates between 0% and 10% of the primary flow at inlet to the cascade, with bleed mass flow rates measured using a square-edged orifice plate.

Numerical computations were performed using the NEWT unstructured tetrahedral flow solver of Dawes [4]. NEWT solves the full three-dimensional Reynolds averaged Navier-Stokes equations on an unstructured mesh of tetrahedral cells, using a finite-volume discretization. Turbulence is modeled via the standard two-equation k-ε model. Use of an unstructured mesh-based solver allowed modeling of the real cascade geometry, including the blade passage, bleed off-take, and bleed collection plenum. A typical calculation mesh contained about 2,800,000 tetrahedral cells and 500,000 nodes. For brevity, further details of the mesh, mesh generation, and the numerical scheme are not given here (see Refs. [3,4]). At the plenum exit, a uniform static pressure boundary condition was applied, and the bleed mass flow rate was calculated for the prescribed exit pressure. Achieving a target bleed rate was therefore an iterative process, in which the plenum exit pressure was changed between calculations. The numerical process, where bleed flow rate was found by setting the static pressure at the plenum exit, was similar to that used in experiments. As a result, the experimental and computational bleed rates that resulted are not entirely consistent; they are zero, between about 3% and 4%, and about 9% of the primary flow. These are sufficiently close, however, to allow the qualitative comparisons and assessments required.

Overall Aerodynamic Behavior

Figure 2 shows measured and calculated bleed characteristics for the ramped slot geometry of Fig. 1, labeled ramp. The bleed characteristic shows the variation of bleed off-take static pressure (expressed as a static pressure coefficient, C_p) with bleed rate. Bleed air pressures were calculated from the average of measured static pressure from 12 wall tappings distributed around the plenum. In Fig. 2 only the increment in C_p is shown on the axis. Measured data are plotted as open symbols, while calculated data are plotted as solid symbols. Also plotted in Fig. 2 for comparison are bleed characteristics for configurations described in earlier papers: Case A from Leishman et al. [1]—a circular hole configuration, labeled hole; and Case E from Leishman et al. [2]—an axisymmetric slot configuration with no inlet ramp surface, labeled slot. The ramped geometry, with contoured inlet to the slot to minimize flow separation, gave high-bleed off-take pressures relative to the simpler configurations without inlet ramp surfaces. Moreover, the rate of static pressure drop with increasing bleed rate was also much less, so that the off-take pressures remains high at high bleed rates. Generally, the measured off-take pressures are well captured by the numerical calculations, especially for the ramped inlet configuration.

Measured contours of stagnation pressure loss coefficienct (Y_p) downstream of the ramped bleed slot and blade row are shown in Fig. 3 for three bleed rates: 0%, 3.6%, and 9.1% of the primary flow at inlet to the blade row. Also shown at the top left is the baseline configuration with no bleed slot (i.e., a solid endwall). The measurements were performed 0.25 axial chord lengths downstream of the blade trailing edge using a calibrated five-hole pneumatic probe. For brevity, computational fluid dynamics (CFD) results are not compared with experimental data in Fig. 3. As demonstrated in Refs. [2,3], however, downstream contours and 2D radial profiles are generally well predicted. (The greatest error in CFD predictions occur at zero bleed rate with the levels of loss and blockage underpredicted relative to measurement.) Compared to the flow downstream of the baseline (no bleed slot) configuration, Fig. 3 shows significant changes to the primary flow aerodynamics resulting from the strong interaction between the bleed slot and the primary flow at the three bleed rates. At zero bleed rate, increased loss and blockage were measured at the suction-surface endwall corner of the blade passage, so that a loss core extended across more than 50% of the blade pitch and nearly 40% of the blade span away from the endwall. At 3.6% bleed there remained a high loss region at the suction-surface endwall corner. At 9.1% bleed rate the bleed flow was sufficient to clear the endwall of high loss fluid and prevent deleterious flow interactions that would increase losses downstream of the blade row.

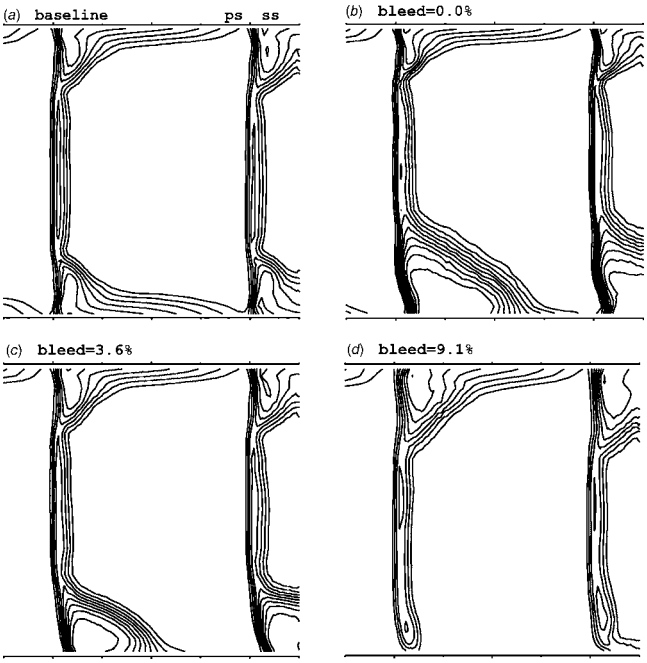

Fig. 3 Measured contours of stagnation pressure loss (Y_p) 0.25 axial chord downstream of the blade row (increment 0.1, minimum contour 0.1)

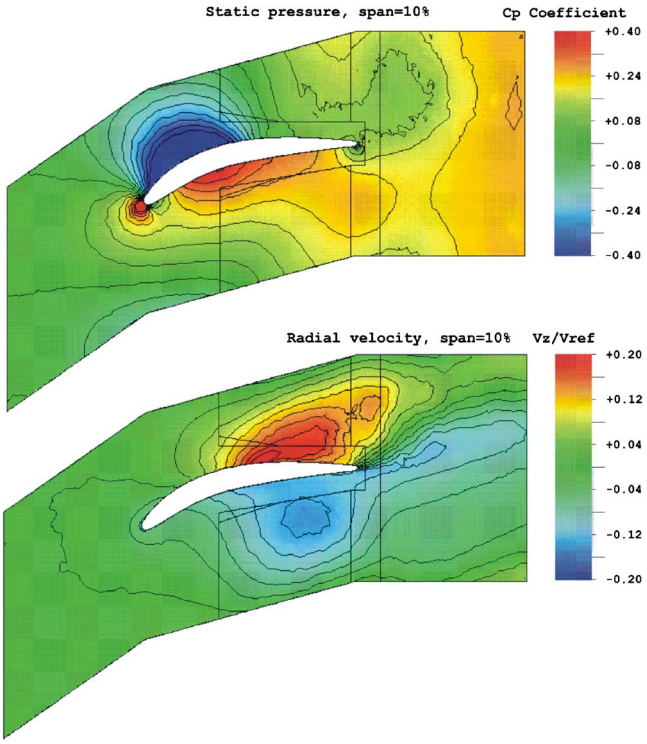

Fig. 4 Calculated contours of: (*a*) static pressure at 10% span; and (*b*) radial velocity at 10% span for 3.2% bleed rate

Figure 3 also shows that blockage at the suction-surface corner of the smooth endwall (i.e., the endwall opposite the bleed slot) increased at higher bleed rates. Increasing amounts of bleed represent mass removal from the blade passage, which causes an increased static pressure rise over the whole span, thereby enhancing the tendency for flow to separate from the suction-surface endwall corner of the blade. It is interesting that the two-dimensional wakes at blade midheight become thinner within increasing bleed rate, but no satisfactory and substantiated cause has been found for this.

Flow Mechanism

The blade-to-blade static pressure field acting on the relatively weak boundary layer fluid at the endwall is known to generate cross-passage secondary flows within a blade row. Similarly, when a hole (or bleed slot) is placed on the endwall, the same gradients of static pressure influence flow into and out of the hole. Figure 4(*a*) plots calculated static pressure contours on a radial plane at 10% blade span away from the bleed slot endwall for 3.2% bleed rate. Despite the presence of the bleed slot, the static pressure distribution at 10% blade span is generally similar to the pressure distribution at midspan (not shown for brevity, but shown in Ref. [3]). The bleed slot geometry is shown as an outline in Fig. 4 and it is evident that there are large static pressure gradients in the primary flow over the ramp.

Static pressure gradients within the blade passage influence where primary flow enters the bleed slot and Fig. 4(*b*) plots calculated contours of radial velocity in the blade passage on the radial plane at 10% blade span away from the endwall. It is evident from Fig. 4(*b*) that primary flow does not enter the bleed slot uniformly across the blade passage; regions of inflow, blue contours in Fig. 4(*b*), are where the static pressure in the primary flow is high near the blade pressure surface, and regions of outflow (red contours) are where the static pressure in the primary flow is low near the blade suction surface.

Calculated contours of radial velocity within the bleed slot are shown in Fig. 5 for three bleed rates, on a radial plane at 90% of the depth of the slot (i.e., near where the slot dumps into the plenum, as indicated by the contour plane in Fig. 6). Flow into the slot is highly nonuniform, with primary flow entering (blue contours) preferentially downstream of the pressure-surface region, towards the rear surface of the slot. The pitchwise nonuniformities are greatest at low bleed rates, and Fig. 5 shows that with increasing bleed rate the flow within the slot becomes progressively more uniform, with a higher portion of radial flow into the slot (blue contours), but always preferentially across the rear surface of the slot.

Primary flow enters the bleed slot preferentially downstream of the pressure surface of the blade and concentrates toward the rear surface of the slot, where the highest radial velocities were show in Fig. 5. Where primary flow enters the slot (i.e., downstream of the blade pressure surface) it stagnates on the rear surface of the slot with a dividing streamline, as sketched in Fig. 6 for a cross section through the bleed slot (note that various measurement locations referenced throughout are also indicated in Fig. 6). The dividing streamline separates the primary flow that enters the bleed slot from the primary flow which passes over the slot and continues downstream. The stagnation point on the rear surface, together with streamline curvature effects as the flow is turned sharply from a near axial direction in the blade passage towards the radial direction within the bleed slot, generates strong static pressure gradients across the rear surface of the slot.

Figure 7 shows calculated static pressure contours over the rear surface of the bleed slot, for 4.2% bleed rate. Surface contours are shown across one blade pitch: each blade passage contains a high- and low-static pressure region being periodic with blade pitch. Stagnating flow and streamline curvature effects create a local increase in static pressure on the rear surface of the slot downstream of the blade pressure surface (shown as red contours).

The pitchwise variation of static pressure was measured across the rear surface of the bleed slot with 16 static pressure surface tappings on the rear surface, 3.5 mm below the endwall surface (which represents 10% of the radial depth of the slot, as indicated in Fig. 6) across one blade pitch. The measured and calculated static pressure variations across the rear surface of the slot at 10% depth are shown in Fig. 8 for three bleed rates between 0% and

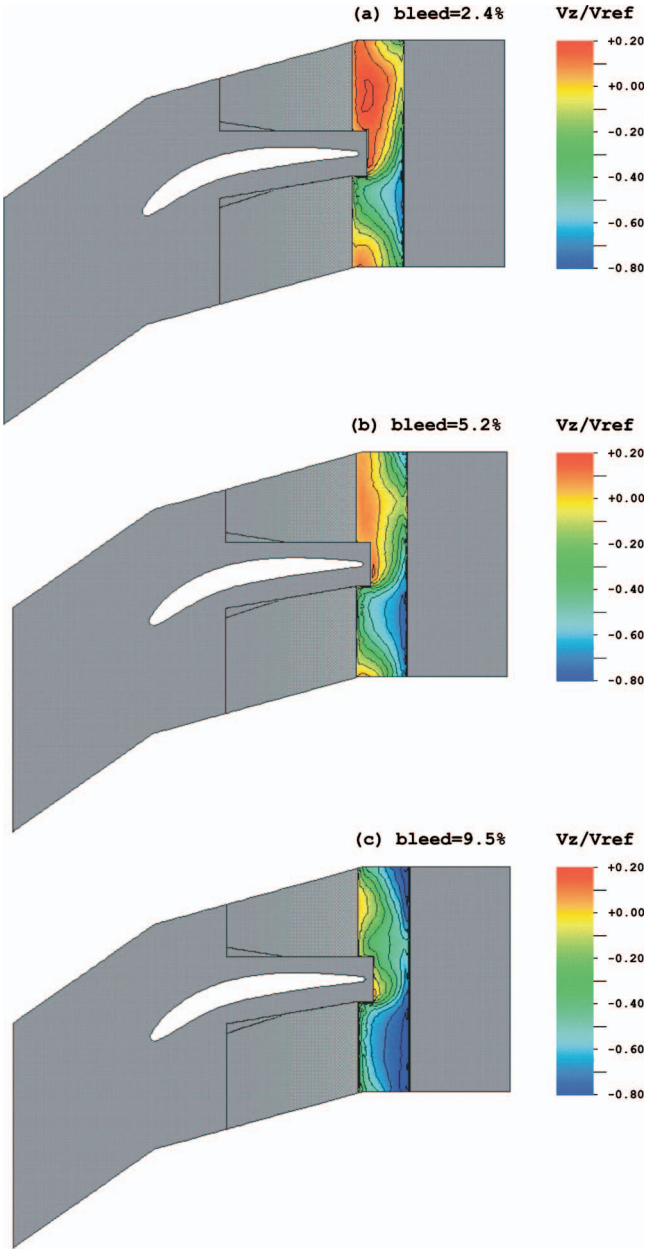

Fig. 5 Calculated contours of radial velocity within slot—(*a*) zero bleed; (*b*) 5.2% bleed; and (*c*) 9.5% bleed

9.5%. The data are for one blade pitch, with the circumferential location of the blade trailing edge corresponding to zero in the figure. Figure 8 shows a region of maximum static pressure downstream of the pressure surface (PS) of the passage, where primary flow enters the slot, and a region of minimum static pressure

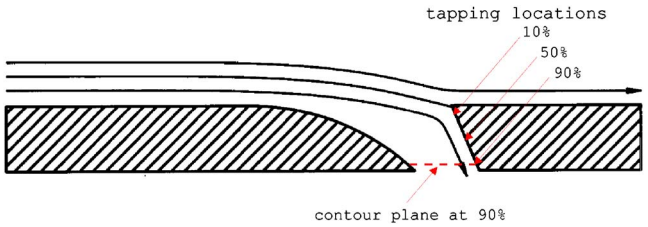

Fig. 6 Dividing streamline stagnating on rear surface of bleed slot

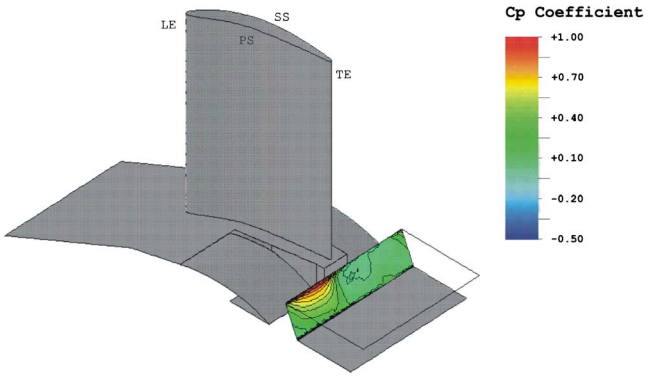

Fig. 7 Calculated (4.2% bleed) contours of static pressure across the rear surface of the bleed slot

downstream of the suction surface (SS) of the passage, where there is less flow entering the slot, and sometimes spillage. Generally the measured trends for pressure are well captured by the CFD.

At all bleed rates, the static pressure coefficient varied by about $\Delta Cp \approx 0.8$ between the pressure-surface and suction-surface sides of the slot (i.e., 80% of the inlet primary flow dynamic pressure, outside the endwall boundary layer). The pitchwise extent of the high-static pressure region was larger for greater bleed rates as flow entered the slot from across more of the blade passage, but the large gradients of static pressure downstream of the pressure surface of the blade persisted at 9.5% bleed. The large pressure gradients, which were the result of pitchwise nonuniform bleed into the slot, completely alter the simplistic view that the slot is a region of near-uniform static pressure downstream of the blade row. For the bleed holes and slot considered in Refs. [1,2], the static pressure variation was produced by the blade row in which they were located. In the ramped slot the variations are produced in the slot by the nonuniform stagnation pressure of the bleed flow and nonuniform radial flow into the slot.

Figure 9 plots the calculated pitchwise variation of static pressure across the rear surface of the bleed slot at three radial depths into the slot (10%, 50%, and 90%) for three bleed rates. The maximum static pressure on the rear surface of the bleed slot is always greatest near the endwall at 10% depth, where primary flow enters the slot and stagnates on the rear surface, and decreases further into the slot, away from the endwall at 50% and 90% depths. For all bleed rates, the largest gradients in static pressure occurred downstream of the blade trailing edge (i.e., moving from the pressure-surface to the suction-surface region of the slot).

Figure 10 shows calculated contours of tangential velocity across the rear surface of the bleed slot; yellow contours correspond to positive tangential velocity in the direction implied for the rotation of a rotor as indicated in Fig. 10, and blue contours correspond to tangential velocity in the opposite direction. (Tangential velocities are shown on the rear surface because the CFD code NEWT uses a nonzero slip velocity at solid surfaces with wall shear stresses modeled using wall function boundary conditions; although nonphysical, this allows a qualitative indication of the flow near to the surface.) Viewed in conjunction with Fig. 7, it can be seen that static pressure gradients across the rear surface of the bleed slot create the tangential components of velocity within the slot, such that flow is directed away from the high-pressure regions towards the adjacent lower pressure regions within the slot.

Calculated pitchwise variations of tangential velocity across the rear surface of the bleed slot are shown in Fig. 11 for three bleed rates, at three depths into the slot. The direction of the flow has a maximum positive component of tangential velocity predominantly downstream of the pressure surface of the blade and has a maximum negative component of tangential velocity downstream

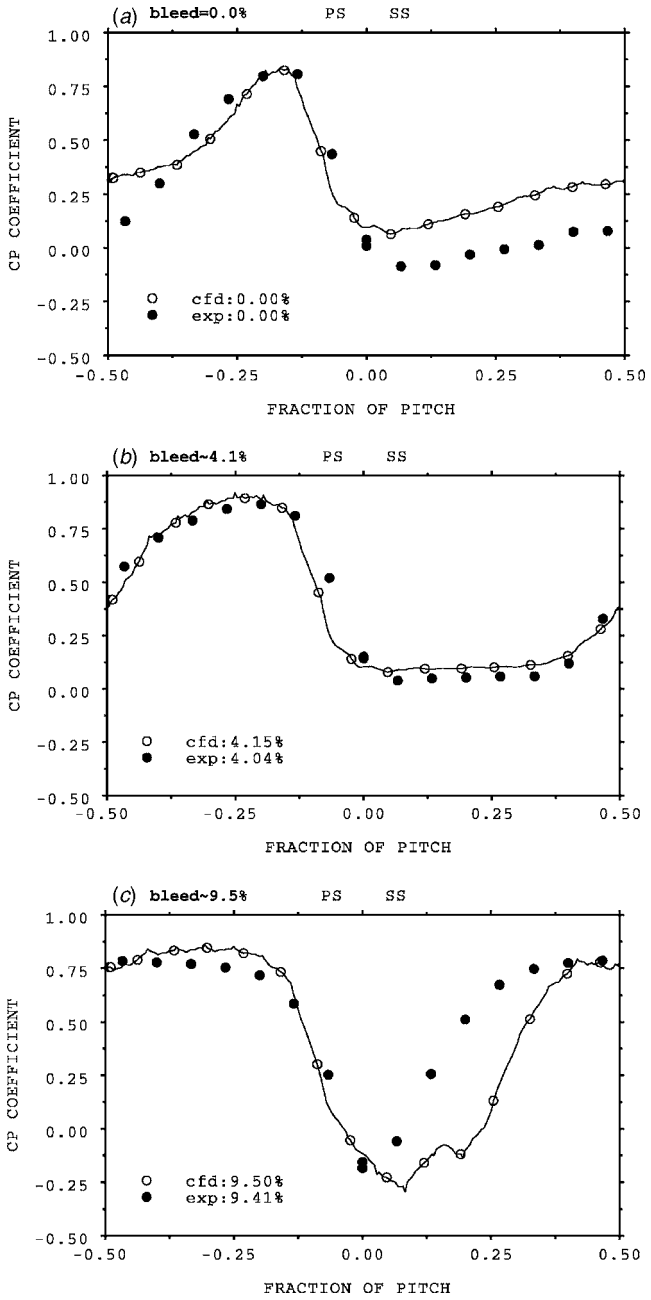

Fig. 8 Measured (exp) and calculated (CFD) pitchwise variation of static pressure (C_p) across the rear surface of the bleed slot for three bleed rates

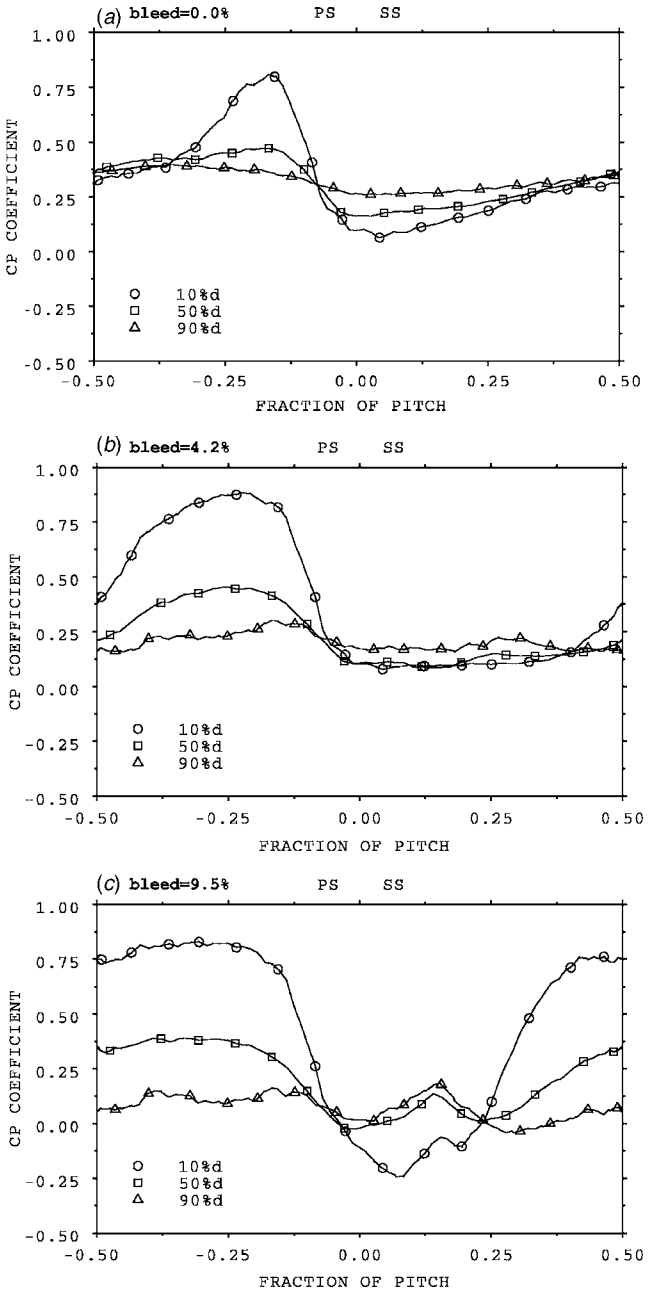

Fig. 9 Calculated pitchwise variation of static pressure (C_p) across rear surface of bleed slot at 10%, 50%, and 90% slot depth, for three bleed rates

of the suction surface of the blade. The maximum tangential velocity across the surface of the slot remained nearly constant at about 0.68 of the inlet freestream velocity for the three bleed rates shown in Fig. 11. Moreover, the magnitude of tangential velocity variations did not decrease through the depth of the slot (whereas the static pressure variations decreased) because the static pressure variations at 10% depth establish a bulk flow pattern within the slot and across the whole rear surface.

The resultant flow pattern within the bleed slot is illustrated in Fig. 12, which shows calculated contours of static pressure, tangential velocity, and axial velocity (with velocity vectors). These are all shown on a plane within the slot at 50% of the depth of the slot, for 3.7% bleed rate. The high-static pressure region (red contours) is shown in Fig. 12(*a*) downstream of the pressure surface of the blade, which is where primary flow enters the slot (Fig. 5). In the slot, flow moves tangentially away from the high-static pressure region, with contours of tangential velocity shown in Fig. 12(*b*). Red contours represent flow behind the blade trailing edge from downstream of the blade pressure surface towards the region of the slow downstream of the suction surface, while blue contours represent a flow in the opposite direction towards the middle of the blade passage and into the region of the slot downstream of the suction surface. Consequently, two flows with opposing tangential velocities collide along the rear surface of the slot, in the region of the slot downstream of the suction surface of the blade, shown by the vectors in Fig. 12(*c*). Where the two opposing tangential flows collide, they are turned away from the rear surface of the slot and are directed upstream in the negative axial direction (blue contours). Clearly, the region of the slot downstream of the suction surface contains backwards flow that is directed onto the

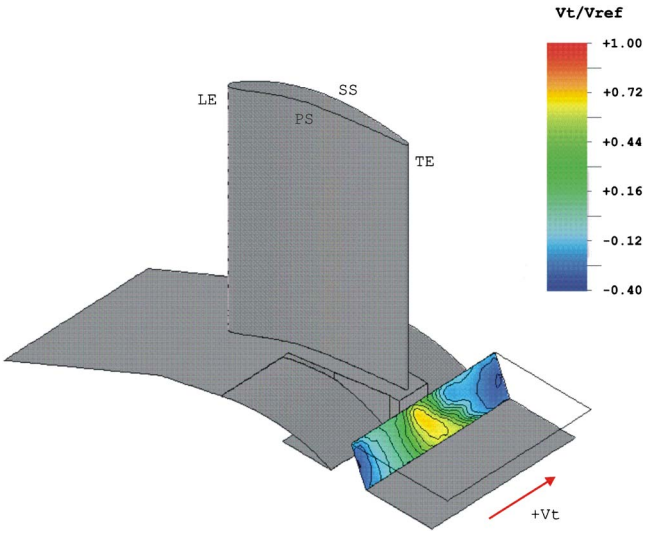

Fig. 10 Calculated (4.2% bleed) contours of tangential velocity (V_t) across the rear surface of the bleed slot

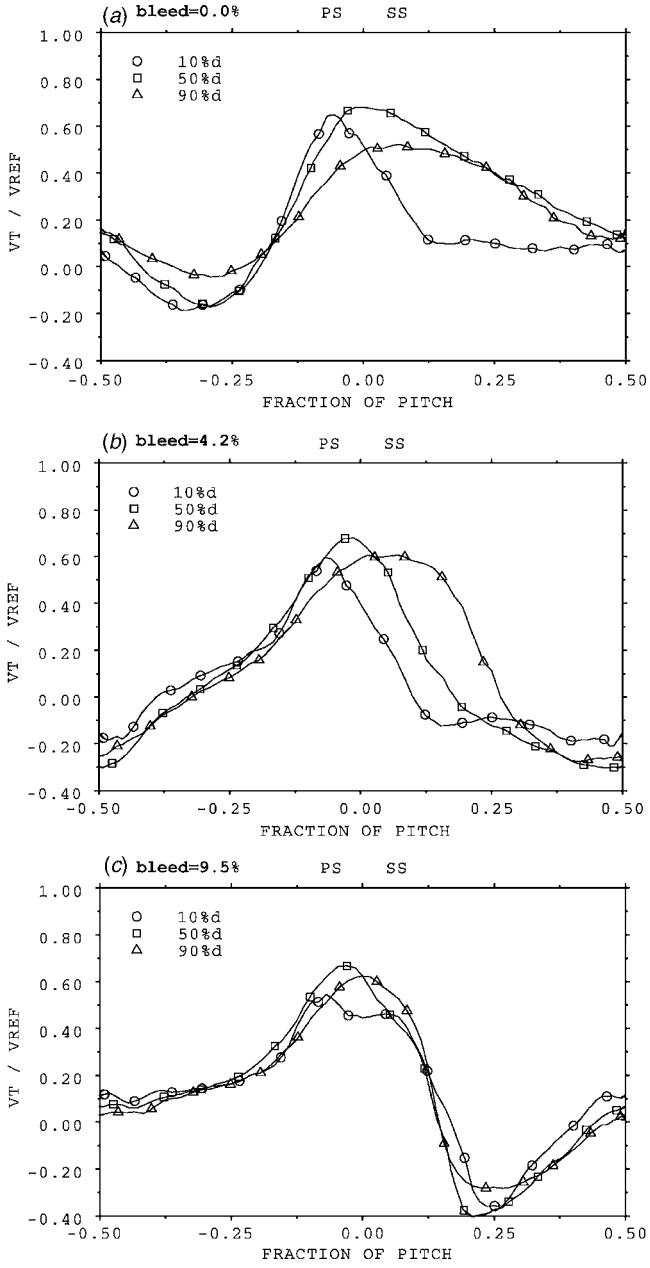

Fig. 11 Calculated pitchwise variation of tangential velocity (V_t) across rear surface of the bleed slot at 10%, 50%, and 90% depth, for three bleed rates

inlet ramp surface near the blade suction surface, causing or exacerbating separated flow over that part of the ramp surface. The flow pattern within the slot, shown in Fig. 12(*c*) and separated flow over the inlet ramp surface creates blockage, thereby preventing primary flow from entering the bleed slot through regions near the suction surface of the blade.

The flow structure illustrated in Fig. 12 makes it unlikely that primary flow enters the bleed slot downstream of the suction surface of the blade except at very high bleed rates. Instead, this region of the slot creates a path for fluid in the bleed slot to spill into the blade passage (i.e., the primary flow). Flow from the slot forms a spillage jet that penetrates the primary flow, as shown in Fig. 13(*a*) using streamlines calculated for 3.2% bleed rate conditions. The spillage flow re-enters the primary flow as a concentrated spillage jet with a strong radial component of velocity. The streamlines trace primary flow entering the bleed slot downstream of the pressure surface of the blade passage, being driven in a tangential direction behind the blade trailing edge into the region of the slot downstream of the blade suction surface, then spilling into the primary flow downstream of the suction surface of the blade passage. This behavior is shown by the calculated contours of radial velocity on a plane at 10% of the depth of the slot (i.e., near the endwall) in Fig. 13(*b*). The primary flow enters the slot (blue contours) near the pressure surface of the blade; downstream of the suction surface of the blade, the spillage jet is shown as a core of radial outflow (red contours). The spillage jet is turned from a nearly radial direction to the axial direction by the cross-flowing primary air stream. Viscous shearing and mixing between the spillage jet and primary flow generates additional loss in the primary flow, as measured downstream of the blade row and shown earlier in Fig. 3.

(The flow pattern illustrated in Fig. 13 for 3.2% bleed rate conditions is generally representative for all bleed rates. However, the amount of spillage and levels of loss are greatest at zero bleed rate and progressively decrease with higher bleed rate until a level of bleed is reached in which there is no spillage, for example the 9.1% bleed case in Fig. 3.)

Effect of Inlet Boundary Layer Thickness

To assess the generality of the flow mechanisms described above for the particular ramped bleed slot geometry, different bleed slot configurations were investigated numerically. These consisted of configurations with different ramp geometries and configurations with increased bleed off-take area. Calculations were also performed with different inlet flow conditions (i.e., boundary layer thickness and levels of boundary layer skew). The objective was first to determine the effect of these changes on the interaction of the slot with the primary flow; and second to identify whether the dominant mechanism of this interaction remained the strong pressure gradients and transverse flow within the slot. In summary the general flow structure described above persisted for all of these variations; the flow mechanism previously described was largely insensitive to details of the ramp geometry, slot area, and inlet boundary layer properties. For brevity, data are presented for only the effect of inlet boundary layer thickness.

The aerodynamic behavior of the ramped bleed slot was investigated using inlet boundary layer thickness from $\delta^*/C=0.007$ to 0.088, thereby covering most of the published range of representative compressor endwall boundary layers by Smith [5] and

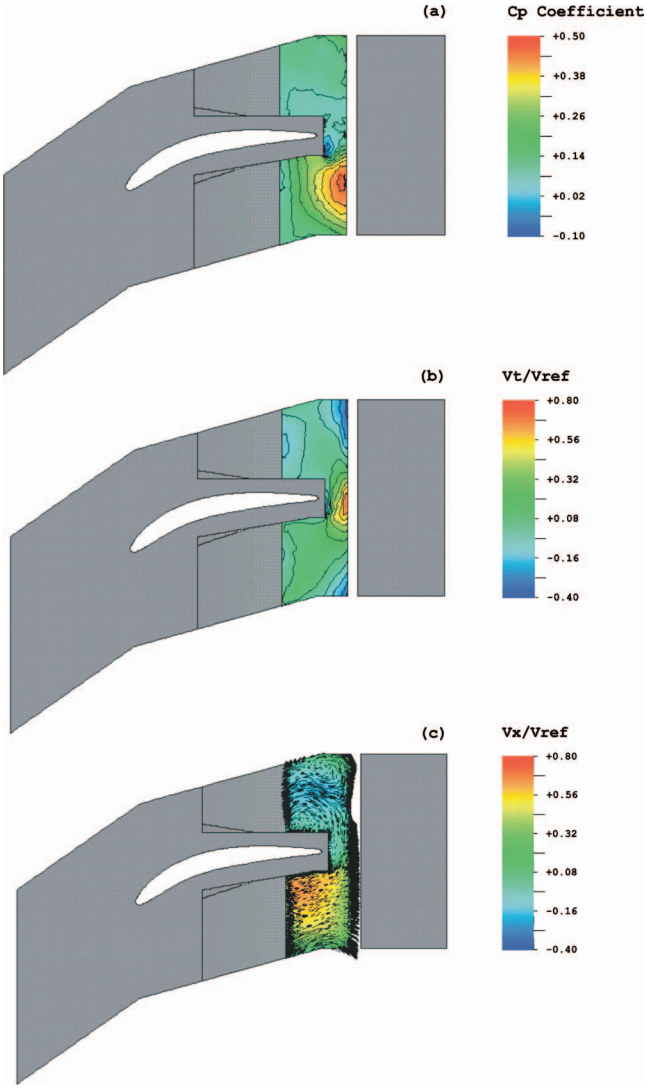

Fig. 12 Calculated (3.7% bleed) flow within bleed slot at 50% slot depth—(*a*) static pressure; (*b*) tangential velocity; and (*c*) axial velocity with vectors

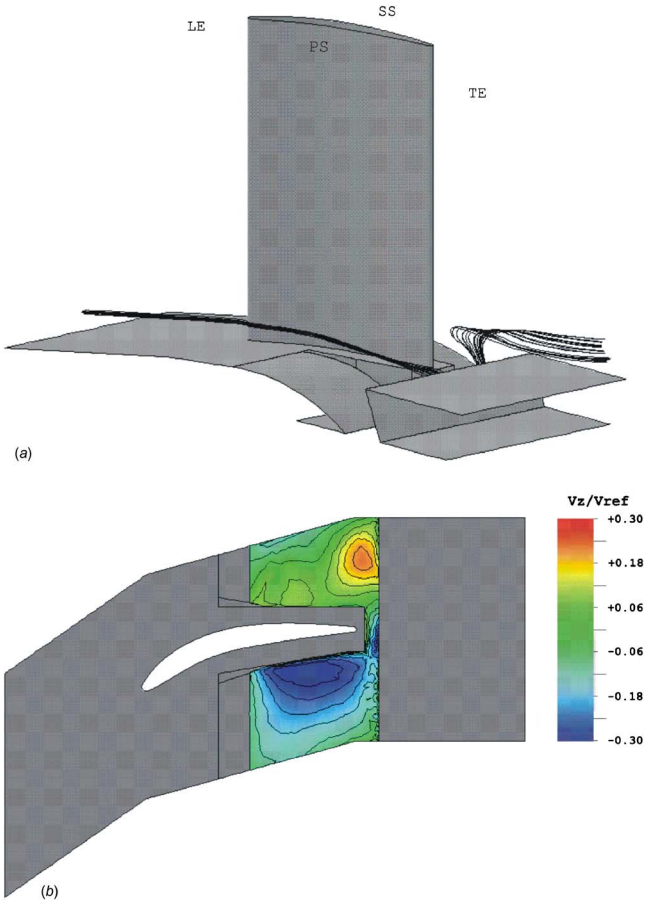

Fig. 13 Calculated (3.2% bleed) spillage jet—(*a*) calculated streamlines; and (*b*) radial velocity contours at 10% slot depth

Hunter and Cumpsty [6]. (The data so far presented in this paper were based on an inlet boundary layer with $\delta^*/C=0.018$.)

Although not shown in the interest of brevity, the primary flow structure downstream of the blade row was generally similar for all inlet boundary layer thicknesses to that shown in Fig. 3 for the case $\delta^*/C=0.018$ variations to the inlet boundary layer profile did not fundamentally change the interaction with the primary flow. As would be expected, as the endwall boundary layer thickness was increased, the size of the endwall suction-surface separation also increased.

Figure 14 plots the calculated pitchwise variation of static pressure across the rear surface of the bleed slot for five inlet boundary layer thicknesses at three bleed rates (note that the increment in boundary layer thickness between the five cases is not uniform). Data are presented on the rear surface of the slot near the endwall, at 10% radial depth into the slot. With increasing inlet boundary layer thickness the magnitude of the maximum static pressure (and the pitchwise static pressure variation) decreased. This decrease is explained by considering the origins of the dividing streamline separating the primary flow that enters the slot from that which passes over the slot, as represented schematically in Fig. 15 for a thin and thick inlet boundary layer profile. The dividing streamline stagnates on the rear surface of the slot causing a local increase of static pressure on the surface, whereby the dynamic pressure of the flow is recovered as static pressure. For a thin inlet boundary layer profile as depicted in Fig. 15(*a*), the dividing streamline originates from fluid near the edge of the boundary layer with total and dynamic pressure near the freestream values. By contrast, the dividing streamline for a thicker inlet boundary layer, Fig. 15(*b*), originates from further within the boundary layer where the total and dynamic pressure is lower.

Figure 16 plots the calculated pitchwise variation of tangential velocity across the rear surface of the slot at 50% slot depth, for five inlet boundary layer thicknesses and three bleed rates. With increasing boundary layer thickness the magnitude of the pitchwise variation of tangential velocity decreased only slightly, less than the relative decrease in the variation of static pressure that was shown in Fig. 14: the magnitude of tangential velocities across the rear surface of the slot always exceeded about 0.45 of the inlet freestream velocity. The flow pattern within the slot for the thin and thick boundary layer cases considered was generally similar to that already shown in Fig. 12.

Calculations were also carried out with skewed inlet boundary layer profiles, representative of that into a stator of a multistage compressor. The effect of skew was found to be small and in the interest of brevity the results are not shown here.

Discussion

It is appropriate to draw together some general features of the operation of the ramped bleed slot. The flow pattern is far from uniform, even though the slot has been positioned downstream of the trailing edge of the blades where, for the baseline (no bleed slot) configuration, the static pressure in the primary flow is nearly

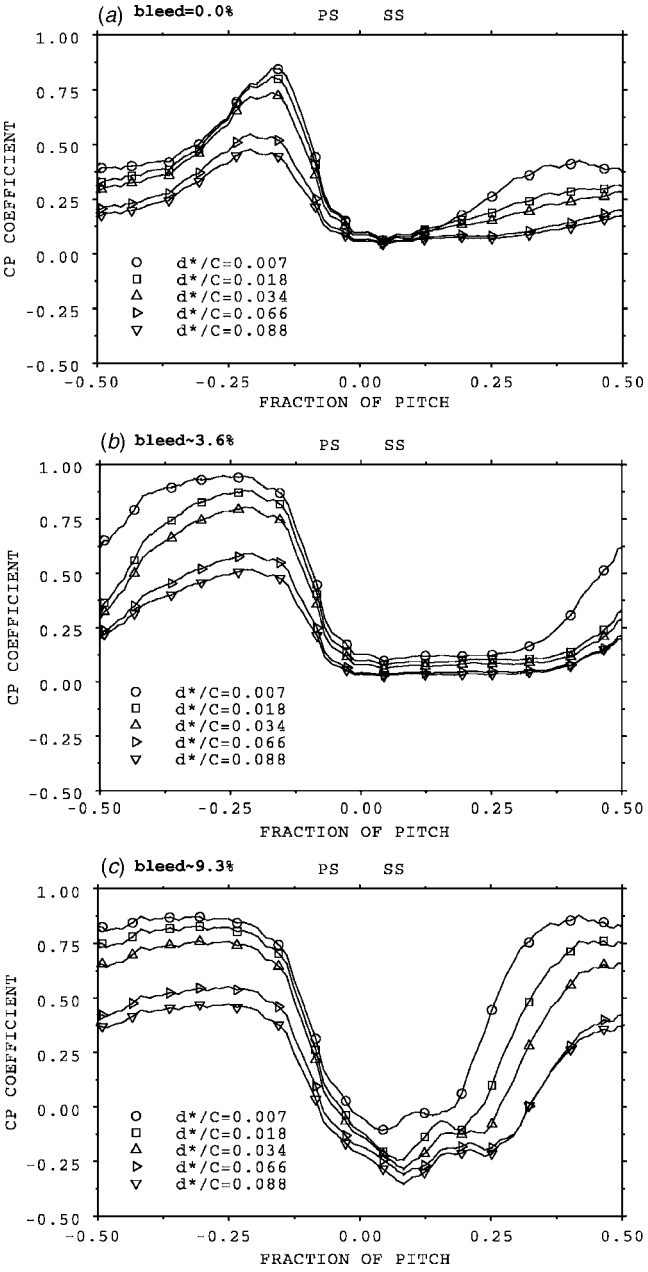

Fig. 14 Calculated pitchwise variation of static pressure (C_p) across rear surface of slot at 10% depth for three bleed rates and different inlet boundary layer thickness

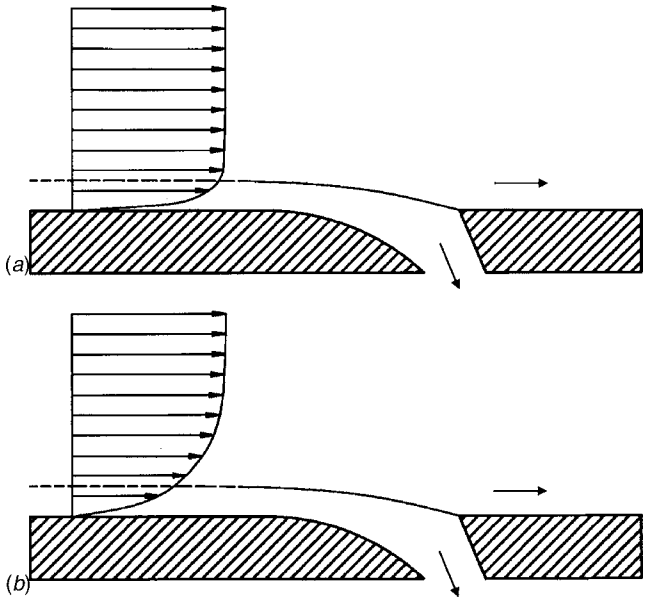

Fig. 15 Dividing streamline stagnating on rear surface of slot with inlet boundary layer total pressure profile—(*a*) thin inlet boundary layer; and (*b*) thick inlet boundary layer

uniform, see Fig. 4(*a*). This is very different from the use of holes or slots inside the blade passages, as in Ref. [1], where the primary flow has large static pressure nonuniformities produced by the lift on the blades themselves.

In the case of the downstream slot the nonuniformity in static pressure is produced by the nonuniformity in stagnation pressure. The flow near the endwall leaving a blade row is always nonuniform in the circumferential direction; in the case of a blade row with no tip clearance this nonuniformity is largely as a result of the three-dimensional separation that forms in the corner formed by the suction surface of the blade and the endwall. (In the case of a blade with tip clearance the clearance flow produces a region of lower stagnation pressure.) When the nonuniform flow hits an obstruction (in the case of the slot this is the downstream surface) the nonuniformity in stagnation pressure is converted into a static pressure nonuniformity and the static pressure field then sets up a pattern of velocities normal to the incident stream. So whereas the nonuniform flow out of the upstream blade row is of almost uniform direction, but varying velocity magnitude, the flow after striking the obstruction is nonuniform in direction as well.

The nonuniformity in direction has important consequences for the operation of the slot. Even if there is no flow withdrawn from the slot (i.e., zero bleed rate), the nonuniform static pressure leads to flow entering where the stagnation pressure is high (downstream of the pressure surface of the blade) and leaving the slot where the stagnation pressure is low (downstream of the suction surface of the blade). A flow moving radially out of the slot into a region of low stagnation pressure (the corner separation at the suction-surface/endwall corner) exacerbates the problem by increasing the size of this separation, leading to increased loss and blockage compared with a geometry with no slot, (Fig. 3).

When flow is withdrawn from the slot a dividing streamsurface exists below which flow is removed from the blade passage by the slot and above which the flow emerges back into the primary stream. At some point on this surface there has to be a stagnation point on the rear surface, with flow radiating away from this point. The flow moves tangentially in both directions to where the static pressure is low, which is in the region downstream of the suction surface. Where the tangential flows in opposite directions collide, in the low-static pressure region, they turn to form a flow radially outward.

The magnitude of the static pressure fields found here are on the same order as the dynamic pressure of primary flow outside the endwall boundary layer, while the magnitude of the tangential and radial velocities are of the same order as the primary flow velocity. The variation in static pressure is comparable to the inlet dynamic pressure of the freestream precisely because the radial velocity outprevents the flow from being brought to rest on the back surface of the slot in regions where the stagnation pressure is low (downstream of the blade suction surface). The large magnitude of the static pressure variation means that even when the amount of flow bled from the slot is large, the disruption caused can still be significant.

In the geometry reported on here there are ramps extending 65% of the axial chord upstream from the trailing edge and these are exposed to the static pressure field produced by the blades. There is no evidence to suggest that this has any major effect on

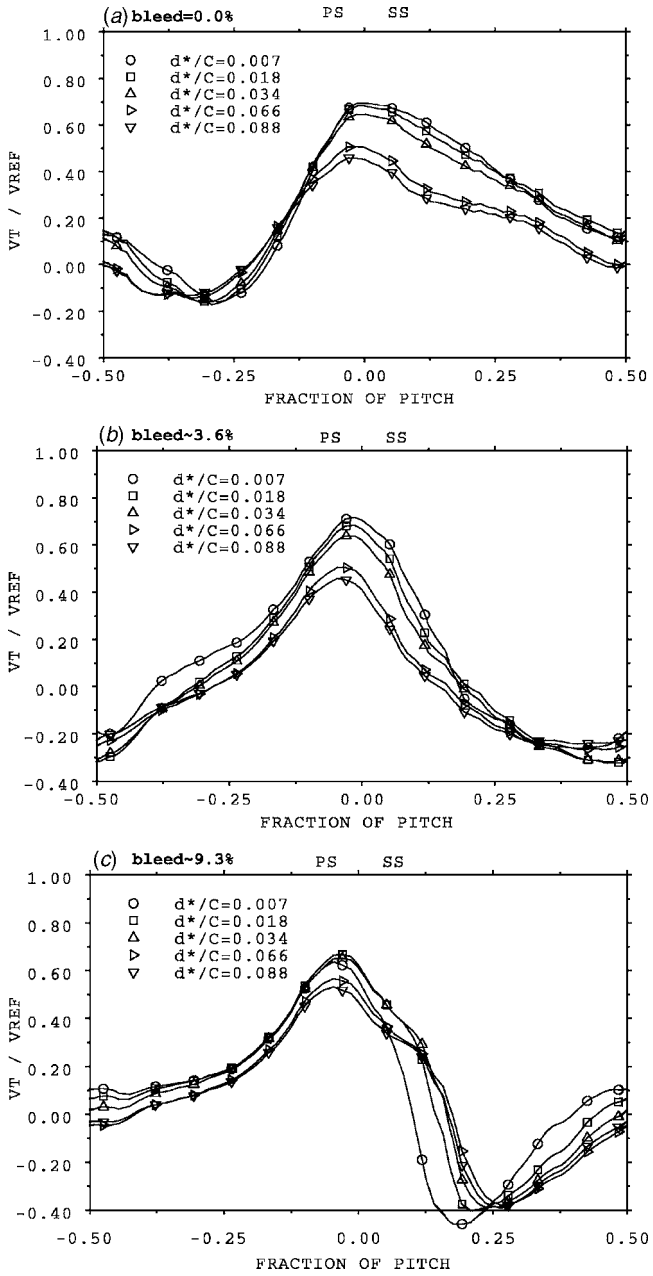

Fig. 16 Calculated pitchwise variations of tangential velocity (V_t) across rear surface of slot at 10% slot depth for different bleed rates and inlet boundary layer thickness

the flow, but it is the nonuniformity of the flow in the slots which is primarily responsible for the effect on the primary flow.

Conclusions

1. The ramped bleed slot provides a high bleed off-take pressure with less reduction in pressure as the bleed flow rate is raised than other holes and slots which have been examined.
2. The ramped bleed slot does produce large disturbances to the primary flow (which manifest themselves as increases in loss, blockage, and deviation) at small bleed off-take rates, even though it is downstream of the blade passages where the static pressure field imposed by the blades is weak.
3. The nonuniform stagnation pressure flow leaving the blade row interacts with the rear surface of the slot to produce static pressure variations in the slot. The static pressure variations are of the same order of magnitude as the dynamic pressure of the freestream primary flow. This is true both when no flow is taken from the bleed slot and when large bleed flow is taken.
4. The static pressure variations in the bleed slot set up tangential and radial velocities with order of magnitude similar to that of the primary flow in the freestream.
5. Whereas flow enters the slot downstream of the pressure surface of the blades, flow leaves the slot in the region downstream of the suction surface of the blades. The flow spilling from the slot into the primary flow interacts with the region of low stagnation pressure out of the blades, exacerbating the loss region.
6. The flow pattern and the slot performance were found to be only weakly affected by the thickness of the endwall boundary layer or by skew in the endwall boundary layer. The static pressure variations within the slot were reduced in magnitude with a thicker endwall boundary layer.
7. The formation of strong static pressure variations, and the consequent large tangential and radial velocities, is a fundamental response of a slot to a nonuniform flow. Therefore it is not surprising that alterations to the bleed slot geometry (for example, the area of the slot or details of the ramp profile) had little effect on the way the slot interacted with the primary flow.

Acknowledgment

The work, which was carried out at the Whittle Laboratory, was supported by Rolls-Royce plc., the Applied Research Programme of the Ministry of Defence, and the Department of Trade and Industry Aeronautical Research Programme. The authors wish to thank the sponsors for permission to publish this paper. However, the opinions expressed here are those of the authors and not necessarily those of any of the sponsoring organizations. The experimental program was greatly assisted by staff of the Whittle Laboratory Workshop, particularly Fred Bryant, John Saunders, and Arthur Davis. The authors acknowledge J. J. Bolger and S. J. Gallimore, from Rolls-Royce, for their support of this research, and W. N. Dawes for the use of his CFD code NEWT. The authors particularly wish to thank J. D. Denton for his contributions to this research project.

Nomenclature

C = blade chord
C_p = $(P_S\text{-}P_{S1})/1/2\rho V_{\text{ref}}^2$, static pressure coefficient
P_0 = local stagnation pressure
P_{01} = inlet freestream stagnation pressure
P_S = local static pressure
P_{S1} = inlet freestream static pressure
V_{ref} = cascade inlet free-stream velocity
V_x = axial velocity
V_z = radial velocity
Y_p = $(P_0\text{-}P_{01})/1/2\rho V_{\text{ref}}^2$, stagnation pressure coefficient
δ_{99} = boundary layer thickness
δ^* = endwall boundary layer displacement thickness
θ = endwall boundary layer momentum thickness
ρ = density

References

[1] Leishman, B. A., Cumpsty, N. A., and Denton, J. D., 2007, "Effects of Bleed Rate and Endwall Location on the Aerodynamic Behavior of a Circular Hole Bleed Off-Take," ASME J. Turbomach., **129**, pp. 645–658.
[2] Leishman, B. A., Cumpsty, N. A., and Denton, J. D., 2007, "Effects of Inlet

Ramp Surfaces on the Aerodynamic Behavior of Bleed Hole and Bleed Slot Off-Take Configurations," ASME J. Turbomach., **129**, pp. 659–668.
[3] Leishman, B. A., 2003, "The Aerodynamic Behaviour and Design of Compressor Bleed Slot," Ph.D. dissertation, University of Cambridge, Cambridge, UK.
[4] Dawes, W. N., 1993, "The Practical Application of Solution-Adaption to the Numerical Simulation of Complex Turbomachinery Problems," Prog. Aerosp. Sci., **29**, pp. 221–269.
[5] Smith, L. H., 1970, "Casing Boundary Layers in Multistage Axial-Flow Compressors," Proceedings of the Symposium on Flow Research on Blading, Brown Boveri & Co Ltd, Baden, Switzerland, *Flow Research on Blading*, L. S. Dzung, ed., Elsevier, New York.
[6] Hunter, I. H., and Cumpsty, N. A., 1982, "Casing Wall Boundary-Layer Development through an Isolated Compressor Rotor," ASME J. Eng. Power, **104**, pp. 805–817.

Interaction of Tip Clearance Flow and Three-Dimensional Separations in Axial Compressors

Semiu A. Gbadebo
Siemens Industrial Turbomachinery,
Lincoln, UK

Nicholas A. Cumpsty
Imperial College,
London, UK

Tom P. Hynes
University of Cambridge,
Cambridge, UK

This paper considers the interaction of tip clearance flow with three-dimensional (3D) separations in the corner region of a compressor cascade. Three-dimensional numerical computations were carried out using ten levels of tip clearance, ranging from zero to 2.18% of blade chord. The 3D separations on the blade suction surface were largely removed by the clearance flow for clearance about 0.58% of chord. For this cascade, experimental results at zero and 1.7% chord tip clearance were used to assess the validity of the numerical predictions. The removal mechanism was associated with the suppression of the leading edge horseshoe vortex and the interaction of tip clearance flow with the endwall boundary layer, which develops into a secondary flow as it is driven towards the blade suction surface. Such interaction leads to the formation of a new 3D separation line on the endwall. The separation line forms the base of a separated stream surface which rolls up into the clearance vortex. [DOI: 10.1115/1.2720876]

Introduction

Tip clearance flow has been found to control the formation of three-dimensional (3D) separation on the blade suction surface near the endwall of compressor stators. This was clearly demonstrated by Dong, Gallimore, and Hodson [1], who showed a clear hub separation on the stator of a single stage compressor with no clearance. With the introduction of a small clearance (of the order of 1% of chord) between the blade and the stationary hub, the separated region on the blade suction surface was greatly reduced and this was reported to result in improved efficiency. McDougall [2] also found a large corner separation for a sealed rotor tip, similar to the separation at a stator hub, but this was virtually removed when a small clearance was introduced. In the above studies, the removal of separation was attributed to leakage flow energizing the low-momentum fluid in the suction surface/endwall corner. The explanations offered for these observations are best described as heuristic and a complete understanding of the process involved in the removal has not been given because of lack of understanding of the formation of the 3D separation itself.

Because of its recognized importance for determining compressor performance (loss, blockage, and surge margin) tip clearance flow has been widely studied. Storer and Cumpsty [3,4] showed the effects of clearance on overall performance and gave an approximate model for estimating the effect of clearance on loss; the simple model agrees well with measurements, establishing that some features of the flow are independent of the fine detail. The effect of tip clearance on the performance of both stationary cascades and rotating turbomachinery was reviewed by Peacock [5,6] from the perspective of the overall flow features. The conventional engineering explanation for the 3D separation is that it occurs due to the influence of both the inherent adverse streamwise pressure gradient and the circumferential pressure gradient in the blade passage. The streamwise pressure gradient causes weakening and thickening of the suction surface and endwall boundary layers, while the circumferential pressure gradient needed to turn the main passage flow causes secondary flow; that is, the endwall boundary layer is driven towards the suction surface. The interaction of the weakened boundary layers under the adverse pressure gradient with the secondary flow results in the three-dimensional nature of the separation.

An alternative basis for description of how a 3D separation forms on the suction surface/endwall corner of compressors was given in Gbadebo [7] for blades without tip clearance. The formation in linear cascades of compressors, together with the types of singular points (points of zero shear stress) associated with the separation, was also described in Gbadebo, Cumpsty, and Hynes [8]. The 3D separation is characterized by the appearance of separation lines along which limiting streamlines (or skin-friction lines) on the suction surface and on the endwall converge. The suction surface and endwall separation lines, both of which are found to originate from a common singular point on the endwall corner, bound the separated region, as illustrated in Fig. 1 for a cascade with no clearance. The point takes the form of a multiple node-saddle singularity (a node (N_2) on the endwall and saddle point (S_3) on the suction surface). The nodal point (N_2) is the point where the suction-side leg of the endwall dividing streamline interacts with the suction surface because of overturning caused by the imposition on the endwall boundary layer of the main passage circumferential pressure gradient. The dividing streamline forms the base of the leading edge horseshoe vortex system; the horseshoe vortex springs from the leading edge stagnation (saddle) point of separation (S_1) and the corresponding nodal point of attachment (N_1).

The flow in the endwall region of unshrouded axial turbomachines is altered by the presence of the tip gap, which allows a high-velocity jet from the pressure side to the suction side of the blade tip; although the geometry is more complex, the flow often appears much simpler in form. The high-velocity leakage jet usually continues across the blade passage from the suction surface towards the pressure surface where it interacts with the endwall secondary flow to form the clearance vortex. Two mechanisms are known to be responsible for tip leakage flow, the principal one being due to the static pressure difference between the pressure and suction surfaces of the blade. The other, found over rotor tips or the tips of unshrouded stators, is due to viscous stresses, which cause the fluid to be drawn through the gap by the relative motion of the blade and the endwall.

This paper is aimed at clarifying the mechanism of alteration or removal of 3D separations on the blade suction surface by the clearance flow. Calculations were performed using ten levels of

Contributed by the International Gas Turbine Institute of ASME for publication in the JOURNAL OF TURBOMACHINERY. Manuscript received August 30, 2006; final manuscript received September 7, 2006. Review conducted by David Wisler. Paper presented at the ASME Turbo Expo 2006: Land, Sea and Air (GT2006), May 8–11, 2006, Barcelona, Spain, Paper No. GT2006-90071.

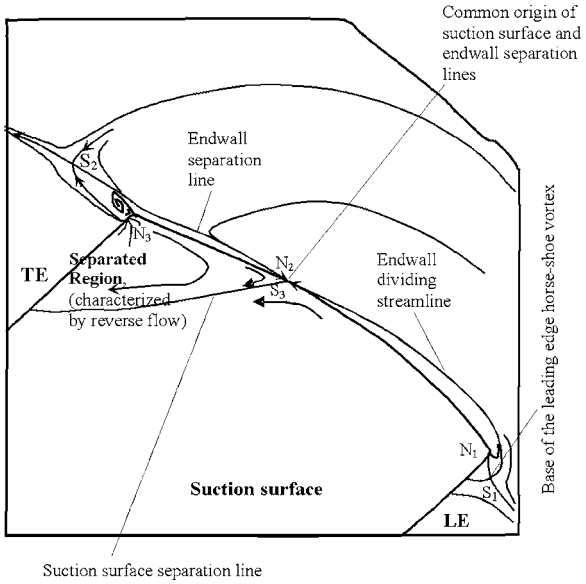

Fig. 1 Description of formation of 3D separation in compressor blade passage. S=saddle point, N=node. (Subscript denotes singular point number.)

tip clearance, ranging from zero to 2.18% chord to study the interaction of the clearance flow with the separated region. Changes in the surface flow pattern and the flow field within the clearance space were examined as 3D separation is removed from the suction surface by the clearance flows. Experimental results at zero and 1.7% chord tip clearance were used to validate the numerical predictions.

Relative rotation between the endwall and the blade will be accompanied by skew within the inlet boundary layer and by the action of increased levels of circumferential frictional forces acting on the clearance and secondary flows. These will influence, to some extent, the interaction of the clearance flow and the flow within the 3D separated region but are beyond the scope of the present study.

Cascade Description, Experimental and Computational Procedures

A low-speed compressor cascade was used in this study. It consists of five blades with a standard NACA-65 thickness distribution on a circular arc camber line. The cascade is described in [8], where it is referred to as cascade 1. The geometric, measured flow, and inlet boundary layer parameters are shown in Table 1. Surface mounted tufts were used for flow visualization on the cascade, while exit area traverses were carried out at about 50% axial chord from the trailing edge. A Kiel probe, positioned in the nominal flow direction (axial), was used so that only total pressure loss was measured. The measurement procedure is the same as that described in [7].

The computational fluid dynamics (CFD) code employed is MULTIP; a fully three-dimensional multi-stage Reynolds averaged Navier-Stokes solver of Denton [9], which is capable of modeling tip clearance and shroud leakage flows in turbomachinery. The calculations were carried out using a control volume formulation on an "H" type mesh. The clearance region is modeled approximately by tapering the blade tip over a small number of mesh planes to a single point. The usual periodic boundary condition is then applied at that point where the blade thickness is zero. Despite this approximation, most features of flows calculated with the code agree well with measurements with clearance [4], although a simulation of the tip gap with a separate block (as in multi-block flow solvers) is likely to improve the agreement further. The numerical scheme is second-order accurate in space and solutions can be obtained for flows with Mach number of about 0.1 to supersonic flows. The wall shear stress is modeled using wall functions that assume the first grid point from the surface to lie at the start of the logarithmic region of a turbulent boundary layer. Away from the surfaces, shear stresses are obtained by a simple eddy-viscosity mixing-length turbulence model.

In order to achieve accurate solutions in reasonable computer run times, the calculations were performed on the cascade from the endwall to the line of symmetry at mid-span. Grid sensitivity tests carried out show that the separated flow pattern is most sensitive to grid distribution in the spanwise direction. Consequently, about seventeen grid points were used to resolve the endwall boundary layer while eleven grid points were used for the boundary layer on the blade surfaces. The total numbers of grid points in the pitchwise, streamwise, and spanwise directions were 49 $\times 158 \times 93$, respectively, while the upstream and downstream boundaries were set at around 50% chord from the leading and trailing edges. The experimentally measured inlet profiles of stagnation pressure and absolute flow angles were used to define the inlet conditions, while the measured inlet and exit static pressures were used as a guide for fixing the pressure ratio. The tip clearance is conventionally non-dimensionalized with respect to blade chord, but it is more appropriate to refer to the tip gap in terms of incoming endwall boundary layer height, since this is a length scale relevant to the secondary flow and the horseshoe vortex. Tip gaps are shown in Table 2 using displacement thickness of the inlet boundary layer, together with the number of grid points across the gaps. The computational procedure is similar to that described in [8].

Table 1 Compressor cascade geometry and inlet boundary layer parameters

Geometric parameters	
Profile	NACA-65
Chord (m)	0.3
Pitch-chord ratio	0.6
Blade height-chord ratio	1.45
Max. thickness chord ratio	0.05
α_1	45.0 deg
Camber angle	45.5 deg
Stagger angle	22.25 deg
Aerodynamic parameters	
Incidence	0.0 deg
Re (inlet)	4.8×10^5
2D diffusion factor	0.47
de Haller no.	0.75
Inlet boundary layer parameters	
δ (mm)	11.5
δ^* (mm)	1.497
H	1.24

Results and Discussion

Datum (Zero Clearance) Case. Figure 2(*a*) shows suction surface tufts for the cascade at zero clearance and these agree well with the computed streamlines shown in Fig. 2(*b*). A separation

Table 2 Cascade tip clearance gaps

τ/c (%)	0.0	0.16	0.24	0.33	0.45
τ/δ^* (%)	0.0	32.0	48.1	66.1	90.2
Grid points	0	4	5	6	7
τ/c (%)	0.58	0.74	1.17	1.73	2.18
τ/δ^* (%)	116.2	148.3	234.4	356.7	436.8
Grid points	8	9	11	13	14

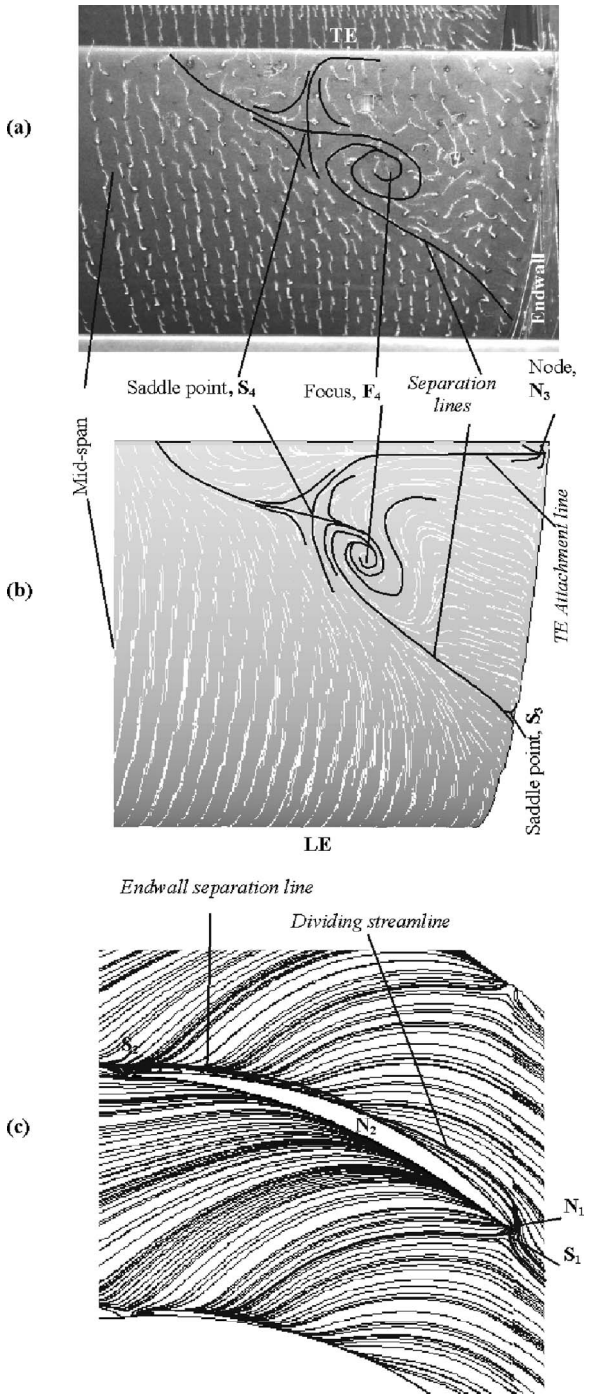

Fig. 2 (*a*) Suction surface tufts. (*b*) Computed suction surface limiting streamlines. (*c*) Computed endwall limiting streamlines pattern for the compressor cascade at zero clearance. S=saddle point, N=node, F=focus. (Subscript denotes singular point number.)

line, marked by the convergence of neighboring streamlines, can be seen originating from a saddle point (S_3) at about 35% chord from the leading edge at the endwall. This separation line stretches diagonally and winds into a spiral node or focus (i.e., a vortex). The line then passes through a saddle point adjacent to the focus and extends spanwise to about 60% chord from the endwall at the trailing edge. The key singularity on the suction surface is this saddle point-focus pair (S_4,F_4). At the trailing edge adjacent to the endwall is the node N_3, from which an attachment line originates, evident by the divergent surface streamlines. This is the line along which some of the separated blade boundary layer and overturned endwall boundary layer interact with the suction surface.

The computed streamlines on the endwall in Fig. 2(*c*) can be seen to reveal a strong secondary flow caused by the drifting of the boundary layer towards the suction surface. It also shows the basic singular points that occur in the region, similar to the illustration presented in Fig. 1.

The good agreement between the measured and predicted surface flow patterns for the cascade is matched by the measured and calculated total pressure loss contours shown in Fig. 3. The maximum loss is found to be about 54% of the inlet dynamic head for both calculation and measurement.

Influence of Clearance Flow on Suction Surface and Endwall Streamlines. Figure 4 shows computed flow patterns for four representative clearances. The 0.16% chord and 0.24% chord clearances are typical of the pattern for clearance with this cascade below about 0.58% of chord. The streamline patterns for these cases have many features in common with that at zero clearance, shown in Fig. 2, so that the separation line on the suction surface serves as a barrier between the separated region downstream and the combination of upstream suction surface boundary layer away from the endwall and the region occupied by the clearance flow near the endwall. It is, however, interesting to see how the clearance flow starts to influence the entire surface flow pattern and singularities. At the smallest clearance (0.16% chord), the main saddle focus pair (S_4,F_4) on the suction surface at zero clearance still exists although somewhat squashed. Both saddle point S_3 and nodal point N_3 from which the original separation line and attachment lines respectively emerge, are now shifted away from the endwall. A new saddle focus pair (S_5,N_5) can also be seen at the trailing edge at a distance of about 44.0% chord (30% span) from the endwall. The separated region on the suction surface can be seen to have widened at this smallest clearance and this is reflected in the increase in the number of singularities and consequent high exit loss (see Fig. 8).

At both 0.16% and 0.24% chord clearances, the endwall limiting streamlines show a "bubble-like" region occupied by the clearance flow, which is bounded by an attachment line near the pressure surface and a separation line near the suction surface respectively. A close inspection suggests the origin of these lines to be a nodal point of attachment in place of the original leading edge saddle-node pair (N_1,S_1), that now seems to have been weakened as clearance increased and eventually disappeared at 0.58% clearance, as shown in Figs. 4 and 6. Similarly the two lines appear to terminate on a nodal point of separation downstream, where the clearance flow and secondary flow converge.

For these small clearances, the flow leaving the clearance gap can be seen to roll up into a vortex formed from a separated stream surface whose base is the separation line on the endwall. However, this has relatively little effect on the overall endwall flow. The secondary flow still significantly dominates the clearance flow, thus forcing the rolled over vortex to interact with the flow on the suction surface of the blade. At these small tip clearances, the vortex appears from the calculations to lose all coherence well before the trailing edge as it merges into the separated corner flow. However, at 0.24% clearance, the interaction of the vortex causes the size of the separated region on the suction surface to be reduced slightly and moved somewhat downstream. As can be seen, only the saddle point of separation (S_4) and the trailing edge nodal point of attachment (N_3) remain on the suction surface.

When the clearance is increased to 0.58% chord there is a radical change in the surface flow pattern with the large roll-over of the clearance flow seeming to remove most of the separation on the suction surface. Although the streamlines still show partial

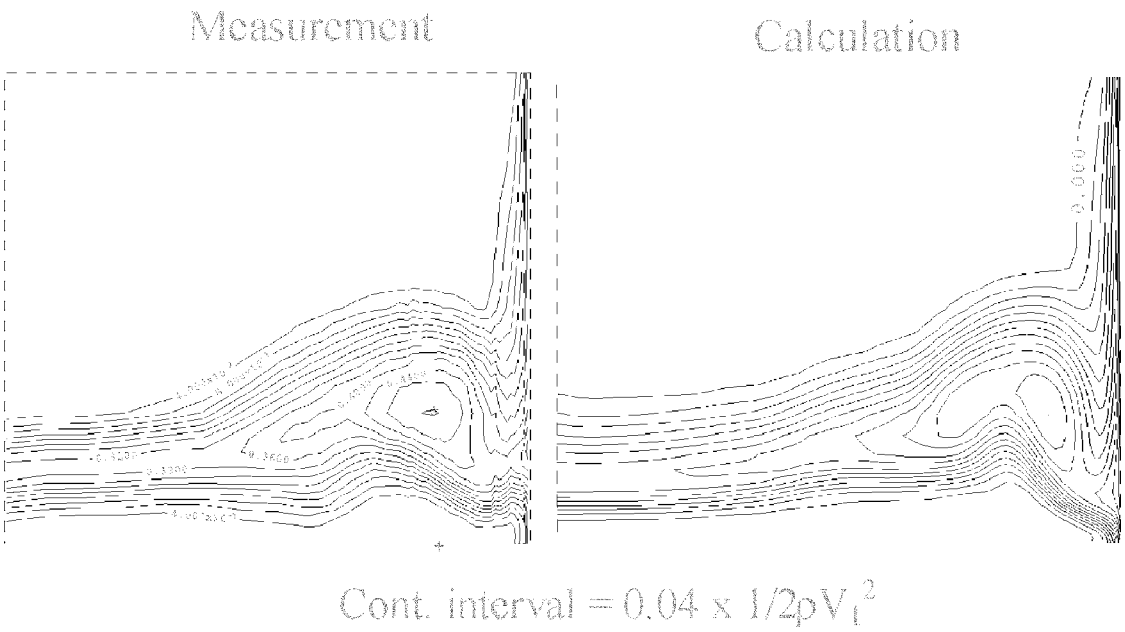

Fig. 3 Contours of measured and computed exit total pressure loss coefficient for the compressor cascade at 50% chord from trailing edge, zero clearance

convergence in the separated region, all singular points have been removed from the suction surface by the clearance flow.

When the clearance is increased to about 1% chord, Fig. 4 shows the pattern changes again. This time the clearance flow is obviously greater and the higher momentum of this causes the separation line, formed where the clearance flow and the secondary flow collide on the endwall, to move towards the middle of the passage. The increased difference in the direction of the two streams and increased strength of the clearance flow leads to a roll-up of the free shear layer into a more coherent vortex, which persists downstream of the blade passage. In this case, the clearance flow mainly blocks off the secondary flow, both of which interact very little with the suction surface, as can be seen from Fig. 4. In other words, 3D separation disappears from the suction surface because the clearance flow prevents the secondary flow from interacting with the suction surface boundary layer near the endwall. The suction surface now has a streamline pattern, which resembles the uniform conditions near mid-span even close to the tip. Computations show similar behavior as the clearance is further increased. The clearance vortex rests between the suction-surface side and the separation line on the endwall, with the vortex center moving spanwise in the streamwise direction. The presence of the vortex near the suction surface is believed to be a cause of the reduction of static pressure on the suction surface near the tip and an increased local blade force.

Figure 5 shows the experimental flow visualization of the endwall and suction surface pattern for 1.7% clearance. This confirms the calculated removal of the 3D-separated region on the suction surface and the strong convergence on the endwall.

Although the singularities associated with separations on the suction surface are predicted to be removed for this blade by tip clearance beyond about 0.55% chord, the Navier-Stokes equations apply in the same way, with the same notion of limits as distance from the surface goes to zero. As a result the topological rule examined in [7,8] requires that with clearance, two more nodes than saddle points should exist within the blade passage. At small clearance the endwall flow pattern in Fig. 4 clearly suggests these two nodes to be the point at which the attachment line begins and the point at which the separation line ends, respectively; the suction surface on its own shows equal number of nodes and saddles, similar to the zero clearance case. The surface flow patterns calculated for all clearances greater than 0.55% do not show the surface singularities evident at small clearances and the experimentally observed tuft patterns for large clearance likewise show none of these features.

Physically, 3D separation would not have been completely removed from the suction surface if any singularity associated with it still exists on the surface. However, the attachment and separation lines still evident on the endwall at high clearances presumably indicate the existence of the two nodes, as observed at small clearance, although the surface flow pattern makes them somehow impossible to visualize. Furthermore, Lighthill's [10] criterion is that appearance of separation and attachment lines on a surface is always associated with singularities. On the other hand, it may be that the nodes are located in corners over the blade tip, but it is impossible to verify this because of the limitation in the modeling of tip clearance in the present computation.

The computed velocity vectors at the leading edge/endwall junction of the blade, shown in Fig. 6, show the influence of the clearance flow on the leading edge horseshoe vortex. The magnified view covers close to about 1% chord from the endwall. An appropriate length scale relevant to the horseshoe vortex would be one of the parameters of the incoming endwall boundary layer height. Hence, Table 2 also refers to the tip gap in terms of boundary layer displacement thickness. At a clearance of 0.24% chord, which is about 48% of the displacement thickness, the size of the horseshoe vortex can be seen to have been diminished, compared with the no-clearance case. At 0.58% clearance, Table 2 indicates the tip gap to be of the order of the displacement thickness itself, and as Fig. 6 shows, there is virtually no horseshoe vortex. Computations show complete removal of the horse-shoe vortex when the clearance is further increased. The reduction or removal of 3D separation on the blade suction surface is therefore believed to be associated with the reduction or elimination of the leading-edge horseshoe vortex, which provides the origin of the dividing streamlines on the endwall observed at zero and small clearance. As explained in the introduction, the suction-side leg of this dividing streamline terminates on the singular point N_2 at the corner from which the original 3D separation lines on the suction surface and endwall begin.

Flow within the Clearance Space. The axial variation of leak-

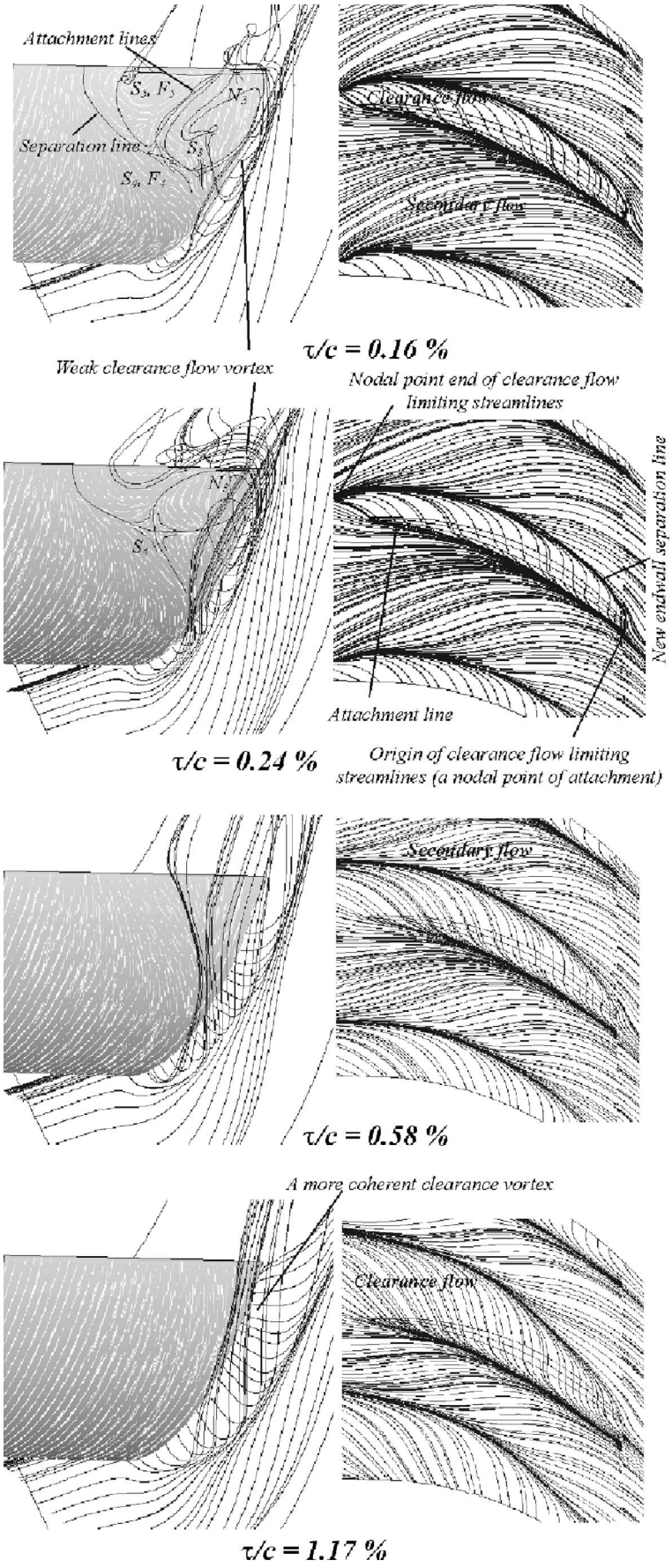

Fig. 4 Influence of clearance flow on suction surface and endwall streamlines; N=node, F=focus, S=saddle point

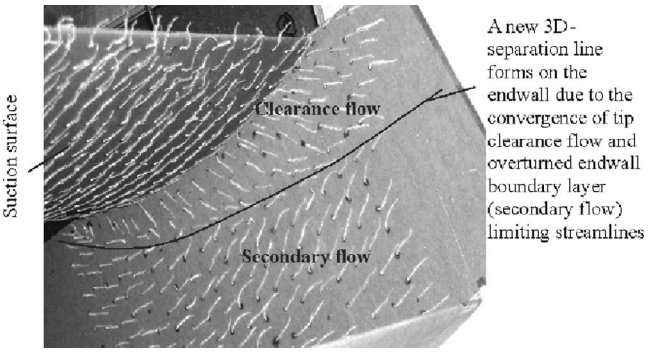

Fig. 5 Cascade endwall tuft flow pattern at 1.7% chord tip clearance

age velocity at the tip gap centerline, normalized by the inlet velocity, is plotted in Fig. 7(*a*) showing clearly how the leakage flow strengthens with increase in tip clearance. The maximum leakage velocity occurs at about 1.7% chord tip clearance with a further increase in clearance leading to a reduction in the peak velocity. It is also evident from the figure that the location of the maximum velocity, which corresponds to the peak loading, shifts backward from near the leading edge at minimum clearance to about 31% axial chord at 1.7% chord tip clearance. The location then remains unchanged with further clearance increase. At the axial location of the peak leakage velocity for each clearance gap, the radial variation of the normalized leakage velocity within the clearance space is plotted in Fig. 7(*b*). This figure suggests that the peak overall leakage velocity increases and the location moves towards the endwall until the clearance reaches about 1.17% or chord, roughly equal to twice the inlet boundary layer displacement thickness, beyond which it remains more or less constant.

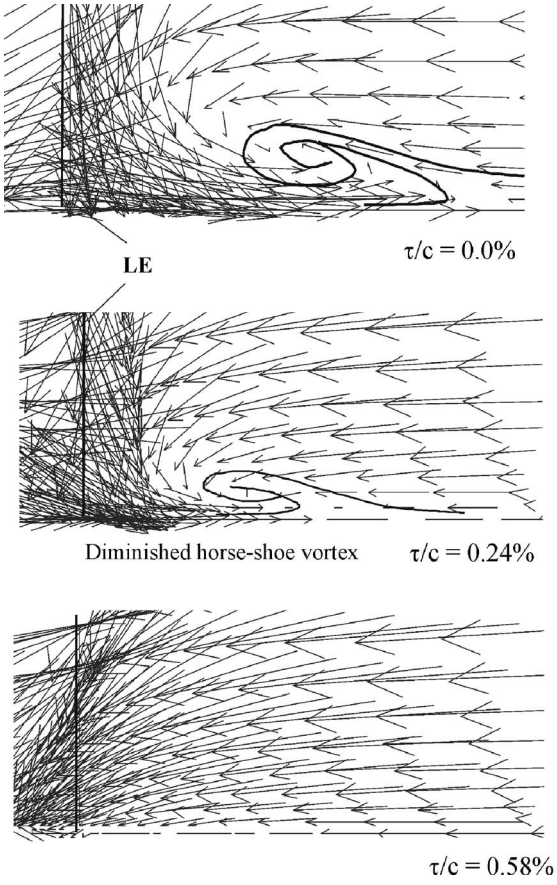

Fig. 6 Velocity vectors at the leading edge/endwall corner of the blade showing the influence of clearance flow on the leading edge horseshoe vortex; clearance values of 0.0, 0.24, and 0.58% chord

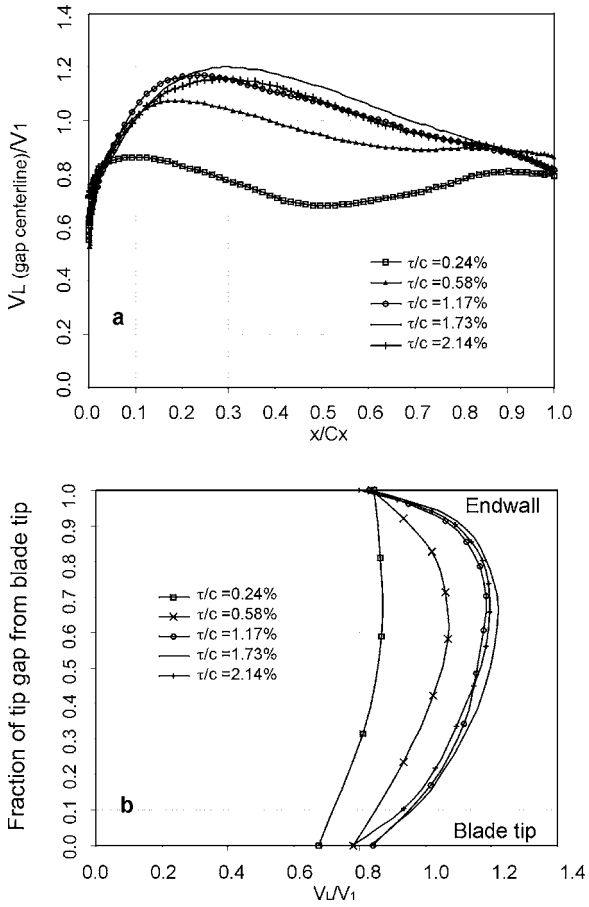

Fig. 7 Influence of tip gap on the leakage velocity for the compressor cascade. (*a*) Axial variation of the clearance centerline velocity. (*b*) Radial profiles of the clearance velocity at peak-loading location for each gap.

Calculated Overall Exit Loss. The calculated overall exit total pressure loss variation is shown in Fig. 8. This is the mass averaged loss, including the loss from the endwall boundary layer out to mid-span. For small clearance, less than about 0.2% chord, the effect of clearance for this cascade is to increase loss consistent with the increase in the number of singularities, as noted in Ref. 8.

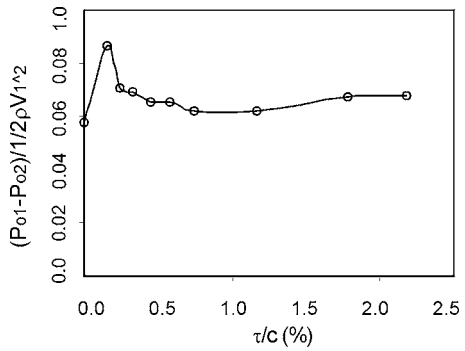

Fig. 8 Influence of clearance gap on calculated exit total pressure loss

Beyond about 0.5% chord clearance the loss is lower but nearly constant, though always greater than the zero clearance case. The overall values are similar to those measured by Storer and Cumpsty [3], though they found the loss coefficient to be highest for zero clearance, falling to a minimum for clearance of about 1% chord.

Conclusions

The following conclusions can be drawn from the present work:

1. For this cascade of blades, the loss was predicted to be highest for a small clearance, approximately 0.2% chord. For a clearance of 0.5% chord, when the clearance was comparable with the inlet boundary layer displacement thickness, the loss was much reduced and fell only slightly to a minimum at about 1% clearance. At a clearance of about 0.2% chord, the calculations showed that the number of surface singularities was larger than for zero clearance, confirming the trend for loss to increase with number of singularities found in an earlier paper [8].
2. The calculations show good agreement with the measurements of surface flow patterns both with and without clearance at the tip of the blade; good agreement is also shown for downstream loss.
3. At zero and small clearance, the calculations and the flow visualization show the presence of singularities on the surface connecting the separation and attachment lines, the general pattern being similar; for clearance above about 0.58% of chord for this cascade, it is impossible to clearly visualize surface singularities on the endwall where separation and attachment lines still exist. The disappearance of the singularities is not clearly understood.
4. For clearance less than 0.58% chord (i.e. comparable to the inlet boundary layer thickness) with this cascade the calculations showed that a horseshoe vortex clearly exists ahead of the blade with a saddle and node evident on the suction surface. A region of separated flow is evident near the suction surface and endwall (as for zero clearance) and for these small clearances, the clearance vortex enters this separated region, where it appears to lose all coherence.
5. For clearance above about 0.58%, the flow pattern is markedly altered, with the region of separated flow on the suction surface reduced compared with small clearance cases. The clearance vortex, arising from the interaction of the clearance flow and endwall secondary flow appears to be strong enough to remain coherent downstream of the blade.
6. As the clearance is increased well beyond 0.58% chord the clearance vortex becomes stronger and remains closer to the endwall. In this case the clearance flow prevents the endwall fluid from interacting with the suction surface boundary layer and thereby precludes the 3D corner separation. The presence of the vortex close to the suction surface reduces the pressure on that surface with the effect of increasing the pressure difference across the blade near the tip and thereby increasing the clearance flow velocity magnitude.

Acknowledgment

This work was supported by Rolls-Royce Plc, the Applied Research Programme of the Ministry of Defence, and the Department of Trade and Industry Aeronautic Research Programme. The authors are very grateful for this and for their permission to publish. The authors would also like to thank Prof. J. D. Denton for the use of his CFD code. The opinions expressed here are those of the authors and not necessarily those of Rolls-Royce plc or any other organization.

Nomenclature

c = chord
H = shape factor= δ^*/θ
i = incidence
P = pressure
Re = Reynolds number
x = axial distance
α = absolute flow angle
β = blade (metal) angle
δ = boundary layer thickness
δ^* = displacement thickness
θ = momentum thickness
ρ = density
τ = clearance gap

Subscripts

L = leakage
x = axial
0 = total, stagnation
1 = inlet
2 = exit

Descriptors

F = focus
LE = leading edge
N = node
PS = pressure surface/side
S = saddle point
SS = suction surface/side
TE = trailing edge

References

[1] Dong, Y., Gallimore, S. J., and Hodson, H. P., 1987, "Three-Dimensional Flows and Loss Reduction in Axial Compressors," ASME J. Turbomach., **109**, pp. 354–361.
[2] McDougall, N. M., 1988, "Stall Inception in Axial Compressors," Ph.D. thesis, University of Cambridge, UK.
[3] Storer, J. A., and Cumpsty, N. A., 1991, "Tip Leakage Flow in Axial Compressors," ASME J. Turbomach., **113**, pp. 252–259.
[4] Storer, J. A., and Cumpsty, N. A., 1994, "An Approximate Analysis and Prediction Method for Tip Clearance Loss in Axial Compressors," ASME J. Turbomach., **116**, pp. 648–656.
[5] Peacock, R. E., 1982, "A Review of Turbomachinery Tip Gap Effect: Part 1 Cascades," Int. J. Heat Fluid Flow, **3**, pp. 185–193.
[6] Peacock, R. E., 1982, "A Review of Turbomachinery Tip Gap Effect: Part 2 Rotating Machines," Int. J. Heat Fluid Flow, **4**, pp. 3–16.
[7] Gbadebo, S. A., 2003, "Three-Dimensional Separations in Compressors," Ph.D. thesis, University of Cambridge, UK.
[8] Gbadebo, S. A., Cumpsty, N. A., and Hynes, T. P., 2005, "Three-Dimensional Separations in Axial Compressors," ASME J. Turbomach., **127**, pp. 331–339.
[9] Denton, J. D., 1999, "Multistage Turbomachinery Flow Calculation Program-MULTIP," Whittle Laboratory, University of Cambridge, UK.
[10] Lighthill, M. J., 1963, "Attachment and Separation in Three-dimensional Flows," *Laminar Boundary Layers*, L. Rosenhead, ed., Oxford Univ. Press, London, Sec. II, pp. 72–82.

Investigation of Unsteady Flow Field in a Vaned Diffuser of a Transonic Centrifugal Compressor

Seiichi Ibaraki

Tetsuya Matsuo

Takao Yokoyama

Nagasaki Research and Development Center,
Mitsubishi Heavy Industries, Ltd.,
1-1 Akunoura-machi,
Nagasaki 850-8610, Japan

Transonic centrifugal compressors are used with high-load turbochargers and turboshaft engines. These compressors usually have a vaned diffuser to increase the efficiency and the pressure ratio. To improve the performance of such a centrifugal compressor, it is required to optimize not only the impeller but also the diffuser. However the flow field of the diffuser is quite complex and unsteady because of the impeller located upstream. Although some research on vaned diffusers has been published, the diffuser flow is strongly dependent on the particular impeller exit flow, and some of the flow physics remain to be elucidated. In the research reported here, detailed flow measurements within a vaned diffuser were conducted using a particle image velocimetery (PIV). The vaned diffuser was designed with high subsonic inlet conditions marked by an inlet Mach number of 0.95 for the transonic compressor. As a result, a complex three-dimensional flow with distortion between the shroud and the hub was observed. Also, unsteady flow accompanying the inflow of the impeller wake was confirmed. Steady computational flow analysis was performed and compared with the experimental results.
[DOI: 10.1115/1.2720505]

Introduction

The authors have previously measured the internal impeller flow of a turbocharger transonic centrifugal compressor using laser Doppler velocimetery (LDV) and high-response pressure sensors, thus clarifying the complex three-dimensional flow fields accompanying shock waves, as well as the mechanism by which loss occurs. [1,2] In continuation, using a transonic centrifugal compressor equipped with the same type of impeller and a vaned diffuser, the internal flow of the diffuser was measured by means of PIV, and the accompanying flow phenomena were elucidated.

Because the inlet velocity of a transonic compressor exceeds the speed of sound, related issues include increased loss due to the shock wave, and the reduced operating range caused by the high Mach number. Improved performance on the part of both the impeller and diffuser is required in order to resolve these issues.

Vaned diffusers are used for centrifugal compressors having a comparatively high pressure ratio, and are effective for improved efficiency and pressure ratio. On the other hand, because the operating range for such compressors is often limited by diffuser surging and choking, the diffuser is an important focus for expansion of the operating range. Since the flow to the diffuser is distorted by the impeller located upstream, performance is heavily affected and the internal flow is extremely complex. Unsteadiness can therefore be expected. Accordingly, in order to achieve higher diffuser performance, aerodynamic design that takes the influence of the impeller into account is considered to be essential. Many research works concerning higher performance vaned diffusers have been undertaken. Hayami et al. [3] applied a low solidity diffuser to increase the operating range. Rodgers [4] reported a tandem-type diffuser with the vanes arranged in two rows, while Zangeneh [5] employed inverse design for optimization of vane load and higher diffuser performance. As noted above, however, the internal flow of the vaned diffuser cannot escape the influence of the impeller. This makes it difficult to achieve a universal interpretation of flow phenomena for appropriate application to all diffusers, and design methods have not yet been sufficiently established.

Notwithstanding, research aimed at elucidating the complex internal flow of diffusers has been conducted. Krain [6,7] measured the unsteady flow of a vaned diffuser by means of laser 2 focus (L2F), indicating that the vane inlet flow angle changes substantially along the direction of vane height, and that the flow angle changes by over 10 degs in an unsteady manner accompanying the rotation of the impeller. L2F time average flow was also reported to agree well with steady analysis results. Ziegler et al. [8,9] also used L2F for unsteady measurement at impeller exit and the diffuser throat, investigating the influence on flow and performance caused by the gap length between the impeller and the diffuser. Wernet et al. [10] applied the PIV to unsteady flow measurement of a diffuser, finding that the impeller wake generated by the clearance flow enters the diffuser, and investigating detail diffuser surge phenomena.

PIV measurement is being increasingly utilized for internal flow measurement in turbomachinery. Compared to LDV point measurement, PIV permits measurement of a plane, and the time required is substantially reduced. In addition to the measurement of stationary flow channels such as for diffusers, Hayami et al. [11] have applied PIV to impeller measurement, and have measured the shock wave associated with a transonic impeller inducer.

In the research reported in the present paper, aimed at obtaining a better understanding of vaned diffuser internal flow phenomena as well as guidelines for greater efficiency, unsteady flow measurement of a centrifugal compressor diffuser was conducted using PIV. Steady flow analysis was also undertaken and compared with the experimental data.

Experimental Apparatus and Procedure

Figure 1 shows the appearance of the transonic compressor impeller and diffuser used in the research reported here. The impeller and diffuser are both of similar configuration to those reported previously [1,2], but a compressor approximately 14% smaller was employed due to test equipment constraints. The impeller used here was a backward swept open shroud impeller, with a diameter of 321 mm, 7 full blades, and 2 stages of 7 splitter

Contributed by the International Gas Turbine Institute of ASME for publication in the JOURNAL OF TURBOMACHINERY. Manuscript received July 23, 2006; final manuscript received August 11, 2006. Review conducted by David Wisler. Paper presented at the ASME Turbo Expo 2006: Land, Sea and Air (GT2006), May 8–11, 2006, Barcelona, Spain. Paper No. GT2006-90268.

Fig. 1 Test impeller and diffuser

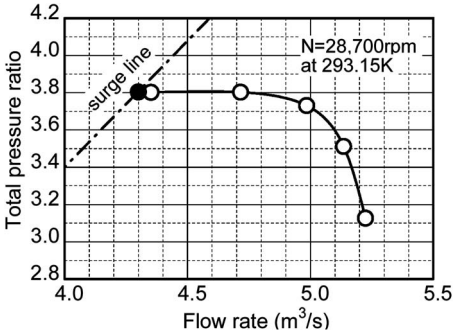

Fig. 3 Compressor stage characteristics

blades each. The relative Mach number of the impeller leading edge tips was about 1.3. The vaned diffuser had 19 vanes, with vane height of 20.2 mm equivalent to the impeller exit width, vane inlet diameter of 369 mm, and a vane inlet angle of 20.5 deg. The inlet Mach number was approximately 0.95, representing a high subsonic inflow.

Figure 2 indicates the meridian configuration and the PIV measurement locations. Diffuser measurement cross sections consisted of three cross sections in the direction of vane height, corresponding to section A in the vicinity of the shroud, section B at the midspan, and section C in the vicinity of the hub. Section A was equivalent to 67% of vane height from the hub, with section B representing 50%, and section C representing 23%. Seeding particles could not be sufficiently supplied above section A, and measurement was not possible.

Figure 3 presents the pressure ratio and flow rate characteristics associated with the test compressor design speed. The design speed was 28,700 rpm (impeller exit speed of 482 m/s), corresponding to the peripheral speed of the impeller in previous reports [1,2]. The pressure ratio was 3.8. Compared with the previous cases [1,2], pressure ratio was slightly down due to the influence of the PIV measurement volute, observation window, etc. (see Fig. 2), including the scale effect. The adiabatic efficiency of the test compressor stage including volute is 82% at peak efficiency. Internal flow measurements were at three flow rates: 4.4 m^3/s in the vicinity of the surge, 4.8 m^3/s in the vicinity of the peak efficiency, and 5.1 m^3/s in the vicinity of the choke.

A two-dimensional PIV system by DANTEC was used. The light source was a pulse YAG laser with output of 8 kW (50 mJ/Pulse). A CCD camera with 1024×1024 pixels was employed, with an interval of 30 frames/s and a minimum frame interval of 1 μs. Polyalcohol has high boiling temperature was used for seeding particles. Figure 4 shows the vaned diffuser and the measurement window, while Fig. 5 presents the conditions of the PIV measurement. The laser sheet, as indicated in Fig. 2, was directed from the optical glass placed downstream from the diffuser, with measurement of a single vane pitch as shown in Fig. 4. In order to prevent reflection of the laser light, a black coating was applied to the diffuser vanes and side plates.

Using a rotational speed sensor to detect passage of the impeller blade tips, flow velocity measurement was conducted in synchronization with the impeller. By matching the measurement times when the impeller and diffuser were in identical phases, flow fields were measured for each phase. This was for data supple-

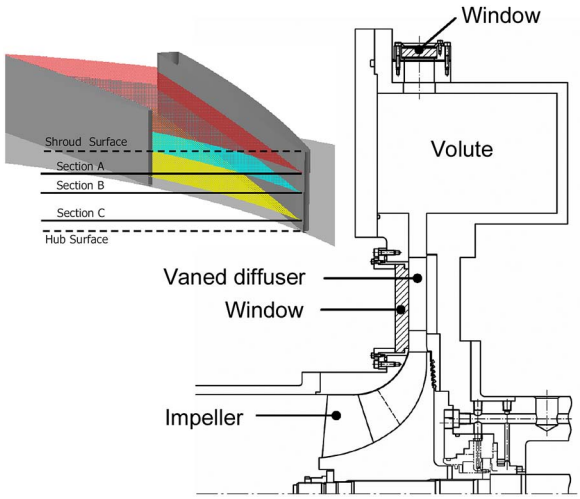

Fig. 2 Cross section and measurement locations

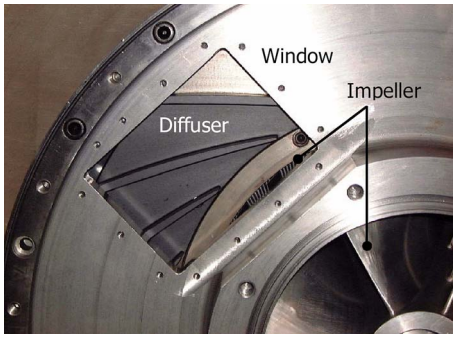

Fig. 4 Test section of diffuser

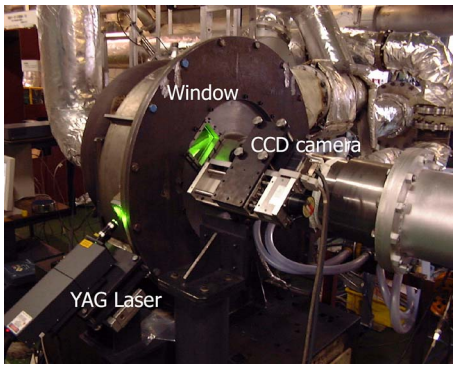

Fig. 5 PIV measurement setup

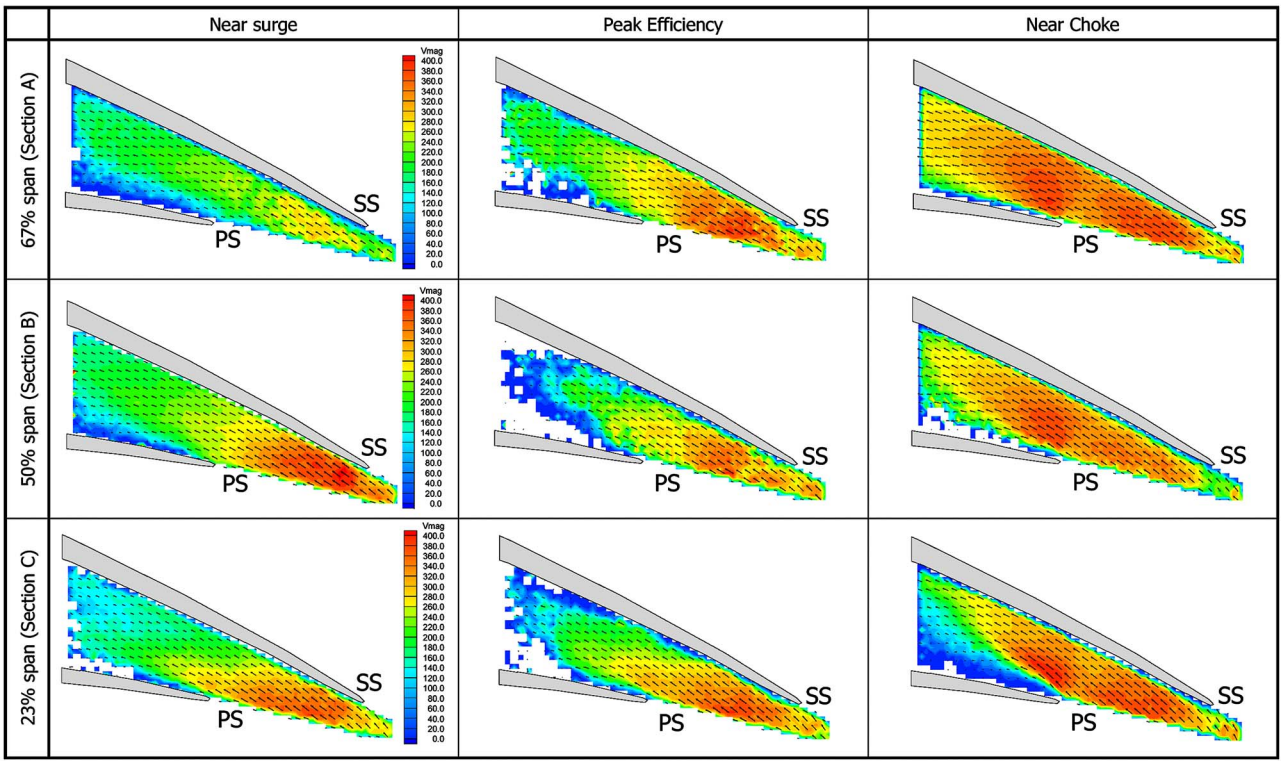

Fig. 6 Absolute velocity distribution and velocity vectors

mentation, necessitated by factors such as insufficient seeding due to the high rotational speed. Images were taken at 12 orientations of the diffuser and impeller passages over a full impeller blade pitch. Fifty images per orientation were aligned for flow velocity measurement.

Experimental Results and Discussion

Time Average Flow Field. Using PIV, unsteady flow velocity was measured in synchronization with impeller rotation. First, in order to evaluate the effect on flow rate and the measurement cross section, the time average flow obtained from the measurement results must be considered. Figure 6 presents the velocity distribution and velocity vector for the time average flow field, while Fig. 7 shows the time average flow angle distribution and velocity vector. The time average flow field was determined by overlaying 100 images of random phases.

It can be seen from Fig. 6 that the flow velocity in the vicinity of the shroud near the surge point is considerably reduced in comparison with velocity at the midspan and the hub area. It can also be observed that, at the midspan, the flow velocity gradually decreases from the diffuser vane leading edge to the throat. In the hub area, the inflow is characterized by negative incidence, such that the flow accelerates in the vicinity of the vane leading edge on the pressure surface, and the flow velocity thus increases on the pressure surface side of the throat. At peak efficiency the flow velocity in the vicinity of the shroud increases to reach or exceed the speed at midspan. The negative incidence increases at midspan and at the hub side, and substantial separation is seen on the vane pressure surface side. In the vicinity of the choke point, the flow velocity increases after the throat in each of the cross sections, and a large separation zone is formed on the hub side pressure surface. From these results, it can be seen that the flow has a strong velocity gradient in the spanwise direction and that a change in flow rate is accompanied by a considerable change in flow velocity in the shroud region.

It can be seen from Fig. 7 that the flow angle is small in the vicinity of the shroud for each flow rate, and large in the vicinity of the hub. At peak efficiency incidence is large at the hub, particularly near choke. A substantial separation zone is formed on the pressure surface, accompanied by low velocity flow. Figure 8 shows a comparison of steady analysis and measurement with respect to the flow angle at the peak efficiency. The flow angle distribution patterns are observed to be in good agreement for each of the cross sections (sections A–C). While the analysis results for the vane upstream flow angle in section A are lower than those measured, the difference is not quantitatively significant.

Figure 9 shows the pitchwise averaged meridional velocity and flow angle at a diameter of 360 mm (12% downstream of the impeller diameter). For each cross section and flow rate, the flow at the vane leading edge becomes an inflow on the vane suction surface side, possessing negative incidence with respect to the vane. This phenomenon is clearly observed in other measurement results as well, such as those of Krain [6,7] and Zangeneh [5]. Because the conventional diffusers have been designed without consideration of the impeller exit distortion generally, negative incidence may be expected to occur.

The CFD results shown in Fig. 9 represent the meridional velocity and flow angle for peak efficiency at the same radius obtained from steady analysis as subsequently discussed. Although there are differences in the absolute values compared to the measurement results for the meridional velocity and flow angle, the qualitative trend is in agreement. However, the CFD results for section A are smaller than the measurement results, suggesting that CFD tends to exaggerate low flow velocity in the vicinity of the shroud. Nevertheless, given that shroud measurement was not possible using PIV, reference to the CFD results makes it easy to predict that the flow angle and the meridional velocity will decrease substantially as the shroud is approached. From Fig. 9, the flow angles for section A (in the vicinity of the shroud) and section C (in the vicinity of the hub) differ by about 9 degs at peak efficiency, and by about 13 degs in the vicinity of choking. In the CFD results, the shroud is subject to reverse flow, and the differ-

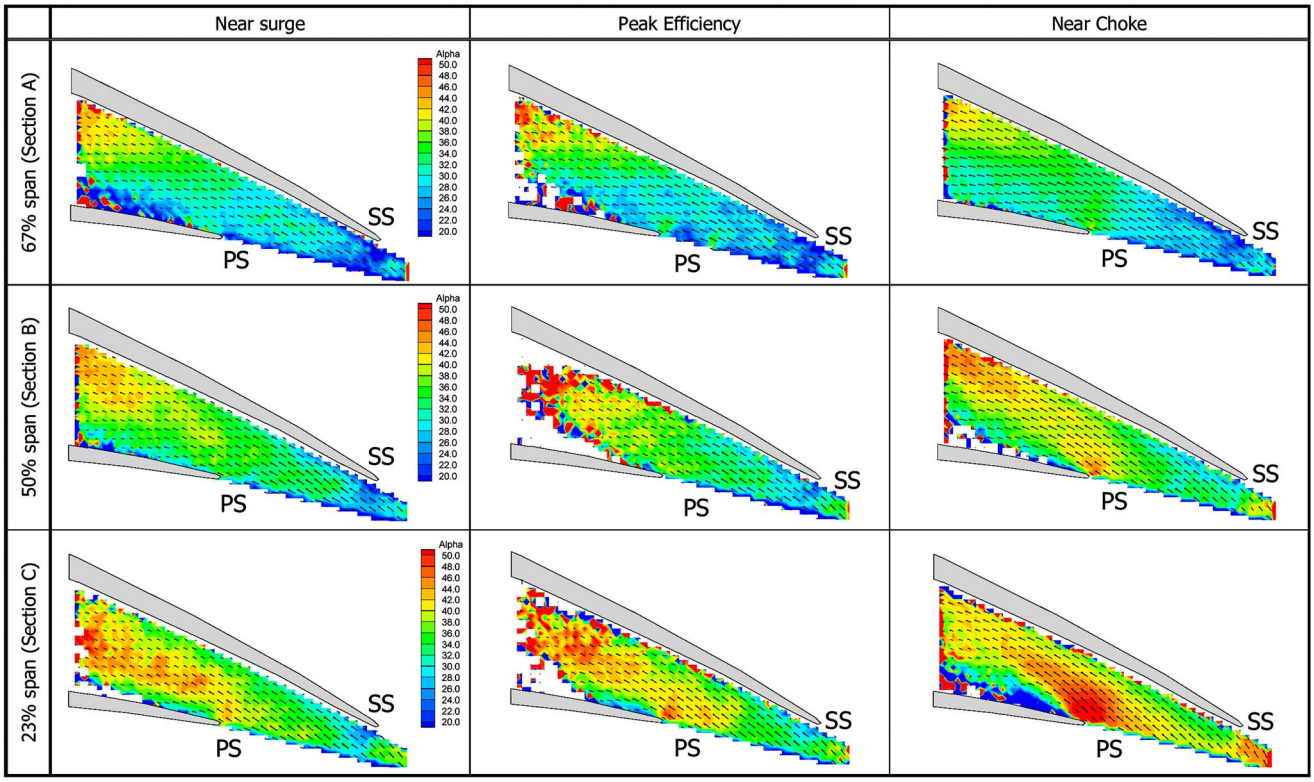

Fig. 7 Flow angle distribution and velocity vectors

ence in flow angle between shroud and hub is about 50 degs. Even considering the overestimation of the low velocity zone by CFD, the deviation in the flow angle between hub and shroud at the efficiency peak point can be estimated to be at least 20–30 degs. Also, the CFD results suggest that the reason why measurement results could not be obtained in the vicinity of the shroud was that, because the flow angle in the vicinity of the shroud was small, with flow being nearly in the peripheral direction, instability occurred in conjunction with separation or reverse flow, such that seeding particles could not be supplied.

Unsteady Flow Field. Next, consideration is given to the unsteady flow velocity measurement results, synchronized with impeller rotation as obtained from PIV measurement. As mentioned

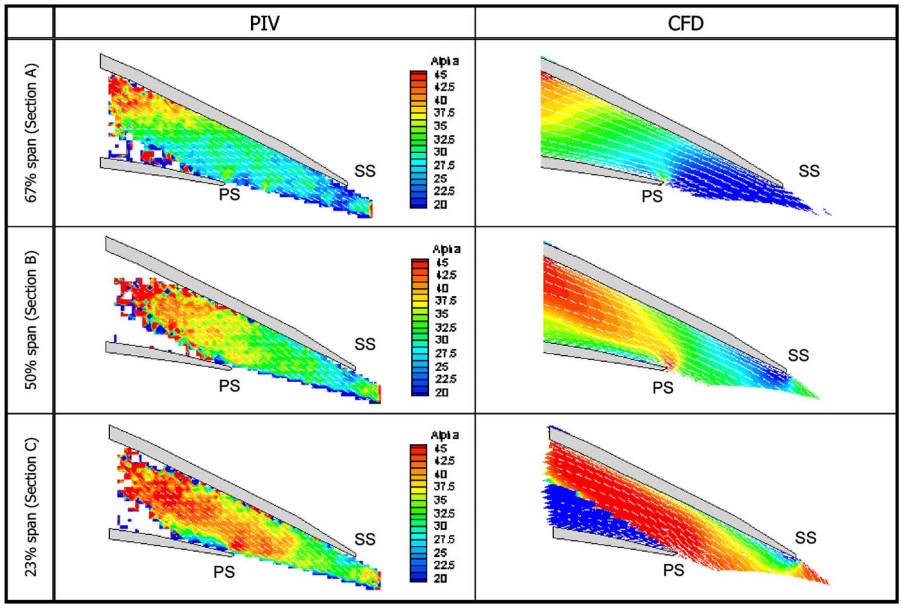

Fig. 8 Comparison of flow angle distribution and velocity vectors at peak efficiency point

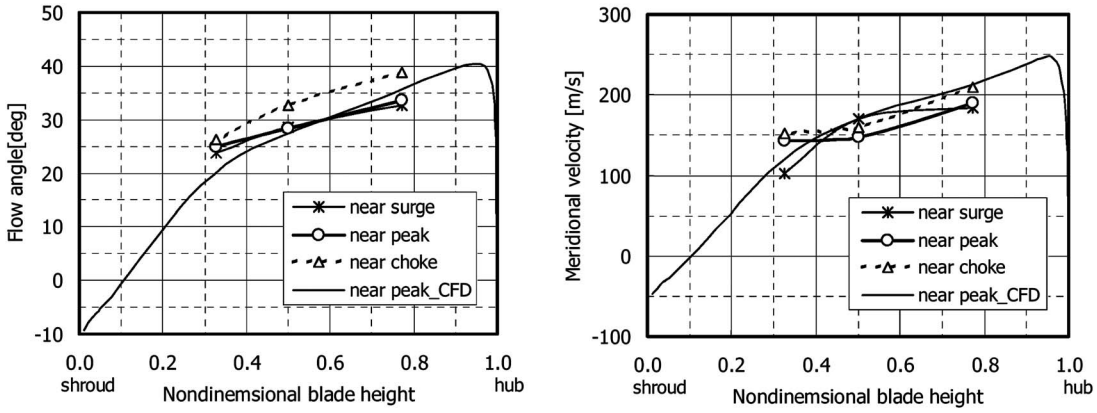

Fig. 9 Comparison of pitchwise averaged flow angle and meridional velocity

before, because the velocity vectors were obtained by matching the measurement time with identical phases of the impeller and diffuser, strictly speaking these results are for quasiunsteady measurement. Figure 10 presents timewise changes in the flow angles and velocity vectors for each phase. These show 6 of the 12 divisions for each interval during which a single diffuser vane pitch is passed by a single impeller full blade pitch. This allows observation of increase or decrease of the flow angle in the direction of flow for each cross section, with the position shifting over time. This is due to the fact that the impeller wake having a small flow angle and the main stream alternately and cyclically enter the diffuser vanes. Naturally, this cycle corresponds to the passage of an impeller blade.

Referring to Fig. 11(*a*), showing the vane inlet, throat and throat downstream as points a, b, and c at the center of the diffuser vane pitch, Fig. 11(*b*) presents the respective time fluctuations of the flow angle. The *x* axis in Fig. 11(*b*) indicates the normalized time at the time of passage by a single impeller full blade pitch. Because the impeller has two rows of splitter blades, four wakes associated with the full blade and the splitter blades enter during the passage of one full blade pitch. This is also confirmed by Fig. 11(*b*). At point a of the diffuser vane inlet, the flow angles corresponding to the vicinity of the shroud, the vane midspan, and the vicinity of the hub each undergo a change from 5 to 10 degs. Also, there is a difference of about 10 degs in the flow angle between the hub and the shroud, with a flow angle distribution in the direction of vane height, and with a three-dimensional unsteady flow field characterized by time-wise change from about 5 to10 degs. Compared to point a, throat center point b has a slightly greater change in the flow angle. As seen in Fig. 10 as well, this is due to the fact that the flow enters with negative incidence, such that fluctuation in the flow angle is substantial at the leading edge of the pressure surface, and the resulting influ-

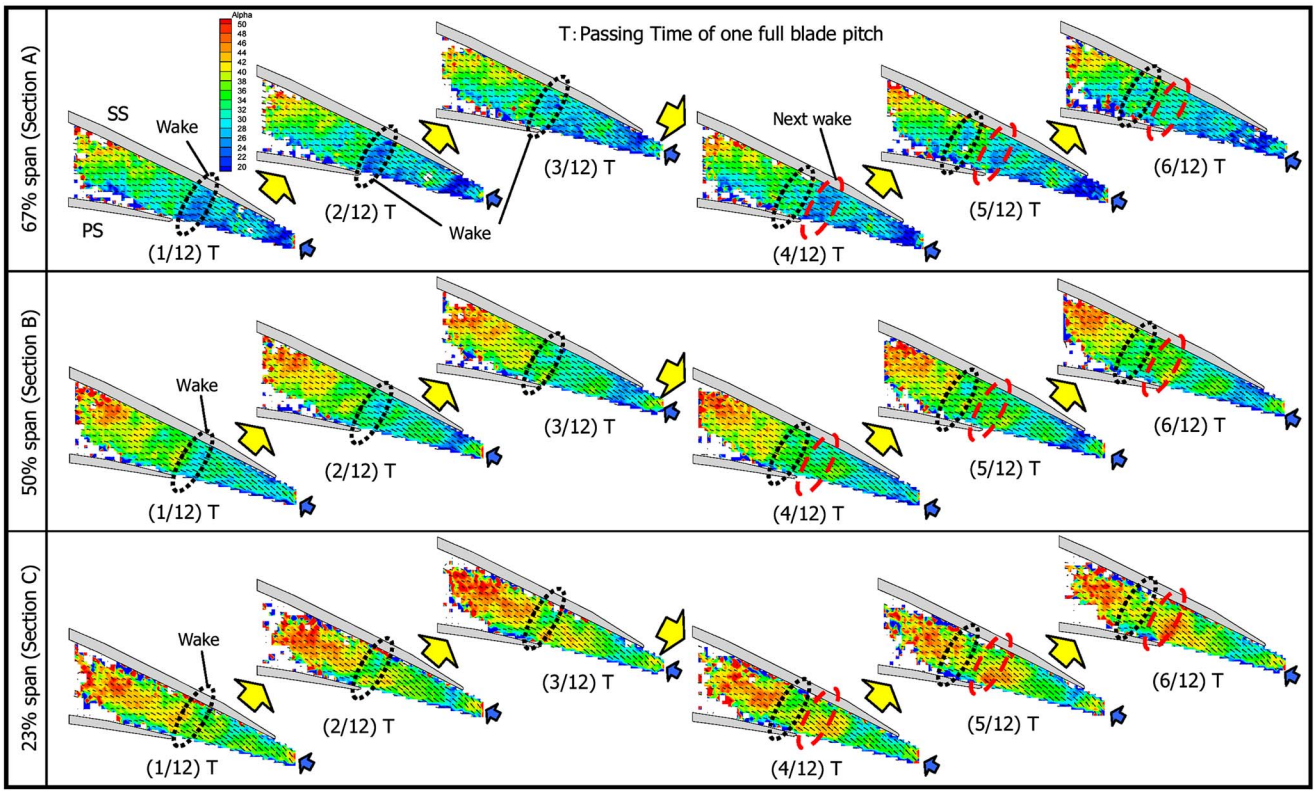

Fig. 10 Unsteady flow angle distribution and velocity vectors measured by PIV

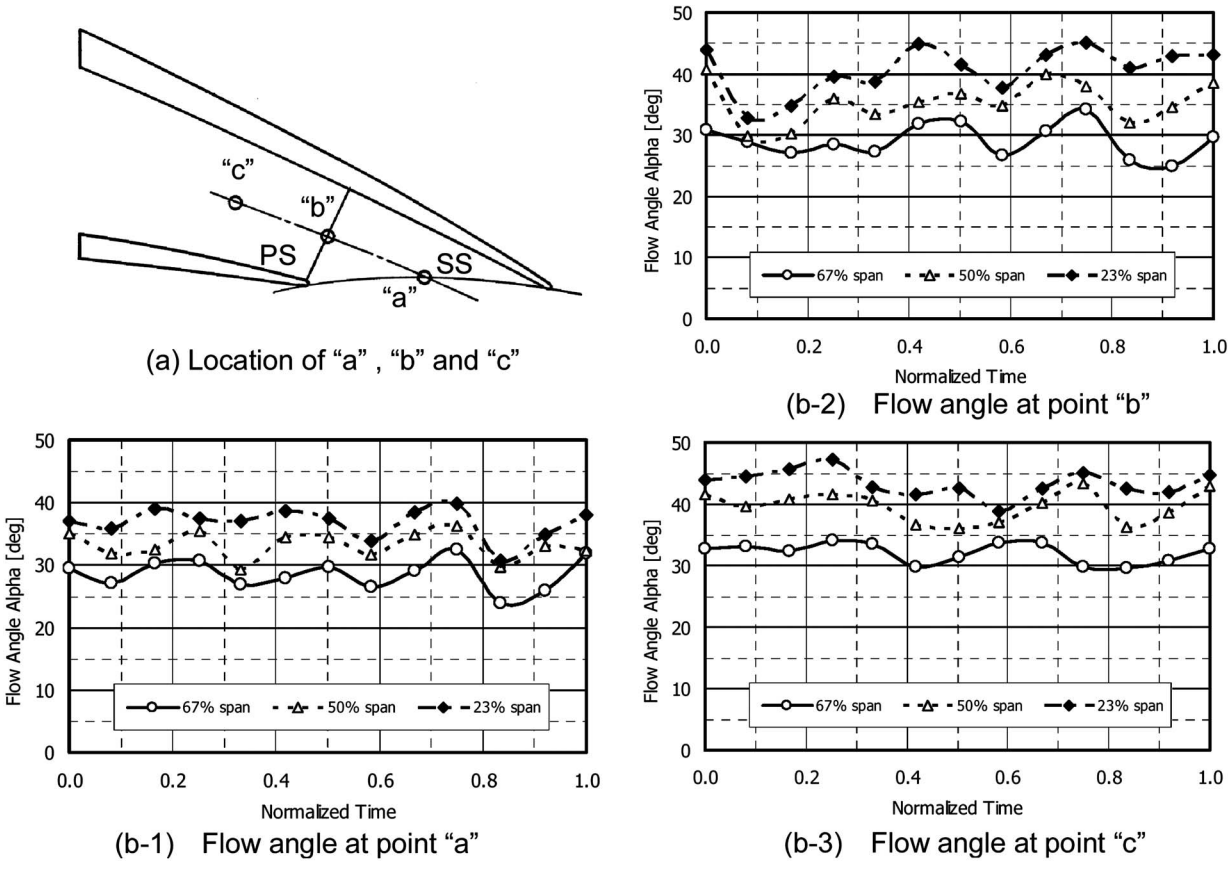

Fig. 11 Time-wise changes of flow angle in the vaned diffuser

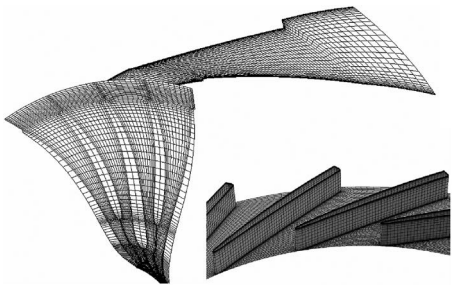

Fig. 12 Computational mesh

ence is considered to be greater at point b than at point a upstream. At the throat downstream point c, although the fluctuation is slightly less than for point b upstream, timewise change in the flow angle was confirmed to be 5 degs at the shroud and just under 10 degs at the midspan and on the hub side. Accordingly, the impeller wake can be identified even downstream from the throat, and without substantial diffusion. Even at point c there is a difference of about 5–15 degs between the shroud and the hub, such that distortion in the direction of vane height remains even downstream from the throat, with extremely late mixing in the direction of vane height.

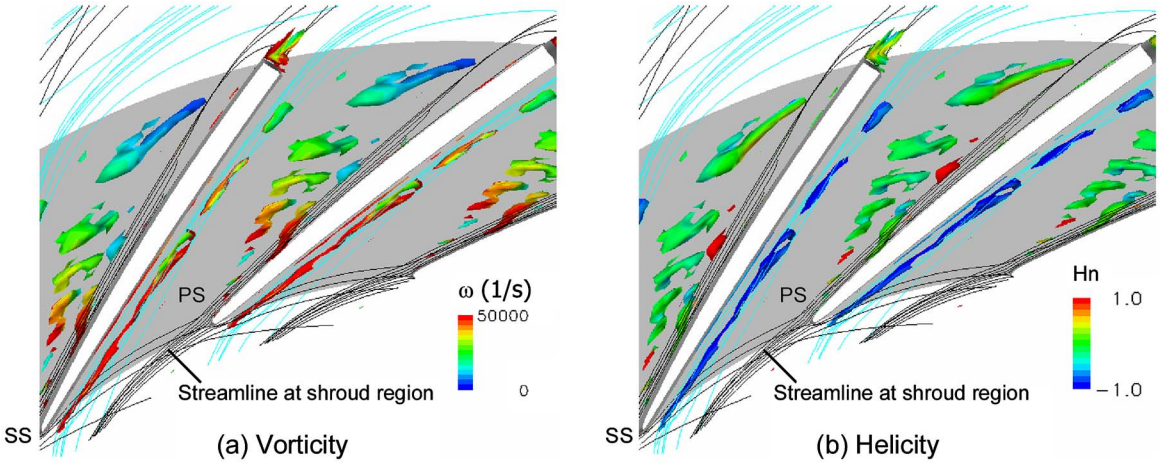

Fig. 13 Vortex core colored with vorticity and normalized helicity

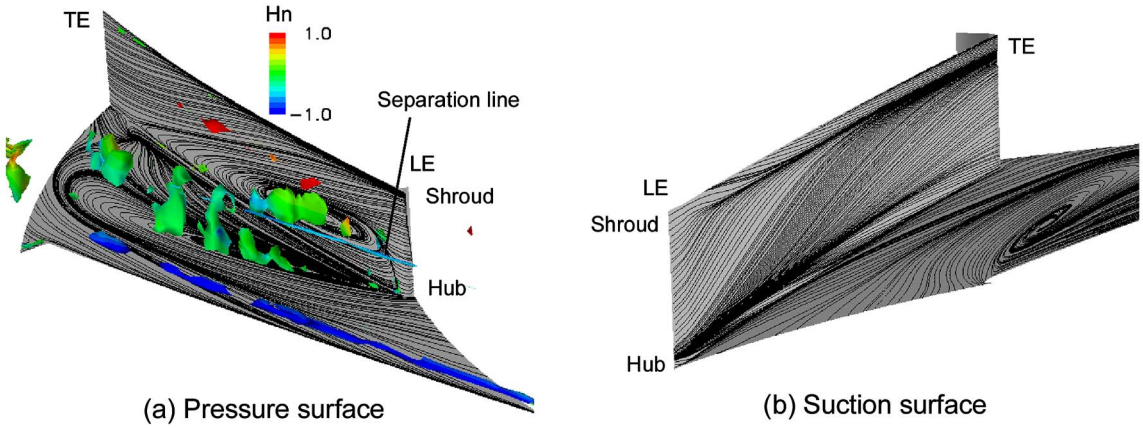

Fig. 14 Limiting streamline on vane and hub surface

3D Viscous Flow Analysis. The flow field resulting from steady analysis of the impeller and diffuser was also considered. The CFD code was TASCflow, a commercial Reynolds average Navier-Stokes code, with the κ-ε model used as the turbulence model. Figure 12 presents the computational mesh. Impeller mesh was composed of 119 nodes streamwise, 57 nodes pitchwise, 21 nodes along the blade height, and 4 nodes for clearance. In the case of the diffuser, there were 78 nodes streamwise, 33 nodes pitchwise, and 21 nodes along the vane height.

Figure 13 gives the visualization results for the diffuser internal flow at peak efficiency, as obtained from steady analysis. The figure shows the vortex core, identified based on critical point theory [12], and the vortex core is colored with vorticity and normalized helicity. Normalized helicity is defined as the cosine of the angle formed by the vorticity vector and the absolute velocity vector, and the region in which its absolute value is 1 is where the strong streamwise vortex exists. The rotational direction of the streamwise vortex is clockwise with respect to the direction of flow when normalized helicity is 1, and counterclockwise when this is −1. Figure 13 also shows the overlay of the streamline in the vicinity of the shroud. The flow angle is small near the shroud, and the flow spirals in the peripheral direction at the vaneless diffuser portion upstream from the diffuser. The spiraled flow enters the pressure surface side of the diffuser vanes, and forms a clockwise vortex as seen from upstream. The vortex core which is considered to be a region of separation can be seen on the pressure surface side and higher vorticity is observed in this region.

The limiting streamlines corresponding to the diffuser vane pressure/suction surfaces and the hub surface are shown in Figs. 14(*a*) and 14(*b*), respectively. From Fig. 14(*a*), leading edge separation is seen to occur from the hub to the midspan. Since excessive negative incidence is associated with the flow from the midspan to the hub, as is also clear from the PIV results, this is deemed to represent separation at the leading edge. Downstream from this region of separation, a secondary flow occurs on the pressure surface from the shroud towards the hub, and large region of separation also forms on the hub surface in conjunction with the leading edge separation. Furthermore, a secondary flow can be observed at the leading edge along the limiting streamline on the suction surface as indicated in Fig. 14(*b*), from the hub towards the shroud. This is understood to be due to the blockage effect of the region of separation on the hub side pressure surface, with the flow pushing against the shroud side on suction surface. On the hub side, a boundary layer can be confirmed as a counterclockwise vortex generated at the leading edge with higher vorticity shown in Figs. 14(*a*) and 13.

Figure 15 presents the total pressure distribution in the direction of flow for the diffuser, while Fig. 16 shows the entropy distribution. Low energy fluid accumulates due to leading edge separation, leading to total pressure loss and substantial entropy generation on the pressure surface side. The main cause of this loss generation at the diffuser can be seen as leading edge separation due to excessive negative incidence. Given that PIV measurement results indicate an unsteady change of 5–10 degs in the flow angle, the incidence would change accordingly, and it is predicted that the size of the region of separation would also change over

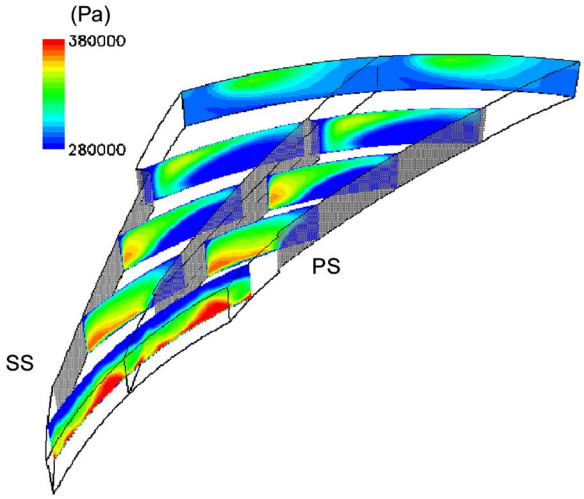

Fig. 15 Total pressure distribution

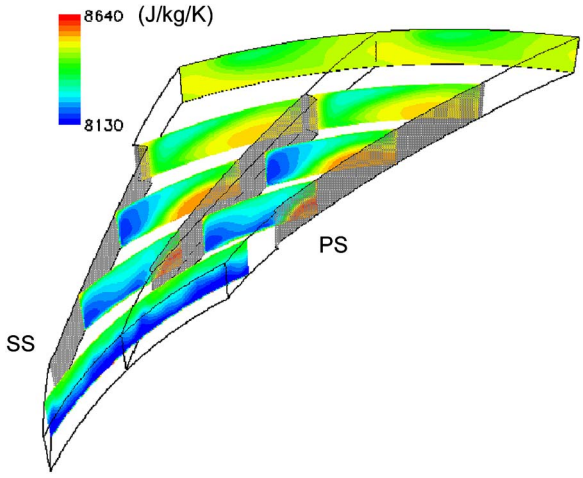

Fig. 16 Entropy distribution

time. However, negative incidence is always present from the midspan to the hub, and suppression of leading edge separation through reduction of incidence is considered to be an effective means of improving diffuser performance.

Conclusion

PIV measurement and CFD verification were applied to a vaned diffuser for a transonic compressor, for ascertainment of flow phenomena and consideration of guidelines to achieve better performance. The results are as follows:

(1) The diffuser inlet flow is affected by the upstream impeller flow, which causes a three-dimensional distorted flow in the spanwise direction. The difference in the time averaged flow angle between shroud and hub is at least 10 degs. Excessive negative incidence occurs from the midspan to the hub side.
(2) The vaned diffuser flow is strongly unsteady, with change in the inlet angle of 5–10 degs during the passage of a single impeller full blade pitch. The flow angle changes by a similar amount downstream from the diffuser throat as well, and it was determined that the impeller wake is present far downstream of the diffuser throat.
(3) Mixing in the spanwise direction of the impeller exit flow is extremely delayed. A difference of more than 10 degs in the flow angle was found close to the throat.
(4) Steady analysis tends to be qualitatively consistent in comparison with the time averaged flow field obtained from PIV measurement, but also tends to overestimate the low velocity region of the shroud.
(5) From midspan to hub leading edge separation was detected by PIV measurement and steady flow analysis. The accumulation of low-energy fluid in conjunction with leading edge separation is the main cause of total pressure reduction and entropy generation.

Acknowledgment

The authors would like to express their appreciation to Mr. Sumida and Mr. Atsushi Matsuo, who helped plan and prepare the test compressor equipment for PIV measurement, and Mr. Taketsugu, who helped execute PIV measurement.

Nomenclature

Alpha = absolute flow angle from tangential, deg
Hn = normalized helicity
N = impeller rotational speed, rpm
PS = pressure surface
SS = suction surface
V_{mag} = absolute velocity m/s
ω = vorticity, 1/s

References

[1] Ibaraki, S., Higashimori, H., and Matsuo, T., 2001, "Flow Investigation of a Transonic Centrifugal Compressor for Turbocharger," 23th CIMAC.
[2] Ibaraki, S., Matsuo, T., Kuma, H., Sumida, K., and Suita, T., 2002, "Aerodynamics of a Transonic Centrifugal Compressor Impeller," ASME Paper No. GT-2002-30374.
[3] Hayami, H., 2000, "Improvement of the Flow Range of Transonic Centrifugal Compressor with a Low-Solidity Cascade Diffuser," ASME Paper No. 2000-GT-0465.
[4] Rodgers, C., 1993, "Compact Diffusers for Small Transonic Compressor," AGARD Meeting.
[5] Zangeneh, M., and Roduner, D. V. C., 2002, "Improving a Vaned Diffuser for a Given Centrifugal Impeller," ASME Paper No. GT-2002-30621.
[6] Krain, H., 1999, "High Pressure Ratio Centrifugal Compressor with Transonic Flow," ASME Paper No. FEDSM99-7801.
[7] Krain, H., 2002, "Unsteady Diffuser Flow in a Transonic Centrifugal Compressor," Int. J. Rotating Mach., **8**(3), pp. 223–231.
[8] Ziegler, K. U., Gallus, H. E., and Niehuis, R., 2002, "A Study on Impeller-Diffuser Interaction: Part 1—Influence on the Performance," ASME Paper No. GT-2002-30381.
[9] Ziegler, K. U., Gallus, H. E., and Niehuis, R., 2002, "A Study on Impeller-Diffuser Interaction: Part 2—Detailed Flow Analysis," ASME Paper No. GT-2002-30382.
[10] Wernet, M. P., Bright, M. M., and Skoch, G. J., 2001, "An Investigation of Surge in a High-Speed Centrifugal Compressor Using Digital PIV," ASME J. Turbomach., **123**, pp. 418–428.
[11] Hayami, H., Hojo, M., and Aramaki, S., 2002, "Flow Measurement in a Transonic Centrifugal Impeller Using a PIV," J. Visualization, **5**(3), pp. 255–261.
[12] Furukawa, M., Inoue, M., Saiki, K., and Yamada, K., 1999, "The Role of Tip Leakage Vortex Breakdown in Compressor Rotor Aerodynamics," ASME J. Turbomach., **121**(3), pp. 469–480.

Aerodynamic Characteristics of Supercritical Outlet Guide Vanes at Low Reynolds Number Conditions

Toyotaka Sonoda
Honda R&D Co. Ltd.,
Aircraft Engine R&D Center,
351-0193, Saitama, Japan
e-mail: toyotaka_sonoda@n.n.rd.honda.co.jp

Heinz-Adolf Schreiber
German Aerospace Center (DLR),
Institute of Propulsion Technology,
51170 Köln, Germany

As a part of an innovative aerodynamic design concept for a single stage low pressure turbine, a high turning outlet guide vane is required to remove the swirl from the hot gas. The airfoil of the vane is a highly loaded compressor airfoil that has to operate at very low Reynolds numbers (Re~120,000). Recently published numerical design studies and experimental analysis on alternatively designed airfoils showed that blade profiles with an extreme front loaded pressure distribution are advantageous for low Reynolds number conditions. The advantage even holds true for an increased inlet Mach number at which the peak Mach number on the airfoils reaches and exceeds the critical conditions ($M_{ss} > 1.0$). This paper discusses the effect of the inlet Mach number and Reynolds number on the cascade performance for both a controlled diffusion airfoil (CDA) (called baseline) and a numerically optimized front loaded airfoil. The results show that it is advantageous to design the profile with a fairly steep pressure gradient immediately at the front part in order to promote early transition or to prevent too large laminar—even shock induced—separations with the risk of a bubble burst. Profile Mach number distributions and wake traverse data are presented for design and off-design conditions. The discussion of Mach number distributions and boundary layer behavior is supported by numerical results obtained from the blade-to-blade flow solver MISES. [DOI: 10.1115/1.2720868]

Introduction

LP turbines in the modern civil aeroengine consist of several stages. Therefore, besides the efficiency, weight, cost and reliability are important factors to be considered in the design process. The weight of the LP turbine accounts for roughly one-third of the total engine weight. The efficiency of the LP turbine has a large effect on the engine specific fuel consumption (SFC). A 1% improvement in LP turbine efficiency gives rise to about 0.9% decrease in engine SFC and would result in saving $52,000 per year per typical aircraft, according to Wisler [1]. Ashpis [2] also showed that the operating Reynolds number for the LP turbine can drop below 100,000 at high-altitude cruise condition, which leads to a 2% drop in efficiency from take-off to cruise. It has been observed that the boundary layers are largely laminar, even in the presence of free-stream turbulence and wakes. As a result, the boundary layers are susceptible to flow separation near the aft portion of the blade suction surface.

Several studies have been published that are related to laminar separation bubbles, boundary layer transition and high lift profiles in LP turbine and which helped to improve efficiency (e.g., Lou and Hourmouziadis [3], Volino and Hultgren [4], Howell et al. [5], Haselbach et al. [6]). Haselbach et al. [6] showed that their new "Ultra High Lift" airfoils achieve a reduction of approximately 11% in airfoil count and significant reductions in turbine weight.

In order to reduce the number of turbine components, new ultrahigh-loaded LP turbine technology is required. While this technology is still under development, it is already worthwhile to include a high turning compressor stator as an Outlet Guide Vane (OGV) just behind an extremely high loaded turbine rotor. Using the OGV, a turbine aerodynamic designer can freely load up the rotor performance and adjust the velocity triangles to an optimal stator, rotor and OGV combination. This leads to a considerable increase of the reaction of the turbine rotor.

However, a wide operating range is required for the OGV, because the exit flow of the rotor changes considerably due to the variation in LP-turbine's expansion ratio between take-off and cruise. Additionally, it should be noted that the Reynolds number varies greatly between take-off and cruise, i.e., Re=1,000,000 for ground condition and about 100,000 for cruise condition. Therefore, low losses for the OGV are required for a wide range of Reynolds numbers. Indeed, the OGV losses could dramatically increase, since it has to operate at Reynolds numbers lower than 200,000, which is well-known to be a critical level for compressor airfoils. Of course such increased losses could compromise the concept of the high loaded turbine rotor with OGV and loss increase at low Reynolds numbers also may compromise the operation of small turbofan engines at high altitude cruise conditions.

In the past, several kinds of airfoils have been developed for subsonic and transonic compressor blades. Rhoden [7] reported that for low-speed cascades a fairly steep pressure gradient immediately after the suction peak near the leading edge seems to be effective in preventing laminar separation. Roberts [8] and Citavy and Jilek [9] e.g., tested low speed compressor cascades at low Reynolds numbers and proposed semiempirical models for the growth and bursting of laminar separation bubbles, but design rules were not reported.

In the early 1980s sub- and transonic controlled-diffusion airfoils (CDA) made their way into modern compressor designs, which were based on both experimental and numerical research [10]. In subsonic blade rows the CDA, that has a velocity maximum around 20–30% of the chord, has been applied to many aeroengines and land-based gas turbines. The blade performance and the range of application, however, depend on the blade chord Reynolds number as illustrated in Fig. 1. The compressor rotor

Contributed by the International Gas Turbine Institute of ASME for publication in the JOURNAL OF TURBOMACHINERY. Manuscript received July 26, 2006; final manuscript received August 19, 2006. Review conducted by David Wisler. Paper presented at the ASME Turbo Expo 2006: Land, Sea and Air (GT2006), May 8–11, 2006, Barcelona, Spain, Paper No. GT2006-90882.

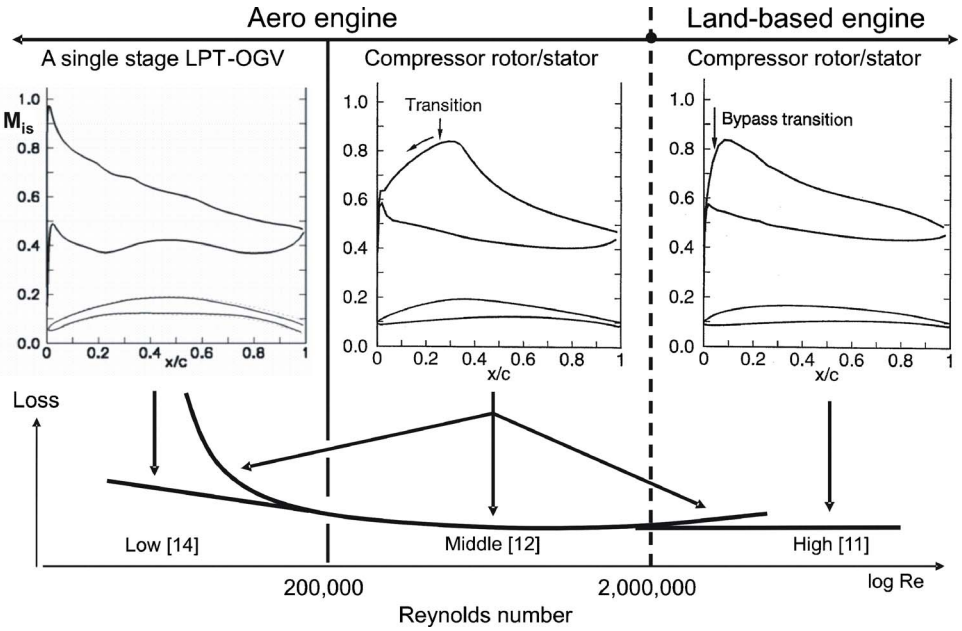

Fig. 1 Reynolds number effect on profile losses for subsonic compressor cascades

and stator airfoils for aeroengines are in operation between roughly Re=200,000 and 2,000,000, whereas compressor blades of land-based engines operate above $2-3\times10^6$.

Recently, Köller et al. [11] and Schreiber et al. [12] showed in their optimization and experiments that the CDA airfoils, that have been primarily developed for aeroengine applications, are not the optimal solution, if directly transferred to the land-based gas turbines, since at very high Reynolds numbers nearly no laminar boundary layer is present on the front portion of the airfoil (Fig. 1). Similar optimized airfoils were found by Sieverding et al. [13], who showed the "ski-slope" pressure distribution that has its peak velocity shortly after the leading edge at about 5% of the chord length. The effectiveness of these profiles, especially the increase of the working range, is confirmed in their three-dimensional CFD simulation and compressor experiments.

Figure 2 shows an example of the reduction of the number of LP-turbine components in a small turbofan engine, using a compressor cascade as OGV behind the highly loaded turbine rotor. In a first step, the OGV has been designed applying the conventional CDA philosophy in which the peak velocity is around 20% of the chord. The OGV, located just downstream of the rotor, has a relatively wide chord in order to cope with the laminar boundary layer separation at the very low Reynolds number conditions. The low Reynolds number design of the OGV for $M_1=0.6$ was very critical, because high flow turning and strong diffusion was required at two-dimensional flow conditions because hub and casing contours were nearly parallel.

In a second step, Sonoda et al. [14] showed an alternative OGV with a unique airfoil Mach number distribution, as shown on the left-hand side of Fig. 1. Their numerical optimization for the very low Reynolds number conditions resulted in a front loaded cascade having the velocity peak just at the leading edge. The optimization confirmed the design concept in which "aerodynamic loading should be imposed on a region where the boundary layer is very thin and healthy" and where early boundary layer transition is enforced to prevent too large laminar separation bubbles [7]. Experimental and numerical analysis confirmed the low losses in the entire relevant Reynolds number range [15].

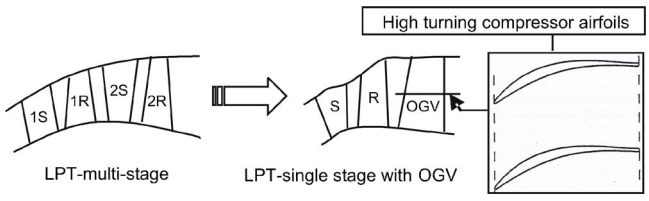

Fig. 2 Reduction of number of LP-turbine components in a small turbofan engine by using a highly loaded compressor airfoil as an outlet guide vane

However, from an engineering point of view two questions must be raised. (1) What is the free-stream turbulent effect on blade performance in such a low Reynolds number region? (2) Is the concept of the extreme front loading still advantageous in the transonic regime? In order to answer these questions, additional experiments were performed with increased free-stream turbulence. Further tests and numerical studies analyzed the blade performance at increased inlet Mach numbers with supercritical flow conditions. If the aerodynamic performance of the OGV at the increased inlet Mach number of $M_1=0.7$ would be similar to those at $M_1=0.6$, this would correspond to an increase of about 1% of LP-turbine efficiency.

Therefore, the main objective of this research is to investigate the aerodynamic characteristics of the two alternatively designed outlet guide vanes and to clarify why the optimized airfoil with its extreme front loaded velocity distribution is superior especially at low Reynolds numbers and at supercritical flow conditions.

Blading Design

Blading design for the outlet guide vanes initially was performed for 2D conditions (AVDR=1.0) at $M_1=0.6$, a flow turning of 43 deg, a diffusion factor of $D_f=0.53$, and a Reynolds number of 130,000, see [14]. Designing the ES airfoil, an evolutionary algorithm, namely evolutionary strategy (ES) (Olhofer et al. [16]) was coupled to a Navier-Stokes blade-to-blade analysis. During the optimization process the pressure loss at design and off-design condition, the deviation angle, and the blade thickness were considered in order to calculate the fitness function. The Navier-Stokes solver of Arima et al. [17] with Chien's low Reynolds k-ε turbulence model was used, since in our project phenomena like large laminar separation bubbles and intensive turbulent separations are likely to play a dominant role. Figure 3 shows the airfoil

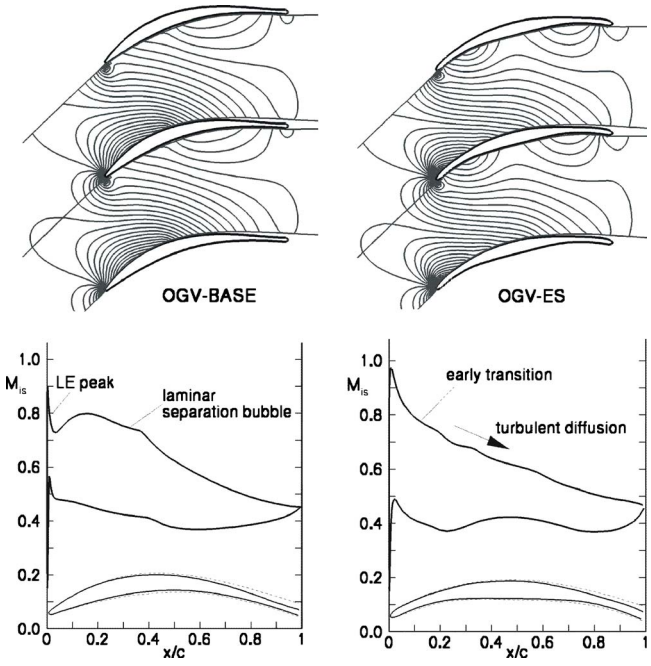

Fig. 3 Baseline and optimized cascade at design condition

geometries and the airfoil surface Mach number distributions for the baseline cascade (OGV-BASE) and the optimized one (OGV-ES).

Approach

Test Setup. The experiments were performed in the transonic cascade tunnel of the DLR Cologne. This tunnel is a closed loop, continuously running facility with a variable nozzle, an upper transonic wall, and a variable test section height. The air supply system enables an inlet Mach number range from 0.2 to 1.4 and a Mach number independent variation of the Reynolds number from about 1×10^5 to 3×10^6. Tunnel sidewall boundary layers ahead of the cascade are removed through protruding slots. Within the blade pack aft of the minimum pressure region endwall boundary layers were controlled by suction through chordwise slots to obtain practically two-dimensional flow condition around the midspan region (AVDR=1.0). Tailboards combined with throttles are used to control inlet and exit boundary conditions. For the present tests seven blades with 65 mm chord and 168 mm blade span were installed in the test section, with the center blades instrumented on the pressure and suction side. A cross-sectional view of the facility and the test section data are shown in Fig. 4 and Table 1, respectively.

In order to obtain tests at low Reynolds numbers, the closed loop system of the facility must be evacuated by additional sets of radial compressors. By adjusting the total pressure between 1.1 and 0.1 bar, blade chord Reynolds numbers were achieved between about 1×10^6 and 1×10^5. The cascades were tested at inlet Mach numbers of 0.5, 0.6, and 0.7 in the entire possible incidence range. The inlet flow angle was measured with probes at the same gapwise locations for three consecutive blade channels. Inlet total temperature was about 305 K and the free stream turbulence level around 0.6%. Table 2 provides some estimated uncertainties for key dependent variables, in which uncertainty is less near design incidence angle and for the higher Reynolds numbers tests and increases at lower Reynolds numbers and approaching the stalled flow conditions.

Blade-to-Blade Flow Solver. The blade-to-blade solver used for the analysis and interpretation of the experimental results is the quasi-three-dimensional viscous/inviscid solver MISES V2.4

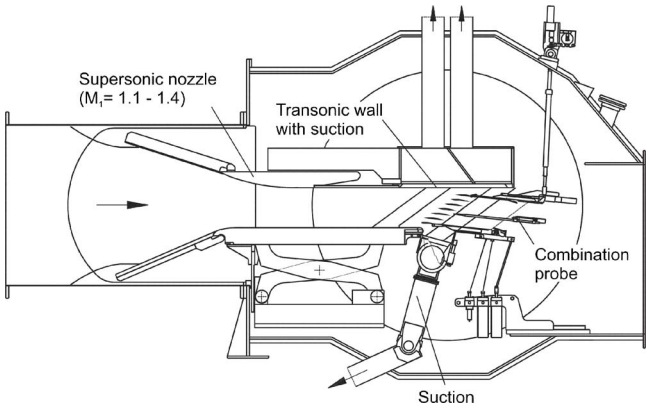

Fig. 4 DLR transonic cascade facility

of Drela and Youngren [18]. This code describes the flow field using the steady Euler equations, while the viscous effects are modeled by the integral boundary layer equations. Boundary layer transition is simulated by a modified criterion of Abu-Ghannam/Shaw [19]. The solver is sufficiently validated for cascade flows at low and high Reynolds numbers and transonic flow conditions with shock-wave boundary layer interaction. Most of the blade-to-blade simulations were performed using a free-stream turbulence level of 0.5% that is similar to the turbulence level observed in the cascade wind tunnel when operating without turbulence generating grids (0.6%).

Results

Effect of Free-Stream Turbulence. The effect of free-stream turbulence on the performance of compressor cascades has been widely studied and the results have been discussed in several publications, e.g., Schlichting and Das, [20], Roberts [8], Citavy and Norbory [21], and Evans [22]. The turbulence in real turbomachinery environments has an important effect on the boundary layer development, on transition, laminar and turbulent separation, the extension of laminar separation bubbles and on the process of turbulent reattachment at the rear part of the bubble. A nearly endless number of papers have been published discussing the effect of free-stream turbulence or wake-passing effects, on laminar separations bubbles, and boundary layer transition (i.e., Mayle [23] and Cumpsty [24]) but blade performance is hardly considered. Especially for medium and low Reynolds numbers, this turbulence effect on blade performance is of greatest interest.

However, the resulting effect on performance strongly depends on the profile design philosophy, i.e., airfoils with different surface pressure distributions respond differently to the outer turbu-

Table 1 Test section data

Inlet Mach number	0.2–1.4
Reynolds number	1×10^5–3×10^6
Turbulence level	0.6–4%
Total pressure	0.1–1.8 bar
Total temperature	300–325 K
Test section height variable	150–330 mm
Blade span	168 mm

Table 2 Estimated uncertainties (experiment)

Upstream flow angle, β_1	±0.2–0.5 deg
Exit flow angle, β_2	±0.3–0.6 deg
Loss coefficient, ω	±0.001–0.01
AVDR	±0.01–0.015

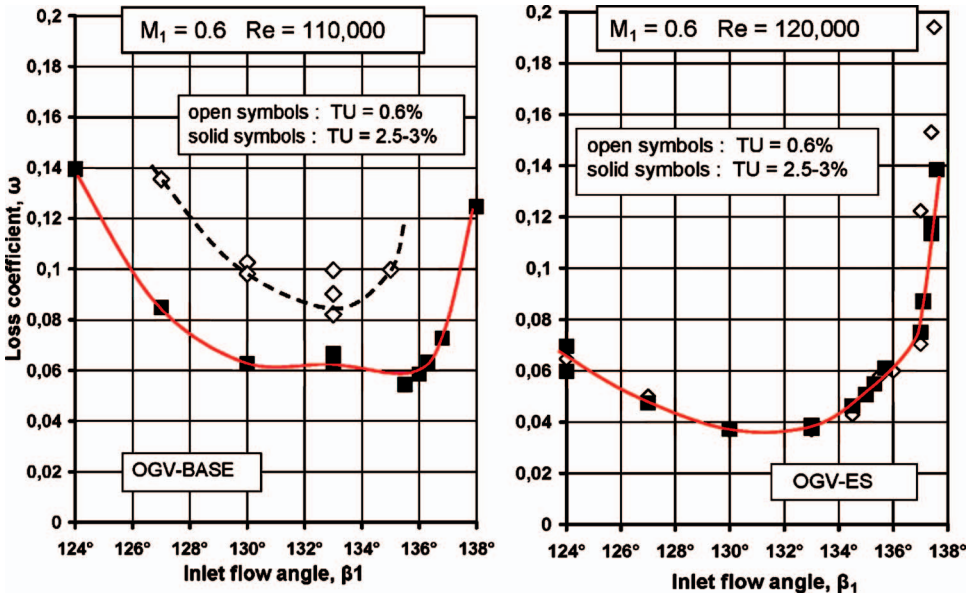

Fig. 5 Effect of free-stream turbulence on total pressure losses at a low Reynolds number. Experimental results for (*a*) OGV-BASE and (*b*) OGV-ES.

lence. A recent study [25] using the present airfoils OGV-BASE and OGV-ES showed that the "conventional" CDA pressure distribution with an accelerated front portion and laminar separation around 25–30% of the chord is more sensitive to an increased free-stream turbulence than the optimized OGV-ES profile which has boundary layer transition relatively close behind the leading edge. By increasing the turbulence level from about 0.6 to 3% the losses of the OGV-BASE are affected in the complete incidence range which is true especially for low Reynolds numbers. In Fig. 5, the total pressure losses of the BASE and ES cascades are shown for the design inlet Mach number of 0.6 and two different turbulence levels. When increasing the turbulence, the losses of the BASE airfoil are slightly reduced because the turbulence influences the reattachment process of the extended laminar bubble and the subsequent downstream turbulent separation.

The losses of the ES airfoil are nearly unaffected due to the early boundary layer transition just after the front portion of the blade [15]. Comparing the losses of both the conventional BASE airfoil and the ES airfoil at the inlet Mach number of 0.6, we clearly observe the essential advantage of the front loaded cascade. The next section will show whether this advantage is true even for increased inlet Mach numbers with supercritical flow conditions.

Effect of Reynolds Number and Inlet Mach Number. It is well known that below critical Reynolds numbers of 200,000 or 150,000 the losses of compressor cascades increase dramatically due to large extensions of the laminar separation bubbles or due to burst of the bubbles with rear turbulent separations. Basically, this is also true for the cascades tested in this research, the baseline cascade, however, showed a higher Reynolds number dependency in relation to the optimized one. Corresponding results were shown already in a previous publication of Schreiber et al. [15]. New results for different inlet Mach numbers and especially for supercritical conditions at $M_1=0.7$ now are provided in Fig. 6. Obviously, the OGV-BASE cascade (Fig. 6, top) is more sensitive to the compressibility effect than the optimized airfoil OGV-ES, Fig. 6 (bottom). For the "nearly supercritical" inlet Mach number of $M_1=0.7$ the losses of the baseline airfoil increase below Re $\approx$400,000 or 350,000, whereas for the ES airfoil the losses remain well below 4% even at the lowest tested Reynolds number of 130,000. These Reynolds number effects are clearly visible also in the incidence characteristics shown in Fig. 7 for $M_1=0.7$. Tests

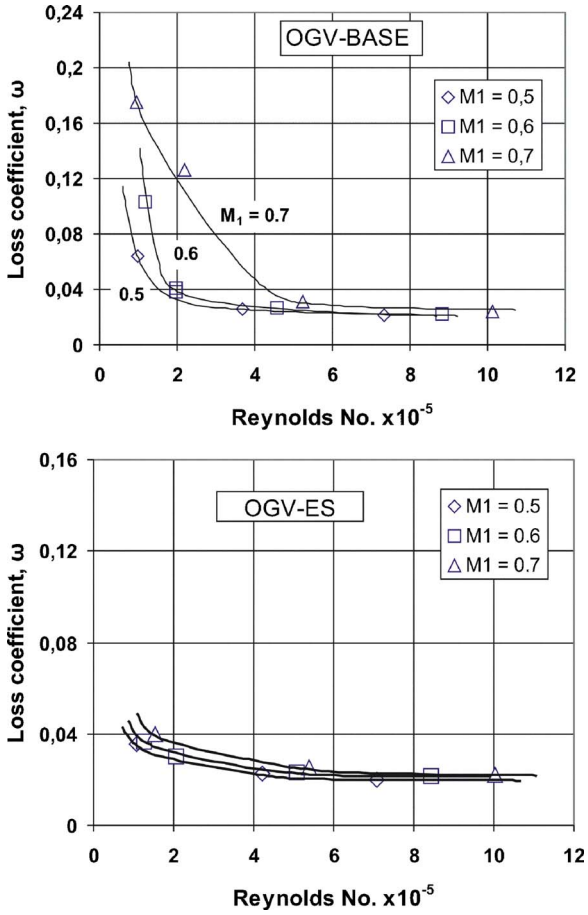

Fig. 6 Total pressure losses as function of blade chord Reynolds number for $M_1=0.5$, 0.6, and 0.7. Experimental results for OGV-BASE (top) and OGV-ES (bottom).

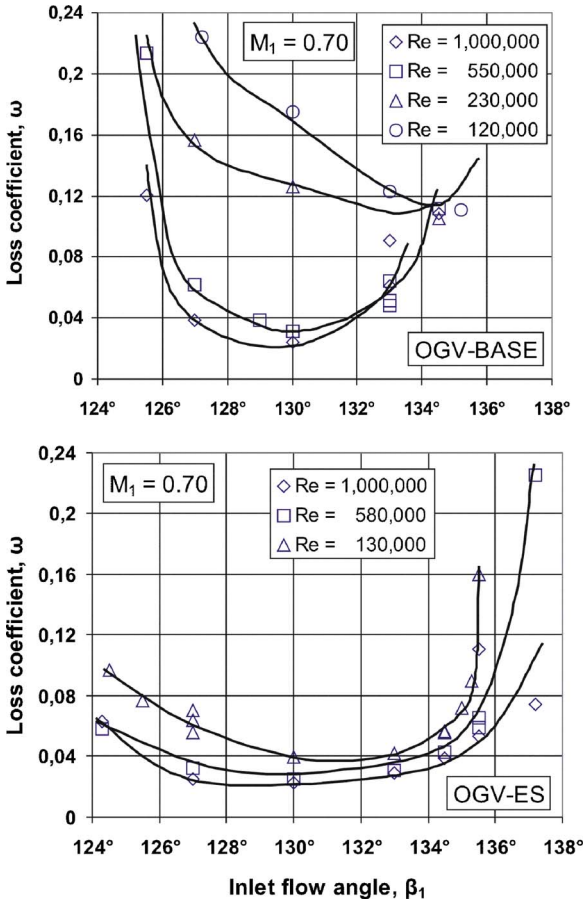

Fig. 7 Reynolds number effect on the incidence characteristic at M_1=0.7. Experimental results for OGV-BASE (top) and OGV-ES (bottom).

confirmed low losses for a wider incidence range for the ES airfoil at Re=130,000, Fig. 7 (bottom). The high losses of the BASE airfoil (Fig. 7, top) result from severe boundary layer separations which are observed even at the design incidence angle.

In order to clarify, whether the outlet guide vane cascades can be used even at higher inlet Mach numbers, their performance has been studied for inlet Mach numbers from M_1=0.5 to about 0.8–0.87 using the blade-to-blade solver MISES. The calculated total pressure losses for Re=120,000 are plotted in Fig. 8 for incidence angles of −6 deg, 0 deg, and +1.5 deg and compared to some experimental losses. When we look at the theoretical results for the design incidence angle (β_1=133 deg) only, it seems possible that the inlet Mach number can be increased from 0.6 to 0.7 for both BASE and ES cascade without seriously decreasing the airfoil's performance. At M_1=0.7 the theoretical losses of ES are 4.48% compared to 4.64% for the BASE airfoil, although the suction side peak Mach number on the ES airfoil is nearly 1.2, whereas the Mach number of the BASE profile remains well below M=1.0, as shown in the next section.

However, as we know already from the experimental data, Fig. 8 center, the actual difference between BASE and ES is considerably bigger. Comparing the experimental losses with the theoretical losses, we see that for BASE there is a large difference between experiment and theory—nearly a factor of 2—but for the ES cascade, the agreement between experiment and MISES simulation is excellent for the design incidence and acceptable at off design points.

Effect of Off-Design Incidence Angle. The differences between BASE and ES in simulation and experiment are even more pronounced for the off design incidence angles shown in Fig. 8 left and right, in Fig. 9, and in Fig. 10 which provides the simulated loss ~ incidence characteristics for Re=860,000 and 120,000. Reasons for these discrepancies and especially for the discrepancies between MISES simulation and the experiments will be explained in more detail in the following sections in particular for the off-design incidence angles at which supercritical flow conditions on the blade surface become relevant.

For a negative incidence angle of i=−6 deg the BASE cascade starts to choke and the laminar suction side accelerates to a maximum Mach number of 1.15 as shown in Fig. 11, top-left. An extended laminar shock wave boundary layer interaction weakens the boundary layer at mid-chord and rear turbulent separation is induced. The ES cascade remains far from choking and the maximum Mach number just exceeds 0.9 (Fig. 11, top-right). At this incidence MISES simulates only 4.9% of loss for the ES airfoil compared to 9.2% for the BASE profile.

At a positive incidence (β_1=134.5 deg) the suction side Mach number of the BASE airfoil still remains below M=1.0 (Fig. 11, bottom-left). However, the peak Mach number of the front loaded airfoil ES, which has a relatively thick leading edge, exceeds M=1.24 (Fig. 11, bottom-right) and even reaches 1.3 at the high Reynolds number (Fig. 13). But the resulting shock wave is weak and has no adverse effect on the blade performance. The thicker but well shaped leading edge of the ES profile makes the cascade less sensitive to incidence variations, as discussed already in [14,15].

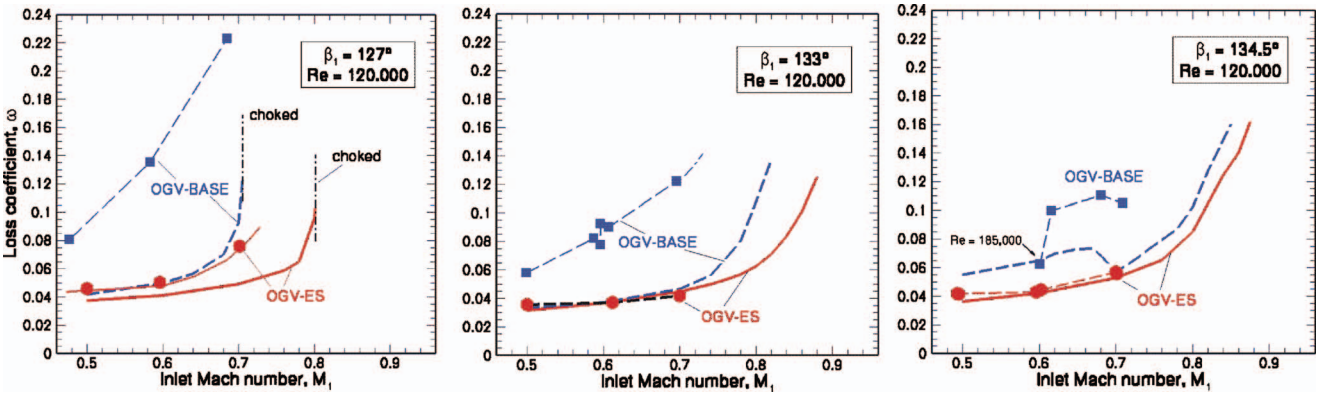

Fig. 8 Mach number influence on losses for i=−6 deg, i=0 deg, and i=+1.5 deg. Experiment (symbol) and MISES simulation (line).

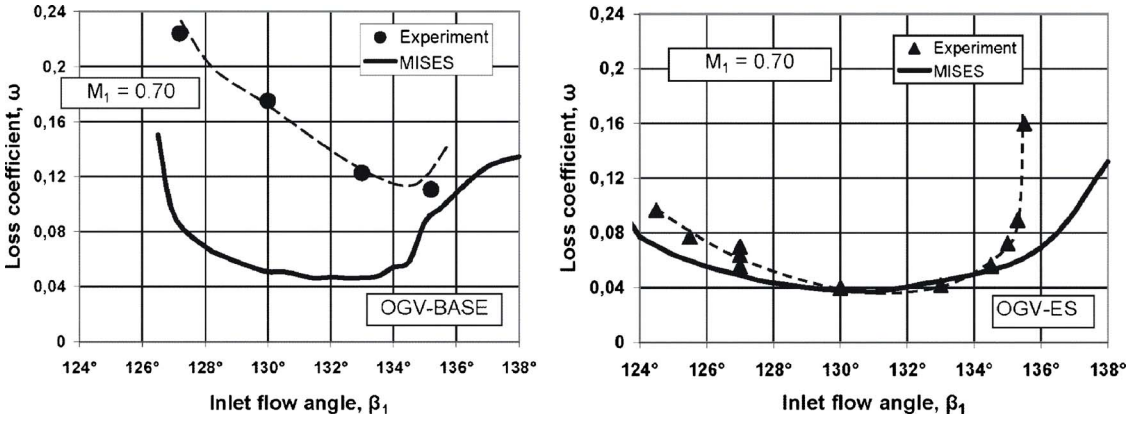

Fig. 9 Comparison of MISES and experiment for low Reynolds number condition (Re=120,000)

Unlike, the circular leading edge of the BASE airfoil induces a more distinct LE peak that weakens the boundary layer from the beginning.

Comparisons between the simulated and experimental Mach number distributions will be discussed in the following two sections for high and low Reynolds numbers.

Simulation and Experiment at High Reynolds Number. From both the experimental as well as theoretical loss ~ incidence characteristics it becomes apparent that the essential differences between BASE and ES becomes visible at off-design conditions. Therefore, the detailed results at $M_1=0.7$ will be discussed for $i=-6$ deg and $i=+1.5$ deg. At the Reynolds number of 860,000 the agreement between experiment and MISES simulation is very good for the low loaded negative incidence condition. In Fig. 12, the surface Mach number distributions of both cascades excellently agree with the simulation and even the loss levels are quite similar. A Schlieren photograph of the BASE cascade clearly visualizes the shock wave pattern within the supersonic bubble, see Fig. 12, left.

Considerable differences between experiment and MISES are observed for the BASE cascade at $i=+1.5$ deg. Figure 13 clearly shows a severe turbulent boundary layer separation starting at about 50% of the chord whereby MISES seriously underpredicts this separation. We believe that MISES fails in simulating the local boundary layer separation induced by the distinct velocity peak of the circular leading edge [15].

For the corresponding test point, the front loaded airfoil ES shows a very high velocity reaching a Mach number level around 1.2, whereby MISES predicts about 1.3. Nevertheless, losses remain relatively low. No boundary layer separation is observed on the entire suction surface, and experiment and MISES results agree quite well. In the Schlieren photograph in Fig. 13 (right) only a nonsignificant shock wave is visible.

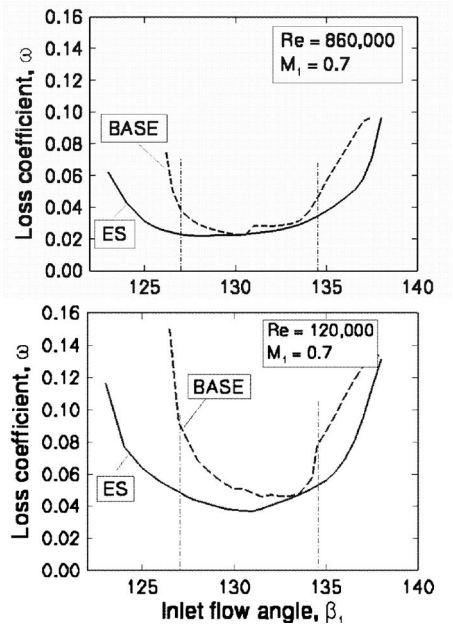

Fig. 10 Simulated loss-incidence characteristics for $M_1=0.7$ at high (top) and low (bottom) Reynolds number

Simulation and Experiment at Low Reynolds Number. At the low Reynolds number of 120,000 differences between MISES simulation and experiment become more evident. For $i=-6$ deg the BASE airfoils completely fail as can be seen in Fig. 14, left. At this test point, the gradient of deceleration behind the extended laminar separation bubble is too high. Hence, the laminar separation bubble at midchord position completely bursts and the circulation around the airfoil breaks down. MISES still predicts reattachment of the bubble with starting rear turbulent separation resulting in 9.2% losses. The experimental losses dramatically increase to about 22%.

The simulation of the ES Mach number distribution is quite good, just the extension of the laminar midchord bubble is slightly underpredicted and the short separation bubble immediately behind the pressure side leading edge is missing, see Fig. 14, right. This also explains the slight differences between experimental and simulated losses of 7% and 4.9%, respectively.

At first sight, the experimental Mach number distribution for BASE at $i=+1.5$ deg looks quite healthy, but effectively the suction side has a strong turbulent separation and losses are twice as high as MISES predicts (Fig. 15, left). The supercritical ES cascade with the theoretical peak Mach number of 1.24 for Re =120,000 can cope with the deceleration on the suction side without separation and the losses of experiment and simulation agree quite well (Fig. 15, right). However, again MISES misses the local—in this case shock induced—leading separation bubble. This bubble reattaches at about 20% of the chord and the rear turbulent boundary layer remains quite healthy.

Boundary Layer Development. The design incidence conditions at $M_1=0.7$ (Fig. 11, center) and the above described critical test points at low Reynolds number (Re=120,000) are analyzed in more detail by studying the boundary layer development of the blade suction side. Figure 16 clearly demonstrates the important differences between the baseline CDA airfoil and the optimized ES airfoil for $i=0$ degree of incidence. The form factor H_{12i} and the skin-friction coefficient C_f of the BASE airfoil indicate a short

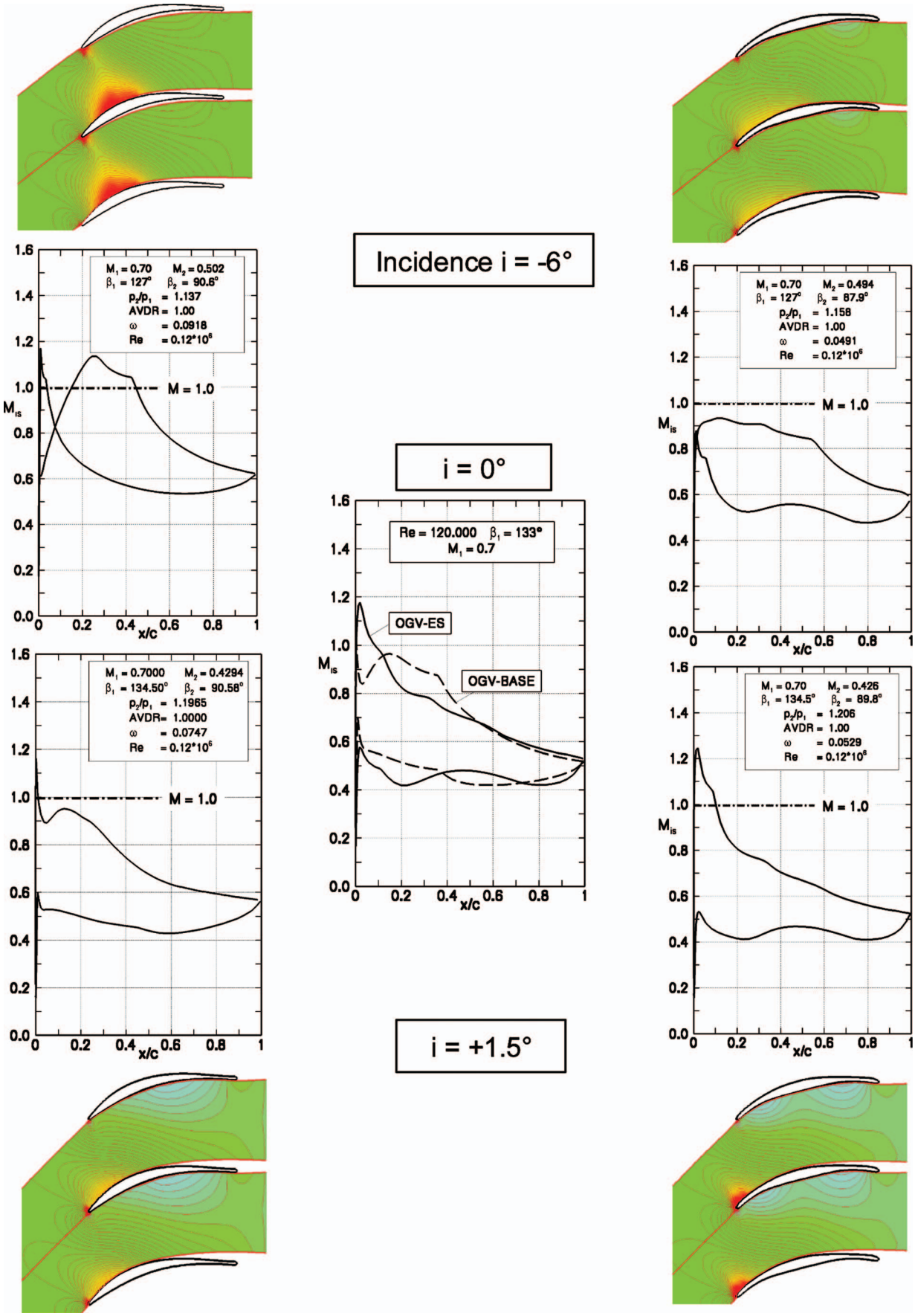

Fig. 11 Simulated Mach number distributions for M_1=0.7 and Re=120,000 at i=−6 deg (top), i=0 deg (center), and i=+1.5 deg (bottom)

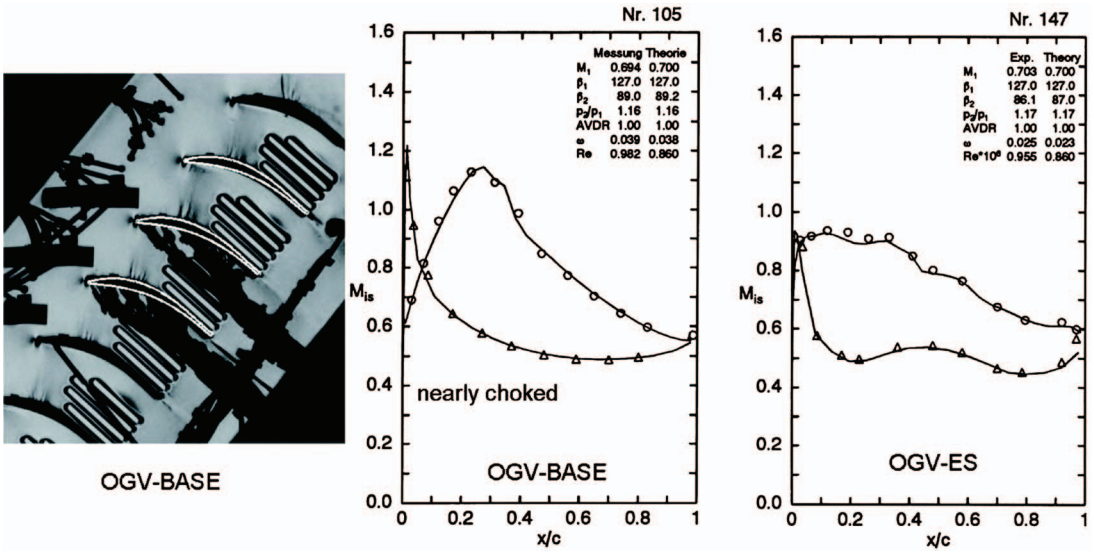

Fig. 12 Schlieren photograph and surface Mach number distributions for $M_1=0.7$ at $i=-6$ deg and Re$\approx 1\times 10^6$. Experiment (symbol) and MISES (line).

bubble behind the distinct LE peak, a relaminarization, and an extended laminar separation bubble from 25 to 40% of the chord. On the rear part of the suction side, we observe rear turbulent separation indicated by the shape factor H_{12i}, that exceeds a value of 2.5.

The boundary layer on the front loaded ES airfoil experiences a thin shock induced laminar separation with turbulent reattachment near 15% of the chord. However, downstream, the suction side boundary layer remains very stable which is shown by the strong increase of the friction coefficient: C_f between 15 and 35% of the chord, see Fig. 16, bottom-right. The weak shock wave behind the LE seems to have no detrimental effect on the very thin and still healthy boundary layer.

At negative incidence angles and supercritical flow conditions still the boundary layer of the suction side must be considered because loading is highest downstream of the midchord supersonic pocket. For the test point ($i=-6$ deg) shown in Fig. 14, the simulated boundary layer parameters are plotted in Fig. 17. Both cascades show a midchord laminar separation bubble, but the bubble on the BASE airfoil does not reattach, whereas the ES airfoils experiences a healthy turbulent reattachment.

Due to the considerable difference between MISES simulation and experiment of the BASE cascade in Fig. 14 (left), another coupled blade-to-blade simulation was performed to find out the shortcomings of MISES for this low Reynolds number test point. A better agreement between simulation and experiment was achieved by reducing the Reynolds number from 120,000 to a fictive Reynolds number of 80,000 and the free-stream turbulence level from 0.5% to 0.1%. The corresponding surface Mach number distribution and boundary layer parameters are plotted in Fig. 17. At these "wrong or artificial" boundary conditions the laminar suction side bubble completely bursts and the losses increase from 9% to about 18%, a level similar to the experimental one.

Finally, the positive incidence angle test points of Fig. 15 are analyzed in Fig. 18. Here the shape factor of the BASE airfoil clearly indicates strong rear turbulent separation. The front loaded

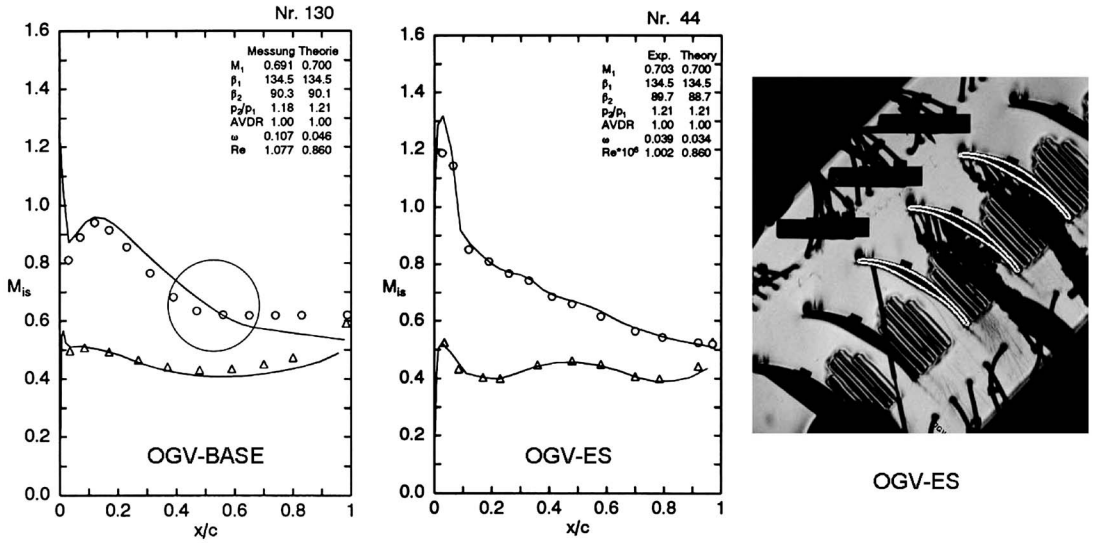

Fig. 13 Surface Mach number distributions and Schlieren photograph for $M_1=0.7$ at $i=+1.5$ deg and Re $\approx 1\times 10^6$. Experiment (symbol) and MISES (line).

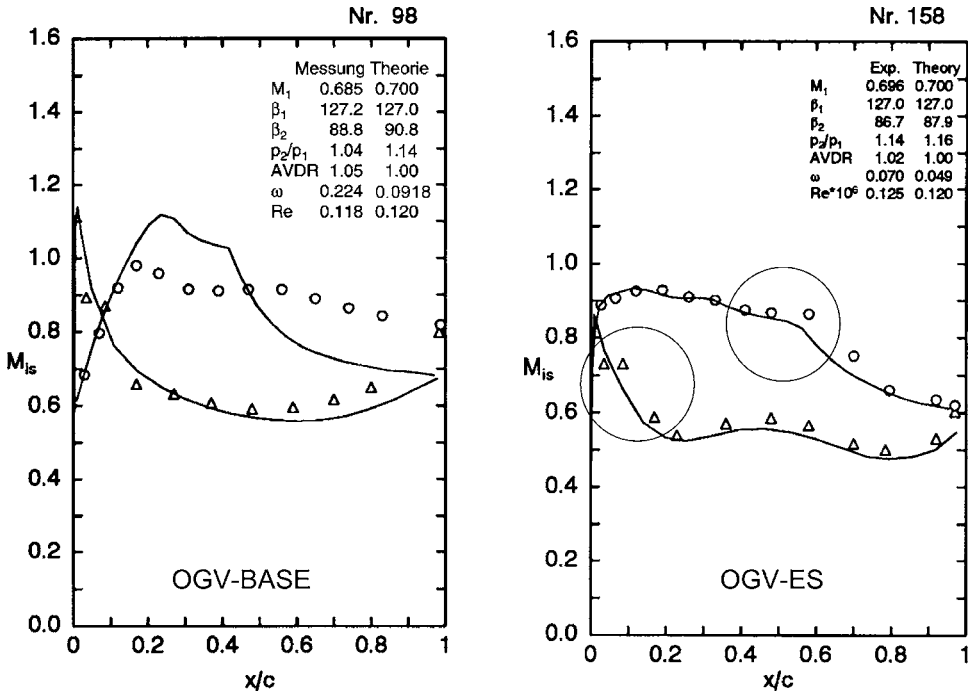

Fig. 14 Surface Mach number distributions for $M_1=0.7$ at $i=-6$ deg and low Reynolds number ($Re\approx 1.2\times 10^5$)

airfoil ES with a simulated peak suction side Mach number of 1.25 shows a shock induced laminar separation with an intensive turbulent reattachment. However, the experiment in Fig. 15 (right) indicates that the peak Mach number remains below 1.1. The shock induced laminar bubble is more extended in the experiment than in the simulation. The boundary layer code in MISES obviously has some difficulties to simulate short separation bubbles immediately behind the leading edge on both pressure and suction side when the blade chord Reynolds number remains below $\approx$500,000.

Conclusions

Two alternative outlet guide vanes designed for low Reynolds number operation have been investigated for a range of Reynolds

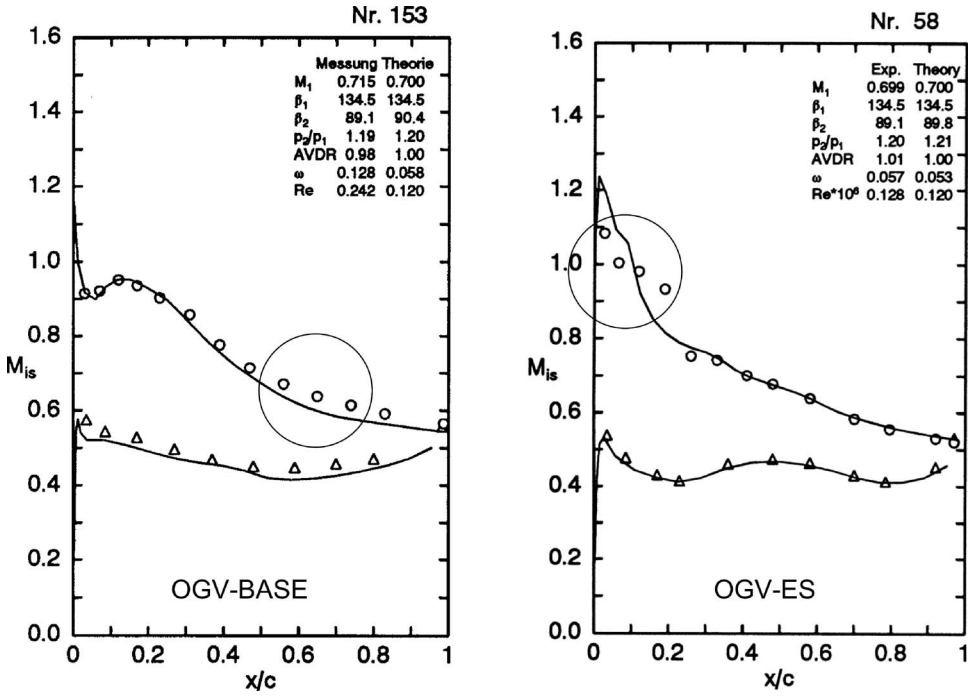

Fig. 15 Surface Mach number distributions for $M_1=0.7$ at $i=+1.5$ deg and a low Reynolds number

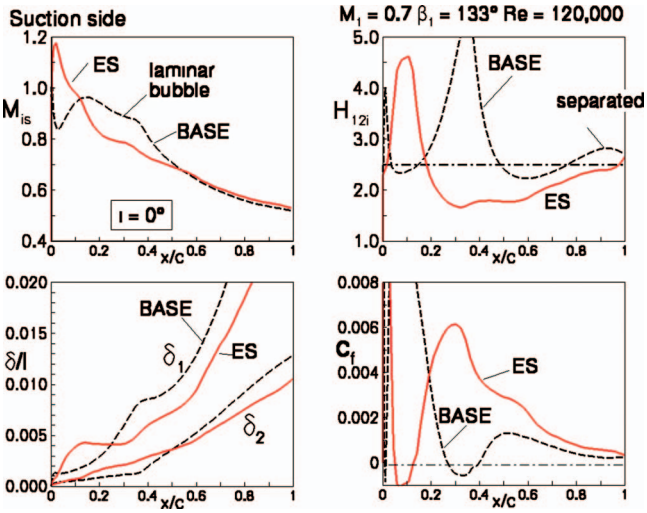

Fig. 16 Boundary layer properties at $i=0$ deg for $M_1=0.7$

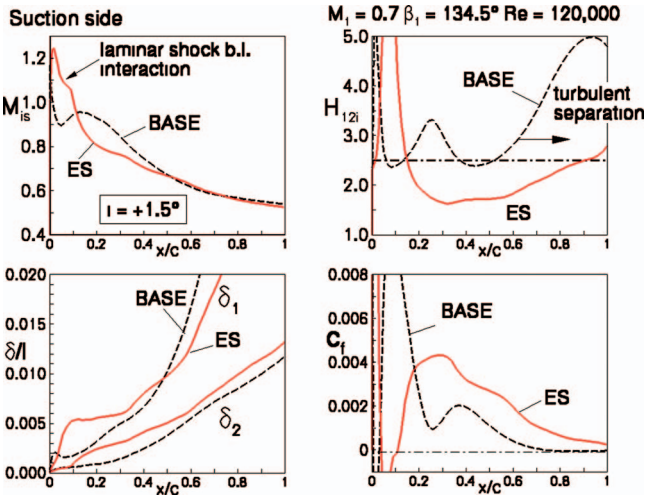

Fig. 18 Boundary layer properties at $i=+1.5$ deg for $M_1=0.7$

numbers and inlet Mach numbers up to supercritical flow conditions. The first baseline cascade consists of conventional controlled diffusion airfoils (CDA) and the second optimized cascade consists of extremely front loaded airfoils with the peak Mach number at the leading edge. The following conclusions can be drawn:

Tests with different turbulence levels show that the CDA pressure distribution with an accelerated front portion and laminar separation is more sensitive to free-stream turbulence than the airfoil with an extremely front loaded distribution, especially at low Reynolds number conditions.

The advantage of the front loaded airfoil holds even at supercritical flow conditions with a suction side peak Mach number up to 1.25–1.3. The steep pressure gradient behind the leading edge induced by the weak shock wave promotes early transition in a region, where the boundary layer is thin and healthy.

At the supercritical conditions ($M_1=0.7$) the difference in losses between the CDA airfoil and the front loaded one is even more evident at off-design incidence angles. This holds true for the simulated losses and even more for the experimental ones.

The blade-to-blade solver MISES used for the analysis excellently simulated the blade performance and profile Mach number distributions, especially at the higher Reynolds numbers. However, at low Reynolds number some discrepancies arise in simulating the extension of laminar separation bubbles and resulting losses. We believe that most of the discrepancies have their origin at the blade leading edge.

The boundary layer code in MISES has some difficulties to simulate short separation bubbles immediately behind the leading edge on pressure and/or suction side when the blade chord Reynolds number is low.

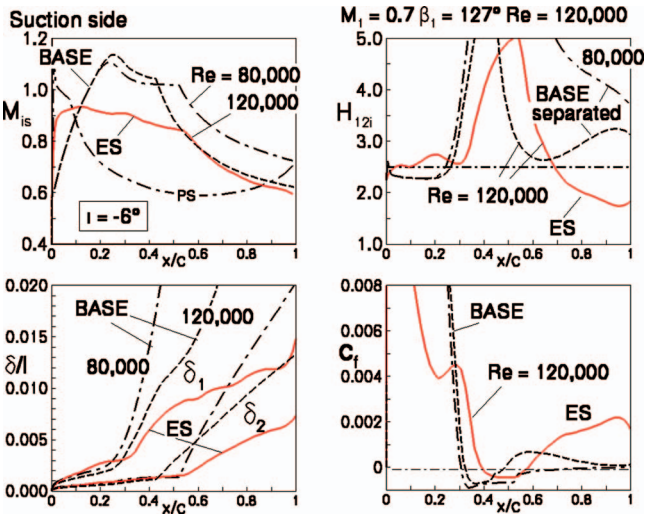

Fig. 17 Boundary layer properties at $i=-6$ deg for $M_1=0.7$ and additional results for a very low Re=80,000

Acknowledgment

The authors are grateful to Wolfgang Steinert from the Institute of Propulsion Technology, DLR Cologne, who performed the test series.

Nomenclature

AVDR = axial velocity density ratio = $(\rho_2 w_2 \sin\beta_2)/(\rho_1 w_1 \sin\beta_1)$
D_f = diffusion factor $=1-w_2/w_1+(w_2/w_1\cos\beta_2-\cos\beta_1)s/2c$
c = chord length
C_f = friction coefficient $=2\tau_w/(\rho w^2)$
H_{12} = shape factor $=\delta_1/\delta_2$ (index i when incompressible)
i = incidence angle $=\beta_1-\beta_{1\text{design}}$
M = Mach number
p = pressure
Re = Reynolds number based on chord length
s = blade spacing
w = velocity
x = chordwise coordinate
β = flow angle with respect to cascade front
δ_1 = boundary layer displacement thickness
δ_2 = boundary layer momentum thickness
ρ = density
ω = total pressure loss coefficient: $\omega=(p_{t1}-p_t)/(p_{t1}-p_1)$

Subscripts

1 = inlet plane, far upstream
2 = exit plane, far downstream
is = isentropic entity
LE = leading edge
TE = trailing edge

References

[1] Wisler, D. C., 1998, "The Technical and Economic Relevance of Understanding Boundary Layer Transition in Gas Turbine Engines," Minnowbrook II, 1997 Workshop on Boundary Layer Transition in Turbomachines, NASA/CP-1998-206958, pp. 53–64.

[2] Ashpis, D., 1998, "The NASA Low-Pressure Turbine Flow Physics Program," Minnowbrook II, 1997 Workshop on Boundary Layer Transition in Turbomachines, NASA/CP-1998-206958, pp. 45–52.

[3] Lou, W., and Hourmouziadis, J., 2000, "Separation Bubbles Under Steady and Periodic-Unsteady Main Flow Conditions," ASME J. Turbomach., **122**, pp. 634–643.

[4] Volino, R., and Hultgren, L. S., 2001, "Measurements in Separated and Transitional Boundary Layers Under Low-Pressure Turbine Airfoil Conditions," ASME J. Turbomach., **123**, pp. 189–197.

[5] Howell, R. J., Ramesh, O. N., Hodson, H. P., Harvey, N. W., and Schulte, V., 2001, "High Lift and Aft-Loaded Profiles for Low-Pressure Turbines," ASME J. Turbomach., **123**, pp. 181–188.

[6] Haselbach, F., Schiffer, H. P., Horsman, M., Dressen, S., Harvey, N., and Read, S., 2002, "The Application of Ultra-High-Lift Blading in the BR715 LP Turbine," ASME J. Turbomach., **124**, pp. 45–51.

[7] Rhoden, H. G., 1952, "Effects of Reynolds Number on the Flow of Air through a Cascade of Compressor Blades," ARC, R&M No. 2919.

[8] Roberts, W. B. 1975, "The Effect of Reynolds Number and Laminar Separation on Axial Cascade Performance," ASME J. Eng. Power, **97**, pp. 261–274.

[9] Citavy, J., and Jilek, J., 1990, "The Effect of Low Reynolds Number on Straight Compressor Cascades," ASME Paper No. 90-GT-221.

[10] Hobbs, D. E., and Weingold, H. D., 1984, "Development of Controlled Diffusion Airfoils for Multistage Compressor Application," J. Eng. Gas Turbines Power, **106**, pp. 271–278.

[11] Köller, U., Mönig, R., Küsters, B., and Schreiber, H. A., 2000, "Development of Advanced Compressor Airfoils for Heavy-Duty Gas Turbines, Part 1: Design and Optimization," ASME J. Turbomach., **122**, pp. 397–405.

[12] Schreiber, H. A., Steinert, W., and Küsters, B., 2002, "Effect of Reynolds Number and Free-Stream Turbulence on Boundary Layer Transition in a Compressor Cascade," ASME J. Turbomach., **124**, pp. 1–9.

[13] Sieverding, F., Ribi, B., Casey, M., and Meyer, M., 2004, "Design of Industrial Axial Compressor Blade Sections for Optimal Range and Performance," ASME J. Turbomach., **126**, pp. 323–331.

[14] Sonoda, T., Yamaguchi, Y., Arima, T., Olhofer, M., Sendhoff, B., and Schreiber, H. A., 2004, "Advanced High Turning Compressor Airfoils for Low Reynolds Number Condition, Part 1: Design and Optimization," ASME J. Turbomach., **126**(3), pp. 350–359.

[15] Schreiber, H. A., Steinert, W., Sonoda, T., and Arima, T., 2004, "Advanced High Turning Compressor Airfoils for Low Reynolds Number Condition, Part 2: Experimental and Numerical Analysis," ASME J. Turbomach., **126**(4), pp. 482–492.

[16] Olhofer, M., Arima, T., Sonoda, T., Fischer, M., and Sendhoff, B., 2001, "Aerodynamic Shape Optimization Using Evolution Strategies," in *Optimization in Industry III*, Springer Verlag.

[17] Arima, T., Sonoda, T., Shiratori, M., Tamura, A., and Kikuchi, K., 1999, "A Numerical Investigation of Transonic Axial Compressor Rotor Flow Using a Low Reynolds number k-ε Turbulence Model," ASME J. Turbomach., **121**(1), pp. 44–58.

[18] Drela, M., and Youngren, H., 1991, "Viscous/Inviscid Method for Preliminary Design of Transonic Cascades," AIAA-Paper No. 91-2364, Sacramento, CA.

[19] Drela, M., 1995, "Implementation of Modified Abu Ghannam Shaw Transition Criterion," *MISES User's Guide*, MIT, Computational Aerospace Science Lab., Cambridge, MA.

[20] Schlichting, H., and Das, A., 1970, On the Influence of Turbulence Level on the Aerodynamic Losses of Axial Turbomachines," *Dzung, Flow Research on Blading*, Elsevier, Amsterdam, pp. 243–268.

[21] Citavy, J., and Norbury, J. F., 1977, "The Effect of Reynolds Number and Turbulence Intensity on the Performance of a Compressor Cascade with Prescribed Velocity Distribution," J. Mech. Eng. Sci., **19**(3), pp. 93–100.

[22] Evans, R. L. 1978, "Boundary Layer Development on an Axial Flow Compressor Stator Blade," ASME J. Eng. Power, **100**, pp. 287–293.

[23] Mayle, R. E., 1991, "The Role of Laminar-Turbulent Transition in Gas Turbine Engines," ASME J. Turbomach., **113**, pp. 509–537, 1991 GTI Scholar Lecture.

[24] Cumpsty, N. A., Dong, Y., and Li, Y. S., 1995, "Compressor Blade Boundary Layers in the Presence of Wakes," ASME Paper No. 95-GT-443.

[25] Schreiber, H.A., and Steinert, W., 2004, "Experimental Investigation of Two Outlet Guide Vane Cascades—Effect of Free-Stream Turbulence on OGV-BASE and OGV-ES," DLR Internal Report No. 325-06-04.

The Effect of Wake Induced Structures on Compressor Boundary-Layers

Andrew P. S. Wheeler[1]
Robert J. Miller
Howard P. Hodson

Whittle Laboratory,
University of Cambridge,
Cambridge, UK

The interaction of a convected wake with a compressor blade boundary layer was investigated. Measurements within a single-stage compressor were made using an endoscopic PIV system, a surface mounted pressure transducer, hotfilms and hotwire traverses, along with CFD simulations. The wake/leading-edge interaction was shown to lead to the formation of a thickened laminar boundary-layer, within which turbulent spots formed close to the leading edge. The thickened boundary-layer became turbulent and propagated down the blade surface, giving rise to pressure perturbations of 7% of the inlet dynamic head in magnitude. The results indicate that wake/leading-edge interactions have a crucial role to play in the performance of compressor blades in the presence of wakes. [DOI: 10.1115/1.2720499]

Introduction

Current compressor design-tools are commonly based on studies of the flow within cascades, where the incoming flow is steady. However, the flows within aeroengine blade-rows are often highly unsteady. The effects that this has on the time-averaged performance, compared to the equivalent cascade test is not well understood. Nonetheless, one area where the effects of unsteady flows have been shown to be important is the effect that upstream wakes have on boundary-layer transition. There is a large amount of literature on boundary-layer transition in turbomachines and Mayle [1] and Walker [2] have provided excellent reviews of the early research. However, the true complexities of boundary-layer transition under the influence of upstream wakes have only been realized in more recent years. Cumpsty et al. [3] and Dong and Cumpsty [4,5] were the first to outline the basic mechanisms with an emphasis on the importance of the calmed region. Halstead et al. [6] performed extensive studies of wake-induced transition in compressors and turbines. Detailed studies of wake-induced transition in compressors can also be found in the work of Hughes and Walker [7] and Solomon and Walker [8].

Wake-induced transition can have both beneficial and detrimental effects on performance. Studies within LP turbine blade-rows have shown that, on the one hand, the increased turbulent wetted-area due to the wake-induced turbulence tends to increase losses, whereas the calmed regions which follow the turbulent spots tend to reduce losses compared to the undisturbed boundary-layer [9]. These ideas have been exploited in new LP turbine designs to increase blade loadings and reduce blade counts while still achieving the same loss level [10].

In compressor blade-rows, the impact of unsteady transition on loss has received little attention in the published literature. Dong [11] reported no significant effect on loss on a controlled diffusion blade. However, the flat-plate studies of Ottavy et al. [12] have shown a large impact on loss, where performance improvements above the steady-flow case were found at certain flow conditions. These and several other studies in compressor blade rows have shown that wake-induced transition generally starts very early on the blade suction surface [8,7,13]. Several empirical correlations based on steady flow transition [1] suggest that turbulent spots cannot form within a boundary-layer where the Reynolds number based on the time-averaged momentum thickness is small, such as close to the leading edge of blades. The early onset of wake-induced transition in compressors is therefore puzzling. This apparent anomaly has been addressed in part by Hughes and Walker [7], who have suggested that early transition in compressor blade-rows occurs due to the amplification of Tollmien-Schlichting disturbances. Nonetheless, the mechanism for the early formation of turbulent spots within compressor blade-rows is still not well understood.

A detailed investigation of the unsteady flow within a single-stage compressor rig has been conducted. The main focus of this was to determine the influence that the wake/leading-edge interaction has on the development of the suction-surface boundary-layer. A number of experimental techniques were used including PIV, unsteady surface pressure measurements, hotfilms and hotwire traverses, as well as high resolution leading-edge pressure measurements. A series of CFD simulations were also used to aid the analysis of the results. In this paper, the time-average and unsteady leading-edge flow-fields are investigated and this identifies a periodically thickened laminar boundary-layer which is formed through the leading-edge/wake interaction. Turbulent spots which form close to the leading edge are found to originate from within this structure, which consequently becomes turbulent and propagates at the front of the turbulent strip. The propagation of the wake and the thickened boundary-layer structure is tracked downstream of the leading edge. The structure is shown to propagate slower than the wake and to cause significant surface-pressure perturbations. A new picture of unsteady transition in compressors is presented, and the effect that the thickened boundary-layer structure has on the unsteady loss is measured.

Experimental and CFD Methods

Experimental Rig Details. The measurements were performed in the stator-blade row of the Deverson single-stage research compressor at the Whittle Laboratory, Cambridge, UK. The rig is a large-scale model of an embedded high-pressure compressor. A schematic of the rig and the working section is shown in Fig. 1. After a 9.3:1 area contraction air passes into a parallel annulus with hub and casing radii of 609.6 mm and 762.0 mm, respectively. A series of hub and casing boundary-layer blockage generators and a turbulence grid situated upstream of the stage simulate the flow conditions of an embedded stage. The air meets a

[1]Corresponding author, and current address: Rolls-Royce Industrial Fellow, St. Catherine's College, University of Oxford, Oxford OX1 3UJ, UK. email: andrew.wheeler@eng.ox.ac.uk

Contributed by the International Gas Turbine Institute of ASME for publication in the JOURNAL OF TURBOMACHINERY. Manuscript received July 31, 2006; final manuscript received July 31, 2006. Review conducted by David Wisler. Paper presented at the ASME Turbo Expo 2006: Land, Sea and Air (GT2006), May 8–11, 2006, Barcelona, Spain.

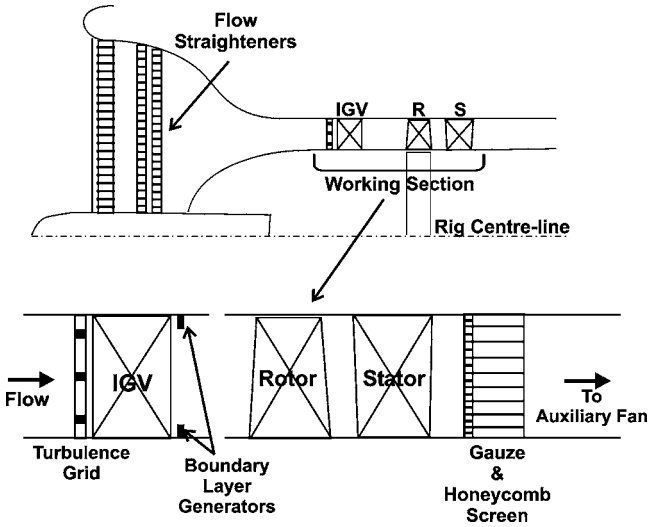

Fig. 1 The Deverson rig and working section

row of inlet guide vanes (IGVs), which produce the swirl required for the following rotor blades. After passing through the rotor blades the air travels through a row of stator blades, which are fixed from the casing and sealed at the hub. A pressure-loss screen and honeycomb are situated approximately 0.4 stator axial chords downstream of the stator trailing edge. These are to simulate the steady potential-field effects of a downstream stage with a fixed characteristic slope. An auxiliary fan and throttle, situated far downstream of the pressure-loss screen allows for the mass flow through the rig to be controlled independently of the rotational speed.

The "Build 2" rig configuration [14] was used for the current investigation. This has 51 rotor blades, 49 stator blades, a design rotational speed of 500 rpm and the design flow coefficient is $\phi = 0.51$. The stator blade inlet and exit Reynolds numbers at midspan, based on the chord are $\mathrm{Re} = 2.8 \times 10^5$ and 1.9×10^5, respectively. The stator inlet and exit flow angles at midspan are $\alpha_1 = 52.7$ deg and $\alpha_2 = 29.5$ deg, respectively. The stator blade has a chord $c = 126$ mm, and a circular leading edge of radius $r/c = 0.0087$ with an included wedge angle of 32.0 deg.

Figure 2 shows the experimentally measured time-averaged pressure distribution for the stator-blades at midspan, along with the CFD predictions which will be discussed later. The stator

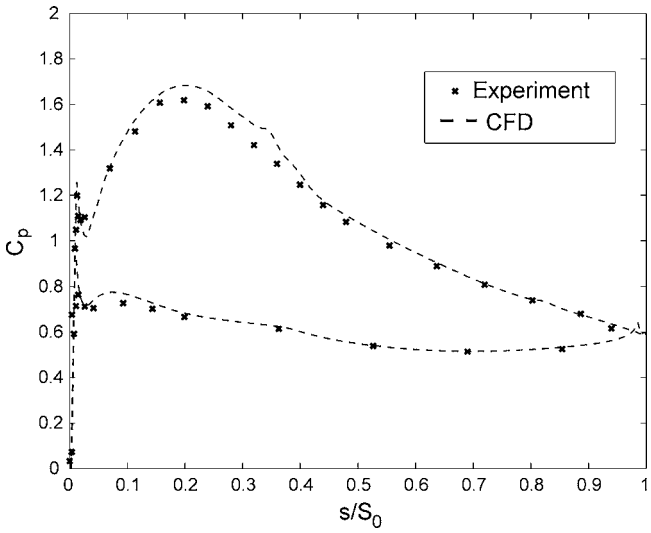

Fig. 2 The stator-blade pressure distribution at midspan, at $\phi = 0.51$

blades are a controlled diffusion aerofoil (CDA) design, as is seen in the figure, where the adverse pressure gradient on the suction surface is initially comparatively steep and then decreases in strength towards the trailing-edge.

Experimental Methods. The unsteady flow field was measured using a LaVision PIV system, which consisted of a frequency-doubled double-pulse 120 mJ Nd-YAG laser and a double frame 12 bit CCD camera. Endoscopes and laser guiding optics were used to obtain optical access for the laser measurements. The flow seeding was produced using a Le Maitre vaporizing fog generator and the seeding was injected into the rig bellmouth.

Measurements of the boundary-layer were made at a surface length of 6.7% S_0 and 97% S_0, with a hotwire probe which was traversed across the boundary-layer at these positions. The hotwire was calibrated for velocity using the King's law method, and the Bearman and Cox correction methods were implemented to correct for ambient temperature variations and wall proximity effects, respectively. For the traverse at 6.7% S_0, the thinness of the boundary-layer required that the distance of the first traverse point from the surface be estimated by comparing the time-average measured profile to that predicted by the CFD calculations.

Time-average surface pressures were obtained using a specially manufactured blade with pressure tappings around the blade circumference. A microtapping technique similar to that used by Bindon [15] was used to obtain high resolution measurements around the leading edge.

Unsteady suction-surface pressures were measured using an Endevco 8507C pressure transducer which was mounted flush with the blade suction-surface by inserting it into a hole through the blade.

An array of surface-mounted hotfilms were used to make quasi shear stress measurements over the stator blade suction surface. The quasi wall shear stress is related to the measured output voltage by the relation [16],

$$\tau_w = \left(\frac{E^2 - E_0^2}{E_0^2} \right)^3 \tag{1}$$

where E_0 is the output voltage under zero flow conditions.

The data logging during all the unsteady measurements was triggered using a once-per-revolution signal from the rotor. The ensemble statistics were then obtained from a number of "phase-locked" time-series. For the PIV measurements, 128 instantaneous vector fields at 8 rotor phase angles were obtained. During the hotfilm and hotwire measurements 256 phase-locked time-series were logged and 512 were logged for the unsteady pressure measurements.

A series of normalizations are used in the paper to aid the analysis of the results. These are defined as

$$f^*(s,t) = \frac{f(s,t) - f_m(s)}{f_m(s)} \tag{2}$$

$$f^{**}(s,t) = \frac{f(s,t) - f_{\max}(s)}{f_{\max}(s) - f_{\min}(s)} \tag{3}$$

$$f^{***}(s,t) = \frac{f(s,t) - f_m(s)}{f_{\max}(s) - f_{\min}(s)} \tag{4}$$

where f represents the measured variable.

CFD Details. The UNSFLO [17] computer program was used to aid the analysis of the experimental results. This program can solve the steady or unsteady, inviscid or viscous equations of motion in two dimensions or in a quasi-three-dimensional mode where a streamtube thickness variation is specified. For viscous calculations, as used in the present work, it solves the thin-layer Navier-Stokes equations on a structured O-grid around the turbomachinery blades. On the rest of the grid, the Euler equations for

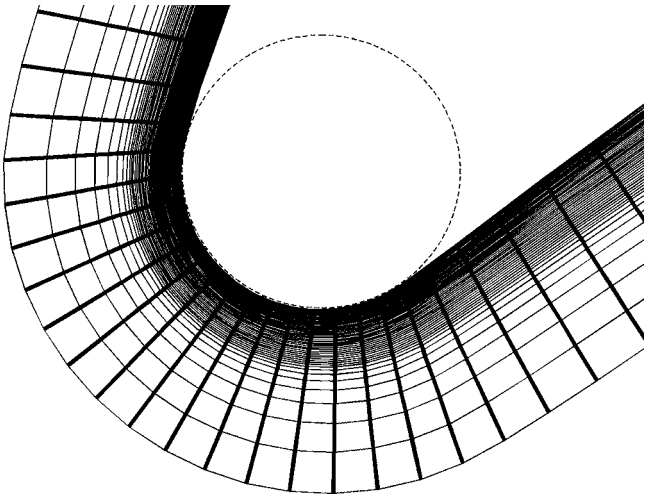

Fig. 3 Computational mesh close to the leading edge

inviscid flow are solved. For the present investigation a streamtube thickness variation was determined from a fully three-dimensional calculation of the flow field in the stator passage.

The 2D computational mesh used for the current work had 24,289 nodes. The leading-edge region of the stator-blade, at midspan, was the main focus of these calculations, and the computational mesh in this region is shown in Fig. 3. Naturally, the boundary-layer in this region was thin and therefore a large number of cells across the viscous O-mesh were required. At the same surface distance as the experimental boundary-layer traverse at $s/S_0=0.067$, there were 30 mesh points across the time-average boundary-layer. The start and end of transition was fixed, and an algebraic turbulence model [17] was implemented downstream of this point. On the suction-surface, transition was prescribed just downstream of where boundary-layer separation occurred at $s/S_0=0.36$. This ensured that laminar flow existed over the front portion of the blade.

The boundary conditions for the calculations were the exit Reynolds number, the exit Mach number, and the inlet flow angle. The exit Reynolds number and inlet flow angle were set to be equal to the experimental values detailed above, whereas the exit Mach number was raised to 0.2 to aid convergence. An unsteady calculation was performed, where a wake profile was prescribed at the inlet in order to simulate the effect of an upstream rotor-blade wake. A Gaussian wake profile was prescribed according to experimental measurements, which gave the wake half-width as $0.1P$ and the velocity defect as $0.4V_{\text{inlet}}$.

Figure 2 shows the predicted time-averaged C_p distribution from the CFD calculation. The agreement between experiment and CFD is quite reasonable over most of the blade surface, with some differences close to the peak suction position. The large spikes in the C_p distributions close to the leading edge will be discussed next.

Results

Leading-Edge Flow Field. Figure 4 shows a comparison of the experimental and CFD time-averaged C_p distribution in the leading-edge region. A spike in the experimental distribution on the suction surface is observed at $s/S_0=0.013$, while no spike is observed on the pressure surface. The spike is caused by the over-acceleration and then rapid deceleration as the flow is turned around the leading-edge circle. The deceleration causes an increase in the boundary-layer thickness and may result in separation [18]. At positive incidences the spike on the suction-surface is increased and the pressure-surface spike is decreased, whereas for negative incidences the opposite is true. The CFD results exhibit a

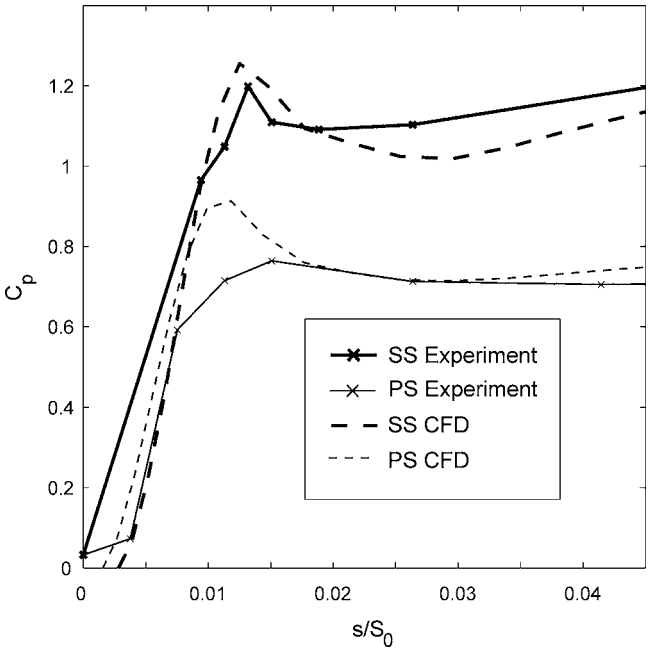

Fig. 4 Leading-edge time-average C_p distribution at midspan

suction-surface spike at a similar position to the experiment, although the predicted spike height is slightly larger. The CFD also predicts a small pressure-surface spike.

The effect that the wake has on the time-resolved suction-surface C_p distribution can be seen in Fig. 5, which has been derived from the CFD calculation. Here the distributions with the largest and smallest spike heights are compared with the time-averaged distribution. The largest spike height occurs when the wake is at the leading edge, as shown in the schematic from the CFD calculation. The figure shows that the spike height is increased significantly by the presence of the wake at the leading edge. The impingement of the wake increases the time-resolved incidence, and hence creates the observed increase in the time-resolved spike height. The T2 and T1 distributions represent the average C_p distributions when the leading edge is encompassed by

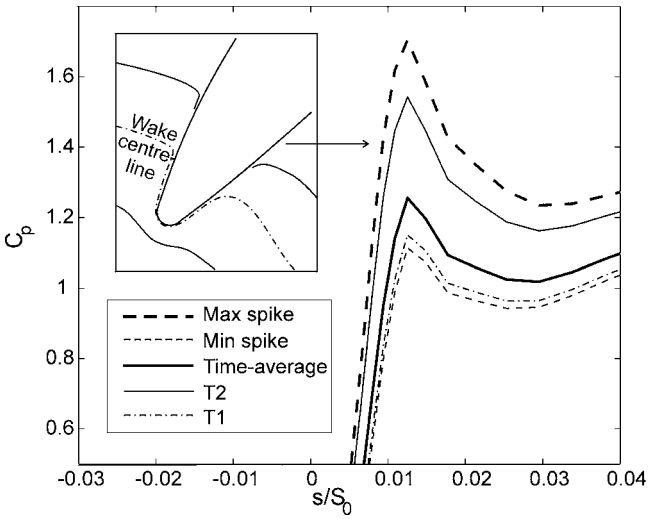

Fig. 5 Leading-edge suction-surface C_p distribution with and without wake impingement, from the CFD solution

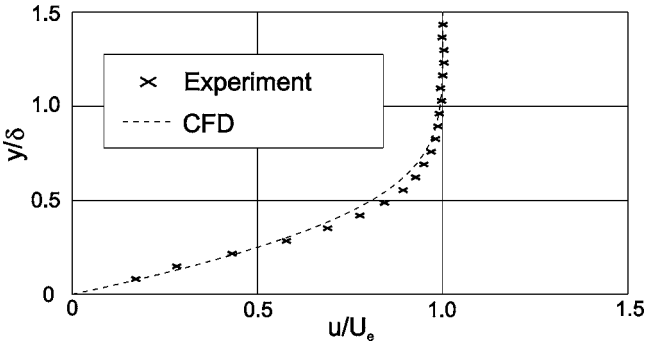

Fig. 6 Measured and predicted time-averaged boundary-layer profile at 6.7% S_0

the wake (22% τ_0) and when the wake is completely clear of the leading edge (50% τ_0). These will be used in an analysis which is discussed later.

The effect that the time-resolved variation of the leading-edge spike had on the boundary-layer development was measured using a hotwire probe, which was traversed across the boundary-layer at 6.7% S_0. A comparison of the CFD and the experimentally measured time-averaged boundary-layer profile are shown in Fig. 6. The CFD prediction matches reasonably well the experimental result, which implies that the boundary-layer is laminar at this point since transition was prescribed in the CFD to be further downstream. Further evidence of this is shown in Fig. 7, which plots the variation of the shape factor (H) with time for the experiment and the CFD prediction. The experimental value of H has a peak variation of 6% about a mean of 2.47, which is in the range where laminar flow would be expected. The CFD predicts a similar mean value of H=2.43, with a variation of 2%.

Figure 8 compares the experimentally measured and computationally predicted variation of momentum thickness divided by the time-average (θ/θ_m). A periodic increase of approximately 17–18% in the experimentally measured θ/θ_m is seen. The CFD prediction gives a similar, although slightly smaller, variation in θ/θ_m of 16.7%.

Predictions of the momentum thickness at this point, using the method of Thwaites, for the velocity distribution of the T1 and T2 cases discussed previously are also marked in Fig. 8. The CFD prediction fluctuates approximately between these two values. This would suggest that the wake impingement at the leading edge

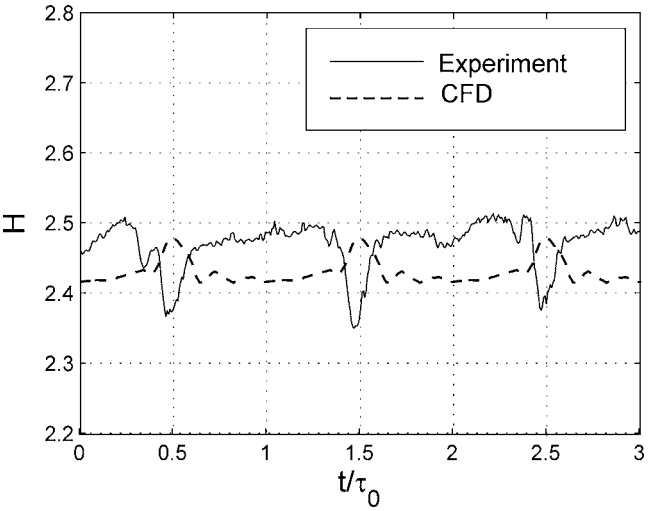

Fig. 7 Measured and predicted variation of H with time at 6.7% S_0

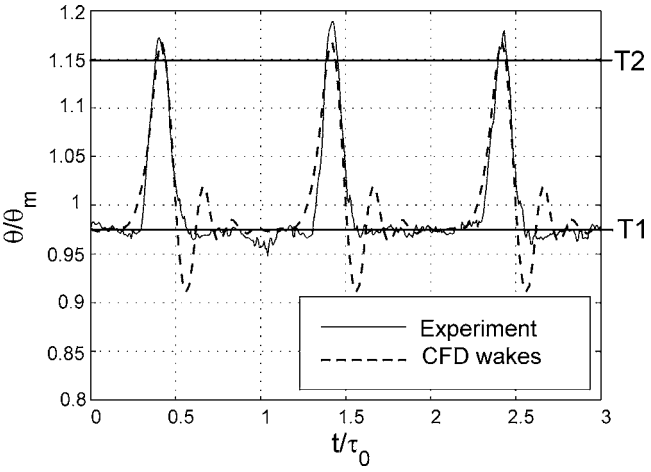

Fig. 8 Measured and predicted variation of θ/θ_m with time at 6.7% S_0

creates large fluctuations in the boundary-layer momentum thickness by changing the velocity distribution around the leading edge. In addition, this implies that the leading-edge boundary-layer responds in a quasi steady way to the wake impingement, (see [19,20]). Since the variations in H are small then this increase in momentum thickness also leads to an increase in boundary-layer blockage and there is a subsequent thickening of the boundary-layer at these times.

Figure 9 plots the Reynolds number based on momentum thickness (Re_θ) at 6.7% S_0 calculated from the hotwire traverse described previously. The critical Reynolds number based on momentum thickness ($\mathrm{Re}_{\theta\mathrm{crit}}$) is also plotted according to the correlation by Mayle [1], using the boundary-layer edge turbulence intensity (Tu) calculated from these experimental results. For boundary-layers where the value of Re_θ is greater than $\mathrm{Re}_{\theta\mathrm{crit}}$, turbulent spots are expected to develop. Figure 9 shows that these conditions are closely met within the region of the thickened boundary-layer, where Re_θ is high and the value of $\mathrm{Re}_{\theta\mathrm{crit}}$ is low due to the raised turbulence level in the wake. The Mayle correlation applies to transition via a bypass mode, however, the probability of natural transition occurring is also increased in regions of high Re_θ.

Convection of Wake and Wake-Induced Structure. The space-time diagram in Fig. 10 was constructed from the PIV measurements to investigate the propagation of the wake over the

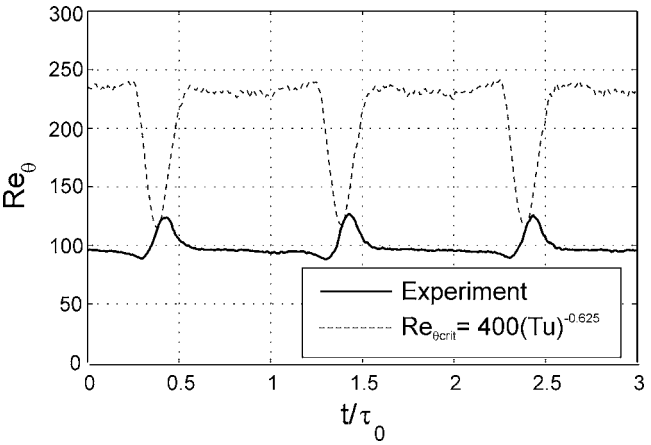

Fig. 9 Measured variation of Re_θ and $\mathrm{Re}_{\theta\mathrm{crit}}$ based on the Mayle correlation [1], at 6.7% S_0

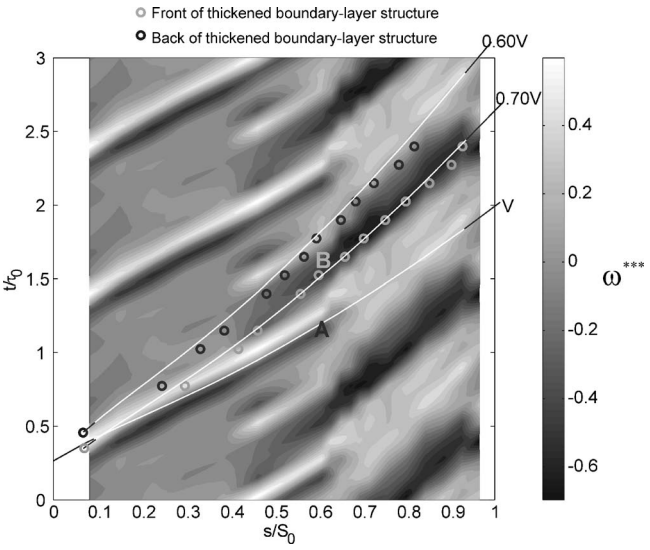

Fig. 10 *S-T* plot of normalized ensemble-averaged vorticity (third normalization, ω^{***}, see Eq. (4)) at $y/c=0.046$ above the suction surface

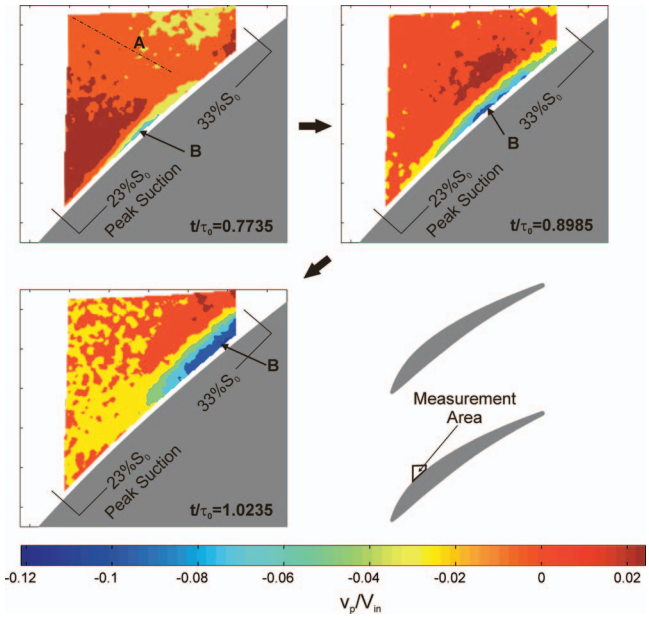

Fig. 12 Contour plots of ensemble-average perturbation velocity (v_p/V_{inlet}) close to peak-suction at 3 rotor phase angles

suction-surface. The space-time diagram was produced by extracting velocity data at a plane $y/c=0.046$ above the blade suction surface. The figure plots normalized ensemble-average vorticity (third normalization, ω^{***}, see Eq. (4)). Several convection lines are plotted which correspond to celerities of the freestream velocity (V) as calculated from the measured blade pressure distribution, and fractions of this speed, $0.6V$ and $0.7V$. The wake is identified as two parallel regions of positive and negative vorticity, caused by the negative-jet effect shown by Meyer [21]. The wake (marked A) convects at the freestream velocity over the blade surface, and therefore the V convection line represents the locus of the wake in space and time. At distances of $s/S_0>0.65$ the measurement plane is within the boundary-layer and hence it is not possible to distinguish the wake in this region.

Figure 11 is a space-time diagram of the unsteady surface pressure, where the measurement locations are indicated at the top of the diagram. The same celerity lines plotted in Fig. 10 are shown. The wake does not appear to significantly affect the pressure downstream of the leading-edge region. However, a pressure drop is observed to propagate at a slower speed than the wake, between the $0.7V$ and $0.6V$ lines.

Figure 12 shows the PIV measurements of the ensemble-averaged flow-field at three rotor-phases close to the peak-suction position on the blade. The figure plots contours of perturbation velocity, which is defined here as

$$v_p = |v| - |v_m| \tag{5}$$

The perturbation velocity will be negative in regions of low velocity flow relative to the time-averaged flow-field. The kinematic effect of the wake near the blade surface creates a region of negative v_p leading the wake and a region of positive v_p flow following the wake [21]. The wake center line is therefore approximately midway between these regions, and is seen at $t/\tau_0=0.7735$ marked A. In addition to the wake, a region of low velocity corresponding to a thickened boundary-layer is observed (marked B). It is clearly seen convecting across the surface at the three rotor-phases shown and the structure lags behind the wake. It can be seen to grow in height while it convects, however at this point it is below the plane at which the space-time diagram of Fig. 10 was constructed. The increase in height of the structure as it convects downstream is likely to be due to the influence of the adverse pressure gradient downstream of peak suction.

The propagation of the wake and the thickened boundary-layer down the late suction-surface was observed using further PIV measurements. These are shown in Fig. 13, which are plots of the ensemble-averaged late suction-surface flow-field at four equally spaced times in the wake-passing period. A schematic of the measurement window and the relative positions of the wake and the thickened boundary-layer are shown next to each plot. Contours of perturbation vorticity (ω_p) are shown which shows the deviation of the vorticity from the time-average. The wake (marked A), is observed as a region of positive and negative ω_p, as observed in Fig. 10. The thickened boundary-layer (marked B) appears as a region of negative ω_p since it acts to increase the magnitude of the vorticity in the outer boundary-layer. Both A and B can clearly be seen to convect over the blade surface and the thickened boundary-layer now significantly lags behind the wake. The thickened boundary-layer can now be identified in the space-time diagram of Fig. 10 as the dark region labeled B, where the height of

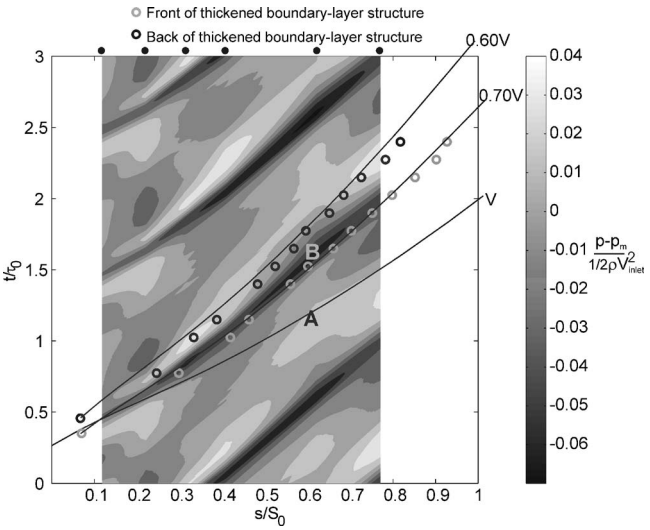

Fig. 11 *S-T* plot of the ensemble-averaged surface pressure perturbation ($(p\text{-}p_m)/1/2\rho V^2_{inlet}$)

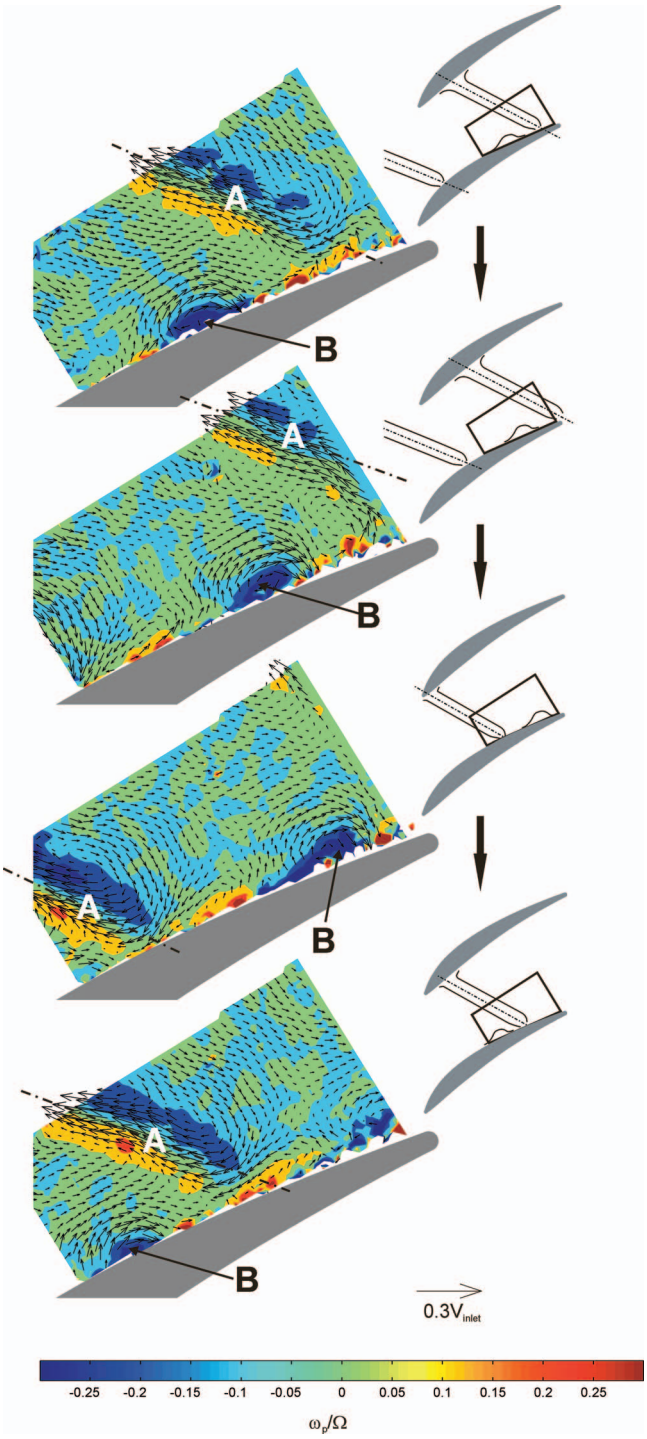

Fig. 13 Contour plots of ensemble-average perturbation vorticity (ω_p) and perturbation vector fields (Reynolds decomposition) at 4 rotor phase angles

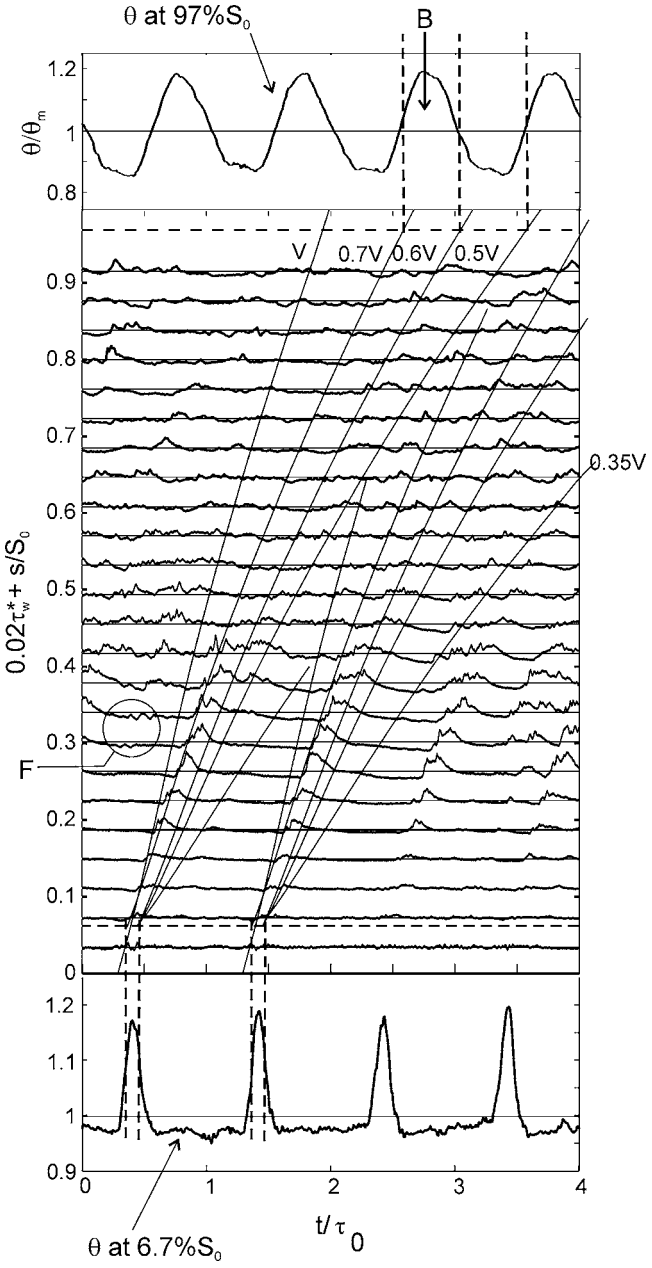

Fig. 14 Raw traces of normalized quasishear stress (first normalization, τ_w^*, see Eq. (2))

the structure is sufficient for it to be observed at this plane. The positions of the front and back of the thickened boundary-layer determined from the PIV data and the hotwire traverse at $6.7\%S_0$, are superimposed on the space-time diagram of Figs. 10 and 11. The front of the structure moves at $0.7V$ and the back moves at $0.6V$, where these lines are plotted such that they begin at the front and back of the thickened laminar boundary-layer seen in Fig. 8. It will be shown later that the thickened laminar boundary-layer undergoes transition and forms a thickened turbulent boundary-layer, which is seen in Fig. 13.

The plots in Fig. 13 also show the ensemble-averaged perturbation vector fields, which are the ensemble-average vectors with the time-average vector field subtracted. This is known as a Reynolds decomposition of the flow. The negative-jet effect is seen in the vector fields, which point away from the suction surface within the wake region. The thickened boundary-layer structure appears as a region of higher streamline curvature. The pressure perturbations seen in Fig. 11 convect within this region and are expected to be due to the increased streamline curvature caused by the thickened boundary-layer.

The size of the pressure perturbations seen in Fig. 11 is observed to increase between $s/S_0=0.2$ and $s/S_0=0.4$, where the structure was shown to grow in size, as is seen in Fig. 12. The maximum perturbation in surface pressure reaches approximately 7% of the inlet dynamic head.

Effect on Transition. Figure 14 shows raw traces of the normalized quasi shear stress (first normalization, τ_w^*, see Eq. (2)) over the suction-surface. As well as the convection lines shown in

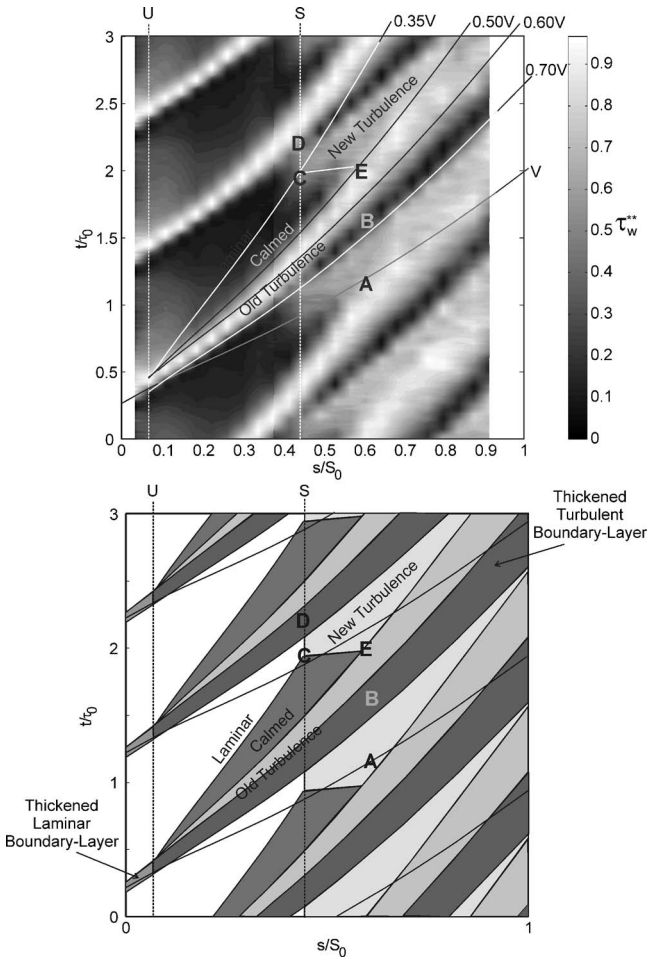

Fig. 15 *S-T* plot and schematic of ensemble-average normalized quasishear stress (second normalization, τ_w^{**}, see Eq. (3)) using the designation of states of [3]

the previous plots, lines at $0.5V$ and $0.35V$ are shown. The variation of momentum thickness (θ) at $6.7\%S_0$, is also reproduced in Fig. 14. According to Fig. 9, turbulent spots are expected to form within the thickened laminar boundary-layer caused by the wake/leading-edge interaction, where θ is high. Turbulent spots are identified by the locally increased shear-stress within them, and are observed to form within the thickened region. They are initiated very early on the suction surface ($s/S_0<0.1$). The thickened laminar boundary-layer seen at $6.7\%S_0$, becomes a thickened turbulent boundary-layer identified as the region marked B in Fig. 13.

In Fig. 14, the leading edge of the spots is observed to travel at close to $0.7V$, which differs significantly from the speed of $0.85V-0.90V$ which has traditionally been observed. The trailing-edge travels at a more typical $0.5V$, which is followed by a calmed region, this trails the turbulent spot between the $0.5V$ and $0.35V$ convection lines and is characterized by a gradual decrease in shear-stress with time. The calmed region is terminated by the onset of new turbulent spots that form in the undisturbed boundary-layer. This is observed in Fig. 14 at F where fluctuations are seen that are characteristic of the behavior prior to separated flow transition. The formation of turbulent spots as a direct result of the influence of the wake is not observed in Fig. 14. This may be a result of the negative-jet effect [21], which will tend to transport any turbulent fluid under the wake center-line away from the suction surface.

Figure 15 is a space-time diagram of the ensemble-averaged normalized quasi shear stress (second normalization, τ_w^{**}, see Eq. (3)) over the suction-surface, with a schematic of this plot outlining the boundary-layer states. At this point it is useful to introduce the designation of states described by Cumpsty et al. [3]. The term "old turbulence" was used to describe the turbulence initiated by the wake, and the term "new turbulence" described the turbulence that formed in the absence of the wake. They found that the part of the old turbulent boundary-layer that was initiated furthest upstream grew thick and was affected more strongly by the adverse pressure gradient. This region was characterized by a low value of shear stress and a high displacement thickness.

In Fig. 15 this designation of states is used to annotate the plots. The new turbulent region exists downstream of the location marked S ($s/S_0\approx0.45$), and transition in the absence of wakes is seen along the line C-D. The development of old turbulence is seen between the $0.70V$ and $0.5V$ convection lines, and begins at the location marked U ($s/S_0\approx0.07$). This is followed by the calmed region, which suppresses the formation of new turbulent spots, seen along the line C–E. The effects of calming extend the region of laminar flow temporarily to ($s/S_0\approx0.55$). The increased turbulent wetted area caused by the turbulent strip is therefore much larger than the increased laminar wetted area due to the effects of calming.

Figure 15 shows that the thickened boundary-layer structure (marked B) propagates at the front of the old turbulent region. Within this region the shear-stress undergoes a distinct change from a relatively high value for $s/S_0<0.4$, to a low value for $s/S_0>0.45$. This, combined with the increased displacement thickness of the structure would identify it as the part of the old turbulent boundary-layer initiated furthest upstream as observed by [3,12]. As discussed previously, however, this part of the old turbulent boundary-layer originates from a thickened laminar boundary-layer caused by the wake/leading-edge interaction, and this is indicated in the schematic shown in Fig. 15. The level of shear stress drops within this region as it is affected more strongly by the adverse pressure gradient, therefore giving a lower skin-friction.

Effect on Loss. The unsteady loss of the blade row can be determined via the relation

$$Y_p \approx \frac{2(\theta_{\text{suction}}+\theta_{\text{pressure}})}{P\cos\alpha_{\text{exit}}}\frac{V_{\text{exit}}^2}{V_{\text{inlet}}^2} \tag{6}$$

where Y_p is the (stagnation pressure) loss coefficient and θ_{suction}, θ_{pressure} are the time-average trailing-edge momentum thicknesses on the suction and pressure surface, respectively. In this way the loss can be estimated by measuring the momentum thickness at the trailing-edge of the blade. Hence, the effect that the thickened boundary-layer structure has on the suction surface loss can then be assessed. For this reason a hotwire traverse was performed across the suction-surface boundary-layer close to the blade trailing-edge (at $97\%S_0$).

The variation of trailing-edge momentum thickness divided by the time-average (θ/θ_m) with time from these results, is shown in Fig. 14. The peak θ is 18% above the time-average, and occurs within the thickened turbulent boundary-layer region (marked B). This region is followed by the remainder of the turbulent strip, where θ falls to a value which is 12.5% lower than the time-average. There is a small drop in momentum thickness prior to the arrival of the next thickened boundary-layer. The schematic in Fig. 15 would suggest that this is the level within the new turbulent boundary-layer, and therefore indicates the loss due to the boundary-layer in the absence of wakes. It is not possible to discern from Fig. 14 any effects due to calming on the trailing-edge momentum thickness. The total size of the fluctuations in θ is 31%, indicating that the early onset of turbulent spots, caused by the thickened laminar boundary-layer has a significant impact on the loss produced.

It is shown in Fig. 15 that the turbulent strip increased significantly the turbulent wetted area over the front portion of the blade

surface. In this region the velocities are high and therefore the entropy production rate ($\dot{s} \propto U_e^3$) will also be high. In contrast, Fig. 15 showed that the effects of calming extended the region of laminar flow further downstream, where the velocities are low, and hence the entropy production rate will also be low. In addition the increased laminar wetted area due to the calming is comparatively small relative to the increased turbulent wetted area. It is hypothesized, therefore, that the measured increase in trailing-edge momentum thickness seen in Fig. 14 is due to the increased turbulent wetted area brought about by the turbulent strip. Given this hypothesis, Eq. (6) indicates that the wake/leading-edge interaction is responsible for approximately 13% increase in the time-average suction surface profile loss.

Conclusions

The current work shows that wake/leading-edge interactions are crucial to early transition in compressor blade-rows. The impingement of an upstream wake onto a compressor-blade leading edge is shown to create a temporarily thickened laminar boundary-layer, with high momentum thickness (and hence high Re_θ). This structure provides a favorable environment for the formation of turbulent spots, which consequently develop. These spots grow to form the well-known turbulent-strips that have traditionally been attributed to the direct influence of the wake on the boundary-layer. The thickened laminar boundary-layer develops into a thickened turbulent boundary-layer structure, the front of which propagates at 70% of the wake speed. As the structure propagates it causes large fluctuations in the surface pressure, which reach a maximum of 7% of the inlet dynamic head in magnitude. Measurements of the trailing-edge momentum thickness indicate that the thickened boundary-layer structure has a significant impact on performance, causing an estimated 13% increase in the time-averaged suction-surface profile loss.

These results indicate that leading-edge shape will play an important role in boundary-layer transition in compressor blade-rows in the presence of wakes. This is due to the influence of wakes on the leading-edge C_p distribution. Hence, there is a potential for performance gains to be achieved through the design of new leading-edge shapes.

The leading-edge wedge angle on the low-speed blade used in the present investigation, is much higher than on a high-speed blade found in a modern aeroengine compressor. Reduced wedge angles tend to increase the size of C_p spikes at the leading edge and this results in low speed blades having a much smaller C_p spike than high speed blades. Therefore the effects of leading-edge/wake interactions observed in this work are likely to be even more important in a typical aeroengine compressors.

Acknowledgment

The authors would like to thank Rolls-Royce plc and the EPSRC for their support.

Nomenclature

C_p = pressure coefficient $(p_{0\mathrm{inlet}}\text{-}p)/(p_{0\mathrm{inlet}}\text{-}p_{\mathrm{inlet}})$
c = chord
E = hotfilm bridge voltage
E_0 = zero flow hotfilm bridge voltage
H = shape factor (δ^*/θ)
P = blade pitch
p = pressure
Re_θ = Reynolds number based on momentum thickness
s = surface distance from the leading edge
S_0 = total surface length
t = time
U = mid-height rotor-blade speed
U_e = boundary-layer edge velocity
u = boundary-layer velocity
v = ensemble-average velocity
V = freestream velocity
y = perpendicular distance from surface

Greek Symbols

δ = boundary-layer thickness
δ^* = boundary-layer displacement thickness
ϕ = flow coefficient V_x/U
ν = kinematic viscosity
ω = ensemble-average vorticity
Ω = rotor rotational speed
θ = boundary-layer momentum thickness
τ_0 = wake period
τ_w = quasi shear stress

Subscripts

exit = stator exit
inlet = stator inlet
m = time-averaged quantity
max = local maximum value
min = local minimum value
p = perturbation (time-average subtracted)

References

[1] Mayle, R. E., 1991, "The Role of Laminar-Turbulent Transition in Gas Turbine Engines," ASME J. Turbomach., **113**, pp. 509–537.
[2] Walker, G. J., 1993, "The Role of Laminar-Turbulent Transition in Gas Turbine Engines: A Discussion." ASME J. Turbomach., **115**(2), pp. 207–218.
[3] Cumpsty, N. A., Dong, Y., and Li, Y. S., 1995, "Compressor Blade Boundary Layers in the Presence of Wakes." ASME Paper No. 95-GT-443.
[4] Dong, Y., and Cumpsty, N. A., 1990, "Compressor Blade Boundary Layers: Part 1—Test Facility and Measurements With No Incident Wakes," ASME J. Turbomach., **112**, pp. 222–230.
[5] Dong, Y., and Cumpsty, N. A., 1990, "Compressor Blade Boundary Layers: Part 2—Measurements With Incident Wakes," ASME J. Turbomach., **112**, pp. 231–240.
[6] Halstead, D. E., Wisler, D. C., Okiishi, T. H., Walker, G. J., Hodson, H. P., and Shin, H. W., 1997, "Boundary Layer Development in Axial Compressors and Turbines: Part 1 of 4—Composite Picture," ASME J. Turbomach., **119**, pp. 114–119.
[7] Hughes, J. D., and Walker, G. J., 2001, "Natural Transition Phenomena on an Axial Compressor Blade," ASME J. Turbomach., **123**, pp. 392–401.
[8] Solomon, W. J., and Walker, G. J., 2000, "Incidence Effects on Wake-Induced Transition on an Axial Compressor Blade," J. Propul. Power, **16**(3), pp. 397–405.
[9] Hodson, H. P., and Howell, R. J., 2005, "The Role of Transition in High-Lift Low-Pressure Turbines for Aero-Engines," Prog. Aerosp. Sci., **41**, pp. 419–454.
[10] Howell, R. J., Hodson, H. P., Schulte, V., Schiffer, H. P., Haselbach, F., and Harvey, N. W., 2001, "Boundary-Layer Development in the BR710 and BR715LP Turbines—The Implementation of High Lift and Ultra High Lift Concepts," ASME Paper No. 2001-GT-0441.
[11] Dong, Y., 1988, "Boundary Layers on Compressor Blades," Ph.D. thesis, University of Cambridge, UK.
[12] Ottavy, X., Vilmin, S., Hodson, H., and Gallimore, S., 2004, "The Effects of Wake-Passing Unsteadiness Over a Highly Loaded Compressor-Like Flat Plate," ASME J. Turbomach., **126**, pp. 13–23.
[13] Mailach, R., and Vogeler, K., 2004, "Aerodynamic Blade Row Interactions in an Axial Compressor—Part 1: Unsteady Boundary-Layer Development," ASME J. Turbomach., **126**, pp. 35–44.
[14] Bolger, J. J., 1999, "Three-Dimensional Design of Compressor Blades." Ph.D. thesis, University of Cambridge, UK.
[15] Bindon, J. P., 1987, "Pressure Distributions in the Tip Clearance Region of an Unshrouded Axial Turbine as Affecting the Problem of Tip Burnout," ASME Paper No. 87-GT–230.
[16] Hodson, H. P., Huntsman, I., and Steele, A. B., 1994, "An Investigation of Boundary-Layer Development in a Multistage LP Turbine," ASME J. Turbomach., **116**, pp. 375–383.
[17] Giles, M., 1991, "Unsflo: A Numerical Method for the Calculation of Unsteady Flow in Turbomachinery," Tech. Report No. 205, GTL.
[18] Walraevens, R. E., and Cumpsty, N. A., 1995, "Leading Edge Separation Bubbles on Turbomachinery Blades," ASME J. Turbomach., **117**, pp. 115–125.
[19] Paxson, D. E., and Mayle, R. E., 1991, "Laminar Boundarylayer Interaction With an Unsteady Passing Wake," ASME J. Turbomach., **113**, pp. 419–427.
[20] Lighthill, M. J., 1954, "The Response of Laminar Skin Friction and Heat Transfer to Fluctuations in the Freestream Velocity," Proc. R. Soc. London, Ser. A, **224**, pp. 1–23.
[21] Meyer, R. X., 1958, "The Effect of Wakes on the Transient Pressure and Velocity Distributions in Turbomachines," Trans. ASME, **80**, pp. 1545–1552.

Experimental Results From Controlled Blade Tip/Shroud Rubs at Engine Speed

Corso Padova
e-mail: padova.1@osu.edu

Jeffery Barton

Michael G. Dunn

Gas Turbine Laboratory,
Ohio State University,
2300 West Case Rd.,
Columbus, OH 43234

Steve Manwaring
GE Aircraft Engines,
Cincinnati, OH 45215

Experimental results obtained for an Inconel® compressor blade rubbing a steel casing at engine speed are described. Load cell, strain gauge, and accelerometer measurements are discussed and then applied to analyze the metal-on-metal interaction resulting from sudden incursions of varying severity, defined by incursion depths ranging from 13 μm to 762 μm (0.0005 in. to 0.030 in.). The results presented describe the transient dynamics of rotor and casing vibro-impact response at engine operational speed similar to those experienced in flight. Force components at the blade tip in axial and circumferential directions for a rub of moderate incursion depth (140 μm) are compared to those for a severe rub (406 μm). Similar general trends of variation during the metal-to-metal contact are observed. However, in the nearly threefold higher incursion the maximum incurred circumferential load increases significantly, while the maximum incurred axial load increases much less, demonstrating the non-linear nature of the rub phenomena. Concurrently, the stress magnification on the rubbing blade at root mid-chord, at tip leading edge, and at tip trailing edge is discussed. The results point to the possibility of failure occurring first at the airfoil trailing edge. Such a failure was in fact observed in the most severe rub obtained to date in the laboratory, consistent with field observations. Computational models to analyze the non-linear dynamic response of a rotating beam with periodic pulse loading at the free-end are currently under development and are noted. [DOI: 10.1115/1.2720869]

1 Introduction

Contemporary gas turbines rely on complex blade-casing rub-in-systems to improve the tip clearance behavior during operation from initial service to maximum lifetime [1,2]. Higher energy efficiency is achieved by reducing tip clearance between the rotor and the stationary casing components, but as the clearance is reduced, the probability of a rub occurring during some operating conditions also increases. Blade-to-case rubs can degrade the operation of an engine through the induction of high-amplitude shaft vibration and severe blade/seal wear, and may lead to catastrophic failure of the engine in the worst occurrence.

Advances in the prediction of the complex dynamic of vibro-impact systems with multiple degrees of freedom are currently needed to enable the formulation of a comprehensive design methodology for rub-in systems, particularly one capable of predicting and taking advantage of the potential offered by new and emerging rotor/blade concepts. This need is driving studies based on recently acquired experimental capabilities such as the one reported in this paper as well as computational studies that analyze the non-linear dynamic response of blades under periodic pulse loading [3,4].

In combination with continuing progress in other more mature allied technologies, such as rotor dynamics under severe disturbances [5–7], forced vibrations of bladed disks [8,9], and abradability of materials [10], the improved understanding of the phenomena that affect blade-casing interactions is expected to result in savings in gas turbine maintenance costs applicable not only in propulsion engines but for stationary advanced power systems as well.

Contributed by the International Gas Turbine Institute of ASME for publication in the JOURNAL OF TURBOMACHINERY. Manuscript received July 31, 2006; final manuscript received August 11, 2006. Review conducted by David Wisler. Paper presented at the ASME Turbo Expo 2006: Land, Sea and Air (GT2006), May 08–11, 2006, Barcelona, Spain-90049, Paper No. GT2006-90049.

2 Experimental Method

The development of an in-ground spin-pit facility (SPF) capable of rotating at engine speed and specifically designed to investigate aeromechanic phenomena for gas turbine engine hardware was recently reported [11]. The underground containment tank that houses both the rotating component and part of a high-stiffness spindle is cylindrical (1.52 m in diameter by 0.65 m high), and has 0.90-m-diameter openings at the top and at the bottom.

Vertical axis spin testing for design validation of turbomachinery components dates back to World War II applications, which sought to solve problems with military aircraft turbochargers. However, the research interest envisioned from the inception of this facility design dictated the use of a high-stiffness spindle. This requirement forced a significant departure from the common way of performing a spin experiment, whereby a rotor is suspended in the heavily armored vacuum tank from a flexible shaft. That shaft arrangement allows the rotor to find its own balance axis and eliminates the need for extreme precision in mounting and balancing. Unfortunately, it is unsuitable to reproduce blade-to-case rub situations for which one wishes to derive physics based modeling of the events occurring at the blade tip/casing interface.

Thus, a major subsystem component required for the facility is a vertical and high-stiffness spindle capable of operating at 20,000 rpm for a reasonable period of time. The system utilized here incorporates hybrid bearings and an oil mist lubrication system. The spindle shaft is driven from the top by an air turbine motor. The single-stage engine rotor is bolted beneath the spindle assembly and is surrounded by the containment test chamber. The first critical speed of the spindle is significantly higher than the maximum operating speed. The analysis of the high-stiffness bearing arrangement indicates a shaft critical speed of 23,500 rpm for the design manufacturing tolerances and assumed operating temperature effects. This component was described in full detail in Ref. [11].

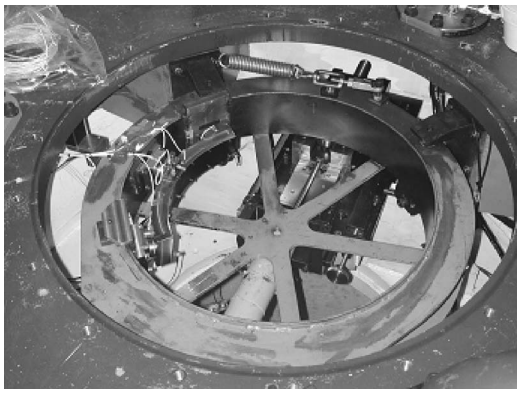

Fig. 1 Incursion mechanism photo

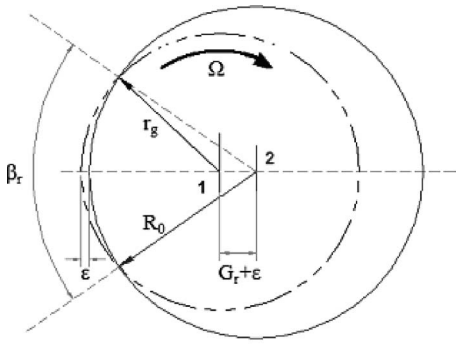

r_g , blade tip path radius at target rub speed
R_0 , casing radius
G_r , radial gap at target rub speed
ε , maximum blade tip interference with casing

Fig. 2 Rub geometry

A second major subsystem required to investigate blade-to-case rubs is a fast-acting mechanism that allows insertion of the engine casing into the path of the bladed rotor under conditions for which the pre-set interference between the casing and the blade can be controlled to within less than 13 μm (0.0005 in.). Such a mechanism was designed and developed to research asymmetric and full rotor clearance closure for engine stages. For single-blade asymmetric clearance closure investigations, a rapid contact of the bladed rotor with its housing is simulated as would occur in an abrupt flight maneuver. For full rotor clearance closure, an extended contact of the bladed rotor with its housing is simulated as could be experienced in some flight phases due to temporary thermal imbalances in different parts of the engine. The known requirements for those types of investigations have defined the general layout of the electromechanical, pneumatic, and measurement subsystems of the facility. The fast-acting incursion mechanism is briefly reviewed below, but was described in full detail in Ref. [11].

The function of the incursion mechanism is to move the engine-case segment into the blade path at an exact time for a precise distance and duration, which determines the number of blade strikes. After a few strikes, the mechanism retracts the casing out of the blade path. The disk containing the blade is operating at engine speed and may contain a single airfoil or multiple airfoils. In the current configuration, a 90 deg sector of a representative engine casing is forced to rub the tip of a single bladed compressor disk for a limited number of times with pre-determined blade incursion into the casing. For the measurements described herein, the speed at the time of rub was on the order of 17,000 rpm. For this rotational speed, the instrumented airfoil returns to the same circumferential position in 3.8 ms; thus, several contacts between blade and shroud are experienced before the eccentricity disturbance is removed.

The compressor disk and blade rotate on a vertical rigid spindle that is driven by an air turbine. The casing sector is mounted on a rigid transfer bar that is backed by three piezoelectric load cells and this assembly (load measuring unit, LMU) is attached to a support ring that swivels in the horizontal plane. A single throw fast acting gas operated piston is attached to a cam follower that is rigidly connected to the support ring and activation of the piston moves the casing in and out of the path of the rotating blade over a time interval of about 20 ms. The incursion of the rubs is prescribed by setting the initial position of the mechanism in increments of 5 μm (0.0002 in.). Figure 1 shows a picture of the subsystem.

2.1 Rub Geometry. The interference between blade tip path and engine casing in ramp-incursion experiments is simply described by Fig. 2. The maximum incursion depends on the initial gap and the eccentricity that is commanded between the casing circle and the spindle axis. For a wide range of interference values, a 90 deg sector of the casing was found sufficient to obtain rubs of significant depth. A similar rub geometry was investigated a few years ago by Ahrens and others [12,13] to derive contact forces during blade rubbing. However, the rotational speed of the blade was 1800 rpm, nearly an order of magnitude smaller than in the experiments that are reported here. In addition, the airfoil consisted of a simple beam of rectangular cross section.

From Fig. 2, consider that a blade of outer radius r_0 is mounted on a disk with center on the spindle axis (point 1). Initially, the casing with larger radius R_0 also has its center on the spindle axis, thus resulting in a clearance G_0. When the rotor is accelerated to an angular velocity Ω, the disk and the blade are subjected to a centripetal force field that moves the blade tip to an outer radius r_g, resulting in a new clearance G_r at the target rub speed.

At the target rotational rub speed, the incursion mechanism commands a displacement of the casing circle equal to $(G_r+\varepsilon)$, where ε is the maximum desired interference for a rub. As a result the casing circle with radius R_0 is now centered away from the spindle axis at point 2 in Fig. 2 and the blade incurs an interference varying from 0 to ε and back to 0 along arc β_r. The angular length of the rub is easily obtained from Fig. 2 as

$$\beta_r = 2\arccos\{(R_0^2 + (G_r+\varepsilon)^2 - r_g^2)/[2R_0(G_r+\varepsilon)]\}$$

In preparation for the metal-on-metal rubs described in this paper, the precise variation of G_r with angular velocity was established experimentally. This was done by first setting a known eccentricity between the casing support ring and the rotor and then bringing the spindle gradually up in speed until a very light touch of the blade was obtained. By repeating the process for several values of the initial eccentricity the gap calibration curve was obtained.

2.2 Instrumentation. The SPF is designed to accept fast response sensors installed both on the rotating disk/blade assembly and on the stationary casing sector or load measuring unit. The shaft of the spindle is hollow and accommodates the bundle of wires from several blade-mounted strain gauges or surface bonded precision resistance temperature devices. For the experiments discussed here, the airfoil was instrumented with miniature dynamic strain gauges arranged on the suction and pressure side of the blade. Eight unidirectional gauges and four rosette gauges were installed. The blade had been fully characterized during compressor development by measurements using multiple strain gauges during excitation by a pulsating air jet. The results from those experiments were used to select a subset of gauge locations best suited to analyze the blade vibratory response during rubs. Excitation power and signal response are carried by electrical wires routed through the spindle to the rotating terminal of a 200-channel slip ring unit. The stationary terminal of the unit is di-

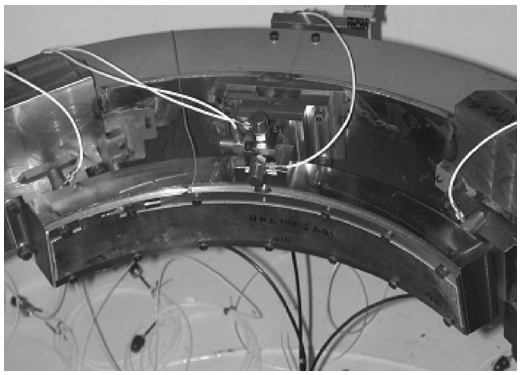

Fig. 3 Load measuring unit (LMU)

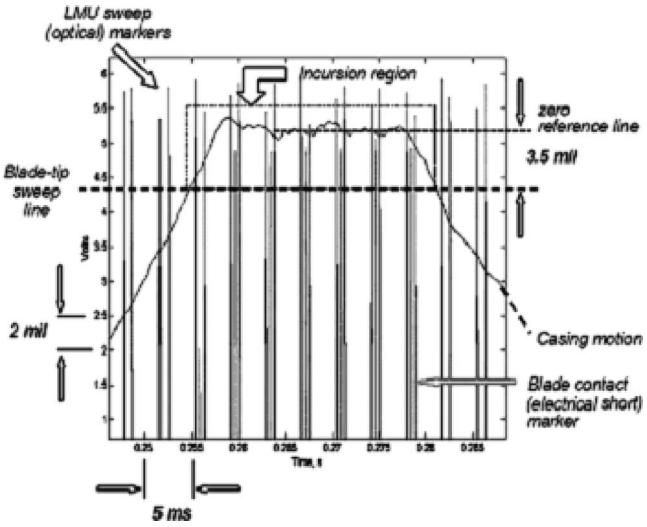

Fig. 4 Casing motion and incursion region

rectly patched into the high-speed data acquisition system. All strain gauges were operated in constant current mode for the present experiments.

The stationary casing (or LMU) is instrumented to measure forces and moments. The segment of engine casing against which the blade rubs is carried by a metric support that includes three load cells. Each piezoelectric load cell measures three force components. Two end cells are placed below the load line, which is located in the mid-plane of the engine case. The center cell is located above mid plane. The arrangement of this LMU is thus designed to minimize the moment loads on each cell and to obtain moment information about three mutually perpendicular axes.

Five accelerometers are also mounted on the LMU, which is shown in Fig. 3. Three radial directions are measured at locations very close to each load cell. A triaxial block, which is mounted near the center load cell, is equipped with the remaining two accelerometers that measure one axial and one circumferential direction in the middle of the LMU.

The dynamic response of the entire LMU was investigated to correctly relate the intensity and frequency of the excitation rub forces to the load cell measurements. The frequency response of an individual piezoelectric load cell is an important parameter. The Kistler Type 9047B sensor selected for the LMU is characterized by high rigidity ($K_x = K_y = 700$ N/μm; $K_z = 6000$ N/μm) and thus has a high natural frequency ($f_0 = 120$ kHz).

The load cell shows relatively little vibration damping at the upper frequency limit. Frequencies can be triggered up to about a third of the natural frequency with very small measuring errors. The lower frequency limit is determined by the drift of the charge amplifier and the quality of the insulation. For the very short measuring times of interest in this application, measurement errors at low frequencies are very small.

A next step in characterizing the dynamic response of the LMU was taken by carefully observing the force response in repeated measurements while applying the same impulsive excitation force with a modal hammer. The observations were then matched with the predictions of a simple one degree of freedom model for the locally dominant mass, stiffness, and damping characteristics. The model indicates the following values for the system parameters

$m = 4.0$ kg (8.81 lb), equal to 49% of the total LMU mass mounted forward of the load cells

$k = 400$ N/μm (2.284 M lbf/in.), equal to 6.7% of the nominal z-direction load cell rigidity

$\zeta = 0.0433$, damping ratio

For such a model, the underdamped vibrations occur at a frequency of 1069.8 Hz (the natural frequency of the system is 1611.3 Hz) and a logarithmic decrement $\delta = 0.272$. This oscillation matches the experimentally observed response over a few periods after the initial transient lasting about 0.75 ms (about 2.68 times the duration of the excitation impulse).

Additional considerations on the investigations of LMU dynamic response are discussed later in the data analysis section.

2.3 Data Acquisition. During a typical experiment, the rotor is accelerated to the target speed in less than 3 min. As the rotor speed approaches the target value selected for a rub to occur, the angular acceleration is gradually decreased so that the airfoil impact with the shoe occurs at a constant rotational speed. For all the experiments presented, the rotational speed at impact was held at 15,990 rpm. A few rubs of the single blade installed onto the bladed disk are then obtained as described in the following paragraphs.

First, the casing movement toward the spinning blade tip is initiated by the triggering system described later in this section. This results in the casing motion shown in Fig. 4 in the initial region of the abscissa (time axis). Each division of the ordinate represents a 2 mil displacement of the casing toward the spinning blade that is located at the top of the figure. Also shown in the figure are the vertical markers that indicate the arrival of the blade at the entrance of the casing sector and the departure of the blade from the casing sector. At a rotational speed of 15,990 rpm the duration of one sweep of the single blade in the disk over the casing sector is about 1 ms. Eleven blade sweeps are shown in the time span given in Fig. 4 (see LMU sweep legend). As the blade passes over the LMU in the initial region of the time axis, there is sufficient clearance between the blade tip and the shroud to avoid a rub.

Second, during the casing motion, the tip sweep line is crossed as depicted in the figure. After this point in time, the LMU is in the path of the spinning blade and a rub is obtained as soon as the blade returns over the LMU sector. This is shown by the appearance of the blade contact marker in the figure. The duration of blade/shroud contact is generally less that the blade sweep duration and depends on the prescribed incursion depth. Except for a range of very small incursions, the rubs begin with the casing still advancing toward the spinning blade. For more severe incursions, more rubs occur before the casing locks into the zero-lead segment of the casing movement (maximum incursion position). The zero-lead incursion duration is clearly indicated in Fig. 4 by the plateau in the casing movement trace and is labeled "zero reference line."

Third, during the time that the casing is in the maximum incursion position, up to six rubs can take place for the values of

rotational speed at which experiments were conducted. Due to the settings chosen in the triggering circuit, five rubs were obtained in most cases. All zero-lead incursions occur with the same nominal interference between the path of the blade tip and the arc of the casing. The deviation of the actual interference from the nominal value was monitored in repeated experiments and found to be less than ±3.8 μm.

Fourth, the continuing motion of the cam forces the casing to begin to retreat. In this phase, the rubs continue because the casing is still inside the incursion region. As before, the more severe the incursion, the more rubs occur before the casing clears the exit boundary of the incursion region.

Finally, the casing crosses the tip sweep line and the rubs end. In the experiments discussed below, the maximum incursion imposed was for 406 μm and resulted in a total of 15 rubs.

The trigger to start both the data acquisition and incursion systems must be precisely controlled. The high-frequency data acquisition system has a selectable window in which to collect data and record the rub events, and must be triggered at the appropriate moment. The individual measurement channels are sampled simultaneously at a rate of 100 Khz using the 12-bit data acquisition system. The triggering circuitry for the ramp-incursion experiments is fairly involved. The object is to get the casing sector to move out and set in place during the time interval when the blade cannot interfere with the casing surface. This time interval spans several blade revolutions, as can be seen from Fig. 4. Using a selectable time delay from a trigger that is related to instantaneous blade position, the objective is achieved by delay increments equal to a fraction of one revolution. An optical sensor placed to sense arrival of the blade at the leading edge of the casing supplies the trigger signal. The incursion system timer can resolve to a millisecond, which is too coarse for this application, so a delay generator capable of resolving to 0.1 ms is placed in front. A manual trigger-enable switch disables the sensor trigger until the rotor set speed is achieved.

The data acquisition system is triggered with the incursion system timer so that casing movement can be monitored during the experiment and correct position relative to blade location can be verified. In each experiment, the data acquisition system is always running in sample-and-hold mode after a manual enable command, and a pre-rub hold time is programmed into the system. Thus any of the measurement histories show typically a pre-rub value for about 200 ms followed by the rub event sequence. Typical histories last 410 ms to 829 ms and consist of a few to several rubs depending on the preset incursion depth and the type of experiment.

3 Data Analysis

The measurements obtained simultaneously from load cells, accelerometers and strain gauges during nearly a second of data acquisition time, when combined, offer a detailed description of the rub phenomena. The purpose of this paper is to describe the results from rubs of an Inconel® compressor blade on a bare steel casing. We do have data for the same blade rubbing on different coatings, but introduction of that material is beyond the scope of this paper. Extensive results from specific applications and research projects on the effect of casing coatings on rub dynamics will be the subject of subsequent papers. In this section load cell, strain gauge and accelerometer measurements are first reviewed qualitatively and then applied to analyze the metal-on-metal interactions.

3.1 Measurements Overview. Typical measurement time histories are shown in Figs. 5 and 6. In these figures, the initial pre-rub level of the sensor signal, the response during multiple rubs, and the post-rub sensor signal are easily identified.

The three load cell measurements from top to bottom of Fig. 5 are for the initial cell, center cell, and last cell passed by the blade during each revolution. Note how quickly after the rub interval the measured loads return to the pre-rub level.

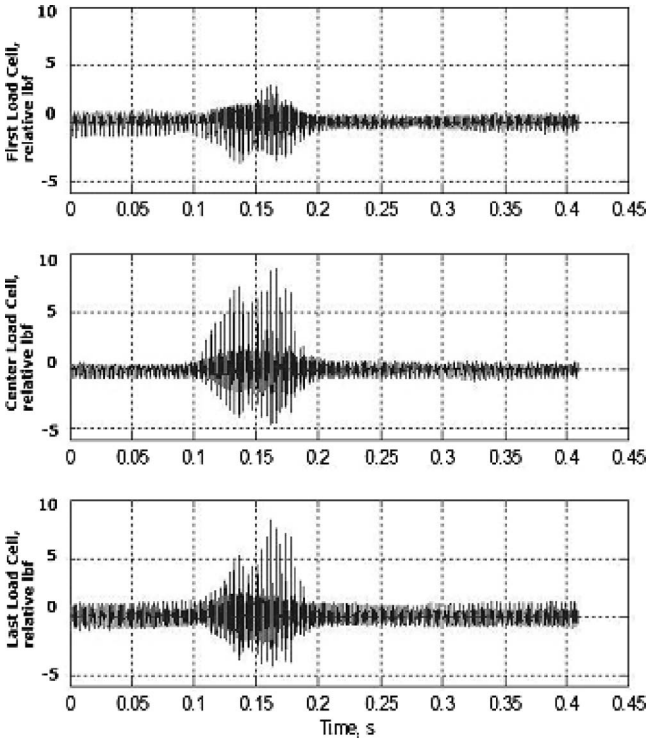

Fig. 5 Typical load cell measurements

The measurements of acceleration are qualitatively very similar to those obtained from the load cells.

The two typical strain gauge measurements from top to bottom of Fig. 6 are for a gauge located at the tip and for a gauge located at the root of the blade, respectively. Note that the tip gauge indicates localized disturbances during the rubs, a displacement of the baseline that is believed to be a temperature-induced, and no post-rub oscillations. In contrast, the root gauge shows oscillations building up from rub to rub followed by an exponential decay after the last rub, but does not show a baseline offset.

3.2 Rub Conditions. It is important to note that the measurements obtained during each experiment should be examined according to a number of different time scales. Five scales are illustrated in Fig. 7. In order of decreasing duration they are: the time

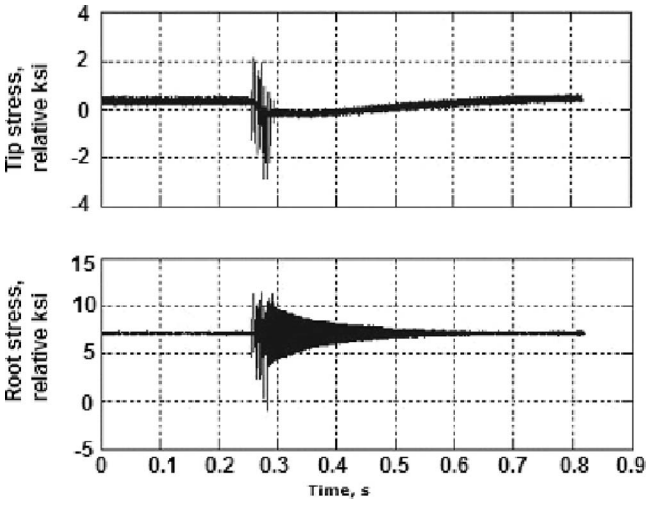

Fig. 6 Typical strain gauge measurements

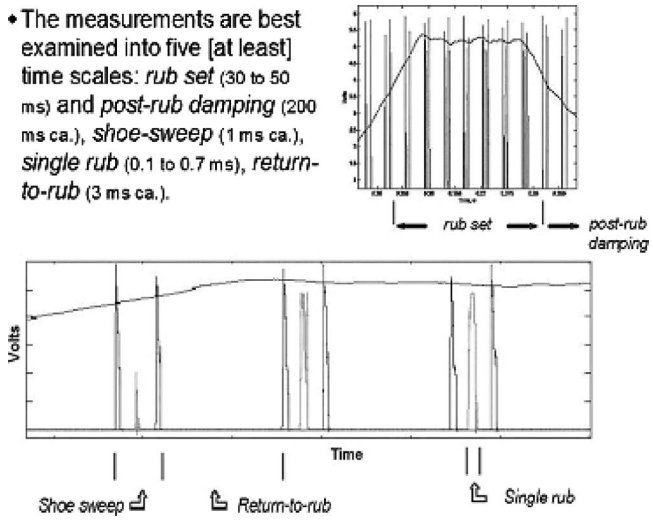

Fig. 7 Time-scales of blade rubs

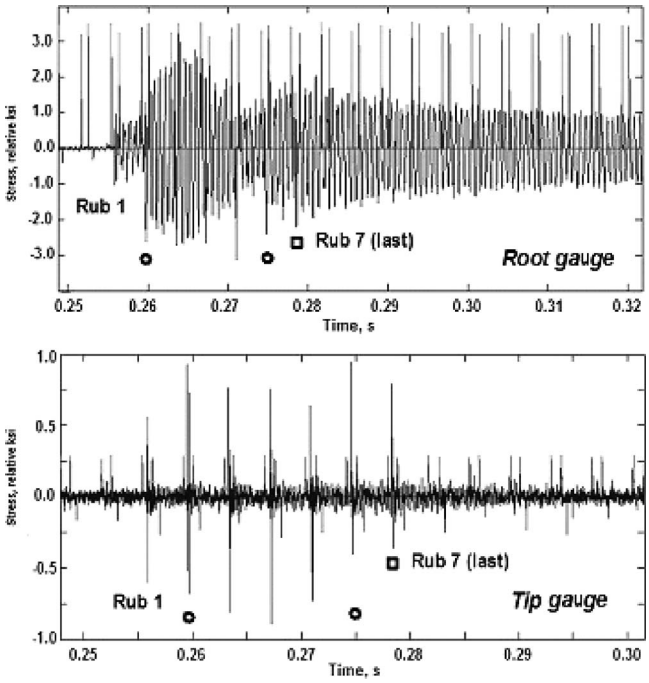

Fig. 8 Strain gauge measurements for rub-set and post-rub damping time scales. Incursion: ε=89 μm (0.0035 in.).

of damping of blade excitation after a set of rubs, the time spanned by an entire set of rubs, the time for one casing (shoe) sweep, the time interval a blade spends in free oscillation after a rub and before returning for a subsequent rub, and the duration of an individual rub. The first two scales are shown in the top part of the figure. The bottom part of the figure zooms in on three distinct blade rubs and shows the three remaining time scales.

The two types of markers discussed earlier are recorded during an experiment to identify the different scales of the rub phenomena. The optical blade-passage markers unequivocally identify the time interval for potential contact and the angular velocity, the electrical blade-contact signal registers actual strikes. In each experiment, the data acquisition system is already running in sample-and-hold mode at the precise instant when the command to acquire measurements is received, and a pre-rub hold time is programmed into the data system. Thus any of the measurement histories shows typically a pre-rub value for about 200 ms, the onset of the rub event, the dynamic response resulting from the impact of the airfoil with the shoe, the release of the airfoil immediately following detachment from the shoe, the vibrational response of the airfoil as it rotates around once more after having been initially excited by the impact, the effect of repeated impacts, and the decay in dynamic response after the conditions causing the incursion have been removed.

One might ask how the above sequence of events is related to rub occurrences in flight. It is clear that in the experiments just like in flight, for a given incursion depth or severity of a rub event, the rate of incursion in each strike will be positive, null or negative during different phases of the set of rubs that makes up an event. By comparing measurements across variables, the effects of incursion depth and rate of incursion can be separated. One way in which the experimental results shown herein differ from the flight situation is that the initial temperature of the components is room temperature and is not elevated as it would be in flight. That difference will be removed in subsequent measurements.

3.3 Vibrations and Loads in Multiple Rubs. The effects of rub repetition can be identified using the measurements presented here. For the example shown above, the first rub is clearly a partial incursion and is followed by rubs of equal duration (250 μs). However, the first rub is important although not a full engagement, because it is this rub that causes the initial vibratory response of the airfoil. In addition, in zero-lead rubs, the deviation of the actual interference from the nominal value was monitored in repeated experiments and found to be less than ±3.8 μm (±.00015 in.). Rubs 2 and 3 are equal in duration and incursion depth. However, as the blade comes around after each rub, it is excited and one would intuitively expect that rubs 2 and 3 will be different in blade vibratory response and in tip loads during contact to the casing. The extent to which this was found to be true is shown in the results that follow.

First we turn to the topic of overall blade/casing response during an entire rub-set and beyond. Figure 8 shows the alternating stresses versus time, on the top is the root strain gauge, and on the bottom is the tip strain gauge. The vertical markers identify the time intervals during which the blade sweeps over the LMU. As shown earlier, during a fraction of this time the blade comes into contact with the casing surface: a strike occurs and this strike may include an initial hit, partial or full detachment, and subsequent hits. Note the different scales on the vertical axes for the root and tip gauge. Also note that the markers have been arbitrarily scaled in the measured voltage for the sole purpose of visualizing the LMU sweeps.

In this rub event (there were seven strikes in total), each of the strikes is identified by labels, numbers, and symbols: the first strike is labeled and the seventh strike is marked with a square symbol, the first and last of all zero-lead strikes (strike numbers 2 to 6) are marked with round symbols. The first strike occurred with an incursion depth of 51 μm (0.002 in.) and an incursion rate estimated at 1 in./s as the casing is advancing into the blade. All zero-lead strikes are at a nominal incursion 89 μm (0.0035 in.). The seventh strike occurred with an incursion depth of 76 μm (0.003 in.) and a negative incursion rate (casing is retreating away from the blade) of 3.8 m/s (1.5 in./s).

Following the root strain gauge measurement in more detail, strike 1 is not a full engagement, but it excites some vibration modes of the blade. This initial rub is followed by several of the zero-lead rubs, all nominally equal in incursion. Yet an uneven progression of alternating stresses results, first increasing then decreasing, then increasing again. This is interpreted as being an effect of different boundary constraints in repeated strikes due to the conical geometry of the casing, the unwrapping motion of the blade and phase differences in the oscillations of the blade as it returns to interact with the casing. After strike 7, stresses decay

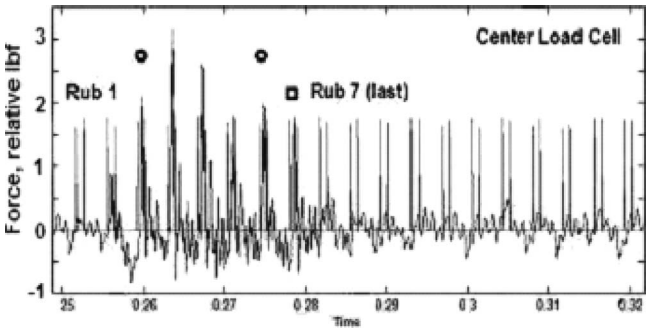

Fig. 9 Center load cell measurement for rub-set time scale. Incursion: ε=89 μm (0.0035 in.).

gradually.

Following the tip measurement in detail, only stress spikes induced by the contact loads are observed. The magnitude of the maxima and minima of stress are indicative of changing boundary conditions of the blade as it returns to interact with the casing. It is also possible that a portion of the observed activity may be the result of the interaction between natural and forced vibration frequencies of the airfoil. Details of the tip loads and waveforms will be discussed later in this section.

Figure 9 shows the load measurement at the center location of the LMU. The peak loads registered in strikes 1 and 7 are consistent with the expectation based on incursion and incursion rate conditions. The peak loads registered in the five zero-lead strikes match the trend shown by blade stresses: increasing load in strikes 2 and 3, decreasing in 3, 4, 5, and the increasing again from 5 to 6.

Moderate variations in the pattern described above for the root alternating stresses were observed as the incursion depth increased from 13 to 406 μm (0.0005 in. to 0.016 in.). Specifically, minor variations were noted in experiments 22, 23, and 24. The pattern changes more markedly in going from incursion depth of 89 μm to 140 μm (0.0035 in. to 0.0055 in.) and above. By contrast, a progressive increase in the measured peak loads was observed as the incursion depth increased from 13 μm to 406 μm (0.0005 in. to 0.016 in.).

3.4 Vibrations and Loads in a Single Rub. Returning to the overview of the shoe-sweep time scale, it is instructive to compare one of the zero-lead rubs, i.e., number 3, to the first rub. Figure 10 shows the data for the root gauge and the tip gauge on an expanded time scale. It is noticeable that the time histories show distinct spikes at the beginning and end of the most perturbed region. The time interval between these two spikes correlates well in all experiments with the indications of electrical contact shown earlier as the blade-contact marker, so the first spike is taken as indicating an attachment stress wave and the last spike a detachment stress wave. In this case the blade contact lasted about 200 μs.

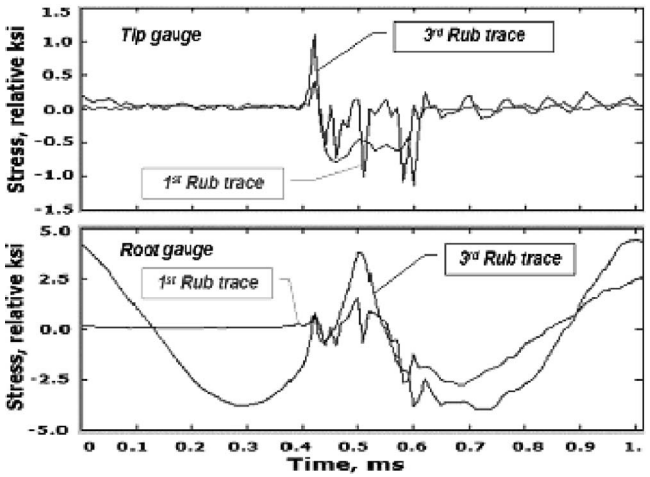

Fig. 10 Strain gauge measurements for shoe-sweep time scale. Incursion: ε=140 μm (0.0055 in.).

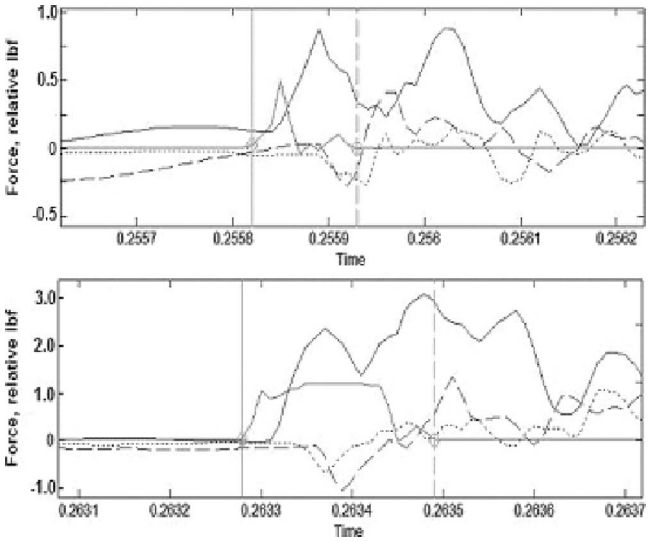

Fig. 11 Load cells measurements for shoe-sweep time scale (first rub: top; third rub: bottom). Incursion: ε=89 μm (0.0035 in.).

It must be stressed that these times are consistent with the durations involved in a real engine rub. It is necessary to understand the physics under these conditions for real engines, not at some longer duration that is easier to obtain experimentally.

Looking first at the root gauge, the first rub is not a full engagement rub. The centrifugal load has been subtracted out and we see that relative stress is zero up to the first attachment. There is some high frequency content probably related to a changing area of contact as the airfoil flexes and twists under load, and after a low-frequency oscillation gradually develops. It is a first flex frequency that persists also at later times. The detachment spike is visible. Notice that it is a bit early relative to the companion event in the third rub. Again, this is not a full engagement strike.

Now let us follow the third rub. The blade comes around and is excited in the first flex mode. The blade attaches first and the resulting history is more suggestive of an increasing-decreasing contact area. The blade then detaches and resumes the first flex motion.

Looking now at the tip, the following occurs: the start of the first rub contact is clearly marked by a first positive spike followed by smaller disturbances because of varying contact area and local blade detachment. A marked negative spike marks final blade detachment. In the third rub the spike marking the initial blade impact is stronger followed by a more uniform load during contact consistent with a deeper incursion. The detachment spike again ends the strike at about the same level encountered during the first rub.

It is now of interest to extend the above overview of the shoe-sweep time scale to the load cell measurements. Figure 11 shows the time histories for the first rub and the third rubs (the second of the zero-lead rubs). In the top frame of Fig. 11, four lines are shown: one line is the record of the electrical blade contact, the three other lines are loads measured from the LMU entrance cell (dotted line), the center cell (solid line), has ordinates above zero only between the vertical marker lines and the exit cell (dashed line). The figure is for the first rub, when the blade makes contact

to the casing just a short distance prior to passing the center load cell. It is seen that the center cell responds immediately measuring a positive load while the entrance and exit cells respond with some delay and a negative load at first. A first bending mode LMU displacement is consistent with these measurements.

The bottom frame of Fig. 11 shows similar histories for the third rub. The general trend observed above is still valid but the increased load levels associated with a deeper and sustained incursion (as evidenced by the solid line for the center cell) are also apparent.

Clearly, even in this very preliminary look at the measurements, purely based on an initial survey of the time-series measurements, one can follow a lot of the physics of rubs at a relevant engine speed. Some fundamental aspects of the phenomena are also well recorded.

3.5 Measurements Processing. As demonstrated by these results, rub phenomena occurring at rub speeds consistent with engine operation are indeed very complex. It is very useful to describe and interpret these results after extensive processing in the frequency domain. To this end, the results that are reported and discussed in the next section have been obtained by applying fast Fourier transform techniques at two levels.

First, for the strain gauge measurements the power spectrum density (PSD) of each signal was obtained and segmented in three relevant frequency domains in order to compare spectral magnitudes to the known blade natural frequencies. Those frequencies were available experimentally from routine compressor qualification tests. The aim at this stage of interpretation of the rub experiments was to identify stress intensification factors during rubs at the natural frequencies or elsewhere in the frequency domain for design purpose. Results from these analyses will be discussed in the next section.

Second, for the load cell measurements, a matrix of frequency response functions (FRF matrix) for known input loads onto the casing surface was generated in pre-experiment broadband modal tests of the LMU. Processing of the load cell signals after the experiments using the inverse of the FRF matrix and the known blade location results in reconstruction of blade tip loads. Currently the algorithms for load cell processing are satisfactory only up to 8 kHz, a frequency cutoff incurred by the application of the reference input loads while using the modal hammer. In principle, that limitation can be removed by a process of PSD averaging over multiple traces. However, that remains to be implemented and signal-to-noise limitations could still limit the accuracy of the process. At the same time narrowband modal testing using a piezoelectric shaker and finite-element modeling of the entire LMU structure are in progress. These steps can be combined and are expected to circumvent the inherent difficulty raised by measuring rub events; namely, the excitation of a wide range of vibrations of the experimental rig due to the high-frequency components in the contact forces. Clearly, excitation of the natural frequencies of the LMU and support structure leads to an amplitude and phase distortion in the load cell measurements that must be properly accounted for in the final data reduction algorithm.

4 Results and Discussion

4.1 Post-Rub Photographs. At this stage in the research, only still photography executed after each experiment has been deployed to document casing and blade conditions following several rub strikes. High speed imaging of the blade deformations during, between, and immediately after successive casing strikes will be available in the near future.

A few photographic records from the growth and ramp-incursion experiments with a single blade on the disk impacting on metal casing are shown in Figs. 12–15. The simple technique of spraying a light coating of machinist blue ink on the metal casing surface before each experiment was sufficient to successfully visualize the location and extent of blade tip contact to the engine casing sector. The method is readily implemented and effective to visualize even grazing rubs, having incursions well below the LMU motion resolution of 5 μm (0.0002 in.). At the most severe incursion investigated to date, this simple method has also recorded the interesting oscillatory pattern of the tip of the blade due to torsional excitation. The obvious drawback of post-experiment photography is that is presents an integrated record of multiple strikes, thus driving one towards instantaneous imaging.

Fig. 12 Blade and casing after very light rub

Figure 12 shows the blade and casing after a very light rub. Pre-test predictions indicated that the combined axial, radial, and circumferential deformation of the airfoil would result in the tip surface coming into contact with the conical casing surface at a location mid-rear chord. The prediction was verified by the experiment. The angular length of the rub was measured at 8 deg, also as predicted by the geometry considerations given earlier.

Figure 13 shows a closeup of the trailing edge of the blade. Under the rub conditions accumulated on this blade there were no signs of plastic deformation or significant burrs at the tip. The discoloration of the epoxy used in bonding and coating the strain gauges is the only indication of the severity of the conditions encountered by the blade. A local instantaneous temperature above 160°F would result in the clear epoxy change in color according to the manufacturer.

Figure 14 shows the casing after experiment 30, for an incursion at 406 μm (0.016 in.) of the single blade rotating at 15,990 rpm. Here, too, the airfoil did not sustain significant damage. The angular extent of rub was measured at 52 deg.

In contrast, Fig. 15(*a*) shows a closeup of the airfoil after experiment 31, where an impact incursion at 762 μm (0.030 in.) was sustained by the single blade rotating at high speed. There is significant plastic deformation of the overall airfoil shape, a removed portion at the trailing edge tip, as well as definite local

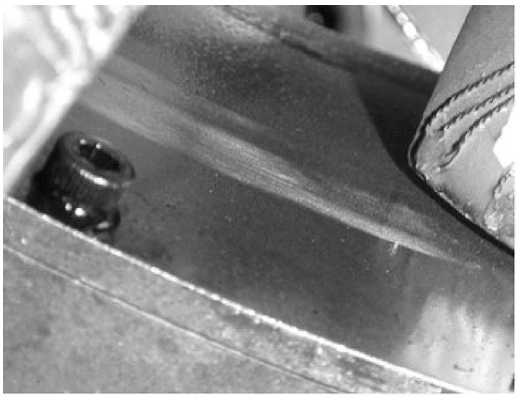

Fig. 13 Closeup of blade trailing edge and casing after several moderately light rub experiments

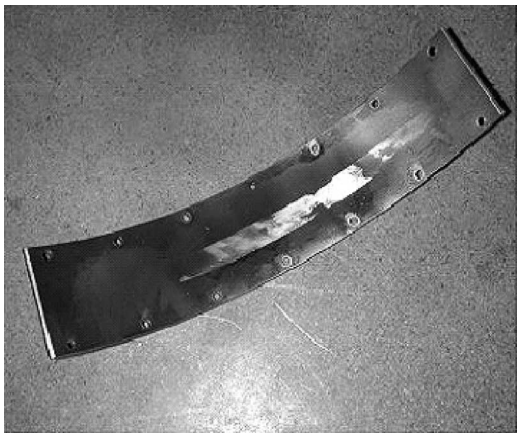

Fig. 14 Casing after rub of experiment no. 30. Incursion: ε =406 μm (0.0160 in.).

damage along the leading edge of the blade. The concomitant rub swath recorded on the casing by the removal of the ink is shown in Fig. 15(*b*). The pattern that is revealed by alternating light and dark areas is consistent with a strong torsional oscillation resulting in alternating high surface stresses toward the leading edge and trailing edge of the tip.

(*a*)

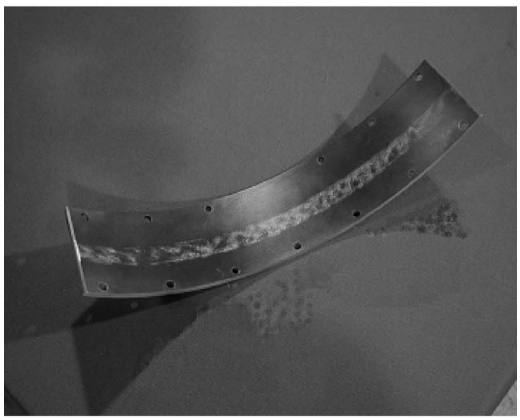

(*b*)

Fig. 15 (*a*) Closeup of blade after experiment No. 31. Impact incursion at ε=762 μm (0.0300 in.). (*b*) Casing after rub of experiment No. 31. Impact incursion at ε=762 μm (0.0300 in.).

4.2 Tip Loads. Results of tip loads will be presented and discussed next. These loads were obtained from the time series of load cell measurements shown earlier as follows.

During a rub experiment, nine response measurements are recorded from an unknown force at the rub surface. It is precisely this resultant force that is computed from the known instantaneous blade position and from the inverse of the output FRF operating on the load cell measurements transformed to the frequency domain. The computation above is then repeated for a discrete set of blade positions during the rub.

At present, issues associated with the detailed requirements of impulse vibration testing have restricted the application of the FRF algorithm to two components of the blade tip load, the axial and the circumferential component. However, finite element structural modeling is in progress to remove such a restriction. In the meantime, even with the restriction to two components, interesting comparisons of tip loads have been obtained, as illustrated below.

Even with the above restrictions, the tip loads indications are very interesting. Figure 16 shows results from the 140 μm (0.0055 in.) incursion (experiment # 26). The axial tip load derived in each of the eight strikes incurred during the experiment is shown in Fig. 16(*a*). The spacing of the data points indicates the angular resolution associated with the processing of the load cell measurements for several airfoil locations. At the rotational speed of 15,990 rpm, a time interval of 100 μs corresponds to about 10 deg rotation. The first two rubs of the single blade installed on the bladed disk are for advancing casing and show axial forces considerably lower than the remaining rubs. In all zero-lead rubs, the maximum axial load is established quickly at the beginning of the event and decreases gradually during the rub. This may result from a relatively large deformation of the airfoil more than compensating for the trend in incursion depth shown earlier in the rub geometry section of this paper. The results for circumferential tip loads are shown in Fig. 16(*b*).

The axial and circumferential tip loads derived in each of the five zero-lead strikes incurred during experiment no. 30 [maximum incursion depth of 406 μm (0.016 in.)] are shown in Fig. 17.

The same general trends are noticed even as the incursion depth of the rub has increased threefold. However, it is interesting to note that while the maximum incurred circumferential load has increased 53%, the maximum incurred axial load has increased only 12%. These results underscore emphatically the highly nonlinear nature of the rub phenomena.

4.3 Blade Vibrations and Stresses. The blade vibratory response was analyzed with the primary objective of deriving design guidelines regarding significant changes in excited frequencies, modal shapes, and stress magnification during rub events. During compressor design, it is industry practice to thoroughly investigate airfoils to identify their dynamic characteristics by analytical methods and testing. Finite-element analysis and experimental techniques are routinely applied to locate the natural frequencies of the blade and to provide information on the modal shapes.

The blade used in the OSU experiments had been fully characterized prior to the rub measurements by finite elements calculations and by measurements using multiple strain gauges during excitation by a pulsating air jet. The air jet was operated at a frequency range of 0–31 kHz, and the responses of the blade were measured. Alternating stresses at discrete frequencies and blade locations on both suction and pressure sides identified mode shapes and natural frequencies of the blade from maximum stress location and stress distribution in nearby gauges. The data from the strain gauges at each natural frequency (1.4, 4, 4.7 kHz,…) identified were available prior to the OSU experiments in a normalized format (percent of maximum value) like that shown, for example, in Table 1.

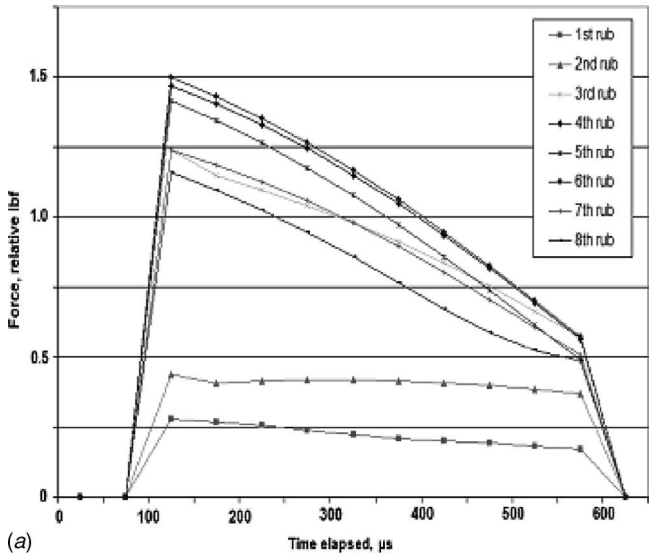

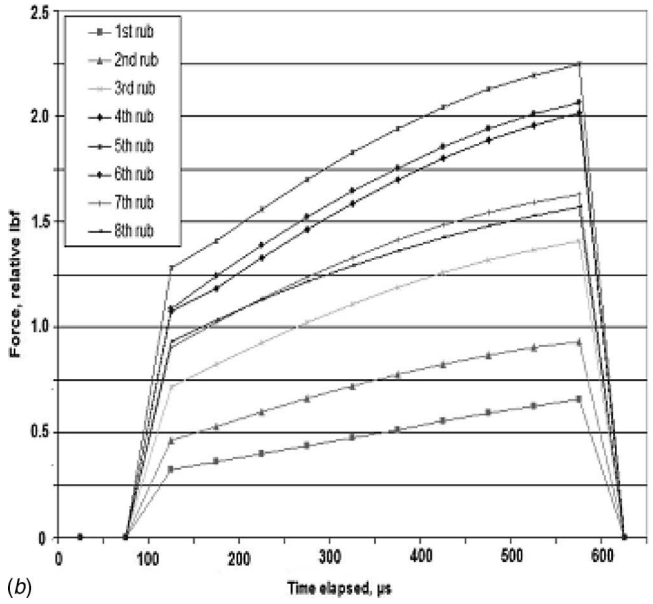

Fig. 16 (*a*) Axial component of tip force on airfoil in experiment no. 26. Incursion: ε=140 μm (0.0055 in.). (*b*) Circumferential component of tip force in experiment no. 26. Incursion: ε=140 μm (0.0055 in.).

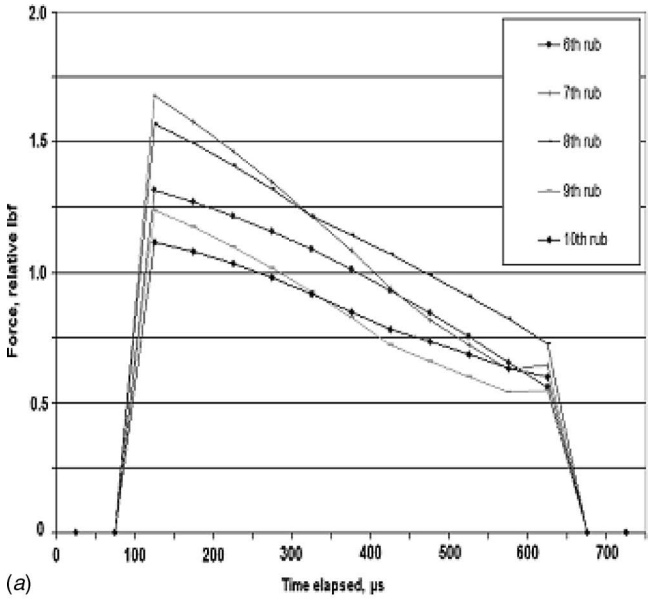

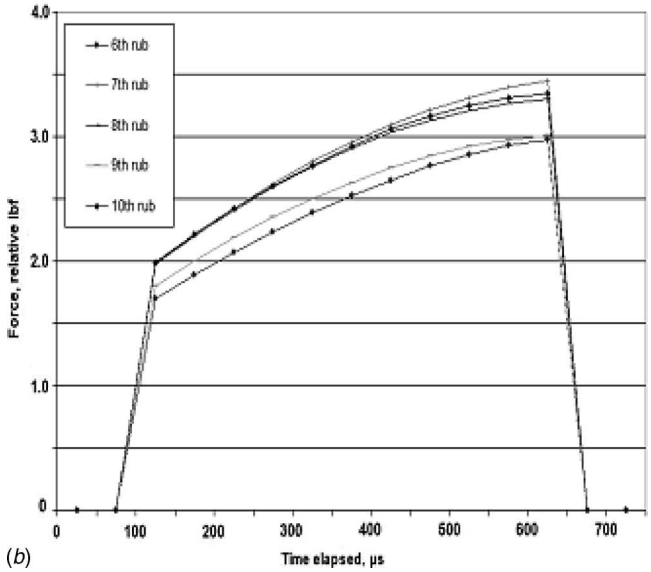

Fig. 17 (*a*) Axial component of tip force on airfoil in experiment no. 30. Incursion: ε=406 μm (0.0160 in.). (*b*) Circumferential component of tip force in experiment no. 30. Incursion: ε=406 μm (0.0160 in.).

In Table 1, five mode shapes are listed: first flex (1F), first torsion (1T), first and second compounds (C1, C2), and second flex (2F). Six strain gauges on the airfoil, i.e., three on the suction side and three on the pressure side, are then listed as an example. Their approximate location on the airfoil is reflected by their label as mid-chord at the airfoil tip (Tip M), trailing edge at the airfoil tip (Tip TE), mid-chord at the airfoil root (Root), leading edge at the airfoil tip (Tip LE), trailing edge at mid-span of the airfoil (TE M), leading edge at mid-span of the airfoil (LE M). The response level of each gauge location for each mode is then shown as percent of maximum value detected at the specific excitation frequency.

To quantify the effect of rub events, the measurements obtained from the OSU experiments were reduced to represent the stress of a particular gauge for a specified blade/casing interaction. Spectral analysis was applied to examine changes in frequency peak location and stress levels in selected frequency sub-domains. Knowledge of the natural frequencies of the blade provided an initial framework in order to isolate specific magnitudes of the power spectral density. This was then used to assess the possibility of severe stress occurring at each significant frequency.

A method of expediting the analysis of the data was conceived to ensure investigation of the appropriate segments of the signal for many different blade strikes. Naturally, the strikes were first grouped into the three main categories: advancing casing, zero-lead, and retreating casing. Only zero-lead rubs will be discussed in the following paragraphs.

For the purposes of creating frequency sub-domains for the spectral analysis, a number of possible filters were considered. A Chebychev II filter was finally selected. This filter allowed for a quick transition from the passband to the stopband region without ripples in the passband. Since the frequencies within the passband region represented information of the blade/engine casing contact, distortion of the response due to ripples was unacceptable. Ripples in the stopband region were permitted to exist however, as only

Table 1 Pre-experiment natural frequency responses

	Gauge	1 F 1.4 kHz	1 T 4 kHz	C1 4.7 kHz	C2 5.4 kHz	2 F 6.9 kHz
Suction Side	Tip M	1	−13	18	22	18
	Tip TE	1	7	−2	9	11
	Root	−100	100	4	62	88
Pressure Side	Tip LE	0	−17	8	3	0
	TE M	47	−67	100	20	−7
	LE M	23	7	24	100	100

the frequency content within the passband parameter was of importance. The choice of a specific filter method allowed for the creation of frequency sub-domains by lowpass, highpass, and bandpass variations of the Chebychev type II filter. These distinctions represented the frequencies that were allowed to pass unaltered in the passband region.

Following the above step, the bandpass filter was used to separate specific frequency ranges of the PSD in two manners: line and bin analyses. For a frequency line filter, the passband parameter was specified to only allow for a very small amount of frequencies to pass unaltered (a ±37 Hz range about the target frequency), while the bin filter extended the total passband range to the mid-interval point based on the data of Table 1. Finally, multiple bandpass filters incorporating these methods were used in succession to isolate the magnitude of the response about the targeted natural frequency.

An example of the final results for rub-induced stress deviations during zero-lead rubs is given in Figs. 18 and 19. The bin-filtered responses were used here based on the ability to more precisely identify the maximum response about the specified natural frequency.

The minimum, maximum and average normalized response is shown in Fig. 18 for the mid-chord root gauge location from experiment no. 26, $\varepsilon = 140$ μm (0.0055 in.). The gauge had recorded the largest stress in the first flexural mode and in the first torsional mode while vibrating as a cantilever beam free at the tip. The same situation occurs while the airfoil vibrates as a cantilever beam rubbing at the tip: the largest stress (normalized as 100%) is incurred in the range centered around 1.4 kHz (first flex) and centered around 4 kHz (first torsion). However, the same root gauge location is stressed differently while rubbing the case than while vibrating freely in the frequency range of the first combined mode C1 (centered around 4.7 kHz). The range of stress deviation over all recorded strikes at that frequencies went from 140% to 203% of the highest stress location on the airfoil for the C1 mode shape, with the average deviation measured at 175%. The effect of rubs at other frequencies is also shown in Fig. 18.

Similar normalized responses from experiment no. 26 are plotted for two tip strain gauge locations in Figs. 19(*a*) and 19(*b*). It is important to note that the leading edge tip strain gauge indicates rub-induced stress deviation from rubs only at the highest fre-

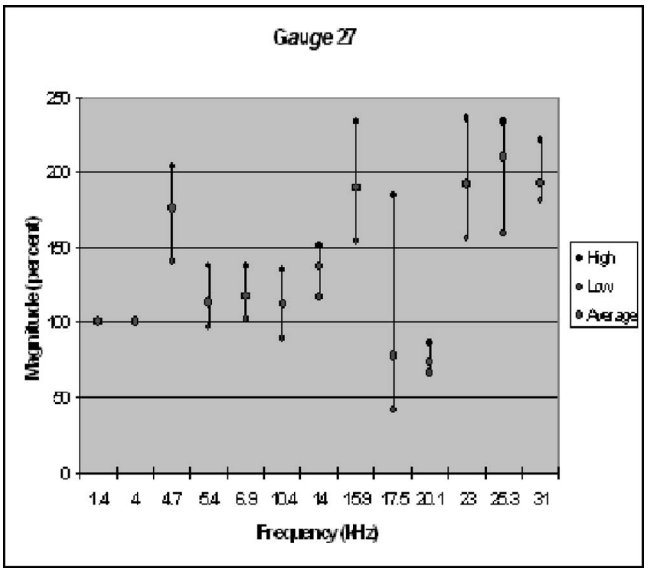

Fig. 18 Percent deviation of mid-chord root stresses on airfoil at selected frequencies

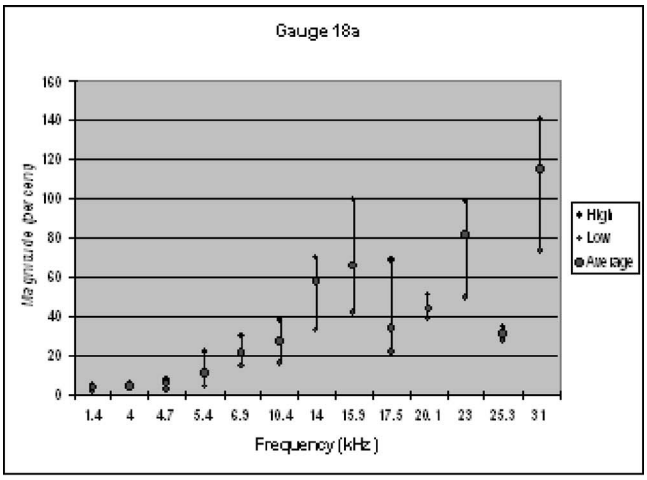

(*a*)

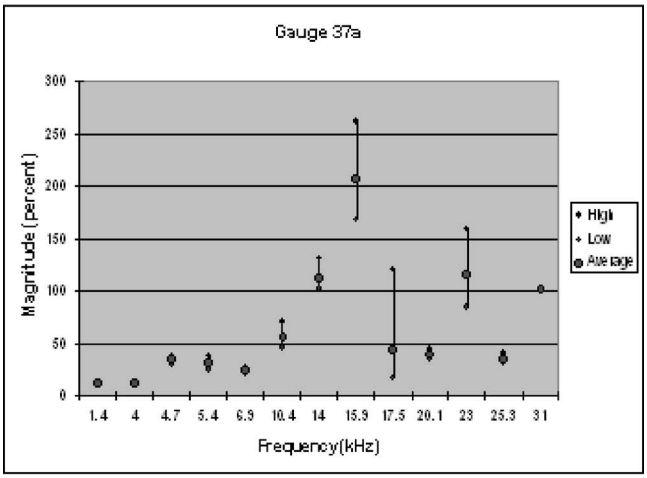

(*b*)

Fig. 19 (*a*) Percent deviation of LE tip stresses on airfoil at selected frequencies. (*b*) Percent deviation of TE tip stresses on airfoil at selected frequencies.

quency range, with a peak value measured at 141% of the highest stress location on the airfoil for the mode shape near 31 kHz. By contrast, the trailing edge tip gauge shows deviations in three of the modes above 11 kHz, with a peak value measured at 261% of the highest stress location on the airfoil for the mode shape near 16.9 kHz. It is conceivable that these levels of rub-induced stress deviation, when sustained over many more cycles than experienced in this experiment, could lead to substantial local damage. The results above would suggest a failure occurring first at the airfoil trailing edge as more likely.

In general, Figs. 18 and 19 are representative of results obtained for each individual strain gauge location for each experiment. They provide initial design guidelines regarding significant changes in blade dynamics during rub events.

In aggregate, the results discussed in this section begin to describe complete transients involving multiple successive incursions, tracking the blade tip contact force distribution and blade stresses throughout the observed rub event time frame, including blade motion during, between, and after successive casing strikes.

5 Conclusions

An in-ground spin-pit facility specifically designed to investigate aeromechanic phenomena for gas turbine engine hardware rotating at engine speed is presently in full operation at the OSU Gas Turbine Laboratory. An engine compressor disk, engine airfoil, and associated casing were used to obtain the blade/casing interaction experiments reported in this paper. The experiments were designed to obtain specific information related to prediction and modeling of blade-casing interactions.

The results presented describe the transient dynamics of rotor and casing vibro-impact response when an Inconel airfoil strikes a bare metal casing for several successive times under operational conditions similar to those experienced in flight. Sudden incursions of varying severity, defined by incursion depths ranging from 13 μm to 762 μm (0.0005 in. to 0.030 in.), were obtained. Tip loads and vibratory stresses occurring in rub events representative of in-flight events including a few rubs of varying incursion depth and positive or negative incursion rate and a few rubs at zero incursion rate have been demonstrated. In addition, the amplification of blade oscillations under successive rubs was obtained. The results discussed in this paper have been applied to advance the understanding of the complex physics of the rub phenomena and to compare the measurements to analytical predictions.

Acknowledgment

The work described in this paper was performed as part of the General Electric University Strategic Alliance program at The Ohio State University. Several GE engineers are contributing valuable research directions and assistance to the tip rub project. The authors wish to especially acknowledge the contributions of Kevin Turner, Dennis Corbly, Jim Rhoda, Alan Turner, A. J. Wang, and Sunil Sinha. We also would like to acknowledge the contributions to this work of Professor Maurice Adams of Case Western Reserve University and Dr. Michael Adams of Machinery Vibrations, Inc.

References

[1] Hermanek, F. J., Jr., 1970, "Coatings Lengthen Jet Engine Life," Metal Progress, **97**, pp. 104–106.

[2] Kosing, O. E., Scharl, R., and Schmuhl, H. J., 2001, "Design Improvements of the EJ 200 HP Compressor. From Design Verification Engine to a Future All Blisk Version," ASME Paper No. 2001-GT-0283.

[3] Sinha, S. K., 2005, "Non-linear Dynamic Response of a Rotating Radial Timoshenko Beam with Periodic Pulse Loading at the Free-end," Int. J. Non-Linear Mech., **40**(1), pp. 113–149.

[4] Turner, K., Adams, M.L., and Dunn, M.G., 2005, "Simulation of Engine Blade Tip-Rub Induced Vibration," ASME Paper No. GT2005-68217.

[5] Muszynska, A., 1989, "Rotor-to-Stationary Element Rub-Related Vibration Phenomena in Rotating Machinery—Literature Survey," Shock Vib. Dig., **21**, pp. 3–11.

[6] Padovan, J., and Choy, F. K., 1987, "Nonlinear Dynamics of Rotor/Blade/Casing Interactions," ASME J. Turbomach., **109**, pp. 527–534.

[7] Adams, M. L., 2000, *Rotating Machinery Vibration. From Analysis to Troubleshooting*, Marcel Dekker Inc., New York.

[8] Manwaring, S. R., and Wisler, D. C., 1993, "Unsteady Aerodynamics and Gust Response in Compressors and Turbines," ASME J. Turbomach., **115**, pp. 724–733.

[9] Kielb, J. J., Abhari, R. S., and Dunn, M. G., 2001, "Experimental and Numerical Study of Forced Response in a Full-Scale Rotating Turbine," ASME Paper No. 2001-GT-0263.

[10] Laverty, W. F., 1981, "Rub Energetics of Compressor Blade Tip Seals," *Proceedings of the 3rd International Conference on Wear of Materials*, pp. 714–721.

[11] Padova, C., Barton, J., Dunn, M. G., Manwaring, S., Young, G., Adams, M. L., and Adams, M., 2004, "Development of an Experimental Capability to Produce Controlled Blade Tip/Shroud Rubs at Engine Speed," ASME Paper No. GT2004-53322.

[12] Jiang, J., Ahrens, J., Ulbrich, H., and Scheideler, E. M., 1998, "A Contact Model of a Rotating Rubbing Blade," *Proceedings of the 5th International Conference on Rotor Dynamics*, Darmstadt, pp. 478–489.

[13] Ahrens, J., Ulbrich, H., and Ahaus, G., 2000, "Measurement of Contact Forces During Blade Rubbing," *Vibrations in Rotating Machinery*, 7th International Conference, Nottingham, September 12-14, ImechE, London, pp. 259–263.

A Simplified Method for Predicting the Stability of Aerodynamically Excited Turbomachinery

Albert F. Storace
Consulting Engineer Dynamics,
Advanced Technology and Preliminary Design,
GE Aviation,
Cincinnati, OH

A modal stability (MS) method is presented for the quick and accurate prediction of the stability of aerodynamically excited turbomachinery using real eigenvalue/eigenvector data obtained from a rotordynamics model. The modal stability method provides a means to compare the work of stabilizing damping forces to the work of destabilizing aerodynamic cross-coupled stiffness forces to predict the onset of whirl instability. The MS method thus indicates that unstable or self-excited whirling (sometimes called whipping) at one of the system's natural frequencies is initiated when the destabilizing work equals or exceeds the stabilizing work. This approach provides a powerful design tool to quickly ascertain the effects of squeeze-film dampers, and turbine engine architecture, including bearing locations and bearing support structure stiffness, on system stability.
[DOI: 10.1115/1.2720870]

Introduction

A major destabilizing force acting on turbomachinery stages is the unsteady aerodynamic force, called the Thomas/Alford force. This force was first postulated by Thomas [1] and Alford [2] to explain rotor whirl instabilities seen in steam turbines and jet engines, respectively. Therefore, this force is generally referred to as the Thomas/Al ford force. It is a cross-coupled stiffness force because its magnitude is proportional to the radial deflection of the rotor and it acts in the direction orthogonal to the deflection. Any radial deflection of the rotor relative to the stator creates circumferentially nonuniform clearances and unsteady aerodynamic blade forces that sum to generate the cross-coupled stiffness force. To further understand the factors involved, consider that the eccentric operation of the rotor results in local changes in mass flow and efficiency for both the rotor blades and the stator vanes. The result is a circumferential perturbation of both the rotor blade and the stator vane forces. Furthermore, for repeating compressor or turbine stages, the change in the tangential momentum across the rotor blades and the stator vanes is essentially equal and thus the tangential forces acting on the rotor blades and the stator vanes are equal. This indicates that the Thomas/Alford force acting on the stator vane row is probably equal and opposite to the Thomas/Alford force acting on the rotor blade row. Consider turbines, where the circumferential variation in radial tip clearance causes a circumferential variation in efficiency so that the rotor blading with the smallest clearance would be the most efficient and would be more highly loaded than the blades with larger clearance. Thus for turbines, the cross-coupled aerodynamic stiffness force tends to promote forward whirl of the rotor and backward whirl of the stator. Actually, the countering cross-coupled stiffness forces reduce the net destabilizing energy fed into the turbomachine system and it would whirl in the forward direction, that is, in the same direction as the turbine rotation (spin) under the influence of the turbine cross-coupled stiffness forces. For compressor eccentric operation, the cross-coupled stiffness force can promote either forward or backward whirl of the turbomachinery system relative to the direction of the compressor rotation based on the test data and analysis results for compressors reported by Ehrich [3] and Storace et al. [5,6]. This is because the local mass flow decreases faster than the efficiency increases on the reduced clearance side of the eccentric compressor rotor. Since torque is directly proportional to mass flow and inversely proportional to efficiency, the more-rapidly decreasing mass flow probably more than counteracts the effect of decreasing efficiency. This suggests that the local reductions in mass flow for the whirling compressor rotor are actually more important than the local reductions in efficiency. The two opposing actions impact both the sign and the magnitude of the Thomas/Alford force for compressors.

Provided herein is a method to predict the onset of instability through a comparison of the destabilizing work done by the Thomas/Alford force and the stabilizing work done by damping forces. An initial version of the method was presented by Storace [4] and this paper expands and refines the methodology to include multiple rotors, the prediction of rotor forward and backward whirl instability, and to reflect further aerodynamic cross-coupled stiffness force test data and analysis results for compressors reported by Ehrich [3] and Storace et al. [5,6].

The method for predicting the onset of instability is called the modal stability criterion (MSC). It provides a simplified approach using real modes to predict rotor stability and goes beyond the theory and mathematical models customarily used to predict rotordynamic instability caused by blading aerodynamic forces in that, as discussed above, it is postulated that the Thomas/Alford force acts on both the rotor blade and the stator vane rows.

Derivation of the Modal Stability Criterion

The following equation defines the rotor and stator physical Thomas/Alford forces acting on both the rotor blade and stator vane rows of a turbine or compressor stage in the ground fixed *X-Y* coordinate system,

$$\begin{Bmatrix} F_{XR} \\ F_{YR} \\ F_{XS} \\ F_{YS} \end{Bmatrix} = \begin{bmatrix} 0 & -K_{XY} & 0 & K_{XY} \\ K_{YX} & 0 & -K_{YX} & 0 \\ 0 & K_{XY} & 0 & -K_{XY} \\ -K_{YX} & 0 & K_{YX} & 0 \end{bmatrix} \begin{Bmatrix} X_R \\ Y_R \\ X_S \\ Y_S \end{Bmatrix} \quad (1)$$

Contributed by the Turbomachinery Division of ASME for publication in the JOURNAL OF TURBOMACHINERY. Manuscript received August 11, 2006; final manuscript received August 29, 2006. Review conducted by David Wisler. Paper presented at the Eleventh International Symposium on Transport Phenomena and Dynamics of Rotating Machinery, 2006.

In Eq. (1), X_R, Y_R, X_S, Y_S are the horizontal and vertical deflections of the rotor and stator at the rotor blade station (axial location). As previously postulated, Eq. (1) indicates that the rotor blade row forces F_{XR}, F_{YR} are equal and opposite to the stator vane row forces F_{XS}, F_{YS}. In addition, it is assumed that the amplitudes of the cross-coupled stiffness coefficients K_{XY}, K_{YX} are equal.

K_{XY} = Thomas/Alford cross–coupled stiffness coefficient

$$\text{for the rotor blade row} = K_{XY} = \frac{T\beta}{D_P H}\frac{lb}{in} \tag{2}$$

where T is the stage rotor blade row torque, in. lb., D_P is the stage rotor blade pitch diameter, in., and H is the stage rotor blade height, in.

β (beta) is the change in thermodynamic efficiency per unit change in blade-tip clearance, expressed as a fraction of blade height (the Thomas/Alford coefficient which represents the nondimensional cross-coupled stiffness). In the development to follow, positive (negative) beta indicates that the cross-coupled stiffness force promotes forward (backward) rotor whirl,

For circular whirl: $X_R = A_R \cos \omega t$

$$Y_R = A_R \sin \omega t$$

and

$$X_S = A_S \cos \omega t$$

$$Y_S = A_S \sin \omega t$$

where A_R and A_S are the amplitudes of the physical whirl displacement vectors of the rotor and stator, respectively, at the rotor blade station and ω rad/s is the whirl frequency. The whirl displacement vectors will be expressed in terms of modal displacements obtained from an undamped mode of the turbomachinery system (turbine engine). Therefore, since the rotating modal displacement vectors obtained from the undamped mode (real mode) are collinear, the physical whirl displacement vectors can be treated like scalars. Transforming the cross-coupled stiffness forces from a ground fixed X-Y Cartesian coordinate system to a polar coordinate system (radial, tangential directions) rotating at angular speed ω gives the following:

Obviously the rotor blade and stator vane row radial forces are zero as the cross-coupled stiffness forces provide no direct stiffness or restoring force component, that is, no structural stiffening is added to the system. Only tangential force components are provided as follows:

Tangential force (cross-coupled stiffness force)

acting on the rotor blade row

$$= F_R = K_{XY}(A_R - A_S) \text{ lbs.}$$

Tangential force (cross-coupled stiffness force)

acting on the stator vane row

$$= F_S = -K_{XY}(A_R - A_S) \text{ lbs.}$$

Define ϕ_R and ϕ_S as the rotor and stator modal displacements, respectively, in an engine plane at the rotor blade station for a given mode. Thus, $A_R = \phi_R SF$ in. and $A_S = \phi_S SF$ in. where SF is the generalized coordinate for the mode (represents the scale factor that converts modal displacements to physical displacements).

Then, for the mode under consideration, the cross-coupled stiffness forces acting on the rotor blade and the stator vane rows are

$$F_R = K_{XY}(\phi_R - \phi_S)SF \text{ lbs.}$$

$$F_S = -K_{XY}(\phi_R - \phi_S)SF \text{ lbs.} \tag{3}$$

Refer to Fig. 1.

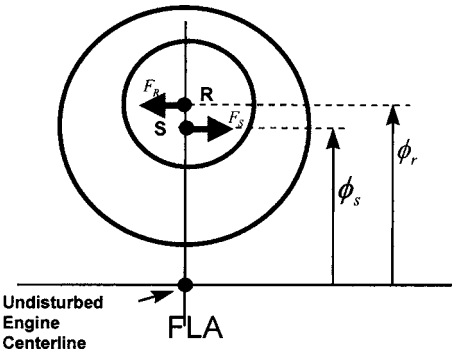

Fig. 1 Cross-coupled stiffness forces acting on the rotor and stator (*forward whirl direction is counterclockwise-forward looking aft (FLA)*)

Assuming forward whirl, the destabilizing rotor blade row work performed by the cross-coupled stiffness force per cycle of vibration at the rotor blade station is

$$W_R = 2\pi K_{XY}(\phi_R - \phi_S)\phi_R SF^2 \text{ in. lb.}$$

The stator vane row work for forward whirl is stabilizing (extracts energy from the system) and is equal to the amplitude of the cross-coupled stiffness force times the distance traveled by the stator center at the stator vane station for one whirl cycle. If the axial offset between the rotor blades and stator vanes of a stage is ignored, then the distance traveled can be approximated as $2\pi\phi_S SF$. Then the stator vane row work for forward whirl is

$$W_s = -2\pi K_{XY}(\phi_R - \phi_S)\phi_S SF^2 \text{ in. lb.}$$

The net destabilizing work for a stage per cycle of vibration is shown in Eq. (4),

$$W = W_R + W_S = 2\pi K_{XY}(\phi_R^2 - \phi_R\phi_S - \phi_R\phi_S + \phi_S^2)SF^2$$
$$= 2\pi K_{XY}(\phi_R - \phi_S)^2 SF^2 \text{ in. lb.} \tag{4}$$

Note that mathematically, the net work $W = 2\pi K_{XY}(\phi_R - \phi_S)^2 SF^2$ can be associated with the work of an equivalent "negative damping element" connecting the rotor and the stator when K_{XY} is replaced by $C_E\omega$, where C_E is the effective damping coefficient.

Summing the destabilizing energy over the compressor and turbine stages of the engine (for both the high and low pressure rotors), the total energy is given by

$$W_T = 2\pi SF^2\left(\sum_{\text{Turb}} K_{XYT}(\phi_{RT} - \phi_{ST})^2 \pm \sum_{\text{Compr}} K_{XYC}(\phi_{RC} - \phi_{SC})^2\right) \text{ in. lb.} \tag{5}$$

where K_{XYT} and K_{XYC} are the individual cross-coupled stiffness coefficients for the turbine and compressor rotor blade rows, respectively. The rotor and stator modal displacements for the turbine rotor blade stations are ϕ_{RT}, ϕ_{ST}, and ϕ_{RC}, ϕ_{SC} are the rotor and stator modal displacements at the compressor rotor blade stations.

The $\pm$ sign for the compressor work summation reflects the sign of the compressor blade row beta coefficients which can be plus or minus. This indicates that the compressor work can be stabilizing (destabilizing) for forward (backward) whirl of the rotor.

The destabilizing energy W_T is compared to the energy absorbed (energy dissipated by external damping) by the turbine engine per cycle vibration for a given mode to establish the potential for whirl instability.

The energy dissipated per cycle of vibration in an engine plane is

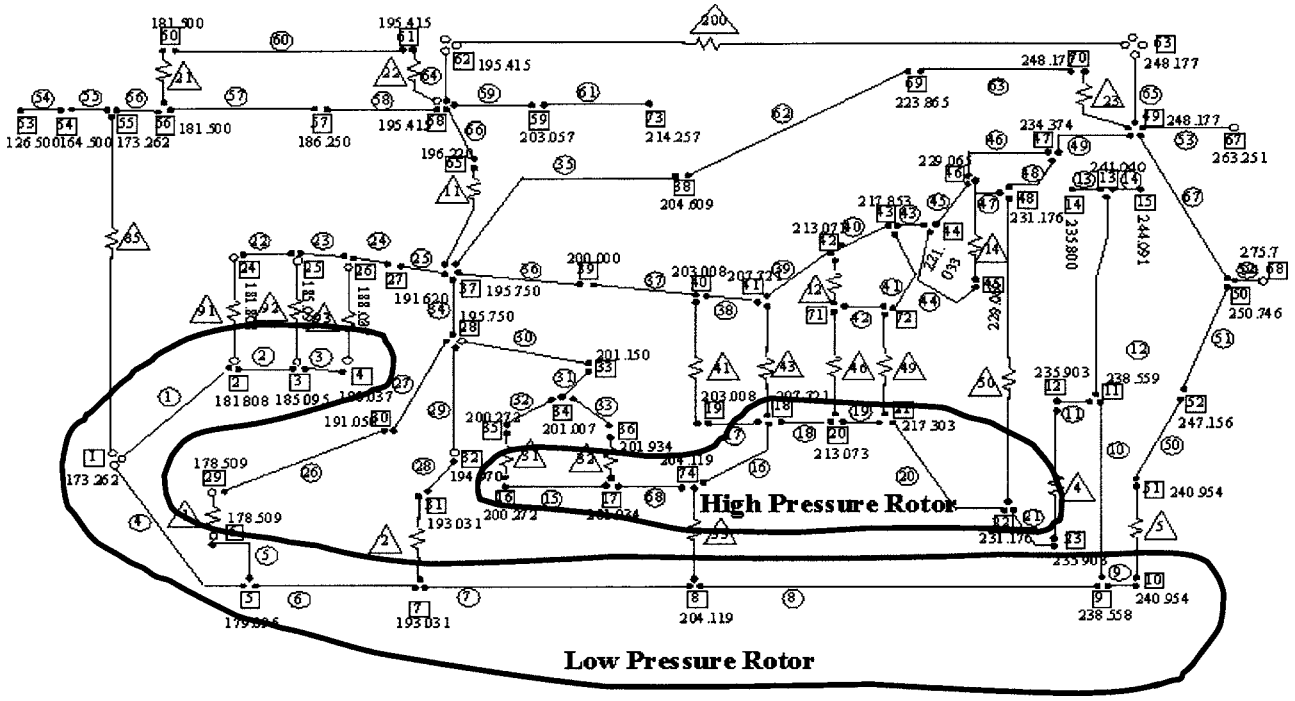

Fig. 2 Structural network for turbine engine rotordynamics model

$$E = \frac{2\pi PE(SF)^2}{Q} \text{ in. lb.}$$

where Q is the turbine engine system Q-factor (generalized or modal Q-factor) for a given mode of vibration. PE=$\frac{1}{2}K_G$=the engine system modal (generalized) potential energy in a single plane, where $K_G=\{\phi\}^T[K]\{\phi\}$ is the generalized stiffness for the mode, $[K]$ is the physical global stiffness matrix, and $\{\phi\}$ is the mode shape vector. The engine system energy dissipated in two planes is

$$E_T = \frac{2\pi}{Q}K_G(SF)^2 \text{ in. lb.} \tag{6}$$

Hence, $E_T/W_T \geq 1.0$ for stability and when the expressions for the destabilizing and stabilizing energies are substituted in this energy ratio, the $(SF)^2$ terms cancel and the result is the modal stability criterion Eq. (7),

$$\text{MSC} = \frac{\dfrac{K_G}{Q}}{\left|\sum_{\text{Turb}} K_{XY_T}(\phi_{RT}-\phi_{ST})^2 \pm \sum_{\text{Compr}} K_{XY_C}(\phi_{RC}-\phi_{SC})^2\right|}$$

$$\geq 1.0 \text{ for stability} \tag{7}$$

The absolute value of the destabilizing energy is shown in the denominator of the modal stability criterion equation to represent the case when the compressor destabilizing work is negative and exceeds the turbine destabilizing work. In this case, the rotor will undergo backward whirl if the magnitude of the negative energy exceeds the stabilizing energy. If the compressor destabilizing energy is negative and the net destabilizing energy is positive, then the compressor provides a stabilizing influence for forward whirl of the rotor. In this case, the compressor cross-coupled stiffness force behaves as a positive damping force.

It is expected that there is potential for only subsynchronous modes to be destabilized. However, for conservatism, the MSC value is calculated at maximum power for modes with natural frequencies extending to 10% above the operating speed range. The cross-coupled stiffnesses K_{XYT} and K_{XYC} are based on the rotor torque values at maximum power.

The modal damping Q for the turbine engine system used in the MSC calculation is obtained by integrating the component (casings, rotors, frames, bearings, dampers, mounts) damping contributions over the mode shape for each of the modes evaluated. Equation (8) gives the equation for Q for a given mode,

$$Q = \frac{\text{PE}}{\sum_{i=1}^{ns}\frac{\text{PE}_i}{Q_i} + \sum_{j=1}^{nr}\left(1-\frac{\Omega_j}{\omega}\right)\frac{\text{PE}_j}{Q_j}} \tag{8}$$

where PE_i are the modal potential energies in the ns stator components (the stator components include stationary housing bearings and squeeze-film dampers), Q_i are the component Q-factors for the stator components, Ω_j are the maximum spin speeds (rad/s) of the nr rotors, PE_j are the modal potential energies in the nr rotors, Q_j are the component Q-factors for the rotor components, and ω is the natural frequency (rad/s) of the mode.

The first summation in the denominator of Eq. (8) represents the external damping contributed by the stationary components. The second summation represents the internal damping contributed by the rotating components. For forward whirl, the rotors included in this summation provide positive damping when the rotor spin speed is below the system natural frequency ω and negative damping when the rotor is spin speed is above the system natural frequency ω.

Stability Calculation Procedure Using the Modal Stability Criterion

For demonstration purposes, consider the rotordynamics finite element model for the 2-spool turbine engine shown in Fig. 2. This is a centerline beam model and represents a single plane of the system and thus the model is termed a planar or 2D model. In Fig. 2, the lines or spans (identified by the numbers enclosed in circles) represent unbranched substructures, typically rotors and

Table 1 Forward whirl natural frequencies, and modal properties calculated for the turbine engine model shown in Fig. 2

Natural Freq. (CPM)	Modal Q	Modal Stiffness (lb.f/in.)	Modal mass (lb.f s^2/in.)
580.007	1.093	1.176E+4	3.187
1895.719	3.593	1.083E+5	2.748
4344.953	4.000	1.238E+5	5.982E−1
5256.637	4.386	3.968E+5	1.310
6430.396	4.245	3.643E+5	8.034E−1
7455.712	4.020	2.237E+6	3.669
7902.187	3.504	1.382E+5	2.018E−1
8786.354	4.708	7.539E+5	8.905E−1
10516.682	4.855	1.133E+6	9.342E−1
12136.527	6.148	1.167E+6	7.226E−1
12959.335	9.172	7.967E+5	4.326E−1
15500.884	6.580	1.058E+6	4.014E−1
16683.307	4.182	1.416E+6	4.639E−1
18046.474	4.000	1.971E+6	5.518E−1
19932.898	8.841	2.716E+5	6.233E−2
20431.859	6.142	4.935E+6	1.078
21121.389	4.297	2.756E+6	5.634E−1
21328.062	5.711	5.417E+5	1.086E−1
23352.399	4.506	1.055E+7	1.763
23727.544	4.159	2.619E+7	4.242

Table 2 MSC values calculated for forward whirl modes for the turbine engine model shown in Fig. 2[a]

Mode	CPM	Modal Q	PE	Stability criterion
1	580.0	1.1	5880.0	27074.053
2	1895.7	3.6	54150.0	362.819
3	4345.0	4.0	61900.0	157.205
4	5256.6	4.4	198400.0	17.572
5	6430.4	4.2	182150.0	97.990
6	7455.7	4.0	118500.0	496.113
7	7902.2	3.5	69100.0	748.802
8	8786.4	4.7	376950.0	11.806[b]
9	10516.7	4.9	566500.0	82.338
10	12136.5	6.1	583500.0	108.510
11	12959.3	9.2	398350.0	37.846
12	15500.9	6.6	529000.0	194.818
13	16683.3	4.2	708000.0	320.073
14	18046.5	4.0	985500.0	876.309
15	19932.9	8.8	135800.0	588.939
16	20431.9	6.1	2467500.0	146.947
17	21121.4	4.3	1378000.0	1948.724
18	21328.1	5.7	270850.0	268.310
19	23352.4	4.5	5275000.0	282.470
20	23727.5	4.2	13095000.0	860.977

[a]Stability criterion >1 implies stability.
[b]Minimum MSC value >1.0 (engine is stable).

casings, and model distributed mass, stiffness, and damping properties. The spring elements (identified by the numbers enclosed in triangles) typically model the stiffness and damping load paths of engine frames, bearings, squeeze-film dampers, centering springs, and engine mounts. The joints at the connections between the spans and springs are identified by the numbers enclosed by boxes. The engine has low- and high-pressure rotors that are corotating and the spans used to model these rotors are identified in Fig. 2. The undamped modes obtained from the engine model along with the modal damping calculated with Eq. (8) are used in the MSC calculation.

The stability for the model is evaluated as follows. If the compressor beta coefficients are positive, then there is only potential for forward whirl instability and obviously only forward whirl modes need be evaluated with the MSC equation. The model is constrained to determine the forward whirl modes and the modal properties are computed. These properties are tabulated in Table 1. Then on a mode-by-mode basis, Eq. (9) (denominator of the MSC equation) is used to calculate the modal destabilizing energy at maximum engine power,

$$\text{Modal destabilizing energy} = \sum_{\text{Turb}} K_{XYT}(\phi_{RT} - \phi_{ST})^2 \pm \sum_{\text{Compr}} K_{XYC}(\phi_{RC} - \phi_{SC})^2 \quad (9)$$

Note that if this energy is positive for a given forward whirl mode, then it is used in the MSC equation to evaluate the forward whirl mode for stability. This indicates that energy is fed into the engine system by the cross-coupled stiffness forces and if this energy is greater than the stabilizing energy, then the MSC value is less than 1.0 and this indicates that the engine will undergo forward whirl at the natural frequency for the mode. If the modal destabilizing energy is negative, then the forward whirl mode cannot be destabilized and the MSC equation does not apply.

Table 2 shows the MSC values computed for the engine forward whirl modes. The engine is predicted to be stable for all of the evaluated modes as all of the MSC values are greater than 1.0. The smallest stability margin (MSC=11.806) is predicted for the 8786 CPM mode.

If the compressor beta coefficients are negative, then backward whirl modes also need to be evaluated for stability. In this case, the model is constrained to determine the backward whirl modes and the modal properties are computed. The procedure is the same as used for the forward whirl modes, except the screening criterion is that only modes with negative modal destabilizing energy (thus, energy is fed into the engine system for backward whirl modes) are evaluated with the MSC equation for backward whirl instability.

Including the Effects of Squeeze-Film Dampers in the Stability Evaluation

Static housing squeeze-film dampers (SFDs) always provide a stabilizing influence on turbine engines. An effective component Q-factor for the damper is used to include its effect on system stability. Figure 3 shows an example map of the component Q-factor versus damper geometry (damper land length and diameter) and clearance for a parallel damper and centering spring combination. In Fig. 3, the damper is modeled using a Reynolds equation solution for small circular orbits to simulate the damper's performance at the onset of instability which is consistent with the MSC energy balance calculation; the component stiffness and damping are contributed by the centering spring and the squeeze-film damper, respectively. The approach is to evaluate the system stability without the damper using the MSC calculation to determine the bearing location where a damper could be used to enhance stability for a given mode. Then a map such as that shown in Fig. 3 is used to determine the component Q-factor to be used in the modal damping equation (Eq. (8)) to determine the system Q-factor used in the MSC calculation for the selected centering spring stiffness and SFD geometry and radial clearance at the natural frequency of the mode. Figure 4 shows an example of the design process for a turbine engine where a range of SFD parameters are evaluated to determine the damper configuration required to meet the desired system stability margin. Shown in this figure is a plot of the MSC value versus the damper + centering spring component Q-factor and the corresponding damper clearance values for constant values of damper land length and diameter. In Fig. 4, a 50% stability margin (MSC=1.5) has been selected as the requirement and damper clearance values less than 7.5 mils meet this requirement.

Conclusion

The modal stability criterion (MSC) provides a convenient and quick means to perform a system stability analysis for aerodynamically excited turbomachinery using the real modes generated

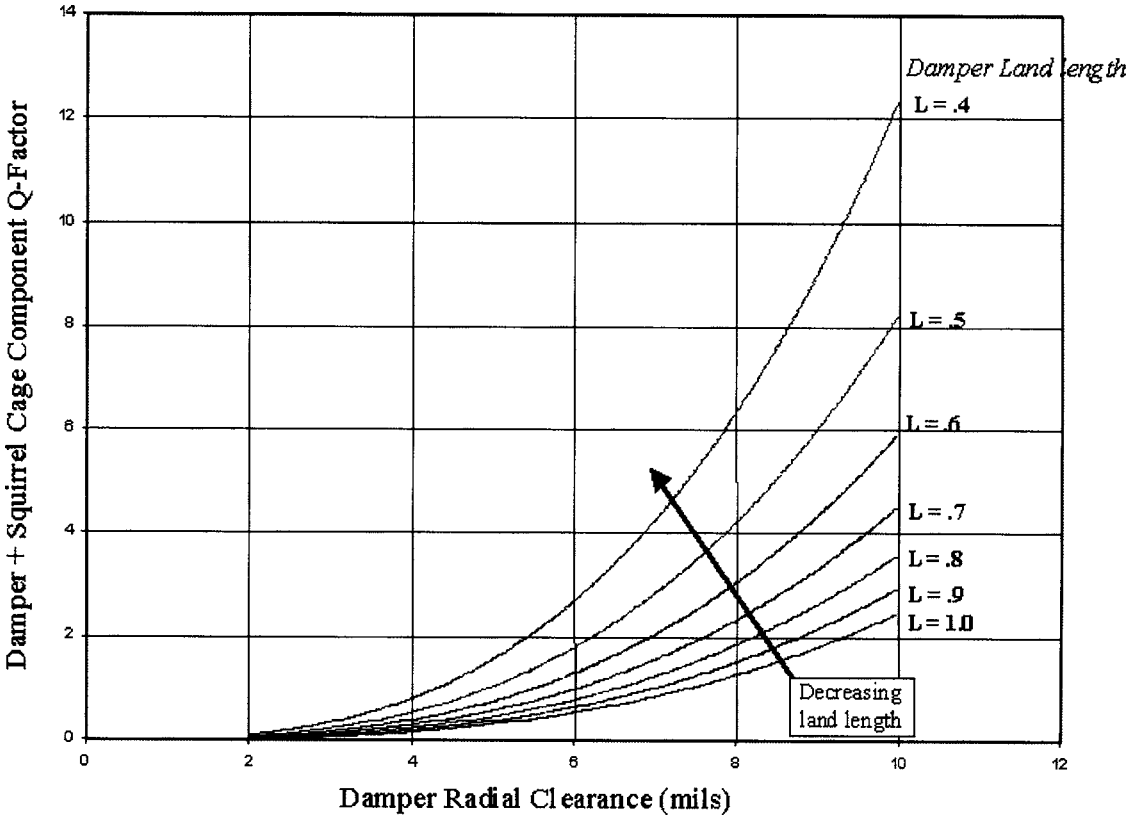

Fig. 3 Squeeze-film damper+squirrel cage component *Q* factor as a function of damper radial clearance and land length

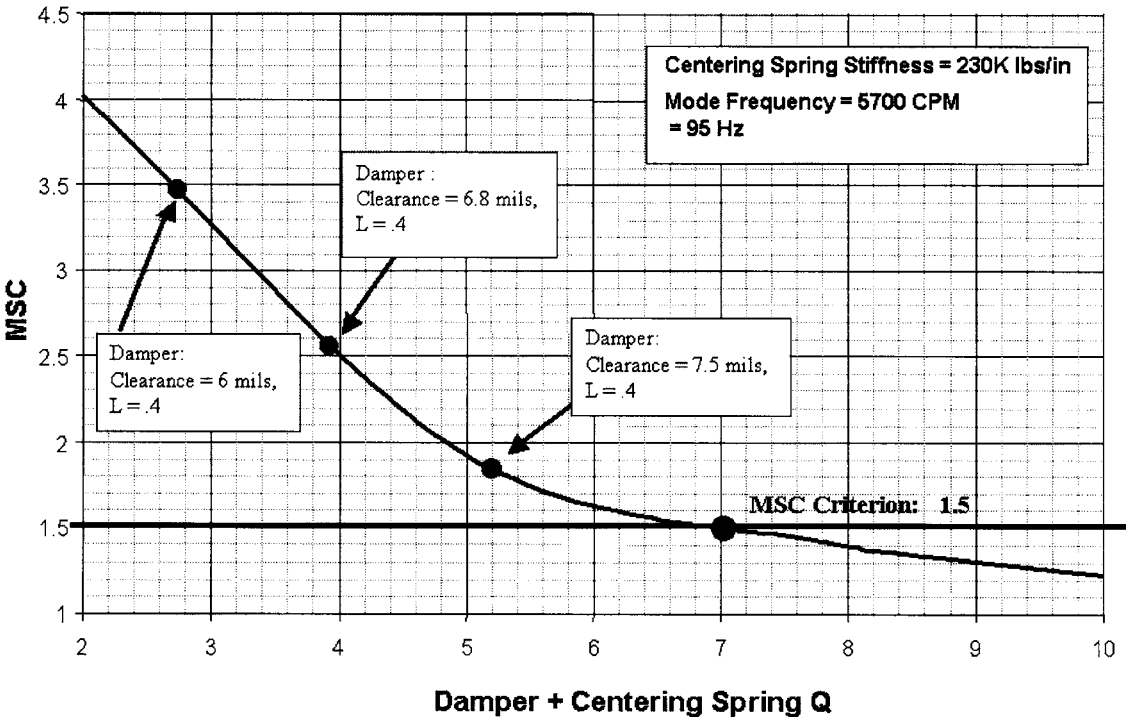

Fig. 4 Modal stability criterion (MSC) value as a function of squeeze-film damper+centering spring component *Q*-factor (damper geometry dependency)

from a system vibration model. It includes all of the significant parameters (forward and backward whirl inducing destabilizing aerodynamic forces, whirl and spin speeds, and engine system damping, including the effects of squeeze-film dampers), and modeling detail needed to make an accurate assessment of engine system stability. Although the stability analysis methodology presented focused on blade tip-clearance related aerodynamic destabilizing forces, it is equally applicable to the modeling of other aerodynamic force destabilizing mechanisms such as that associated with secondary flow swirl in labyrinth seals. All that is required in the modeling of destabilizing aerodynamic forces is the inclusion of the appropriate cross-coupled stiffness in the MSC criterion. The assumption of circular whirl means that the stabilizing effects of nonaxisymmetric rotor and/or engine support stiffness are not included, and this may result in built-in conservatism, depending on the modal characteristics of the engine system modes.

References

[1] Thomas, H. J., 1958, "Unstable Natural Vibration of Turbine Rotors Induced by the Clearance Flow in Glands and Blading," Bull. De l' A. I. M., **71**(11/12), pp. 1039–1063.

[2] Alford, J., 1965, "Protecting Turbomachinery From Self-Excited Rotor Whirl," J. Eng. Power, **97**, pp. 333–334.

[3] Ehrich, F. F., 1993, "Rotor Whirl Forces Induced by the Tip Clearance Effect in Axial Flow Compressors," J. Vibr. Acoust., **115**, pp. 509–515.

[4] Storace, A. F., 1990, "Predicting the Stability of Aerodynamically Excited Turbomachinery," The Sixth Workshop on Rotordynamic Instability Problems in High-Performance Turbomachinery, Texas A&M University, pp. 272–286.

[5] Storace, A. F., Wisler, D. C., Shin, H.-W., Beacher, B. F., Ehrich, F. F., Spakovszky, Z. S., Sanchez, M. Martin, and Song, S. J., 2000, "Unsteady Flow and Whirl-Inducing Forces in Axial-Flow Compressors, Part I—Experiment," ASME Paper No. 2000-GT-0565.

[6] Ehrich, F. F., Spakovsky, Z. S., Sanchez, M. Martin, Song, S. J., Wisler, D. C., Storace, A. F., Shin, H.-W., and Beacher, B. F., 2000, "Unsteady Flow and Whirl-Inducing Forces in Axial-Flow Compressors, Part II—Analysis," ASME Paper No. 2000-GT-0566.

M. Nikolic
e-mail: marija.nikolic@imperial.ac.uk

E. P. Petrov
e-mail: y.petrov@imperial.ac.uk

D. J. Ewins
e-mail: d.ewins@imperial.ac.uk

Mechanical Engineering Department,
Centre of Vibration Engineering,
Imperial College London,
South Kensington Campus,
London SW7 2AZ, UK

Coriolis Forces in Forced Response Analysis of Mistuned Bladed Disks

The problem of estimating the mutual interaction of the effects of Coriolis forces and of blade mistuning on the vibration characteristics of bladed disks is addressed in this paper. The influence of different degrees of mistuning on forced response and amplification factors are studied in the presence of Coriolis forces and then compared to their non-Coriolis counterparts using a computationally inexpensive, yet representative, model of a bladed disk. The primary objective of the study reported in this paper is to establish whether current mistuned bladed disk analyses should incorporate Coriolis effects in order to represent accurately all the significant factors that affect the forced response levels. [DOI: 10.1115/1.2720866]

Introduction

One of the major problems in turbomachinery bladed disk vibration is related to scatter in the blades' forced response amplitudes (resulting from variability in blades' properties) as this might lead to excessive vibration levels confined to few blades and, subsequently, might cause a high cycle fatigue failure. As a result, throughout the past decade, much research effort has been dedicated to the development of computationally efficient "reduced order methods" for predictions of the forced response characteristics using large-scale finite element models of bladed disks [1–4]. However, despite the exploitation of state-of-the-art model reduction techniques, the acquired predictions are only as good as the initial bladed disk model provided. Thus, unless all physical phenomena affecting the behavior of bladed disks are included accurately in the model, the forced response predictions may be doubtful and somewhat unreliable. The failure to include *all* the factors that have a nontrivial contribution to the vibration characteristics of bladed disks could provide an explanation for a recurring mismatch observed between theoretical predictions and experimental measurements, particularly for individual blades in the assembly.

Turbomachinery components such as bladed disks are exposed to effects of forces caused by bladed disk rotation, acting on the system in a rotating frame of reference, such as centrifugal and Coriolis forces. While the influence of centrifugal forces on the vibration characteristics of bladed disks is commonly recognized and integrated in contemporary analysis, the effects of the Coriolis forces are usually considered to be negligible. In contrast, classical rotor-dynamic studies that account for shaft dynamics with rigid disks traditionally incorporate the "gyroscopic effects" which are a direct result of forces of the Coriolis type. The disregard of the effects of Coriolis forces in the context of bladed disk analysis is attributed to a belief that Coriolis forces usually alter natural frequencies, mode shapes, and other dynamic properties of bladed disks by an insignificant amount when the analysis is aimed at modes of vibration with the numbers of nodal diameters greater than one.

However, as will be shown in this paper, the effects of Coriolis forces can generate significant changes in the dynamic properties for bladed disks, and especially for mistuned assemblies. When analyzed in the absence of Coriolis forces, perfectly tuned cyclically symmetric bladed disks are characterized by double modes with identical natural frequencies for each number of nodal diameters. When Coriolis forces are taken into account, these pairs of double modes split into single modes with the natural frequencies of each corresponding to a forward or backward traveling wave mode for each nodal diameter number. Moreover, it has been found that the order of magnitude of the Coriolis-induced natural frequency splits of the tuned bladed disk can be the same as the splits caused by blade mistuning. This suggests that the effects of Coriolis forces may have important implications for predictions and interpretations of the forced response behavior of mistuned bladed disks.

In traditional mistuned bladed disk analysis, similarly to the analysis of tuned structures, the effects of Coriolis forces have previously been considered to be negligible. To the authors' best knowledge, there are no investigations available in the published literature on the effects of mutual influence of Coriolis forces and mistuning.

The main goals of the study reported here are: (i) to determine the mutual influence of the effects of Coriolis forces and blade mistuning on vibration characteristics of bladed disks; and (ii) to establish whether the Coriolis forces should be included as a missing link in the analyses of mistuned bladed disks. The impact of different mistuning degrees on forced response and amplification factors is investigated for several bladed disk designs incorporating varying strengths of Coriolis forces.

This paper is organized as follows. In the first section, an underlying physical mechanism of the Coriolis forces action on tuned bladed disk vibration properties is demonstrated. Subsequently, crucial results from an experimental validation study of the predictions including the Coriolis forces using a practical bladed disk are presented, which then leads to a definition of the problem to be resolved. In the third section, a lumped parameter mass–spring model, which permits both the Coriolis forces and blade mistuning to be simulated simultaneously, is introduced. Several designs of bladed disk are analyzed exhibiting weak-to-strong Coriolis forces effect, while the forced response predictions are obtained for different degrees of blade frequency mistuning. Some statistical results are presented in the fourth section, followed by a discussion of bladed disk designs that would be more affected by the Coriolis forces effects and, as a result, intensify the mutual interaction of Coriolis forces and blade mistuning on forced response levels. Finally, conclusions drawn from this study are given in the fifth section.

Contributed by the International Gas Turbine Institute of ASME for Publication in the JOURNAL OF TURBOMACHINERY. Manuscript received July 13, 2006; final manuscript received August 15, 2006. Review conducted by David Wisler. Paper presented at the ASME Turbo Expo 2006: Land, Sea and Air (GT2006), Barcelona, Spain, May 8–11, 2006. Paper No. GT2006-90315.

Effects of Coriolis Forces on Tuned Bladed Disks

Tuned Bladed Disk Vibration Properties. In traditional analyses of perfectly tuned cyclically periodic bladed disks, in which all blades are identical, the effects of Coriolis forces have usually been neglected. Such systems are characterized by pairs of "double" modes with identical natural frequencies and mode shapes orthogonal in spatial orientation.

Tuned bladed disk mode shapes can be expressed in polar coordinates as

$$\phi_{n,s}^{\cos}(r,\theta) = R_{n,s}(r)\cos(n\theta), \quad \phi_{n,s}^{\sin}(r,\theta) = R_{n,s}(r)\sin(n\theta) \tag{1}$$

where r and θ are polar coordinates and n and s are the numbers of nodal diameters and nodal circles, respectively. Mode shapes of the two modes with identical natural frequencies differ only in the angular orientation of the nodal lines, and any combination of the two individual mode shapes is also a possible mode shape, including ones which rotate around the structure in a traveling wave motion.

Coriolis Forces in Blade Vibration. Coriolis forces are associated with the components of blade and disk motion along axes which are perpendicular to the primary axis of rotation (or "spinning") of the disk on which they are carried, while the component of motion parallel to the rotation axis does not contribute to the Coriolis forces

$$\vec{F}_{\text{Coriolis}} = -m(2\vec{\omega} \times \vec{r}') \tag{2}$$

where Coriolis force, $\vec{F}_{\text{Coriolis}}$, normal to the rotating frame velocity, $\vec{r}'$, and to the rotation vector, $\vec{\omega}$, causes the blade particle velocity to change direction, but not the magnitude, and is thus a deflecting force.

Hence, in the investigation of the Coriolis forces' influence on vibration characteristics, we confine ourselves to study the in-plane radial and tangential blade vibrations only, as there is no coupling between out-of-plane and in-plane blade vibrations due to Coriolis forces. The effects of Coriolis forces arising from simultaneous rotation and in-plane tangential or in-plane radial vibration of the bladed disk are illustrated in Fig. 1 for the case of a three nodal diameter (3ND) mode shape.

Rotating Bladed Disk System With the Effects of Coriolis Forces. For rotating bladed disks, the general equation of motion for forced vibration in the time domain is known to be "nonself-adjoint" [5,6] and is presented as

$$[M]\{\ddot{q}(t)\} + [G(\Omega) + [D]]\{\dot{q}(t)\} + ([K] + [K_S(\Omega)] + [M(\Omega)])\{q(t)\} = \{f(t)\} \tag{3}$$

where, in a fixed frame of reference, $\{q\}$ is a response of the system; $\{f\}$ is the vector of applied external forces; Ω is rotation speed; $[M]$, $[K]$, and $[D]$ are mass, stiffness, and damping matrices, respectively; $[G(\Omega)]$ is a speed-dependent skew-symmetric matrix due to Coriolis forces; and $[K_S(\Omega)]$ is a speed-dependent stress stiffening matrix due to centrifugal forces; and $[M(\Omega)]$ is a speed-dependent spin softening matrix.

Assuming, for the sake of simplicity, that there is no structural damping and that the mass and stiffness matrices are speed independent, Eq. (3) becomes

$$[M]\{\ddot{q}(t)\} + [G(\Omega)]\{\dot{q}(t)\} + [K]\{q(t)\} = \{f(t)\} \tag{4}$$

In contrast to "self-adjoint" nonrotating structures, whose system matrices are symmetric [6], the inclusion of Coriolis terms, which increase in magnitude with rotation speed, gives rise to asymmetric equations of motion and asymmetric system matrices, so that

$$[M] = [M]^T, \quad [K] = [K]^T, \quad [G] = -[G]^T \tag{5}$$

We shall seek the free response solution of Eq. (4) in the form [7]

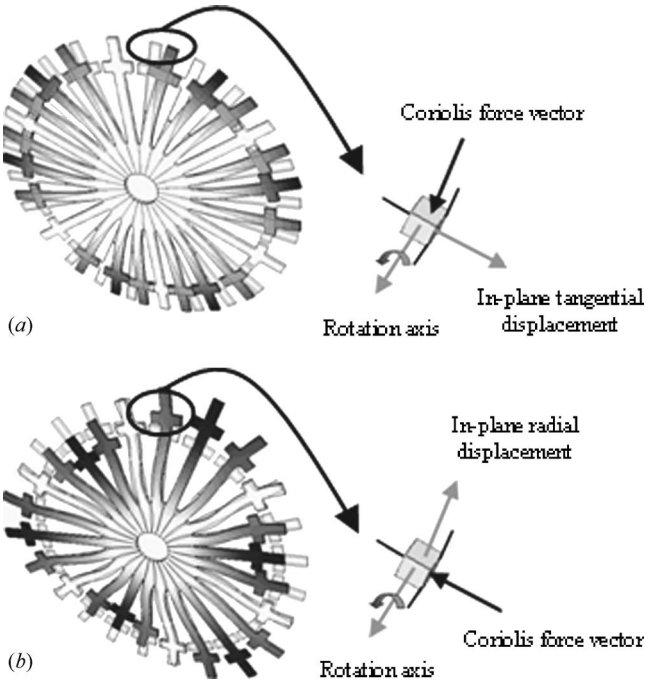

Fig. 1 The action of Coriolis forces: 3ND mode shapes of a bladed disk: (*a*) blade tangential vibration; and (*b*) blade radial vibration

$$q(t) = \psi e^{\lambda t}, \quad \text{where } q(t), \psi, \lambda \in \mathbb{R}^N \tag{6}$$

Substituting Eq. (6) into Eq. (4), we obtain an expression for the dynamic stiffness matrix

$$\chi(\lambda)\psi = 0, \quad \text{where } \chi(\lambda) = (\lambda^2[M] + \lambda\Omega[G] + [K]) \tag{7}$$

A set of N homogenous algebraic equations possesses a nontrivial solution if, and only if, the determinant of the coefficients vanishes

$$\det \chi(\lambda) = 0 \tag{8}$$

The solution to Eq. (8) constitutes the eigenvalues, λ_r, and the associated two different kinds of eigenvectors due to asymmetry of the velocity- and displacement-dependent matrices: "right" and "left" eigenvectors, both of which are complex [8]. A right-hand eigenvector, ψ_r, satisfies $\chi(\lambda_r)\psi_r = 0$, while the left-hand eigenvector, ψ_l, complies with $\psi_l^T \chi(\lambda_r) = 0$. While the former vector is generally known as the "mode shape," the latter is the second set of eigenvectors that contains the information regarding the ability of excitation forces to produce a vibration corresponding to a specific mode when applied to the structure [8].

It is known that the eigenvalues of Eq. (8) consist of N complex conjugate pairs and, correspondingly, the eigenvectors also occur in complex conjugate pairs [7]. Thus, it is possible to express the eigenvector as $\psi_r = y + iz$, where y is the real part and z is the imaginary part of the eigenvector, ψ_r. Hence, by premultiplying Eq. (7) by $\bar{\psi}_r^T$, we obtain

$$\{\bar{\psi}\}^T(\lambda^2[M] + \lambda\Omega[G] + [K])\{\psi\} = 0$$

$$(y - iz)^T(\lambda^2[M] + \lambda\Omega[G] + [K])(y + iz) = 0 \tag{9}$$

It can be shown that Eq. (9) leads to

$$\lambda^2 m + 2i\lambda\Omega g + k = 0 \tag{10}$$

where

$$m = y^T[M]y + z^T[M]z, \quad k = y^T[K]y + z^T[K]z, \quad g = z^T[G]y$$

Solving Eq. (10) yields the eigenvalues as complex conjugate pairs, given $m>0$, $k>0$, $g \in \mathbb{R}^N$

$$\lambda = \frac{-i\Omega g \pm \sqrt{\Omega^2 g^2 + mk}}{m} \tag{11}$$

Finally, after substituting the standard $\omega_n^2 = k/m$ and $\mu = g/m$, the expression for λ becomes

$$\lambda = -i\Omega\mu \pm \sqrt{(\Omega\mu)^2 + \omega_n^2} \tag{12}$$

which demonstrates the important result of the split in double natural frequencies of the tuned bladed disk system due to effects of Coriolis forces.

Experimentally Validated Bladed Disk Predictions With the Effects of Coriolis Forces. In the previous section it has been established theoretically that the inclusion of Coriolis forces into the analysis of tuned bladed disks introduces qualitative changes in their free vibration characteristics and, consequently, forced response predictions, predominantly by *Coriolis splitting* of the natural frequencies into pairs of distinct modes. Furthermore, in this section the influence of Coriolis forces on tuned bladed disks is demonstrated by presenting some key results obtained from a study of the experimental validation of the predictions made for natural frequency splits arising from the effects of Coriolis forces using a carefully designed testpiece. Theoretical predictions have been acquired using the finite element software package SAMCEF which permits the modal analysis of rotating bladed disks with the Coriolis and centrifugal forces included. The eigenvalue solver implemented in this software is based on a pseudomodal method that uses the Lanczos algorithm [9].

The testpiece has been designed so as to display clearly the effects of Coriolis forces on first bending family of the bladed disk modes, and thereby, to facilitate an unambiguous experimental validation of predictions made including the Coriolis forces. These forces are generated when there is bladed disk rotation and significant radial and tangential components in blade vibratory displacements. Coriolis forces produce coupling between these displacements, and the higher the coupling, the more prominent the effect of Coriolis forces is on the natural frequencies. A strong coupling can be achieved in several ways. One way to increase the coupling is by introducing "swept" blades, i.e., blades which lean in the axial direction. The higher the angle by which the blades lean or, as will be referred in this paper, the higher the "sweep" angle, the greater the influence of Coriolis forces, as there is a strong in-plane vibration coupling. In light of this, a so-called "swept" testpiece has been selected with a sweep angle of 15 deg, which produces large enough radial component of displacements to allow observation of the Coriolis effects while still accommodating geometric constraints of the existing test rig. Figure 2 depicts photographs of a "swept" testpiece with 24 blades and its finite element model, comprising about 783,216 degrees of freedom (DOF).

The natural frequencies have been measured and calculated using the SAMCEF code [9] for the first 2ND and 3ND mode pair and are shown in Fig. 3. It is important to note that while a 3ND is a perfectly tuned mode pair exhibiting double natural frequencies under stationary conditions, the 2ND mode pair is slightly mistuned at 0 rpm by 0.5%. Under rotating conditions, the natural frequencies in each pair of modes have different values, and the two mode shapes are believed to be a pair of forward and backward traveling waves with the same number of nodal diameters as viewed in a rotating frame of reference. One can observe that theoretical and experimental natural frequencies are in good agreement.

Measured and predicted natural frequency splits for the cases of the first 2ND and 3ND mode pairs are further illustrated in Fig. 4 and Table 1. The maximum measured natural frequency split for the 2ND mode pair was found to be 1.65% at 700 rpm, whereas the corresponding maximum split for the 3ND mode pair was 1.78% at 510 rpm. A relatively close agreement was achieved between theoretical predictions including the effects of Coriolis forces and measured natural frequency splits. The relatively small discrepancies observed between the two sets of results could be attributed to an inevitable amount of inherent mistuning of a testpiece and slight differences in disk center fixation conditions. However, most importantly, the phenomenon of splitting of double mode natural frequencies of a nearly tuned bladed disk mode due to effects of Coriolis forces has clearly been experimentally validated.

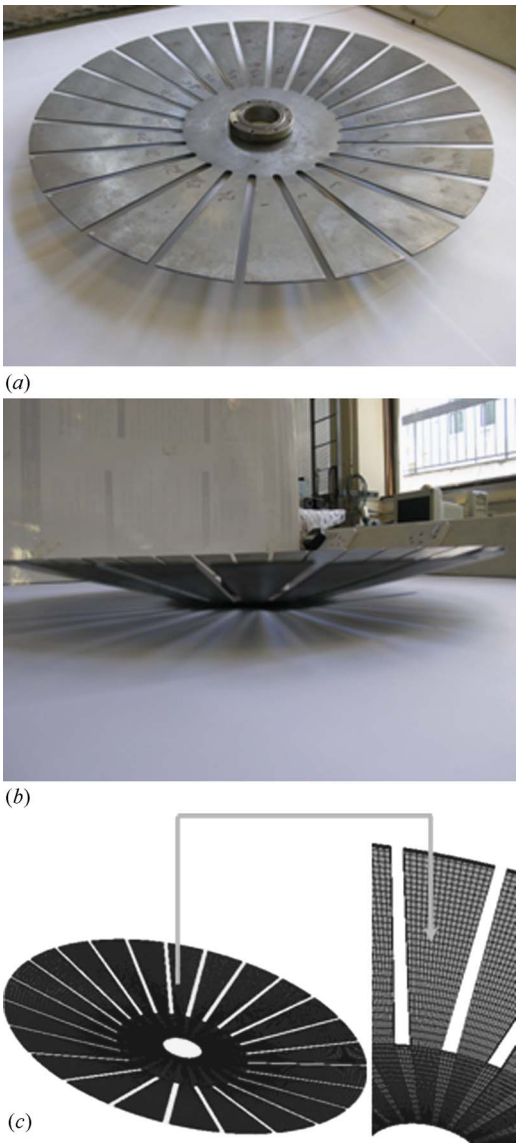

Fig. 2 Photographs of a testpiece (*a*)-(*b*); and its finite element model (*c*)

Problem Definition

It is well known that blade mistuning, which is inevitable in all practical bladed disks, results in a scatter of natural frequencies and mode shapes. In a previous section, the influence of Coriolis forces was shown to induce a split in natural frequencies that is of the same order as the split present in a typically mistuned system. This suggests that Coriolis forces may have important implications for predictions and interpretations of the forced response

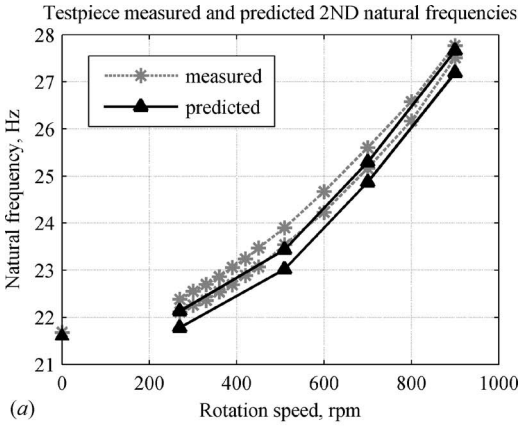

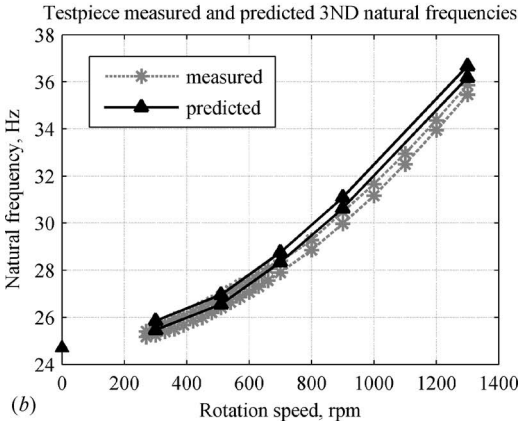

Fig. 3 Measured and predicted natural frequencies for first 2ND mode pair (*a*); and first 3ND mode pair (*b*)

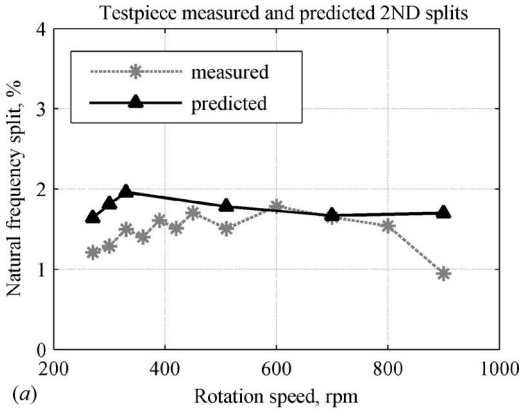

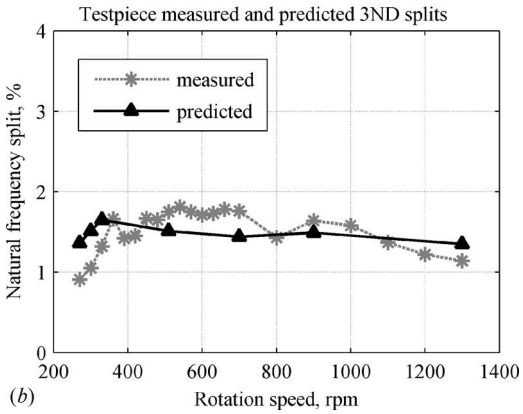

Fig. 4 Measured and predicted natural frequency splits for first 2ND mode pair (*a*); and first 3ND mode pair (*b*)

behavior of mistuned bladed disks. The problem of estimating the mutual interaction of effects of Coriolis forces and blade mistuning on vibration characteristics of bladed disks is addressed in the subsequent sections of this paper.

Lumped Parameter Mass Model Analysis

Model Description. In view of the lack of finite element codes capable of forced response analysis of rotating bladed disks with Coriolis forces and blade mistuning included, a simple lumped parameter mass model was chosen to study the mutual influence of Coriolis forces and blade mistuning. It is believed that a small system will serve as a useful tool to explore the underlying physics of the complex combined effect of the two phenomena. Since there is no coupling between out-of-plane and in-plane blade vibrations due to Coriolis forces, the model includes in-plane radial and tangential vibration only. Thus, a suitable lumped parameter model of bladed disk dynamics must comprise four DOF per sector with two DOF per mass. The bladed disk chosen for this study contains 24 sectors. The model, depicted in Fig. 5, contains two masses representing the blade and the disk segments and a series of springs in the x and y directions representing radial and tangential vibrations. It is assumed that the springs in the radial direction are much greater than those in the tangential direction. The values for the lumped parameter mass model are listed in Table 2. It should be noted that these values are not intended to represent any particular bladed disk, but are chosen with the aim of demonstrating the appropriate physics. Therefore, no units are connected with these values, simply the assurance that they are consistent.

The most important feature of this model is related to the added disk-to-disk cross-coupling stiffness terms, which simulate the strength of in-plane tangential and radial coupling.

Let the stiffness matrix, which connects the nth disk mass to the $(n-1)$th mass be of the form

$$k_{11} = \begin{bmatrix} kdd_x & kdd_{xy} \\ kdd_{yx} & kdd_y \end{bmatrix} \tag{13}$$

Table 1 Measured and predicted natural frequency splits for first 2ND (a) and 3ND (b) mode pair

	2ND		% diff.
(a) Speed (rpm)	Measured	Predicted	Measured versus predicted
300	1.29	1.81	+28.73
330	1.50	1.96	+23.47
510	1.51	1.78	+15.17
700	1.65	1.67	+1.20
900	0.95	1.70	+44.12
1300	—	—	—
	3ND		% diff.
(b) Speed (rpm)	Measured	Predicted	Measured versus predicted
300	1.05	1.51	+30.46
330	1.32	1.65	+20.00
510	1.78	1.51	−15.17
700	1.76	1.44	−18.18
900	1.64	1.49	−9.15
1300	1.14	1.35	+15.56

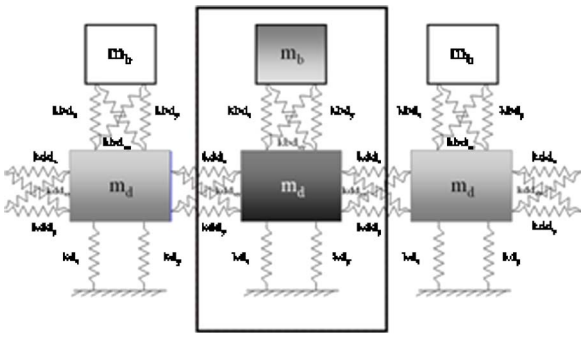

Fig. 5 Lumped parameter mass model

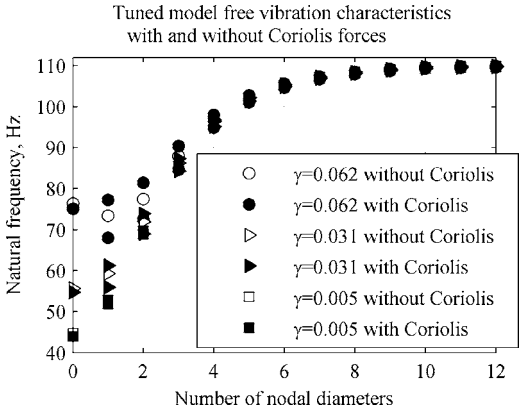

Fig. 6 Tuned model free vibration properties dependence on coupling parameter γ

where k_{11} is a symmetric positive matrix, $kdd_{yx}=kdd_{xy}$.
$_{(2\times2)}$

Hence, the total disk-to-disk coupling stiffness matrix can be expressed as

$$\begin{Bmatrix} F_1 \\ F_2 \end{Bmatrix} = \begin{bmatrix} k_{11} & k_{12} \\ k_{21} & k_{22} \end{bmatrix} \begin{Bmatrix} q_1 \\ q_2 \end{Bmatrix} = \begin{bmatrix} k_{11} & k_{11}R^T \\ Rk_{11} & Rk_{11}R^T \end{bmatrix} \begin{Bmatrix} q_1 \\ q_2 \end{Bmatrix} \quad (14)$$

where

$$R = -\begin{bmatrix} \cos\gamma & -\sin\gamma \\ \sin\gamma & \cos\gamma \end{bmatrix} \quad (15)$$

$$q_{1,2} = \begin{Bmatrix} x \\ y \end{Bmatrix}_{1,2} \quad \text{and} \quad F_{1,2} = \begin{Bmatrix} F_x \\ F_y \end{Bmatrix}_{1,2} \quad (16)$$

Blade-to-disk cross-coupling stiffness terms are expressed in a similar way.

The choice of the form of stiffness matrix in Eq. (14) is not unique and is just one of the ways of representing the degree of coupling. A parameter of radial–tangential coupling, which will be further referred to as "coupling parameter," or γ, is used as a control parameter to regulate the Coriolis forces' strength: the higher the value of γ, the stronger the effect of Coriolis forces. For the case when $\gamma=0$, there is no radial–tangential coupling and, as a result, no Coriolis forces effect. This is demonstrated in Figs. 6 and 7 and Table 3.

The choice of coupling parameter value was determined by the desired shape of the natural frequency versus number of nodal diameters plot. As the coupling parameter is increased from 0.005 to 0.062, the split of the otherwise identical double natural frequencies due to Coriolis forces only in the 2ND mode pair has increased from 1% to 11%. While a similar increase in the split of natural frequencies is observed for 5ND and 10ND mode pairs, the actual split magnitudes are much smaller than that corresponding to the 2ND mode pair. The reason for such a result is due to the fact that the amount of blade-to-blade coupling decreases with the number of nodal diameters, which in turns reduces the effects of Coriolis forces.

Forced Response Considerations. In this section, the main forced response characteristics of the combined system, including the effects of Coriolis forces and mistuning, are presented. The coupling parameter γ was initially set to 0.005, so that the influence of Coriolis forces only on tuned natural frequencies was relatively small (2ND split being approximately 1%). A random mistuning pattern, denoted in Fig. 8 as "ref. mist. pat.," was chosen as a reference pattern and was generated within a frequency mistuning range of ±5%, which is typical for bladed disks. Subsequently, several other frequency mistuning patterns were created in order to study the effect of increasing mistuning ranges on the forced response of a system with Coriolis forces. These patterns were based on a reference pattern, but spanned different mistuning ranges. The secondary patterns were obtained by multiplying in-

Table 2 Lumped parameter mass model properties

Parameter	Value
m_d	8
m_b	3
kdd_x	5.8×10^6
kbd_x	15.4×10^5
kd_x	0.9×10^6
kdd_y	$kdd_x\times100$
kbd_y	$kbd_x\times100$
kd_y	$kd_x\times100$
kdd_{xy}	5.0×10^3
kbd_{xy}	5.0×10^4

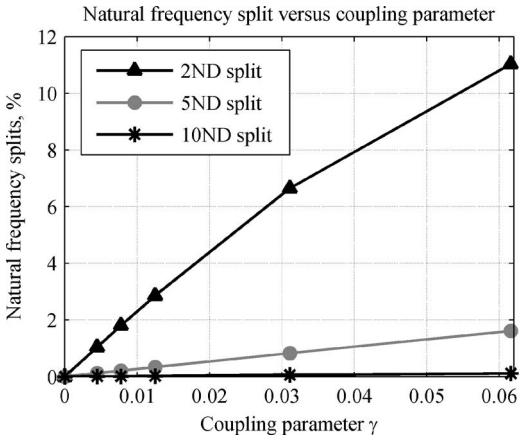

Fig. 7 Tuned model natural frequency split as a function of coupling parameter γ

Table 3 Tuned model dependence on coupling parameter

Coupling parameter γ	2ND split (%)	5ND split (%)	10ND split (%)
0.000	0.00	0.00	0.00
0.005	1.04	0.12	0.01
0.008	1.81	0.21	0.01
0.013	2.86	0.34	0.02
0.031	6.65	0.83	0.06
0.062	11.03	1.61	0.11

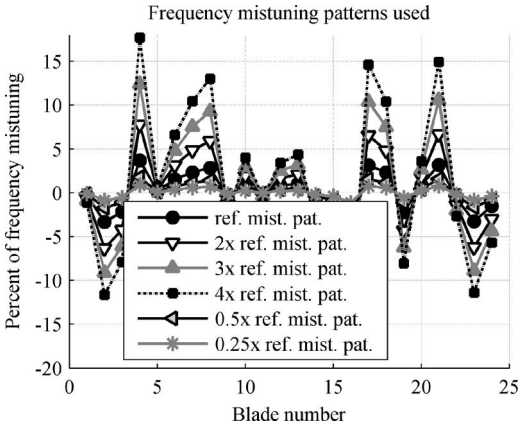

Fig. 8 Frequency mistuning patterns used

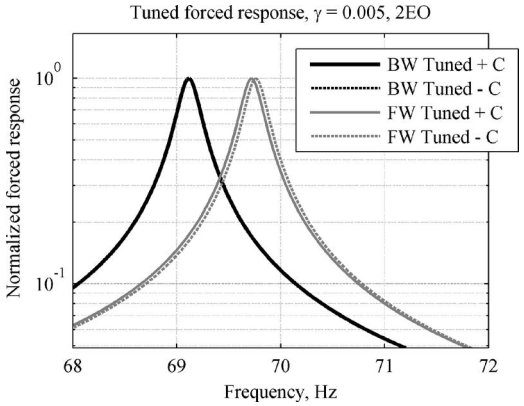

Fig. 9 Tuned forced responses, coupling parameter γ=0.005, 2EO

dividual blade mistuning values in the reference pattern by an identical multiplier for all blades. The following values of these multipliers were considered: 0.25, 0.5, 2.0, 3.0, and 4.0, which cover wide and practically attainable mistuning ranges. A relatively large blade mistuning of 17% is represented for the mistuning pattern resulting from the multiplier 4.0, and while not very common, it is not implausible in practice for bladed fan disks, where large differences may exist from blade to blade (see e.g., Ref. [10]).

The damping loss factor was set to 0.003. A simple engine order forcing field was applied of the form

$$F(\theta,t) = F_0 e^{\mathrm{iEO}(\Omega t \pm \theta)} \tag{17}$$

where F_0 is the force amplitude; EO is the engine order; Ω is the rotating speed; t is time, and θ is the circumferential position around the disk. A forward (response backward) traveling wave was obtained by applying a positive imaginary term in Eq. (17).

Forced response levels were calculated from the following equation

$$\{Q\} = ([K] - \omega^2([M] + [\Delta M]) + i[D] + i\omega[G])^{-1}\{F\} \tag{18}$$

where $\{Q\}$ is the forced response; $[K]$ is the system stiffness matrix; $[M]+[\Delta M]$ represents mass-mistuned system; $[D]=\eta[K]$ is the structural (hysteretic) damping matrix; η is the damping loss factor; $[G]$ is the Coriolis matrix; and $\{F\}$ is the applied force.

Tuned bladed disk backward (EO=+2) and forward (EO=−2) forced responses,[1] with and without Coriolis forces, are shown in Fig. 9. The so-called "forward" traveling wave response does not have immediate practical interest, but is physically possible under certain circumstances. As expected, in the case of a tuned system without Coriolis forces, the responses to the backward and forward waves are identical, whereas the presence of Coriolis forces generates the forced responses at distinct frequencies.

Normalized mistuned forced responses and their envelopes, with and without Coriolis forces taken into account, are illustrated in Fig. 10, with response normalization being made with respect to the maximum tuned response levels in the frequency range of interest. It can be observed from Fig. 10 that the backward and forward mistuned traveling wave responses obtained for 2EO with Coriolis forces are "nearly" mirror images of each other. A lower amplitude peak in each mistuned frequency response function (FRF) with Coriolis forces can be considered as a small contribution of a traveling wave component to the main stationary component. Mistuned responses without Coriolis forces are also not identical due to the blade mistuning which has been introduced and to the coupling between tangential and radial vibrations (see Eq. (14)). If the model had no tangential–radial coupling, then mistuned forward and backward forced responses would have been identical to each other. Moreover, envelopes of the maximum forced responses are clearly dissimilar for the cases of calculations with and without Coriolis forces included.

The results in Fig. 11 demonstrate that the individual (specifically, blade No. 10, which is representative of the others) frequency response functions are different when the Coriolis forces are present compared to their non-Coriolis counterparts, which could provide an explanation for a mismatch observed sometimes between theoretical predictions and experimental data for bladed

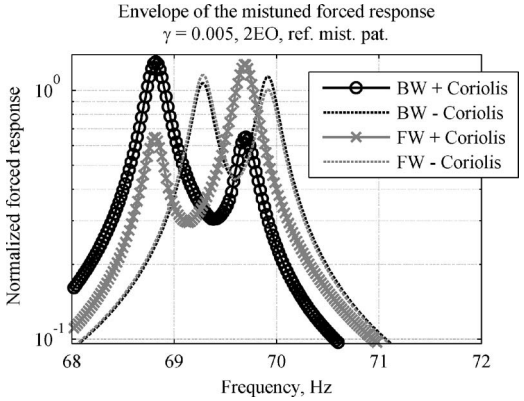

Fig. 10 Envelope of the mistuned forced responses, coupling parameter γ=0.005, 2EO

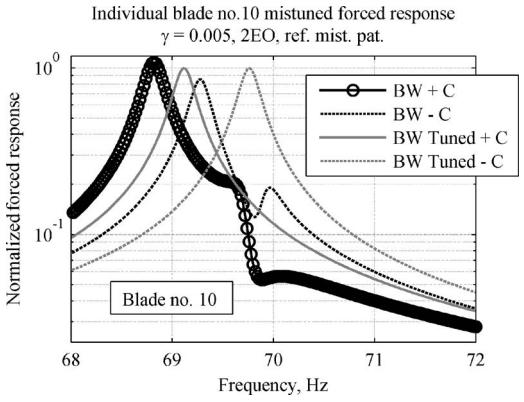

Fig. 11 Individual blade No. 10 mistuned forced responses, coupling parameter γ=0.005, 2EO

[1]"Forward" and "backward" forced responses are defined with respect to rotating frame of reference.

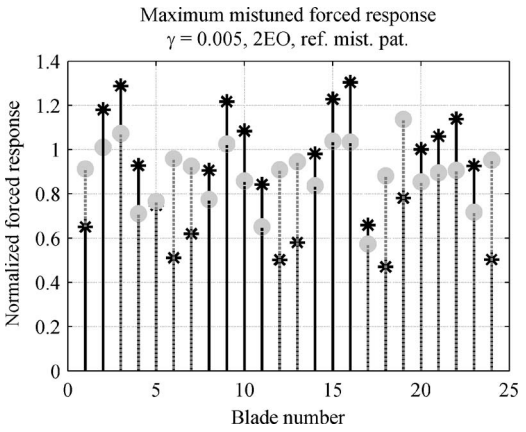

Fig. 12 Maximum blade amplitudes with (star) and without (circle) Coriolis forces, coupling parameter γ=0.005, 2EO

disks.

The amplitude distribution as a function of blade number, depicted in Fig. 12, shows that the maximum blade amplitude can be higher by 14% when the Coriolis forces are included in the analysis compared to that for a mistuned-only system.

Influence of Mistuning Ranges on Forced Response With and Without Coriolis Force

Weak Influence of Coriolis Forces, Coupling Parameter γ =0.005. In the following sections, for each coupling parameter value manifesting the strength of Coriolis forces, the backward forced response will be shown for different frequency mistuning ranges, based on a reference mistuning pattern, as shown in Fig. 8.

Envelopes of the mistuned forced responses for different blade frequency mistuning degrees under 2EO and 5EO are given in Fig. 13. They show shapes of the FRFs under different EOs and their gradual peak separation from a nearly tuned to a heavily mistuned system. In the case of 5EO, the forced response functions with and without Coriolis forces are very similar and, thus, overlapping in Fig. 13(*b*).

Maximum forced responses for coupling parameter γ=0.005 with Coriolis forces included are compared with their non-Coriolis counterparts for different mistuning degrees and EOs in Fig. 14.

It is seen that in the case of 2EO, for relatively small frequency mistuning, the forced response without Coriolis forces is higher, whereas for most of other mistuning degrees, the forced responses including Coriolis forces are above those for mistuned-only system by approximately 15%. For 5EO and 10EO, there is almost no difference in maximum forced responses.

Strong Influence of Coriolis Forces, Coupling Parameter γ =0.062. Figure 15 demonstrates a rather different envelope of the mistuned forced response for different blade frequency mistuning degrees for 2EO and similar features for 5EO, obtained for a system with coupling parameter γ=0.062, simulating a strong influence of Coriolis forces.

The maximum forced responses obtained for strong Coriolis forces influencing the case are presented in Fig. 16. The response with Coriolis forces included for 2EO is much higher than that corresponding to the mistuned-only system, reaching levels which are 75% greater at mistuning equal to three times the original mistuning pattern. The responses with and without Coriolis forces are much more similar for 5EO and 10EO.

Statistical Characterization of Forced Response. Figures 17–20 represent selected statistical results for forced responses obtained from Monte Carlo simulations of 500 randomly generated mistuning patterns, with and without the effects of Coriolis forces. Blade

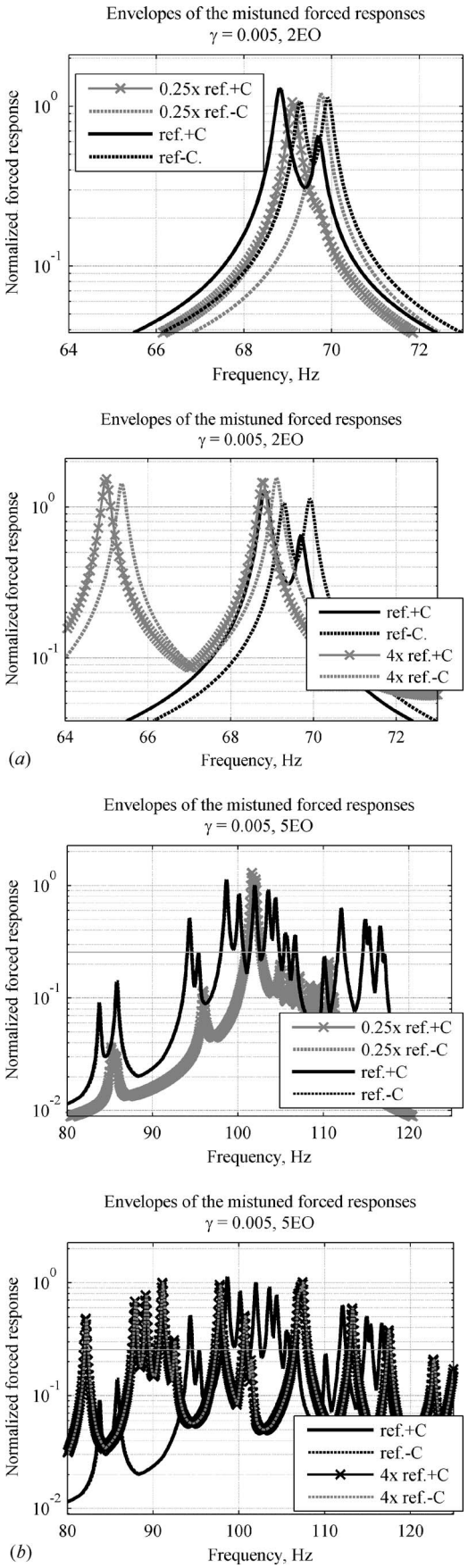

Fig. 13 Envelopes of mistuned forced responses for different blade frequency mistuning ranges, coupling parameter γ =0.005; (*a*) 2EO; (*b*) 5EO

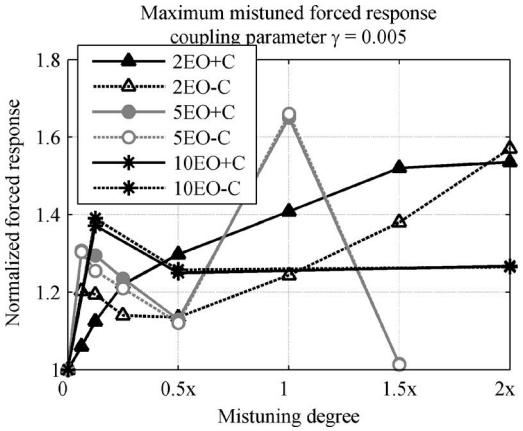

Fig. 14 Maximum mistuned forced responses with and without Coriolis forces, coupling parameter $\gamma = 0.005$

frequency mistuning was assumed to lie in the typical range for bladed disks of ±5% of the nominal first blade-alone frequency. The maximum forced responses calculated for each blade and for all mistuning patterns generated are plotted in Figs. 17 and 18 for a case of 2EO excitation. One can see significant differences in blade amplitudes determined with and without Coriolis forces included. As the coupling parameter γ increases from 0.005 to 0.062, the effects of the Coriolis forces on blade amplitudes rise. Hence, for the same degree of mistuning, the maximum forced response with Coriolis forces included obtained in Fig. 19 over all 500 mistuning patterns is higher by approximately 40% than that corresponding to the mistuned-only system. For 5EO and 10EO, the maximum forced response levels with and without Coriolis forces calculated over 500 mistuning patterns are very similar.

Histograms shown in Fig. 20 demonstrate the statistical distributions of maximum mistuned forced responses with and without Coriolis forces. In the case of 2EO, the statistical distributions are significantly different for a strong coupling case with γ=0.062. For 5EO, the difference between the histograms of maximum forced responses is minimal for both weak and strong coupling cases.

Discussion. In the previous section, it has been demonstrated that for lower nodal diameter modes the maximum forced response level of the combined Coriolis-mistuned system depends on the amount of coupling between tangential and radial component of displacements, represented in a simple lumped parameter mass–spring model by the coupling parameter. The stronger the coupling, the more pronounced the effects of Coriolis forces are, which in turn produce higher maximum forced response levels compared with their non-Coriolis counterparts. In practice, the above-mentioned coupling could be characterized by the amount of radial flexibility inherently present in a bladed disk. For example, a nonstaggered flat bladed disk does not include a prominent radial component, and thus, its vibration properties would not be affected notably by Coriolis forces. Conversely, contemporary, increasingly complex three-dimensional designs of bladed disks incorporate a more significant radial flexibility, for which the inclusion of Coriolis forces into mistuned analysis may be important. Further work will concentrate on assessing the mutual influence of Coriolis forces and blade mistuning on industrial bladed disk geometries.

Conclusions

For the first time, the experimental validation of the natural frequency splits due to Coriolis forces has been made, and the mutual influence of the effects of Coriolis forces and blade mistuning on forced response characteristics of bladed disks has been studied. A simple, yet representative, lumped parameter model has

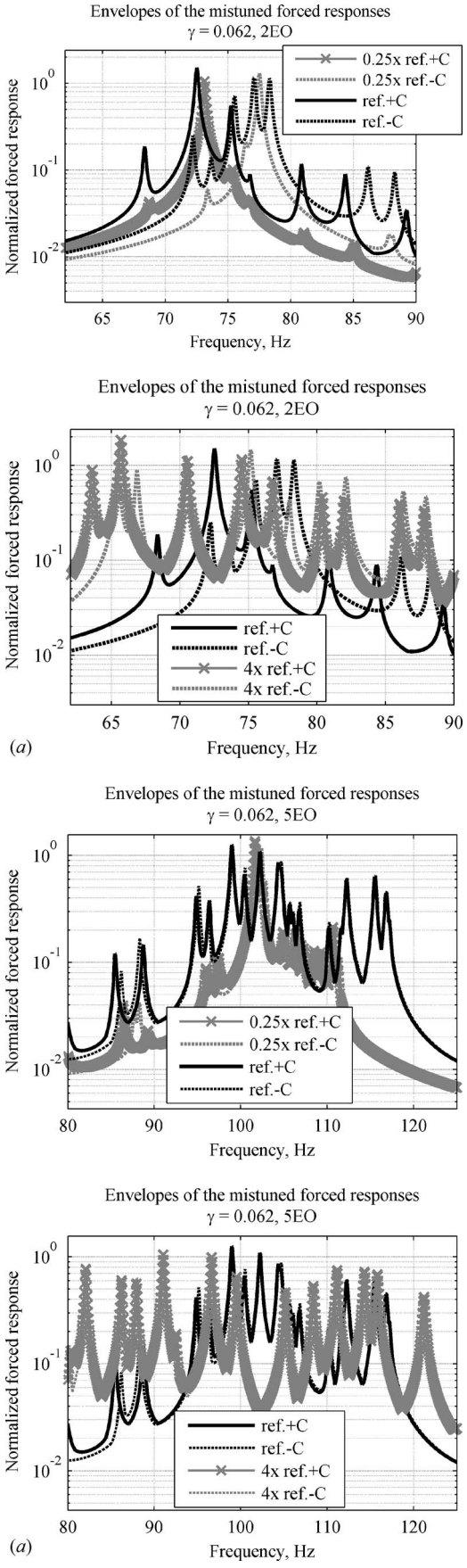

Fig. 15 Envelopes of mistuned forced responses for different blade frequency mistuning ranges, coupling parameter γ =0.062; (*a*) 2EO; (*b*) 5EO

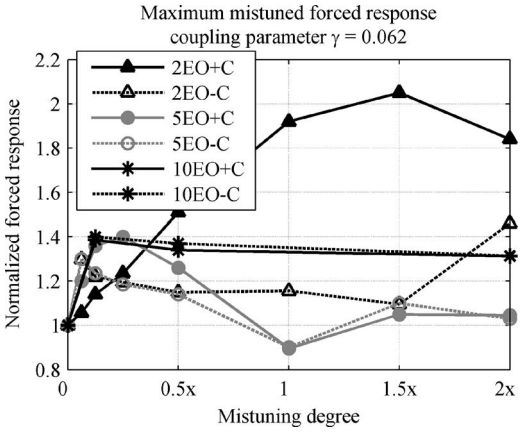

Fig. 16 Maximum mistuned forced responses with and without Coriolis forces, coupling parameter γ=0.062

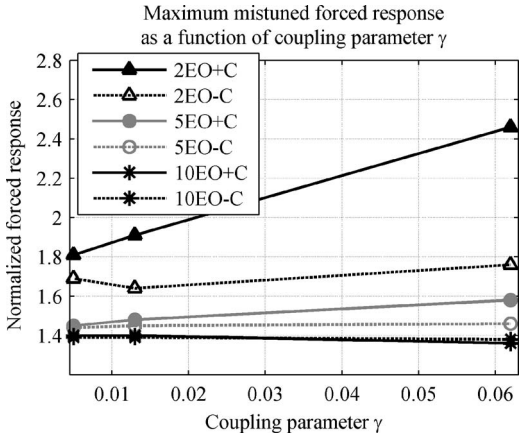

Fig. 19 Maximum mistuned forced response over all 500 mistuning patterns

been developed to demonstrate the effects of Coriolis forces for varying strengths of in-plane blade-to-blade coupling, which was found to be the most significant feature that affects the maximum forced response amplification factors of the combined Coriolis-mistuned system.

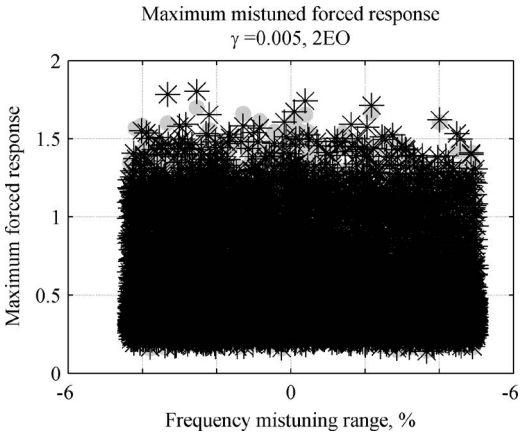

Fig. 17 Statistical 2EO results for the maximum mistuned forced response for each blade for γ=0.005 with (star) and without (circle) Coriolis forces

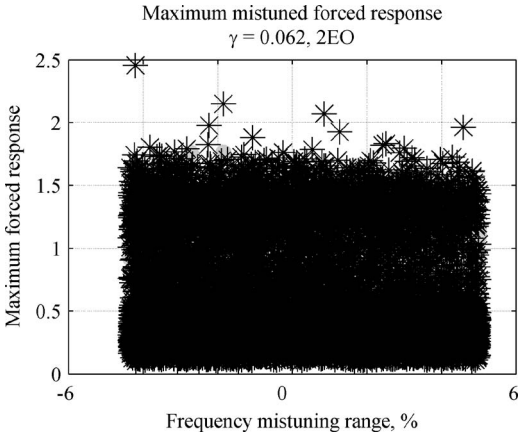

Fig. 18 Statistical 2EO results for the maximum mistuned forced response for each blade for γ=0.062 with (star) and without (circle) Coriolis forces

The results obtained in this study indicate that in some of the cases considered the additional effects of Coriolis force could be considered as "minor" in comparison with the typical blade mistuning influence on maximum amplification factors attainable in bladed disks. However, there are particular designs of bladed disks with a prominent radial flexibility where the Coriolis force effects could not be neglected and require careful examination. Such systems were found to have maximum forced response levels with the Coriolis effects included much higher (approximately 40% in the case of frequency mistuning within a ±5% range) and their statistical distributions significantly different from those corresponding to a mistuned-only system. Moreover, the variation

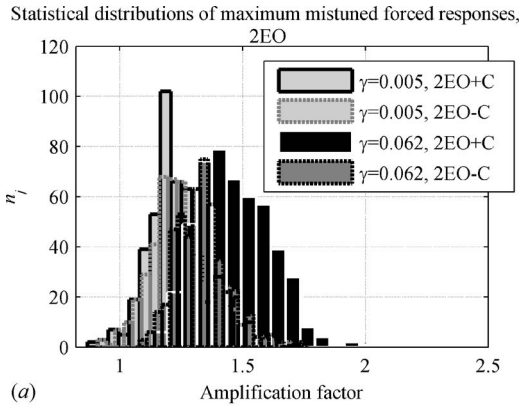

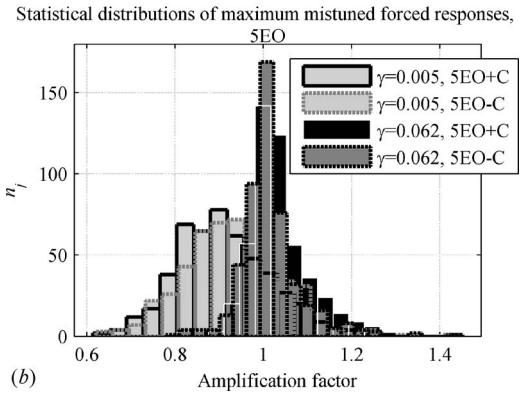

Fig. 20 Histograms of maximum mistuned forced responses with and without Coriolis forces for: γ=0.005 and γ=0.062 for: (*a*) 2EO; and (*b*) 5EO

between the maximum forced responses with and without Coriolis forces was seen to depend on a specific degree of mistuning. As a result of this study, the individual blade frequency response functions were found to be different when the Coriolis forces are present compared to their non-Coriolis counterparts. This could provide an explanation for a recurrent mismatch between theoretical predictions and experimental measurements for bladed disks.

Acknowledgment

The authors gratefully acknowledge contributions in the experimental validation study from Dario Di Maio.

References

[1] Petrov, E. P., Sanliturk, K. Y., and Ewins, D. J., 2002, "A New Method for Dynamic Analysis of Mistuned Bladed Disks Based on the Exact Relationship Between Tuned and Mistuned Systems," ASME J. Eng. Gas Turbines Power, **124**, pp. 586–597.

[2] Yang, M.-T., and Griffin, J. H., 2001, "A Reduced Order Model of Mistuning Using a Subset of Nominal System Modes," ASME J. Eng. Gas Turbines Power, **123**, pp. 893–900.

[3] Feiner, D. M., and Griffin, J. H., 2002, "A Fundamental Model of Mistuning for a Single Family of Modes," ASME J. Turbomach., **124**, pp. 597–605.

[4] Castanier, M. P., Ottarsson, G., and Pierre, C., 1997, "Reduced Order Modelling Technique for Mistuned Bladed Disks," ASME J. Vibr. Acoust., **119**, pp. 439–447.

[5] Bucher, I., and Ewins, D. J., 2001, "Modal Analysis and Testing of Rotating Structures," Philos. Trans. R. Soc. London, Ser. A, **359**, pp. 61–96.

[6] Meirovitch, L., and Ryland, G., 1979, "Response of Slightly Damped Gyroscopic Systems," J. Sound Vib., **67**(1), pp. 1–19.

[7] Meirovitch, L., 1980, *Computational Methods in Structural Dynamics*, Sijthoff & Noordhoff, International Publishers, Alphen aan den Rijn, The Netherlands.

[8] Ewins, D. J., 2000, *Modal Testing: Theory, Practice and Application*, Research Studies Press, Baldock, Herfordshire, UK.

[9] *SAMCEF V11.0-06 Manual*, 2005, SAMTECH S.A.

[10] Petrov, E. P., Sanliturk, K. Y., Ewins, D. J., and Elliott, R., 2000, "Quantitative Prediction of the Effects of Mistuning Arrangement on Resonant Response of a Practical Turbine Bladed Disc," *Proceedings of the 5th National Turbine Engine High Cycle Fatigue (HCF) Conference*, Chandler, AZ.

Assessing Convergence in Predictions of Periodic-Unsteady Flowfields

J. P. Clark
Turbine Branch,
Turbine Engine Division,
Propulsion Directorate,
Air Force Research Laboratory,
Building 18, Room 136D,
1950 5th Street,
WPAFB, OH 45433
e-mail: john.clark@pr.wpafb.af.mil

E. A. Grover
Turbine Aerodynamics,
United Technologies Pratt & Whitney,
400 Main Street,
M/S 169-29,
East Hartford, CT 06108
e-mail: eric.grover@pw.utc.com

Predictions of time-resolved flowfields are now commonplace within the gas-turbine industry, and the results of such simulations are often used to make design decisions during the development of new products. Hence it is necessary for design engineers to have a robust method to determine the level of convergence in design predictions. Here we report on a method developed to determine the level of convergence in a predicted flowfield that is characterized by periodic unsteadiness. The method relies on fundamental concepts from digital signal processing including the discrete Fourier transform, cross correlation, and Parseval's theorem. Often in predictions of vane–blade interaction in turbomachines, the period of the unsteady fluctuations is expected. In this method, the development of time-mean quantities, Fourier components (both magnitude and phase), cross correlations, and integrated signal power are tracked at locations of interest from one period to the next as the solution progresses. Each of these separate quantities yields some relative measure of convergence that is subsequently processed to form a fuzzy set. Thus the overall level of convergence in the solution is given by the intersection of these sets. Examples of the application of this technique to several predictions of unsteady flows from two separate solvers are given. These include a prediction of hot-streak migration as well as more typical cases. It is shown that the method yields a robust determination of convergence. Also, the results of the technique can guide further analysis and/or post-processing of the flowfield. Finally, the method is useful for the detection of inherent unsteadiness in the flowfield, and as such it can be used to prevent design escapes. [DOI: 10.1115/1.2720504]

Introduction

As the state of the art for computational fluid dynamics (CFD) calculations in the gas turbine industry has progressed from single-row potential flow calculations to time-resolved, multistage unsteady Navier–Stokes simulations, the fidelity of flowfield predictions has increased accordingly. The increased predictive capability of the codes have allowed for better turbomachinery designs and improved understanding of the physical mechanisms that are prevalent in turbomachines, especially when used to complement experimental findings. This is the crux of a pair of recent review papers by Adamczyk [1] and Dunn [2] concerning the state of the art in aerodynamic and durability predictions in the gas turbine industry, respectively.

Turbomachinery designers often employ both steady-state and time-resolved predictive tools during the development of new engines. The major difference between the methods is the numerical treatment of the inter-row boundary. For steady-state turbomachinery simulations, common methodologies include the average-passage formulation of Adamczyk [1] and the mixing plane as employed in the Ni code [3–6]. In the latter, the flow from an upstream blade row is circumferentially averaged and then the flow properties are passed into the downstream row as a radial profile. For many situations the difference between the steady-state flowfield and the time average of an unsteady solution is minor. However, it is the time-resolved information that is often of critical importance to the designer, as in the case of predicting resonant stresses in the machine.

Predicting the time-resolved behavior of the engine requires the transport of discrete flow structures from one airfoil row into an adjacent airfoil row. The steady-state practice of averaging flows between airfoil rows of different rotation speeds acts to smear out the discrete structure, thus eliminating its specific influence on the system. An unsteady CFD simulation passes information between airfoil rows as a complete two-dimensional (2D) profile, thus maintaining any discrete flow structures present in the flowfield and allowing their influence on downstream airfoil rows.

Examples of such discrete flow structures are airfoil wakes, potential fields, and shocks that can travel downstream and/or upstream through the engine [7]. Turbine airfoil surfaces constantly encounter fluctuating flowfields induced by such flow structures. These can manifest as pressure fluctuations that impart time-varying forces which result in the generation of cyclic rotor vibratory stresses that have the potential to reduce the life of the airfoil. Design methodologies are constantly being improved to predict these airfoil vibratory stresses, and such computations are now routinely performed in the design cycle at some companies [8–11]. The time-varying pressure field, as predicted using unsteady simulations, is critical to this effort, and hence a robust technique for ensuring the validity of the computations is a necessity.

In terms of engine performance, a number of studies have involved the intentional shifting of circumferential position between successive blade and/or vane rows [12–15]. Known as airfoil clocking, this relative difference in circumferential position is used to control the location of upstream airfoil wakes as they propagate through downstream airfoil passages in order to achieve a performance benefit in terms of increased efficiency. Such calculations rely on the structure of an airfoil wake to remain intact as it progresses downstream through the engine. Again, the presence of a mixing plane would average out the wake structure between airfoil rows and hence would eliminate the ability of the simulation to predict clocking effects.

Another phenomenon of concern involves the interaction of a combustor hot streak with the downstream rows of the turbine

Contributed by the International Gas Turbine Institute of ASME for publication in the JOURNAL OF TURBOMACHINERY. Manuscript received July 18, 2006; final manuscript received August 9, 2006. Review conducted by David Wisler. Paper presented at the 2006 IGTI Turbo Expo, Paper No. GT2006-90735.

[16–19]. Hot streaks have the potential to impact negatively the life of downstream airfoil rows if not anticipated during the turbine design phase. Unsteady CFD provides a means to track the development of a combustor hot streak as it persists through the turbine, thereby identifying which airfoils are at risk for a hot streak encounter and predicting the potential impact on airfoil life.

There are well established means for determining the accuracy of CFD simulations with respect to grid- and time-step convergence [20,21]. This has led to policy statements from the engineering societies with respect to code verification and validation in general [22] and numerical accuracy in particular [23]. Of interest here is "iterative convergence." The policy statement from the ASME Journal of Fluids Engineering [23] states that, "stopping criteria for iterative calculations must be precisely explained, [and] estimates must be given for the corresponding convergence error." Iterative convergence criteria for steady-state simulations are well established: convergence is typically measured by tracking the iteration-to-iteration change of one or more flowfield quantities and looking for this value either to drop below a minimum threshold or to reach a zero slope. In an unsteady CFD simulation, the time-periodic nature of the flowfield precludes such a measure of convergence so some other technique is required.

In the gas-turbine industry designers often make simple qualitative judgments as to periodicity of the flow, and this is seldom based on interrogation of more than a few signals. Further, in most publications, discussion of unsteady convergence is cursory. One exception is due to Laumert et al. [24], who defined convergence of their unsteady simulation as occurring when the maximum deviation in static pressure between two periodic intervals was less than 0.1% over the airfoil surface at midspan. More recently, Ahmed and Barber [25] defined unsteady convergence in terms of time-varying fast Fourier transform (FFT) magnitudes calculated as the solution progresses. As time-resolved flowfield predictions become an ever increasing part of physics-based design systems the need for quantitative measures of iterative convergence becomes critical. This is particularly true when time-resolved CFD is used during detailed design where both rapid turn-around time and predictive accuracy are critical.

Design-optimization systems are becoming more and more prevalent within the industry [26], and using time-accurate CFD within such a system necessarily requires quantitative convergence monitoring. During a typical optimization study, the largest bottleneck is the computational time required to obtain a valid solution when considering the currently perturbed design parameter. Without a converged solution from which to extract one or more parameters used in an objective (or fitness) function, it is not possible to determine a correct relationship between the perturbed design parameters and the design objective. One is left with little choice but to set each optimization perturbation to run a high number of iterations to ensure convergence. Consequently, the potential savings in the wall-clock time required to achieve a given objective is significant if a time-resolved convergence criterion is available.

A robust, quantitative process for assessing the level of convergence of a time-accurate simulation is required. Ideally, the method should consist of calculations that both track the progress of the simulation and allow for the detection of inherent unsteadiness in the flowfield. Here we define a measure of time-periodic convergence and apply the technique to a number of unsteady simulations relevant to modern gas-turbine design. Again, application of the technique ensures the effective usage of time-accurate analyses during traditional design exercises and enables effective unsteady optimization.

Qualities of an Unsteady Convergence Criterion

Often in flowfield predictions in turbomachines, the period of the most significant unsteady fluctuations is expected from the circumferential interval modeled and the known wheel speed. During the execution of the time-accurate simulation, various aspects of the flowfield can be monitored at discrete intervals equal to some multiple of the computational time step. One can then calculate time-mean and time-resolved quantities of interest, and these may include but are not limited to the mass flow rates through domain inlet and exit boundaries, total pressures and temperatures (to obtain aero-performance), and static pressures on airfoil surfaces (to calculate resonant stresses). The collection of these quantities over the iteration history of the solution provides a set of discrete, time-varying signals which can be processed using standard signal processing techniques. Here, a set of signal processing operations, described in more detail by Ifeachor and Jervis [27] and in Ref. [28], were selected carefully for their relevance to both the design process in general and the case of periodic unsteadiness in particular.

As mentioned above, designers primarily perform unsteady simulations either to determine the effect of design changes on the time-mean characteristics of the machine (e.g., aero-performance or heat load) or to estimate resonant stresses on the airfoils. So, the development of both time-mean and time-resolved quantities is important for unsteady convergence monitoring. It is straightforward to track the former over periodic intervals, but the latter requires some consideration. Resonant stress analyses are typically performed at discrete engine orders consistent with the Campbell diagram of the airfoil row [9]. Such calculations require accurate data on the unsteady forces to the airfoil row implying both magnitude and phase information at the frequencies of interest. These frequencies are driven by the airfoil counts in the machine where both the fundamental frequencies and a number of harmonics may be important. So, it is necessary at a minimum to track the development of the magnitude and phase of relevant frequencies from periodic interval to periodic interval as well as time-mean quantities.

An effective convergence criterion for unsteady flows also allows for the possibility of inherent unsteadiness existing in a flowfield. This often occurs in turbomachinery as a consequence of vortex shedding at the trailing edge of the airfoil. Such shedding can occur whether or not a significant separation zone exists on the airfoil suction surface, and the frequency is dictated by the relevant Strouhal number of the flow over the airfoil. Fortunately, two other signal analysis measures, cross correlation and the power spectral density, are useful under such circumstances.

One can cross correlate a time-varying signal determined over one expected periodic interval with the same signal calculated over the next period. The result is itself a repeating signal that should have the same period as that expected in the simulation. Further, the magnitude of the cross-correlation coefficient at zero lag is a direct measure of how alike the signal is over each of the pairs of expected periodic intervals. If significant inherent unsteadiness exists in the flowfield, then the magnitude at zero lag can be significantly less than one, and the period of the cross-correlation coefficient can occur at a number of lags that is inconsistent with that expected in the simulation.

In signal processing Parseval's theorem states that the integral of the power spectral density over a defined range of frequencies is equal to the contribution of fluctuations on that interval to the overall mean square of the signal. Consequently, one can sum the power spectral densities over all significant frequencies expected in the simulation and compare that to the overall mean square. If the summed signal power is not a large fraction of the overall signal variance, then either inherent unsteadiness exists in the flowfield or a higher harmonic of the fundamental passing frequencies is more significant than expected. Of course, it is also possible to use the level of the power spectral density to determine the frequencies associated with the inherent unsteadiness and/or the higher harmonics, and one can then alter the execution of the unsteady simulation (and subsequent post-processing and resonant stress analysis) accordingly.

It is clear that all of the above measures are important for an

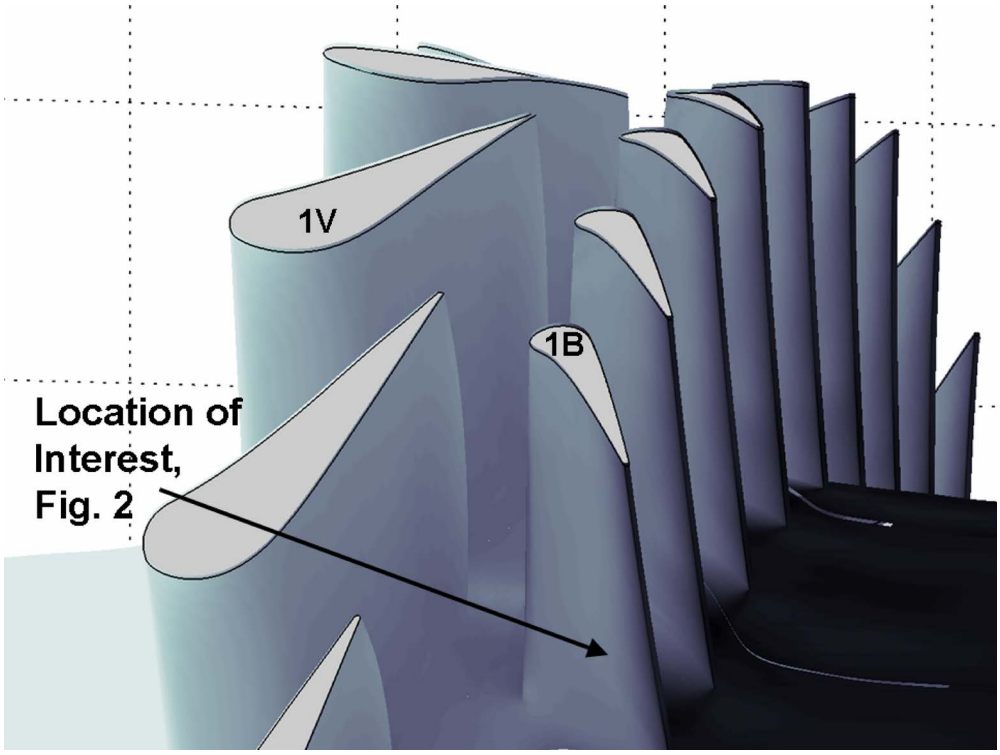

Fig. 1 Instantaneous static pressure on the no-slip surfaces of the HIT turbine rig simulation (HPT1)

assessment of unsteady convergence, and a means for combining all the relevant information into a single measure may be obtained from the field of fuzzy logic. Klir et al. [29] describe the process of "fuzzy decision making" that applies in situations such as these, and Clark and Yuan [30] have previously used the method to detect the edges of turbulent spots in a transitional flowfield consistent with a turbine blade. Further details regarding decision making with fuzzy sets can be found in Zimmermann [31] and Klir and Yuan [32]. The process employed here is described below along with complete details of the convergence assessment method.

A Method for Unsteady Convergence Assessment

It is useful to describe the details of the current method with respect to an example of periodic-unsteady simulation. A machine that is convenient for this purpose is the AFRL high impact technologies research turbine (HIT RT). An early design iteration of the turbine, denoted here as HPT1, is described in detail by Johnson [33]. The geometry is a single-stage high-pressure turbine consistent with an engine cycle envisaged for 2017 and beyond. The vane and blade airfoil counts of HPT1 are 22 and 44, respectively. The turbine was analyzed via the 3D time-accurate Reynolds-averaged Navier–Stokes (RANS) solver of Dorney and Davis [34], which is itself a further development of the Rai code [35,36].

The turbine geometry is shown in Fig. 1 as the portion of the wheel (1/22nd) modeled in the simulation. Colorization of the nonslip surfaces in the figure is based on instantaneous static pressure. The wheel speed at conditions consistent with a short-duration rig experiment for design-system code validation in the AFRL Turbine Research Facility [37,38] is 7050 rpm, and with 1/22nd of the annulus modeled the expected periodicity occurs on an interval equal to approximately 0.387 ms. This interval corresponds to one vane passing per blade or the passage of two blades per vane. At the time step depicted in Fig. 1, the simulation had completed approximately 19 periodic cycles (vane passings), and the time-varying pressure at the location indicated on the blade pressure side for the two subsequent cycles is plotted in Fig. 2(*a*). While a surface static pressure on the blade pressure side is used in the present example, it is possible to use the method with any flow variable at any location of interest in the domain that is relevant to the design issue at hand.

All signal-analysis operations required to apply the convergence–assessment method are illustrated in Figs. 2(*a*)–2(*e*). Again, these are the calculations of the time mean of the flow quantity over each periodic cycle, the discrete Fourier transform (DFT), the cross-correlation coefficient (CCF), and the power spectral density (PSD). The time mean of the static pressure over a single periodic cycle is

$$\bar{p} = \frac{1}{N}\sum_{n=0}^{N-1} p(n+1) \tag{1}$$

where N is the number of time steps per period, and $p(n+1)$ is the static pressure calculated at an integer multiple, $n+1$, of the time step, Δt. In Fig. 2(*a*) the time-mean levels calculated over each of the two periodic cycles are plotted as well as the raw pressure trace. Complete convergence of the time-averaged signal is achieved when there is no difference in signal mean from one periodic interval to the next.

The DFT of the fluctuating pressure, p', evaluated at an integer multiple, $k+1$, of the signal sampling frequency, $\Delta f = (N\Delta t)^{-1}$ is given by

$$P(k+1) = \sum_{n=0}^{N-1} p'(n+1)e^{-i(2\pi kn/N)} \tag{2}$$

where Fourier components are defined for values of k between 0 and $N-1$. Each Fourier component is a phasor

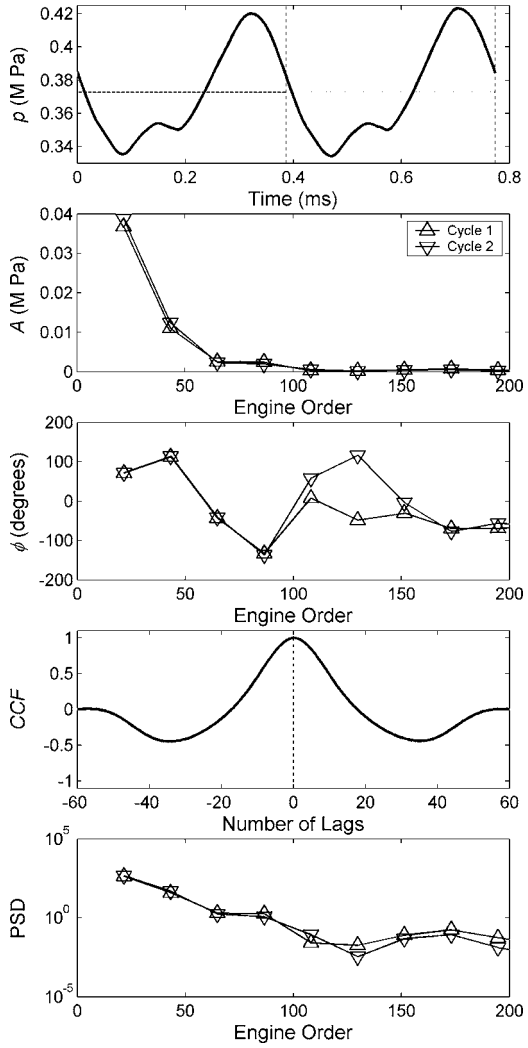

Fig. 2 An example of signal-analysis techniques used in the current method for HPT1: (*a*) time mean; (*b*) DFT magnitudes; (*c*) phase angles; (*d*) cross-correlation coefficients; and (*e*) power-spectral densities

$$P(k+1) = \mathrm{Re} + \mathrm{Im}\, i \tag{3}$$

and the time-periodic fluctuation at a given multiple of the sampling frequency can be reconstructed by

$$p(t) = \mathrm{Re}\{Ae^{i(\omega t+\phi)}\} = A\cos(\omega t + \phi) \tag{4}$$

In Eq. (4), A is the normalized DFT magnitude, given by

$$A = 2(\mathrm{Re}^2 + \mathrm{Im}^2)^{1/2}/N \tag{5}$$

Φ is the phase angle defined as $\tan^{-1}$ (Im/Re), and ω is the circular frequency corresponding to the integer multiple of the sampling frequency, $2\pi\Delta f(k+1)$. DFT magnitudes and phase angles are plotted in Figs. 2(*b*) and 2(*c*), respectively, for each of the periodic intervals plotted in Fig. 2(*a*). Convergence of the simulation at a given frequency is complete when there is neither a change in magnitude nor a difference in phase between the DFT results for two consecutive periodic intervals at frequencies of interest to the designer.

The results of a cross correlation of the signals from the two periodic cycles of Fig. 2(*a*) are plotted in Fig. 2(*d*). In the time domain the CCF is given by

$$\mathrm{CCF}(L) = \frac{\frac{1}{N}\sum_{n=0}^{N-1} p'((n+1)+L)p'((n+1)+N)}{\frac{1}{N}\left[\sum_{n=0}^{N-1} p'^2(n+1)\sum_{n=0}^{N-1} p'^2((n+1)+N)\right]^{1/2}} \tag{6}$$

The calculation at a given time lag, L, is accomplished first by multiplying the time-lag-shifted fluctuating pressure over the first interval by the fluctuating pressure signal for the second periodic interval, summing products, and then dividing by the number of samples per period. The result is then normalized by the product of the root-mean-square levels for the two signals. Complete convergence of the unsteady simulation yields a cross-correlation coefficient equal to 1 at zero lag. This implies that the signals from the first and second periodic intervals are exactly alike and that N is the true period of the signals.

The PSDs of the signals from the two periodic intervals plotted in Fig. 2(*a*) are shown in Fig. 2(*e*). The PSD at a given multiple of the sampling frequency is defined as the product of the Fourier component at that frequency and its complex conjugate divided by the number of samples, N. Convergence of a time-resolved turbomachinery simulation occurs when a large fraction of the overall signal power occurs at frequencies of interest and when that portion of the mean square does not change from one periodic interval to the next.

It is useful to calculate a single parameter that can be used to gauge the level of convergence of the simulation, and multivalued logic provides a convenient means of accomplishing this objective [29]. One can use the calculated time-mean levels, DFT magnitudes and phase angles, cross-correlation coefficients at zero lag, and fraction of overall signal power at frequencies of interest to define a series of fuzzy sets that express various aspects of the degree of convergence. These fuzzy sets are as follows

$$f_M = 1 - \left|1 - \frac{\bar{p}_2}{\bar{p}_1}\right| \tag{7}$$

$$f_A = 1 - \left|1 - \frac{A_2}{A_1}\right| \tag{8}$$

$$f_\phi = 1 - \left|\frac{\phi_2 - \phi_1}{\pi}\right| \tag{9}$$

$$f_S = |\mathrm{CCF}(0)| \tag{10}$$

$$f_P = \frac{\sum_{k_{\mathrm{expected}}} \mathrm{PSD}(k+1)}{\sum_{k=0}^{N-1} \mathrm{PSD}(k+1)} \tag{11}$$

where the subscripts 1 and 2 refer to the first and second cycles, respectively. Evaluation of Eqs. (7)–(11) gives membership grades in fuzzy sets that describe consistent mean level, amplitude, phase angle, overall signal shape, and fractional signal power, respectively. The amplitude and phase membership grades of Eqs. (8) and (9) are calculated for each frequency of interest as defined, for example, by an airfoil Campbell diagram. The numerator in Eq. (11) is a summation over all frequencies expected to produce significant signal power in the simulation. A level substantially less than 1 implies the presence of either inherent unsteadiness in the simulation or a significant signal level due to some higher harmonic of the expected fundamental frequencies.

The overall convergence level is then itself a fuzzy set defined as the intersection of the others

$$f_C = f_M \cap f_A \cap f_\phi \cap f_S \cap f_P \tag{12}$$

and this is in turn given by the standard fuzzy intersection [29]

Table 1 Results of the fuzzy-set convergence analysis as applied to the signals in Fig. 2

Fuzzy set	Membership grade
f_M	0.999
f_A (22E)	0.947
f_Φ (22E)	0.991
f_A (44E)	0.886
f_Φ (44E)	0.990
f_A (66E)	0.933
f_Φ (66E)	0.988
f_S	0.999
f_P	0.997
f_C	0.886

$$f_C = \min(f_M, f_A, f_\phi, f_S, f_P) \tag{13}$$

Here we define $f_C \geq 0.95$ for two consecutive cycles to be consistent with convergence of the periodic-unsteady flowfield. To continue this example, Eqs. (7)–(13) were evaluated for the signals plotted in Fig. 2, and the results are shown in Table 1. For this simulation, significant unsteadiness was expected to occur due to the fundamental vane-passing frequency (22E) as well as two harmonics of that frequency (44E and 66E). Note that more than 99% of the overall signal power is contained in the expected frequencies, so there is not any significant inherent unsteadiness evidenced in the signal. Also note that the signals are 99.9% correlated between the two periodic intervals, so the overall signal shape is very well converged. There is very little phase difference between cycles at the frequencies of interest, and the variation of amplitudes between cycles is greatest for the first harmonic of the fundamental. As a consequence, the overall convergence level of the simulation is 0.886, and this is dictated by the change in amplitude of that engine order (44E) from cycle to cycle.

At this point, it is worth noting that the fuzzy sets f_M and f_S taken together are akin to the sort of information that an "expert user" of unsteady CFD employs to judge the convergence of a simulation. Such an expert would typically plot the time variation of flowfield quantities for two of more periodic cycles and make a judgment as to how alike the dc and ac components of the signal are from one cycle to the next. In this example, there is very little change in both the time-mean level and the overall signal shape between the cycles plotted in Fig. 2. An expert user would undoubtedly come to the same conclusion from a visual inspection of the pressure trace plotted in Fig. 2(a). However, one can see in Table 1 that the amplitude of the first harmonic of vane passing is still changing significantly over the two periods plotted in Fig. 2(a). Since simulations of this type are often performed to assess vibratory stresses during the design cycle of an engine, there is a clear advantage to the application of a more robust method of convergence assessment like that described here. For example, an 11% variation in the amplitude of unsteady forcing could well mean the difference between passing and failing an FAA certification test for resonant stresses.

To complete this example, Fig. 3 is a plot of the fuzzy convergence level versus the periodic cycle number for 34 periodic intervals (i.e., 34 vane-passing events). The fuzzy sets that dictate the outcome of the overall level are also indicated in the figure. The convergence behavior of the simulation is in this case controlled by the variations of the magnitude and phase of harmonics of the fundamental from cycle to cycle. While this convergence behavior is typical of simulations where simple vane–blade interaction effects dominate the flowfield, the importance of tracking more than the Fourier components as the solution progresses is illustrated below with reference to other turbine geometries.

Again, it is important to recognize that the flowfield parameter selected for convergence monitoring is case dependent: the most important quantities are dictated by the reasons for performing the simulation. If the designer is assessing the expected level of resonant stress due to a specific forcing function on the airfoil surface, then the amplitude and phase angle at that frequency must be monitored at a number of locations on the airfoil surface. Alternatively, the amplitude and phase angle of the integrated aerodynamic load on the surface can be monitored. In addition, if the purpose of the analysis is to quantify a change in the time-mean performance resulting from the latest design iteration, then the mass- or mixed-out-averaged efficiency of the stage is the quantity to monitor.

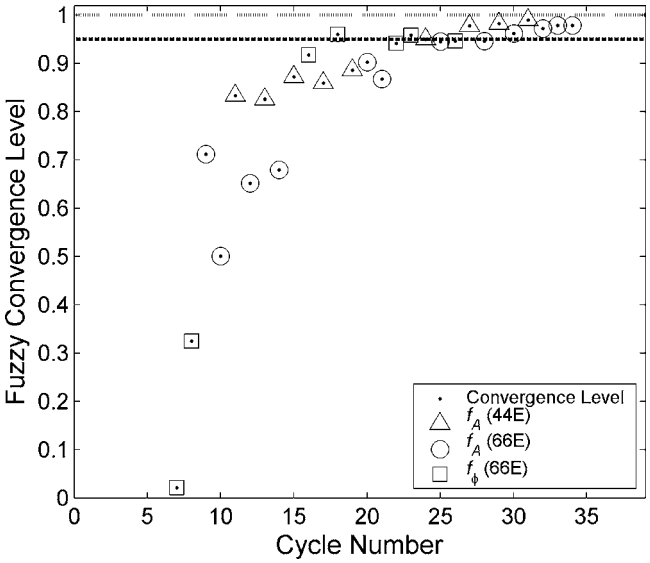

Fig. 3 Convergence behavior of the flowfield at the location of interest given in Fig. 1 for HPT1

One must also keep in mind that some quantities within the simulation converge well before others: for example, the pressure field typically becomes truly periodic well in advance of the entropy field due to the disparate propagation rates of finite pressure waves and viscous disturbances. So, great flexibility was built into the implementation of the convergence-assessment algorithm described above. The user can monitor a large number of flow quantities at any point in the flowfield. This is very useful when determining overall simulation convergence in post-processing mode. Also, one can estimate the convergence of arbitrary signals generated as the solution progresses (e.g., mass-flow rates, efficiencies, integrated airfoil loadings, etc.), and that can be used to control an unsteady optimization routine. Further examples of the application of this algorithm to a number of periodic-unsteady flowfields predicted in turbines during the design cycle are described next.

Convergence Behavior of Simulations of Vane–Blade Interaction

A primary reason for executing an unsteady CFD simulation during the turbomachinery design cycle is to predict airfoil resonant stresses. If vibratory stress problems are detected early enough during detailed design, then they can be mitigated [9]. However, if unacceptable vibratory stresses are discovered after the engine has been put into service, significant warranty costs could be involved if changes to the geometry are required. Avoidance of design escapes is thus critically dependent upon accurate predictions of unsteady loads on airfoil surfaces.

Predictive tools for vibratory stresses rely on accurate Fourier analysis of time-resolved pressure fields [8,10], and true periodicity is required to avoid errors resulting from spectral leakage [27]. Thus it is necessary for designers to quantify convergence levels

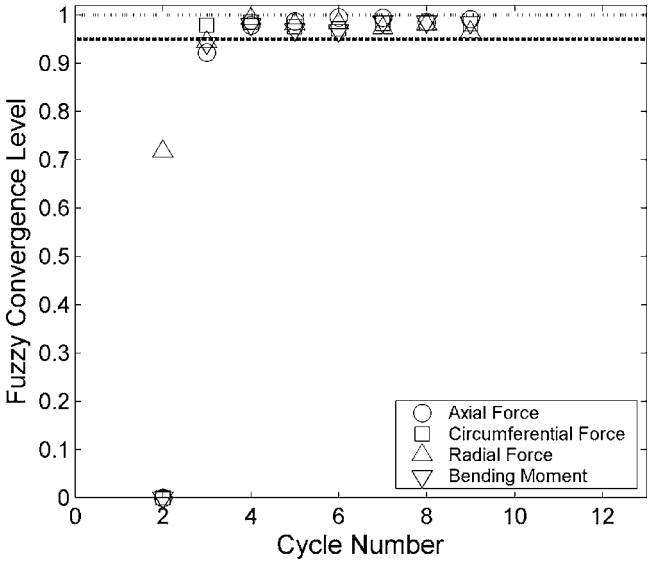

Fig. 4 Convergence levels for blade force components as a function of periodic cycle for HPT2

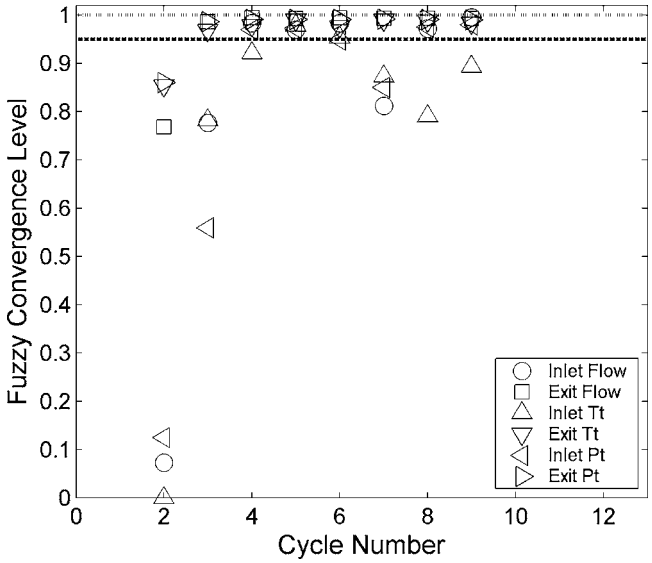

Fig. 5 Convergence of flow rates, total pressures, and total temperatures at the blade interrow boundaries for HPT2

prior to determining vibratory stresses. When predicting a flowfield to assess vibratory stresses, time-resolved traces of the integrated airfoil loading provide a suitable means to monitor convergence. Airfoil surface static pressure fluctuations are the root cause of vibratory stresses, and when integrated over the airfoil surface, these static pressures provide the airfoil loading.

As an example, a stage-and-one-half calculation was performed for a high-pressure turbine (HPT2) with 48 first vanes, 72 first blades, and 84 second vanes, modeled as 1/12th of the full-wheel geometry. Based on these airfoil counts, one would expect blade vibratory stresses to arise due to the $48E$ and $84E$ vane-passing frequencies as well as their harmonics. However, it is unlikely that resonant crossings due to frequencies larger than $168E$ would occur in the operating range of the turbine. So, the fundamental and first harmonic of each vane-passing frequency is considered in the analysis.

Figure 4 is a plot of the convergence level, f_C, calculated using integrated blade loadings on a cycle-by-cycle basis for the high-pressure turbine blade. Separate values of f_C were calculated for each of the time-trace signals representing the axial, tangential, and radial forces on the blade as well as the bending moment. The integrated blade loadings are very well converged after five periodic cycles with values of f_C greater than 0.95 for all force components as well as the moment.

Convergence of the blade integrated loading occurs rapidly in this example, and that is an indication that the unsteadiness in static pressure is primarily driven by potential field and/or shock interaction effects. The propagation rate of viscous disturbances in a turbine flowfield is much smaller than that of finite pressure waves, so one would expect that the level of convergence of total quantities entering and exiting the blade row is correspondingly lower at a given periodic cycle. Inspection of Fig. 5 confirms this supposition. The figure is a plot of convergence levels for inlet and exit mass-flow rates as well as total pressures and temperatures. For all periodic cycles a comparison of f_C levels between Figs. 4 and 5 indicates that the static pressure field of the turbine converges faster than the viscous flowfield. Therefore, if the current example was used to determine the effect of a design change (e.g., vane clocking) on unsteady loss levels as well as to predict resonant stresses, then the simulation requires a longer run time prior to post-processing.

For another example of the performance of the present method, consider a stage-and-one-half calculation for a high-pressure turbine (HPT3) having airfoil counts equal to 36, 72, and 48 in the first vane, first blade, and second vane row, respectively. Again, 1/12th of the wheel was modeled in the simulation with the purpose of the analysis to assess drivers due to the fundamental vane-passing frequencies only. The solution was run for six complete cycles, and that was enough to yield convergence of the unsteady loadings in the previous example. However, inspection of Fig. 6 reveals that convergence was not achieved on that interval in the current example. In fact, a convergence level of less than 0.7 was achieved for the axial force component.

Since the level of convergence achieved by the axial component was lower than that of all the others, it was selected for further investigation. Figure 7 is a plot of the normalized axial force signal as well as the membership grades in the fuzzy sets defined in Eqs. (7)–(11) as a function of periodic cycle number. The convergence level is dictated by the lowest membership grade over all the membership functions, namely, the fractional signal power, f_P. A low level of f_P implies that there is significant unsteadiness due to an unexpected frequency. Also note that low levels of the cross correlation at zero lag, f_S were obtained. This implies a significant

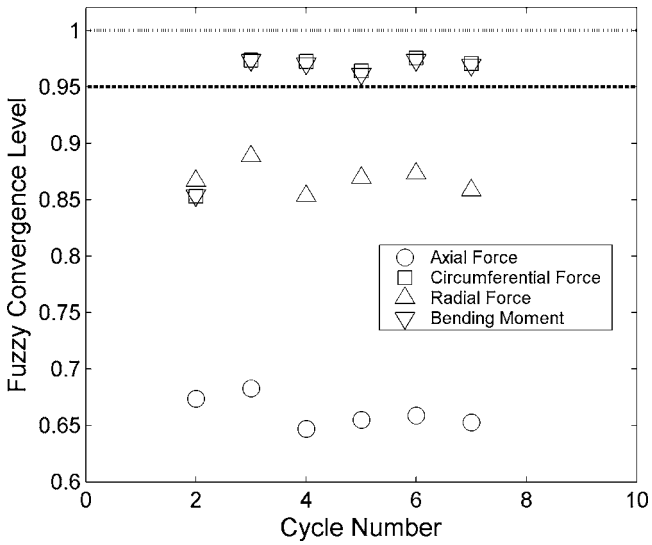

Fig. 6 Convergence levels for blade force components as a function of periodic cycle for HPT3

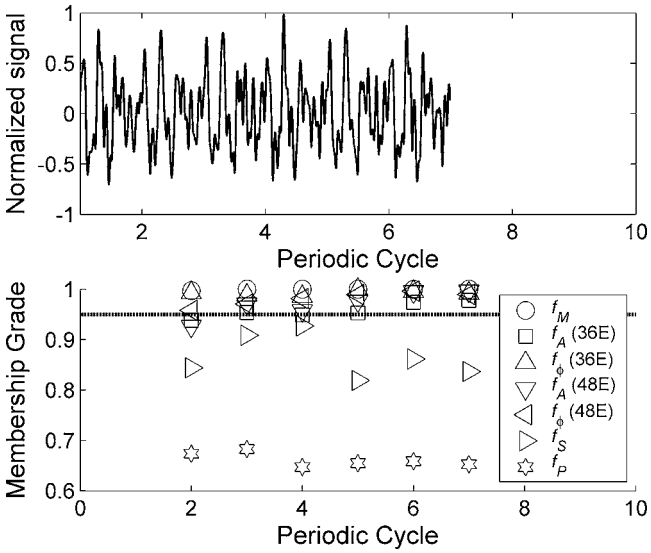

Fig. 7 Plots of time-resolved blade axial force and fuzzy-set membership grades as functions of the periodic cycle (HPT3)

change in signal shape from cycle to cycle, and this can mean that the primary periodicity occurs in the simulation over some unanticipated time scale, calling into question the validity of the DFT results used throughout the method. In any case, the results suggest that rigorous interrogation of the unsteady flowfield predicted in the turbine is warranted.

Figure 8 is a plot of fractional signal power due to engine orders of excitation up to 300. There is significant unsteadiness in the axial force exerted on the blade due to the first harmonic of the second-vane passing frequency, and this contributes to the low level of f_P. Consideration of the blade Campbell diagram might lead one to conclude that no resonance is to be expected due to that forcing function. However, more problematic is the signal power detected at the engine orders above 150. While 180*E* is the fourth harmonic of the first-vane passing frequency, the significant peak that occurs at 168*E* is spurious, and it warrants further investigation.

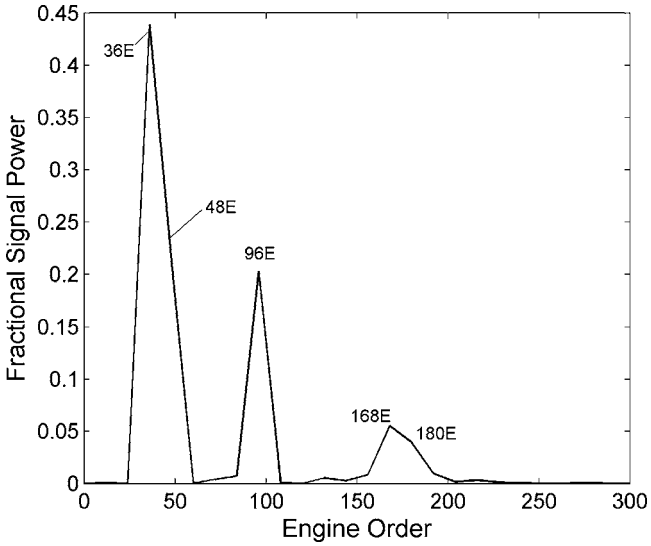

Fig. 8 The results of a PSD analysis performed on cycle seven of the axial force signal for the blade of HPT3. Power contributions from unexpected frequencies are apparent.

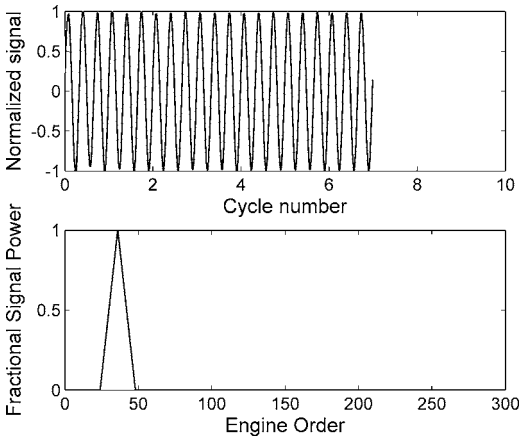

Fig. 9 Normalized flow rate into the blade row versus periodic cycle number and the results of a PSD analysis of the signal (HPT3)

Plots of normalized, time-resolved flow rates entering and exiting the blade row are plotted in Figs. 9 and 10, respectively, along with fractional signal power as functions of frequency resulting from PSD analysis. The unsteady blockage effect of the upstream vanes is very clearly evident in the inlet flow plots of Fig. 9. In Fig. 10, however, there is significant unsteadiness associated with the blockage of the downstream airfoils as well as high-frequency unsteadiness at 168*E* and 180*E*. A high-frequency blockage effect is suggestive of inherent unsteadiness (i.e., vortex shedding). Further, the unsteadiness is broad banded and suggests that the shedding is actually occurring at a frequency between 168*E* and 180*E* with an attendant picket-fencing effect on the spectral analysis.

Additional evidence of vortex shedding is discernible in Figs. 11 and 12. Figure 11 is a plot of the DFT magnitude calculated from the time-resolved entropy rise through the blade row at 168*E* ($\approx$31 kHz). A midspan plane is shown for a single blade passage, and the highest magnitude of the unsteady entropy rise is found in the vicinity of the blade trailing edge. Again, this is characteristic of vortex shedding. A calculation of the Strouhal number of the oscillations based on trailing-edge diameter and the local velocity in the vicinity of the trailing edge gives a value of $\approx$0.16. Figure 12 is a plot of the local DFT magnitude of unsteady static pressure at the same midspan plane for the 168*E* frequency. High levels of unsteady static pressure occur near the blade throat and down-

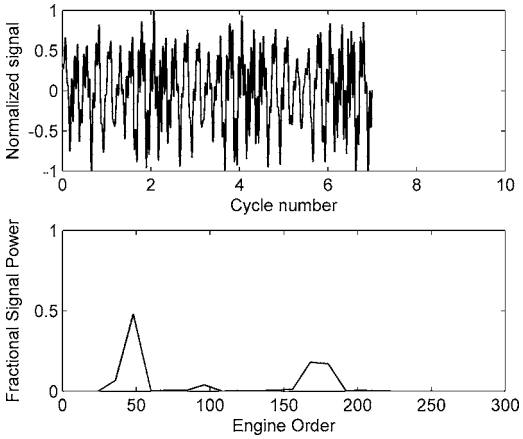

Fig. 10 Normalized flow rate out of the blade row versus periodic cycle number and the results of a PSD analysis of the signal (HPT3)

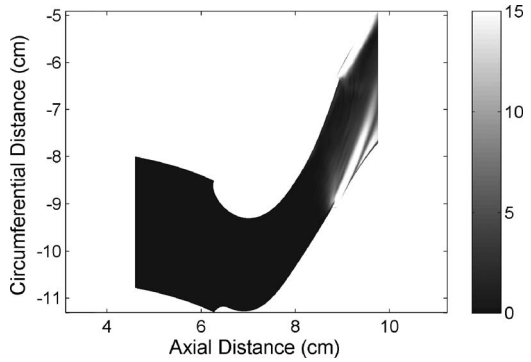

Fig. 11 Contours of DFT magnitude at 168*E* calculated from time-resolved entropy rise (J/kg/K) at midspan through the blade passage (HPT3)

stream of the trailing edge at a location consistent with a reflected cross-passage shock. It is concluded that the unsteady blockage caused by the vortex shedding produces enough of an instantaneous variation in the throat area to cause a shock to form. Consequently exceptionally high levels of unsteady pressure occur on the blade suction side at the vortex-shedding frequency.

Note that the simulation described above represents an early iteration in the design cycle for a turbine. In part as a consequence of these results, the design parameters of the turbine changed markedly before the final geometry was obtained. Consequently, no significant high-frequency unsteadiness occurred in the product. So, it is unclear whether or not the phenomenon described here could in fact lead to an airfoil failure. However, Doorly and Oldfield [39] have noted the presence of instantaneous local separation on a turbine blade in conjunction with shock passing, and their Schlieren images were suggestive of the occurrence of the phenomenon described here in the vicinity of the blade trailing edge. In any case, it is clear from this example that application of the present method to assess convergence in predictions of vane–blade interaction provides designers and analysts with significant direction as to the interrogation of the flowfield and the health of the design.

Convergence Behavior of Simulations of Hot-Streak Migration

During the design cycle, unsteady analysis is used to assess the effect of hot streaks on the aero-performance and durability of downstream rows, and one can employ the present method to judge convergence in such flowfields. As an example, consider a simulation of hot-streak migration through the first stage of another high pressure turbine (HPT4). The geometry consists of a

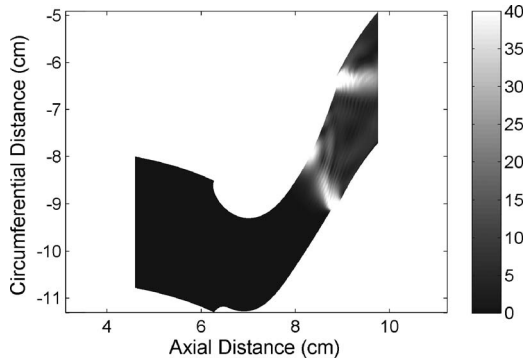

Fig. 12 Contours of DFT magnitude at 168*E* calculated from time-resolved static pressure (kPa) at midspan through the blade passage (HPT3)

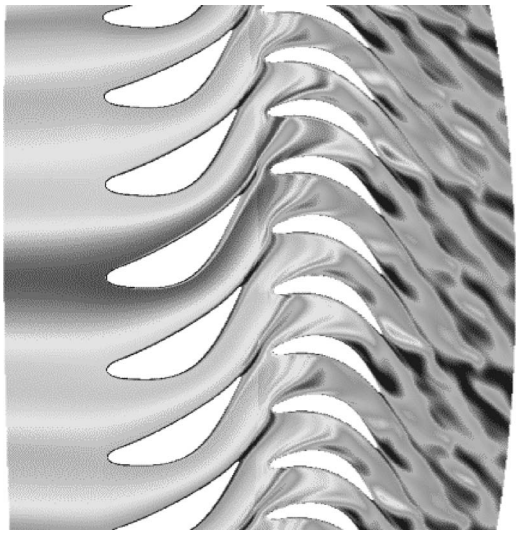

Fig. 13 Instantaneous total temperatures through HPT4 for the hot-streak simulation

vane/blade configuration with a combustor thermal exit profile mapped onto the vane inlet boundary. The CFD model contains 48 stator airfoils and 72 rotor airfoils as well as 24 regions of distinctly higher-enthalpy fluid corresponding to the location of the combustor nozzles. The hot streaks are aligned with the leading edges of alternating vanes, and one-third of the hot streaks are at an elevated temperature with respect to the other two-thirds. The remainder of the inlet profile is adjusted to maintain a given area averaged inlet total temperature. Contours of local total temperature are shown in Fig. 13.

For such a configuration, the convergence of the system should be calculated using rotor-based quantities. As the blades traverse behind the circumference of the vane ring, they pass through a number of regions of alternating enthalpy as well as the vane wakes, and the blade flowfield responds accordingly. Further, one might hypothesize that for a well designed vane row at subsonic vane exit Mach number, the hot streaks comprise the major sources of unsteadiness for the blade airfoils. So, Fig. 14 is a plot

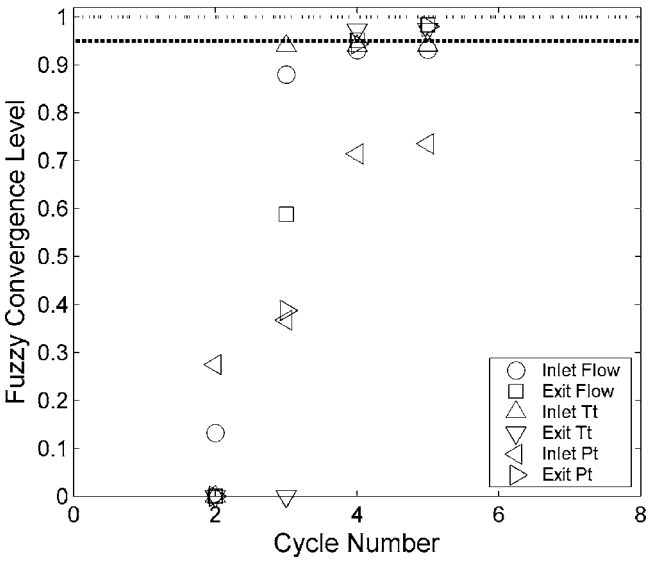

Fig. 14 Convergence levels for the blade flowfield variables considering the 8*E* and 24*E* frequencies associated with the hot-streak inlet profile (HPT4)

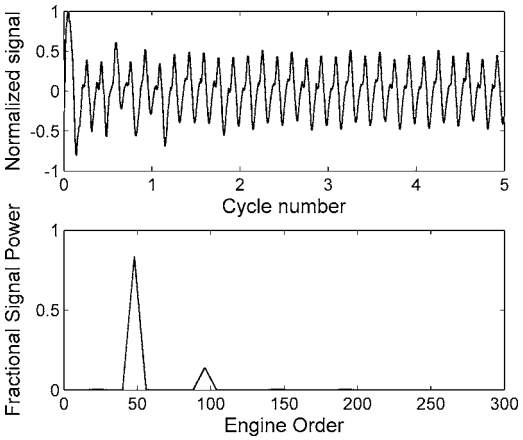

Fig. 15 Normalized total pressure upstream of the blade row versus cycle number and a PSD analysis of the signal (HPT4)

of convergence levels versus periodic cycle number for the inlet- and exit mass flow, total temperature, and total pressure obtained by considering the 8*E*, 24*E*, and 48*E* drivers as dominant. In Fig. 14 good levels of convergence are seen for all quantities except the upstream total pressure.

A power-spectral analysis of the upstream total pressure signal is plotted in Fig. 15 along with the time variation of that quantity, normalized by the peak value. All signal power in the upstream total pressure trace comes not from the hot streaks (8*E* and 24*E*) but from the vane wakes (48*E* and 96*E*), and this is consistent with the Munk and Prim [40] substitution principle. Accordingly, the effect of the hot streaks is not seen in the comparatively steady aerodynamics of the vane: instead, it is manifested in the unsteady flow through the blade row [16,17]. A final check of the convergence behavior of the case with respect to the tangential component of the force on the blade is presented in Fig. 16. The membership grades of all the fuzzy sets are greater than 0.95 by the fifth cycle, and this confirms that the case is approaching true periodicity with respect to the blade loading.

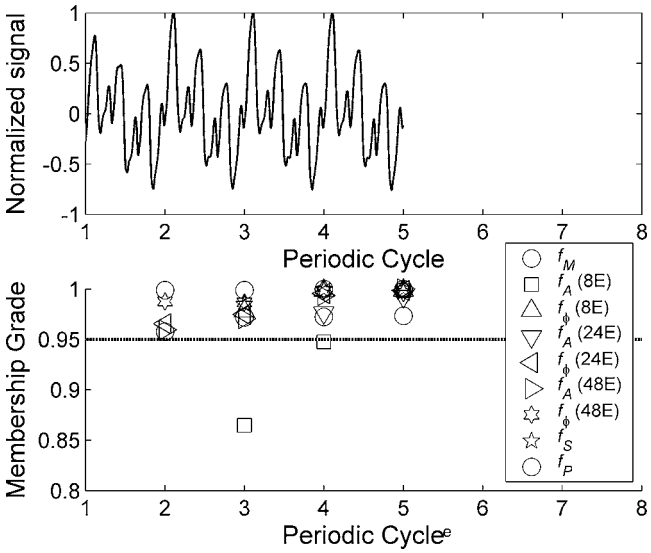

Fig. 16 Plots of time-resolved blade tangential force and fuzzy-set membership grades as functions of the periodic cycle (HPT4)

Table 2 Operating conditions of the example turbines

	Re (1 V, exit)	Vane M_{exit}	Blade M_{exit}
HPT1	2.4×10^6	0.82	1.40
HPT2	2.1×10^6	1.09	1.24
HPT3	2.0×10^6	0.75	0.94
HPT4	2.0×10^6	0.61	0.81

Conclusions

A quantitative method to assess the level of convergence of a periodic-unsteady simulation was described. The method was based on well known signal-processing techniques, and these were used in conjunction with fuzzy set theory to define a single overall convergence level of the simulation. The development of the method was illustrated with reference to a prediction of vane–blade interaction in a transonic high-pressure turbine. The robustness of the technique was then demonstrated by application to a number of simulations consistent with turbine aerothermodynamic design in industry (see Table 2). It was shown that the technique is very useful as an indicator of the overall quality of the simulations as well as guide to further investigations of the flowfield and characterization of the design. For example, the method was shown to be useful in detecting inherent unsteadiness in the prediction of the flow through a high-pressure turbine, and therefore judicious application of the technique can be a significant factor in preventing design escapes.

Acknowledgment

The impetus for this work came from discussions that the authors had with Mr. R. K. Takahashi of Mitsubishi Heavy Industries. The authors would also like to thank Mr. Joel Wagner of Pratt & Whitney as well as the three anonymous reviewers for their helpful suggestions to improve the manuscript. Those interested in applying this method to specific problems may contact john.clark@pr.wpafb.af.mil.

Nomenclature

A = DFT magnitude
CCF = cross-correlation coefficient
DFT = discrete Fourier transform
E = engine order=frequency/(rpm/ 60)
f = membership grade in a fuzzy set
k = integer multiple of sampling frequency
L = number of lags
Ma = Mach number
N = number of samples per periodic cycle
n = integer multiple of sampling interval
P = Fourier component of static pressure signal
Pt = total pressure (MPa)
p = static pressure (MPa)
PSD = power spectral density
Re = Reynolds number based on axial chord
Tt = total temperature (K)

Greek

Δf = spectral resolution (Hz) of a signal=$1/(N\Delta t)$
Δt = sampling rate, temporal resolution of a signal (s)
Φ = DFT phase angle (radians, deg)
ω = circular frequency (radians /s)

Subscripts/Superscript

A = fuzzy set for convergence of DFT amplitude
C = fuzzy set for overall convergence
M = fuzzy set for time-mean convergence
P = fuzzy set for fraction of overall signal power

S = fuzzy set for convergence of overall signal shape
Φ = fuzzy set for convergence of DFT phase angle
$'$ = Fluctuating component

References

[1] Adamczyk, J. J., 2000, "Aerodynamic Analysis of Multi-Stage Turbomachinery Flows in Support of Aerodynamic Design," ASME J. Turbomach., **122**, pp. 189–217.
[2] Dunn, M. G., 2001, "Convective Heat Transfer and Aerodynamics in Axial Flow Turbines," ASME J. Turbomach., **123**, pp. 637–686.
[3] Ni, R. H., 1982, "A Multiple-Grid Scheme for Solving the Euler Equations," AIAA J., **20**(11), pp. 1565–1571.
[4] Ni, R. H., and Bogoian, J. C., 1989, "Prediction of 3-D Multistage Turbine Flow Field Using a Multiple-Grid Euler Solver," AIAA Paper No. 89-0203.
[5] Ni, R. H., 1999, "Advanced Modeling Techniques for New Commercial Engines," Proceedings 14th ISOABE Conference, Florence, Italy, 5–10 September.
[6] Davis, R. L., Shang, T., Buteau, J., and Ni, R. H., 1996, "Prediction of 3-D Unsteady Flow in Multi-Stage Turbomachinery Using an Implicit Dual Time-Step Approach," AIAA Paper No. 96-2565.
[7] Tyler, J. M., and Sofrin, T. G., 1970, "Axial Flow Compressor Noise Studies," SAE Trans., **70**, pp. 309–332.
[8] Hilbert, G. R., Ni, R. H., and Takahashi, R. K., 1997, "Forced-Response Prediction of Gas Turbine Rotor Blades," *Proceedings ASME Winter Annual Meeting*, Dallas, TX.
[9] Clark, J. P., Aggarwala, A. S., Velonis, M. A., Magge, S. S., and Price, F. R., 2002, "Using CFD to Reduce Resonant Stresses on a Single-Stage, High-Pressure Turbine Blade," ASME Paper No. GT2002-30320.
[10] Green, J. S., and Marshall, J. G., 1999, "Forced Response Prediction Within the Design Cycle," IMechE Conf. Trans., **1999-1A**, pp. 377–391.
[11] Weaver, M. M., Manwaring, S. R., Abhari, R. S., Dunn, M. G., Salay, M. J., Frey, K. K., and Heidegger, N., 2000, "Forcing Function Measurements and Predictions of a Transonic Vaneless Counter-Rotating Turbine," ASME Paper No. 2000-GT-375.
[12] Huber, F., Johnson, P. D., Sharma, O. P., Staubach, J. B., and Gaddis, S. W., 1996, "Performance Improvement Through Indexing of Turbine Airfoils: Part 1—Experimental Investigation," ASME J. Turbomach., **118**, pp. 630–635.
[13] Griffin, L. M., Huber, F. W., and Sharma, O. P., 1996, "Performance Improvement Through Indexing of Turbine Airfoils: Part 2—Numerical Simulation," ASME J. Turbomach., **118**, pp. 636–642.
[14] Dorney, D. J., and Sharma, O. P., 1996, "A Study of Turbine Performance Increases Through Clocking," AIAA Paper No. 96-2816.
[15] Haldeman, C. W., Dunn, M. G., Barter, J. W., Green, B. R., and Bergholz, R. F., 2004, "Experimental Investigation of Vane Clocking in a One and 1/2 Stage High Pressure Turbine," ASME Paper No. GT2004-5347.
[16] Shang, T., and Epstein, A. H., 1997, "Analysis of Hot Streak Effects on Turbine Rotor Heat Load," ASME J. Turbomach., **119**(3), pp. 544–553.
[17] Takahashi, R. K., Ni, R. H., Sharma, O. P., and Staubach, J. B., 1996, "Effects of Hot Streak Indexing in a 1-1/2 Stage Turbine," AIAA Paper No. 96-2796.
[18] Dorney, D. J., and Gundy-Burlet, K., 2000, "Hot-Streak Clocking Effects in a 1-1/2 Stage Turbine," J. Propul. Power, **12**(3), pp. 619–620.
[19] He, L., Menshikova, V., and Haller, B. R., "Influence of Hot Streak Circumferential Length-Scale in a Transonic Turbine Stage," ASME Paper No. GT2004-53370.
[20] Roache, P. J., 1998, *Verification and Validation in Computational Science and Engineering*, Hermosa Publishers, Albuquerque, NM.
[21] Gokaltun, S., Skudarnov, P. V., and Lin, C-X., 2005, "Verification and Validation of CFD Simulation of Pulsating Laminar Flow in a Straight Pipe," AIAA Paper No. 2005-4863.
[22] AIAA Policy Board, 1998, "Guide for the Verification and Validation of Computational Fluid Dynamics Simulations," AIAA Policy Paper No. G-077-1998.
[23] Freitas, C. J., 1993, "Editorial Policy Statement on the Control of Numerical Accuracy," ASME J. Fluids Eng., **115**(2), p. 339.
[24] Laumert, B., Martensson, H., and Fransson, T. H., 2001, "Investigation of Unsteady Aerodynamic Blade Excitation Mechanisms in a Transonic Turbine Stage, Part I: Phenomenological Identification and Classification," ASME Paper No. 2001-GT-0258.
[25] Ahmed, M. H., and Barber, T. J., 2005, "Fast Fourier Transform Convergence Criterion for Numerical Simulations of Periodic Fluid Flows," AIAA J., **43**(5), pp. 1042–1052.
[26] Staubach, J. B., 2003, "Multidisciplinary Design Optimization, MDO, the Next Frontier of CAD/CAE in the Design of Aircraft Propulsion Systems," AIAA Paper No. 2003-2803.
[27] Ifeachor, E. C., and Jervis, B. W., 1996, *Digital Signal Processing*, Addison-Wesley, New York.
[28] Mathworks, 2000 *Signal Processing Toolbox User's Guide*, Version 5, Natick, MA.
[29] Klir, G. J., St. Clair, U. H., and Yuan, B., 1997, *Fuzzy Set Theory: Foundations and Applications*, Prentice–Hall PTR, Upper Saddle River, NJ.
[30] Clark, J. P., and Yuan, B., 1998, "Using Fuzzy Logic to Detect Turbulent/Non-Turbulent Interfaces in an Intermittent Flow," *Intelligent Automation and Control*, Vol. 6, TSI Press, Albuquerque, NM, pp. 113–118.
[31] Zimmermann, H. J., 1990, *Fuzzy Set Theory and Its Applications*, 2nd ed., Kluwer, Boston, MA.
[32] Klir, G. J., and Yuan, B., 1995, *Fuzzy Sets and Fuzzy Logic: Theory and Applications*, Prentice–Hall PTR, Upper Saddle River, NJ.
[33] Johnson, P. D., 2005, "Consortium Turbine Research Rig, Aerothermal and Mechanical Design," AFRL, WPAFB, OH, AFRL Technical Report No. AFRL-PR-WP-TR-2005-2157.
[34] Dorney, D. J., and Davis, R. L., 1992, "Navier–Stokes Analysis of Turbine Blade Heat Transfer and Performance," ASME J. Turbomach., **114**, pp. 795–806.
[35] Rai, M. M., 1987, "Navier-Stokes Simulations of Rotor-Stator Interaction Using Patched and Overlaid Grids," J. Propul. Power, **3**, pp. 387–396.
[36] Rai, M. M., and Madavan, N. K., 1990, "Multi-Airfoil Navier-Stokes Simulations of Turbine Rotor-Stator Interaction," ASME J. Turbomach., **112**, pp. 377–384.
[37] Polanka, M. D., Hoying, D. A., Meininger, M., and MacArthur, C. D., 2003, "Turbine Tip and BOAS Heat Transfer and Loading, Part A: Parameter Effects Including Reynolds Number, Pressure Ratio and Gas to Metal Temperature Ratio," ASME J. Turbomach., **125**, pp. 97–106.
[38] Clark, J. P., Polanka, M. D., Meininger, M., and Praisner, T. J., 2006, "Validation of Heat-Flux Predictions on the Outer Air Seal of a Transonic Turbine Blade," ASME J. Turbomach., **128**, pp. 589–595.
[39] Doorly, D. J., and Oldfield, M. L. G., 1985, "Simulation of the Effects of Shock Wave Passing on a Turbine Rotor Blade," ASME J. Eng. Gas Turbines Power, **107**, pp. 998–1006.
[40] Munk, M., and Prim, R., 1947, "On the Multiplicity of Steady Gas Flows Having the Same Streamline Pattern," Proc. Natl. Acad. Sci. U.S.A., **33**, pp. 137–141.

Predicting Transition on Concave Surfaces

Mark W. Johnson
Department of Engineering,
University of Liverpool,
Liverpool L69 3GH, UK

Boundary layers on concave surfaces differ from those on flat plates due to the presence of Taylor-Goertler (T-G) vortices. These vortices cause momentum transfer normal to the blade's surface and hence result in a more rapid development of the laminar boundary layer and a fuller profile than is typical of a flat plate. Transition of boundary layers on concave surfaces also occurs at a lower Re_x than on a flat plate. Concave surface transition correlations have been formulated previously from experimental data, but they are not comprehensive and are based on relatively sparse data. The purpose of the current work was to attempt to model the physics of both the laminar boundary layer development and transition process in order to produce a transition model suitable for concave surface boundary layers. The development of the laminar boundary layer on a concave surface was modeled by considering the profiles at the upwash and downwash locations separately. The profiles of the boundary layers at these two locations were then combined to successfully approximate the spanwise averaged profile. The ratio of the boundary layer thicknesses at the two locations was found to be as great as 50 and this leads to laminar boundary layer shape factors as low as 1.3 and skin friction coefficients up to 12 times the value for a flat plate laminar boundary layer. Boundary layers therefore grow much more rapidly on concave surfaces than on flat plates. The transition model assumed that transition commenced in the upwash location boundary layer at the same transition inception Re_θ observed on a flat plate. Transition at the downwash location then results from the growth of turbulent spots from the upwash location rather than through the initiation of spots. The model showed that initially curvature promotes transition because of the thickened upwash boundary layer, but for strong curvature the T-G vortices effectively stabilize the boundary layer and transition then occurs at a higher Re_θ than on a flat plate. Results from the transition model were in broad agreement with experimental observations. The current work therefore provides a basis for the modeling of transition on concave surfaces. [DOI: 10.1115/1.2720865]

Introduction

Traditional transition prediction models developed from flat plate data fail to predict the transitional behavior of boundary layers on the pressure surface of gas turbine blades. This is because of the destabilising effect of the centrifugal pressure gradient induced by the blade curvature which leads to the formation of Taylor-Goertler (T-G) vortices. These vortices can only be observed in the quiescent conditions of a laboratory wind tunnel, but the consequences of their presence in terms of increased skin friction coefficient and premature transition is observed on gas turbine blades. Many researchers e.g. [1–10] have studied the transition of boundary layers on concave surfaces over several decades through experiment, but to date no reliable predictive technique has been developed for either the enhanced development of the laminar boundary layer or its transition. The objective of the current work is to address these issues.

Taylor-Goertler Vortices

T-G vortices have been observed in several experimental studies e.g., Shigemi et al. [2]. These vortices have fixed spanwise locations for Goertler numbers G_θ less than about 2 and distinct upwash and downwash boundary layer profiles can be measured at fixed spanwise locations. At higher G_θ, e.g., Hachem and Johnson [4] the vortices start to meander in the spanwise direction and hence time averaged boundary layer profiles are invariant with spanwise position. Although the T-G vortices can not be observed at high G_θ, their influence is apparent through the distorted boundary layer profiles and enhanced skin friction.

Laminar Boundary Layer Profiles

It should be noted that all the boundary layer profiles discussed in this paper are flat plate equivalent boundary layer FPEBL profiles. The FPEBL is derived from the actual boundary layer profile using the procedure of Riley et al. [5] given in the Appendix.

Shigemi et al. [2] took detailed measurements of laminar boundary layers on a concave surface at low G_θ, where the T-G vortices had stable positions. Their measurements showed that the boundary layer thickness varied by at least a factor of two between the upwash (U) and downwash (D) locations. The boundary layer profiles at each location were however undistorted from the flat plate profile with shape factors H of approximately 2.5. For boundary layers at a higher G_θ the spanwise averaged boundary layer profiles have a very characteristic shape as shown in Fig. 1. The velocity gradient at the wall is high, but once the velocity reaches 60–80% of the freestream velocity a distinct kink is seen in the profile and a much lower velocity gradient exists in the outer part of the layer. The reason for this sudden change in velocity gradient is the large boundary layer thickness variation in the spanwise direction. To illustrate this consider the boundary layer thickness to vary in the spanwise direction according to the square wave shown in Fig. 2. The upwash and downwash profiles are also assumed to be zero pressure gradient Pohlhausen profiles such that

$$\frac{u}{U} = 2\left(\frac{y}{\delta}\right) - 2\left(\frac{y}{\delta}\right)^3 + \left(\frac{y}{\delta}\right)^4 \quad (1)$$

Contributed by the International Gas Turbine Institute of ASME for publication in the JOURNAL OF TURBOMACHINERY. Manuscript received July 13, 2006; final manuscript received August 18, 2006. Review conducted by David Wisler. Paper presented at the ASME Turbo Expo 2006: Land, Sea and Air (GT2006), May 8–11, 2006, Barcelona, Spain, Paper No. GT2006-90455.

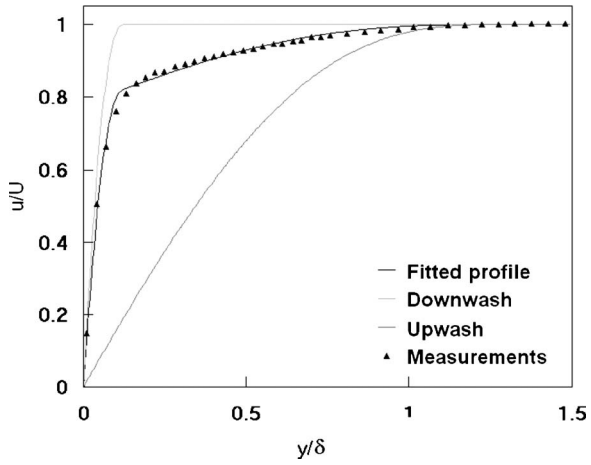

Fig. 1 Typical laminar boundary layer profile on a concave surface

Now considering the profile in Fig. 1, we can determine the values of the three quantities shown in Fig. 2, i.e., the upwash boundary layer thickness δ_U, the proportion of the span occupied by the upwash profile s_U and the upwash to downwash boundary layer thickness ratio r_δ, using a least rms error technique. This leads to the upwash and downwash profiles and overall fitted profile shown in Fig. 1. The figure shows that although a square wave is a very crude approximation to the actual spanwise variation an acceptable fit to the measured data is obtained. The figure also clearly shows that the kink in the overall profile is due to the rapid change in velocity gradient associated with the edge of the downwash boundary layer.

The square wave model is used throughout this paper to represent the spanwise variation in boundary layer thickness resulting from the action of the T-G vortices. However the model can only be used to predict the growth of laminar boundary layers on concave surfaces, if a relationship between s_U and r_δ and the flow conditions can be established. The experimental results of Hachem and Johnson [3] were used for this purpose. Hachem and Johnson measured laminar boundary layer development on two constant radius concave surfaces at two different tunnel speeds and subjected to nominally zero freestream pressure gradients. In the present work, their profiles are defined by two parameters, the shape factor H and $C_f \mathrm{Re}_\theta$, which characterizes the velocity gradient at the wall. For a flat plate zero pressure gradient boundary

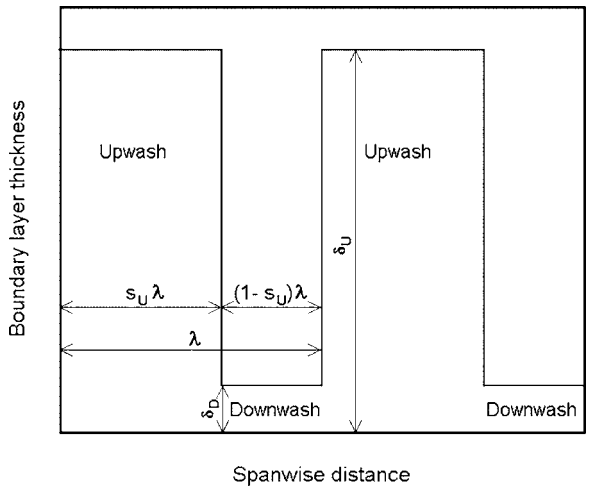

Fig. 2 Square wave model for spanwise variation in boundary layer thickness

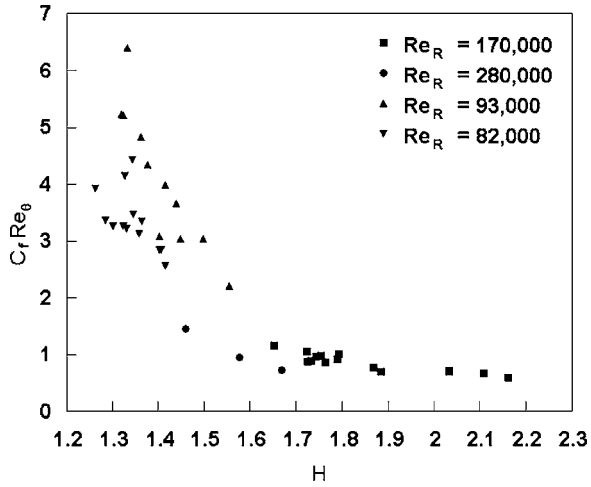

Fig. 3 Skin friction coefficient and shape factors for laminar boundary layers on concave surfaces

layer these parameters have the values 2.54 and 0.47, respectively, but it can be seen from Fig. 3 that Hachem and Johnson measured shape factors as low as 1.3 and $C_f \mathrm{Re}_\theta$ values as high as 6 on their concave surfaces.

The boundary layer profile depends on the blade radius R, the freestream velocity U, the fluid density ρ, and viscosity μ, and the distance x along the blade at which the profile is measured. In terms of dimensionless parameters this reduces to

$$C_f \mathrm{Re}_\theta = f\left(\mathrm{Re}_R, \frac{x}{R}\right) \tag{2}$$

and

$$H = f\left(\mathrm{Re}_R, \frac{x}{R}\right) \tag{3}$$

Hence

$$s_U = f\left(\mathrm{Re}_R, \frac{x}{R}\right) \tag{4}$$

and

$$r_\delta = f\left(\mathrm{Re}_R, \frac{x}{R}\right) \tag{5}$$

s_U and r_δ were evaluated for the data in Fig. 3 and are shown as functions of x/R in Figs. 4 and 5.

Figure 4 suggests that the dependence of s_U on x/R is much stronger than on Re_R and hence the equation

$$s_U = 0.1 + 0.9\left(1 - \exp\left(-0.8\frac{x}{R}\right)\right) \tag{6}$$

is a reasonable fit to the data. r_δ on the other hand does show dependence on both Re_R and x/R. The discontinuity in Fig. 5 at $x/R=0.85$ suggests that r_δ scales with $1/\mathrm{Re}_R$. A least rms curve fit to the data replotted against $(x/R)(1/\mathrm{Re}_R)$ (see Fig. 6) provides the correlation equation

$$r_\delta = 1 + 2.5 \times 10^6 \frac{x}{R}\frac{1}{\mathrm{Re}_R} \tag{7}$$

Equations (6) and (7) therefore provide a model for the boundary layer profile on a constant curvature concave surface with a zero streamwise pressure gradient.

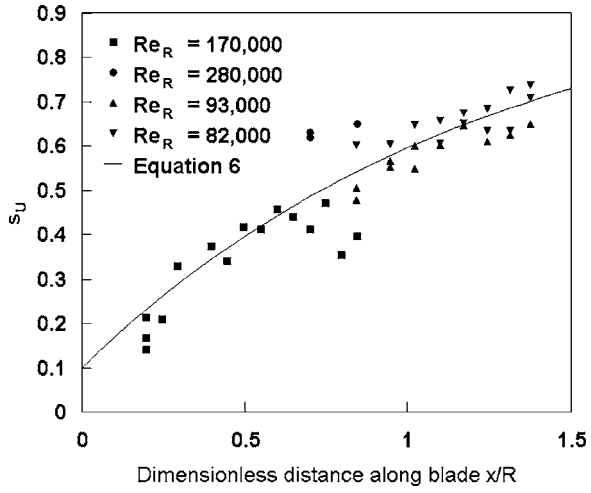

Fig. 4 Evolution of the proportion of the span occupied by the upwash profile

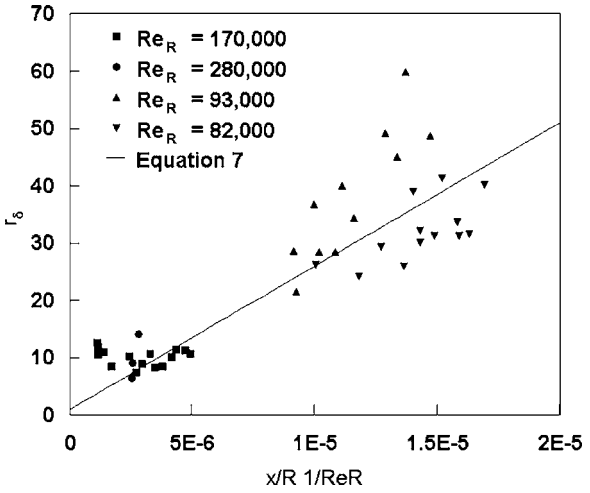

Fig. 6 Correlation for ratio of upwash to downwash boundary layer thickness

Laminar Boundary Layer Development

The overall skin friction coefficient C_f and displacement thickness δ^* are given by simple weighted averages of the upwash and downwash values

$$C_f = s_U C_{fU} + (1 - s_U) C_{fD} \tag{8}$$

and

$$\delta^* = s_U \delta^*_U + (1 - s_U) \delta^*_D \tag{9}$$

The velocity product within the momentum thickness integral gives rise to an $s_U(1-s_U)$ term

$$\frac{\theta}{\delta} = s_U \frac{37}{315} + (1 - s_U) \frac{37}{315 r_\delta} + s_U (1 - s_U) \frac{115 r_\delta^5 - 263 r_\delta^4 + 168 r_\delta^3 - 27 r_\delta + 7}{630 r_\delta^5} \tag{10}$$

Equations (8)–(10) can therefore be used to determine the laminar boundary layer development from the boundary layer momentum equation

$$\frac{d\theta}{dx} = \frac{C_f}{2} \tag{11}$$

Figure 7 shows the predicted laminar boundary layer development for a range of blade radius Reynolds numbers. The flat plate boundary layer development is shown for comparison. For low Re_x, before the T-G vortices have developed significantly, the boundary layer growth is identical to that on a flat plate. The T-G vortices develop most rapidly on the blades with low Re_R and hence the boundary layer growth increases above the flat plate value earliest for the lowest Re_R values.

Figure 8 shows the development of the laminar boundary layer for a blade where Re_R=800,000. The T-G vortices begin to influence the flow at about Re_x=30,000 when the upwash boundary layer begins to develop faster than the flat plate profile and the downwash boundary layer more slowly. By Re_x=250,000 the T-G vortices are sufficiently strong to remove low energy fluid from the downwash location faster than it is formed and hence the boundary layer at this location begins to thin. At Re_x=1,000,000 the upwash boundary layer is more than four times the thickness of the downwash boundary layer. The pretransitional measurements of Zhang et al. [6], which were taken on a constant curvature blade also with Re_R=800,000, are shown in the figure. The measured Re_θ values are lower than the predictions, but the ratio

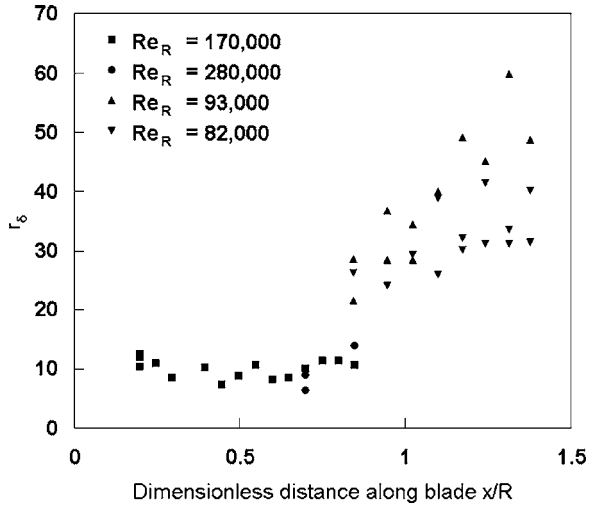

Fig. 5 Evolution of the ratio of the boundary layer thickness at upwash and downwash locations

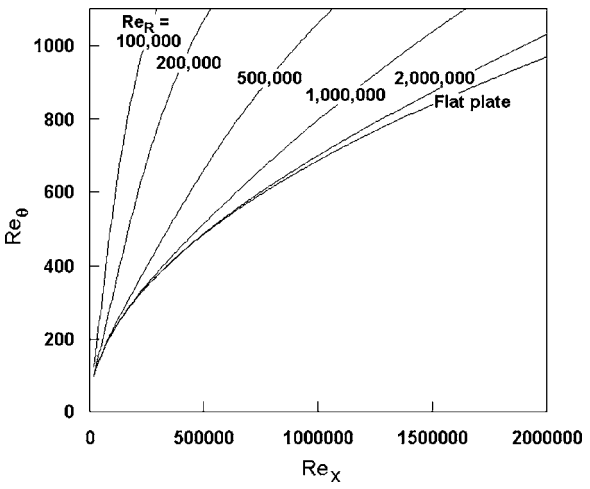

Fig. 7 Laminar boundary layer development for a range of blade radius Reynolds numbers

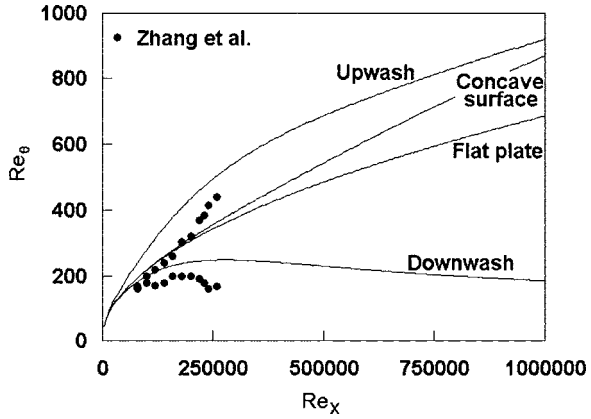

Fig. 8 Laminar boundary layer development for Re_R=800,000

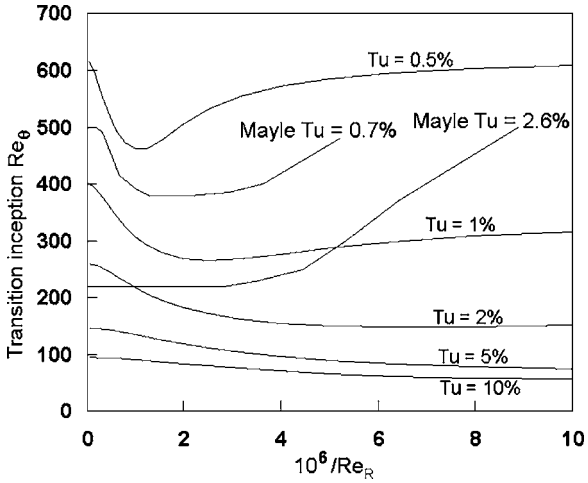

Fig. 9 Predicted transition inception on concave surfaces

between the values at up and downwash is reliably predicted. The discrepancy in the absolute values could be due to a slightly favorable pressure gradient upstream of the first measurement point or because of the limitations of the square wave model.

Transition Inception

Shigemi et al. [2] determined transition inception at both the upwash and downwash spanwise locations and found that transition occurred slightly earlier at the upwash location. The transition inception Re_θ at the upwash location was very similar to that for a flat plate boundary layer transition, whereas the value at the downwash location was much lower than the flat plate value. If it is assumed that transition commences at the upwash location in a similar manner to transition on a flat plate and then the spots spread laterally into the neighboring downwash regions, this would lead to the observed premature transition at the downwash locations. Shigemi et al. observed T-G vortices at a regular spacing of 25 mm across the span of their blade. If their spots spread at a typical angle of 10 deg, then they would spread laterally by a quarter vortex wavelength in a streamwise distance of about 35 mm which is consistent with their experimental observations. A transition model where transition commences when the upwash Re_θ reaches the value required for transition on a flat plate will therefore be used in the current work. Mayle's [10] criterion for transition on a flat plate

$$Re_{\theta\ start} = 400\ Tu^{-0.625} \tag{12}$$

is used as the upwash Re_θ value at the transition inception.

Transition inception Re_θ results for concave surfaces have been correlated by previous researchers, against a number of different dimensionless parameters including the Goertler number G_θ, the boundary layer momentum thickness to radius ratio x/R, and the blade radius Reynolds number Re_R. As G_θ, x/R, and Re_R are all related through Re_θ, any correlation can be formulated in terms of any one of these parameters. In the current paper, the predicted transition inception Re_θ values are plotted against the inverse of the blade radius Reynolds number Re_R in Fig. 9. This figure shows how curvature can reduce the transition Re_θ by up to 50%. This effect occurs at low curvature for low freestream turbulence levels as the T-G vortices are able to develop to a greater extent prior to transition occurring. Stronger curvature (higher $1/Re_R$) does not, however, continue to promote transition. This is because ultimately the T-G vortices mix out the differences between the upwash and downwash locations ($s_U \approx 1$) and transition is predicted at the same Reynolds number as on a flat plate. The empirical concave curvature transition correlation of Mayle [10] is also shown in the figure. Mayle's correlation for Tu=0.7% shows good agreement with the current prediction, however for Tu =2.6% the correlation suggests that transition is delayed by increasing curvature, whereas the prediction indicates the opposite. Although the square wave model used in this paper can lead to a modest increase in the transition inception Reynolds number from the flat plate value, this increase is limited because the up and downwash boundary layers are assumed to retain zero pressure gradient Pohlhausen profiles. It must be concluded therefore that when the curvature effects are strong, the boundary layer profiles at the up and downwash locations are distorted by the TG vortices. Profiles measured by, e.g., Winoto and Low [3] show distortions which can not be approximated by the current simple square wave model.

Transition Path

Johnson and Ercan [11] developed a transition prediction method for flat plate boundary layers and showed that it was capable of accurately predicting the transition process for the ERCOFTAC T3A, B and C test cases. This predictive procedure is used in the current paper to predict transition on concave surfaces. The only modification which has been made is to make the same assumption which was made to obtain Fig. 9, namely, that transition will commence in the laminar boundary layer at the upwash location.

Calculations were performed for four constant radius concave surfaces and a flat surface. The freestream velocity and freestream turbulence level were U=6 m/s and Tu=1%, respectively. The Johnson and Ercan transition model is also sensitive to the freestream turbulence length scale. This was set at 6 mm which results in a transition inception location of Re_θ=404 on the flat plate which is consistent with the Mayle transition inception correlation (Eq. (12)).

Figure 10 shows the variation of the shape factor H through transition on each of the blades. The points in the transition process where the intermittency was 1%, 25%, 50%, 75%, and 99% are also marked. On the flat plate transition follows the classic path commencing at Re_x=345,000 when H=2.54 and completing at Re_x=708,000 when H=1.46. Curvature has the effect of reducing the Re_x at which transition commences, although the transition length remains more or less constant. The shape factor value at the transition inception also drops with increasing curvature, until for Re_R=200,000 the value is only 1.65, which is lower than for a turbulent boundary layer with the same Re_θ and so the shape factor actually increases during the early part of transition up to an intermittency of 25%. The measurements from Zhang et al. [6] in the figure for Re_R=800,000 show transition inception close to the predicted value, however, the measurements indicate a shorter transition length.

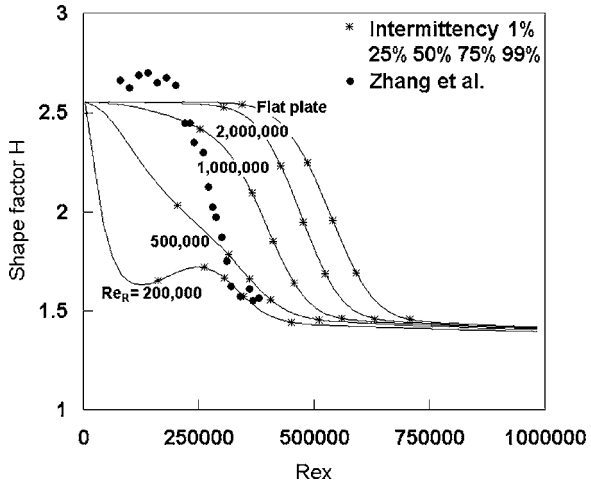

Fig. 10 Shape factor *H* variation through transition on constant curvature blades

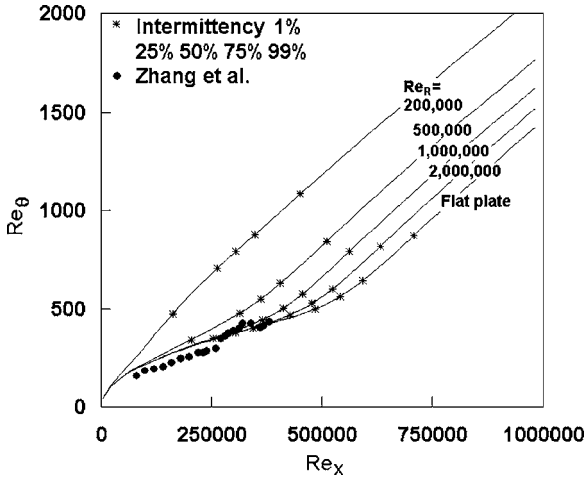

Fig. 12 Boundary layer development through transition

The variation in the skin friction coefficient C_f along each of the blades is plotted in Fig. 11. Increased curvature increases the skin friction in the laminar boundary layer due to the action of the T-G vortices. The effect is most dramatic for the Re_R=200,000 blade where C_f is approximately three or four times the flat plate value up to Re_x=500,000. The implications of this are important in gas turbine blade design where the Re_R values are commonly in the range 200,000–500,000. The current results clearly show that if flat plate boundary layer theory is used the skin friction and hence heat transfer rate will be grossly under predicted.

The boundary layer growth is shown in Fig. 12 where Re_θ is plotted against Re_x. The enhancement of C_f due to curvature also greatly increases the growth rate of the laminar boundary layer, such that for Re_R=200,000, there is little apparent change in growth rate between the laminar, transitional, and turbulent regimes. An interesting feature of these results is that although curvature initially leads to a reduction in the Re_θ value at which transition commences, for the highest curvature blade Re_R =200,000, the value of Re_θ is 477, which is significantly above the flat plate value. This is because the overall Re_θ value can exceed the value at both the upwash and downwash locations due to the final $s_U(1-s_U)$ term in Eq. (10). The Re_θ results of Zhang et al. are lower than predicted as previously discussed, but the overall trend is reliably predicted.

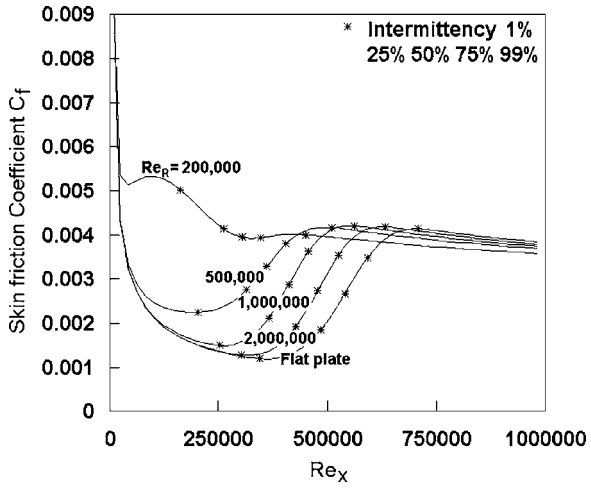

Fig. 11 Skin friction coefficient C_f variation through transition

Conclusions

1. Laminar boundary layer profiles on concave surfaces have a distinct characteristic "kink." This occurs because of the large spanwise variation in boundary layer thickness between the downwash and upwash locations.
2. For modest curvature, laminar concave boundary layer profiles can be accurately modeled as a weighted mean of two (an upwash and a downwash) zero pressure gradient flat plate boundary layer profiles.
3. The proportion of the boundary layer span occupied by the upwash profile s_U increases progressively with development of the boundary layer.
4. The ratio of the upwash to downwash boundary layer thickness r_δ increases progressively with the development of the boundary layer.
5. The T-G vortices can remove sufficient low momentum fluid from the downwash location to result in a thinning of the boundary layer at this location.
6. The present study suggests that transition commences at the upwash location, where the boundary layer has its maximum thickness, when Re_θ at that location reaches the value which would initiate transition on a flat plate at the same freestream turbulence level.
7. The present study suggests that spreading of turbulent spots from the upwash location rather than the initiation of turbulent spots causes transition at the downwash location.
8. Curvature promotes transition initially, because the T-G vortices produce a thickened boundary layer at the upwash location. For strong curvature however the transition inception Re_θ can exceed the flat plate value.
9. The current work implies that if the laminar boundary layer development on a concave surface can be predicted using a RANS calculation then transition can be predicted successfully using a flat plate correlation and the upwash Re_θ value.

Further Work

(1) The model used in the current paper for the development of the laminar boundary layer is crude. The model can be improved by using more detailed experimental or numerical results from laminar boundary layers on concave surfaces.

(2) The current work has only been undertaken for zero streamwise pressure gradient flows. The work suggests however that with a streamwise pressure gradient the boundary layer development could be modeled by assuming that the boundary layer profiles at the upwash and

downwash locations are the appropriate nonzero pressure gradient flat plate profiles. This needs to be verified from experimental or numerical results.

(3) The current work only considers constant curvature blades and therefore has limited application for turbomachinery blades which have variable curvature. The method can be extended to variable curvature blades if a suitable laminar boundary layer model can be developed.

Acknowledgment

The author would like to thank Dr. Farouk Hachem for providing his detailed experimental data for this study.

Nomenclature

C_f = skin friction coefficient
G_θ = Goertler number
H = shape factor
r_δ = ratio of upwash to downwash boundary layer thickness
R = blade radius
Re_R = blade radius Reynolds number
Re_x = surface length Reynolds number
Re_θ = momentum thickness Reynolds number
s_U = proportion of span occupied by upwash profile
Tu = freestream turbulence level
u = local velocity
U = freestream velocity
x = distance measured along the blade from the leading edge
y = wall normal coordinate
δ = boundary layer thickness
θ = boundary layer momentum thickness
λ = Taylor-Goertler vortex spanwise wavelength
ν = kinematic viscosity

Subscripts

D = downwash location
U = upwash location

Appendix

On a concave surface with a constant radius of curvature R, the freestream velocity U varies with the distance y from the wall according to the free vortex condition $U(R-y)=$constant. The fact that the velocity continues to increase beyond the boundary layer edge means that this point cannot be identified as simply as for a flat plate boundary layer. To overcome this problem the flat plate equivalent boundary layer (FPEBL) was determined from the experimental velocities for each boundary layer using the technique due to Riley et al. [9]. The FPEBL is the boundary layer which would be formed if the boundary layer on the concave surface were to flow on to a flat plate with no further viscous dissipation such that the normal pressure gradient is relieved. The Bernoulli and continuity equations together with the free vortex condition lead to

$$u_e^2 = u_m^2 + 2\int_0^{y_m} \frac{u_m^2}{R - y_m} dy_m \tag{A1}$$

and

$$\int_0^{y_e} u_e dy_e = \int_0^{y_m} u_m dy_m \tag{A2}$$

where the m and e subscripts refer to the measured and FPEBL values, respectively. These equations are integrated numerically to obtain the FPEBL. The boundary layer integral parameters were evaluated from the FPEBL profile.

References

[1] Liepmann, H. W., 1943, "Investigations on Laminar Boundary-Layer Stability and Transition on Curved Boundaries," NACA Wartime Report No. W-107.
[2] Shigemi, M., Gibbings, J. C., and Johnson, M. W., 1987, "Boundary Layer Transition on a Concave Surface," I. Mech. E. International Conference on Turbomachinery, Cambridge, September, pp. 223–230.
[3] Winoto, S. H., and Low, H. T., 1989, "Transition of Boundary Layers in the Presence of Goertler Vortices," Exp. Fluids, **8**, pp. 41–47.
[4] Hachem, F., and Johnson, M. W., 1990, "A Boundary Layer Transition Correlation for Concave Surfaces," ASME paper No. 90-GT-222.
[5] Riley, S., Johnson, M. W., and Gibbings, J. C., 1989, "Boundary Layer Transition on Strongly Concave Surfaces," ASME paper No. 89-GT-321.
[6] Zhang, D. H., Winoto, S. H., and Chew, Y. T., 1995, "Measurement in Laminar and Transitional Boundary Layer Flows on Concave Surfaces," Int. J. Heat Fluid Flow, **16**, p. 88.
[7] Volino, R. J., and Simon, T. W., 1997, "Measurements in a Transitional Boundary Layer with Görtler Vortices," ASME J. Turbomach., **119**, p. 562.
[8] Schultz, M. P., and Volino, R. J., 2003, "Effects of Concave Curvature on Boundary Layer Transition Under High Freestream Turbulence Conditions," ASME J. Fluids Eng., **125**, p. 18.
[9] Dris, A., and Johnson, M. W., 2005, "Transition on Concave Surfaces," ASME J. Turbomach., **127**, p. 507.
[10] Mayle, R. E., 1991, "The Role of Laminar-Turbulent Transition in Gas Turbine Engines," ASME J. Turbomach., **113**, p. 509.
[11] Johnson, M. W., and Ercan, A. H., 1999, "A Physical Model for Bypass Transition," Int. J. Heat Fluid Flow, **20**, pp. 95–104.

The Effects of Varying the Combustor-Turbine Gap

N. D. Cardwell

N. Sundaram

Mechanical Engineering Department,
Virginia Polytechnic Institute and
State University,
Blacksburg, VA 24061

K. A. Thole

Mechanical and Nuclear Engineering Department,
Pennsylvania State University,
University Park, PA 16802

To protect hot turbine components, cooler air is bled from the high pressure section of the compressor and routed around the combustor where it is then injected through the turbine surfaces. Some of this high pressure air also leaks through the mating gaps formed between assembled turbine components where these components experience expansions and contractions as the turbine goes through operational cycles. This study presents endwall adiabatic effectiveness levels measured using a scaled up, two-passage turbine vane cascade. The focus of this study is evaluating the effects of thermal expansion and contraction for the combustor-turbine interface. Increasing the mass flow rate for the slot leakage between the combustor and turbine showed increased local adiabatic effectiveness levels while increasing the momentum flux ratio for the slot leakage dictated the coverage area for the cooling. With the mass flow held constant, decreasing the combustor-turbine interface width caused an increase in uniformity of coolant exiting the slot, particularly across the pressure side endwall surface. Increasing the width of the interface had the opposite effect thereby reducing coolant coverage on the endwall surface. [DOI: 10.1115/1.2720497]

Introduction

Core flow temperatures within the hot section of a gas turbine commonly exceed the metal melting temperature. Cooling techniques are needed to protect turbine components from the harsh environment. To accomplish this cooling, high pressure air is bled from the compressor, bypassed around the combustor, and then routed into the turbine where it is used for internal and external cooling purposes.

Since the entire turbine is not manufactured as a single component, numerous gaps exist between mating parts allowing leakage of high pressure coolant. Thermal expansion and mechanical stresses within the turbine make it especially difficult to seal these interfaces. One such interface is the slot between the combustor and the first stage of the turbine since the combustor and turbine are not rigidly connected. The gap between adjacent vane sections is another area that allows leakage of high pressure coolant. Leakages result in a significant loss in overall efficiency.

Turbine components are typically cast with high nickel super alloys because of their high strength at elevated temperatures. While the exact materials are proprietary, these alloys are similar in composition to Inconel 625. The average coefficient of thermal expansion for Inconel 625 is equal to 0.138 mm per cm of unrestrained metal over the standard to operating temperature range of 1075°C [1]. If one considers an unrestrained 30 cm combustor, it would result in an expansion of 4 mm. This 4 mm is on the order of the change in slot width we are modeling for this paper.

The work presented in this paper evaluates the effects of expansion and contraction of the combustor-turbine interface on endwall cooling performance. Also compared in this paper is the effect of leakage flowrates from a mid-passage gap between two mating vanes on the overall endwall cooling performance.

Relevant Past Studies

Significant work has been performed documenting the effects of leakage from the slot at the combustor-turbine interface. There have also been studies in the literature analyzing the combined effects of a combustor-turbine slot leakage and film-cooling. Very few studies exist on either the effect of a realistic mid-passage gap or the effect of changes in the combustor-turbine slot width on endwall cooling effectiveness for an actual airfoil passage.

The majority of the studies concerned with leakage flow have focused on a slot upstream of the first stage vane meant to simulate the leakage flow that occurs between the combustor and the turbine. One of the earliest works was presented by Blair [2]. Blair's study included a two-dimensional slot upstream of the vane. An enhanced cooling benefit was observed for increases in leakage flow. In a similar study, Burd et al. [3] studied the effects of coolant leaking from an upstream slot. As with Blair, Burd et al. reported better endwall cooling for leakage flows as high as 6% of the total passage flow. Colban et al. [4,5] studied the effects of changing the combustor liner film-cooling and upstream slot leakage flows on endwall effectiveness levels for a first vane cascade. Their results, like others, showed that the upstream slot flow does not evenly distribute along the endwall, with the majority of the cooling benefit along the suction side of the vane. Pasinato et al. [6] studied the effects of injecting air upstream of the vane stagnation through a series of discrete slots. These slots were oriented in the slot in such a manner that the coolant was injected tangentially to the leading edge of their contoured endwall. Pasinato et al. [6] found that this secondary air injection strongly distorted the flowfield upstream of the vane stagnation.

Some studies have combined the effects of upstream slot leakage with endwall film-cooling. The main studies performed are those of Zhang and Jaiswal [7], Kost and Nicklas [8], Nicklas [9], and Knost and Thole [10,11]. Kost and Nicklas [8] and Nicklas [9] reported that coolant ejection from an upstream slot causes radical changes in the near wall flowfield signifying an intensification of the horseshoe vortex, which was observable in their flow angle diagrams. This increase in intensity resulted in the slot coolant being moved off of the endwall surface and heat transfer coefficients that were over three times that measured for no slot flow injection. Endwall studies by Knost and Thole [10,11] investigated endwall effectiveness levels for a vane passage with both film-cooling and upstream slot injection. For increasing slot mass flow, Knost and Thole reported higher local effectiveness levels with the same coolant coverage area on the endwall

Several studies have documented the effect of flow from a gap between two adjacent airfoils. Aunapu et al. [12] showed that blowing through a passage gap could be used to reduce the negative effects of the passage vortex, but with significant aerody-

Contributed by the International Gas Turbine Institute of ASME for publication in the JOURNAL OF TURBOMACHINERY. Manuscript received July 18, 2006; final manuscript received July 26, 2006. Review conducted by David Wisler. Paper presented at the ASME Turbo Expo 2006: Land, Sea and Air (GT2006), May 8–11, 2006, Barcelona, Spain. Paper No. GT2006-90089.

namic losses. Another study done by Ranson and Thole [13] used a mid-passage gap between two blades for their experimental and computational studies. Their results showed that the flow through the gap was initially directed toward the blade pressure side, due to the incoming velocity vectors, and then convected towards the suction side of the adjacent airfoil. Yamao et al. [14] reported changes in film-cooling effectiveness levels due to leakage air injected from both an upstream slot and mid-passage gap. Their study indicated that film-cooling effectiveness was enhanced with an increase in sealing flow through both leakage interfaces.

Piggush and Simon [15,16] analyzed the effect of leakage flows on aerodynamic losses for a vane cascade. It was concluded that the mid-passage gap blowing caused both an increase in passage losses and the creation of a second smaller passage vortex which was located below the primary passage vortex. Piggush and Simon [15,16] also concluded that the majority of mid-passage gap blowing became entrained in the formation of a second vortex within the passage. Reid et al. [17] studied the effect of interplatform leakage on overall efficiency for an axial flow turbine stage. They determined that the largest drop in efficiency associated with interplatform leakage was 1.5% when compared to the stage efficiency with no slot present. The main difference in interplatform gap geometry between these two studies is that Reid et al. [17] modeled the internal seal strip of the interplatform gap and Piggush and Simon [15,16] did not.

Cardwell et al. [18] analyzed the effect of a mid-passage gap with a seal strip and platform misalignment on endwall cooling effectiveness. They determined that misalignment between adjacent vanes and between the combustor-turbine interface can significantly affect upstream slot coolant trajectory and effectiveness. Cardwell et al. [18] reported that a backward facing step (cascade configuration) between the combustor-turbine interface greatly reduced the need for suction side endwall film-cooling due to an increased utilization of upstream slot leakage.

The effect of a step in hub diameter just ahead of a blade row on aerodynamic blade performance was evaluated by de la Rosa Blanco et al. [19]. They also determined that a backward facing step at this location can lead to a reduction in endwall and mixing losses when compared to a flat endwall while a forward facing step produces higher losses than a flat endwall. Piggush and Simon [15,16] also agreed with the pressure loss results of de la Rosa Blanco et al. [19] for a turbine vane indicating increased losses with a forward and decreased losses with a backward facing step upstream of the vane stagnation.

To date there has been significant research on the effect of upstream slot flow on the passage fluid dynamics and endwall heat transfer, but no study on the effects of varied upstream slot widths. This study improves upon previous works by studying the realistic effect of combustor-turbine slot expansion and contraction on endwall adiabatic effectiveness levels given a vane passage with other realistic features such as a mid-passage gap and film-cooling.

Vane and Endwall Geometry

The flat endwall used in the linear cascade has three cooling features: a combustor-turbine slot, a mid-passage vane-to-vane gap with accompanying seal strip, and discrete film cooling holes. The same film cooling pattern as shown in Fig. 1, which was originally designed and tested by Knost and Thole [10,11], was used in this study. Figure 1 shows the film cooling hole injection angles, the upstream slot, and the mid-passage gap discussed above. All film cooling holes were cylindrical and inclined at an angle of 30 deg with respect to the endwall surface. Table 1 provides a brief description of the turbine vane geometry and operating conditions. Significant studies were performed on this particular vane geometry with a more detailed description given in Radomsky and Thole [20].

Figure 1 also shows a two-dimensional slot upstream of the vane leading edge, which represents the mating interface of the turbine and combustor. This slot had an injection angle of 45 deg and was located 30% of the axial chord upstream of the vane stagnation location. This leakage interface will be referred to as the upstream slot. Table 2 provides a summary of parameters relevant to the film-cooling holes and upstream slot geometries.

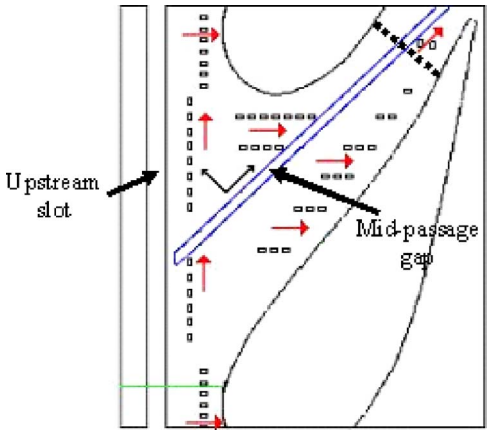

Fig. 1 Endwall geometry with film-cooling holes, an upstream slot, and a mid-passage gap

As discussed in the Introduction, the primary focus of this work was to analyze the endwall cooling effect of upstream slot expansion and contraction. For this study the metering slot width was expanded by 50% and contracted by 50%, which will be referred to as double width and half width, respectively. As with the nominal slot, both the double width and half width slots had a 45 deg surface injection angle. For these studies, the upstream slot was expanded and contracted while keeping the slot centerline fixed relative to the vane stagnation.

The gap between adjacent vane sections will be referred to as the mid-passage gap. A cross section of the mid-passage gap is shown in Fig. 2. Unlike the upstream slot, the mid-passage gap had a recessed seal strip as found in many engine designs, which influenced its interaction with the coolant and mainstream flow. To allow flow control, the mid-passage gap had a separate supply plenum which did not open into the upstream slot. The cross section of the mid-passage gap is also shown in Fig. 2. This gap, which was described in the previous study by Cardwell et al. [18],

Table 1 Geometric and flow conditions

Scaling factor	9
Scaled up chord length (C)	59.4 cm
Scaled up axial chord length (C_a)	29.3 cm
Pitch/chord (P/C)	0.77
Span/chord (S/C)	0.93
Re_{in}	2.1×10^5
Inlet and exit angles	0 to 72 deg
Inlet, exit Mach number	0.017, 0.085
Inlet mainstream velocity	6.3 m/s

Table 2 Summary of endwall geometry

	Parameter	Experimental
Upstream slot	Nominal slot width	0.024 C
	Double slot flow length to width	0.94
	Nominal slot flow length to width	1.9
	Half slot flow length to width	3.8
	Upstream slot surface angle	45 deg
Film cooling	FC hole diameter (cm)	0.46
	FC hole L/D	8.3
	Film-cooling surface angle	30 deg

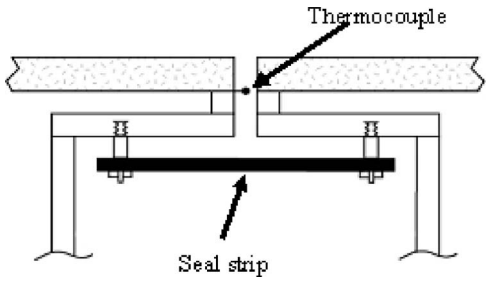

Fig. 2 Cross section view of the mid-passage gap geometry with an accompanying seal strip

had a 90 deg surface injection angle, a width of 0.635 cm, and a gap flow length to width ratio of 5. For this study, the mid-passage gap width was not varied.

Similar to the previous study reported by Cardwell et al. [18], the endwall surface was covered with a uniform roughness. To simulate a random array of a uniform roughness level, wide-belt industrial sandpaper was used to cover the entire endwall. The sandpaper had a closed coat 36 grit surface and a grade Y cloth backing. A closed coat surface had roughness elements arranged in a random array over 100% of its surface. The 36 grit sandpaper had an average particle size of 538 microns [21] which was roughly twice that observed by Bons et al. [22] for in service turbine endwalls. A custom construction technique was used to guarantee a uniform and uniform fit around each film-cooling hole. This technique ensured a uniform interaction between the rough surface and coolant jets for the entire endwall.

Experimental Methodology

The experimental facility used for this study consisted of a linear cascade test section placed in a closed loop wind tunnel, as shown in Fig. 3. Flow within the wind tunnel was driven by a 50 hp axial vane fan, which was controlled by a variable frequency inverter. After being accelerated by the fan, the flow turned 90 deg and then passed through a primary finned-tube heat exchanger. This heat exchanger was used to precool the bulk flow. After passing through the primary heat exchanger, the flow encountered another 90 deg turn before entering a three way split. This split simulated the primary core flow through the combustor and the bypass flow around the combustor. The flow split was achieved by using a porous plate with a 25% open area to act as a valve thereby directing a portion of the flow into the upper channel. The primary core flow passed through a resistance heater bank where its temperature was increased to 60°C. The secondary flow in the top channel passed through a secondary finned-tube heat exchanger where the flow temperature was lowered to 10°C. The mainstream flow continued through the middle channel into the test section. The cooler bypass flow was pulled into a 2 HP blower where it then flowed into the test section for the coolant supplies.

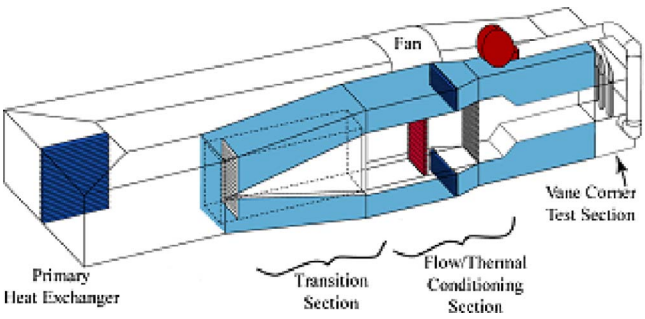

Fig. 3 Illustration of the wind tunnel facility

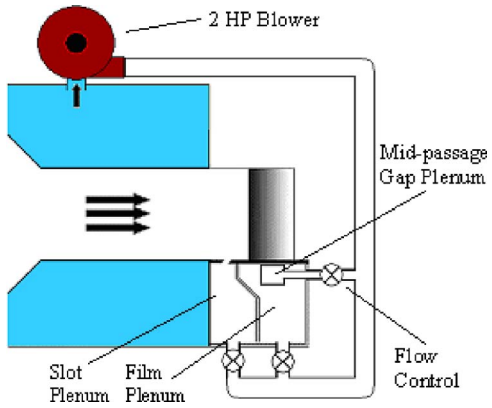

Fig. 4 Separate plenums for film-cooling, upstream slot, and mid-passage gap provided by independent flow control

The test section consisted of a vane cascade comprised of two full passages with one center vane and two half vanes, an endwall with film cooling holes, an upstream slot, and mid-passage gap geometries, which were scaled up by a factor of 9. A detailed account of its construction has been previously described by Cardwell et al. [18]. The two main differences between the current test section and the one described by Cardwell et al. [18] were a change in the upstream approach flow and the ability to vary the upstream slot metering width. The previous upstream approach flow had a 15.6 deg contraction directly upstream of the test section while the upstream flow path used in this study had a 45 deg contraction that was 2.9 chords upstream of the vane giving a longer constant flow area into the test section. The upstream slot was interchangeable so that the flow metering width could be adjusted. The endwall, which was the main focus of the study, was constructed of low thermal conductivity foam (0.033 W/m K). The endwall foam was 1.9 cm thick and was mounted on a 1.2 cm thick Lexan plate. The cooling hole pattern was cut using a five-axis water jet machine to ensure proper hole placement and tight dimensional tolerances. The upstream slot, which needed to be stiffer, was constructed of hard wood which also has a low thermal conductivity value (0.16 W/m K).

Adiabatic endwall temperatures were taken for the different slot geometries and flowrates and also for different gap flowrates. Each coolant path had its own separate plenum for independent control of the flow through the film-cooling holes, upstream slot, and mid-passage gap as shown in Fig. 4. For the studies reported in this paper, film cooling was not varied so a nominal value was set for all cases. The mid-passage gap was maintained even when no coolant was supplied to its plenum. Experiments were conducted for both a sealed and leaking mid-passage gap. Sealing of the mid-passage gap plenum was accomplished by closing the appropriate coolant feed pipe.

The inlet turbulence was measured to be 1.3%. The turbulent inlet boundary layer thickness was measured as 22% of the span at a location 15 slot widths upstream of the center vane stagnation location. During steady state operation, a temperature difference of 40°C was maintained between the mainstream and the coolant. From a room temperature start, the typical time to achieve steady state conditions was 3 h.

Coolant Flow Settings. As stated earlier, all three coolant plenums were sealed with respect to each other and had independent flow control. CFD studies reported by Knost and Thole [10] were used to set the coolant mass flows through the film-cooling holes through the use of a predicted discharge coefficient. The method previously described by Knost and Thole and Cardwell et al. [18] was used whereby a global discharge coefficient was found through CFD analysis. Only one film-cooling flowrate was used

for these studies, which was 0.5% of the core flow.

A discharge coefficient of 0.6 was chosen for the upstream slot. This is a typically assumed value for a flow through a sharp-edged orifice. No assumed discharge coefficient was needed for the mid-passage gap as the coolant flow rate was measured directly using a laminar flow element placed downstream of the coolant control valve. Feeding this plenum differently was necessary due to the high amounts of ingestion seen in the mid-passage gap, which will be explained later in the paper.

Instrumentation and Measurement Techniques. Spatially-resolved adiabatic endwall temperature contours were recorded using an FLIR P20 infrared camera. The test section had multiple viewing ports on the top endwall through which measurements were taken until the entire endwall surface was mapped. At each viewing location the camera was placed perpendicular to the endwall surface at a distance of 55 cm. Given the camera's viewing angle, each picture covered an area of 24 cm $\times$ 18 cm, with the resolution being 320×240 pixels. The camera's spatial integration was 0.16 hole diameters (0.71 mm). Postcalibration of the images was accomplished using actual temperature values taken by thermocouples placed on the endwall surface. The surface emissivity was assumed to be 0.92, which is a commonly reported value for the material type and surface structure associated with coarse grit sandpaper [23]. During postcalibration, the image background temperature was adjusted until the thermocouple data and infrared image data were within 0.01°C. Typical values of background temperature were 55°C (note the freestream temperature was typically 60°C). Six images were taken at each viewing location, of which five were used to obtain an average image using an in-house Matlab program. The same program then scales, rotates, and assembles the averaged images at all locations. This fully assembled contour gives a complete temperature distribution for the endwall surface.

Freestream temperature values were measured at 25%, 50%, and 75% of the vane span at four locations across the passage pitch. Maximum variations along the pitch and span were less than 0.5°C and 1.0°C, respectively. Three thermocouples were attached in the upstream slot plenum and two thermocouples were attached in the film cooling plenum to measure the respective coolant temperatures. Differences in temperature between the plenums were typically less than 1°C. Eleven thermocouples were placed within the mid-passage gap to measure the air temperature profile. These thermocouples were located six seal strip thicknesses beneath the endwall surface (see Fig. 2). A 32 channel data acquisition module by National Instruments was used with a 12-bit digitizing card to measure and record the thermocouple voltage data. All temperature data was recorded and compiled after the system had reached steady state.

A one-dimensional conduction correction as described by Ethridge et al. [24] was applied to all adiabatic effectiveness measurements. This correction involved measuring the endwall surface effectiveness with no coolant flow. This was accomplished by blocking off the film-cooling holes within the passage. The resulting η correction was 0.16 at the entrance for an η value of 0.9 and 0.02 at the exit region at a measured η value of 0.5.

An uncertainty analysis was performed on the measurements of adiabatic effectiveness using the partial derivative method described at length by Moffat [25]. The precision uncertainty was determined by taking the standard deviation of six measurement sets of IR camera images with each set consisting of five images. The precision uncertainty of the IR camera measurements was ±0.0143°C and the bias uncertainty was ±1.02°C, based on the calibration of the image. The precision uncertainty and bias uncertainty of the thermocouples was ±0.1°C and ±0.5°C, respectively. The total uncertainty was then calculated as ±1.02°C for the IR images and ±0.51°C for the thermocouples. Uncertainty in effectiveness, η, was found based on the partial derivative of η with respect to each temperature in its definition and the total uncertainty in the measurements. Uncertainties of $\delta\eta = \pm 0.028$ at $\eta = 0.1$ and $\delta\eta = \pm 0.028$ at $\eta = 0.8$ were calculated.

Table 3 Upstream slot coolant setting

	% mass flow	M	I
Double width slot	0.85%	0.22	0.04
	1.13%	0.29	0.08
Nominal slot width	0.75%	0.29	0.08
	0.85%	0.33	0.10
	1.00%	0.39	0.13
Half-width slot	0.38%	0.29	0.08
	0.85%	0.66	0.39

Discussion of Results

A number of tests were conducted for this study with the most representative results being given in this paper, as described in the next section on the test matrix. First, the effect of varying upstream slot width will be discussed for constant mass flow rate and a constant momentum flux ratio. Second, the effect of a fixed slot width for varying upstream slot mass flow rate will be discussed. Last, a mid-passage gap comparison with and without flow width will be discussed.

Derivation of Test Matrix. Significant consideration was given to the creation of a test matrix (shown in Table 3), which would be of particular use to the turbine designer. Mass flowrates are reported on a percent basis with respect to the total mass flowrate through the passage. For all cases, the film-cooling mass flow was set at 0.5% and, unless specified, the mid-passage gap was at 0%.

The first comparison done was for a 0.85% matched mass flow for expanding and contracting the slot width by 50%. The mass flow was kept constant by increasing or decreasing the plenum pressure accordingly, which resulted in a matched mass flow but varying momentum flux and mass flux ratios. While a sensible choice from an experimental point of view, this does not necessarily correlate to that of an actual engine.

Within the engine, the pressure difference between the coolant and exit static pressure typically remains constant resulting in a matched momentum flux ratio (given that $\Delta p \sim U^2$). The second comparison was for an average slot $I = 0.08$ while expanding and contracting the slot width 50%. Total coolant pressure to static gas pressure was held at a constant value, which resulted in nominally the same average slot velocity (and momentum flux ratio) but differing slot mass flows as the slot metering width was contracted or expanded. Next, the effect of varying slot mass flow was analyzed for the nominal slot width. The last effect to be analyzed was the mid-passage gap leakage. The mid-passage gap mass flow was set at 0.1%, 0.2%, and 0.3% of core passage flow.

Matched Mass Flow Ratios for Differing Slot Widths. For nominal slot flow rate of 0.85%, Fig. 5 compares adiabatic effectiveness for different slot widths. It is important to note that while the slot mass flow remained constant for all slot widths, the average slot momentum flux ratio changed by a factor of 10 between the half and double width slots.

The effect of expanding the slot is shown in Fig. 5(*a*). No coolant was observed exiting the upstream slot on the pressure side of the mid-passage gap. The hot ring observed on the vane's leading edge was apparent and effectiveness levels on the entire pressure side and suction side had decreased substantially relative to Fig. 5(*b*). The effect of contracting the slot is shown in Fig. 5(*c*). Figures 5(*a*) and 5(*b*) show the upstream slot coolant had been primarily confined to the suction side surface by the presence of the mid-passage gap. In Fig. 5(*c*) for the half width slot the leakage flow seems evenly distributed over the entire slot pitch with a substantial increase in cooling on the pressure side of the mid-passage gap. Film-cooling holes upstream of the vane stagnation are redundant and the hot ring around the vane pressure

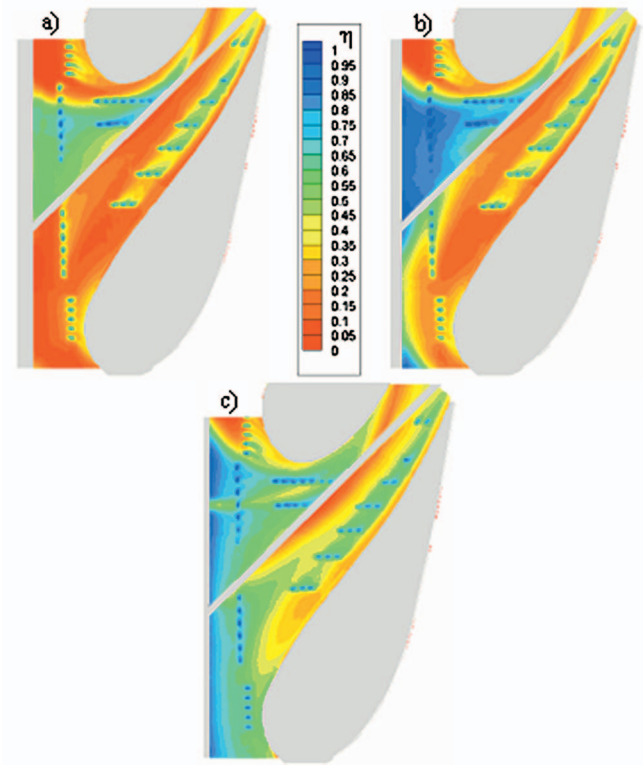

Fig. 5 Contours of adiabatic effectiveness for (*a*) double, (*b*) nominal, (*c*) half-width upstream slot with 0.85% slot mass flow ratio

side shown in other cases which extends from the leading edge into the passage is no longer apparent. More even cooling was observed on the mid-passage gap suction side as well in Fig. 5(*c*), while the locally high values of effectiveness seen using the nominal upstream slot width (Fig. 5(*b*)) were less apparent.

Pitchwise averaged values of effectiveness for varied slot width with matched mass flow ratios are shown in Fig. 6. Expanding the slot shows a decrease in averaged effectiveness levels along much of the platform while contracting the slot increases the averaged effectiveness. This can be explained by the contours shown in Fig. 5 where the coverage area was greater in Fig. 5(*c*) and more localized in Fig. 5(*a*). The contracted slot shows better coolant coverage than nominal with higher averaged effectiveness levels than both the nominal and double-width slot. This result is expected based on the viewpoints of coolant momentum and mass flow (see Table 3). The higher plenum pressure required to supply

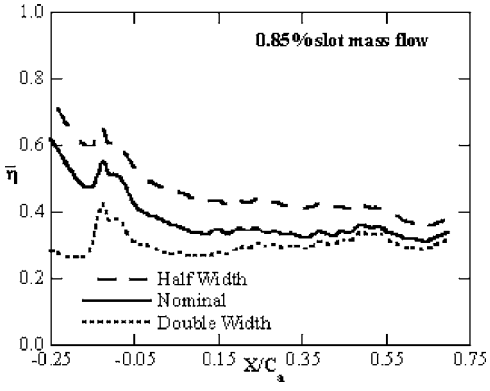

Fig. 6 Pitchwise averaged adiabatic effectiveness for the entire passage with varied upstream slot widths

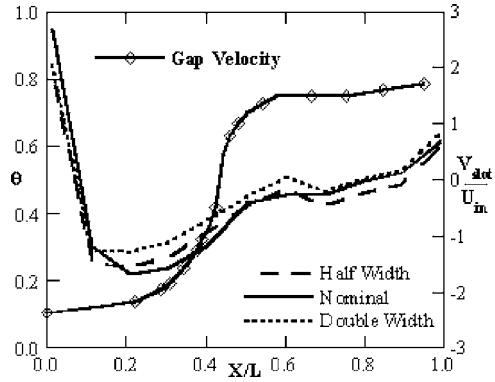

Fig. 7 Nondimensionalized mid-passage gap temperature profiles with varied upstream slot widths

0.85% from the contracted slot has resulted in an increase in the coverage uniformity. This improvement in uniformity can be explained by considering that with a higher plenum pressure there is less sensitivity to the exit static pressure variation due to the presence of the vane. For the expanded slot, lower plenum pressures are required to supply 0.85% mass flow thereby resulting in more sensitivity to the exit static pressure.

Through observation of Fig. 5(*a*) it was concluded that a portion of the slot was ingesting hot mainstream air since no coolant was observed exiting the slot on the mid-passage gap pressure side. Therefore, the ejected coolant on the suction side was already premixed with hot main gas within the upstream slot, which explains the strong reduction in averaged effectiveness levels for the expanded slot.

Mid-passage gap temperature profiles are shown in Fig. 7. This information is important as turbines are typically designed so that ingestion of hot mainstream gas into the gaps is minimized. The nondimensional gap temperature, θ, was based on the mainstream and the coolant temperatures where θ values of zero and one signify maximum and minimum gap temperatures, respectively. Again, Fig. 2 illustrates the thermocouple location for the mid-passage gap. Also shown in Fig. 7 are the calculated inviscid gap velocities based on the local static pressure at the gap exit, which was known from previous studies [26]. Note that this calculation assumed a constant total plenum pressure difference between the mainstream and the gap plenum. An iterative procedure was used to calculate the pressure difference which resulted in zero net mass flow from the slot (ingested flow equals ejected flow). For zero net mass flow through the mid-passage gap, negative velocity values (signifying ingestion) were predicted for $X/L<0.45$ and positive velocity values (signifying ejection) were predicted for $X/L>0.45$.

The gap leading edge ingested a substantial amount of coolant from the upstream slot. In the location $0<X/L<0.2$, this ingested coolant resulted in cooler temperatures with the amount of coolant being ingested decreasing with increasing X/L. There was also increased ingestion of the hot mainstream flow which caused a rapid increase in the gap air temperature. Temperature in the gap increased dramatically as hot mainstream flow was ingested at $X/L<0.2$. The increase in θ observed at $X/L=0.2$ was most likely caused by ingestion of fresh coolant from film-cooling holes in the vicinity of $X/L=0.2$ as well as continued mixing of previously ingested upstream slot coolant and main gas. This mixture of coolant and hot mainstream gas convects inside the mid-passage gap until the exit static pressure is low enough for it to exit the gap. Up to $X/L=0.45$, the inviscid velocity is indicated to be into the slot (static endwall pressure is higher than the plenum pressure), which is consistent with the fact that flow is ingesting into the gap. Beyond $X/L=0.45$, Fig. 7 shows that flow is exiting the mid-passage gap.

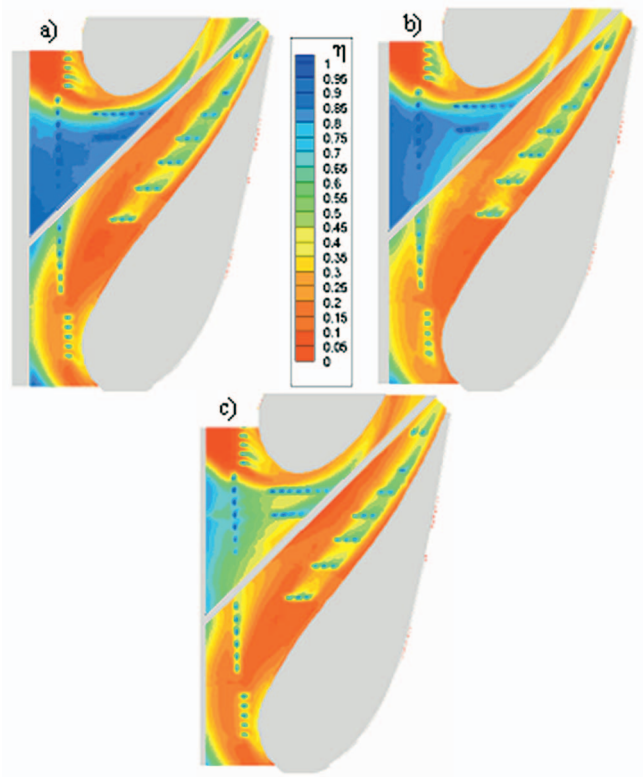

Fig. 8 Contours of adiabatic effectiveness for (*a*) double, (*b*) nominal, (*c*) half-width upstream slot with *I*=0.08 average slot momentum flux ratio

All θ profiles for varying slot width in Fig. 7 are very similar to values slightly lower for both the double and half-width upstream slots. Since the coolant exiting the half-width slot has a relatively high momentum compared with the nominal, it is less likely that it will be ingested into the mid-passage gap than for the double-width slot.

Matched Momentum Flux Ratios for Differing Slot Widths. Upstream slot momentum flux ratios were matched to an average value of $I=0.08$, which corresponded to a nominal width upstream slot flow of 0.75%. As shown previously, the upstream slot width was contracted and expanded by 50%. There was 0% flow in the mid-passage gap.

Figure 8 shows contours of adiabatic effectiveness and Fig. 9 shows pitchwise averaged values of adiabatic effectiveness on the endwall for an average upstream slot momentum flux ratio of

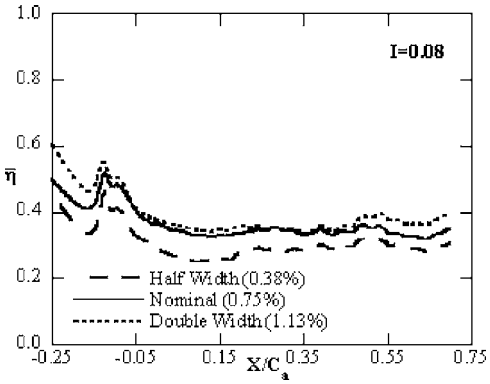

Fig. 9 Plots of pitchwise averaged adiabatic effectiveness for the entire passage with varied slot widths

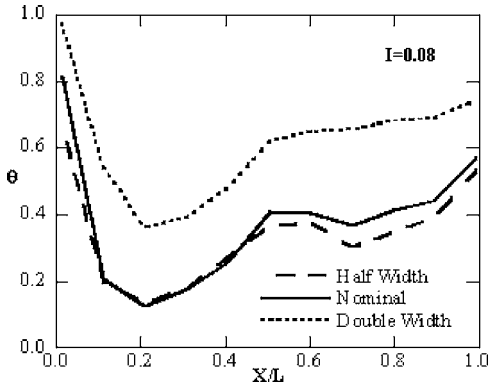

Fig. 10 Nondimensionalized mid-passage gap temperature profiles varied upstream slot widths given a nominal slot momentum flux ratio

0.08. The coolant coverage area is very similar for all three slot widths, illustrating that coverage area is a function of the coolant to mainstream momentum flux ratios rather than the coolant mass flow rate. By contracting the slot and keeping the plenum-to-mainstream pressure difference the same, the mass flow of coolant exiting the upstream slot was reduced (see Table 3). This reduction in coolant flow explains the observed reduction in effectiveness on the suction side platform and the lower values of averaged effectiveness. By the same reasoning, the coolant mass flow would be higher for the expanded slot, thus explaining the increase in averaged coolant effectiveness on the suction side platform.

Figure 8 shows there is also an effect of slot width on the mid-passage gap trailing edge. In this region, the mid-passage gap ejects a mixture of the coolant and main gas which was ingested in the leading edge region. A slight increase in effectiveness levels for the nominal and double slot cases relative to the half slot width were observed on the suction side of the mid-passage gap trailing edge. The cooler region near the trailing edge indicates different amounts of coolant were being ingested into the mid-passage gap near the leading edge and then ejected near the trailing edge. Upstream slot momentum flux was the same for all cases, but coolant mass flow was higher for the double slot and lower for the half slot.

By examining the mid-passage gap temperature profiles in Fig. 10, we see that by matching the upstream slot coolant momentum flux ratios the amount of coolant being ingested into the mid-passage gap changed with slot width. Expanding the slot width dramatically decreased gap temperature, sometimes by as much as 70% from nominal. The effect of contracting the slot is not observed until $X/L=0.45$, where ejecting mid-passage gap temperatures were observed to be 10–20% lower.

Adiabatic Effectiveness With Varying Slot Leakage Flows. For a constant upstream slot width and a varying difference between the coolant and the mainstream static pressures, the coolant flow rate exiting the slot varies. To determine this effect, tests were conducted, as before, with no mid-passage gap flow and upstream slot mass flow rates were set to 0.75%, 0.85%, and 1.0%. The effect of varying upstream slot flowrate was analyzed for a nominal slot width. Contours of adiabatic effectiveness for the effect of coolant mass flux ratio are shown in Fig. 11.

The primary result was that for all three cases the coverage area had not changed significantly but the cooling benefit had increased. It is important to note that upstream slot momentum flux ratio increased with slot mass flow by a factor of 1.6 from the lowest to highest slot flowrate studied. This increase was much smaller than the factor of 10 discussed in the previous section. For each case, there was very little coolant flow from the upstream slot crossing over the mid-passage gap as shown before by Card-

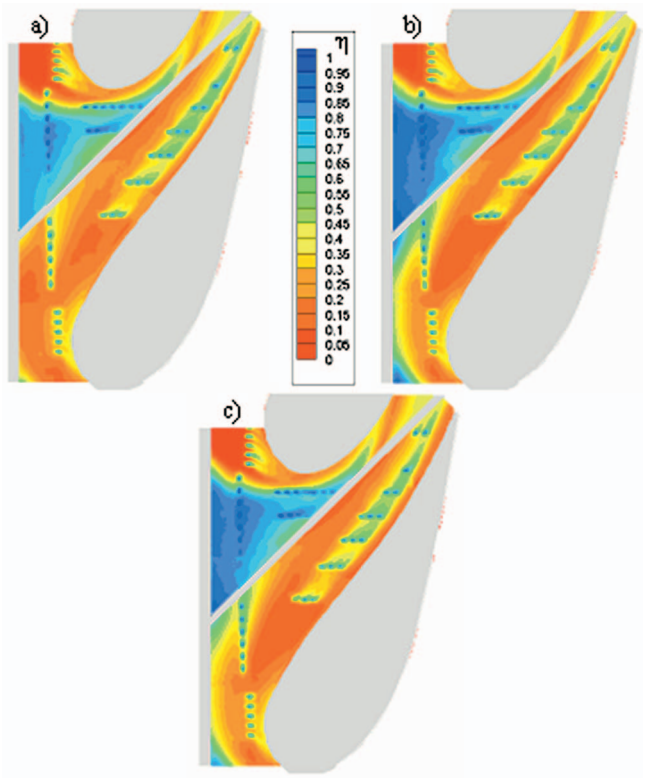

Fig. 11 Contours of adiabatic effectiveness for (*a*) 0.75%, (*b*) 0.85%, (*c*) 1.0% upstream slot mass flow rate for a nominal slot width

well et al. [18]. The coolant convected along the gap until the end of the vane passage where it exited the gap. The effect of film-cooling was also nominally the same for all upstream slot flows. As the slot mass flow rate was increased, the amount of coolant observed on the pressure side of the slot increased slightly. The suction side of the gap, which was well cooled for all flow rates, showed higher adiabatic effectiveness levels when the slot flow rate was increased. Although the coolant mass flow rate through the slot was increased substantially, much of the pressure side endwall continued to show lower values of adiabatic effectiveness. To quantify the effect of increasing slot flow at these levels, the adiabatic effectiveness values were pitchwise averaged for all flow rates, as shown in Fig. 12. Increasing the upstream slot cooling showed increased values of pitchwise averaged adiabatic

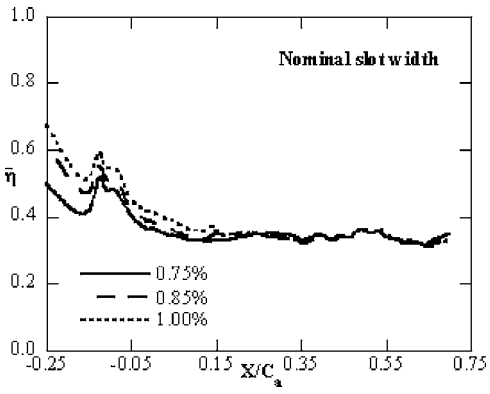

Fig. 12 Plots of laterally averaged adiabatic effectiveness for the entire passage with varied upstream slot mass flow

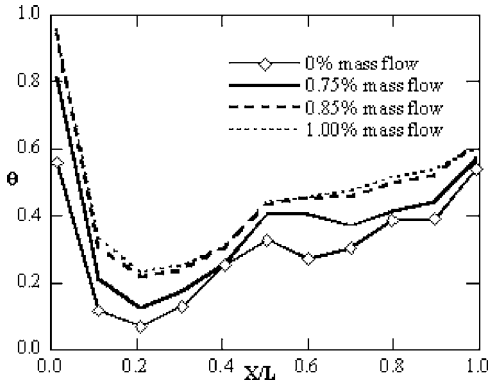

Fig. 13 Nondimensionalized mid-passage gap temperature profiles varied upstream slot mass flow

effectiveness.

Since there was more coolant on the endwall for increased upstream slot leakage, it was hypothesized that more coolant was being ingested into the mid-passage gap. The measured nondimensional gap temperature profiles for the above mentioned cases are shown in Fig. 13. Note that again, no coolant mass flow was provided to the gap. The increase in slot flow rate from 0.75% to 0.85% showed a substantial decrease in gap temperatures. The ratio of ingested coolant to hot gas was higher, thus explaining the decrease in ejected gap temperatures beyond $X/L=0.45$. In contrast, negligible changes in gap temperatures were recorded for the increase to 1% upstream slot flow. Most likely the gap was saturated with coolant from the upstream slot at the 1% case.

Adiabatic Effectiveness Varying Mid-Passage Gap Flows. The last comparison completed for this study was for a variation in the mid-passage gap leakage. These experiments were conducted with a nominal upstream slot width and a 0.75% upstream slot mass flow rate ($I=0.08$). Mid-passage gap mass flow rates were set to 0.1%, 0.2%, and 0.3%.

The contours of adiabatic effectiveness for the varying gap flows are shown in Fig. 14. These contours are very similar to each other with no large effect due to varied mid-passage gap flow. As before, the contours were pitchwise averaged, which is shown in Fig. 15. No effect is observed in the leading edge region of the slot. It appears that the mid-passage gap flow has little to no effect on the endwall surface for the entire passage in this flow rate range. The presence of the gap, however, does affect the endwall effectiveness patterns relative to a continuous endwall as previously described by Cardwell et al. [18].

There was a slight effect of the coolant flow rate on the nondimensional temperature distribution within the gap. Figure 16 shows the nondimensional gap temperature profiles for the three cases as compared to the no flow case. As compared to the no gap flow condition, the gap temperature was lower relative to all values of coolant mass flow. Increasing the mid-passage gap flow rate reduced the temperature measured within the gap for $0.45<X/L<1$. For between $0.45<X/L<1$, decreases in gap temperatures were observed for increases in mid-passage gap flow. Note that the ejected fluid was a mixture of ingested upstream slot coolant, ingested main gas, and mid-passage gap coolant.

Figure 17 shows thermal field profiles which were taken within the passage for 0% and 0.3% mid-passage gap flow. The measurement plane was located at $s/C=0.5$, which is illustrated by the dashed line in Fig. 1. There was little change in the passage temperature profiles indicating little change in the secondary flows. Again as previously noted when comparing gap temperature profiles, the interaction of the mid-passage gap was only slightly affected by changes in leakage flow and was primarily driven by the endwall static pressure distribution throughout the passage.

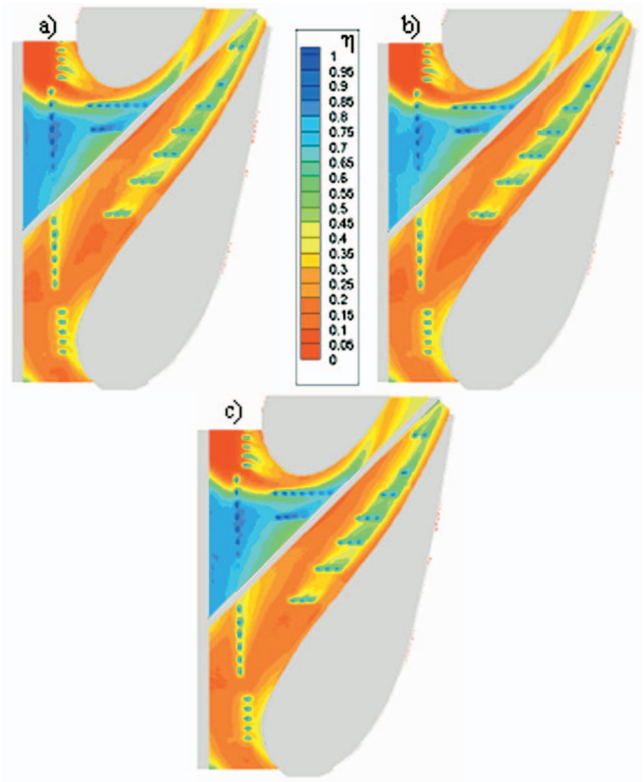

Fig. 14 Contours of adiabatic effectiveness for (*a*) 0.1%, (*b*) 0.2%, and (*c*) 0.3% mid-passage gap mass flow with nominal upstream slot width

Conclusions

Measurements of endwall adiabatic effectiveness and nondimensional mid-passage gap temperature profiles were presented for a double, nominal, and half-width combustor to turbine interface. Two parameters were used to compare the different configurations: mass flow and momentum flux ratios.

When comparing varying slot width while matching mass flow, it was observed that decreasing the slot width caused the coolant to be more evenly distributed on the endwall. Increasing the slot width while matching mass flow indicated a reduced coverage with no coolant observed on the pressure side of the passage. Moreover, the effectiveness values on the suction side were lower that those observed at the same flow rate for a nominal slot width. This decrease was caused by ingesting hot mainstream gas. Averaged effectiveness values were found to be the lowest for the double slot relative to the nominal and half-width.

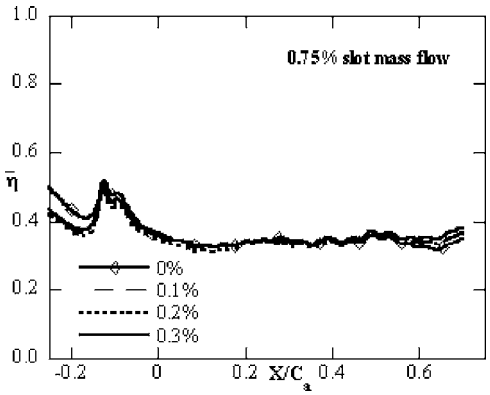

Fig. 15 Plots of laterally averaged adiabatic effectiveness for the entire passage with varied mid-passage gap cooling

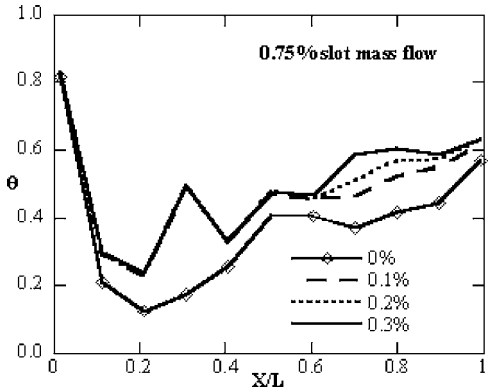

Fig. 16 Nondimensionalized mid-passage gap temperature profiles with varied mid-passage gap cooling

Matching the slot momentum flux ratios for the three slot widths resulted in endwall contours that looked nominally the same in terms of upstream slot coolant coverage. These results indicated that the upstream coolant coverage area was a function of momentum flux ratio, not mass flow rate. The cooling from the upstream slot had a beneficial effect only along the suction side endwall surface. Doubling the slot width resulted in better endwall cooling on the suction side platform and significantly lowered temperatures within the mid-passage gap. Given the same slot momentum flux ratio, halving the slot resulted in less coolant mass flow and higher temperatures within the gap.

With a nominal width, increasing upstream slot cooling resulted in improved endwall adiabatic effectiveness values and lower gap temperatures. Even at 1.0% mass flow, the upstream coolant momentum was still too low to adequately cool the pressure side platform due to the presence of the ingesting mid-passage gap.

Mid-passage gap leakage flows proved to have little effect on endwall adiabatic effectiveness levels, though gap temperatures were lower for increased leakage flows. Since the gap plenum was ingesting, it was at an equilibrium pressure somewhere between the passage inlet static wall pressure, which was higher, and the passage exit static wall pressure, which was lower. By introducing coolant flow to the gap plenum, the temperature of the gap fluid was effectively lowered while the equilibrium pressure stayed nominally the same. Thus it would require much higher coolant pressure to significantly affect the mid-passage gap velocity distribution.

These results indicate that the leakage through the combustor-turbine interface can provide cooling to the endwall. Since this interface width changes as the turbine and combustor heat up, it is important to account for the associated changes in coolant cover-

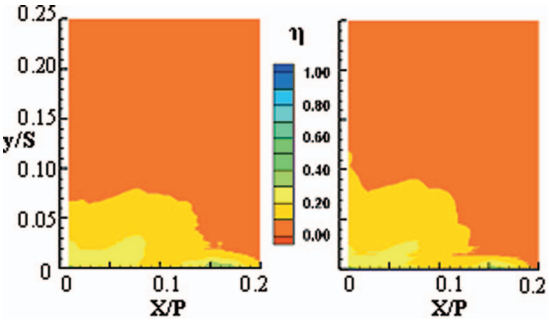

Fig. 17 Plots of thermal field data for (*a*) 0% flow and (*b*) 0.3% flow within the mid-passage gap

age area and local coolant levels thereby reducing the need for film-cooling on certain areas of the vane-endwall surface.

Acknowledgment

This publication was prepared with the support of the U.S. Department of Energy, Office of Fossil Fuel, and National Energy Technology Laboratory and the South Carolina Institute for Energy Studies (SCIES) University Turbine Systems Research program (UTSR). However, any opinions, findings, conclusions, or recommendations expressed herein are solely those of the authors and do not necessarily reflect the views of the DOE, SCIES, or the UTSR Program. The authors would also like to thank Mike Blair (Pratt & Whitney), Ron Bunker (General Electric), and John Weaver (Rolls Royce) for their input on the modeling of realistic turbine features.

Nomenclature

C = true chord of stator vane
C_a = axial chord of stator vane
D = diameter of film-cooling hole
I = average momentum flux ratio, $I=(\rho_c U_c^2/\rho_\infty U_\infty^2) = \rho_s(\dot{m}/\rho_s A_s)^2/\rho_\infty U_\infty^2$
L = length of mid-passage gap
$\dot{m}$ = mass flowrate
M = average blowing ratio
p = static pressure
P = vane pitch, hole pitch
Re_{in} = Reynolds number, $\mathrm{Re}_{in}=\mathrm{CU}_{in}/\nu$
S = span of stator vane
T = temperature
X = local coordinate
U = velocity
s = distance along vane from flow stagnation

Greek

η = adiabatic effectiveness, $\eta=(T_\infty-T_{aw})/(T_\infty-T_c)$
ρ = density
ν = kinematic viscosity
θ = nondimensional gap effectiveness, $\theta=(T_\infty-T_G)/(T_\infty-T_c)$

Subscripts

aw = adiabatic wall
c = coolant conditions
G = gap air temperature
in = inlet conditions
s = upstream slot
∞ = freestream conditions

References

[1] Electronic Space Products International "Inconel 625," http://www.espimetals.com/tech/Tech%20Inconel%20625.htm (Ashland, OR).
[2] Blair, M. F., 1974, "An Experimental Study of Heat Transfer and Film-Cooling on Large-Scale Turbine Endwall," ASME J. Heat Transfer, **96**, pp. 524–529.
[3] Burd, S. W., Satterness, C. J., and Simon, T. W., 2000, "Effects of Slot Bleed Injection Over a Contoured Endwall on Nozzle Guide Vane Cooling Performance: Part II—Thermal Measurements," ASME Paper No. 2000-GT-200.
[4] Colban, W. F., Thole, K. A., and Zess, G., 2002, "Combustor-Turbine Interface Studies: Part 1: Endwall Measurements," J. Turbomach., **125**, pp. 193–202.
[5] Colban, W. F., Lethander, A. T., Thole, K. A., and Zess, G., 2002, "Combustor-Turbine Interface Studies: Part 2: Flow and Thermal Field Measurements," J. Turbomach., **125**, pp. 203–209.
[6] Pasinato, H. D., Squires, K. D., and Roy, R. P., 2004, "Measurement and Modeling of the Flow and Heat Transfer in a Contoured Vane-Endwall Passage," Int. J. Heat Mass Transfer, **47**, pp. 5685–5702.
[7] Zhang, L. J., and Jaiswal, R. S., 2001, "Turbine Nozzle Endwall Film-Cooling Study Using Pressure Sensitive Paint," J. Turbomach., **123**, pp. 730–738.
[8] Kost, F., and Nicklas, M., 2001, "Film-Cooled Turbine Endwall in a Transonic Flow Field: Part I—Aerodynamic Measurements," ASME Paper No. 2001-GT-0145.
[9] Nicklas, M., 2001, "Film-Cooled Turbine Endwall in a Transonic Flow Field: Part II—Heat Transfer and Film-Cooling Effectiveness," J. Turbomach., **123**, pp. 720–729.
[10] Knost, D. G., and Thole, K. A., 2003, "Computational Predictions of Endwall Film-Cooling for a First Stage Vane," ASME Paper No. GT2003-38252.
[11] Knost, D. G., and Thole, K. A., 2005, "Adiabatic Effectiveness Measurements of Endwall Film-Cooling for a First Stage Vane," J. Turbomach., **127**, pp. 297–305.
[12] Aunapu, N. V., Volino, R. J., Flack, K. A., and Stoddard, R. M., 2000, "Secondary Flow Measurements in a Turbine Passage With Endwall Flow Modification," J. Turbomach., **122**, pp. 651–658.
[13] Ranson, W., Thole, K. A., and Cunha, F., 2005, "Adiabatic Effectiveness Measurements and Predictions of Leakage Flows Along a Blade Endwall," J. Turbomach., **127**, pp. 609–618.
[14] Yamao, H., Aoki, K., Takeishi, K., and Takeda, K., 1987, "An Experimental Study for Endwall Cooling Design of Turbine Vanes," IGTC-1987, Tokyo, Japan.
[15] Piggush, J. D., and Simon, T. W., "Flow Measurements in a First Stage Nozzle Cascade Having Endwall Contouring, Leakage, and Assembly Features," ASME Paper No. GT2005-68340.
[16] Piggush, J. D., and Simon, T. W., 2005, "Flow Measurements in a First Stage Nozzle Cascade Having Leakage and Assembly Features: Effects of Endwall Steps and Leakage on Aerodynamic Losses," ASME Paper No. IMCE2005-83032.
[17] Reid, K., Denton, J., Pullan, G., Curtis, E., and Longley, J., "The Interaction of Turbine Inter-Platform Leakage Flow With the Mainstream Flow," ASME Paper No. GT2005-68151.
[18] Cardwell, N. D., Sundaram, N., and Thole, K. A., 2006, "Effects of Mid-Passage Gap, Endwall Misalignment and Roughness on Endwall Film-Cooling," J. Turbomach., **128**, pp. 62–70.
[19] de la Rosa, Blanco E., Hodson, H. P., and Vazquez, R., "Effect of Upstream Platform Geometry on the Endwall Flows of a Turbine Cascade," ASME Paper No. GT2005-68938.
[20] Radomsky, R., and Thole, K. A., 2002, "Detailed Boundary Layer Measurements on a Turbine Stator Vane at Elevated Freestream Turbulence Levels," J. Turbomach., **124**, pp. 107–118.
[21] "Sandpaper—Coated Abrasives," www.sizes.com/tools/sandpaper.htm (11 August 2004).
[22] Bons, J. P., Taylor, R. P., McClain, S. T., and Rivir, R. B., 2001, "The Many Faces of Turbine Surface Roughness," J. Turbomach., **123**, pp. 739–748.
[23] Modest, M. F., 2003, *Radiative Heat Transfer*, 2nd ed., pp. 743–758.
[24] Ethridge, M. I., Cutbirth, J. M., and Bogard, D. G., 2000, "Scaling of Performance for Varying Density Ratio Coolants on an Airfoil With Strong Curvature and Pressure Gradients," J. Turbomach., **123**, pp. 231–237.
[25] Moffat, R. J., 1988, "Describing the Uncertainties in Experimental Results," Exp. Therm. Fluid Sci., **1**, pp. 3–17.
[26] Kang, M., Kohli, A., and Thole, K. A., 1999, "Heat Transfer and Flowfield Measurements in the Leading Edge Region of a Stator Vane Endwall," J. Turbomach., **121**(3), pp. 558–568.

Influence of Aerodynamic Loading on Rotor-Stator Aerodynamic Interaction in a Two-Stage Low Pressure Research Turbine

Edward Canepa
e-mail: edward.canepa@unige.it

Piergiorgio Formosa
e-mail: piergiorgio.formosa@unige.it

Davide Lengani
e-mail: davide.lengani@unige.it

Daniele Simoni
e-mail: daniele.simoni@unige.it

Marina Ubaldi
e-mail: zunmp@unige.it

Pietro Zunino
e-mail: pietro.zunino@unige.it

DIMSET—Università di Genova,
I-16145 Genova, Italy

The unsteady flow within a two-stage low-pressure research turbine equipped with high lift profiles has been investigated in detail for three different aerodynamic loading conditions. Experiments have been carried out at low speed. Velocity and turbulence intensity in the blade-to-blade plane at midspan have been measured by means of a crossed hot-wire probe, upstream and downstream of each blade row. The probe has been traversed circumferentially over 1.5 bladings pitch and the phase-locked data acquisition and ensemble average technique have been used to reconstruct the flow in space and time. The effects of multistage configuration have been identified and analyzed by considering the velocity components and turbulence intensity. Potential interaction from the downstream blading in relative motion, periodic wake perturbations from the upstream blading and preceding stage perturbations make the flow in the second stage extremely complex. Overall the flow downstream of rotors is perturbed in space by upstream and downstream stators, while flow downstream of stators is mostly perturbed in time by rotor effects. As expected, high lift profiles are significantly sensitive to incidence variation, with this effect further enhanced by the multistage cumulative interactions.
[DOI: 10.1115/1.2720498]

Introduction

In modern aeroengines the reduction of fuel consumption and consequently CO_2 emissions mainly depend on the possibility to increase the bypass ratio and the propulsion efficiency. The fan of a high bypass ratio turbofan engine generates up to 80% of the global thrust and the required power is supplied by the LP turbine. This is the reason why the LP turbine efficiency has a large impact on the entire engine efficiency. This single component is often also the heaviest of the entire engine.

Hence the chance to reduce the LP turbine weight, while maintaining the same efficiency level, becomes very interesting both for manufacturers and customers. It can be achieved by using high lift or ultrahigh lift profiles [1], characterized by large pitch to chord ratio and Zweifel lift coefficient close to unity, which lead [2] to a reduction of the number of blades up to 20%.

Unfortunately LP turbines in cruise conditions work at low Reynolds numbers, typically in the range between 0.8×10^5 and 3.0×10^5, where the high diffusion levels occurring in the rear of the profile may lead the suction side boundary layer to separate massively, determining a dramatic LP turbine performance breakdown [3].

Moreover because of the large blade aspect ratios typical of LP turbines, profile losses are the largest portion of the total [4]. Such losses depend upon the boundary layer development and changes on both the transition onset location and transition mechanism can influence significantly the aerodynamic performance of the bladings.

Hence the possibility to employ high lift profiles requires a deep knowledge of the steady and unsteady flow phenomena occurring in a real LP turbine environment, which can affect the profile behavior.

Aerodynamic rotor-stator interaction is the main cause of unsteadiness in turbomachines working at nominal conditions. Both viscous and potential effects determine a nonuniform flow field at the outlet of a blade row. Such spatial perturbations become periodic unsteady inlet flow conditions for the following blade row, which is in relative motion. The potential effect of a blade extends both upstream and downstream, and at low Mach numbers decays exponentially in a chord or pitch order length [5]. Differently viscous wake effects are convected downstream and show a longer permanence in the flow.

Generally unsteady perturbations determine an increase in the stage loss compared to the ideal steady case. Sometimes these perturbations may have a positive effect, as it happens when a turbulent perturbation determines an earlier boundary layer transition before laminar separation takes place [6–8]. This is the case of high lift profiles used in LP turbines at low Reynolds number operation.

Currently turbine design is carried out by means of three-dimensional steady calculation models, even if unsteadiness is a major characteristic in a real turbine flow environment. Loss-generating mechanism models for unsteady flows are not completely developed at the moment, and empirical correlations are used to take into consideration unsteady effects. Indeed, an increased knowledge of the rotor-stator interactions is required in order to improve the performance of turbines.

The present work main objective is to analyze the rotor-stator interactions for different profile loading conditions in a multistage research turbine.

Contributed by the International Gas Turbine Institute of ASME for publication in the JOURNAL OF TURBOMACHINERY. Manuscript received July 24, 2006; final manuscript received August 4, 2006. Review conducted by David Wisler. Paper presented at the ASME Turbo Expo 2006: Land, Sea and Air (GT2006), May 8–11, 2006, Barcelona, Spain. Paper No. GT2006-90753.

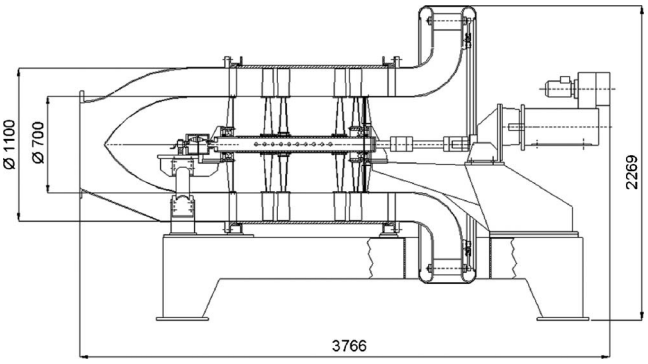

Fig. 1 Meridional section of the turbine model

Table 1 Turbine and blade parameters

	Stator	Rotor
Number of blades	30	30
Chord length at midspan c	120 mm	120 mm
Blade span l	200 mm	200 mm
Blade pitch at midspan g	94.2 mm	94.2 mm
Aspect ratio l/c	1.66	1.66
Pitch to chord ratio g/c	0.785	0.785
Inlet blade angle α_1, β_1	−37.7 deg	63.2 deg
Outlet blade angle α_2, β_2	63.2 deg	−37.7 deg
Inner diameter D_i	700 mm	
Outer diameter D_o	1100 mm	
Tip clearance	0.8 mm	
Stator/rotor axial gap	38 mm	

Test Facility and Experimental Procedure

Axial Flow Turbine. Measurements have been performed on a large-scale low-speed two-stage axial flow research turbine (Fig. 1), designed and built with the purpose of investigating unsteady flow phenomena representative of a low pressure gas turbine. It consists of four rows of unshrouded blades, which can be moved both axially and circumferentially, in order to allow gapping and clocking. Atmospheric air, used as working fluid, is fed by a centrifugal fan located downstream of the turbine. The fan is driven by a 60 kW electric motor, and the turbine shaft is braked by means of a 40 kW dc. reversible electric motor. Both motors are equipped with a variable speed electronic control. A variable stagger angle centripetal flow distributor is adopted to generate a preswirled flow upstream of the first stator, in order to obtain repetitive conditions and to vary the operational point. Operating conditions can be varied continuously acting on both the rotational speed and the guide vane stagger angle.

The stator rows are equipped with MTU T106 prismatic blade profile stacked on the trailing edge. The rotors have twisted blades, designed to obtain an outlet flow similar to the one generated by the distributor at the turbine inlet. All the blades are made of epoxy resin in order to allow the use of hot-film instrumentation minimizing the conductive heat exchange from the sensors. The two stages are repetitive.

The outer casing is plexiglas-made and can be independently rotated. In the upper part a longitudinal opening has been obtained, where modular caps may be fitted, allowing probes insertion or optical access. A photograph of the blade rows is shown in Fig. 2.

Probe positioning in axial and radial directions is obtained by means of a two-axis traversing system mounted on the top of the casing. Circumferential positioning is obtained by casing rotation. All the three movements are computer controlled with minimum steps of 10 μm.

The main turbine and blade geometrical parameters are reported in Table 1. The meridional channel mean diameter is 900 mm. Chord-based Reynolds number can be continuously varied from 50,000 up to 500,000. The bladings can be axially moved within a range of 925 mm.

At design operating conditions the rotational speed is 450 rpm and the mass flow rate is 11.8 kg/s, with a total pressure drop of 1200 Pa per stage and an overall power of 24 kW.

The stages configuration is symmetric at midspan and is provided with MTU T106 blade profiles for which extensive cascade investigations can be found in the literature [9,10]. At nominal conditions the Zweifel coefficient is 1.055.

The experiments reported in this paper have been performed at constant chord based Reynolds number equal to 200,000. Three different conditions of aerodynamic loading on the profiles have been adopted and obtained by varying the incidence angle, i.e., the rotational speed. The incidence values considered are equal to $i = +3, -5, -10$ deg, corresponding to high, intermediate, and low loading conditions. The respective rotational speeds are $\omega = 110$, 180, 260 rpm.

The first stator inlet flow angle was kept constant and equal to the nominal value $\alpha_0 = -37.7$ deg.

Measuring Techniques. Velocity components have been measured by means of a two-component crossed miniature hot-wire probe (Dantec P64) connected to a six-channel Dantec Streamline CTA system. A Metrabyte DAS 58 sample and hold AD converter board has been used for data sampling. The signal has been low pass filtered at 20 kHz. The instantaneous velocity components are determined by using the directional calibration and noniterative hot-wire analysis procedure of Schroeder [11].

Measurements have been performed at midspan in 60 equally spaced circumferential points, covering 1.5 blade vanes, in 5 axial positions upstream and downstream of each blade row (Fig. 3). A phase-locked acquisition technique, driven by the shaft encoder, has been used in order to collect a total number of 150,000

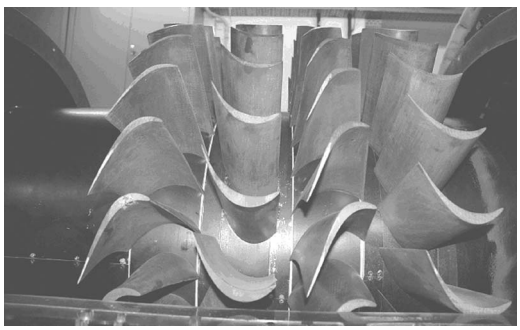

Fig. 2 Two-stage low-pressure turbine bladings

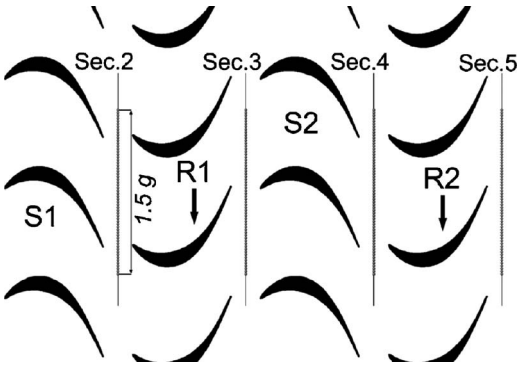

Fig. 3 Measuring point locations

samples in each measuring point. The two-dimensionality of the flow at midspan has been previously verified for the three loading conditions, through measurements carried out using a 5-hole aerodynamic probe. In the worst case (high loading condition) the ratio between the radial and axial velocity components was about 0.08. However, especially at high loading, the secondary flows have a significant effect on the flow distribution all over the blade span, therefore caution should be exercised when interpreting results with 2D models.

Experimental Procedure. The ensemble average technique [12] has been applied to separate periodic oscillations associated with the blade passing frequency from random fluctuations. The reference signal has been derived from the shaft encoder.

A generic instantaneous quantity (i.e., velocity component) is a function of time (t_j) or rotor circumferential coordinate, of the data record (n) and of the stationary probe circumferential position with respect to the stator vane (θ_k).

The equations defining the ensemble average procedure are as follows:

- instantaneous quantity

$$q(t_j,\theta_k,n) = \tilde{q}(t_j,\theta_k) + q'(t_j,\theta_k,n)$$

- ensemble-averaged quantity

$$\tilde{q}(t_j,\theta_k) = \frac{1}{N}\sum_{n=1}^{N} q(t_j,\theta_k,n)$$

- root mean square of the random unsteady fluctuations

$$\mathrm{r\tilde{m}s}(q) = \sqrt{\tilde{q'^2}(t_j,\theta_k)} = \sqrt{\frac{1}{(N-1)}\sum_{n=1}^{N}[q(t_j,\theta_k,n) - \tilde{q}(t_j,\theta_k)]^2}$$

- skewness coefficient

$$\tilde{S}k(q) = \frac{\frac{1}{N}\sum_{n=1}^{N}[q(t_j,\theta_k,n) - \tilde{q}(t_j,\theta_k)]^3}{[\mathrm{r\tilde{m}s}(q)]^3}$$

For present investigations typical data acquisition parameters are as follows: number of data for each rotor blade passage, $I=100$; number of measured contiguous blade passages, $z=6$; dimension of each sampled record, $J=zI=600$; number of rotor revolutions, $N=250$.

Experimental uncertainties for the x-wire probes measurements and the noniterative hot-wire analysis method employed were evaluated in detail in [11]. Systematic errors are ±1% for the instantaneous velocity magnitude, and ±1 deg for the yaw angle.

Statistical uncertainties of ensemble averaged quantities due to finite number of samples, evaluated with a confidence level of 95%, a turbulence intensity of 20%, and a number of 250 samples, are as follows: $\varepsilon_c = \pm 2.5\%$, $\varepsilon_{c'} = \pm 7.4\%$.

The dimension of the probe volume is approximately 1 mm $\times$ 1 mm $\times$ 1 mm, while the dimension of the apparent probe volume due to rotor measurements in the absolute frame of reference is less than 0.5 mm.

Results and Discussion

Space-time contour plots have been adopted in order to analyze the blade row interaction effects on the flow at midspan (see, for example, Fig. 4). The normalized circumferential probe position in the absolute frame of reference y/g is plotted on the horizontal axis, while the normalized time scale t/T is plotted on the vertical one.

For each section the displayed quantities are: velocity, flow angle, and turbulence intensity defined as $\tilde{\mathrm{Tu}} = \sqrt{(\tilde{c_a'^2} + \tilde{c_t'^2})/2}/\bar{c}_a$.

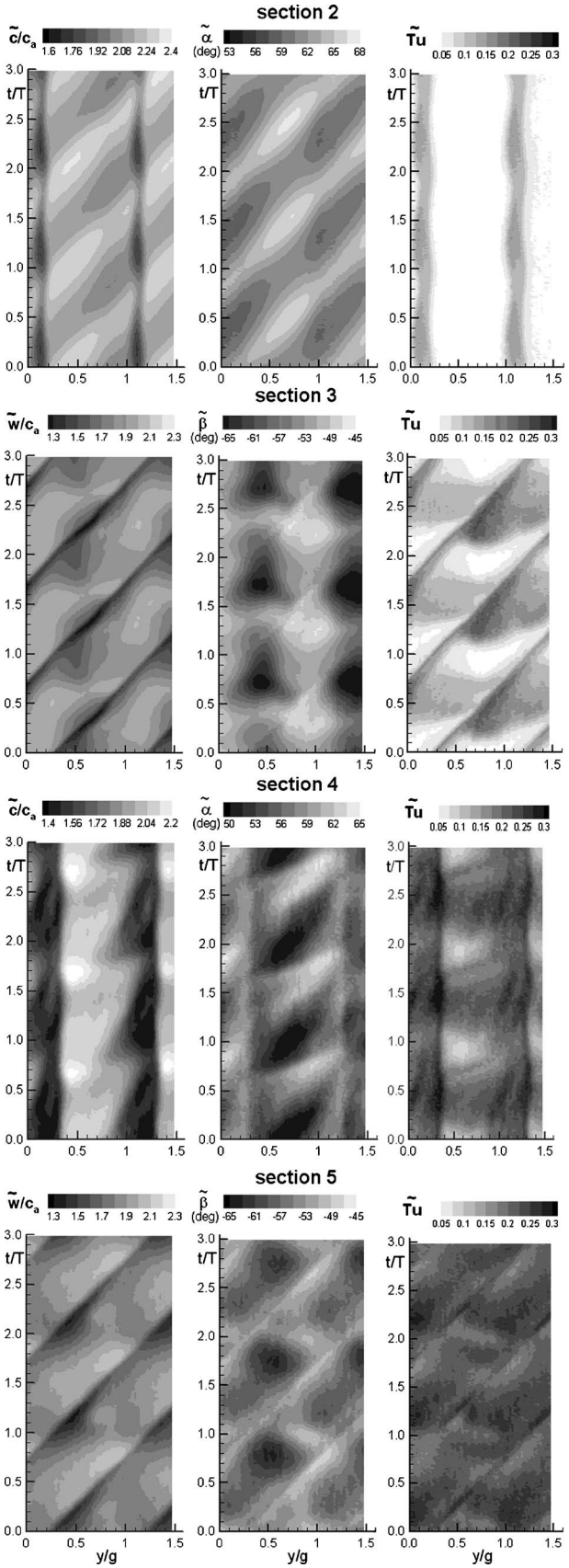

Fig. 4 Intermediate loading conditions flowfield

For each diagram the absolute spatial coordinate has been adopted. In the sections placed downstream of the stators (Secs. 2

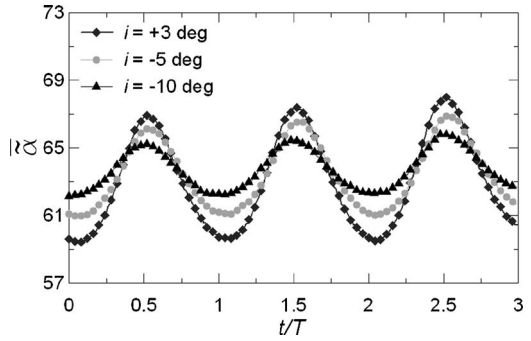

Fig. 5 Time evolution of the absolute flow angle for $y/g=0.75$ at section 2

and 4) the absolute quantities have been depicted, while the relative ones has been used downstream of the rotors (Secs. 3, 5).

In this kind of diagram stator blade wakes are identified by vertical stripes present at fixed circumferential positions, while the rotor wakes appear as 45 deg inclined lines, resulting as a consequence of the relative motion between the probe and the rotor blades and of the equality between the stator and the rotor pitches. In the stator wakes the suction side is located on the left of the stripe, because the probe was traversed through the vane wake from the suction to the pressure side.

The rotor wake suction side can be identified on the lower side of the inclined stripe, because the turbine rotor blades are passing in front of the probe with the suction side before (with the pressure side after).

Intermediate Incidence Flowfield. Space-time diagrams for the intermediate loading conditions are shown in Fig. 4, each row corresponding to a different measuring section.

Section 2 (first row of Fig. 4). The velocity defects relative to vane wakes are clearly visible for $y/g=0.15$ and $y/g=1.15$. These areas are characterized by a turbulence intensity variable between 10–12%, while in the free stream the turbulence lowers to 5–6%. Remarkable periodic perturbations of both the ensemble averaged absolute velocity and angle are present.

This indicates strong potential flow effects from the downstream rotor blades, which determine oscillations of nearly 20% for the absolute velocity and of about 7 deg for the absolute flow angle. Another important aspect is that the potential perturbations act in the way to reduce the velocity close to the vane wake suction side, increasing it near to the pressure side, which consequently shows periodic areas of accelerated flow.

Section 3 (second row of Fig. 4). The main flow feature is represented by the rotor wakes identified as the inclined streaks present in both the relative velocity and turbulent intensity contour plots. In the wake regions unresolved unsteadiness rises up to 22%, while areas of undisturbed flow are still present.

Traces of the preceding stator wakes, convected and stretched through the rotor vanes, can be identified as wide spots of large turbulent intensity close to the wakes' suction side in the range $y/g=0.6-1.1$. Similar distributions can be found in the literature [13,14].

Other important spatial nonuniformities are the fluctuations in the rotor wake velocity defects, and the presence of nuclei of small and large absolute value of the relative flow angle, respectively, at $y/g=0.9$ and $y/g=0.4$. These perturbations, present at fixed absolute circumferential positions, can be probably referred to the potential effect caused by the following stator vane pressure distributions, which also are present at fixed absolute circumferential positions.

Section 4 (third row of Fig. 4). The flow pattern downstream of the second stator is similar to the one shown in section 2, but a

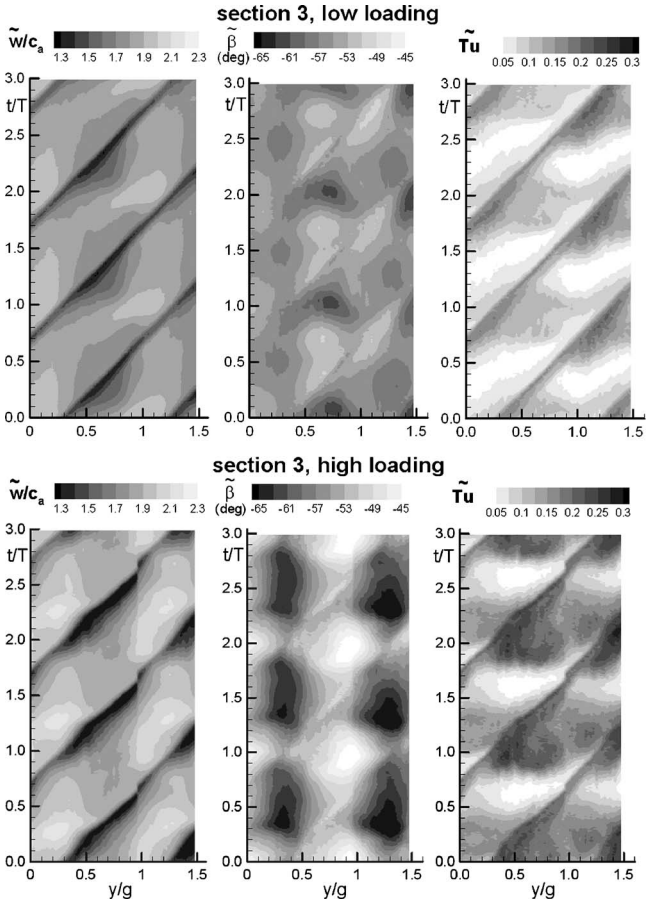

Fig. 6 Comparison of flowfields at section 3 for high and low loading

relevant increase of the width and depth of the stator wake velocity defect is present. The flow shows a general augmentation in the turbulence level, which at midpitch reaches averaged values of about 20%. High turbulence traces of the rotor wakes are periodically present close to the stator wake suction side. The absolute flow angle behaviors are also qualitatively similar to the first stator outlet section, but in section 4 the mean flow is overall more axial. This aspect can be explained by the presence of large and deep second stator wakes, which suggest an extended boundary layer development that leads to a larger outlet flow deviation.

Section 5 (last row of Fig. 4). The relative velocity contour plot shows overall milder velocity variations if compared with section 3, caused mainly by the absence of the aerodynamic blockage induced by the following stator. The turbulence intensity mean

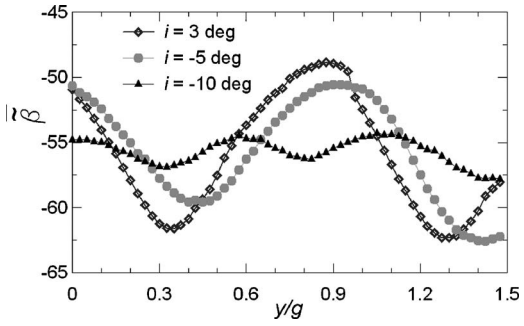

Fig. 7 Time averaged flow angle circumferential distribution in section 3

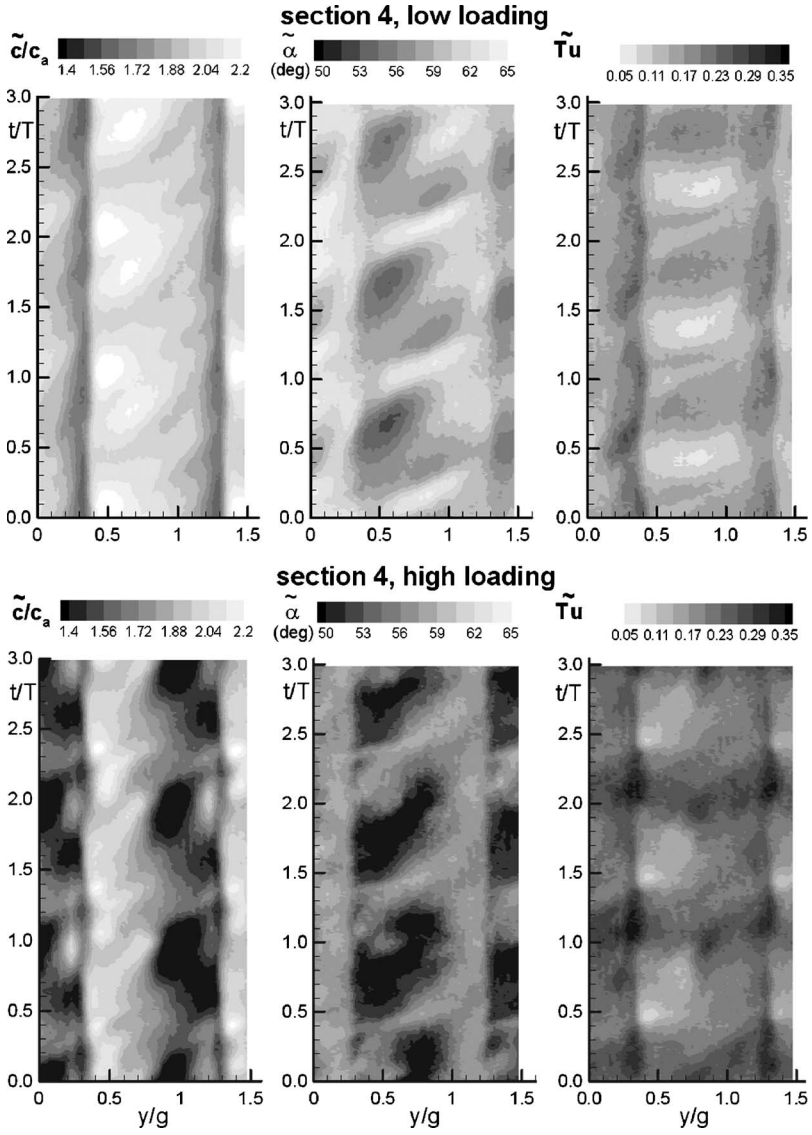

Fig. 8 Comparison of flowfields at section 4 for high and low loading

value rises to values higher than 20%.

Comparing the results of sections 3 and 5 the most striking feature is the difference in the relative flow angle distributions. The low and high absolute value nuclei, present in section 3, respectively, at $y/g=0.9$ and $y/g=0.4$, appear strongly weakened in section 5, indicating the lack of downstream potential effects.

Loading Variation Effects on the Flowfield. The loading conditions have been modified changing the incidence angle. The high loading condition is characterized by $i=+3$ deg and the low loading condition by $i=-10$ deg.

Section 2. The flow leaving section 2 is not significantly affected by loading modifications, mainly because the inlet absolute flow angle upstream of the first stator was kept constant. Nevertheless it is interesting to underline the variation in the rotor upstream potential effects, which determine larger periodic oscillations in the absolute flow angle as the blade loading increases.

The time evolution of the ensemble-averaged angle $\tilde{\alpha}$ in the circumferential position $y/g=0.75$ is represented in Fig. 5. In the low loading case the oscillation amplitude is about 4 deg, while in the high loading one it rises up to 8 deg.

Section 3. The relative velocity contours (first column of diagrams in Fig. 6) indicate that the velocity defects in the rotor wakes increase particularly close to the wake suction side, when the blade loading is increased. The velocity gradients present inside the rotor passages (i.e., between two successive wakes) are strengthened as the loading level increases.

Random unsteadiness distributions (last column of diagrams in Fig. 6) show a peculiar behavior, characterized by the rotor wake stripes and by the presence of turbulent nuclei whose intensity enlarges with load augmentation. Moreover such large intensity cores expand progressively in the rotor channel. Considering that the turbulence level present in section 2 is not affected by loading variation, the differences in nuclei extension and intensity in section 3 can be caused by different turbulent kinetic energy production inside the rotor, due to the interactions between blade boundary layer and vanes wakes [14]. Differences in nuclei locations for the three loading conditions can be explained by different convection mechanisms determined by different pressure gradients.

The downstream stator potential effects act in the way to determine two areas of strong flow acceleration both in the low loading conditions and the high loading one, which are present in the relative velocity contour plots at $y/g=0.2$ and, according to flow

periodicity, at $y/g=1.2$. The velocity peaks present in these circumferential positions are 5% larger in the case of high loading than in the low one.

At the same circumferential coordinates (i.e., $y/g=0.2,1.2$) the relative flow angle distributions (central column of diagrams in Fig. 6) report the presence of zones characterized by large absolute values. In a different way cores of low absolute value of the $\tilde{\beta}$ angle are present at $y/g=0.8$. These circumferential periodic perturbations together with the presence of the rotor wakes determine a periodic flow pattern both in space and in time. This behavior is strongly enhanced by increasing the incidence angle.

In order to quantify the influence of the downstream pressure field on the $\tilde{\beta}$ angle, the circumferential distributions of the time-averaged relative flow angle at the rotor outlet are depicted in Fig. 7. The oscillation amplitudes range from nearly 2 deg in the low loading conditions up to more than 12 deg in the high loading case.

Section 4. The flow leaving the second stator is depicted in Fig. 8. The absolute velocity contours (first column of diagrams in Fig. 8) indicate strong effects of the loading conditions. The previously described potential interactions (see Fig. 4, sections 2 and 4, absolute velocity diagrams), which reduce the absolute velocity in regions close to the vane wake suction side, and at the same time determine flow acceleration on the other wake side, seem to have a different behavior between the low loading condition and the high loading one.

At low incidence angle conditions the main effect is represented by the presence of nuclei of large amplitude of the absolute velocity, displaced close to the wake pressure side at $y/g=0.5$ and $y/g=0.6$. At high loading condition the viscous effects strengthen the vane wake velocity defects and the potential perturbations from downstream, tending to periodically increase the velocity, are attenuated.

The turbulence intensity distributions both in high and low loading conditions (last column of diagrams in Fig. 8) indicate that the upstream rotor wakes, chopped and distorted by the velocity gradients, exit from the vane in nearly horizontal stripes. The turbulence level grows as the load increases.

The absolute flow angle contours (central column of diagrams in Fig. 8) show similar features for the different loading conditions. The effect of incidence is relevant on the flow deviation at stator trailing edge. In fact the mean absolute flow angle calculated in section 4 in the low loading case is of about 59 deg, while it lowers to nearly 54 deg in the high loading conditions.

The time-averaged circumferential distributions of the absolute velocity and turbulence intensity at the second stator exit are represented in Fig. 9. The velocity profiles, for all the three incidence angles, reach the maximum values in points, $y/g=0.5$, close to the stator wakes pressure side.

In the low loading condition the time averaged velocity moderately decreases in the vane passage until a new wake is present. The turbulence intensity inside the vane passage is nearly constant, characterized by values of about 12%, while in the wake it increases to more than 20%.

In the intermediate incidence angle condition the vane wake velocity defect increases, and it is not possible to separate the wake from the area of low velocity present in the vane passage in the range $y/g=0.7-1$. At same incidence angle random unsteadiness increases progressively in the vane passage, ranging from 16% at $y/g=0.5$ to 24% at $y/g=1.2$, moreover at $y/g=1.4$ a peak related to the stator wake is present.

At high loading condition the velocity profile is characterized by a strong defect near midpitch which determines a local minimum at $y/g=1.0$. Increasing the circumferential coordinate the velocity slightly increases until $y/g=1.2$, where the pressure side vane wake is present. This local velocity minimum is characterized by a turbulence level nearly 3–4% larger than the turbulence intensity of the free stream close to the wake pressure side. In the turbulence intensity profile at large incidence condition a well distinct peak is also present at $y/g=1.3$ representative of the pressure side of vane wake.

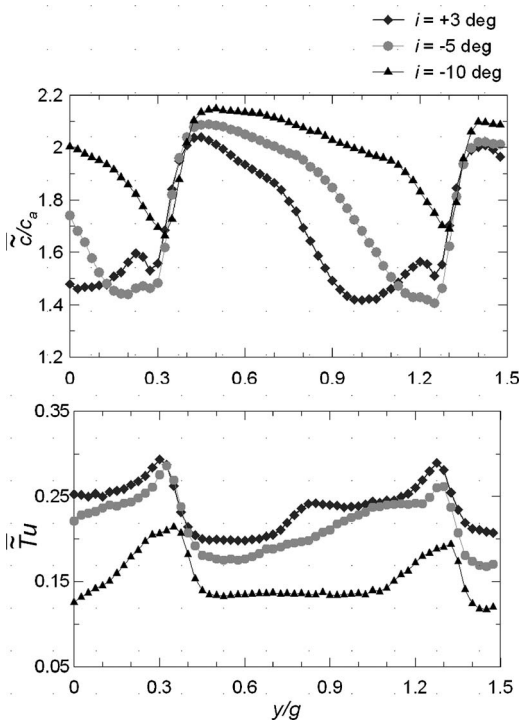

Fig. 9 Time averaged absolute velocity and turbulence intensity circumferential distribution in section 4

Section 5. The flow in section 5 is depicted in Fig. 10. The relative velocity contour plots (first column of diagrams in Fig. 10) show the growth of the velocity defects in the rotor wakes, as the loading increases. As a consequence the relative velocity increases in the area between two successive wakes.

The turbulence intensity contours (last column of diagrams in Fig. 10) indicate, at low loading condition, a low turbulence intensity in all the flowfield. The rotor wakes are very thin and lower turbulence values are displaced in areas close to the wake pressure sides.

According to the loading augmentation, turbulence levels grow substantially but at the same time, the qualitative pattern remains similar except for the positions of the large value cores, which indicate different convection mechanism and turbulent diffusion of the upstream generated wakes.

In order to compare the potential perturbations effects on the flow at the rotors outlet, the circumferential distributions of the time averaged relative flow angle representative of section 3 and section 5, in high and low loading conditions, are depicted in Fig. 11. In section 3 the circumferential fluctuations of the relative angle are negligible at low loading condition, while at high loading condition the amplitude of the fluctuations increases beyond 10 deg. Differently, the flow leaving the second rotor shows slight circumferential oscillations of the relative angle in both low and high loading conditions.

Conclusions

Detailed experimental investigations have been performed in a two-stage low-pressure large-scale research turbine, equipped with high lift profiles, for three different loading conditions. By means of an X-hot-wire probe the velocity components and turbulence intensity have been measured in the blade-to-blade plane at midspan, upstream and downstream of each blade row. For each

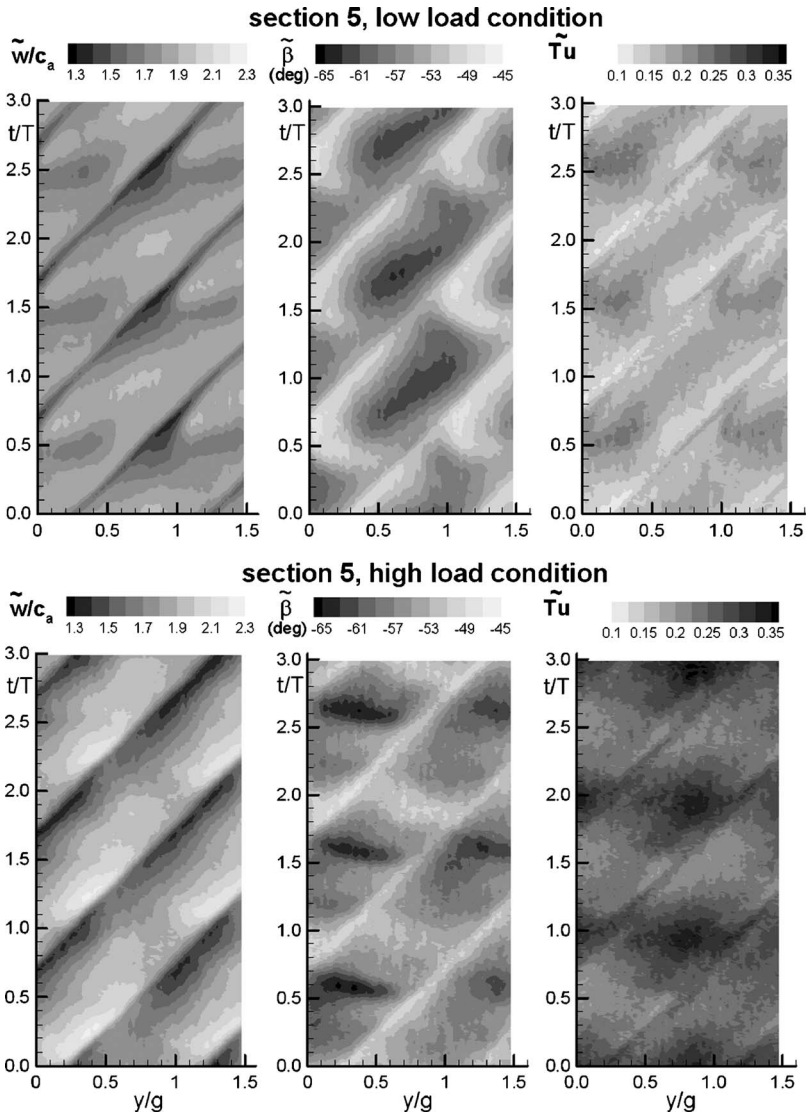

Fig. 10 Comparison of flowfields at section 5 for high and low loading

axial measuring station the probe was traversed circumferentially in order to solve the multiple blading interaction both in time and space.

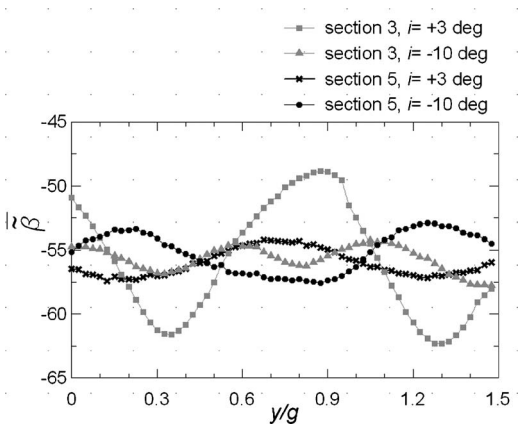

Fig. 11 Time averaged relative flow angle circumferential distributions in sections 3 and 5, at two different loading conditions

Results indicate that both potential and viscous effects are significantly present in the flow for all the three loadings conditions.

Downstream of the stators the rotor potential perturbations determine periodic temporal oscillations on both the absolute velocity and angle distributions. The oscillations amplitudes are strongly influenced by the loading condition, and their values are comparable with the ones of the spatial periodic perturbations determined by the vane wakes.

Downstream of the first rotor, which is followed by a stator, potential effects determine circumferential periodic perturbations on the relative velocity and flow angle. As the loading increases, the strength of circumferential perturbations is enhanced. Downstream of the second rotor, which is not followed by any stator, potential effects are weak for all the three incidence angles.

Turbulence intensity increases continuously through each blade row. Loading augmentation determines an increase of turbulence level in each measuring section, and influences transport phenomena which drive the wake segments through both rotor and stator channels.

At high loading condition the effect of multiple rotor-stator interaction is cumulative and the flow is completely dominated by interaction unsteady viscous and potential effects.

Acknowledgment

This work was supported by MIUR (Italian Ministry of Education, University and Research) through the PRIN 2003 Research Program.

Nomenclature

c = chord length at midspan
C = absolute velocity
D_i = inner diameter
D_o = outer diameter
g = stator and rotor pitch at midspan
i = incidence angle
l = blade span
r = radial coordinate
t = time
T = rotor blade passing period
Tu = turbulence intensity
W = relative velocity
α = absolute flow angle with axial direction
β = relative flow angle with axial direction
ε_c = statistical uncertainty associated to ensemble averaged velocity
$\varepsilon_{c'}$ = statistical uncertainty associated to ensemble averaged rms
ω = rotational speed

Subscripts

a = in the axial direction
t = in the circumferential direction

Superscripts and Overbars

$'$ = fluctuating component
$-$ = time averaged
$\sim$ = ensemble averaged

References

[1] Curtis, E. M., Hodson, H. P., Banieghbal, M. R., Denton, J. D., and Howell, R. J., 1996, "Development of Blade Profiles for Low Pressure Turbine Applications," ASME Paper No. 96-GT-358.
[2] Cobley, K., Coleman, N., Siden, G., and Arndt, N., 1997, "Design of New Three Stage Low Pressure Turbine for BMW Rolls-Royce BR715 Engine," ASME Paper No. 97-GT-419.
[3] Lou, W., and Hourmouziadis, J., 2000, "Separation Bubbles Under Steady and Periodic-Unsteady Main Flow Conditions," ASME J. Turbomach., **122**, pp. 634–643.
[4] Schulte, V., and Hodson, H. P., 1996, "Unsteady Wake Induced Boundary Transition in Highly Loaded LP Turbines," ASME Paper No. 96-GT-486.
[5] Hodson, H. P., 1984, "Boundary Layer and Loss Measurements on the Rotor of an Axial-Flow Turbine," J. Eng. Gas Turbines Power, **106**, pp. 391–399.
[6] Schroeder, Th., 1991, "Investigations of Blade Row Interaction and Boundary Layer Transition Phenomena in a Multistage Aero Engine Low-Pressure Turbine by Measurements With Hot-Film Probes and Surface-Mounted Hot-Film Gauges," *Boundary Layer in Turbomachines* (Lecture Series 1991–06), VKI.
[7] Halstead, D. E., Wisler, D. C., Okiishi, T., Walker, G. J., Hodson, H. P., and Shin, H. W., 1997, "Boundary Layer Development in Axial Compressor and Turbines: Part 1 of 4—Composite Picture," ASME J. Turbomach., **119**, pp. 114–127.
[8] Halstead, D. E., Wisler, D. C., Okiishi, T., Walker, G. J., Hodson, H. P., and Shin, H. W., 1997, "Boundary Layer Development in Axial Compressor and Turbines: Part 3 of 4—LP Turbines," ASME J. Turbomach., **119**, pp. 225–237.
[9] Hoheisel, H., Kiock, R., Lichtfuss, H. J., and Fottner, L., 1987, "Influence of Free-Stream Turbulence and Blade Pressure Gradient on Boundary Layer and Loss Behavior of Turbine Cascades," ASME J. Turbomach., **109**, pp. 210–219.
[10] Acton, P., 1998, "Untersuchung des Grenzschichtumschlages an einem Hochbelasteten Turbinengitter unter Inhomogenen und Instationären Zuströmbedingungen," Ph.D. Thesis, Universität der Bundeswehr, München.
[11] Schröder, Th., and Zunino, P., 2000, "A New Method for the Calibration of the Directional Sensitivity of X-Hot-Wire Probes," *Proceedings of the XVth Bi-Annual Symposium on Measuring Techniques in Transonic and Supersonic Flows in Cascades and Turbomachines*, Florence, Italy.
[12] Lakshminarayana, B., 1981, "Techniques for Aerodynamic and Turbulence Measurements in Turbomachinery Rotors," ASME J. Eng. Power, **103**, pp. 374–392.
[13] Elsner, W., and Bijak-Bartosik, E., 2003, "Analysis of the Wake Transport in the Turbine Blade Channel," *Proceedings of the 12th Conference on Fluid Flow Technologies*, Budapest, Hungary.
[14] Stieger, R. D., and Hodson, H. P., 2004, "The Unsteady Development of a Turbulent Wake Through a Downstream Low-Pressure Turbine Blade Passage," ASME Paper No. GT2004-53061.

Conjugate Heat Transfer Analysis of a Cooled Turbine Vane Using the V2F Turbulence Model

Jiang Luo
e-mail: jluo@solarturbines.com

Eli H. Razinsky

Solar Turbines Incorporated,
A Caterpillar Company,
San Diego, CA 92101

The conjugate heat transfer methodology has been employed to predict the flow and thermal properties including the metal temperature of a NASA turbine vane at three operating conditions. The turbine vane was cooled internally by air flowing through ten round pipes. The conjugate heat transfer methodology allows a simultaneous solution of aerodynamics and heat transfer in the external hot gas and the internal cooling passages and conduction within the solid metal, eliminating the need for multiple/decoupled solutions in a typical industry design process. The model of about 3 million computational meshes includes the gas path and the internal cooling channels, comprising hexa cells, and the solid metal comprising hexa and prism cells. The predicted aerodynamic loadings were found to be in close agreement with the data for all the cases. The predicted metal temperature, external, and internal heat transfer distributions at the midspan compared well with the measurement. The differences in the heat transfer rates and metal temperature under different running conditions were also captured well. The V2F turbulence model has been compared with a low-Reynolds-number k-ε model and a nonlinear quadratic k-ε model. The V2F model is found to provide the closest agreement with the data, though it still has room for improvement in predicting the boundary layer transition and turbulent heat transfer, especially on the suction side. The overall results are quite encouraging and indicate that conjugate heat transfer simulation with proper turbulence closure has the potential to become a viable tool in turbine heat transfer analysis and cooling design. [DOI: 10.1115/1.2720483]

Introduction

It is well known that the steady increase in turbine inlet temperature over the last several decades has significantly enhanced the efficiency and performance of gas turbine engines. The tendency for higher turbine inlet temperature is continuing and posing considerable challenges for the analysis and design of turbine cooling schemes [1,2]. Computational fluid dynamics (CFD) techniques based on Reynolds-averaged Navier–Stokes (RANS) equations have matured in recent years and are routinely used to predict the pressure loadings of vanes and blades, but their applications to predicting turbine heat transfer have achieved only limited success [1–3]. Dunn [3] concludes that heat transfer predictions for gas turbines are very difficult because the boundary conditions are not well known. The difficulty is also often attributed to the deficiency of current turbulence closures [1–3].

Dunn [3] notes that the ability of most RANS CFD codes to predict surface–pressure distribution is significantly better than the corresponding heat transfer distributions. Perhaps due to such difference in accuracy, turbine aerodynamics and heat transfer are usually treated separately or in a decoupled manner though they're coupled closely in reality. Typically the external and internal heat transfer coefficients (HTC) on a cooled turbine blade are obtained from boundary layer codes or empirically derived correlations, using surface pressure distributions from three-dimensional (3D) RANS analyses. This information is then passed as boundary conditions to finite-element codes to obtain the metal temperature. The decoupled approaches require multiple iterations and some accuracy may have been lost in the decoupling.

Recently there have been increased research efforts in applying the conjugate heat transfer (CHT) methodology to solve turbine heat transfer problems by Bohn et al. [4] and other researchers [5–14]. The CHT methodology allows a simultaneous and coupled solution of aerodynamics and heat transfer in the external hot gas and the internal cooling passages and conduction within the solid metal, hence eliminating the need for multiple and decoupled solutions. Unlike a decoupled approach in which external and internal heat transfer coefficients need to be assigned on the walls, the conjugate heat transfer method requires flow boundary conditions only at the inlet and exit of the gas and coolant passages.

Recent CHT computations have offered promising results and have been applied to realistic vanes and blades with complex film cooling and serpentine rib-roughened passages (e.g., Refs. [7,8,14]). However, the predictive accuracy of metal temperature by the CHT method is still limited by the accuracy of turbulence closures, as observed in York and Leylek [9] and Facchini et al. [10], among others. The results in Refs. [9,10] using two-equation eddy–viscosity models showed that the error of metal temperature prediction was within or around 10% for a relatively simple cooled vane (the same C3X vane as in this paper). This is equivalent to an error of 150 K (270 ^0R) for a moderate turbine inlet temperature of 1500 K (2240 ^{0}F), hence exceeding the desirable limit of the industry design practice. These and other recent CHT studies indicate that there is a strong need for improved turbulence models. The present paper attempts to address this issue with the V2F model.

The V2F model was developed by Durbin [15,16] to model the near-wall turbulence behavior and nonlocal effects by using an elliptic relaxation methodology. It differs from the widely used two-equation models (e.g., k-ε and k-ω) in that two additional turbulence quantities are solved, $\overline{v^2}$, the wall-normal Reynolds stress component, and F_{22}, the redistribution term in the equation of $\overline{v^2}$. Unlike the conventional low-Reynolds-number eddy–viscosity models, the V2F model does not require damping functions and removes the need to calculate the near-wall distance,

Contributed by the International Gas Turbine Institute of ASME for publication in the JOURNAL OF TURBOMACHINERY. Manuscript received July 13, 2006, final manuscript received July 24, 2006. Review conducted by David Wisler. Paper presented at the ASME Turbo Expo 2006: Land, Sea and Air (GT2006), Barcelona, Spain, May 08–May 11, 2006. Paper No. GT2006-91109.

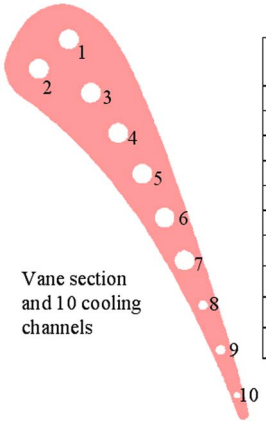

Cooling channel #	Diameter (mm)	C_r in Eq. (2)
1	6.30	1.118
2	6.30	1.118
3	6.30	1.118
4	6.30	1.118
5	6.30	1.118
6	6.30	1.118
7	6.30	1.118
8	3.10	1.056
9	3.10	1.056
10	1.98	1.025

Fig. 1 The C3X vane and cooling channels' property

which is difficult in a complex 3D geometry. The V2F model has been applied to various turbulent flows with improved accuracy over two-equation eddy–viscosity models for flow separation, heat transfer, and wall friction (e.g., Refs. [17,18]). Medic and Durbin [19] found that the V2F model provided a substantial improvement to the predictive accuracy of turbine heat transfer over the standard two-equation models (e.g., k-ε and k-ω). There has been growing interest in this model in the turbomachinery community [e.g., Refs. [20–24]]. However, its performance in conjugate heat transfer prediction of cooled turbine blades has not been assessed.

The present paper aims to develop an improved numerical procedure for conjugate heat transfer analysis using the V2F model. The CHT method will be applied to study a benchmark test case, the NASA C3X turbine vane measured by Hylton et al. [25]. The V2F model will be first validated using the data of a flat plate boundary layer flow. It will be compared with a low-Reynolds-number (LRN) k-ε model and a LRN nonlinear quadratic k-ε model. The predicted flow and thermal properties, including the vane metal temperature and external and internal heat transfer rates, will be evaluated against the data at three operating conditions.

Numerical Method

Model. The C3X transonic turbine guide vane of Hylton et al. [25] was selected as the test case in the present work, as this case has detailed measurement of the external and internal convection and the metal temperature. The experiment consisted of a linear cascade of three vanes, and the center vane was cooled by air flowing radially through ten round pipes from the hub to the shroud. The cross section of the C3X turbine vane is shown in Fig. 1, along with the dimensions and location of the ten cooling channels. The constant Cr is for Eq. (2) below and accounts for the thermal entrance effects for the cooling channels [25]. Detailed geometric parameters of the vane are listed in Table 1. The 3D computational domain included one vane in the middle, with periodic boundary conditions employed to simulate the cascade test condition. The domain extended 76.2 mm from the hub to the

Table 1 Geometry parameters for C3X vane

Stagger angel (deg)	59.89
Air exit angle (deg)	72.38
Throat (mm)	32.9
Vane spacing (mm)	117.7
Vane height (mm)	76.2
Suction surface arc (mm)	177.8
Pressure surface arc (mm)	137.2
True chord (mm)	144.9
Axial chord (mm)	78.2

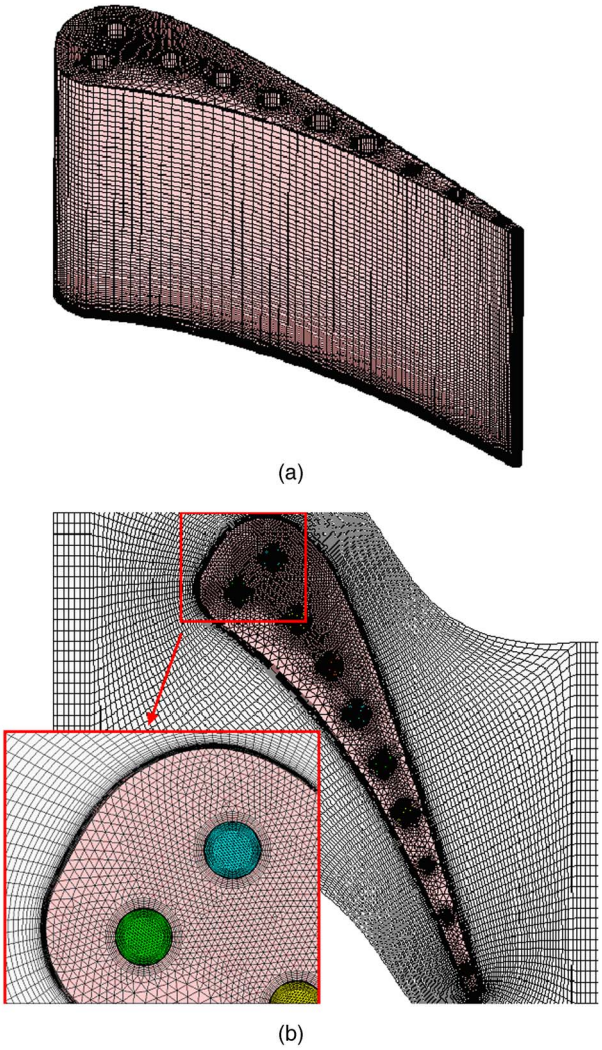

Fig. 2 Computational meshes for the gas and coolant passages and the solid vane; (*a*) mesh on vane surface (pressure side view); (*b*) midspan mesh with zoom-up near LE

shroud (Fig. 2(*a*)), where both end walls were specified to be adiabatic and noslip. The computational inlet was located at 140 mm (about one chord length) upstream of the vane leading edge, which was the same as the measurement inlet [25]. The computational exit was located at 140 mm downstream of the trailing edge.

A total of 18 test runs for C3X were documented in Ref. [25]. Three representative cases with different Reynolds numbers and coolant flow rates have been analyzed in the present work. The operating conditions are listed in Table 2. The exit Mach number Ma_2 is about 0.90 for both Case 1 (R112) and Case 3 (R158), and Case 2 (R154) is transonic with $Ma_2=1.06$. The Reynolds number Re_2, based on the chord length and exit velocity, ranges from 1.5×10^6 (Case 3) to 2.5×10^6 (Case 2). The inlet gas total temperature T_{t1} ranges from 783 K to 808 K. Though the vane surface and gas temperatures are relatively low, their ratio T_w/T_{t1} is representative of those in modern jet engines.

The total pressure and total temperature were specified at the inlet, with the static pressure (derived using P_{t1} and Ma_2) specified at the exit. For the hot gas flow at the inlet, the turbulence intensity Tu_1 was specified to be the experimental value of 8.3%. The inlet turbulence length scale L_{t1} (unknown from the test) was specified to be 0.4 mm (0.5% of the vane axial chord) for all three cases. This length scale was found to provide a proper free stream

Table 2 Flow conditions of three cases analyzed

Case No./(Run)	P_{t1} (bar)	T_{t1} (K)	Ma_2	Re_2	Tu_1 (%)	T_w/T_{t1}
1/(R112)	3.217	783	0.90	2.0E+06	8.3	0.84
2/(R154)	3.867	790	1.06	2.5E+06	8.3	0.76
3/(R158)	2.435	808	0.91	1.5E+06	8.3	0.73

turbulence level outside the vane boundary layers (especially on the suction side), as discussed later. Both the molecular viscosity and conductivity were specified as a function of static temperature using Sutherland's law. The specific heat is specified as a function of temperature with a user subroutine.

The measured mass flow rates (MFRs) and the averaged midspan total temperature ($T_{c\text{-mid}}$) of the coolant are listed in Table 3 for the three cases. There are significant differences in the coolant flow rates from channel to channel and case to case, which have significant impact on the vane metal temperature distribution and gradient, as shown later. The coolant flows in the ten channels were independent from one another and reported to be fully developed at the channel inlet (i.e., the hub of the vane) because there were long tubes upstream [25].

The midspan coolant total temperature $T_{c\text{-mid}}$ is from Ref. [25] where it was averaged from the hub and the shroud measurement, assuming a linear rise of T_c through the cooling pipe. Because the hub temperatures T_{c1} were not documented in Ref. [25], they were specified with proper values (Table 3) in the present work to match the midspan $T_{c\text{-mid}}$. The inlet coolant temperatures T_{c1} were different from channel to channel and case to case. The magnitudes of the coolant inlet velocity were derived using the given mass flow rates and its profiles followed the 1/7th power law. The inlet pressure values were not known from Ref. [25] and specified to match the corresponding Reynolds number of each channel under each case.

The vane material is stainless steel (ASTM Type 310), which has a relatively low thermal conductivity. The vane material has a constant density of 7900 kg/m^3 and specific heat of 585.2 J/Kg/K. The thermal conductivity K (from Ref. [11]) was specified as

$$K = 0.0182T + 6.13 \quad (1)$$

Solver and Turbulence Models. The flow solver was the commercial CFD package STAR-CD [26] Version 3.26, released in 2005. STAR-CD solves 3D RANS equations on unstructured meshes that can be mixed hexa, tetra, prism, and polyhedral cells. It is an implicit finite volume solver that employs a variant of the well-known SIMPLE algorithm for velocity–pressure correction. For conjugate heat transfer analysis, the energy equations for the fluid and solid are solved simultaneously and continuity of energy flux is enforced at the fluid/solid interfaces. The energy equation for solids is a degenerate form of the energy equation for fluids (obtained by setting the velocity to zero). The fluid/solid thermal coupling is treated in an implicit fashion.

The turbulent eddy viscosity (μ_t) was obtained from three turbulence closures: (1) the V2F model that solves three transport equations (for k, ε, and $\overline{v^2}$) and the elliptic equation for the redistribution term F_{22}; (2) the LRN nonlinear quadratic k-ε (QKE) model with the damping function of Lien and Leschziner; and (3) the LRN k-ε (KE) model with the damping function of Lien and Leschziner. The details of the turbulence equations, functions, and constants are available in the methodology [26]. The low-Reynolds-number k-ε models were chosen because they were known to be able to simulate (to some degree) the turbine boundary layer transition subject to free stream turbulence (i.e., the type of bypass transition), which is one of the key features of the C3X vane heat transfer. These models were developed originally for the near-wall turbulence modeling rather than the bypass transition. Schmidt and Patankar [27] explained the mechanisms by which the LRN k-ε models were able to simulate approximately the bypass transition process.

The convective fluxes in all the mean-flow equations (for velocity components and temperature) were discretized with the second-order accurate self-filtered central differencing (SFCD) scheme [26]. The turbulence transport equations were discretized using the first-order accurate upwind differencing (UD) scheme to ensure convergence for all the cases. It was observed in the present work that the numerical diffusion error introduced by the UD scheme in solving turbulence equations was negligible with the present fine meshes.

Mesh. Since the C3X vane had a constant cross section, a 2D mesh (quads) for the external gas path was first generated with ES-TURBO, a mesh-generation code within the STAR-CD software package. Then triangles and quads for the solid and coolant pipes were generated using ICEMCFD, a commercial mesh-generation package. The combined 2D mesh was then stacked up to form the 3D mesh using ICEMCFD. The spanwise grid stretching was employed only near the hub to reduce the total mesh size, because the current focus was on the portion from the hub to the midspan (Fig. 2(*a*)). In total, there were about 3.1 million cells (a combination of hexahedrons and prisms) for the entire domain,

Table 3 Coolant flow conditions of the three cases

No.	MFR Case1 (g/s)	MFR Case2 (g/s)	MFR Case3 (g/s)	T_c-mid Case1 (K)	T_c-mid Case2 (K)	T_c-mid Case3 (K)	T_{c1} Case1 (K)	T_{c1} Case2 (K)	T_{c1} Case3 (K)
1	7.79	20.80	16.70	409.1	369.4	358.1	393.3	357.9	348.3
2	6.58	22.20	17.40	409.4	369.2	359.4	393.1	358.9	349.7
3	6.34	21.30	14.80	391.5	352.9	350.0	375.2	343.6	340.0
4	6.66	21.80	16.50	397.2	355.9	351.5	381.0	346.3	341.5
5	6.50	22.70	17.50	376.9	344.6	342.6	359.2	334.1	331.4
6	6.72	22.90	16.50	434.9	386.7	371.9	419.1	376.1	361.4
7	6.33	16.90	16.10	391.5	355.6	351.9	373.0	342.6	338.2
8	2.26	7.43	5.50	107.6	391.3	386.0	371.6	363.9	363.1
9	1.38	4.57	3.49	466.4	433.7	413.2	426.9	407.1	383.2
10	0.68	2.42	1.71	516.2	482.6	454.9	451.4	443.2	390.9

with about 1.4 million (45% of total) for the hot gas path, 0.7 million (23%) for the solid, and 1.0 million (32%) for the ten cooling channels.

One layer of the computational meshes near the midspan is shown in Fig. 2(*b*), and with a zoom-up view of the leading edge region. In the 38,000 cells on each layer, there are 17,000 cells for the hot gas path, with 240 grid points around the vane. This gas path mesh size was determined from grid-independence studies with 7,000, 17,000, and 30,000 cells. The near-wall spacing of both gas and coolant meshes is below y^+ of 1.0, as required by the low-Reynolds-number turbulence models. The meshes near the vane surface are nearly orthogonal due to the *O*-mesh topology employed around the vane.

Flat Plate Validation (T3B Case). To assess the capability of the V2F model for predicting boundary layer transition, a flat plate flow case T3B [28] was analyzed. This is one of the classical benchmark test cases [28] that have been used to assess the predictions of bypass boundary layer transitions. A laminar boundary layer develops from the leading edge of an adiabatic flat plate of about 1500 mm long, with the free stream speed of 9.4 m/s and the turbulence intensity of 6.0%. The Reynolds number Re_x, based on the free stream speed and the distance from the leading edge, is around 1.0 million at the plate end. The experiment indicates that the boundary layer transition starts around $\mathrm{Re}_x=50{,}000$ and finishes around $\mathrm{Re}_x=125{,}000$.

A 2D mesh of 250×120 cells with near-wall spacing of $y^+<1$ was employed in the present analysis (Fig. 3(*a*)). A uniform flow speed of 9.4 m/s was specified at the inlet. The inlet turbulence length scale was assumed to be 1 mm, following other authors (e.g., Ref. [23]), as it was unknown from the test. As seen in Figs. 3(*b*) and 3(*c*), the V2F model was able to simulate the boundary layer transition process approximately. The predicted skin friction coefficient C_f (Fig. 3(*b*)) is seen to generally follow the test data, transitioning from the level of a laminar boundary layer to the turbulent level, given by the respective equations in the figure. Correspondingly, the boundary layer shape factor (SF) drops from 2.5 representing a laminar boundary layer to slightly above 1.4, typical of a turbulent boundary layer. The V2F prediction is again in good agreement with the test data (Fig. 3(*c*)). It should be noted that the V2F model appears to predict an earlier onset of transition, compared to the data. It overpredicts the transition length, as it also predicts a delayed ending of the transition.

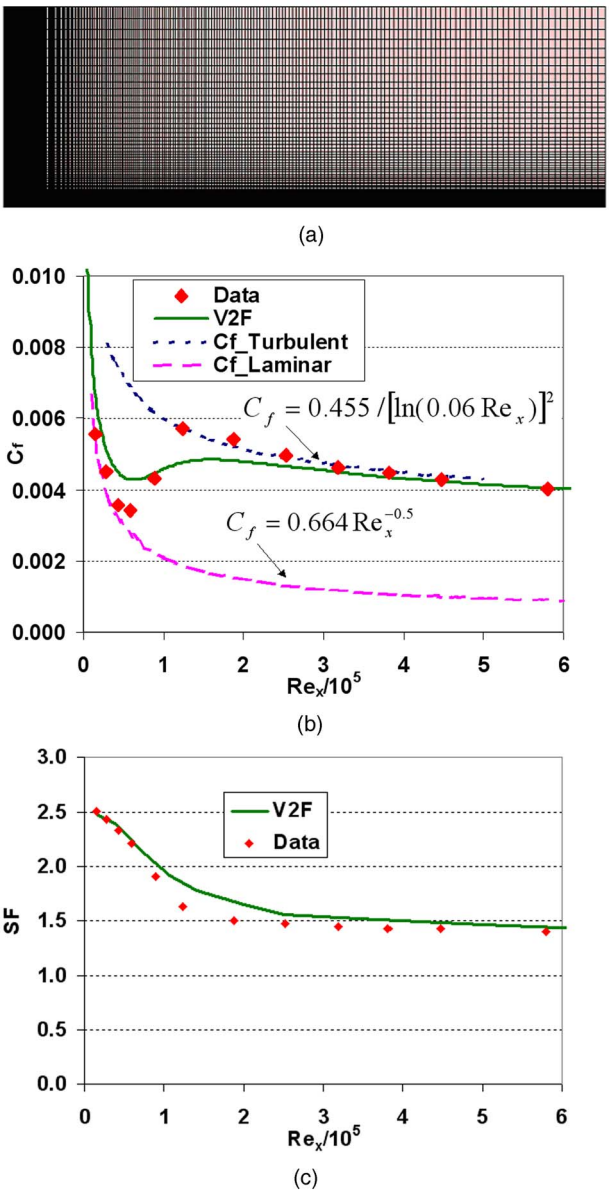

Fig. 3 Simulation of a flat plate boundary layer (T3B): V2F versus data and correlations; (*a*) mesh for T3B case (horizontal axis: *X*); (*b*) predicted and measured skin friction coefficient; and (*c*) predicted and measured shape factor

Results and Discussion

A series of CHT analyses have been performed for the C3X turbine vane under three flow conditions as listed in Tables 2 and 3. The predicted vane pressure loadings and thermal properties, including the external and internal heat transfer rates and the metal temperature, will be compared with the data from Hylton et al. [25].

Case 1. The three turbulence models were applied to compute Case 1 under identical boundary conditions, differencing schemes and convergence criteria. The turbulence intensity and length scale at the cooling channels' inlets were unknown and specified to be 5.0% and 1 mm, respectively (the same as in Ref. [10]).

The predicted and measured pressure (normalized by P_{t1}) distributions on both the pressure and suction sides at the vane midspan are shown in Fig. 4. Because there is no flow separation on the vane, the results from the three turbulence models are almost identical and in good agreement with the measurement. There is slight difference between the predictions and data on the suction side around two data points ($X/C_x=0.58$ and 0.64). This small discrepancy also appeared in recent predictions for this vane [e.g., Ref. [9,10]]. The exact reason for it is not clear.

On the suction side, the gas flow accelerates rapidly from the stagnation point toward the throat, reaching the maximum speed (corresponding to the minimal value of $P/P_{t1}=0.51$) around $X/C_x=0.45$ (Fig. 4). The flow then decelerates until the location around $X/C_x=0.70$, before resuming a mild acceleration toward the trailing edge. The flow is under a favorable pressure gradient on the entire pressure side. It starts with a slow acceleration from the stagnation point for about half of the chord length and then speeds up toward the trailing edge. It is known that a proper prediction of the vane surface pressure distribution is a necessity but not a guarantee for a proper prediction of the corresponding heat transfer distribution [1,3].

The predicted external heat transfer coefficients on the pressure and suction sides are shown in Fig. 5, along with the data and the correlations for turbulent boundary layers ($H_{\mathrm{TBL}}=0.0298\,\mathrm{Pr}^{1/3}\,\mathrm{Re}_S^{0.8}\,K/S$) and laminar boundary layers ($H_{\mathrm{LBL}}=0.332\,\mathrm{Pr}^{1/3}\,\mathrm{Re}_S^{0.5}\,K/S$) on flat plates. Due to the effects of free stream turbulence, flow transition, and pressure gradient, the actual heat transfer is much higher than the laminar correlation while lower than the turbulent correlation. The V2F prediction is

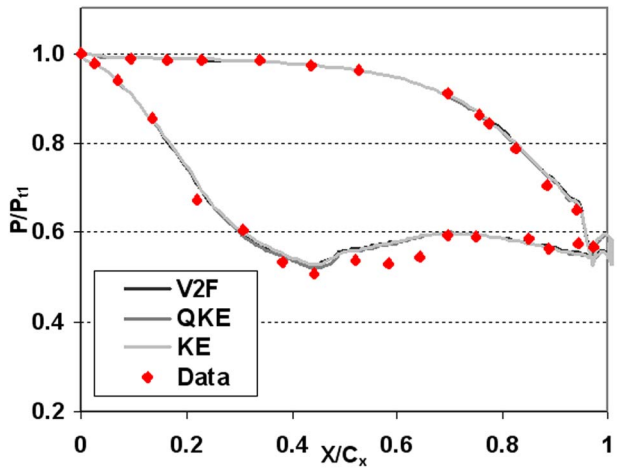

Fig. 4 Predicted and measured vane surface pressure distributions at the midspan: Case 1 with the V2F, quadratic *k-ε* (QKE); and *k-ε* (KE) models

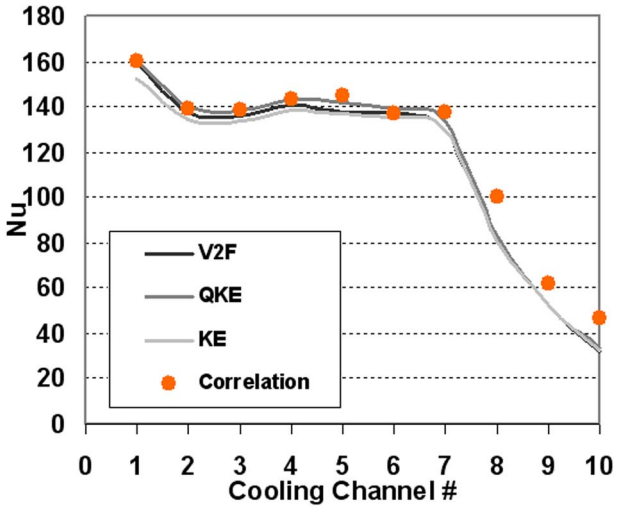

Fig. 6 Predicted Nusselt number of internal cooling channels at the midspan versus Eq. (2): Case 1 with the V2F, quadratic *k-ε*, and *k-ε* models

in excellent agreement with the data on the entire pressure side, from the stagnation point (X/C_x=0.0) to the trailing edge (X/C_x =−1.0). The V2F model was also observed by other authors to yield good performance for the pressure side HTC (e.g., Refs. [20,22,23] for vanes, and [21] for a blade). The quadratic *k-ε* prediction is in reasonable agreement with the data, but the *k-ε* model yields an overprediction. All the models have overpredicted the heat transfer at the stagnation point, with the *k-ε* prediction being the worst (almost 100% higher than the data). This is due to the "stagnation point anomaly" of *k-ε* models, which has been discussed by many authors (e.g., Ref. [29,19]). This problem does not exist for Reynolds stress models [29] that solve the transport equations directly for Reynolds stresses without using the eddy viscosity. The V2F and QKE models have largely mitigated this problem.

The three predictions display a large difference on the suction side, from the stagnation point to the trailing edge (X/C_x =0.0–1.0) in Fig. 5, however. The *k-ε* model significantly overpredicted the heat transfer rate on the entire suction side, because of its anomalous generation of turbulent kinetic energy near the stagnation point and immediately downstream on the suction side due to the existence of large rates of strain. Due to the employment of the nonlinear relationship between the Reynolds stresses and the strain rates, the quadratic *k-ε* model was able to reduce the spurious generation of turbulent kinetic energy in that region. Consequently, its prediction is in good agreement with the data. But the transition onset around X/C_x=0.26 was not captured well by this model. Instead, it predicted an abrupt transition around X/C_x=0.47. The V2F prediction was in the best agreement with the data in the quasi-laminar and transitional flow regions. Perhaps due to the adverse pressure gradient, the V2F model predicted a shorter transition length, an opposite behavior from the flat plate flow. Note all the models overpredicted the HTC at the end of transition and in the turbulent flow region.

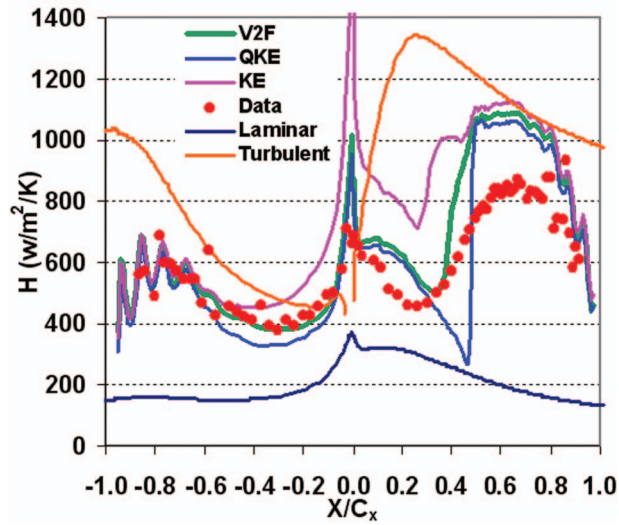

Fig. 5 Predicted and measured vane external heat transfer coefficients at the midspan: Case 1 with the V2F, quadratic *k-ε*, and *k-ε* models

An internally cooled turbine vane like the current one consists of three heat transfer processes that are closely coupled: the external convection, the internal convection, and the conduction within the metal. The metal temperature is determined by convection on both sides. The predicted Nusselt numbers for the internal coolant flows are shown in Fig. 6. As the coolant flow in the channels was fully developed, its Nusselt number was given by the following equation from Ref. [25]

$$\mathrm{Nu} = 0.022\mathrm{Cr}\,\mathrm{Pr}^{0.5}\mathrm{Re}_D^{0.8} \tag{2}$$

The Cr values in Eq. (2) are listed in Fig. 1, and Pr is the flow Prandtl number around 0.70 for the given coolant temperature range. The Reynolds number Re_D is based on the pipe diameter and the bulk velocity. The Nusselt number from Eq. (2) for each coolant channel at the midspan is shown in Fig. 6 as the data correlation. It is evident that all the predictions are in good agreement with the correlation, except for the last three channels where the Nusselt numbers have been underpredicted by 15%–30%.

The predicted metal temperature (T_w) distributions at the midspan are shown in Fig. 7. The V2F prediction is in excellent agreement with the data on the entire pressure side, with an error less than 2%. The quadratic *k-ε* model also yields good prediction there. The *k-ε* model overpredicts T_w due to its overprediction of the external HTC on the pressure side (Fig. 5). On the suction side, the V2F prediction follows the measured wavy pattern and is in good agreement with the data, with an error less than 3%. As expected, the *k-ε* model overpredicts the metal temperature due to its overprediction of the external HTC. The quadratic *k-ε* model yields a reasonable prediction, except a dip near X/C_x=0.46 where it underpredicts the external HTC earlier in Fig. 5. All the

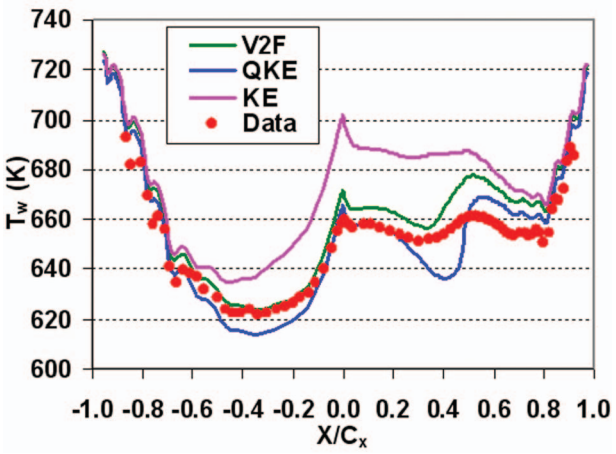

Fig. 7 Predicted and measured vane metal temperature distribution at the midspan: Case 1 with the V2F, quadratic *k*-ε, and *k*-ε models

models overpredicted the temperature in the region with $X/C_x = 0.6-0.8$ due to their overprediction of the external HTC (Fig. 5). However, the predictive accuracy for T_w is better than that for the external HTC there, probably because of the larger contribution to the overall thermal resistance from the internal convection, as discussed by York and Leylek [9].

It is clear from the above figures that the predictive accuracy of the external HTC plays an important role in the predictive accuracy of the vane metal temperature. The external HTC prediction is affected strongly by the turbulence closure's capability in modeling turbine boundary layer transition. As discussed by Mayle [30], such transition bypasses the linear stability mechanism (Tollmien–Schlichting instability wave) due to the infusion of turbulent energy into the boundary layer from the free stream turbulence. While the quadratic *k*-ε model produced a similar accuracy, the V2F model produced better prediction of the transition length and severity.

The predicted values of μ_t/μ and turbulence level (TL) around the vane are shown in Fig. 8. The turbulent viscosity μ_t is an important parameter, as it is the only value passed to the mean-flow equations from the turbulence equations. The differences in μ_t/μ upstream of the vane in Figs. 8(*a*)–8(*c*) are caused by the differences in the μ_t formula and the different decay rates of turbulence predicted by the three models. The V2F (also the quadratic *k*-ε) solution shows a reduction of turbulence in the strong flow acceleration region downstream of the stagnation point on the suction side. This appears to be in agreement with the physical observation that the turbulence is suppressed in a highly accelerating flow over a convex surface. The V2F model also predicts a steady increase of turbulent viscosity going downstream on the suction side, reaching a ratio (μ_t/μ) of about 100 near the trailing edge, which indicates a turbulent boundary layer. The quadratic *k*-ε model predicts a seemingly unphysical level of μ_t/μ outside the boundary layer further downstream on the suction side. The *k*-ε model generated unphysically excessive turbulence due to the "stagnation point anomaly," causing the over-prediction of the HTC values earlier in Fig. 5.

The predicted turbulence level TL in Fig. 8 shows the evolution of the free stream turbulence through the gas passage, which is controlled by both the inlet turbulence intensity Tu and the length scale L_{t1}. Note that $TL = 100 \cdot \sqrt{2/3k}/U_1$ (%) is based on the *inlet* mean flow velocity, rather than the *local* velocity as for Tu. Inside the vane passage, the predicted turbulence level is higher near the boundary layers than in the main stream (Fig. 8). It should be noted that the current turbulence length scale L_{t1} of 0.4 mm or $0.5\% C_x$ is much smaller than $5\% C_x$ or larger values used by

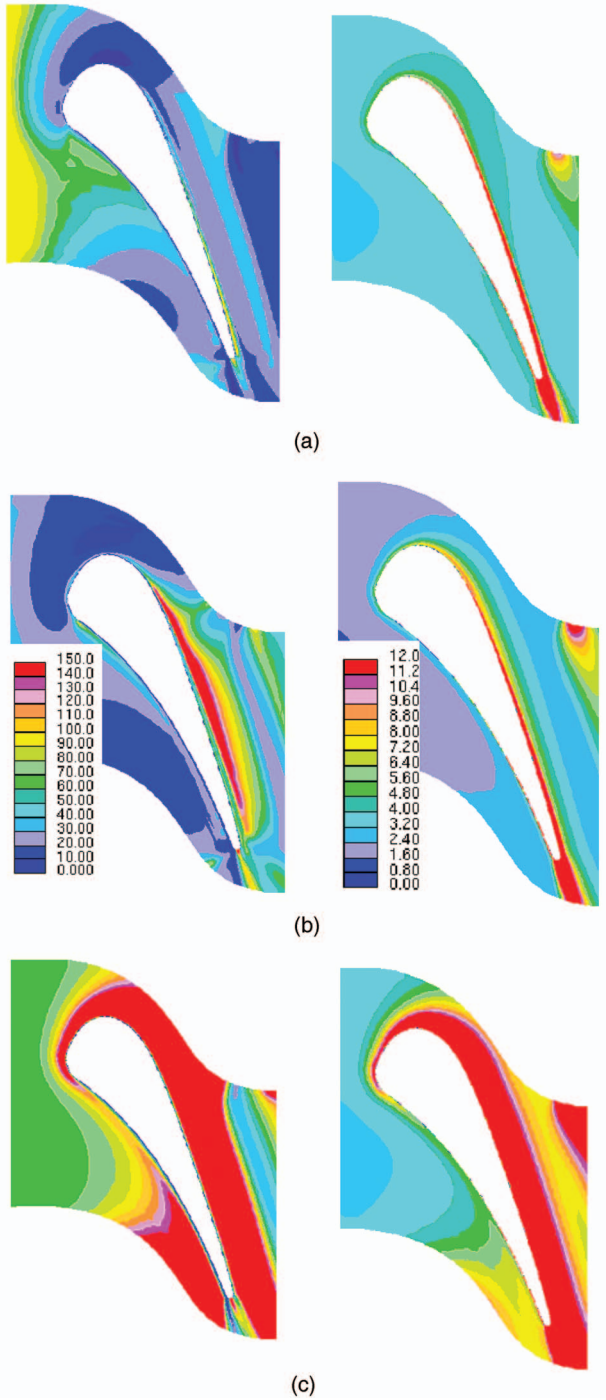

Fig. 8 Predicted turbulence values: viscosity ratio μ_t/μ on the left and turbulence level (TL) (%) on the right at the midspan by the V2F, quadratic *k*-ε, and *k*-ε models (legends in *b*); (*a*) V2F; (*b*) quadratic *k*-ε; and (*c*) *k*-ε

some authors (e.g., Refs. [9,10]). While able to preserve the free stream turbulence level *upstream* of the vane, such large length scales often result in unphysically high turbulence levels near the vane surface in the gas passage, due to the "stagnation point anomaly" effect discussed earlier. As a result of this erroneously generated turbulence, earlier computations typically overpredicted the turbine vane HTC (e.g., Ref. [10]).

The small scale was selected here to maintain a free stream turbulence level around 6–7% *just outside* the boundary layers near the vane LE (Figs. 8(*a*) and 8(*b*)). This level was expected

from the measured Tu_1 of 8.3% about one chord upstream of the LE. With the V2F and QKE models, the current low L_{t1} is able to provide a proper turbulence level for the crucial region just outside the boundary layer, rather than the region upstream of the vane. The k-ε model, however, was unable to predict a reasonable free-stream turbulence near the vane surface with the same low length scale, due to the excessive generation of turbulence near the stagnation point and the suction side.

The V2F-predicted metal temperature distribution on the vane surface is shown in Fig. 9. While there are no corresponding data, the good agreement achieved by this model at the midspan (Fig. 7) provides confidence in the accuracy here. The vane surface temperature rises in a layered wavy pattern from the hub to the tip (Figs. 9(*a*) and 9(*b*)), mainly due to the effect of heat pickup by the coolant in the ten channels. The trailing edge near the tip is the hottest region. The leading edge also shows high temperature. The interior distribution and gradient of metal temperature at the midspan are shown in Fig. 9(*c*), where the cooling effects are evident.

Case 2 and Case 3. From the above comparisons of the three turbulence models for Case 1, it was concluded that the V2F model provided the overall best prediction. Hence only the V2F model was used to compute Cases 2 and 3, as listed in Table 2. The aim was to assess the model's capability under different gas and coolant flow conditions. The same numerical schemes and convergence criteria have been employed. Also, the same turbulent flow conditions (intensity Tu_1 and length scale L_{t1}) have been specified at the gas inlet. The coolant flow conditions were specified per Table 3.

The aerodynamic loadings on the vane for Cases 2 and 3 (not shown) have been predicted very well, with accuracy similar to Fig. 4. The computed and measured external heat transfer rates at the midspan are shown in Fig. 10. The difference in the measured HTC levels of the two cases is caused primarily by the difference in the gas Reynolds numbers. The higher Re_2 of 2.5×10^6 in Case 2 leads to higher HTC on both sides than that of Case 3, with Re_2 of 1.5×10^6. The V2F predictions on the pressure side ($X/C_x=-1.0-0.0$) are in excellent agreement with the data, as seen earlier in Case 1. The prediction of Case 3 on the suction side, including the transition onset near $X/C_x=0.4$, is in good agreement with the data. Similar to the overprediction observed in Fig. 5, the V2F model overpredicts the HTC values for Cases 2 and 3 (at a lesser degree) in the fully turbulent region.

The V2F-predicted vane metal temperature distributions at the midspan for all the three cases are shown in Fig. 11. All the predictions are in excellent agreement with the corresponding data on the entire pressure side, with an error less than 2%. On the suction side, the V2F predictions follow the measured wavy pattern and are in good agreement with the data, with an error less than 3%. It is also interesting to notice that the model has captured the high-temperature region around $X/C_x=0.55$ in Case 3.

The good prediction of the metal temperature should be a result of good predictions of both external and internal heat transfer rates. This is confirmed in Fig. 12, in which the V2F-predicted Nusselt numbers for the internal convection are in good agreement with the correlation Eq. (2) for fully developed pipe flows. The differences in the internal HTC values from case to case are primarily caused by the differences in the coolant mass flow rates and Reynolds numbers.

The V2F predictions of the vane metal temperature (Fig. 11) are mostly within 10 K at the midspan and within 30 K in the peak-error region, compared to the test data. The predictive accuracy of the V2F model appears to be the best for the C3X vane, compared with earlier results using other variants of the k-ε model (e.g., Refs. [9,10]). Although the current internal cooling scheme is much simpler than the realistic ones, this level of good agreement is still quite encouraging. The current study indicates that the conjugate heat transfer methodology with advanced turbulence closures such as the V2F model has a potential to return good predictions of heat transfer rates, as well as the vane/blade metal temperature. Further explorations using this model for complex geometries with realistic cooling schemes should be pursued.

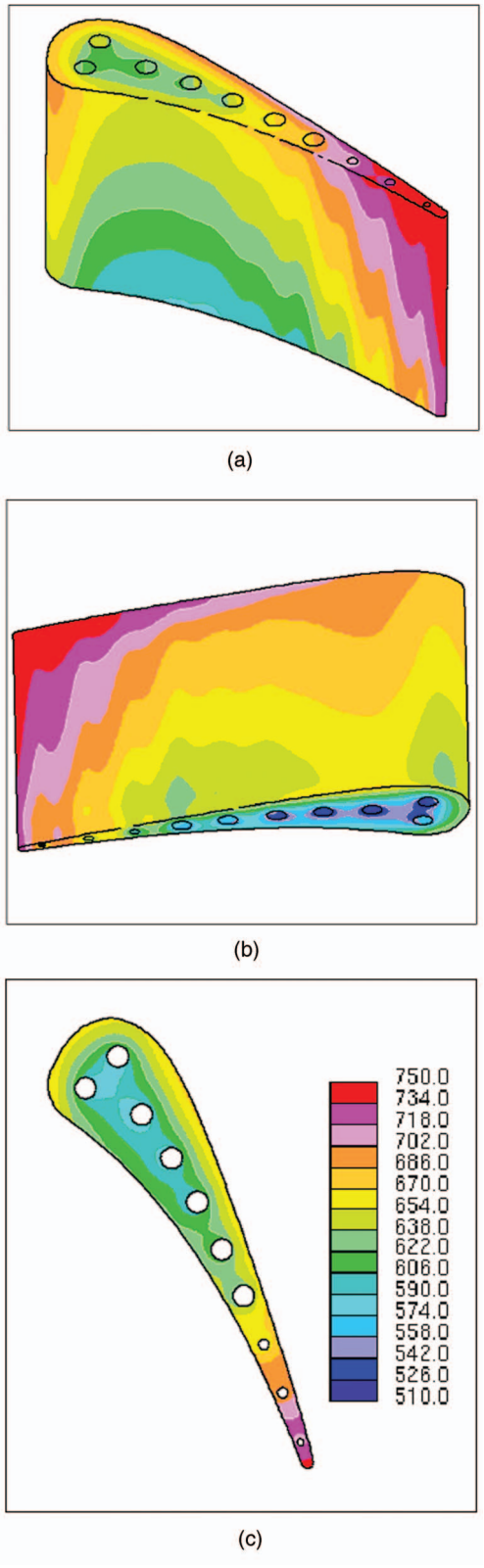

Fig. 9 Predicted vane metal temperature (in K) distribution of Case 1 by the V2F model (legend in *c*); (*a*) pressure side view; (*b*) suction side view; and (*c*) midspan section

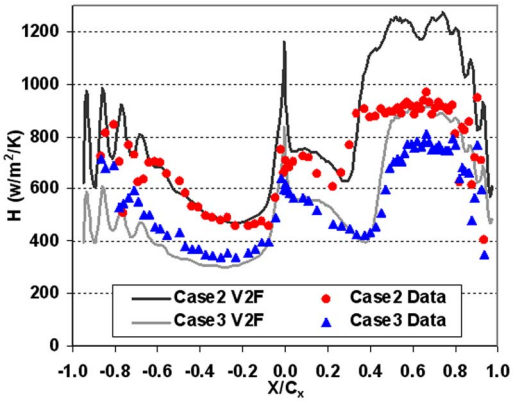

Fig. 10 Predicted and measured vane external heat transfer coefficients at the midspan: Cases 2 and 3 with V2F model

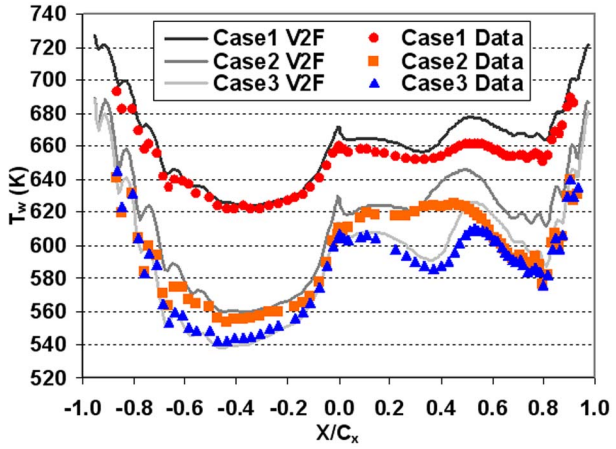

Fig. 11 Predicted and measured vane metal temperature at the midspan: all 3 cases with the V2F model

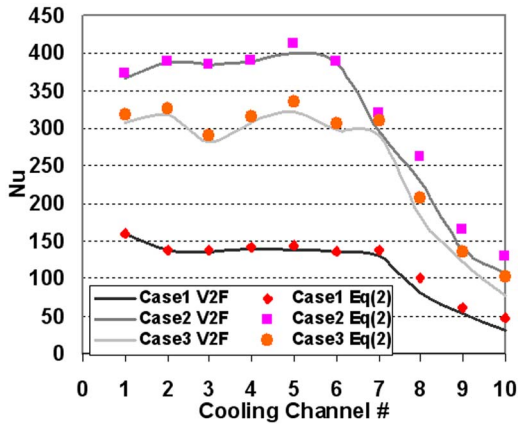

Fig. 12 Predicted Nusselt numbers of the ten cooling channels versus correlation Eq. (2) at the midspan: all three cases with the V2F model

Conclusions

The conjugate heat transfer methodology has been applied to predict the flow and thermal properties of the NASA C3X turbine vane at three operating conditions. The results have been assessed with the test data of both aerodynamic and thermal properties. The V2F model has been compared with a low-Reynolds-number k-ε model and a nonlinear quadratic k-ε model. The predicted aerodynamic loadings by all the turbulence closures are in close agreement with the data. However, it is found that the V2F model provides the closest agreement with the data for the external and internal heat transfer coefficients and ultimately the metal temperature.

The differences in the heat transfer rates and metal temperature under different flow conditions are also captured well by the V2F model. The V2F model has returned accurate predictions of heat transfer for the entire pressure side and a large portion of the suction side. The V2F-predicted metal temperature at the vane midspan follows the measured pattern and is within 3% discrepancy from the data. This is shown to be a result of accurate predictions of heat transfer on both the external gas/metal and internal metal/coolant interfaces.

While the overall agreement is good, it should be noted that the V2F model still has room for improvement in predicting the boundary layer transition and the subsequent turbulent heat transfer, especially on the suction side. Further explorations using the V2F model for realistic cooled blades and vanes are worthwhile. The current results are quite encouraging and indicate that the conjugate heat transfer simulation with a proper turbulence closure has the potential to become a viable tool in turbine heat transfer analysis and cooling design.

Acknowledgment

We would like to thank Solar Turbines Inc. for permission to publish this work.

Nomenclature

C = vane chord length (m)
C_f = skin friction coefficient
C_r = constant in Eq. (2), listed in Fig. 1
C_x = vane axial chord length (m)
D = diameter of coolant channel (m)
F_{22} = redistribution term in V2F model
H = heat transfer coefficient, $\dot{Q}_w/(T_{t1}-T_w)$ ($W/m^2/K$)
k = turbulent kinetic energy (m^2/s^2)
K = thermal conductivity (W/m/K)
L_t = turbulence length scale (m)
LE = leading edge
Ma = Mach number
MFR = mass flow rate (kg/s) or (g/s)
Nu = Nusselt number, HD/K
P_{t1} = inlet total pressure (Pa, or bar (10^5 Pa))
P = static pressure (Pa, or bar)
Pr = Prandtl number
PS = pressure side
$\dot{Q}_w$ = wall heat flux (W/m^2)
Re = Reynolds number
Re_S = Reynolds number based on S and U
S = vane surface distance from leading edge
SF = shape factor of boundary layer
SS = suction side
T = temperature (K)
T_{t1} = inlet total temperature (K)
TL = turbulence level, $100\cdot\sqrt{2/3k}/U_1$ (%)
Tu = turbulence intensity, $\sqrt{2/3k}/U$
U = free stream flow velocity (m/s)
$\overline{v^2}$ = wall-normal Reynolds stress component
X = axial coordinate from LE (X=0.0)
y^+ = nondimensional distance from wall
ϵ = dissipation rate of turbulent energy (m^2/s^3)
μ = molecular viscosity (Pa s)
μ_t = turbulent eddy viscosity (Pa s)

Subscripts

1, 2 = cascade or coolant pipe inlet, exit condition
c = coolant total value
t = total (stagnation) condition
w = wall property
x = axial

References

[1] Lakshminarayana, B., 1996, *Fluid Dynamics and Heat Transfer of Turbomachinery*, J Wiley, New York.
[2] Han, J. C., Dutta, S., and Ekkad, S. V., *Gas Turbine Heat Transfer and Cooling Technology*, Taylor and Francis, London, U.K.
[3] Dunn, M. G., 2001, "Convective Heat Transfer and Aerodynamics in Axial Flow Turbines," J. Turbomach., **123**, pp. 637–686.
[4] Bohn, D. E., Bonhoff, B., and Schonenborn, H., 1995, "Combined Aerodynamic and Thermal Analysis of a Turbine Nozzle Guide Vane," IGTC Paper No. 95-108.
[5] Han, Z. X., Dennis, B., H., and Dulikravich, G. S., 2000, "Simultaneous Prediction of External Flowfield and Temperature in Internally-Cooled 3-D Gas Turbine Blade Material," ASME Paper No. GT2000-253.
[6] Rigby, D. L., and Lepicovsky, J., 2001, "Conjugate Heat Transfer Analysis of Internally-Cooled Configurations," ASME Paper No. GT2001-0405.
[7] Bohn, D. E., Ren, J., and Kusterer, K., 2003, "Conjugate Heat Transfer Analysis for Film Cooling Configurations with Different Hole Geometries," ASME Paper No. GT2003-38369.
[8] Heidmann, J. D., Kassab, A. J., Divo, E. A., Rodriguez, F., and Steinthorsson, E., 2003, "Conjugate Heat Transfer Effects on Realistic Film-Cooled Turbine Vane," ASME Paper No. GT2003-38553.
[9] York, D. W., and Leylek, J. H., 2003, "Three-Dimensional Conjugate Heat Transfer Simulation of an Internally-Cooled Gas Turbine Vane," ASME Paper No. GT2003-38551.
[10] Facchini, B., Magi, A., and Greco, A., S., 2004, "Conjugate Heat Transfer of a Radially Cooled Gas Turbine Vane," ASME Paper No. GT2004-54213.
[11] Zecchi, S., Arcangeli, L., and Facchini, B., 2004, "Features of a Cooling System Simulation Tool Used in Industrial Preliminary Design Stage," ASME Paper No. GT2004-53547.
[12] Takahashi, T., Watanabe, K., and Sakai, T., 2005, "Conjugate Heat Transfer Analysis of a Rotor Blade with Rib-roughened Internal Cooling Passages," ASME Paper No. GT2005-68227.
[13] Agostini, F., and Arts, T., 2005, "Conjugate Heat Transfer Investigation of Rib-Roughened Cooling Channels," ASME Paper No. GT2005-68166.
[14] Kusterer, K., Hagedorn, T., Bohn, D., Sugimoto, T., and Tanaka, R., 2005, "Improvement of a Film-Cooled Blade by Application of the Conjugate Calculation Technique," ASME Paper No. GT2005-68555.
[15] Durbin, P. A., 1991, "Near-Wall Turbulence Closure Modeling without Damping Functions," Theor. Comput. Fluid Dyn., **3**, pp. 1–13.
[16] Durbin, P. A., 1993, "Application of a Near-Wall Turbulence Closure to Boundary Layers and Heat Transfer," Int. J. Heat Fluid Flow, **14**(4), pp. 316–323.
[17] Iaccarino, G., 2000, "Advanced Turbulence Modeling for RANS Simulations," *Proceedings STAR-CD European Users' Meeting*.
[18] Ooi, A., Iaccarino, G., Durbin, P., and Behnia, M., 2002, "Simulation of Turbulent Flow and Heat Transfer in Complex Passages," Int. J. Heat Fluid Flow, **23**, pp. 750–757.
[19] Medic, G., and Durbin, P. A., 2002, "Toward Improved Prediction of Heat Transfer on Turbine Blades," ASME J. Turbomach., **124**, pp. 187—192.
[20] Hermanson, K., Kern, S., Picker, G., and Parneix, S., 2002, "Predictions of External Heat Transfer for Turbine Vanes and Blades with Secondary Flowfields," ASME Paper No. GT2002-30206.
[21] Ameri, A. A., and Ajmani, K., 2004, "Evaluation of Predicted Heat Transfer on a Transonic Blade Using v2-f Models," ASME Paper No. GT2004-53572.
[22] Sveningsson, A., and Davidson, L., 2004, "Computations of Flow Field and Heat Transfer in a Stator Vane Passage Using the V2F Turbulence Model," ASME Paper No. GT2004-53586.
[23] Pecnik, R., Pieringer, P., and Sanz, W., 2005, "Numerical Investigation of the Secondary Flow of a Transonic Turbine Stage Using Various Turbulence Closures," ASME Paper No. GT2005-68754.
[24] Ibrahim, M., Kochuparambil, B. J., Ekkad, S. V., and Simon, T. W., 2005, "CFD for Jet Impingement Heat Transfer with Single Jets and Arrays," ASME Paper No. GT2005-68341.
[25] Hylton, L. D., Mihelc, M. S., Turner, E. R., Nealy, D. A., and York, R. E., 1983, "Analytical and Experimental Evaluation of the Heat Transfer Distribution Over the Surface of Turbine Vanes," NASA Paper No. CR-168015.
[26] *STAR-CD Version 3.20-Methodology*, 2004, CD-adapco Group, New York.
[27] Schmidt, R., and Patankar, S., 1992, "Simulating Boundary Layer Transition with Low-Reynolds-Number k-ε Turbulence Models: Part 1-An Evaluation of Prediction Characteristics," ASME J. Turbomach., **113**, pp. 10–17.
[28] Savill, A. M., 1993, "Some Recent Progress in the Turbulence Modeling of By-Pass Transition," *Near-Wall Turbulent Flows*, R. M. C. So, et al., ed., Elsevier, New York.
[29] Taulbee, D. B., and Tran, L., 1988, "Stagnation Streamline Turbulence," AIAA J., **26**(8), pp. 1011–1013.
[30] Mayle, R. E., 1991, "The Role of Laminar-Turbulent Transition in Gas-Turbine Engines," ASME J. Turbomach., **113**, pp. 509–537.

Heat Transfer Measurements in a First-Stage Nozzle Cascade Having Endwall Contouring: Misalignment and Leakage Studies

J. D. Piggush
Turbine Module Center,
Pratt and Whitney,
East Hartford, CT
e-mail: justin.piggush@pw.utc.com

T. W. Simon
Heat Transfer Laboratory,
Department of Mechanical Engineering,
University of Minnesota,
Minneapolis, MN 55455
e-mail: tsimon@me.umn.edu

This work supports new gas turbine designs for improved performance by evaluating endwall heat transfer rates in a cascade that is representative of a first-stage stator passage and incorporates endwall assembly features and leakage. Assembly features, such as gaps in the endwall and misalignment of those gaps, disrupt the endwall boundary layer, typically leading to enhanced heat transfer rates. Leakage flows through such gaps within the passage can also affect endwall boundary layers and may induce additional secondary flows and vortex structures in the passage near the endwall. The present paper documents leakage flow and misalignment effects on the endwall heat transfer coefficients within a passage which has one axially contoured and one straight endwall. In particular, features associated with the combustor-to-turbine transition piece and the assembly joint on the vane platform are addressed. [DOI: 10.1115/1.2720506]

Introduction

In order to achieve the highest possible efficiency and specific power, gas turbines are designed to run at high temperatures. The temperature of the gas entering from the combustor may be in excess of 1600°C. Such extreme temperatures place high thermal loads on engine components which, without proper attention to cooling, quickly become compromised by oxidation, thermally induced fatigue or, in the case of blades, creep. Maintaining the components at relatively cool temperatures is therefore essential to engine durability.

The challenges associated with elevated temperatures are further compounded by the complex flow field within the engine passage. As the fluid stagnates on the leading edge of the vane and is then turned circumferentially, a complex three-dimensional boundary layer forms. This boundary layer is responsible for both highly nonuniform heat transfer rates on the endwall and additional aerodynamic losses. The situation is further complicated by the introduction of leakage flows and film cooling. A survey of endwall flow and heat transfer literature is presented by Simon and Piggush [1].

The final engine design is the result of numerous compromises between aerodynamic efficiency, durability, cooling requirements, and cost of production. Actual engines must therefore include features that are not entirely desirable from a heat transfer or aerodynamic standpoint. These features include the transition section gap, which is the junction between the combustor section and the vane section. The gap must be made large enough to allow the individual pieces to expand as the engine passes through the thermal cycles of start up and shut down. A second feature is a gap in the endwall between vane castings. The complete stator section is typically composed of individual vane castings assembled around a hub. A gap, referred to as the slashface gap, or gutter, is created between each of the vane castings which, similar to the transition section gap, must be wide enough to allow expansion and contraction of the pieces during thermal cycling. Ingestion of hot mainstream gas into the core of the engine is highly undesirable since the passage materials cannot withstand the extreme temperatures of the passage flow. To seal the gaps and prevent ingression, the core is maintained at a higher pressure than the passage pressure and a leakage flow from the engine core into the passage is established. The presence of the gap and the flow through it may significantly change the flowfield within the turbine passage.

To address real problems associated with assembly misalignment and in-use thermal growth, several flow path geometries that replicate less than ideal alignment of components are considered in the present experiment. Gaps with forward-or backward-facing steps are introduced to the test geometry to allow studying their effects on heat transfer from the turbine vane endwall.

Work to describe the complexities of the passage flow field in axial turbines began as early as 1953. Herzig et al. [2] documented their observation of secondary flow moving in an endwall boundary layer from the pressure surface of the vane to the suction surface. This flow resulted from the turning of the main flow. Another secondary flow is the horseshoe vortex, created as the inlet boundary layer stagnates against the leading edge of the vane. The fluid outside of the endwall boundary layer has not suffered viscous losses and therefore stagnates to a higher pressure than the fluid within the boundary layer. The resulting pressure gradient forces the roll up of a vortex ahead of the stagnation line. Legs of this vortex are convected through the passage. A discussion of the phenomena can be found in Ref. [3]. The interaction of the passage flow described by Herzig et al. [2] and the pressure side leg of the horseshoe vortex was well described by Langston et al. [4]. The endwall passage flow merges with the pressure side leg of the horseshoe vortex to create what is referred to as the passage vortex. This vortex gains strength and size as it moves through the passage. The studies of Chung and Simon [5] and Wang et al. [6] confirm and extend the understanding of secondary flows within the passage.

Many attempts have been made to control secondary flows within passages of gas turbine engines (see Simon and Piggush [1] for a review); two of the more successful techniques include endwall contouring and boundary layer blowing. Endwall contouring

Contributed by the Turbomachinery Division of ASME for publication in the JOURNAL OF TURBOMACHINERY. Manuscript received July 23, 2006; final manuscript received August 11, 2006. Review conducted by David Wisler. Paper presented at the ASME Turbo Expo 2006: Land, Sea and Air (GT2006), Barcelona, Spain, May 8–11, 2006. Paper No. GT2006-90575.

typically gives a contraction in the area of the passage (and associated flow acceleration) that is superposed on the acceleration due to the airfoil shape. A favorable pressure gradient thins the endwall boundary layer reducing secondary flow strength. Several studies have shown the net aerodynamic benefits of endwall contouring. The work of Morris and Hoare [7] showed that contouring can effectively reduce pressure loss for some contour shapes. The study was confirmed by Kopper et al. [8], and others. The work of Burd and Simon [9] characterizes the flowfield on a contoured endwall while Piggush and Simon [10] detail the effects of contouring on the aerodynamic losses of the passage.

Injecting fluid into the boundary layer has also been shown to reduce passage losses by re-energizing the boundary layer. Such blowing must be located carefully and must be done with a streamwise momentum that is comparable to the streamwise momentum of the mainstream. Granser and Schulenberg [11] describe the effects of such blowing. Zhang and Jaiswal [12] report on interactions of injected flows with passage secondary flows. High jet momentum was credited with suppressing passage secondary flows. Several studies documenting the effects of injection of fluid within the passage have been documented. The study of Aunapu et al. [13] attempted to reduce passage secondary flow with the injection of fluid near the center of the passage endwall. Injection was positioned to divert the horseshoe vortex and thereby lessen the strength of the passage secondary flow. The study did not produce an overall reduction in loss. The study of Yamao et al. [14] included leakage through a slashface gap and a gap ahead of the leading edge. This study found little impact of leakage flows on passage losses.

Several important studies, which document heat transfer coefficients on turbine passage endwalls, have been made. They include the works of Blair [15] and Graziani et al. [16]. The second includes a full description of the heat transfer coefficient distribution on the vane endwall. Heat transfer rates are strongly affected by conditions of the incoming boundary layer flow. A region of high heat transfer is seen around the leading edge of the vane where the roll up of the horseshoe vortex brings hot mainstream gases toward the endwall. Moving deeper into the passage, one observes that heat transfer rates first drop, as the horseshoe vortex mixes the boundary layer fluid with the passage fluid and a new, initially laminar, boundary layer forms. Higher heat transfer rates are then produced as acceleration in the passage thins the boundary layer and transitions it to turbulence. Goldstein and Spores [17] used mass transfer techniques to confirm the heat transfer measurements. The mass transfer technique allows high spatial resolution. They discussed the vorticity created at the leading edge and the mass transfer results in the wake of the vane. Recent work by Pasinato et al. [18] in a blown, contoured vane cascade indicates relatively low heat transfer rates at the inlet, followed by higher heat transfer rates as the flow accelerates and the boundary layer thins. The results also indicate that blowing ahead of the leading edge plane tends to increase heat transfer, particularly in the downstream portion of the passage.

Misalignment of components along the gas path also affects endwall heat transfer. Though many studies investigating the effects of backward or forward facing steps on heat transfer are available, relatively few exist for cascade geometries, particularly when leakage flow is introduced through the gap. One study of this sort, but without airfoils and the associated flow turning, is by Chyu et al. [19]. The test section includes a gap with blowing and misalignment. As one might expect, the study indicates a large effect on heat transfer rates of forward facing and backward facing steps. The forward facing step produces a slight reduction of heat transfer rates ahead of the gap leading edge, then an increase downstream of the gap. The backward facing step produces a large area of decreased heat transfer rates downstream of the step and in the recirculation zone. Blowing through the gap which has a fore step or backstep does not change these trends, although heat transfer rates downstream of the gap tend to be increased by the leakage flow. Yu and Chyu [20] studied the influence on film cooling performance of leakage. Moderate film cooling upstream of the gap provided some protection. Increased leakage flow led to decreased cooling protection. Zhang and Moon [21] investigated in a cascade the effects of a gap ahead of the airfoil row with leakage flow through it and a backward facing step at it. The step is shown to create an unstable boundary layer that reduces the effectiveness of cooling. They later showed that the effect of the backstep could be reduced and acceptable film cooling effectiveness due to leakage could be attained by proper choice of the injection velocity [22]. Colban et al. [23,24] also investigated the effects of steps and leakage flow on endwall aerodynamics and cooling. Their work shows sensitivities to various parameters and indicates the importance of fully characterizing the inlet flow.

A series of papers by Wu et al. [25–27] investigate the effects of steps on the endwall of a cascade. Two of the studies [25,26], include a forward facing step. The first uses the transient liquid crystal method to show the heat transfer coefficients on the vane endwall. With an entrance step height of 4% of the chord length, separation and reattachment of the boundary layer over the step causes an area of higher heat transfer just downstream of the leading edge. The step is also credited with weakening the horseshoe vortex. Wu and Lin [26] investigated endwall film cooling effectiveness with a similar forward facing step ahead of the leading edge plane and ahead of the injection holes. They found that the step caused a very significant reduction in the film cooling effectiveness, particularly in the forward part of the passage. The latest study [27] investigates a backward facing step. A region of high heat transfer corresponding to the reattachment of the flow was noted downstream of the step.

The present paper documents a portion of a study on endwall cooling with leakage flows. A first of the series [10] discusses the effects of leakage rates and geometric features of the contoured endwall on passage aerodynamic losses. Results of a scoping study done under the 2^n factorial experimental design scheme are presented. The study shows a dominant effect due to introducing a gap on the platform within the passage. A second paper [28] presents the results of a sensitivity study on aerodynamic losses where parameters were changed one at a time. These parameters include changes in the transition section leakage and gap configuration, steps up and down as seen by the approaching flow, and slashface leakage and gap configuration changes, steps up, and down as seen by the flow traveling across the endwall from pressure to suction surfaces. The nominal case is with 0.5% leakage rate through the transition section and slashface gaps, with no steps. Perturbation cases with steps up and down and increased blowing rates are compared. A third paper [29] shows the effects of varying leakage flow rates on endwall convective heat transfer coefficients. The strongest effects are seen downstream of the slashface where interaction of the leakage flow and the downstream passage flow lead to strong mixing and high heat transfer coefficients. A fourth paper (the present paper) presents the effects of steps at the two gap locations on the endwall convective heat transfer coefficient distributions. The fifth and last of this series [30] discusses the effects of the leakage and steps on the adiabatic effectiveness value distributions. Details of the entire study can be found in the thesis of Piggush [31].

Test Facility

A low speed wind tunnel is used in conjunction with a linear cascade test section. The wind tunnel consists of three fans, a turbulence generator, and a contraction nozzle. The turbulence generator produces flow with large-scale, high-intensity turbulence, similar to that produced in a low-NO_x combustor. The original turbulence generator design comes from the work of Ames [32]. The turbulence generator is connected to a nozzle that transitions from 88.1 cm by 44.5 cm to 64.8 cm by 44.5 cm over a 58.4 cm length.

Table 1 Test vane dimensions and flow parameters

Vane true chord length, C	395.7 mm
Vane axial chord length, C_{ax}	198.5 mm
Vane span (inlet), S_0	315.4 mm
Vane span (outlet), S_1	244 mm
Aspect ratio, S_0/C (inlet)	0.8
Aspect ratio, S_1/C (outlet)	0.62
Fillet radius (nominal)	7.5 mm
Vane pitch	318 mm
Solidity, C/P	1.24
Max thickness	86 mm
Stagger angle	72 deg
Angle of incidence	0 deg
Chord Reynolds number (based on exit velocity and true chord)	9.01×10^5
Exit Mach number	0.11

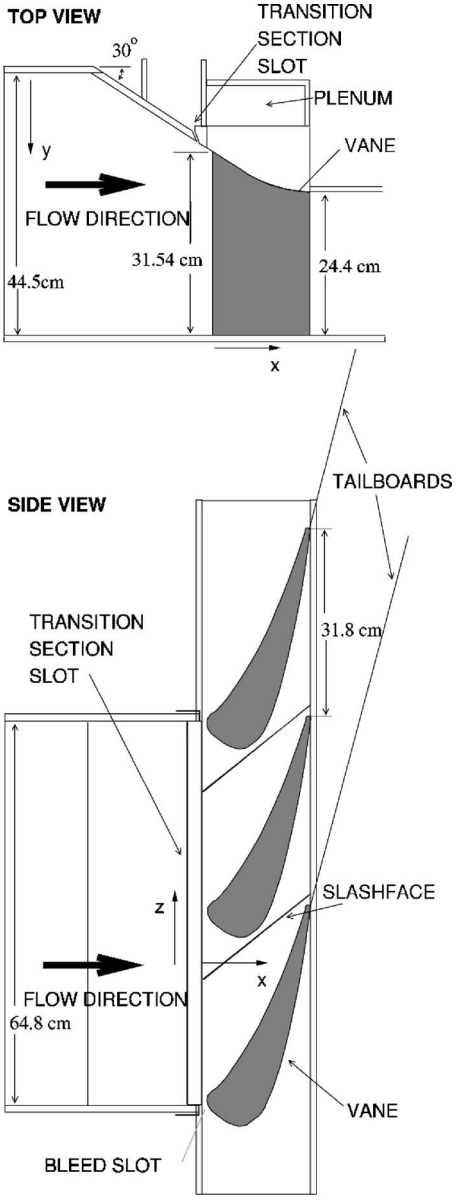

Fig. 1 Schematic of test section

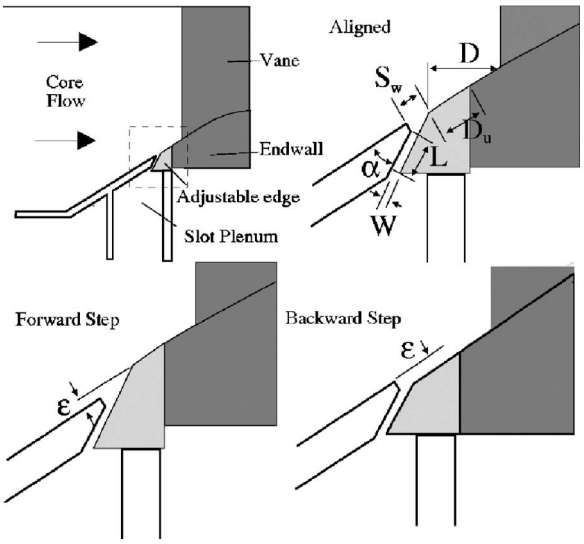

Fig. 2 Schematic of the transition section slot geometry. Details are of the portion enclosed in the dashed square. Note that the dark gray portion indicates the heated sections of endwall and vane. The light gray piece was switched to create steps at the transition section slot.

The test section has three vanes and two passages (see Table 1 and Fig. 1). Though a larger number of passages would be desirable, this would require a sacrifice of some spatial resolution. Data are taken only in the upper passage. Though not visible in the measurements taken, the suction side leg of the horseshoe vortex in the upper passage may be influenced at the leading edge region by the presence of the bleed slot. However, this leg is of minor importance relative to the pressure side leg which traverses the passage. The test section airfoils are of a profile taken from the midsection of a first stage stator of a midsized industrial engine having contoured endwalls. The present facility has similar endwall contouring to that of the pattern engine. The vanes are made of aluminum and are heated with four embedded heaters each. The heated vanes are designed to model the boundary conditions within the engine. Fluid convected from the vane surfaces to the endwall by secondary flows properly simulates the thermal conditions of similar flows in actual engines. The conductivity of the aluminum smoothes temperature gradients on the vane and endwall surface, making the surface nearly isothermal, but not perfectly so (the temperature distribution is shown in Fig. 5(*b*)).

One passage endwall has strong contouring (see Fig. 1) while the other endwall is flat. The contoured endwall of the test section is aluminum. It includes arrays of embedded heaters and thermocouples. Upstream of the leading edge, the test endwall is made of acrylic (see Fig. 2 and Table 2). This essentially creates an unheated starting length after the slot. The unheated starting length is given in Table 2. The endwall contour was chosen to mimic that used in the studies of Oke et al. [33] while incorporating a different angle of contraction (changed from 45 deg to 30 deg). The contour was suggested by engine designers to simulate the transition duct used in an actual engine. It includes a single, continuous, and thin slot ahead of the leading edge plane to simulate the transition-duct-to-vane-row gap and a slot within the passage to simulate the gutter or slashface gap. Both gaps are on the contoured endwall. More details of the facility may be found in Refs. [10,29,31].

The test section is designed to allow certain features of the geometry to be varied. As shown in Fig. 2, the endwall can be raised or lowered at the transition section gap. This creates a forward-or rearward-facing step. Also, the endwall position may be varied on either side of the slashface gap (Fig. 3 and Table 3) to simulate misalignment between individual vane pieces. Leak-

Table 2 Endwall transition section gap parameters (see Fig. 2): location and blowing rates

	Aligned	$\left[\frac{x}{C_{ax}}\right]$ (%)	Back step	$\left[\frac{x}{C_{ax}}\right]$ (%)	Fore step	$\left[\frac{x}{C_{ax}}\right]$ (%)
Vane axial chord, C_{ax}	198.5 mm	—	No change		No change	
Angle of inclination, α	30 deg	—	No change		No change	
Step height, ϵ	0	0	3 mm	1.5	3 mm	1.5
Slot width, W	2.0 mm	1.0	No change		No change	
Distance from slot trailing edge to leading edge, D	22.5 mm	11.3	27.0 mm	13.6	18.0 mm	9.1
Slot opening width, S_w	6 mm	3.0	1 mm	0.4	11 mm	5.6
Ratio of slot length (L) to slot width (W)	0.073	—	No change		No change	
Mass leakage to core flow rate	0–1.5%	—	0–1.0%	—	0–1.0%	—
Average velocity ratio, V_c/V_∞	0–2.4	—	0–1.6	—	0–1.6	—
Unheated starting length, D_u	15.0 mm	7.6	18 mm	9.1	11 mm	5.5

age flow from each of the gaps can be set separately. The overall mass flow rate is monitored using laminar flow elements calibrated to a Meriam Instruments 50MC2-4 laminar flow element. The temperature of the injected flow is maintained at the core flow temperature (to within 5% of the endwall to core flow temperature difference).

Probe access to the test section is through the flat endwall over the axial length $-0.1 < x/C_{ax} < 1.1$. Further details are available in Ref. [10].

Locations within the test section are described using an x, y, z coordinate system (Fig. 1). The x direction is defined as the coordinate which is orthogonal to the plane of the vane leading edges, at which $x=0$. The y direction is defined as the spanwise coordinate and is orthogonal to the flat endwall. The position where $y=0$ is the contoured endwall surface. Finally, the z coordinate is taken to be the pitchwise coordinate. It is orthogonal to the x and y coordinates. The $z=0$ line is horizontal in Figure 1, passing through the stagnation line of the center airfoil.

The cascade Reynolds number (see Table 1) is high enough to avoid flow separation on the airfoils or endwalls. Engine Mach numbers are not matched. Giel et al. [34] investigated the differences between endwall heat transfer coefficients in subsonic flows and transonic flows. Transonic flows were shown to have decreased heat transfer rates when compared to similar subsonic flows.

Nominal values of inlet ($x/C_{ax}=-1.5$) velocity and turbulence intensity are 7.0 m/s (23 ft/s) and 21%, respectively. Autocorrelations and power spectral distributions taken at the plane $x/C_{ax}=-1.5$ near the center of the passage were used to compute the turbulence scales. Values for the integral length scale of u' fluctuations, Λ_f/C_{ax}, are between 0.28 and 0.40 and values for the energy length scale, Λ_u/C_{ax}, are a consistent 0.127. The energy length scale is calculated as, $1.5(u')/\epsilon$, where u' is the fluctuation level of turbulence $\sqrt{\overline{u'^2}}$ and ϵ is the turbulence dissipation [35]. Further details on test section qualification may be found in Refs. [10,31].

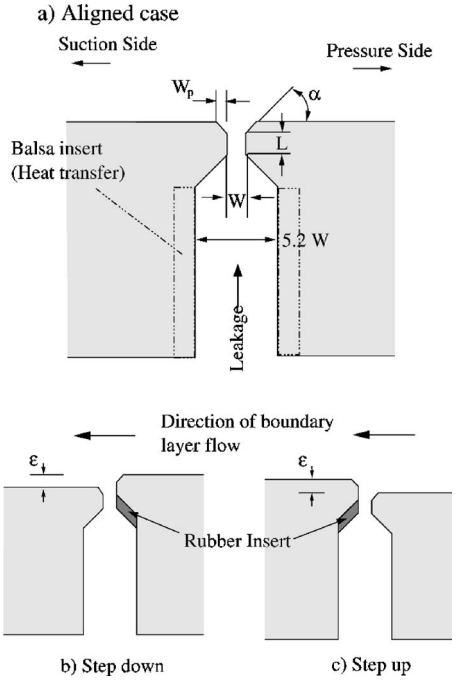

Fig. 3 Schematic of the slashface slot geometry. The balsa insulation is included for the heat transfer studies.

Experimental Procedure

The heat transfer data in this study were calculated from direct measurements of the thermal boundary layer. The method of gathering the boundary layer profiles and the method of data reduction are outlined in this section.

The primary heat transfer quantity presented in this paper is the convective heat transfer coefficient, h, nondimensionalized as the Stanton number (Eq. (1)) where n is normal to the contoured endwall

$$\mathrm{St} = \frac{h}{\rho U_\infty C_p} = \frac{-k\left(\left.\frac{dT}{dn}\right|_w\right)}{\rho U_\infty C_p (T_w - T_\infty)} \tag{1}$$

When the leakage flow temperature is different than the passage flow temperature, the adiabatic wall temperature is substituted for T_∞. Measurement of adiabatic wall temperature distributions is the subject of the paper of Piggush and Simon [30]. For the present

Table 3 Endwall slashface gap parameters: location and blowing rates

		$\left[\frac{x}{C_{ax}}\right]$ (%)
Blade axial chord length, C_{ax}	198.5 mm	—
Gap width, W	3 mm	1.5
Ratio of slot length (L) to slot width	1.0	—
Distance on leading edge plane from pressure side stagnation point toward suction surface	200 mm	101% (62.9% pitch)
Angle from axial	37.5 deg	—
Passage entry width, W_p	2.5 mm	1.25
Passage entry angle, α	45 deg	—
Step height, ϵ	3 mm	1.5
Mass leakage to core flow rate	0–1%	—

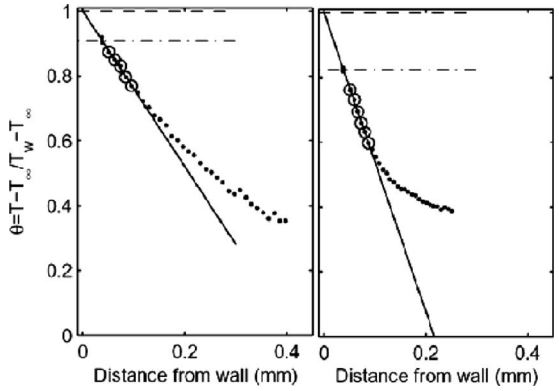

Fig. 4 Typical boundary layer profiles. The profile on the left is approximately St×1000=5; on the right St×1000=10. The solid line is the gradient $dT/dn|_w$, the dashed line is the calculated wall temperature, and the dot-dash line is the temperature measured when the thermocouple is on the wall. The intersection of the solid line and the dot-dash line occurs one thermocouple radius away from the wall.

measurements, the leakage flow and passage flow are of the same temperature, though the endwalls and vane surfaces are heated.

Thermal boundary layer temperature profile data are gathered using a fine wire thermocouple probe. The probe is designed based on the recommendations of Blackwell and Moffat [36]. A 76 μm (0.003 in.) butt-welded, Chromel-Constantin, E-type thermocouple is used. A 12.7 mm (0.5 in.) section of the wire is exposed between two hypodermic needle supports. The exposed section of wire is given a slight curve so that when it approaches the wall, the smooth, butt-welded junction is the first part to touch. Before each test run, the probe is observed under a microscope to verify that the junction is against the wall.

The temperature profile at a given x and z location may be analyzed to provide all the quantities necessary for determining the local Stanton number. The first measured points are taken when the thermocouple is pressed against the wall. Here, electrical continuity is used to indicate when the probe has just touched the endwall. The measured temperature at this point is not the wall temperature but approximately the fluid temperature at a distance of one wire radius from the wall. The next portion of the profile is taken while traversing the probe through the conduction sublayer. In this region, the temperature profile is linear. A line may be fit to these points which, when extrapolated back to the location of the wall, indicates the wall temperature, T_w, in Eq. (1). This method has been verified by comparison with embedded thermocouples. The slope of the profile is the quantity $dT/dn|_w$ of Eq. (1). The quantity T_∞ is measured by moving the probe far from the wall, into the mainstream fluid. Several temperature points are taken when the probe is initially against the wall. This is because the probe is sprung against the wall. As the traverse moves away from the wall, the thermocouple junction remains on the wall. When the temperature measured by the probe begins to drop, the probe has lifted off the wall. Typical profiles include approximately 8–10 points taken on the wall (the cluster of points in Fig. 4), 4–8 points in the conduction sublayer (the circled points in Fig. 4), and several more points outside the conduction sublayer. The wall temperature is calculated using the temperature gradient line and the liftoff point. The study of Qiu et al. [37] found the liftoff point to be one thermocouple radius away from the wall. Thus, the wall temperature is found by extrapolation of the gradient, $dT/dn|_w$, a distance from the wall of one thermocouple radius. This value is consistent with readings from embedded thermocouples.

Only the initial linear portion of the temperature profile is required, along with a single point far into the freestream. To reduce the experimental run time, a computer algorithm is used to end data collection when the probe has moved out of the conduction sublayer. The temperature at each location on the profile is sampled for a total of 4 s. Each profile requires about 120 s to gather.

Each experimental run begins with a test section warmup. During the warmup and during the experiment, the endwall and vane temperatures are monitored continuously. The warmup to steady state typically requires approximately 1 h, after which data collection begins. At steady state, the vane and endwall surfaces are maintained to within approximately 3 °C. During the run, the test section is shut down five times to switch the location of the probe and positioning system. The shutdowns last approximately 2 min. Data acquisition is paused briefly after the shutdown to allow the test section to return to steady-state conditions. Total data collection time is approximately $6\frac{1}{2}$ h for each set of test conditions.

After each run, the temperature profiles are individually analyzed and a line is fit to the linear portion of the profile. Stanton numbers are calculated following the method described above. Using linear interpolation between measurement locations, a contour plot of the heat transfer coefficients within the passage is generated. Figs. 5(*a*) and 6(*a*)–6(*d*) of this paper plot the local Stanton number multiplied by 1000. Dotted contour lines are included using intervals of 0.5×10^{-3} for Stanton numbers under 7×10^{-3}. Heat transfer measurements were taken in the upper passage (of the two passages of this test section). These data are replotted, without contour lines, in the adjacent passages.

This method of obtaining heat transfer coefficients is particularly suitable for application to this vane passage experiment. First, it does not require the surface to be isothermal or of a uniform heat flux. With an aluminum wall and embedded heaters, the thermal boundary condition is nearer to a constant temperature condition than to a constant heat flux condition. The constant temperature condition more closely reproduces the passage thermal boundary conditions in an engine.

To establish the validity of experimental results, it is necessary to determine the accuracy and repeatability of the method. For test cases similar to a turbine endwall, the calculated Stanton numbers were found to agree with those taken through traditional methods to within 11% [37]. The method was also successfully used in a turbine passage with endwall contouring by Burd et al. [38].

Direct verification of the method is difficult to do for the test section is not designed for other methods of finding heat transfer rates. However the method may be verified in a somewhat indirect manner. The determination of the wall temperature relies on both the slope of the line and the method of extrapolation. Thermocouples embedded in the endwall are used to measure the wall temperature; the temperature calculated from the boundary layer profile is then compared to temperature measured with the embedded thermocouple. Comparisons show that wall temperatures calculated in regions with high heat transfer rates ($St>0.01$) tend to overpredict wall temperature by 1.1% of the temperature difference between the wall and the freestream. Wall temperatures calculated in areas of low heat transfer rates ($St<0.06$) tend to underpredict the wall temperature by 3.3%. Both errors are considered acceptable.

To establish the repeatability of the method, the nominal case was repeated a total of four times. As discussed in Ref. [29], the standard deviation ranges from 2% of the average heat transfer coefficient near the inlet plane to 7% of the average heat transfer coefficient behind the slashface gap. These values are acceptable considering the difficulty in obtaining accurate heat transfer measurements.

Results

The cases presented in this study complement those presented in Ref. [29]. For the convenience of the reader, the results of the nominal configuration are recapitulated here.

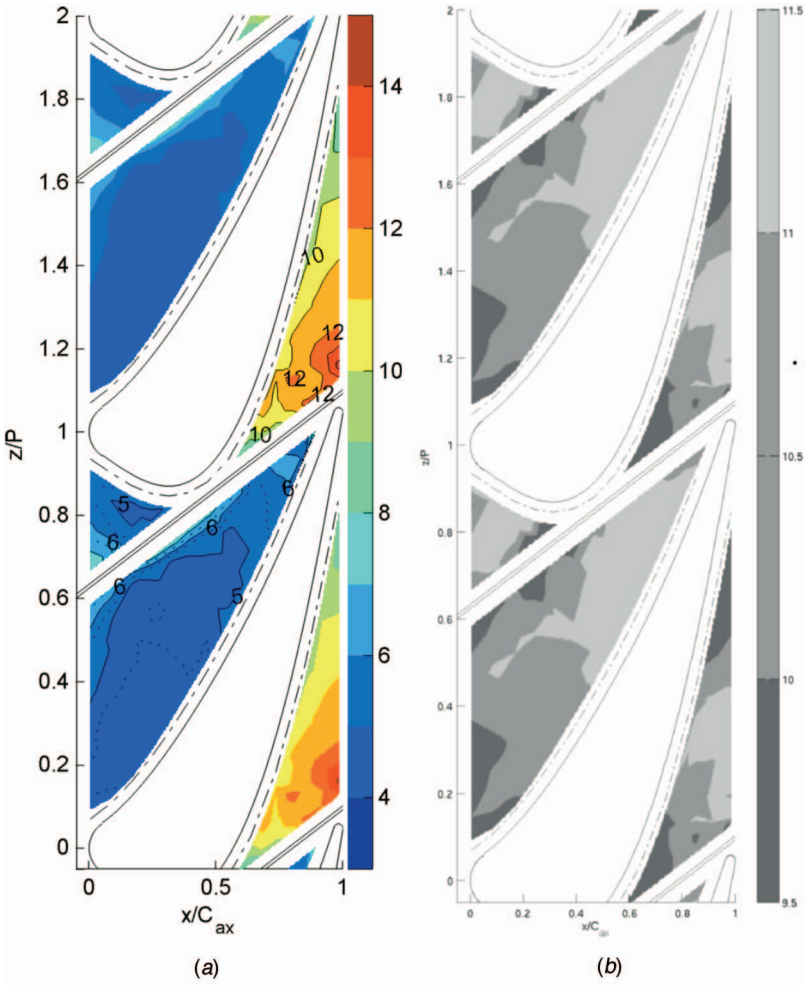

Fig. 5 Nominal Stanton number×1000 distribution (*a*) and endwall surface temperatures (*b*)

The Nominal Case. The nominal case includes blowing from both the transition section and slashface gaps. The leakage from the transition section gap is 0.5% of the passage mass flow rate (MFR) an additional 0.5% MFR is leaked through the slashface gap. Flow from the slashface gap does not exit uniformly. Upstream, the gap ingests fluid from the main flow. Downstream of about $x/C_{ax}=0.42$, fluid is expelled from the gap. The distribution of flow through the slashface gap was discussed in detail in Ref. [10].

Figure 5(*a*) shows the heat transfer distribution obtained for the nominal case. As indicated, the gaps play an important role in determining heat transfer rates on the passage endwall. There is generally a slight reduction at the inlet (compared to endwall heat coefficients in a passage without endwall gaps, presented Ref. [29]) which is attributable to a thickening of the inlet boundary layer due to flow injected at the transition section gap. In the entry plane region near the slashface gap, the heat transfer rates are increased, somewhat. The slashface gap ingests flow at this location. Some of the flow that it ingests is taken from the endwall boundary layer. This acts to thin the boundary layer around the entrance of the gap, thus increasing heat transfer rates compared to the smooth passage case values. One may think of the near-gap region as a sink flow.

Deeper into the passage, 20% of the chord length, the slashface gap is clearly defining the heat transfer distribution. A small zone of high heat transfer rates is apparent near the slashface gap on the pressure side. The momentum of the passage flow moving from the pressure surface to the suction surface causes more fluid to be ingested from the boundary layer along the pressure surface side of the gap. This produces the zone of high heat transfer on the pressure surface side of the gap without a similarly high heat transfer zone being produced on the suction surface side of the gap. At $x/C_{ax}>0.42$, flow emerges from the slashface gap. This provides partial blockage and spilling of the flow around the blockage, with its associated vorticity. The low streamwise momentum flow from the gap combines with the passage flow, thickening the endwall boundary layer and greatly augmenting the passage vortex at the exit of the passage.

Downstream of about $x/C_{ax}=0.6$, the slashface gap and flow continue to strongly affect heat transfer rates. The flow emerging from the gap pushes the boundary layer off the endwall. A reattachment point, with associated high heat transfer rates, may be observed just downstream of the slashface gap. As the fluid is accelerated through the throat of the passage, the boundary layer remains thin and heat transfer rates remain high. Also, increased levels of local turbulence resulting from the emerging flow from the gap raise heat transfer coefficients. The characteristic high heat transfer rates in the wake region of the vane are again observed. Downstream of the passage throat, heat transfer rates begin to drop, as the boundary layer thickens.

The Forward Facing Transition Section Step. In this configuration of the test section, the vane endwall is raised above the exit of the combustor transition section. This creates a forward facing step. As evidenced by the heat transfer coefficients (Fig. 6(*a*)), the development of the thermal boundary layer continues deeper into

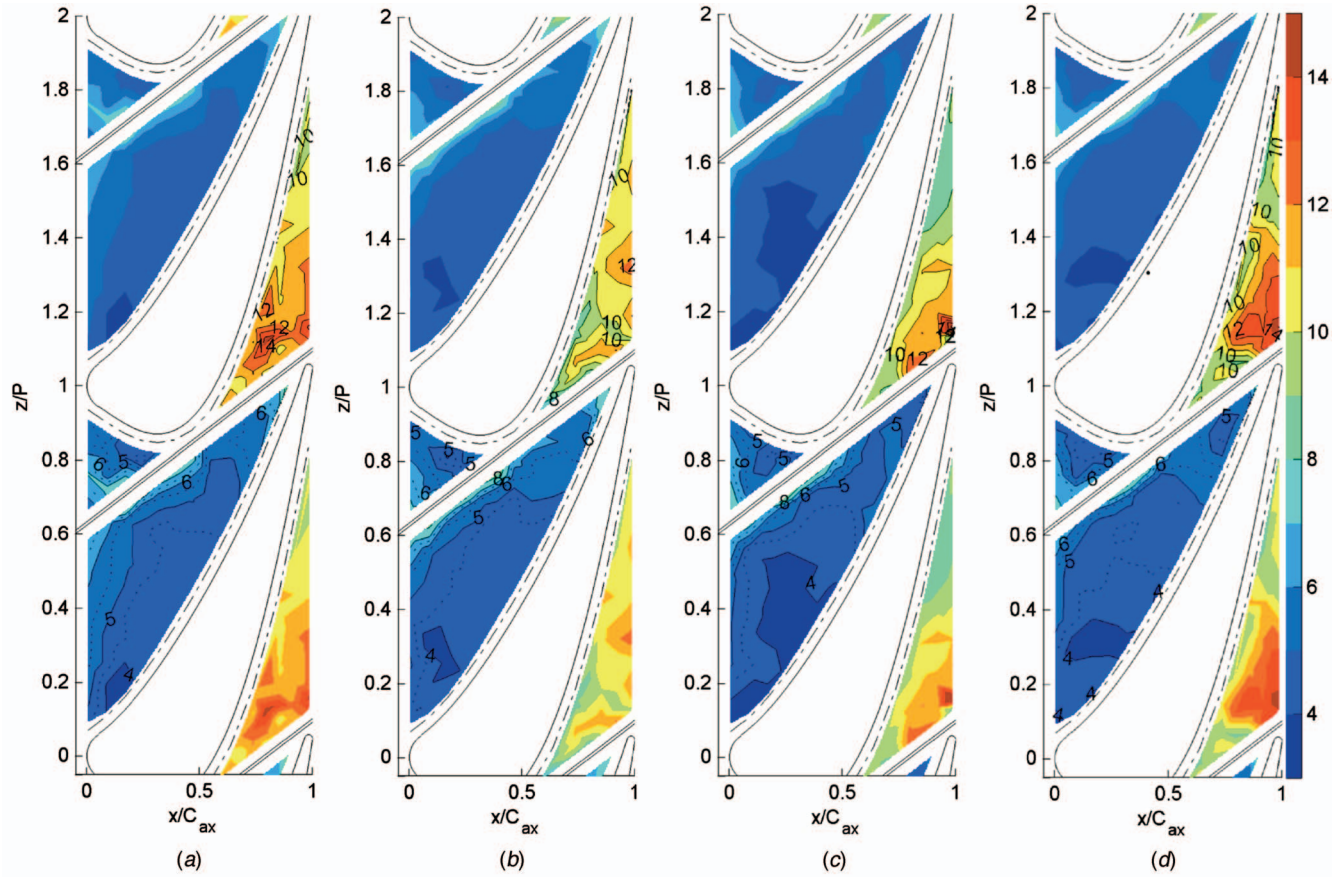

Fig. 6 Stanton number×1000 of the transition section forward facing step (*a*); transition section backward facing step (*b*); slashface forward facing step (*c*); and the slashface backward facing step (*d*)

the passage in this case as compared to that of the nominal case. This is because the step up creates a local acceleration of the flow which contributes to thinning of the momentum boundary layer and forces it to redevelop.

At the very beginning of the measurement zone and above the slashface gap ($x/C_{ax} \approx 0$ and $z/P \approx 0.7$) one can see a small effect of the forestep (relative to Fig. 5(*a*)) as a small zone of lower Stanton number values.

Just downstream, at about $x/C_{ax}=0.2$, the slashface is clearly ingesting fluid as in the nominal case. This, again, is observed as higher Stanton number values on the pressure side of the gap. Since the thickness of the momentum boundary layer is reduced due to the acceleration associated with the forestep, heat transfer coefficients are more readily influenced by the slashface gap. Values are increased over a larger region (compared to the nominal case) just downstream of the transition section gap and between the suction side of the vane and the slashface.

Downstream of the slashface, there is a clear reattachment point defined by the associated high heat transfer rates. This zone is centered at about $z/P=1.1$ and $x/C_{ax}=0.8$. The high heat transfer rates which begin there remain slightly higher than those observed in the nominal case. This continues to the end of the passage. This may be due to the thinner boundary layer, discussed previously.

The Backward Facing Transition Section Step. The test section was also run with the vane endwall positioned below the surface of the transition section, creating a backward facing step at the transition section gap. In this configuration, the flow injected at the transition section gap enters underneath the momentum boundary layer formed upstream of the transition section gap. Though both the thermal boundary layer and the momentum boundary layer must form in this configuration, there is a local deceleration of the flow behind the gap, allowing the boundary layers to thicken more rapidly, compared to the case with the forward facing step. The result is a heat transfer coefficient distribution at the inlet that is similar to that found in the nominal case (see Figs. 6(*b*) and 5(*a*)).

A notable deviation from the nominal case heat transfer coefficient distribution appears at the slashface gap. At the inlet to the passage, a greater amount of fluid appears to be taken from the endwall boundary layer, creating a larger region of influence for the slashface gap. This is consistent with the increased boundary layer thickness brought about by the separation zone and the local deceleration created by the backward facing gap. The zone of influence of the slashface gap extends further away from the slashface gap (in the direction of the pressure side of the passage). This indicates a stronger passage flow being developed in this region (more low momentum fluid moving from the pressure side to the suction side is available for ingestion into the gap). The larger passage flow is consistent with the increased losses for the backward facing step case documented in the pressure loss study [10].

Downstream of the slashface (as seen by the endwall secondary flow), a clear reattachment zone is identifiable in roughly the same position as in the forward facing transition section step study, $z/P=1.1$ and $x/C_{ax}=0.8$ (see Fig. 6(*b*)). However, the heat transfer rates in this region are lower than in the previously discussed studies. This is due to the thickened boundary layer which forms behind the transition section step.

Downstream of the reattachment point, there is an initial decrease in heat transfer rates, followed by a subsequent increase in heat transfer rates. The decrease is consistent with boundary layer thickening, which will take place since there is actually a slight

deceleration of the flow in this region (from about $x/C_{ax}=0.5$ to 0.7) as indicated by the static pressure profile of the suction side of the vane (see Ref. [10]). The increase in the heat transfer coefficient is due to the slight amount of acceleration imposed near the suction side of the vane, from about $x/C_{ax}=0.7$ to 0.9 (see Ref. [10] for the pressure profile of the vane).

The Forward Facing Slashface Step. The influences of steps at the slashface gap were also investigated. In the first configuration, the flow in the endwall boundary layer, which is moving from the pressure side to the suction side, encounters a forward facing step at the slashface gap. The step is formed by holding the pressure side section of the endwall in the nominal position and raising the suction side section of the endwall. This means that there is a forestep at the transition section gap for the portion of the endwall that is between the suction surface and the slashface gap.

The inclusion of a slashface forward facing step changes the heat transfer coefficients at the inlet to the passage, slightly (see Fig. 6(*c*)).

The geometry change is at the slashface gap, therefore discussion will focus on this region. For the forward facing step (as seen by the endwall secondary flow), the heat transfer rates at the leading edge plane are slightly augmented for the region between the slashface gap and the suction side of the vane. This is the result of local acceleration imposed on the flow by raising this section of the endwall. The comments in the section that discusses the forward facing transition section step and explains the increases in the heat transfer rates at the leading edge plane are also applicable to this geometry. This is due to the passage flow. The inclusion of the step increases the preference for ingestion of the pressure side boundary layer fluid, thinning the boundary layer in this region below the boundary layer thickness of the nominal case. As a result, heat transfer rates are higher. In the portion of the test section which is between the suction surface and the slashface slot, heat transfer rates are reduced from levels seen in the nominal case. Just downstream (as seen by the endwall secondary flows) of the gap, very near its edge, a region of reattachment is observed. This small zone is centered at $z/P=1.05$ and $x/C_{ax}=0.8$. Downstream of reattachment (again, as seen by the endwall secondary flow), the thermal boundary layer thickens and heat transfer rates drop.

The Backward Facing Slashface Step. In this configuration, the endwall boundary layer flow moving from the pressure side to the suction side encounters a backward facing step. To create this step, the suction side of the endwall is dropped down while the pressure side is held in the nominal position. Thus, at the transition section, there is a backstep on the endwall section between the suction side and the slashface gap.

Similar to the case of the forward facing slashface step, the backward facing slashface step has only a small effect on heat transfer rates at the inlet plane (see Fig. 6(*d*)).

Just downstream of the inlet plane, the region of influence for the slashface sink flow is shifted slightly toward the suction side of the passage. Consequently, the region of high heat transfer coefficients, beginning after about $x/C_{ax}=0.2$, is shifted slightly toward the suction side. Since the passage flow detaches off the edge of the step, the suction side of the slot tends to provide the low momentum fluid for ingestion (sink flow).

In the section of the passage downstream of the slashface slot (as seen by the endwall secondary flow), high heat transfer rates are observed. The passage flow separates off the edge of the slot and is pushed further away by the injected fluid. This causes a relatively large separation bubble, as evidenced by the large region downstream of the slot where Stanton number values $\times 1000$ range between St=9 and 11. Downstream of this zone (as seen by the endwall secondary flow), the detached flow impinges sharply on the surface as it reattaches, causing high heat transfer rates downstream of the separation bubble. Further downstream in the passage (in the direction of the secondary flow), the thermal boundary layers thicken and the heat transfer rates decrease.

Conclusion

A linear cascade incorporating endwall contouring and endwall assembly features has been used to investigate heat transfer rates. Results show the effects of steps and leakage flows on the endwall heat transfer rates. In brief, a forward facing step at the transition section gap imposes a local acceleration on the flow, thinning boundary layers and causing slightly higher heat transfer rates across the whole test section endwall. The backward facing transition section step has the opposite effect, thickening the boundary layer and reducing heat transfer rates, particularly downstream of the slashface gap (as seen by the endwall secondary flow). Steps at the slashface gap also affect the endwall heat transfer. In the forward portion of the passage, slashface steps cause a redistribution of the heat transfer rates. The portion of the passage between the suction surface and slashface slot is significantly affected by the slashface step. A forward facing step reduces the heat transfer rates by lessening the strength of impingement as the passage boundary layer reattaches. The backward facing step has the opposite effect, increasing the strength of impingement, and thereby shows increased heat transfer rates.

The data presented in this study provide a more complete picture of endwall flow physics as affected by steps, gaps, and leakage in the passage geometry.

Acknowledgment

The results presented in this paper come from research funded under the UTSR program of DOE. The grant monitor is Richard Wenglarz. Guidance in facility and test program design was provided by Edward North and Ihor Diakunchak of Siemens-Westinghouse, Ronald Bunker of the General Electric Company, and Steven Burd of Pratt and Whitney, Incorporated.

Nomenclature

Constants

C = vane true chord length
C_p = constant pressure heat capacity
C_{ax} = vane axial chord length
D = distance from slot trailing edge to airfoil leading edge
D_u = unheated starting length
h = convective heat transfer coefficient
k = thermal conductivity
L = slot length
MFR = ratio of leakage to passage mass flow rates
P = pitch length
S = vane span
S_w = slot opening width
St = Stanton number
T = temperature
u' = rms fluctuation of streamwise velocity
W = gap width
W_p = passage entry width
x = distance in the streamwise direction
y = distance in the spanwise direction
z = distance in the pitchwise direction

Greek

α = slot angle, angle of inclination (see Figs. 2 and 3)
ϵ = step height, turbulent dissipation
Λ_f = integral length scale of turbulence
Λ_u = energy length scale of turbulence
ρ = density

Subscripts

$_0$ = at the inlet of the passage
$_1$ = at the exit of the passage
$_w$ = at the wall
$_\infty$ = condition in the freestream

References

[1] Simon, T., and Piggush, J., 2006, "Turbine Endwall Aerodynamics and Heat Transfer," AIAA J Power Propul., **22**, pp. 301–312.
[2] Herzig, H. Z., Hansen, A. G., and Costello, G. R., 1953, "Visualization Study of Secondary Flows in Cascades," National Advisory Committee for Aeronautics, Washington, D.C., NACA Technical Report No. 1163.
[3] Eckerle, W. A., and Langston, L. S., 1987, "Horseshoe Vortex Formation Around a Cylinder," J. Turbomach., **109**(2), pp. 278–285.
[4] Langston, L. S., Nice, M. L., and Hooper, R. M., 1977, "Three-Dimensional Flow Within a Turbine Cascade Passage," J. Eng. Power, **99**, pp. 21–28.
[5] Chung, J. T., and Simon, T. W., 1990, "Three-Dimensional Flow Near the Blade/Endwall Junction of a Gas Turbine. Visualization in a Large-Scale Cascade Simulator," ASME Paper No. 90-WA/HT-4.
[6] Wang, H. P., Olson, S. J., Goldstein, R. J., and Eckert, E. R. G., 1997, "Flow Visualization in a Linear Turbine Cascade of High Performance Turbine Blades," J. Turbomach., **119**, pp. 1–8.
[7] Morris, A. W. H., and Hoare, R. G., 1975, "Secondary Loss Measurements in a Cascade of Turbine Blades With Meridional Wall Profiling," ASME Paper No. 75-WA/GT-13.
[8] Kopper, F. C., Milano, R., and Vanco, M., 1981, "Experimental Investigation of Endwall Profiling in a Turbine Vane Cascade," AIAA J., **19**(8), pp. 1033–1040.
[9] Burd, S., and Simon, T., 2000, "Effects of Slot Bleed Injection Over a Contoured Endwall on Nozzle Guide Vane Cooling Performancd: Part I—Flow Field Measurements," ASME Paper No. 2000-GT-199.
[10] Piggush, J., and Simon, T., 2005, "Flow Measurements in a First Stage Nozzle Cascade Having Endwall Contouring, Leakage and Assembly Features," ASME Paper No. GT2005–68340.
[11] Granser, D., and Schulenberg, T., 1990, "Prediction and Measurment of Film Cooling Effectiveness for a First-Stage Turbine Vane Shroud," ASME Paper No. 90-GT95.
[12] Zhang, L. J., and Jaiswal, R. S., 2001, "Turbine Nozzle Endwall Film Cooling Study Using Pressure-Sensitive Paint," J. Turbomach., **123**(4), pp. 730–738.
[13] Aunapu, N. V., Volino, R. J., Flack, K. A., and Stoddard, R. M., 2000, "Secondary Flow Measurements in a Turbine Passage With Endwall Flow Modification," J. Turbomach., **122**, pp. 651–658.
[14] Yamao, H., Aoki, S., Takeshi, K., and Takeda, K., 1987, "An Experimental Study for Endwall Cooling Design of Turbine Vanes," *Proceedings of the International Gas Turbine Society of Japan*, Paper No. 87-TOKYO-IGTC-67.
[15] Blair, M. F., 1974, "Experimental Study of Heat Transfer and Film Cooling on Large-Scale Turbine Endwalls," ASME J. Heat Transfer, **96**, pp. 524–529.
[16] Graziani, R. A., Blair, M. F., Taylor, J. R., and Mayle, R. E., 1979, "Experimental Study of Endwall and Airfoil Surface Heat Transfer in a Large Scale Turbine Blade Cascade," ASME Paper No. 79-GT-99.
[17] Goldstein, R. J., and Spores, R. A., 1988, "Turbulent Transport on the Endwall in the Region Between Adjacent Turbine Blades," ASME J. Heat Transfer, **110**, pp. 862–869.
[18] Pasinato, H. D., Liu, Z., Roy, R. P., Howe, W. J., and Squires, K. D., 2002, "Prediction and Measurement of the Flow and Heat Transfer Along the Endwall and Within an Inlet Vane Passage," ASME Paper No. GT-2002-30189.
[19] Chyu, M. K., Hsing, Y. C., and Bunker, R. S., 1998, "Measurements of Heat Transfer Characteristics of Gap Leakage around a Misaligned Component Interface," ASME Paper No. 98-GT-132.
[20] Yu, Y., and Chyu, M. K., 1998, "Influence of Gap Leakage Downstream of the Injection Holes on Film Cooling Performance," J. Turbomach., **120**, pp. 541–548.
[21] Zhang, L., and Moon, H. K., 2003, "Turbine Nozzle Endwall Inlet Film Cooling—The Effect of a Back-Facing Step," ASME Paper No. GT2003-38319.
[22] Zhang, L., and Moon, H.-K., 2004, "Turbine Nozzle Endwall Inlet Film Cooling: The Effect of a Back-Facing Step and Velocity Ratio," ASME Paper No. IMECE2004-59117.
[23] Colban, W. F., Thole, K. A., and Zess, G., 2003, "Combustor Turbine Interface Studies—Part I: Endwall Effectiveness Measurement," ASME J. Turbomach., **125**, pp. 193–202.
[24] Colban, W. F., Lethander, A. T., Thole, K. A., and Zess, G., 2003, "Combustor Turbine Interface Studies—Part II: Flow and Thermal Field Measurements," ASME J. Turbomach., **125**, pp. 203–209.
[25] Wu, P.-S., Lin, T.-Y., and Lai, Y.-M., 2001, "Heat Transfer Coefficient Distribution in the Endwall Region of a Vane With a Finite-Step Entrance Condition," *Proceedings 3rd Pacific Symopsium on Flow Visualization and Image Processing*, Maui, HI.
[26] Wu, P.-S., and Lin, T.-Y., 2003, "Effects of a Forward-Facing Entrance Step on Film Cooling Effectiveness in the Endwall Region of a Vane," *Recent Progress in Transport Phenomena*, pp. 573–578.
[27] Wu, P.-S., Chiu, Y.-C., Chen, L.-Y., and Chang, S.-F., 2005, "Effects of a Backward-Facing Entrance Step on Heat Transfer and Film Cooling of the Endwall Surface of a Vane Passage," *6th World Conference on Experimental Heat Transfer, Fluid Mechanics and Thermodynamics*, Orlando, FL.
[28] Piggush, J., and Simon, T., 2005, "Flow Measurements in a First Stage Nozzle Cascade Having Leakage and Assembly Features: Effects of Endwall Steps and Leakage on Aerodynamic Losses," ASME Paper No. IMECE2005-83032.
[29] Piggush, J., and Simon, T., 2005, "Heat Transfer Measurements in a First Stage Nozzle Cascade Having Endwall Contouring, Leakage and Assembly Features," ASME Paper No. HT2005-72573.
[30] Piggush, J., and Simon, T., 2006, "Adiabatic Effectiveness Measurements in a First Stage Nozzle Cascade having Endwall Contouring, Leakage and Assembly Features," ASME Paper No. GT2006-90576.
[31] Piggush, J., 2005, "An Experimental Investigation of Endwall Leakage Flows and Misalignment in a Gas Turbine Nozzle Guide Vane Cascade," Master's thesis, University of Minnesota, Minneapolis, MN.
[32] Ames, F., 1994, "Experimental Study of Vane Heat Transfer and Film Cooling at Elevated Levels of Turbulence," NASA, Washington, DC, Technical Report No. CR-19825.
[33] Oke, R., Simon, T., Shih, T., Zhu, B., Lin, L., and Chyu, M., 2001, "Measurements Over a Film-Cooled, Contoured Endwall With Various Coolant Injection Rates," ASME Paper No. 2001-GT-0140.
[34] Giel, P. W., Thurman, D. R., Fossen, G. J. V., Hippensteele, S. A., and Boyle, R. J., 1996, "Endwall Heat Transfer Measurements in a Transonic Turbine Cascade," ASME Paper No. 96-GT-180.
[35] Hancock, P., and Bradshaw, P., 1983, "The Effect of Free-Stream Turbulence on Turbulent Boundary Layer Flow and Heat Transfer," J. Fluids Eng., **105**, p. 284.
[36] Blackwell, B., and Moffat, R., 1975, "Design and Construction of a Low-Velocity Boundary Layer Temperature Probe," J. Heat Transfer, **97**, pp. 313–315.
[37] Qiu, S., Simon, T. W., and Volino, R. J., 1995, "Evaluation of Local Wall Temperature, Heat Flux, and Convective Heat Transfer Coefficient From the Near-Wall Temperature Profile," *Heat Transfer in Turbulent Flows*, ASME, New York, HTD-318, pp. 45–52.
[38] Burd, S., Satterness, C., and Simon, T., 2000, "Effects of Slot Bleed Injection over a Contoured Endwall on Nozzle Guide Vane Cooling Performance: Part II—Thermal Measurements," ASME Paper No. 2000-GT-200.

Three-Dimensional Numerical Analysis of Curved Transpiration Cooled Plates and Homogenization of Their Aerothermal Properties

Gottfried Laschet
e-mail: g.laschet@access.rwth-aachen.de

Stephan Rex

ACCESS e.V.,
Intzestrasse 5,
D-52072 Aachen, Germany

Dieter Bohn

Robert Krewinkel

Institute of Steam and Gas Turbines,
Aachen University of Technology,
D-52056 Aachen, Germany

Three different designs of a transpiration cooled multilayer plate—plane, convex, and concave—are analyzed numerically by application of a 3D conjugate fluid flow and heat transfer solver. The geometrical setup and the fluid flow conditions are derived from modern gas turbine components. The conjugate analysis of these designs focus on the influence of the surface curvature, the cooling film development on the plate surface, the fluid structure in the cooling channels, and on the cooling efficiency of the plate. Moreover, to predict the effective thermal properties and the permeability of these multilayer plates, a multiscale approach based on the homogenization technique is employed. This method allows the calculation of effective equivalent properties either for each layer or for the multilayer of superalloy, bondcoat, and thermal barrier coating (TBC). Permeabilities of the different designs are presented in detail for the TBC layer. The influence of the plate curvature and the blowing ratio on the effective orthotropic thermal conductivities is finally outlined. [DOI: 10.1115/1.2720867]

Keywords: transpiration cooling, conjugate heat transfer, homogenization, permeability, thermal conductivity

1 Introduction

The increase of the total efficiency of modern gas turbines is today an important ecological and economical goal. Reduction of the cooling mass flow in thermally high loaded components is one of the most promising solutions to reach this goal. The cooling efficiency, classically realized by film cooling configurations [1], can be improved by a full coverage cooling system. In this case, the cooled walls of gas turbine components are covered with an array of small shaped cooling holes so that a quasihomogeneous cooling film is developed on the surface. Such a cooling system is realized by drilling fine laser holes in multilayer plates. Several cooling configurations for the flat plate have been investigated previously [2,3] by adopting a fine discretization of each cooling channel and by using a 3D Conjugate Heat Transfer and fluid flow solver, CHTflow. These analyses have lead to define efficient outflow shapes for the considered plate.

As the gas turbine components like the combustion chamber wall are often curved, the main objective of this paper is to quantify the influence of the plate curvature on the cooling film structures, the cooling efficiency, and on the effective material properties. Three different cooled multilayer plates—flat, convex, and concave—are selected for the detailed conjugate analysis.

As such detailed analysis requires meshes of more than one million finite volumes, needing several weeks on a supercomputer to reach the steady state, a multiscale approach based on the homogenization technique [4–6] is introduced here. This homogenization technique allows the calculation of equivalent thermophysical properties either for each layer separately or for the multilayer. In a further step, it allows us to calculate the aerothermal behavior of complex gas turbine components by replacing the heterogeneous material by a continuous, equivalent one. For this purpose a reference unit cell with periodic boundary conditions is extracted from the 3D conjugate model (see Fig. 1).

Since the pioneering work of Sanchez-Palencia [4] in the 1980s, the application of the homogenization method to the heat and mass transport through porous media is well documented in the literature [5,6]. But, to our knowledge, the influence of the design of cooling channels on the effective permeability and thermal properties of porous multilayer materials has been investigated only in our previous papers [7–9]. In Refs. [7,8] a theoretical description of the method applied either to advective nonlinear heat transfer problems or to the fluid flow of a compressible cooling gas can be found. In Ref. [9] the focus was on the numerical prediction of effective permeabilities and thermal conductivities for different cylindrical and shaped cooling configurations of a flat plate.

As in Ref. [9], this paper outlines mainly numerical results. Therefore, only a brief synthesis of the conjugate heat transfer and fluid flow solver and of the implemented multiscale technique is given here. After describing the geometric configurations and the boundary conditions of the 3D conjugate model, numerical results about the cooling film structure, the temperature distribution, and the local cooling efficiency are discussed for the selected plate designs. Then, the influence of the curvature on the predicted effective permeabilities is examined. In Sec. 6, the effective thermal conductivities of each layer and of the multilayer are compared for the same flow conditions and the influence of the blowing ratio on these conductivities is depicted.

2 Conjugate Heat Transfer and Fluid Flow Solver

The numerical scheme of the in-house CHTflow code works on the basis of an implicit finite volume method combined with a

Contributed by the International Gas Turbine Institute of ASME for publication in the JOURNAL OF TURBOMACHINERY. Manuscript received July 19, 2006; final manuscript received September 5, 2006. Review conducted by David Wisler. Paper presented at the IGTI TURBO EXPO Conference 2006 in Barcelona, Spain, Paper No. GT2006-90377.

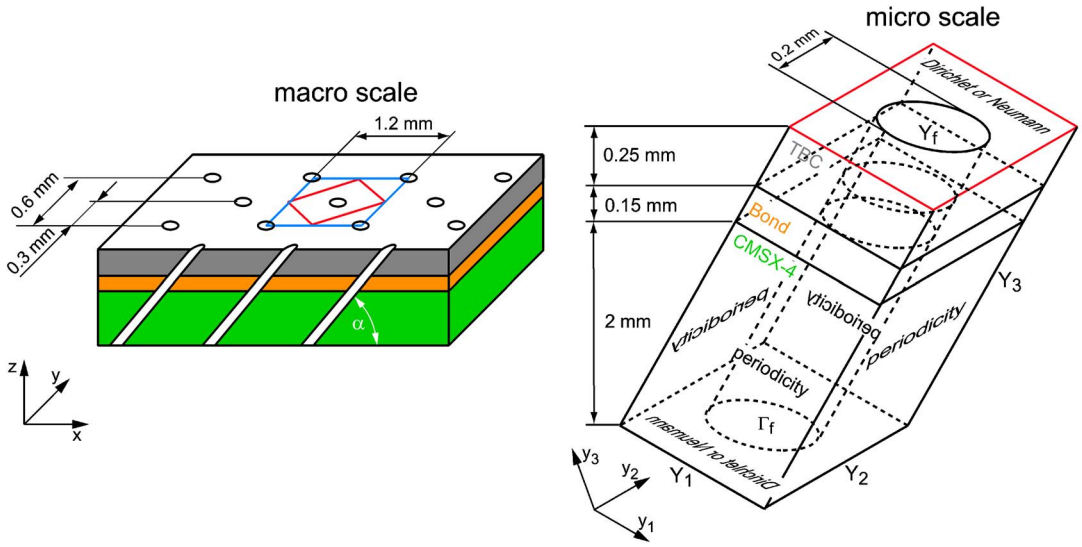

Fig. 1 Definition of a unit cell of periodicity Y_1, Y_2, Y_3 for the transpiration cooled multilayer plate

multiblock technique. The physical domain is divided into separate blocks and the full, compressible, 3D Navier-Stokes equations are solved in the fluid blocks. The governing equations for the conservative variables are formulated in arbitrary, body-fitted coordinates to allow the simulation of complex geometries. The conservation equations are first order implicitly discretized in time by using the Newton method [10]. Upwind discretization is used for the inviscid fluxes. The viscous fluxes are there approximated by central differences. The resulting system of linear equations is solved by a Gauss-Seidel scheme.

The system of the governing equations in the solid body region is reduced to the Fourier equation, which is solved directly and coupled to the fluid flow region. This coupling of fluid and solid blocks is achieved via a common wall temperature, resulting from the equality of the local heat fluxes passing through the contacting cell faces. A detailed description of the conjugate calculation method and its validation can be found in Ref. [11]. For the closure of the conservation equations the algebraic eddy-viscosity turbulence model by Baldwin and Lomax is used. The conjugate analyses are assumed to be converged when, in a run of 10,000 time steps, the temperature changes at the solid/fluid interfaces become lower than 1.0°C. Note that a high resolution grid is needed for the conjugate analysis to compute the heat transfer into the solid body with sufficient accuracy. In former publications [2,3] it has been proven that the conjugate method is an excellent tool for designing multilayer cooling designs.

3 Homogenization of the Heat Transfer and Fluid Flow Through a Porous Material

3.1 Heat Transfer Problem. The homogenization technique assumes that the porous material like the cooled multilayer of superalloy CMSX-4, bondcoat, and thermal barrier coating (TBC) is built up at the microscale by the periodic repetition of a representative volume Y, named unit cell (see Fig. 1). This technique, more detailed in Ref. [7], is based on the formal asymptotic expansion of the temperature T^h on the porous material with the aspect ratio ε between micro- and macroscale,

$$T^h(x) = T^0(\mathbf{x},\mathbf{y}) + \varepsilon T^1(\mathbf{x},\mathbf{y}) + 0(\varepsilon^2) \tag{1}$$

with $\mathbf{x}$, the macroscopic variable, which measures the mean field variation (i.e., temperature) from unit cell to unit cell and $\mathbf{y}=\mathbf{x}/\varepsilon$, the periodic microscopic variable, which describes the strong field variations within each unit cell.

The serial expansion (1) and the differential operator

$$\frac{D}{Dx_i} = \frac{\partial}{\partial x_i} + \frac{1}{\varepsilon}\frac{\partial}{\partial y_i}$$

are then introduced in the steady state advective heat transport equations,

$$\frac{D}{Dx_i}\left(k_{ij}(\mathbf{y},T^h)\frac{DT^h}{Dx_j}\right) + \rho c_p v_j^* \frac{DT^h}{Dx_j} = 0 \tag{2}$$

where $v_i^* = v_i^h$ in the fluid and $v_i^* = 0$ in the solid part.

This leads to a system of differential equations, which is sorted with respect to ε and outlined in Ref. [7]. The ε^{-2} term provides $T^0(\mathbf{x},\mathbf{y}) = T^0(\mathbf{x})$. Therefore, the first expansion term depends only on the macroscopic variable $\mathbf{x}$ and not on the microscopic variable $\mathbf{y}$.

To solve the ε^{-1} term, a special solution of the type,

$$T^1(\mathbf{x},\mathbf{y}) = -\chi^\lambda(\mathbf{y})\frac{\partial T^0(\mathbf{x})}{\partial x_\lambda} \tag{3}$$

where χ^λ $(\lambda = 1,2,3)$ is a periodic displacement field on Y, is introduced in the corresponding linear differential equation (see Eq. (2.6) of Ref. [7]) and leads to

$$\frac{\partial k_{i\lambda}(\mathbf{y},T^0)}{\partial y_i} - \frac{\partial}{\partial y_i}\left[k_{ij}(\mathbf{y},T^0)\frac{\partial \chi^\lambda}{\partial y_j}(\mathbf{y})\right] = 0 \tag{4}$$

A variational formulation of Eq. (4) is introduced in Ref. [7] to determine the unknown displacements χ^λ. The finite element discretization of this weak formulation leads to additional microscopic problems on the unit cell, which are solved numerically. These problems take into account respectively the jump of thermal conductivity at solid/liquid interfaces by implicit fluxes and the temperature variation of k_{ij} in the unit cell by equivalent source terms. The establishment and resolution of the microscopic problems constitute the main task of the developed homogenization program HOMAT (HOMogenization of MATerial properties).

Finally, the resolution of the ε^0 term requires the definition of the following effective, homogeneous thermal conductivities:

$$k_{i\lambda}^{\text{hom}} = \frac{1}{|Y|}\int_Y \left[k_{i\lambda}(\mathbf{y},T^0) - k_{ij}(\mathbf{y},T^0)\frac{\partial \chi^\lambda}{\partial y_j}\right] dy \tag{5}$$

with $|Y|$: volume of the unit cell.

Thus, the effective conductivity (5) is a function of the thermal

properties of each component, the microscopic displacements χ^{λ}, and of the stationary aerothermal behavior of the cooled body through the macroscopic temperature T^0.

3.2 Fluid Flow Problem

.

3.2.1 Homogenization by Asymptotic Expansion. The cooling channel (see Fig. 1) is filled with a compressible gas whose density is small and varies mainly with the temperature due to the low pressure drop predicted in the 3D conjugate analyses of the considered multilayer plates (see Sec. 4). Thus, by adopting the Boussinesq approximation, the state equation of the cooling gas is expressed by $\rho^h = \rho_0(1-\beta T^h)$.

Following the standard setup of the homogenization technique developed in Ref. [4], formal asymptotic expansions of the form,

$$\mathbf{v}^h(\mathbf{x}) = \mathbf{v}(\mathbf{x},\mathbf{y}) = \varepsilon^2\mathbf{v}^0(\mathbf{x},\mathbf{y}) + \varepsilon^3\mathbf{v}^1(\mathbf{x},\mathbf{y}) + 0(\varepsilon^4) \tag{6}$$

$$p^h(\mathbf{x}) = p(\mathbf{x},\mathbf{y}) = p^0(\mathbf{x},\mathbf{y}) + \varepsilon p^1(\mathbf{x},\mathbf{y}) + 0(\varepsilon^2) \tag{7}$$

are specified for the velocity and pressure fields. These serial developments and the differential operator, $D/Dx_i = \nabla_{x_i} + \varepsilon^{-1}\nabla_{y_i}$ are then introduced into the steady state Navier-Stokes equations and into the no-slip boundary condition $\mathbf{v}=0$ on the fluid/solid interfaces Γ_{fs}. This introduction leads to a system of differential equations which must be solved.

The ε^{-1} term of the momentum equation becomes

$$-\nabla_{y_f} p^0(\mathbf{x},\mathbf{y}) = 0 \rightarrow p^0 = p^0(\mathbf{x}) \tag{8}$$

Thus p^0 is independent of the periodic variable $\mathbf{y}$ and all terms involving $\nabla_{y_f} p^0(\mathbf{x},\mathbf{y})$ vanish. Moreover, the ε^0 term of the momentum equation, the $\varepsilon^{-1/2}$ term of the continuity equation, and the $\varepsilon^{1/2}$ term of the boundary condition lead to the following differential system expressed on the unit cell:

$$\begin{aligned} &\rho^*(v_k^0 \cdot \nabla_{y_k} v_i^0) = -\nabla_{x_f} p^0 - \nabla_{y_f} p^1 + \mu_0 \Delta_y v_i^0 + \rho^* g_i \quad \text{in } Y_f \\ &\rho^* \nabla_{y_i} v_i^0 = 0 \quad \text{in } Y_f \\ &v_i^0 = 0 \quad \text{at } \Gamma_{f_s} \end{aligned} \tag{9}$$

with $\rho^*(\mathbf{x}) = \rho_0[1-\beta T^0(\mathbf{x})]$

As detailed in Ref. [8], a variational formulation is introduced to solve the microscopic boundary value problem (9) on the unit cell Y. This formulation leads to determine additional velocity fields $\omega^j \in V_f, j=1,2,3$ satisfying

$$\int_{Y_f} \nabla_{y_k}\omega^j \cdot \nabla_{y_k}\mathbf{q}\, dy = \int_{Y_f} q_j(\mathbf{y}) dy \quad \text{for any } \mathbf{q} \in V_f \tag{10}$$

where V_f is the space of periodic velocities defined by $V_f = \{\nabla_{y_i} q_i = 0, q_i = 0 \text{ on } \Gamma_{fs};\ q_i \text{ is } Y\text{-periodic}\}$.

With the following definition of the permeability tensor of the porous material [4]

$$P_{ij} = \langle \omega_i^j \rangle = \frac{1}{Y}\int_Y \omega_i^j(\mathbf{y}) dy \tag{11}$$

it is possible to deduce the classical Darcy law as macroscopic equivalent behavior (see [8])

$$\mu_0 \langle v_i^0 \rangle(\mathbf{x}) = P_{ij}[-\nabla_{x_f} p^0(\mathbf{x}) + \rho^* g_j] \tag{12}$$

Thus, P_{ij} is defined as the mean value of the component i of the velocity ω^j. It is a symmetric, positive definite tensor, whose components depend only on the geometry of the unit cell Y and not on the thermophysical data like the viscosity or the density.

3.2.2 Numerical Evaluation of the Permeability. Numerical evaluation of the permeability is based on the fact that each variational expression of Eq. (10) corresponds to a special Stokes flow problem on the unit cell Y,

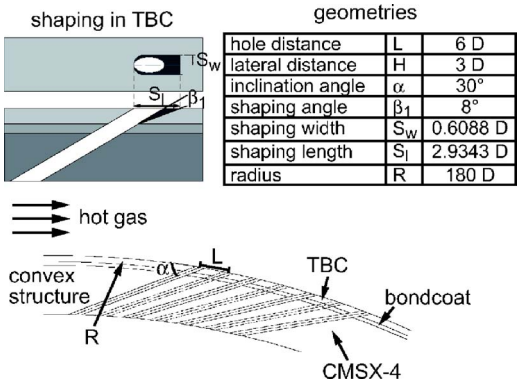

Fig. 2 Geometry of the convex multilayer plate

$$\Delta_{y_i}\omega^{\mathbf{j}} = \mathbf{e}^{\mathbf{j}}; \quad \nabla_{y_i}\omega_i^j = 0 \text{ on } Y_f \quad \text{and} \quad \omega^{\mathbf{j}} = 0 \text{ on } \Gamma_{fs} \tag{13}$$

which expresses the flow of a unit viscosity fluid on the unit cell Y driven either by a negative unit pressure gradient or by positive unit body forces in direction j. Periodic boundary conditions must be imposed on $\omega^{\mathbf{j}}$ components and on the pressure field.

As a stationary Stokes flow problem has to be solved on the unit cell, the well-known analogy with incompressible elasticity can be used here [12]. Thus, the velocity vector of the Stokes problem corresponds to the displacement vector in the elasticity problem. The continuity equation (incompressibility) is satisfied by using a Poisson's ratio very close to 0.5. This analogous elasticity problem is solved with the finite element program ABAQUS [13] by using hybrid linear volume elements, suitable for modeling near-incompressible materials. The ABAQUS results are finally transferred to HOMAT in order to evaluate the effective permeability tensor of the porous material by averaging the obtained velocities (see Eq. (11)).

4 Plate Designs and Model for Conjugate Analysis

4.1 Geometric Configurations. In this study cooled plates composed of three material layers are investigated. Their substrate layer is made of superalloy CMSX-4 with a thickness of 2.0 mm (Fig. 2). The bondcoat consists of a MCrAlY layer (0.15 mm thick). The thermal barrier coating (TBC) is an yttrium stabilized ZrO_2 layer with 0.25 mm thickness. In this analysis three different plate designs are considered: a plane, a convex, and a concave one. These plates are perforated by a laser treatment with seven rows of staggered cooling holes with a diameter of $D=0.2$ mm. The radius of both curved plates is set to 36 mm, which corresponds to 180 times the cooling hole diameter. The axial ($L=6D$) and lateral ($H=3D$) distances of the cooling holes and the angle of inclination ($\alpha=30$ deg) are identical for all configurations at the TBC outlet surface. This means that, for the convex design, the inclination angle is reduced at the plenum side but, for the concave geometry, it increases. All configurations have the same diffusor that expands the outlet area of the cooling holes in the direction of the hot gas flow. This diffusor is characterized by the shaping width and length given in Fig. 2. This shaping is applied only in the TBC region, measured by the angle $\beta_1 = 8$ deg.

4.2 Conjugate Analysis Model. The boundary conditions (see Fig. 3) for the fluid flow are derived from modern gas turbine combustion chambers and first turbine stage flow conditions. 3D conjugate analyses were performed for plates of 28 mm length which represent either a small part of the combustion chamber wall or of the surface of a turbine blade. This cutout of gas turbine components leads to small pressure ratios along the main flow direction compared to real applications.

To reduce the numerical effort only the area between the center

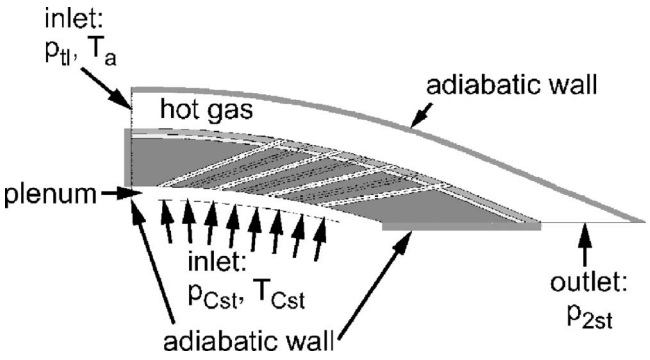

Fig. 3 Boundary conditions

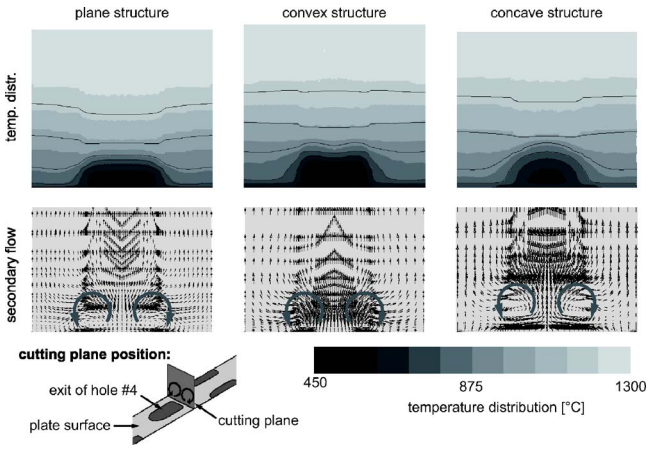

Fig. 4 Temperature distribution and secondary flow in a cutting plane perpendicular to the outlet surfaces

lines of two lines of rows is discretized by imposing symmetry boundary conditions in the y direction (see Fig. 1). Nevertheless, the realized grids consist of approximately 1,800,000 cells due to very fine meshes at solid/gas walls. Typically, several grid nodes are located in the viscous sublayer. In order to keep the total amount of cells manageable, the grid spacing increases in regions further away from the walls.

The inlet and outlet boundary conditions are specified as sketched in Fig. 3. In a distance of 5 mm from the plate surface an adiabatic wall boundary condition is applied. Setting the adiabatic wall at this distance will prevent any influence of this boundary condition on the results in the plate boundary layer. The inlet of the plenum has a distance of 2 mm from the bottom of the plate. On the left- and right-hand side of the plenum, adiabatic wall boundary conditions are also imposed to close the simulation domain. These boundary conditions are the same for the three analyzed plate designs.

For the main flow on the plate surface, the inlet temperature T_{t1} is fixed to 1302.8°C and the total inlet pressure p_{t1} is always set to 2.112 MPa. These boundary conditions lead to a Mach number of Ma=0.25 in the main flow. The static outlet pressure p_{2st} is always set to 1.998 MPa and the static inlet temperature T_{Cst} of the cooling fluid is fixed to 450°C. Depending on the blowing ratio M, the required static inlet pressure p_{Cst} for the cooling fluid in the plenum is given in Table 1. Furthermore, it is assumed that all materials are optically opaque and no radiation boundary conditions are taken into account.

5 Results of the 3D Fluid Flow and Heat Transfer Analysis

In this section we analyse for the same hot gas and cooling conditions (Ma=0.25 and M=0.28) the influence of the plate curvature on the cooling film structure, the temperature distribution on the TBC upper surface, the vortex structure inside the cooling holes, the cooling efficiency distribution on the plate surface and in the CMSX-4 layer.

The presented results correspond to the aerothermal plate behavior around the fourth cooling hole. This central hole was chosen because the cooling film structure as well as the temperature distribution in the plate is fully developed there.

5.1 Temperature Distribution and Flow Structures

5.1.1 Plate Surface. The development of the kidney vortices structure Ω_0 is influenced significantly by the curvature of the plate. This leads also to changes in the cooling film vortex structures Ω_1. In Fig. 4 the structure of the cooling film downstream the fourth row of cooling holes is shown in a 2D cutting plane, perpendicular to the hot gas flow direction and to the plate surface. The cutting plane is located directly behind the downstream edge of the hole, as sketched at Fig. 4. This figure shows the temperature distribution and the secondary flow vectors in the cooling film. Note that velocity vectors are scaled by the same factor.

Comparing the convex with the plane structure, the changes in the cooling film can be seen clearly. The temperature distribution shows that, for the convex design, the center of the cooling film is lifted slightly from the plate surface to the outer bounds of the ejected jet. This lift is mainly due to the different pressure gradients on the flat and convex plate surfaces. The secondary flows are reduced significantly for the convex structure. This reduction is even more pronounced for the concave plate. The vortices are extremely weak there and relatively far away from the surface. The weakening of the Ω_0 vortices implies an increased velocity component in flow direction in the cooling holes. This influences the position of the Ω_1 vortices on the plate surface. The hot gas is there pressed against the surface due to the pressure gradient on the concave design. Note that a rather homogeneous cooling film is developed on the TBC surface for all cases and no hot gas is in direct contact with this surface. However, its spread is the smallest for the concave design.

5.1.2 Cooling Channel. The vortex system of the secondary flow on the plate surface is mainly influenced by the kidney vortex structure inside the cooling holes. In Fig. 5 the temperature distribution and the secondary flow vectors inside the fourth cooling hole are shown. A 2D cutting plane is positioned perpendicular to the main cooling flow direction at 1.2 mm from the plate surface for every design.

Differences are observed for the different plate designs with respect to the origin and spread of the Ω_0 structure in the cooling holes. For the flat plate the vortex centers are displaced to the upper part of the hole. As for the convex case the inclination angle is lower than 30 deg at the cooling hole inlet; modified kidney vortices are generated there. In the middle of the cooling channel the kidney vortices are moved to the lower hole edge and their intensity is reduced due to the increased intensity of the counter rotating vortex at the higher hole edge. On the other hand, the concave plate presents a larger inclination angle at the cooling hole inlet and even though Ω_0 vortices are induced, their intensity is very weak, as shown in Fig. 5. These vortices are also displaced further towards the hole center. Note that these phenomena directly influence the heat transfer in the cooling hole and on the

Table 1 Boundary conditions

Design	Plane		Convex			Concave
M	0.28	0.48	0.11	0.28	0.48	0.28
p_{Cst} (MPa)	2.04	2.08	2.01	2.026	2.055	2.028

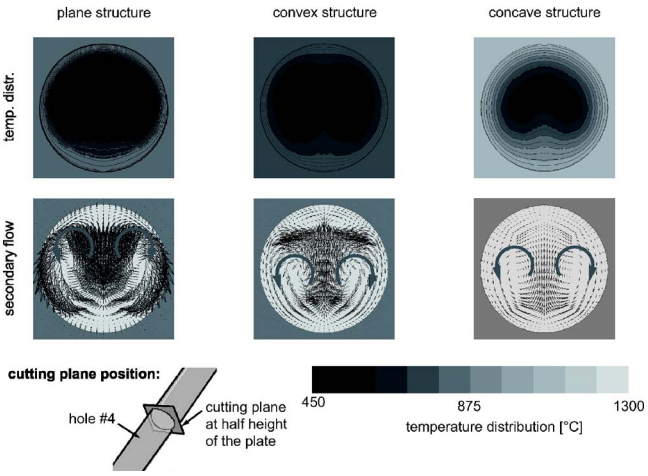

Fig. 5 Temperature distribution and secondary flow in the cooling hole

plate surface. Moreover, the temperature in the cooling fluid and in the solid material increases slightly for the convex plate and significantly for the concave structure. This is a result from two simultaneous effects: the lower intensity of the Ω_0 vortices induces a reduced cooling in the hole; the weaker vortices lead to a lower cooling efficiency on the plate surface, whereby the heat flux into the material increases.

5.2 Cooling Efficiency

5.2.1 Plate Surface. Figure 6 shows the distribution of the cooling efficiency η_c on the upper plate surface near the fourth hole. The outlet area of this hole is depicted there as a white recess. The area of the highest cooling efficiency is located downstream of the fourth hole for all designs. Taking the flat design as reference, the cooling efficiency on the convex plate surface is reduced significantly for the adopted flow conditions. As the cooling film has the tendency to detach from this surface, the contact area of the cooling fluid on the surface decreases, leading to the observed lower cooling efficiency on the plate surface. Furthermore, the relative poor cooling performance of the concave geometry has two origins. At first, the hot gas is pressed against the

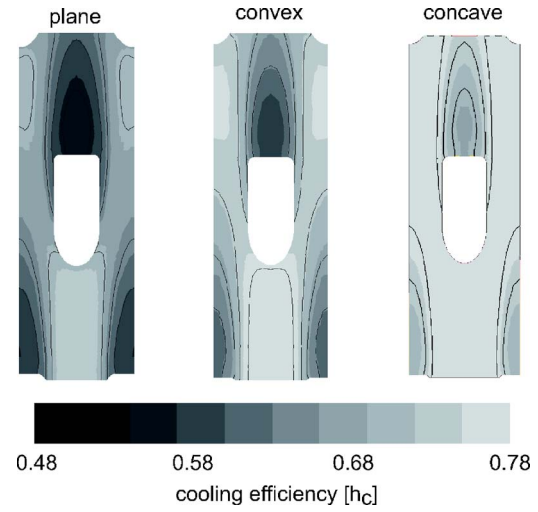

Fig. 6 Cooling efficiency on the plate surface near the fourth hole

Table 2 Permeabilities P_{ij} (μm^2) of each layer

Design	Layer	P_{xx}	P_{yy}	P_{zz}	α_{xz}	$\alpha_{r\theta}$
S30-F	TBC	**140.08**	25.22	29.61	**22.5**	**22.5**
	Bond	69.91	0.037	24.66	30.4	30.4
	CMSX-4	75.52	0.802	25.93	30.2	30.2
S30-conv	TBC	**172.94**	24.91	22.23	**6.7**	**21.75**
	Bond	90.11	1.285	11.56	15.4	30.4
	CMSX-4	89.62	2.589	14.98	15.8	30.8
S30-conc	TBC	**114.78**	23.90	68.54	**35.5**	**19.8**
	Bond	48.95	0.243	49.42	44.8	29.1
	CMSX-4	39.07	2.058	38.99	45.0	29.3

plate surface, thus leading to an increased heat flux into the material. At the same time, due to the very low intensity of the Ω_0 vortices, the cooling is reduced significantly.

5.2.2 Substrate Layer. The quality of the considered cooling designs can be checked by analyzing the cooling efficiency in the substrate layer. In order to determine this cooling efficiency, cycle analyses of an entire combined power plant have been performed. These calculations show that the maximum thermal efficiency is obtained when a hot gas temperature of T_H=1320°C and a cooling fluid temperature of T_C=420°C are achieved. With these values a minimum cooling efficiency of η_c=0.579 for the full-coverage cooling can be determined.

The superalloy CMSX-4 is the most critical material: its maximum allowed temperature is T=900°C. Using this material temperature, a minimum required cooling efficiency of η_C=0.579 in the substrate can be determined for full-coverage cooled multilayer plates. Then, using the calculated maximum temperatures in the substrate, the cooling efficiency in the CMSX-4 layer is, respectively, 0.666 for the flat plate, 0.632 for the convex design, and 0.573 for the concave one. These results clearly show that the concave plate has the lowest cooling efficiency of the three designs and needs a marginal higher blowing ratio than the present one in order to achieve the prescribed value of 0.579.

6 Effective Permeabilities of the Cooling Designs

Effective Darcy permeabilities are evaluated for the three plate designs by using the analogy between stationary Stokes flow and incompressible elasticity [12]. For each design of the cooled plate, effective permeabilities are calculated for each individual layer.

In Table 2, the diagonal terms and the angle of the principal permeability direction are reported, respectively, in the structural $[x\text{-}z]$ plane, α_{xz}, and in the local system, $\alpha_{r\theta}$. These results show that, independent of the plate design, *the permeability tensor is orthotropic*. This behavior can be explained by the analysis of the velocity fields on the unit cell. In Fig. 7 arrows are drawn for the convex design. They correspond either to the velocity norm at the outflow face of the central hole, induced by a negative pressure gradient in the y direction, or to the one generated, respectively, by $\Delta p/\Delta x=-1$ and $\Delta p/\Delta z=-1$ in the cutting plane of the central hole.

Due to the channel inclination, the x velocity component induced by a body force in the same direction is larger than the other two components excited in their direction. As the y direction is normal to the channel inclination, the corresponding body forces induce very small velocities in the cooling channel except at the TBC outer surface where inflow and outflow arrows are present (see Fig. 7(*b*)). Per analogy, this flow structure corresponds to a sheared TBC outlet face. Due to the presence of an outflow diffusor, the TBC permeability P_{yy} is larger than its value for the CMSX-4 and bondcoat layers. Moreover, due to its shaping (angle β_1), larger body forces are applied there in the x direction thus leading to greater velocity norms and to a larger P_{xx} permeability component than for the other two layers.

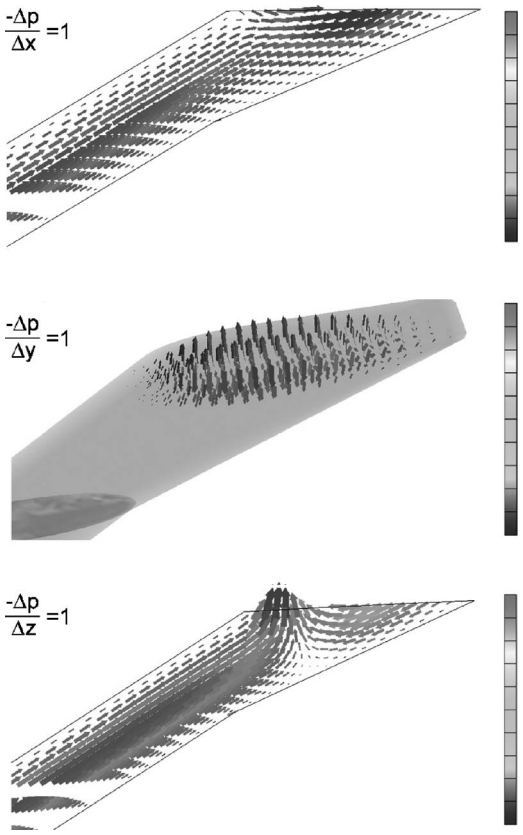

Fig. 7 Velocity profiles on the convex plate due to a negative unit pressure gradient, respectively, in *x*, *y*, and *z* directions

In order to analyze the influence of the plate curvature on the permeability tensor of each layer, the velocity norms in the x and z directions are drawn in Fig. 8 for the concave unit cell. Analogous results for the flat plate are given in Ref. [9]. It is worthwhile to point out that the velocity shape induced by the x body forces is not altered in the midsection plane by the change of plate curvature (see Figs. 7(a) and 8(a)). Nevertheless, the velocity profiles induced by z body forces are completely different, when the plate curvature changes. The combination of shaping and convex curvature increases the body forces near the right outflow wedge whereas the concave curvature leads to a body force decrease at this wedge. These different velocity results have a direct impact on the orthotropy of the effective permeability tensor of the TBC layer. Indeed, the orthotropy, measured by the ratio P_{xx}/P_{zz}, grows from **4.75** for the flat plate up to **7.78** for the convex one whereas the concave design leads to a reduced orthotropy, P_{xx}/P_{zz}=**1.67**.

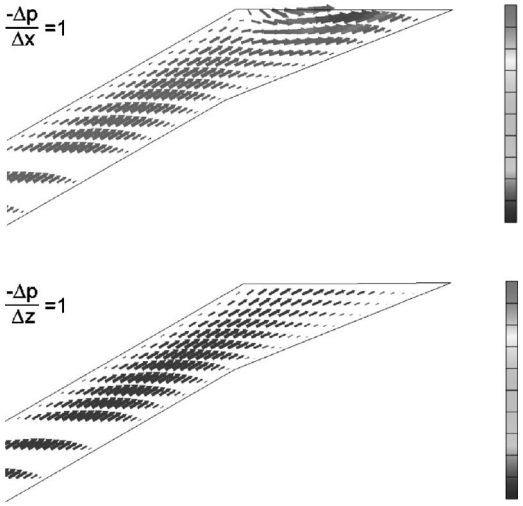

Fig. 8 Velocity profiles in the midplane section of the central hole of the concave unit cell due to a negative unit pressure gradient respectively in *x* and *z* directions

Table 3 Effective thermal conductivities (W/(mK))

Design	Layer	k_x^{hom}	k_y^{hom}	k_z^{hom}	$\Delta k_{y\bar{k}}$	$\bar{T}_{\text{lay}}$
Flat	TBC	1.177	1.120	1.211	−4.15%	778.34
	Bond	29.82	28.89	30.30	−2.63%	735.99
	CMSX-4	16.36	15.73	16.19	−3.01%	697.96
Convex	TBC	1.177	1.100	1.139	−5.13%	797.97
	Bond	29.83	28.11	29.89	−4.71%	760.13
	CMSX-4	16.40	15.35	16.20	−5.23%	722.29
Concave	TBC	1.159	1.103	1.148	−3.95%	843.85
	Bond	29.68	28.72	30.87	−2.82%	803.55
	CMSX-4	17.06	16.47	17.19	−3.36%	765.33

A second significant influence of the curvature is observed by looking to the principal permeability direction, α_{xz}, in the x-z plane. This angle is obtained by diagonalizing the permeability tensor. For the CMSX-4 and bond coat layers of the flat plate, the principal permeability direction corresponds nearly to the channel inclination. The channel shape is there cylindrical. The plate curvature increases/decreases, respectively, this angle by nearly **15** deg. But, expressed in the local coordinate system $[r;\theta]$, the principal permeability direction $\alpha_{r\theta}$ remains for both curved designs nearly constant in the TBC layer and approximately equals the channel inclination in the CMSX-4 and bondcoat layers. Due to additional contour shaping, the principal permeability direction α_{xz} of the TBC layer presents, independent of the plate curvature, a further decrease of about **9** deg. Thus, the principal permeability direction tends there more to the hot gas direction.

7 Effective Thermal Conductivities of the Different Cooled Plates

At first, the influence of the plate curvature on the effective thermal properties is analyzed for the same hot gas and cooling conditions (Ma=0.25, M=0.28, and α=30 deg). Effective values are calculated either for the multilayer or for each layer of the perforated plates. In this analysis the parallelepiped unit cell with four 1/4 channels and one central hole is always used (see Fig. 1). Then, the influence of the blowing ratio on the effective thermal properties is outlined at a given hot gas velocity (Ma=0.25).

7.1 Monolayer Results. The predicted effective thermal conductivities for each layer and design are reported in Table 3. In order to measure the orthotropy of each equivalent monolayer, the relative difference of k_y^{hom} to the mean value $\bar{k}^{\text{hom}}$ is given in column 4. The mean layer temperature $\bar{T}_{\text{lay}}$ is outlined in column 5.

Independent of the cooling configuration, *an orthotropic equivalent behavior* is predicted for each layer. This orthotropy is slightly more pronounced for the convex design. As the cooling efficiency of both curved designs is lower than the flat one, the mean layer temperature increases, mostly for the concave design. But, in spite of a temperature increase, mainly the thermal conductivity k_z^{hom} of these designs changes, respectively, by −5.94% (convex case) and −5.20% (concave one) compared to the flat one. This behavior is due to their larger corrections of the corresponding isotropic mean value k_{va}.

7.2 Multilayer Results. In Table 4(a) the predicted effective thermal conductivities, their volume average value, the mean tem-

Table 4 (a) Effective thermal conductivities (W/(mK)) of the multilayer; (b) their relative difference in (%) to the flat plate values and the corresponding mean temperature variation in (°C)

(a)

Design	k_x^{hom}	k_y^{hom}	k_z^{hom}	k_{va}	$\Delta k_{z,xy}$	$\bar{T}_{\text{lay}}$
Plane	15.61	15.01	12.06	15.83	−21.23%	708.71
Convex	15.33	14.60	11.01	15.76	−26.43%	732.88
Concave	16.11	15.60	14.38	16.75	−9.30%	775.60

(b)

Design	Δk_x^{hom}	Δk_y^{hom}	Δk_z^{hom}	Δk_{va}	$D\bar{T}_{lay}$
Convex	−1.79%	−2.73%	**−8.71%**	−0.47%	24.2
Concave	3.20%	3.93%	**19.24%**	5.78%	66.9

perature, and an orthotropy measure are reported. In order to quantify the impact of the curvature on the effective conductivities, their relative difference to the reference flat plate are outlined in Table 4(b).

In contrast to the monolayer homogenization, where implicit fluxes are evaluated only at the solid/gas interfaces, additional fluxes in the z direction (see axes system in Fig. 1) are generated in the multilayer homogenization at the solid/solid interfaces. Independent of the plate curvature, these high fluxes lead to a larger χ^z displacement field, increasing so the extension of the solid part (see Fig. 9). This field induces an important reduction of the mean isotropic conductivity in the z direction. This way, *the multilayer has a pronounced orthotropic equivalent behavior*, illustrated by the relative difference $\Delta k_{z,xy}$ in Table 4(a).

Compared to the flat design, the convex curvature increases the solid extension and leads to larger χ^z variations on the unit cell, as shown in Fig. 9(*b*). Therefore, *the orthotropy is accentuated and, in spite of a temperature increase of 24.2°C, the effective thermal conductivities decreases mainly in the z direction*. In contrast, the concave shape reduces the solid extension of the flat design and leads to smaller variation of χ^z on the unit cell Y (see Fig. 9(*c*)). Thus, *its equivalent orthotropic behavior is less pronounced* and, parallel to the mean temperature raise, the thermal conductivities augment sligthly in the x-y directions and significantly in the z direction, **+19.24%**.

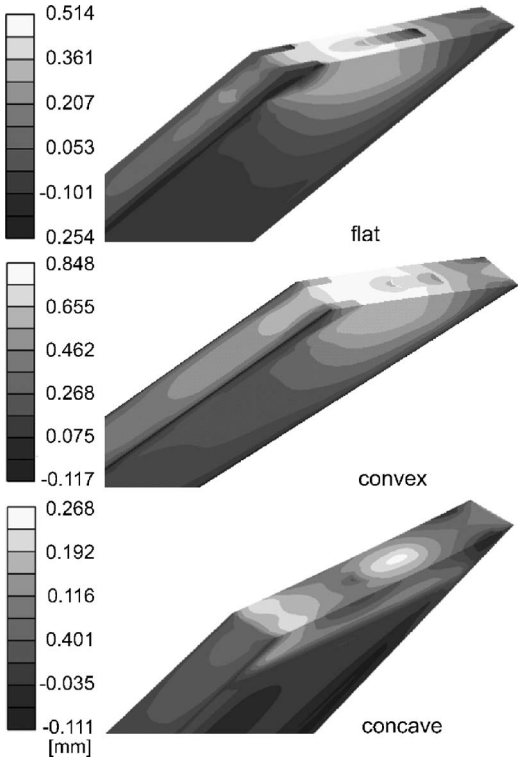

Fig. 9 Microscopic displacements χ^z of the multilayer homogenization for the flat (*a*), convex (*b*), and concave (*c*) designs of the larger unit cell of Fig. 1

7.3 Influence of the Blowing Ratio on the Effective Thermal Conductivities. In combination with the same hot gas velocity (Ma=0.25), two additional blowing ratios, $M=0.11$ and $M=0.48$, have been evaluated for the convex plate and the case $M=0.48$ for the flat design. All mono- and multilayer homogenization results are summarized in Fig. 10. In this figure the effective conductivities are drawn as function of the mean material temperature of each layer or of the multilayer.

The results for the monolayers TBC and bondcoat are eloquent: although the temperature increases, respectively, about 129.3°C (TBC) and 110.8°C (bond) for the convex design, the effective thermal conductivities remain quasiconstant: max. variation of 1.04% for k_z^{hom} of the TBC layer and 1.27% for k_y^{hom} of the bondcoat layer. Moreover, Fig. 10 points up the orthotropy of the

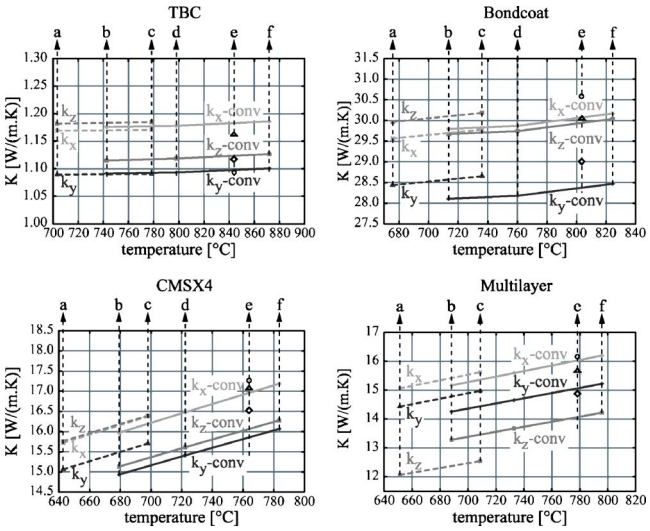

Fig. 10 Mono- and multilayer effective thermal conductivities as function of the mean material temperature for the test cases: (*a*) flat, 0.48 M; (*b*) convex, 0.48 M; (*c*) flat, 0.28 M; (*d*) convex, 0.28 M; (*e*) concave, 0.28 M with ⊗: k_x^{hom}, Δ: k_z^{hom}, ◇: k_y^{hom} and (*f*) convex, 0.11 M

equivalent mono- and multilayers, mainly for the TBC layer. *Independent of the plate curvature, the effective thermal conductivities decreases quasilinearly with the blowing ratio.*

As the thermal conductivity of the superalloy is more temperature sensitive, a more pronounced variation is observed for the CMSX-4 layer and subsequently for the multilayer. Indeed, as the mean CMSX-4 temperature in the convex plate varies from 688.2°C at the high blowing rate $0.48M$ to 783.6°C for the low blowing ratio $0.11M$, k_y^{hom} increases by **7.04**%. This variation cannot be neglected in further industrial applications.

The comparison of the curved designs with the flat one reveals another interesting property of the effective conductivities: for each layer and subsequently for the multilayer we have for the curved designs: $k_x^{\text{hom}} \geq k_z^{\text{hom}} \geq k_y^{\text{hom}}$ instead of $k_z^{\text{hom}} \geq k_x^{\text{hom}} \geq k_y^{\text{hom}}$ for the reference plane plate. This means that for each layer of the curved designs, the thermal conductivity in z direction becomes smaller than its value in the x direction. The origin of this stronger decrease in z direction lies in the modified ratio between the implicit fluxes in x and z direction.

8 Conclusions

A general approach combining 3D conjugate fluid flow and heat transfer with a homogenization method based on asymptotic expansions of the temperature, velocity, and pressure fields for periodic materials has been adopted here. This procedure has been applied successfully to predict the aerothermal behavior of flat, convex and concave multilayer plates with full-coverage cooling holes. A detailed analysis of the flow structures and the cooling efficiency in these plates is presented. The results show that the curvature influences the kidney vortices inside the hole and, thus, the flow structure on the plate surface significantly. For the convex/concave design, the cooling film attempts to be pressed against the plate surface and is reduced there. As the secondary flows in the holes also diminish, the cooling efficiency decreases, mainly for the concave design. The linked homogenization technique allows the prediction of effective permeabilities and thermal conductivities either for each layer or for the multilayer. The permeability and conductivity tensors of each layer and multilayer are orthotropic for the analyzed cooling designs. The numerical results also show that the convex/concave design increases/decreases the orthotropy of both equivalent properties in the channel plane but its transverse value remains nearly unaffected. Moreover, the conductivity results for different curvatures and blowing ratios reveal that essentially the plate geometry (curvature, shape, …) and not the flow conditions (blowing ratio, hot gas velocity, …) defines the orthotropy of the effective thermal conductivities. An experimental validation of the 3D conjugate analyses is under development by building an appropriate ring test stand at the Institute for Steam and Gas Turbines. In further investigations, the influence of deviations in the ideal cooling hole cooling geometry, caused by either the drilling process or oxydation, will be investigated.

Acknowledgment

The authors thank the Deutsche Forschungsgemeinschaft (DFG) for their financial support within the Collaborative Research Center 561: "Thermally Highly Loaded, Porous and Cooled Multilayer Systems for Combined Cycle Power Plants."

Nomenclature

C, H = indices for cooling or hot gas conditions
D = diameter of the cooling channel
$\mathbf{e}^j$ = unit vector
k_{ij} = thermal conductivity tensor
$\bar{k}^{\text{hom}}$ = mean effective thermal conductivity
k_{ij}^{hom} = effective thermal conductivity tensor
k_{iso} = conductivity of the material without cooling channel
k_{va} = volume averaged thermal conductivity
L = row spacing of cooling channels
$M=(\rho\mathbf{v})_C/(\rho\mathbf{v})_H)$ = blowing ratio
P_{ij} = permeability tensor of the porous material
p^h, v^h = pressure and velocity of the cooling gas in the porous material
p^0, p^1 = order zero and one of the pressure serial development
p_{t1} = total inlet pressure of the main flow
p_{Cst} = static inlet pressure of the cooling fluid in the plenum
$\mathbf{q}$ = admissible periodic velocity field on Y
S_l, S_w = shaping length and width of the diffusor
T_{t1} = total inlet temperature of the main flow
T^0, T^1 = order zero and one of the temperature serial development
V_f = space of periodic velocity fields
$\mathbf{v}^0, \mathbf{v}^1$ = order zero and one of the velocity serial development
$\mathbf{x}$ = macroscopic length variable
x, y, z = coordinates and components of $\mathbf{x}$
Y = volume of the unit cell
$\mathbf{y}$ = periodic, microscopic length variable
y_1, y_2, y_3 = coordinates of $\mathbf{y}$ at the microscale
Y_1, Y_2, Y_3 = periodicity of the unit cell, respectively, in y_1, y_2, y_3 direction
Y_f, Y_s = volume of the fluid or solid part of the unit cell
α = channel inclination
β = thermal expansion coefficient of the fluid
β_1 = diffusion angle of shaped holes
Γ_{fs} = interface between solid/gas domains
$\varepsilon=x/y_1=y/y_2=z/y_3$ = aspect ratio between micro- and macroscale
$\eta_c=(T-T_H)/(T_C-T_H)$ = cooling efficiency
μ^h, ρ^h = viscosity and density of the porous material
μ_0, ρ_0 = viscosity and density at the reference temperature
χ^λ = microscopic periodic displacement field
Ω_0 = vortices structure in the cooling channel
Ω_1 = vortices structure in the main flow
ω^j = special velocity fields on the unit cell

References

[1] Kercher, D. M., 2000, "Turbine Airfoil Leading Edge Film Cooling Bibliography: 1972–1998," Int. J. Rotating Mach., **6**(5), pp. 313–319.
[2] Bohn, D., and Moritz, N., 2001, "Comparison of Cooling Film Development Calculations for Transpiration Cooled Flat Plates With Different Turbulence Models," ASME Paper No. 01-GT-0132.
[3] Bohn, D., and Moritz, N., 2003, "Numerical Parametric Study on Full Coverage Cooled Multilayer Plates," Paper No. IGTC2003-TS-084.
[4] Sanchez-Palencia, E., 1980, *Non Homogeneous Media and Vibration Theory* (Lecture Notes in Physics No. 127), Springer, Berlin, Germany.
[5] Ene, H. I., and Polisevski, D., 1987, *Thermal Flow in Porous Media*, Reichel, Dordrecht, Netherlands.

[6] Hornung, U., 1997, *Homogenization and Porous Media*, Springer-Verlag, Berlin, Germany.
[7] Laschet, G., 2002, "Homogenization of the Thermal Properties of Transpiration Cooled Multilayer Plates," Comput. Methods Appl. Mech. Eng., **191**(41-42), pp. 4535–4555.
[8] Laschet, G., 2004, "Homogenization of the Fluid Flow and Heat Transfer in Transpiration Cooled Multilayer Plates," J. Comput. Appl. Math., **168**, pp. 277–288.
[9] Laschet, G., Rex, S., Bohn, D., and Moritz, N., 2003, "Homogenization of Material Properties of Transpiration Cooled Multilayer Plates," ASME Paper No. GT2003-38439.
[10] Schmatz, M. A., 1988, *Three-Dimensional Viscous Flow Simulations Using an Implicit Relaxation Scheme* (Notes on Numerical Fluid-Mechanics (NNFM), 22), Vieweg, Brunswick, pp. 226–242.
[11] Bohn, D., Bonhoff, B., Schönenborn, H., and Wilhelmi, H., 1995, *Validation of a Numerical Model for the Coupled Simulation of Fluid Flow and Diabatic Walls With Application to Film-Cooled Turbine Blades*, VDI Berichte.
[12] Hughes, T. J. R., 1987, *The Finite Element Method: Linear Static and Dynamic Finite Element Analysis*, Prentice-Hall, Englewood Cliffs, NJ.
[13] ABAQUS/Standard User Manual, Hibbitt, Karlsson and Sorensen, Version, 6.3, 2002.

An Experimental and Numerical Study of Heat Transfer and Pressure Loss in a Rectangular Channel With V-Shaped Ribs

Michael Maurer
e-mail: itlr@itlr.uni-stuttgart.de

Jens von Wolfersdorf
e-mail: itlr@itlr.uni-stuttgart.de

Institute of Aerospace Thermodynamics,
University of Stuttgart,
Stuttgart, D-70569 Germany

Michael Gritsch
ALSTOM (Switzerland) Ltd.,
Technology Center TTC-TT,
Birr, CH-5242 Switzerland
e-mail: michael.gritsch@power.alstom.com

An experimental and numerical study was conducted to determine the thermal performance of V-shaped ribs in a rectangular channel with an aspect ratio of 2:1. Local heat transfer coefficients were measured using the steady state thermochromic liquid crystal technique. Periodic pressure losses were obtained with pressure taps along the smooth channel sidewall. Reynolds numbers from 95,000 to 500,000 were investigated with V-shaped ribs located on one side or on both sides of the test channel. The rib height-to-hydraulic diameter ratios (e/D_h) were 0.0625 and 0.02, and the rib pitch-to-height ratio (P/e) was 10. In addition, all test cases were investigated numerically. The commercial software FLUENT™ was used with a two-layer k-ε turbulence model. Numerically and experimentally obtained data were compared. It was determined that the heat transfer enhancement based on the heat transfer of a smooth wall levels off for Reynolds numbers over 200,000. The introduction of a second ribbed sidewall slightly increased the heat transfer enhancement whereas the pressure penalty was approximately doubled. Diminishing the rib height at high Reynolds numbers had the disadvantage of a slightly decreased heat transfer enhancement, but benefits in a significantly reduced pressure loss. At high Reynolds numbers small-scale ribs in a one-sided ribbed channel were shown to have the best thermal performance. [DOI: 10.1115/1.2720507]

Introduction

Throughout the past decades the importance of stationary gas turbines has increased within the field of electric power generation. One of several challenging tasks is to realize high temperature combustion within the combustion chamber while simultaneously maintaining sufficient cooling for the combustion chamber walls. Former generations of gas turbines achieved this task with film cooling. With this method, a nontrivial amount of compressor air is lead around the combustor and injected into the combustion chamber through holes or slots along the combustor wall to reduce temperatures near the combustor walls. This technique has the advantage of simplicity and is technically mature. On the other hand, film cooling has the negative effect that only a part of the compressor air is usable in the combustion process and that in the region of film cooling the combustion process is choked. This leads to undesired levels of unburned hydrocarbons and carbon monoxide emissions.

During the last few years the influence of environmental protection on the design of stationary gas turbines has increased. The reduction of emissions is now a key goal, focusing on unburned hydrocarbons and carbon monoxide as well as on NO_x. Among others, Sattelmayer and Polifke [1] have shown that this is possible using lean premixed combustion. The desire for lean combustion is accompanied by an economically required efficiency improvement, which is obtained by increasing turbine inlet temperatures. Therefore, the trend of combustor design leads towards enhanced backside cooled combustion chamber walls [2,3]. With this technique, higher amounts of compressor air are directly available in the combustion process. The principles of the described combustion chamber designs are sketched in Fig. 1.

To achieve sufficient cooling, several enhancement features may be used to increase the heat transfer on the backside of the combustor wall, where most of these features have arisen from experience in internal blade cooling. Here, the pressure drop available for the implemented heat transfer enhancement technique is often prescribed by the design and the mass flow in such passages should be low. In the case of combustor cooling, the mass flow is high and a low pressure drop is desired. Within the field of internal blade cooling many studies have been conducted (e.g., [4,5]), in which the possible enhancement techniques are compared for their heat transfer enhancement potential and pressure drop behavior with varying Reynolds numbers. Aiming for a high heat transfer enhancement with a low pressure drop at the same time, one could choose V-shaped ribs for the Reynolds number range investigated. Lau et al. [6] and Han et al. [7] conducted studies of heat transfer enhancement for various rib configurations including 90 deg ribs, angled ribs and V-shaped ribs. Lau et al. [6] investigated Reynolds numbers from 10,000 to 60,000, whereas Han et al. [7] varied the Reynolds numbers from 15,000 to 90,000. Both investigated ribbed channels with a dimensionless rib height e/D_h of 0.0625. Taslim et al. [8] investigated similar rib configurations with Reynolds numbers varying from 5,000 to 30,000. In their study, the dimensionless rib height e/D_h was set to 0.0833 in the case of V-shaped ribs. Focusing on V-shaped ribbed channels, further studies are found in the literature. Hadhrami et al. [9] performed a study using V-shaped ribs with a dimensionless rib height e/D_h of 0.094, where the Reynolds number range was between 5,000 and 40,000. Cho et al. [10] conducted a study with V-shaped ribs with dimensionless rib heights e/D_h of 0.04, 0.06, and 0.078. In this study the Reynolds number

Contributed by the International Gas Turbine Institute of ASME for publication in the JOURNAL OF TURBOMACHINERY. Manuscript received July 26, 2006; final manuscript received August 9, 2006. Review conducted by David Wisler. Paper presented at the ASME Turbo Expo 2006: Land, Sea and Air (GT2006), May 8–May 11, 2006, Barcelona, Spain.

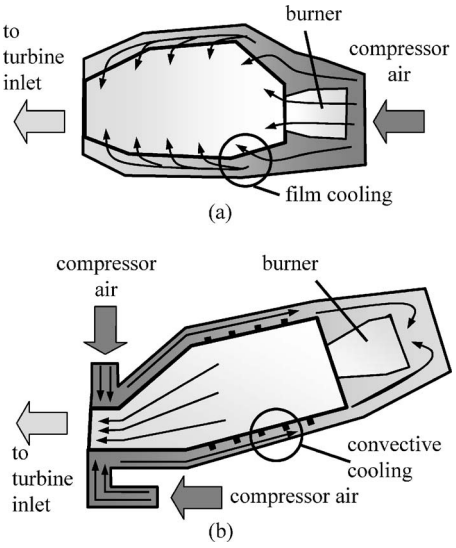

Fig. 1 Principle mass flow in a combustor with (*a*) film cooling and with (*b*) convective cooling

range was between 10,000 and 30,000. Wright et al. [11] investigated V-shaped ribs with a dimensionless rib height e/D_h of 0.078. The Reynolds numbers varied from 10,000 to 40,000. For the same rib geometry and Reynolds numbers up to 500,000 a numerical study has been conducted by Su et al. [12]. In a study by Gao and Sundén [13], V-shaped ribs were investigated at a lower Reynolds number range from 1,000 to 6,000. The dimensionless rib height e/D_h was set to 0.06. Lee et al. [14] conducted a study with V-shaped ribs in a rotating channel. Along with the influence of rotation, nonrotating data were also given. The V-shaped ribs had a dimensionless rib height e/D_h of 0.078. All above mentioned studies above dealt with channels having two opposite ribbed walls. An investigation analyzing one-sided ribbed channels has been performed by Momin et al. [15]. Here, the V-shaped ribs had a dimensionless rib height e/D_h from 0.02 to 0.034. The Reynolds numbers varied from 2,500 to 18,000. An overview over the references cited above investigating V-shaped ribbed channels is presented in Table 1.

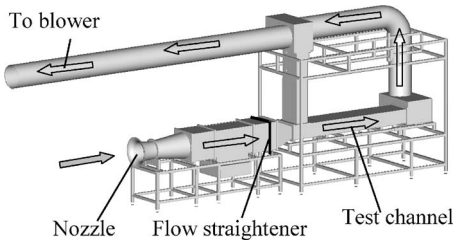

Fig. 2 Schematic of test rig

At the moment no experimental studies could be found providing detailed information on a V-shaped rib configuration in cooling passages for conditions found in combustion chambers, where the typical Reynolds numbers vary up to 500,000 and the ribs are usually placed on one side only.

Experimental Setup

Test Facility. For the present study an open loop wind tunnel has been used. A sketch of the test rig is presented in Fig. 2. The blower operates in suction mode and provides sufficient pressure below atmosphere to obtain Reynolds numbers in the test channel from 95,000 to 550,000. The air flow enters the experimental rig through a nozzle, which is equipped with static pressure taps that allows calculation of the mass flow. The air flow passes through a flow straightener and then into the test channel. The test channel has a length of 2.4 m and a cross section of 400 mm $\times$ 200 mm and is built out of Plexiglas plates with a thickness of 20 mm, allowing for visual access and an adequate thermal insulation due

Table 1 Parameter comparison of V-shaped ribbed channel references

Reference	Configuration	Aspect ratio	e/D_h	P/e	α	Re	Type
Present study	one sided/ two sided	2:1	0.02/ 0.0625	10	45 deg	95,000–500,000	Expt./CFD
Lau et al.[a]	two sided	1:1	0.0625	10/20	45 deg/60 deg	10,000–60,000	Expt.
Han et al.[b]	two sided	1:1	0.0625	10	45 deg	15,000–90,000	Expt.
Taslim et al.[c]	two sided	1:1	0.0833	10	45 deg	5,000–30,000	Expt.
Hadhrami et al.[d]	two sided	2:1	0.094	10	45 deg	5,000–40,000	Expt.
Cho et al.[e]	two sided	6.82:1/ 5:1/3:1	0.04/ 0.06/0.078	10	60 deg	10,000–30,000	Expt.
Wright et al.[f]	two sided	4:1	0.078	10	45 deg	10,000–40,000	Expt.
Su et al.[g]	two sided	4:1	0.078	10	45 deg	10,000–500,000	CFD
Momin et al.[h]	one sided	10.15:1	0.02/0.022/ 0.028/0.034	10	30 deg/45 deg/60 deg/75 deg	2,500–18,000	Expt.

[a]Reference [6].
[b]Reference [7].
[c]Reference [8].
[d]Reference [9].
[e]Reference [10].
[f]Reference [11].
[g]Reference [12].
[h]Reference [15].

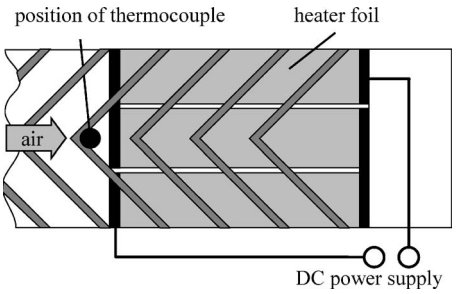

Fig. 3 Sketch of the bottom wall rear part of the test channel

to the low thermal conductivity of the material. The ribs are also manufactured from Plexiglas. After the test channel the air flow is turned 180 deg and enters the blower via a circular channel.

Test Section. The test channel is instrumented to have the ability to obtain friction factors of the periodic rib segments and detailed information on the local heat transfer enhancement.

The friction factors of the periodic rib segments are determined by measuring the pressure loss in the test channel. A total of 14 pressure taps are installed on the midplane of the smooth channel sidewall. The pressure taps are linked to a digital sensor module and an integrated 16 bit A/D converter allows high frequency data acquisition.

To obtain detailed information on local heat transfer enhancement due to the investigated rib configurations, the steady state liquid crystal technique [16] is used. In particular narrowband liquid crystals from Hallcrest-type BM/R31C1W/C17-10 have been used. The thermochromatic liquid crystals (TLC) were calibrated on a separate test rig to ensure correct color versus temperature dependency. To apply the steady state TLC technique, three lanes of steel foil with 600 mm in length and 133 mm in width and 25 μm in thickness were glued on the bottom wall at the rear part of the test channel using an adhesive tape. On top of the foil a black coating was added via airbrush to enhance the contrast of the TLCs, which are sprayed on top of the black coating. To create a constant heating of the covered bottom wall, all heater foils were connected in series to a dc power supply. The electric power was obtained by measuring the heater foil resistance and the voltage potential across the heater foil. In addition, information provided by the TLCs was captured by a CCD camera. Finally the mass flow bulk temperature is measured using a *K*-type thermocouple, which is located in the middle of the test channel cross section. A sketch of the instrumented bottom wall is presented in Fig. 3. Additionally a picture of the instrumented bottom wall is given in Fig. 4. Here one can observe the repeatability of the typical TLC color distribution. Therefore, the number of ribs placed on the area, which is covered by the heater foil, seems to be sufficient to assume periodic conditions.

Axial velocity profiles and turbulence levels have been measured by a hot wire probe upstream of the ribs. The averaged velocity profiles confirmed the mean velocity measurements from the nozzle and a turbulence level of about 4% was measured for all Reynolds numbers investigated.

Table 2 Test case configurations

Test case	e/D_h	No. of ribbed walls
0	...	smooth channel
1	0.0625	1
2	0.0625	2
3	0.02	1
4	0.02	2

Rib Configurations. Four test cases have been identified for investigation. The rib height-to-hydraulic diameter ratios (e/D_h) were 0.0625 and 0.02. All configurations had a pitch-to-rib height (P/e) of 10. Both geometries have been tested in a one and a two-sided configuration with the ribs on the larger channel walls. In the case of a two-sided ribbed channel the rib arrangement was in-line. The ribbed channel length-to-hydraulic diameter (L/D_h) was 7.5 for test cases 1 and 2 and 4.8 for test cases 3 and 4. A minimum of five ribs were placed in front of the measurement region to achieve nearly periodic flow conditions. An overview over all test cases is given in Table 2.

Numerical Setup

In addition to experimental investigations, all test cases were numerically investigated. A fully three-dimensional and steady-state CFD analysis was conducted using the commercial solver FLUENT™. This software was applied to solve the Reynolds averaged Navier-Stokes equations (RANS) with a second order volume discretization scheme. Throughout this study the fluid is considered incompressible and hence the flow field and the energy equation were uncoupled. All computations were performed with a two-layer k-ε turbulence model.

To reduce the computational effort the channel geometry was reduced and only a periodic rib segment was investigated assuming periodic conditions in the channel flow. Looking at Fig. 5 one can observe that the domain may be further reduced by assuming symmetries in the periodic segments. In the case of a one-sided ribbed segment, only the half of the segment is discretized, whereas in the case of a two-sided ribbed segment the volume mesh is applied to one quarter of the whole segment. For all test cases a block-structured grid was generated using the commercial software GAMBIT™. The number of nodes for each mesh varies from 400,000 to 730,000 so that values of the dimensionless first layer height y^+ were always lower than 1 for all Reynolds numbers investigated.

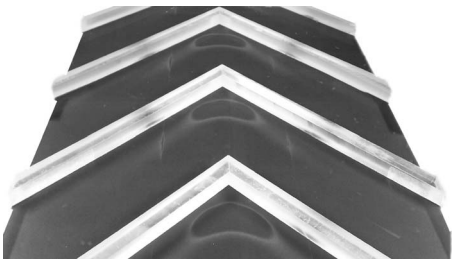

Fig. 4 Typical TLC color distribution during measurement

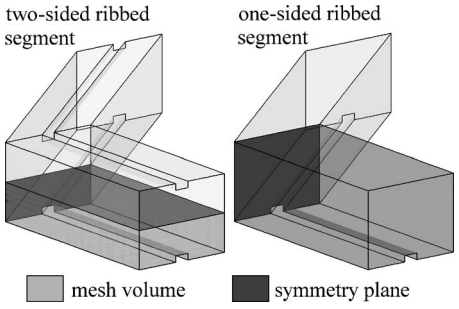

Fig. 5 Mesh volume for one-sided and two-sided ribbed segments

Data Reduction

Pressure taps were located in the mid part of the test channel to avoid inlet and outlet effects. This allowed for static pressure measurements which were used to form a regression line for the pressure losses. With the constant gradient of this regression line the friction factor can be calculated using Eq. (1),

$$f = \frac{(\Delta p/\Delta x)D_h}{2\rho u^2} \tag{1}$$

All friction factors presented in this study are normalized by the friction factor for fully developed turbulent flows in a smooth circular tube ($10^4 < \mathrm{Re} < 10^6$) proposed by Blasius as

$$f/f_0 = \frac{f}{0.046\ \mathrm{Re}^{-0.2}} \tag{2}$$

For the calculation of the heat transfer coefficient the heat flux at the wall must be determined. Therefore the electric power in the heater foil must be corrected for radiation and conductivity losses. In addition the value of the bulk temperature and the local wall temperature is required to obtain the local heat transfer coefficient. The values of the local wall temperatures are provided by the analysis of the TLC. Finally the heat transfer coefficient can be calculated as

$$h = \frac{\dot{Q}_w}{A_H(T_W - T_B)} \tag{3}$$

The local Nusselt number was calculated and normalized by the Dittus-Boelter correlation for a fully developed turbulent flow in a smooth circular tube. The equation of the Nusselt number ratio is presented in Eq. (4),

$$\mathrm{Nu/Nu_0} = \frac{\mathrm{Nu}}{0.023\ \mathrm{Re}^{0.8}\ \mathrm{Pr}^{0.4}} \tag{4}$$

The possible sources of error were investigated and the maximum uncertainties were obtained using the method of propagation of error. Uncertainty analysis for the heat transfer coefficient gives a maximum overall uncertainty of ±12.5% based on the relative measurement errors for temperature (2%), electrical power (2.5%), size of the area covered with heater foil (3%), and an estimated uncertainty for calculation of radiative and conductive losses (5%). Taking the relative errors for mass flow (2%), gradient of pressure distribution (6%), and air properties (2%) into account the maximum uncertainty for the friction factor is ±10%.

Results and Discusion

Velocity Field. For the following analysis of the investigated test cases it is essential to understand the basic characteristics of the fluid flow. As determined by the rib geometry, the air flow in a channel with one V-shaped ribbed wall develops two counter rotating vortices, each of them filling out half of the channel cross section. For a better understanding a CFD plot of the typical flow structure is provided in Fig. 6. Examining test case 1, one can locate one of the counter rotating vortices. Looking at a channel with two opposed V-shaped ribbed walls, four vortices are found. Each of them fills out one quarter of the channel cross section, keeping in mind that only one quarter of the channel is presented in Fig. 6. Investigating the flow structures near the bottom wall one observes that the flow in front of the rib is diverted towards the wall. This is associated with an increasing boundary layer thickness and therefore leads to decreasing heat transfer enhancement. Right behind the rib another vortex is located. Close to the symmetry wall the heat transfer enhancement is maximized due to the reattachment of the flow.

The flow structures in the axial direction also have an influence on the velocity profiles across the channel cross section. In Fig. 7 a 3D velocity profile of the channel cross section of test case 1 is presented. In the region of the vortex center the maximum axial velocity is reached.

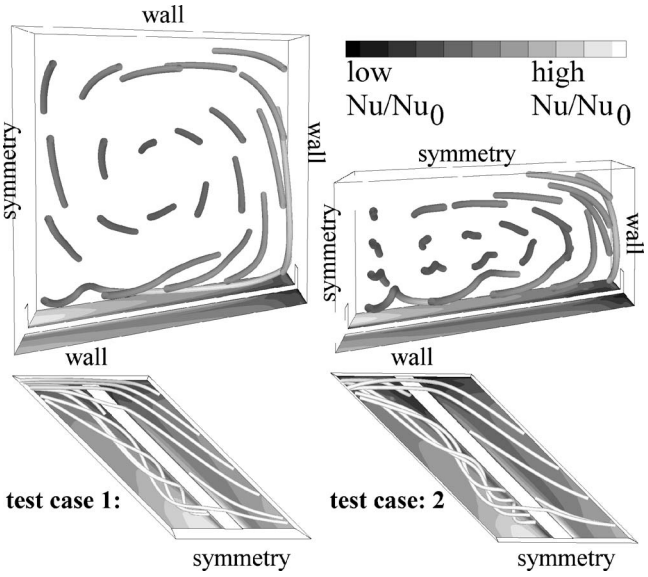

Fig. 6 Flow structures (top) in the axial direction and (bottom) close to the bottom wall

In Fig. 8, 2D velocity profiles are presented for test case 1 with ribs on one side wall. There an interesting observation is revealed. The position of the axial velocity maximum is located in the middle of the channel height in the case of slice $z/W=0.25$ and $z/W=0.375$, whereas the maximum is shifted towards the ribbed wall in the case of slice $z/W=0$. As described by Hanjalić and Launder [17] one would expect a fully asymmetric flow behavior as investigated for 90 deg ribbed channels. Here, the influence of the secondary flow vortices seems to shift the velocity profile and reduces the asymmetric behavior of the flow field with a slight maximum even towards the ribbed wall.

For test case 2, a 3D velocity profile of the channel cross section is presented in Fig. 9. Comparing the velocity profile with the

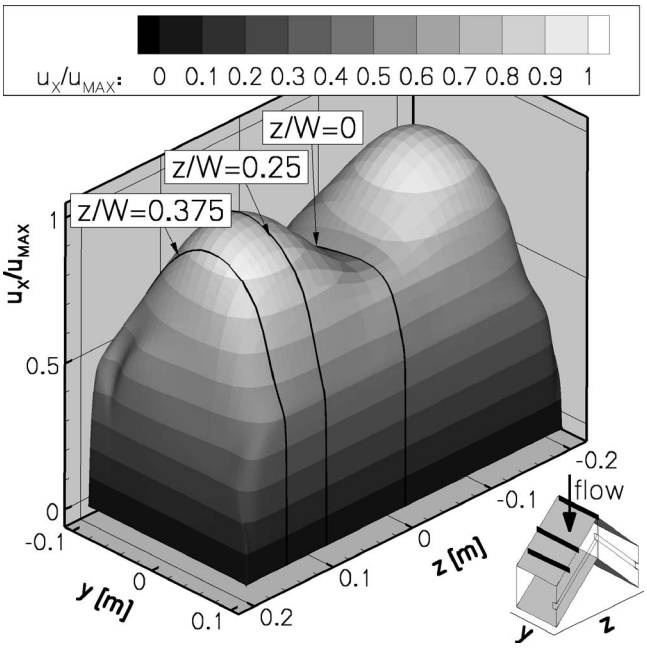

Fig. 7 Velocity profile of test case 1 at Re=130,000

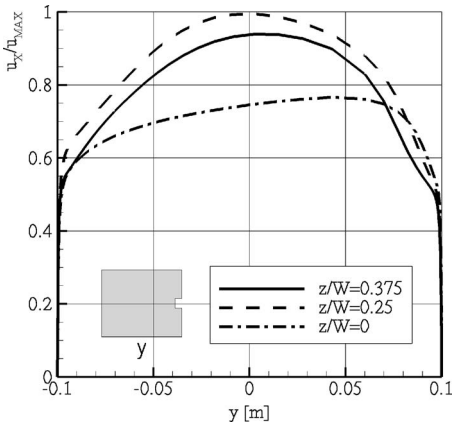

Fig. 8 Slices of velocity profiles of test case 1 at Re=130,000

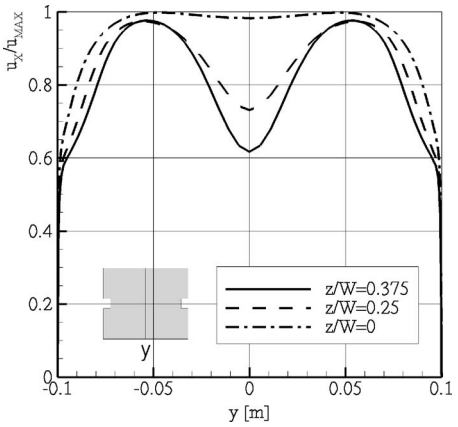

Fig. 10 Slices of velocity profiles of test case 2 at Re =130,000

data from test case 1 relative velocity maxima are located at the center of the four vortices, but the absolute maximum is found at $z/W=0$.

This observation is seen more clearly in Fig. 10 where the differences between test case 1 and test case 2 are emphasized. Moving from $z/W=0.375$ to $z/W=0$, the reduction of the axial velocity between the two relative velocity maxima almost vanishes.

Friction Factor. To be in a position to asses the thermal performance of the different rib geometries, it is not only important to investigate the heat transfer enhancement ratios, it is also critical to discuss the pressure penalty caused by the implementation of flow turbulators. Therefore the friction factor ratios f/f_0 are presented in Fig. 11.

The friction factor ratio of the smooth channel shows nearly a constant trend with an increasing Reynolds number as should be expected. The values of the friction factor are slightly higher then the results of the Blasius equation, whereas the measurements proved to be extremely sensitive due to the relative low pressure differences.

Looking at the friction factor ratios, test case 1 shows increasing values for rising Reynolds numbers. This was also true for the remaining test cases. The experimentally and numerically obtained values of test case 1 show that the obtained results were in good agreement for Reynolds numbers up to 150,000. For higher Reynolds numbers, the experimental data was underpredicted by

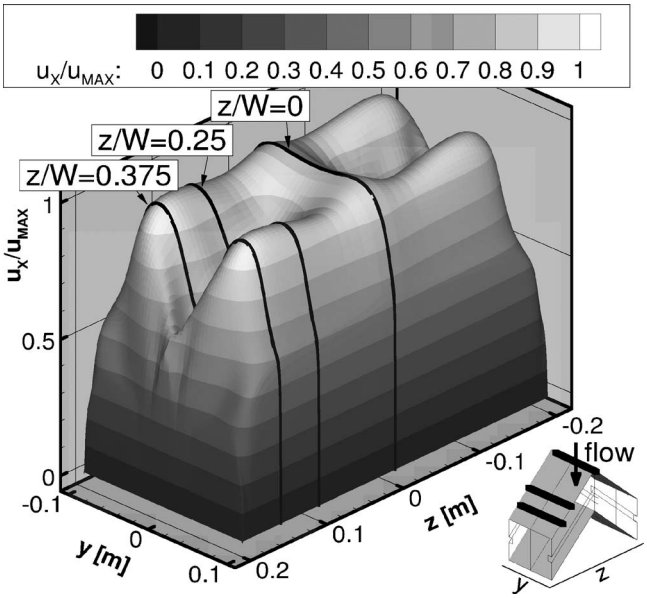

Fig. 9 Velocity profile of test case 2 at Re=130,000

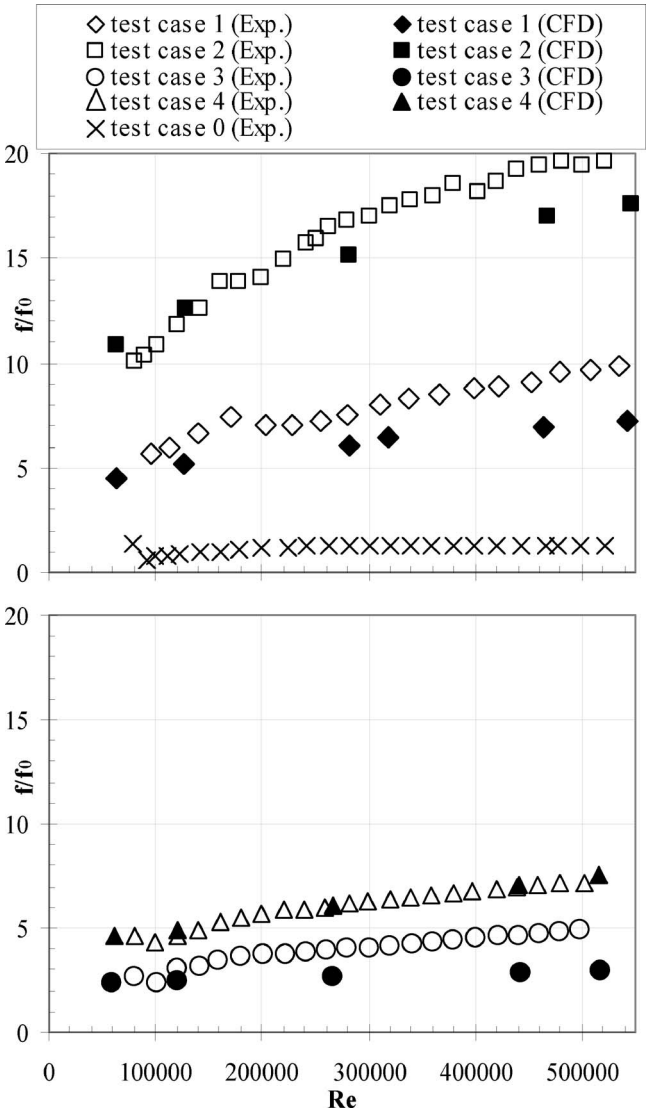

Fig. 11 Friction factor ratios f/f_0 for investigated cases

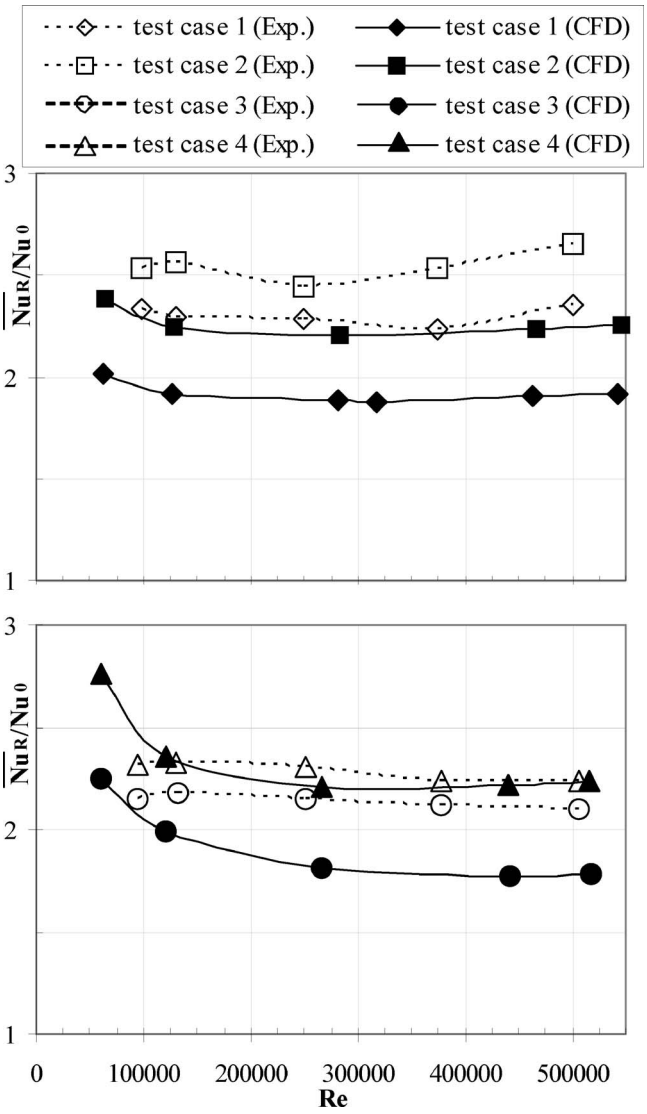

Fig. 12 Area averaged Nusselt number ratios

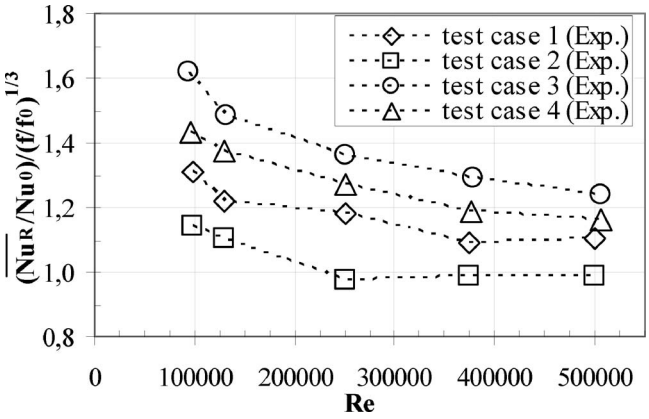

Fig. 13 Thermal performance

the numerical computation. The same trend occurred for test cases 2 and 3. Good agreement between experimental and numerical results was found for test case 4. Comparing the friction factor ratios of one-sided and two-sided ribbed channels it is evident that the existence of a second ribbed wall doubles the pressure penalty in the case of test case 1 and 2, whereas for test case 3 and 4 this was only the case for the numerical results. Here the gap between the experimental data of the one-sided and two-sided ribbed channel was smaller than that of the numerical results.

In the study of Han et al. [7] a geometry corresponding to test case 2 was investigated. Here, a friction factor ratio f/f_0 of 9.98 was measured at a Reynolds number of 90,000. This data agrees reasonably well with the data presented in the present study, keeping in mind that Han et al. [7] conducted their study in a channel with an aspect ratio of 1:1.

Area Averaged Heat Transfer Enhancement. Area averaged and local heat transfer enhancement results are presented, here starting with the area averaged heat transfer as shown in Fig. 12.

In the experimentally and numerically obtained data for test cases 1 and 2, introducing a second ribbed wall to the channel increases the heat transfer. In test cases 3 and 4 this was also the case. Furthermore, an overall decrease in heat transfer can be seen for the smaller rib configurations. In addition, the Nusselt number ratio levels off for $Re > 200{,}000$, except for the experimental data of test cases 1 and 2. Here the Nusselt number ratio tends to increase slightly for rising Reynolds numbers.

Analyzing the numerical and the experimental results for each test case, one can see that the experiment is underpredicted by CFD except for test case 4. At a Reynolds number of 90,000 an area averaged Nusselt number ratio of 2.34 was reported by Han et al. [7] corresponding to test case 2. Once again, there was good agreement with the data presented in the present study even though Han et al. [7] conducted their study in a channel with an aspect ratio of 1:1.

Thermal Performance. To assess the benefits of the rib configurations in the different test cases the heat transfer efficiency at constant pumping power was computed and is presented in Fig. 13. Here, only the thermal performance of the ribbed side is considered. The smaller rib configurations of test cases 3 and 4 performed better than the larger rib configurations in test cases 1 and 2, whose efficiency was close to the value of the smooth wall at higher Reynolds numbers.

Local Heat Transfer Enhancement. Experimental results for the local heat enhancement ratio Nu_R/Nu_0 are presented in contour plots Fig. 14 for test cases 3 and 4. Comparing the contour plots for the one-sided and two-sided ribbed channel, a decreasing heat transfer peak for increasing Reynolds numbers is seen. Similar findings were reported in a numerical study by Su et al. [12]. In the case of equal Reynolds numbers, the heat transfer peak of the two-sided ribbed channel is more enhanced than the heat transfer peak of the one-sided ribbed channel.

Looking at test cases 1 and 2 as shown in Fig. 14, similar observations may be concluded. With an increasing Reynolds number, the heat transfer ratio peak is reduced in intensity. Comparing one-sided and two-sided ribbed channels, the heat transfer ratio peak enhancement between both configurations is more intense than the enhancement between test cases 3 and 4.

The experimental and numerical results for the local heat enhancement ratio are compared in Fig. 15. Previously, the Reynolds numbers of the experimental and numerical data points are not matched exactly. Therefore, the numerical results are compared with the experimental data with the closest Reynolds number. The local heat transfer ratio distribution of all test cases and for two different Reynolds numbers is presented in Fig. 15. For test cases 3 and 4 a similarity in the pattern of the Nusselt number contours can be seen for a Reynolds number of about 130,000. Similar to experimental data, the calculations show an increasing heat transfer enhancement peak going from a one-sided to a two-sided ribbed channel. In the case of a channel with one ribbed wall this peak is underpredicted, whereas in the case of two ribbed walls the heat transfer peak calculated with CFD is even higher than the one found in experiment. The comparison of test cases 3 and 4 at

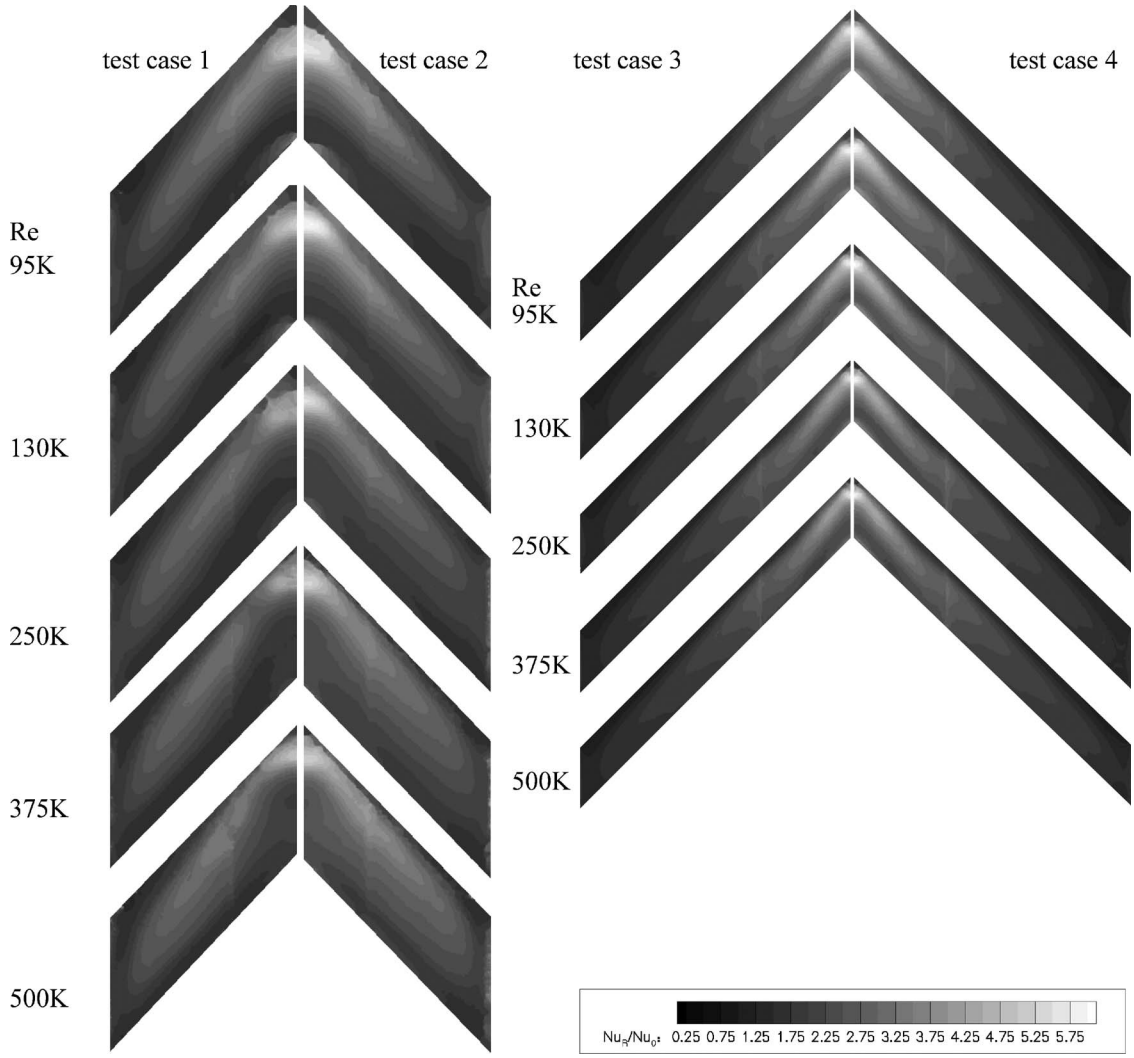

Fig. 14 Experimental local heat transfer ratios

a Reynolds number of about 500,000 reveals that here the heat transfer peak is underpredicted by CFD in both test cases. Still the increase of the heat transfer peak was shown when going from one-sided to two-sided ribbed channels.

In test cases 1 and 2 a similarity in the heat transfer ratio contours may also be seen. Both cases are underpredicted by the numerical simulation compared with data found by experiment. As in the investigations above an increasing heat transfer peak with an increasing number of ribbed channel walls may be observed.

Conclusions

In this study measurements and computations of heat transfer and friction factors have been conducted for V-shaped ribbed channels. The analysis of the friction factor for different Reynolds numbers indicates that there is an increase in pressure penalty if the number of ribbed walls is increased. It was also shown that introducing a second ribbed wall to the test channel enhances both the global and the local heat transfer ratio with an increase in the region of highest heat transfer. This heat transfer peak is reduced with increasing Reynolds number. Therefore experimental data from two sided ribbed channels (e.g., from studies related to gas turbine blade cooling) cannot be taken directly in applications with ribs on only one wall as for combustor liner cooling. Furthermore, for an increasing Reynolds number, the global heat transfer ratio decreases and levels off for Reynolds numbers above 200,000. The best thermal performance for the investigated cases was achieved with small ribs placed on one side of the cooling channel only. Numerical simulations provide the same trends as experimentally observed but underpredict the heat transfer enhancement. The simulations showed the change in flow structures and positions of maximum velocity going from one-sided to two-sided ribbed channels.

Acknowledgment

The authors gratefully acknowledge the financial support provided within the research and innovation initiative KW21 by the Ministry of Baden-Württemberg, Germany and ALSTOM Power. Additionally the permission to publish this paper by ALSTOM Power is appreciated.

Nomenclature

A_H = area covered with heater foil, m^2
D_h = hydraulic diameter, m
e = rib height, m
f = friction factor
f_0 = friction factor of fully developed turbulent flow in a smooth circular tube
h = heat transfer coefficient, W/m^2 K
H = test channel height, m
k = thermal conductivity of air, W/mK

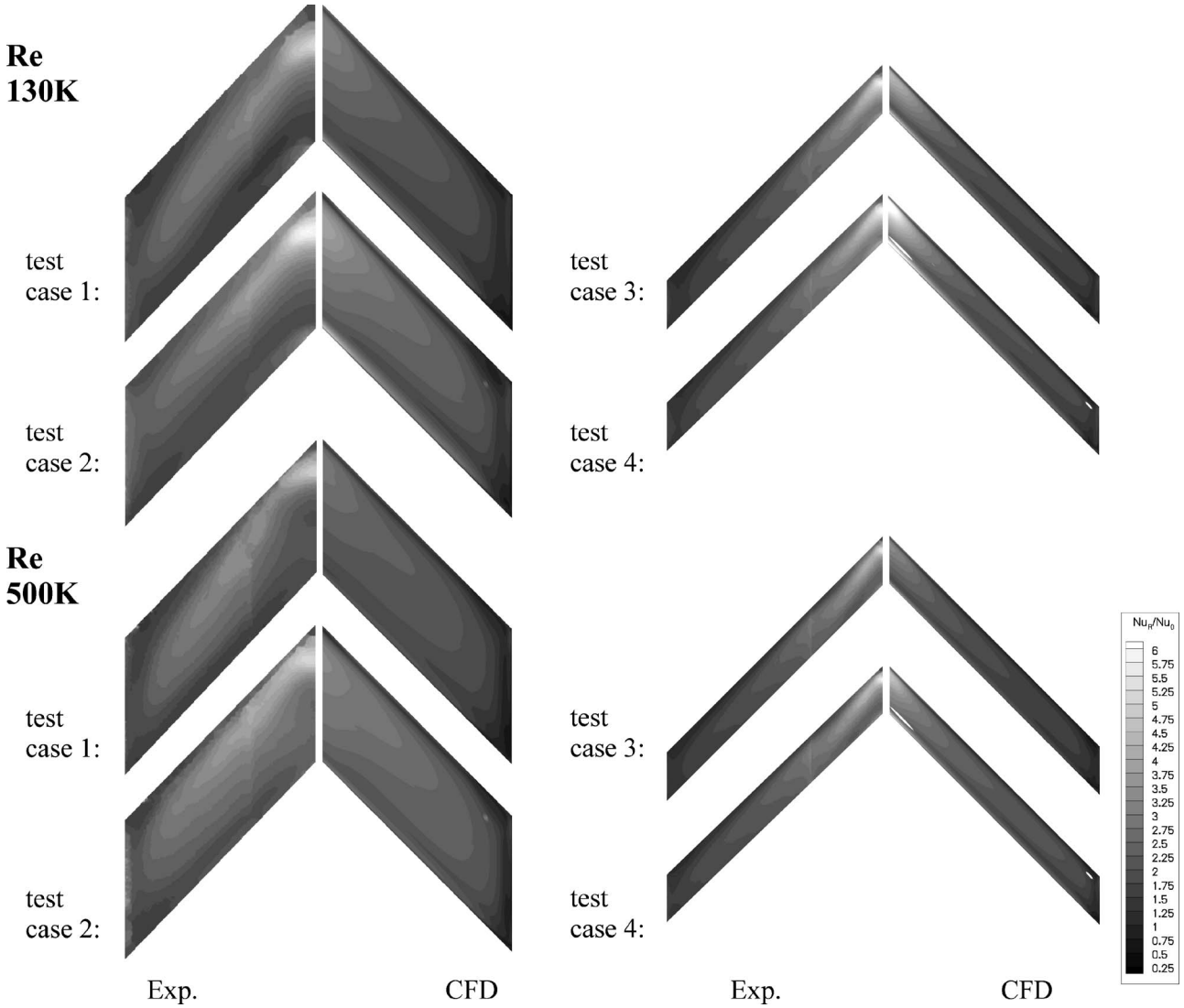

Fig. 15 Comparison between experimentally and numerically obtained local heat transfer ratio for Re∼130 K and Re ∼500 K

L = ribbed channel length, m
Nu = Nusselt number=hD_h/k
Nu_0 = Nusselt number of fully developed turbulent flow in a smooth circular tube
$\overline{\mathrm{Nu}_R}$ = area averaged Nusselt number of the ribbed wall
Nu_R = local Nusselt number of the ribbed wall
P = rib pitch, m
$\Delta p/\Delta x$ = regression line gradient of pressure distribution, Pa/m
Pr = Prandtl number of air
$\dot{Q}_w$ = wall heat flux, W
Re = Reynolds number=$\rho D_h u/\eta$
T_B = bulk temperature,
T_W = local wall temperature, K
u = mean velocity, m/s
u_{MAX} = maximum velocity in the x direction, m/s
u_X = velocity magnitude in the x direction, m/s
W = test channel width, m
x = coordinate in the axial direction, m
y = coordinate in the channel width direction, m
y^+ = dimensionless first layer height
z = coordinate in the channel height direction, m
η = dynamic viscosity of air, kg/(ms)
ρ = density of air, kg/m^3

References

[1] Sattelmayer, T., and Polifke, W., 1998, "NO_x-Abatement Potential of Lean-Premixed GT-Combustors," ASME J. Eng. Gas Turbines Power, **120**, pp. 48–59.
[2] Kim, W. K., Arellano, L., Vardakas, M., Moon, H., and Smith, K., 2003, "Comparison of Trip-Strip/Impingement/Dimple Cooling Concepts at High Reynolds Numbers," ASME Paper No. GT2003-38935.
[3] Bailey, J. C., Tolpadi, A. K., Intile, J., Fric, T. F., Nirmalan, N. V., and Bunker, R. S., 2002, "Experimental and Numerical Study of Heat Transfer in a Gas Turbine Combustor Liner," ASME Paper No. GT2002-30183.
[4] Ligrani, P. M., Oliveira, M. M., and Blaskovich, T., 2003, "Comparison of Heat Transfer Augmentation Techniques," AIAA J., **41**, pp. 337–362.
[5] Cakan, M., 2000, "Aero-Thermal Performance of Internal Cooling Systems in Turbo Machines," Lecture Series 2000–03, von Karman Institute for Fluid Dynamics.
[6] Lau, S. C., Kukreja, R. T., and McMillan, R. D., 1991, "Effects of V-Shaped Rib Arrays on Turbulent Heat Transfer and Friction of Fully Developed Flow in a Square Channel," Int. J. Heat Mass Transfer, **34**, pp. 1605–1616.
[7] Han, J. C., Zhang, Y. M., and Lee, C. P., 1991, "Augmented Heat Transfer in Square Channels With Parallel, Crossed, and V-Shaped Angled Ribs," ASME J. Heat Transfer, **113**, pp. 590–596.
[8] Taslim, M. E., Li, T., and Kercher, D. M., 1996, "Experimental Heat Transfer and Friction in Channels Roughened With Angled, V-Shaped, and Discrete Ribs on Two Opposite Walls," ASME J. Turbomach., **118**, pp. 20–28.

[9] Al-Hadhrami, L., Griffith, T., and Han, J. C., 2003, "Heat Transfer in Two-Pass Rotating Rectangular Channels (AR=2) With Five Different Orientations of 45 deg V-Shaped Rib Turbulators," ASME J. Heat Transfer, **125**, pp. 232–242.
[10] Cho, H. H., Rhee, D. H., and Lee, D. H., 2002, "Effects of Duct Aspect Ratio on Heat/Mass Transfer With Discrete V-Shaped Ribs," ASME Paper No. GT2002-38622.
[11] Wright, L. M., Fu, W. L., and Han, J. C., 2004, "Thermal Performance of Angled, V-Shaped, and W-Shaped Rib Turbulators in Rotating Rectangular Cooling Channels (AR=4:1)," ASME Paper No. GT2004-54073.
[12] Su, G., Teng, S., Chen, H. C., and Han, J. C., 2003, "Computation of Flow and Heat Transfer in Rotating Rectangular Channels (AR=4) With V-Shaped Ribs by a Reynolds Stress Turbulence Model," ASME Paper No. GT2003-38348.
[13] Gao, X., and Sundén, B., 2001, "Heat Transfer Distribution in Rectangular Ducts With V-Shaped Ribs," Heat Mass Transfer, **37**, pp. 315–320.
[14] Lee, E., Wright, L. M., and Han, J. C., 2003, "Heat Transfer in Rotating Rectangular Channels (AR=4:1) With V-Shaped and Angled Rib Turbulators With and Without Gaps," ASME Paper No. GT2003-38900.
[15] Momin, A. E., Saine, J. S., and Solanki, S. C., 2002, "Heat Transfer and Friction in Solar Air Heater Duct With V-Shaped Rib Roughness on an Absorber Plate," Int. J. Heat Mass Transfer, **45**, pp. 3383–3396.
[16] Ireland, P. T., and Jones, T. C., 2000, "Liquid Crystal Measurements of Heat Transfer and Surface Shear Stress," Meas. Sci. Technol., **11**, pp. 969–986.
[17] Hanjalić, K., and Launder, B. E., 1972, "Fully Developed Asymmetric Flow in a Plane Channel," J. Fluid Mech., **51**, pp. 301–335.

Double-Jet Ejection of Cooling Air for Improved Film Cooling

Karsten Kusterer
Jülicher Strasse 338,
B&B-AGEMA GmbH,
D-52070 Aachen, Germany
e-mail: kusterer@bub-agema.de

Dieter Bohn
Institute of Steam and Gas Turbines,
Aachen University,
Templergraben 55,
D-52056 Aachen, Germany
e-mail: post-bohn@idg.rwth-aachen.de

Takao Sugimoto
e-mail: sugimoto_t@khi.co.jp

Ryozo Tanaka

Gas Turbine & Machinery Company,
Kawasaki Heavy Industries, Ltd.,
Akashi 673-8666 Japan

Film cooling in gas turbines leads to aerodynamic mixing losses and reduced temperatures of the gas flow. Improvements of the gas turbine thermal efficiency can be achieved by reducing the cooling fluid amount and by establishing a more equal distribution of the cooling fluid along the surface. It is well known that vortex systems in the cooling jets are the origin of reduced film-cooling effectiveness. For the streamwise ejection case, kidney vortices result in a liftoff of the cooling jets; for the lateral ejection case, usually only one dominating vortex remains, leading to hot gas flow underneath the jet from one side. Based on the results of numerical analyses, a new cooling technology has been introduced by the authors, which reaches high film-cooling effectiveness as a result of a well-designed cooling hole arrangement for interaction of two neighboring cooling jets (double-jet film cooling (DJFC)). The results show that configurations exist, where an improved film-cooling effectiveness can be reached because an anti-kidney vortex pair is established in the double-jet. The paper aims at the following major contributions: (1) to introduce the DJFC as an alternative film-cooling technology to conventional film-cooling design; (2) to explain the major phenomena, which leads to the improvement of the film-cooling effectiveness by application of the DJFC; and (3) to prove basic applicability of the DJFC to a realistic blade cooling configuration and present the first test results under machine operating conditions. [DOI: 10.1115/1.2720508]

Keywords: film cooling, film-cooling effectiveness, double-jet, kidney vortices

Introduction

Due to high turbine inlet temperatures in gas turbine cycles, film cooling is widely used for the vanes and blades of the front stages in order to reduce material temperatures as far as necessary for an acceptable life span of the components. As the cooling fluid is extracted from the compressor at high-pressure levels, the reduction of the cooling fluid effort for the cooling task will lead to increased thermal efficiencies. As film cooling leads to mixing losses and a reduced temperature of the gas flow, improvements can be achieved by reducing the cooling fluid amount and by establishing a more equal distribution of the cooling fluid on the surface.

The cooling fluid ejection through a hole leads to a "jet in crossflow" situation. It is well known that the cooling jet vortices are generated due to the friction of the jet flow and the crossflow. In the case of a streamwise ejection, the vortices are called kidney vortices because of their shape. A large number of publications deal with the visualization or calculation of these vortices and the publications of Bergeles et al. [1], Leylek and Zerkle [2], and Walters and Leylek [3] are mentioned as examples.

In a numerical investigation of a showerhead cooling configuration by Hall et al. [4] it was observed that effects caused by secondary flows could lead to a cooling flow effectiveness degradation and liftoff of the cooling jet. This liftoff effect has been investigated in detail by Bohn and Kusterer [5] for a turbine blade cooling configuration with leading edge ejection. As shown in Fig. 1, hot gas from the upper and lower side flows underneath the cooling jet. A second vortex system (Ω_{1b}) under the cooling jet is generated and the jet is pushed away from the blade surface.

Compound-angle ejection leads to an asymmetric vortex system [6]. A detailed numerical analysis of the film cooling physics in the case of a flat plate has been performed by McGovern and Leylek [7]. The numerical work of Baier et al. [8] focuses on the influence of the laterally inclined jets on film cooling in the case of a suction side ejection. Recent numerical studies on the leading edge film-cooling physics by York and Leylek [9,10] also focus on the determination of the adiabatic film cooling effectiveness and heat transfer coefficients.

In the case of compound-angle ejection, liftoff of cooling jets is reduced in comparison to the streamwise ejection. For example, Goldstein and Jin [11] have presented experimental results for a flat plate that indicate reduced liftoff effects at high blowing ratios in comparison to the streamwise ejection. Nevertheless, they found liftoff effects for compound-angle film cooling due to the asymmetric motion developed from the down-sweeping of the mainstream under the jets. Results of Bohn and Kusterer [12], for leading edge ejection with radially inclined cooling holes, have shown the presence of a dominating vortex ($\Omega_{1,1-b}$) in the jet, which leads to a rotation of the complete jet. Thus, hot gas is transported underneath the jet and finally leads to a liftoff of the jet. However, the liftoff effect is reduced compared to the case with streamwise ejection. As an example of these results, Fig. 2 shows the development of the dominating vortex in a cooling jet on the suction side of the blade and a comparison to the measurements by Ardey [13].

The question is, how to reduce the negative effect of the jet liftoff. One answer is the implementation of holes with shaped exits that reduce the momentum of the ejection. Although the positive influence of shaped holes on film cooling has been well known for a long time [14], a large number of publications still focus on this topic for detailed understanding of the secondary flow development in the jets and aim to create a reliable database on the adiabatic film cooling effectiveness and heat transfer conditions [15–18]. Numerical investigations by Bohn et al. [19] have shown that in cases of high heat flux rates an influence on the secondary flow phenomena in the jets can be observed.

A second possibility that has been discussed in the literature is the influence of the internal geometry on the vortex generation. It is known that including the internal geometry of the supply within numerical investigations is of significant importance in order to

Contributed by the International Gas Turbine Institute of ASME for publication in the JOURNAL OF TURBOMACHINERY. Manuscript received July 28, 2006; final manuscript received August 8, 2006. Review conducted by David Wisler. Paper presented at the ASME Turbo Expo 2006: Land, Sea and Air (GT2006), Barcelona, Spain, May 8–11, 2006, Paper No. GT2006-90854.

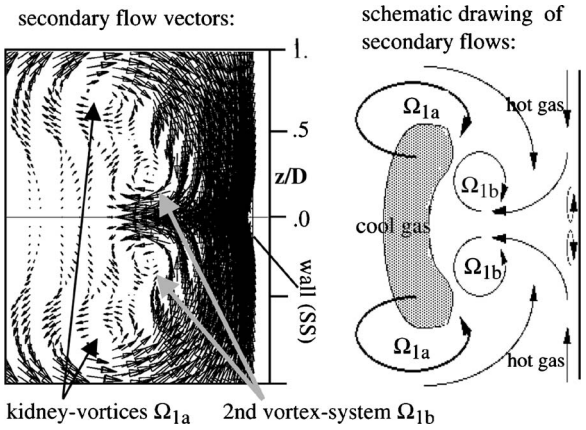

Fig. 1 Secondary flows in suction side jet (leading edge ejection, Bohn and Kusterer [5])

take into account the influence of vortices generated inside the hole before ejection [2,20–22]. Heidmann et al. [23] were also able to show this for a complex cooling geometry within a coupled internal/external simulation of a film-cooled vane. Depending on the direction of the cooling air supply, vortices are generated in the holes that might support or reduce the external liftoff effect of the jet, Vogel [24] has shown that a left-curved inflow creates a vortex system in the hole that rotates differently from the external kidney vortices. This additional vortex system can be found on top and beside the kidney vortices of the jet and leads to an improved wall contact. Due to special geometry parameters of a shaped hole, it might also be possible to create an anti-kidney pair of vortices in the external jet as it has been reported by Haven et al. [25]. Some researchers recommended manufacturing curved holes that also can create an additional anti-kidney vortex system in the hole, that might reduce the negative effect of the external kidney vortices in the jet.

A third recommendation on reducing the liftoff effect is given in this paper by introducing the double-jet film-cooling (DJFC) technology [26].

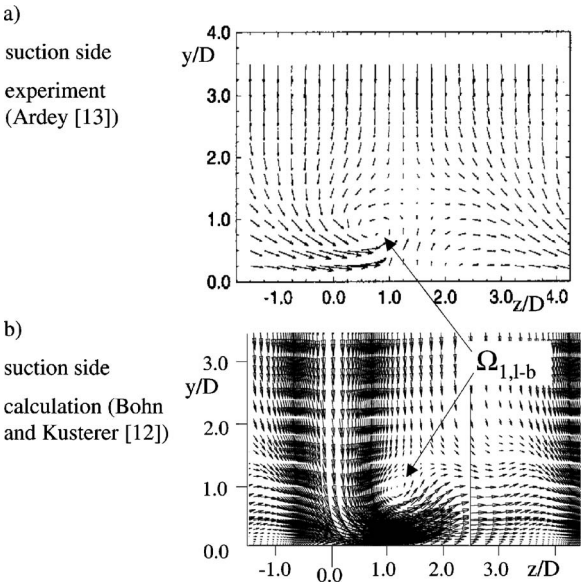

Fig. 2 (*a*)–(*b*): Lateral ejection secondary flows

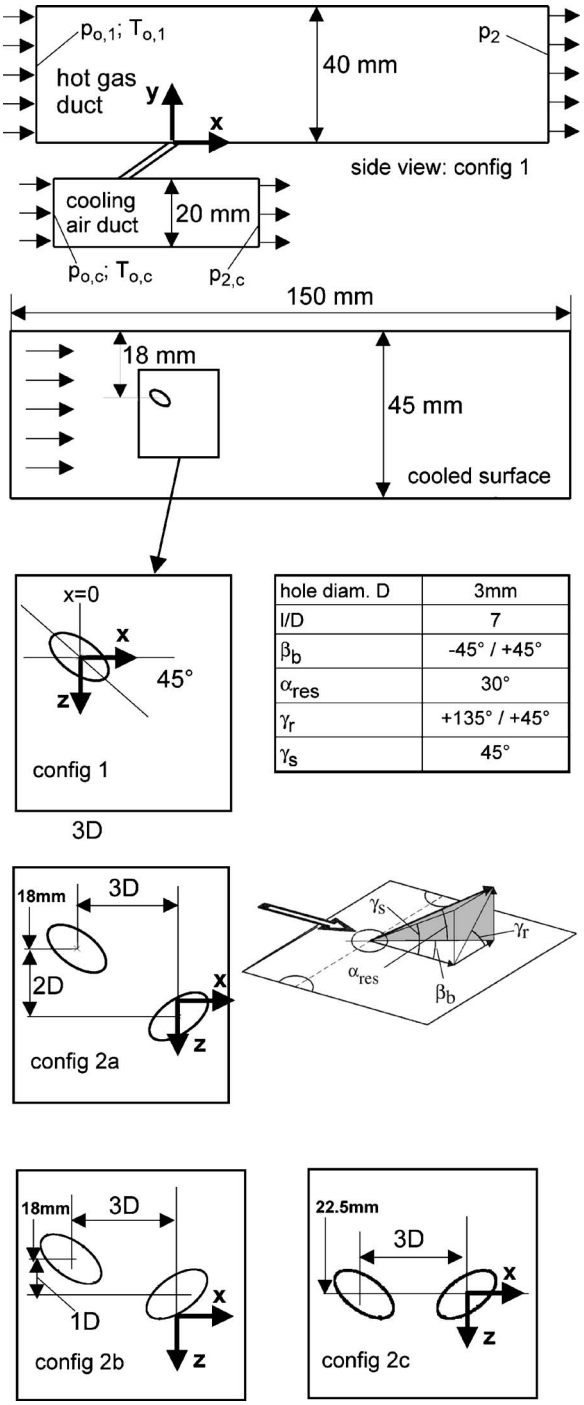

Fig. 3 Duct and hole geometry

Double-Jet Film-Cooling

We know that an anti-kidney vortex system will increase significantly the wall contact of the jet and will also improve the lateral distribution of the cooling air on the surface. Thus, it is the aim of the DJFC to establish an anti-kidney vortex system in the jet as the major secondary flow phenomenon. We also know that a single jet from a cylindrical hole with lateral ejection leads to a dominating vortex in the jet. Therefore, the DJFC aims to place a second ejection hole in a double-hole arrangement that creates a second jet with another dominating vortex rotating in opposite direction to the first one and then combines both jets to one jet (or double jet). As a result, a more or less symmetrical anti-kidney

Table 1 Boundary conditions (DJFC test cases)

$T_{o,1}$	1600 K
$p_{o,1}$	13.128×10^5 N/m^2
Ma_1	0.33
p_2	12.1×10^5 N/m^2
	Cooling air
$T_{o,c}$	700 K
$p_{o,c}$	15×10^5 N/m^2
$p_{2,c}$	14.9×10^5 N/m^2
Ma_c	0.1

vortex pair should be generated. It prevents the flow of hot gas underneath the jet and also prevents the liftoff of the jet. Thus, the wall contact of the jet is significantly enhanced as the secondary flows in the jet push the jet towards the wall. Furthermore, the cooling fluid will be distributed in the lateral direction, too, leading to a more efficient use of the cooling fluid with high cooling effectiveness values.

Geometry of DJFC Test Cases

The basic configuration investigated by means of three-dimensional (3D) flow simulation consists of two ducts: one for the hot gas flow and another one for the cooling air supply of the ejection holes. Figure 3 gives a detailed description on the duct geometry and the hole geometry. The hole diameter is 3 mm and the length of the ejection hole is seven times the hole diameter. The radial ejection angle γ_r and the streamwise ejection angle γ_s of the hole result in a cooling fluid ejection with an angle of $\alpha_{res}=30$ deg relative to the lower duct wall. Definitions of the ejection angles are indicated in the drawing of Fig. 3. Configuration 1 is the basic configuration with only one ejection hole.

Configurations 2a–c are configurations with a double-hole arrangement with oppositely orientated directions of ejection as also indicated in Fig. 3 and an additional cooling air supply for the second hole. The parameter varied for the configurations is the lateral distance between the two holes (from $2D$ to $0D$). For Configuration 2c both holes are in line and at the midposition of the wall.

Model and Boundary Conditions

For the 3D numerical simulations, the conjugate fluid flow and heat transfer simulation code (CHTflow [27]) has been used, but only adiabatic walls have been implemented to the numerical model. Thus, all calculated surface temperatures are adiabatic surface temperatures. Full, compressible three-dimensional Navier–Stokes equations are solved in the fluid regions. All fluids are calculated as perfect gas (air). The closure of the Reynolds averaged equations is provided by the Baldwin–Lomax algebraic eddy–viscosity turbulence model [28]. Full turbulent flow field has been assumed.

The physical domain is divided into separate blocks for the fluid regions (multiblock technique). The 3D model for the DJFC cases includes both supply channels, the cooling holes, and the main flow duct (hot air region). The total number of grid points is approximately 700,000.

Boundary conditions for the inlets and the outlets are chosen as given in Table 1. Total values have been used at the inlets and static pressures have been fixed at the outlets. Temperatures and pressures are close to values of real operating conditions in a modern gas turbine.

Results of the Test Cases

Single Jet (Config 1). Calculations with Configuration 1 have been performed in order to evaluate whether the single jet development meets the expectations as described in the reference literature. Figures 4(*a*)–4(*c*) give the temperature field of the cooling jet in three different axial cutting planes and the secondary flow vectors additionally. As the boundary conditions lead to a high blowing ratio of $M=1.7$, there is a strong interaction of the cooling jet and the hot duct flow. As a result, a strong dominating vortex is created in the jet. Furthermore, the vortex transports hot gas from one side underneath the jet leading to a partial liftoff.

As the development of the single jet meets the requirements on the size and strength of the vortex, the geometry for the DJFC test cases has been derived as presented.

Blowing Ratios (Config 2a–c). Boundary conditions were kept the same for all DJFC test cases. The blowing ratio

$$M = (\rho_c c_c)/(\rho_g c_g) \tag{1}$$

which is the ratio of density and velocity values for the cooling flow and the hot gas flow, is a result of these boundary conditions. Thus, a slight variation of the local blowing ratios of the single holes in the DJFC test cases occur as given in Table 2. However, the single blowing ratios are always close to $M=1.7$. In the test case with "config 2c," the blockage effect of the second hole, is the reason for the lower blowing ratio of the first hole.

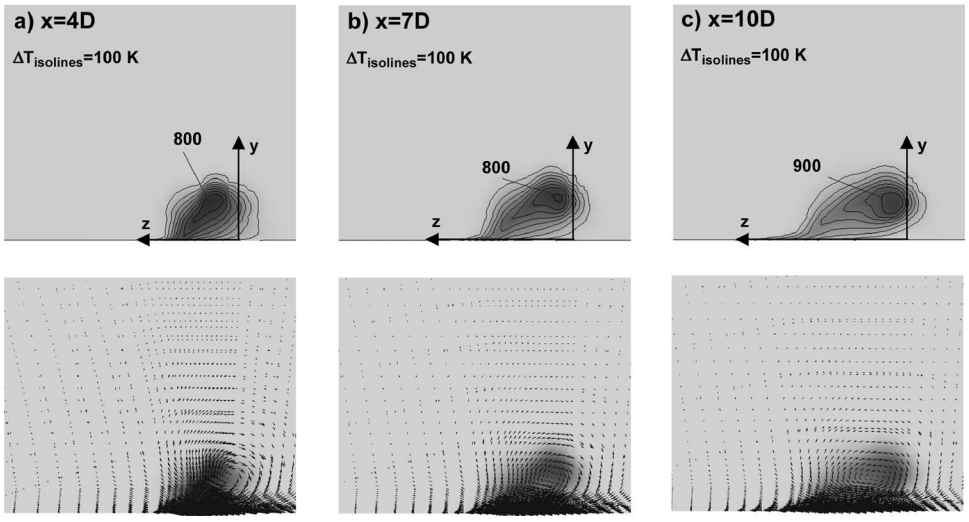

Fig. 4 (*a*), (*b*), (*c*) Development of cooling jet vortex and jet liftoff (Config 1)

Table 2 Blowing ratios for DJFC test cases

	Config 2a	Config 2b	Config 2c
$M_{\text{hole }\#1}$	1.70	1.74	1.61
$M_{\text{hole }\#2}$	1.78	1.74	1.77

Adiabatic Film-Cooling Effectiveness. The performance of cooling can be expressed as the adiabatic film cooling effectiveness

$$\eta_f = (T_{\text{aw}} - T_r)/(T_{0c} - T_r) \tag{2}$$

Here, T_{0c} is the stagnation temperature of the cooling fluid near entry; and T_{aw} is the adiabatic wall temperature. Without film cooling, T_{aw} will be the recovery temperature T_r of the hot gas flow. For reasons of simplification in the determination of the adiabatic cooling effectiveness, the total temperature of the hot gas at the inlet (1600 K) has been used in the evaluation instead of the recovery temperature.

Figures 5(*a*)–5(*c*) show the distribution of the calculated adiabatic film-cooling effectiveness on the surface. Whereas for Configurations 2a and 2b there is hardly any wall contact of the double-jets downstream of the ejection holes, the situation for Configuration 2c is completely different. It is not only possible to detect high values of effectiveness over a long distance behind the holes, but in the downstream area, starting at approximately $x/D=8$, there is also a significant lateral extension of the area in contact with the cooling air. Even very far downstream, at approximately $x/D=30$, relatively high values (>0.2) can be found. However, it is well known that without anisotropic turbulence modeling the process of mixing out of cooling air and hot gas is underestimated. Therefore, lower values of effectiveness are likely in cases with a more sophisticated turbulence modeling, which should be part of further numerical studies. Nevertheless, it is obvious that a major flow phenomenon in the double jet has been changed so that a very much improved wall contact has been established.

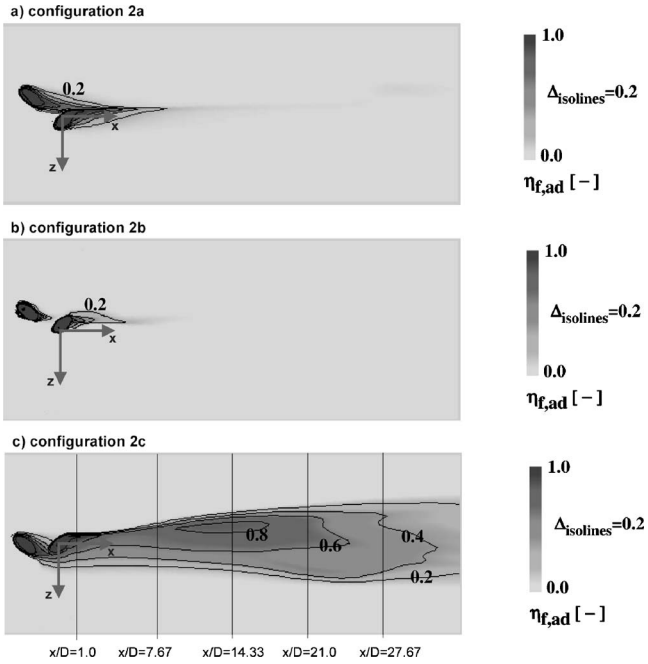

Fig. 5 (*a*), (*b*), (*c*) Calculated adiabatic film-cooling effectiveness for DJFC configurations

Temperature Field. Figures 6(*a*)–6(*c*) present the evaluation results for the temperature field in the double jets in different axial cutting planes. View direction is upstream. In the case of Configuration 2a, the two single jets create a double jet that is similar to a jet from a streamwise ejection through a single cylindrical hole with two cores and a kidney shape. Due to the high blowing ratio, a liftoff of the double jet is forced. The same situation can be found for Configuration 2b (Fig. 6(*b*)). The situation is even worse with an increased liftoff effect.

Now, for Configuration 2c (Fig. 6(*c*)) it can be seen that a liftoff is prevented. The cooling air remains close to the duct wall and further downstream it seems to be pushed toward the wall so that the cool air distributes also in the lateral direction.

Secondary Flows. The reason for the large differences in the temperature fields can be found in the visualization of the secondary flows (Figs. 7(*a*)–7(*c*)). Whereas for the liftoff configurations (Config 2a and 2b), the rotation of the vortex pair in the double jet is similar to the kidney vortex pair in the jet of the streamwise ejection from a cylindrical hole, the secondary flow vectors for Configuration 2c reveal the expected anti-kidney vortex pair. Due to the change in direction of the rotation, the jet is pushed toward the wall and, furthermore, the desired distribution of the cooling air in a lateral direction can also be reached. Therefore, the flow situation is close to the idealized flow directions for an optimized DJFC geometry as drawn in the idealized schematic drawing of Fig. 7(*d*).

The basic numerical study shows that it is possible to find a double-hole arrangement, which is able to create a jet out of the two single jets that establishes anti-kidney vortices. Therefore, significant improvements of the film-cooling effectiveness can be reached without manufacturing shaped holes. However, the applicability for more complex flow situation and within complex cooling configurations needs further investigation.

Application of DJFC for GT Blade

Based on the promising results of the DJFC for the simple numerical test case as described above, it has been decided to investigate the applicability of the DJFC for cooling a blade in a gas turbine. For this purpose, the DJFC has been included in the cooling configuration of a test blade for the first blade row of the L20A gas turbine. As indicated by the schematic drawing in Fig. 8, it should be possible to find a double-hole arrangement on the suction side or pressure side of the blade with an internal cooling air supply by a serpentine-shaped channel. Two rows with cylindrical ejection holes are placed on the surface in a way that the positive effect of the anti-kidney vortex pair in the jets can be realized for a complex cooling configuration and under real operating conditions.

It has been decided that the DJFC replaces the cooling air ejection through the row of shaped holes on the suction side of the original blade, which has high efficient cooling of the blade suction side in the original design for machine application. The internal cooling duct geometry and all other cooling arrangements have to be kept the same as for the other test blades. Due to the restrictions in the possibilities to change the internal geometry design, it has been found that it is not possible to establish the necessary arrangement of cooling holes over the complete height of the blade. Furthermore, the location of the hole exits is also somewhat further downstream than in the original design with a row of shaped holes.

From the original design, it is known that cooling air ejected through the row of shaped holes on the suction side is able to establish a quite efficient cooling film. Thus, in cases where a similar thermal load level of the suction side with application of the DJFC design would be reached, this might indicate that the DJFC is providing a similar contribution to the cooling performance of the blade as the shaped holes.

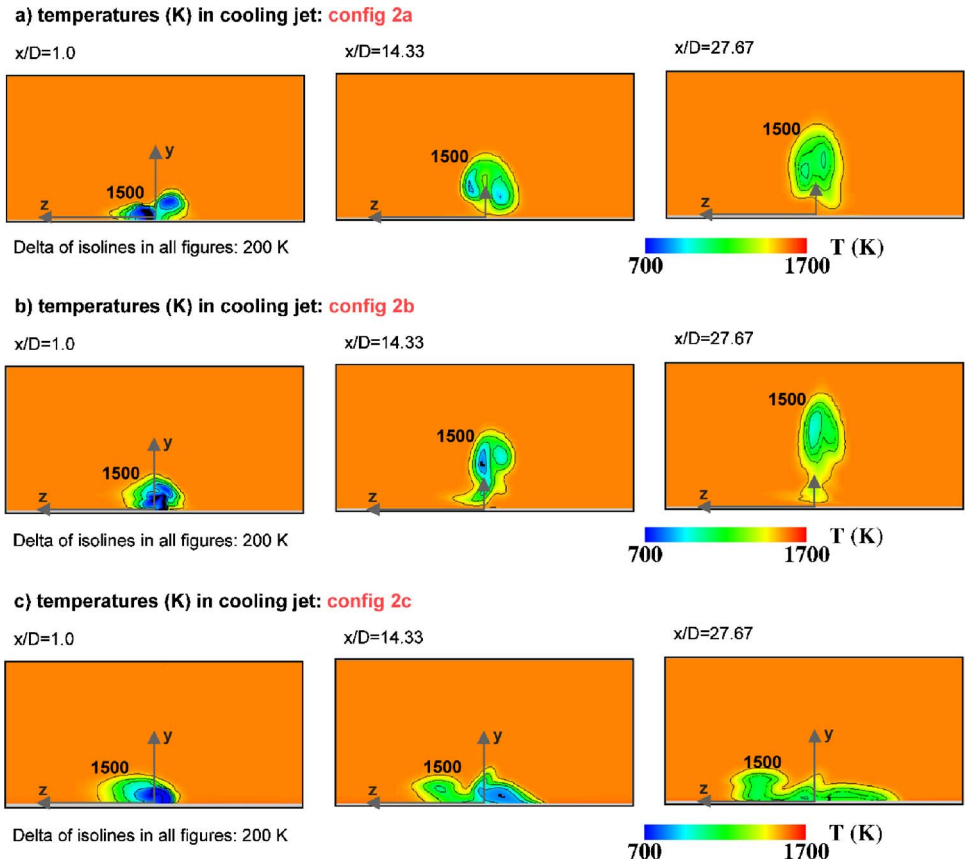

Fig. 6 (*a*), (*b*), (*c*) **Calculated temperature distributions in the double jets**

Figure 9 shows the calculated distribution on the blade surface of the adiabatic temperatures (suction side view) for the initial configuration with DJFC design. The calculation takes into account the passage flow, internal flow of the serpentine-shaped passage for supply of the two rows of the DJFC, and the blade tip hole. It can be clearly seen that behind the holes the double jet reaches low adiabatic surface temperatures (high adiabatic film-cooling effectiveness) and that there is also a lateral extension of the jets. However, the lateral distribution of the cooling air is limited and high-temperature streaks between the jets can be expected.

The interaction with major passage flow phenomena (passage vortex, tip clearance vortex) also results in negative effects on the cooling air distribution. A large amount of cooling air is ejected through the tip hole and that cooling air becomes a major part of the tip clearance vortex. Based on comparison of 3D aerothermal calculations with the computational fluid dynamics (CFD) code for the original configuration and the DJFC configurations, it has been assumed that the overall cooling air amount supplied to the internal cooling supply channel will be over 10% lower in the

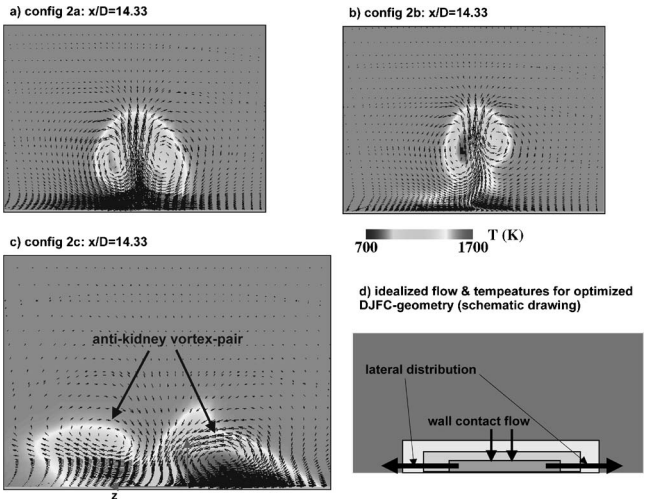

Fig. 7 (*a*), (*b*), (*c*) **Calculated secondary flows in the double jets**

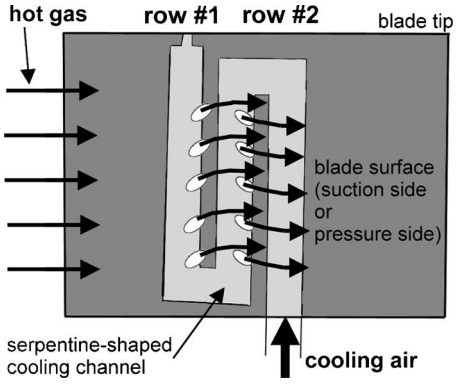

Fig. 8 Application of the DJFC to a cooled GT blade (schematic drawing)

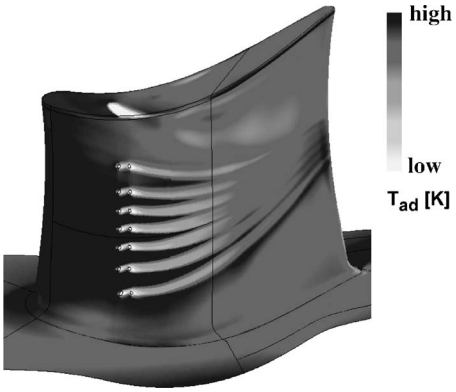

Fig. 9 3D CFD result (adiabatic surface temperatures) of a DJFC design for a test blade

case of the DJFC configuration. Thus, a reduction of the convective cooling for the test blade with DJFC can be expected.

Several turbine blades with the DJFC design on the suction side have been manufactured. Based on an initial DJFC design, a blade with a further refined DJFC design has also been manufactured. In the refined configuration, it had been possible to improve the locations of the hole exits with respect to the generation of the anti-kidney vortex system. These blades have been tested under hot gas operating conditions in the gas turbine. Thermal load measurements have been performed by application of the pyrometer measurement technique.

Figures 10(*a*)–10(*c*) present the results of the pyrometer measurements for the rear part of the suction side for different configurations. Unfortunately, the midpart of the suction side is not accessible for pyrometer measurements in the machine. The comparison of the initial DJFC design (Fig. 10(*b*)) with the original design of the test blade (Fig. 10(*a*)) shows that cooling performance of the rear part of the suction side is similar. Thermal load appears to be slightly higher for the initial DJFC design. For the refined DJFC design (Fig. 10(*c*)), the main features are still the same as in the original design but overall thermal load is lower despite the fact that the calculated cooling air amount is lower by approximately 10% for the suction side ejection.

These results indicate that the DJFC basically provides a similar cooling performance as the row of shaped holes. But it cannot be stated at the moment that the cooling performance is better than in the original design because the location of cooling air ejection is somewhat downstream of the original position of the row with shaped holes. Due to this fact, higher thermal loads have been observed for the leading edge region in both DJFC test cases. However, the first results are promising with respect to applicability of the DJFC technology for blade cooling. Further studies and testing are under consideration.

Conclusions

The paper has presented the numerical results for the DJFC, which consists of a double-hole arrangement with laterally inclined holes of cylindrical shape. Due to an optimized position of the single holes, high film-cooling effectiveness values can be reached in a wide region on the surface behind the cooling air ejections. The major findings have been as follows:

1. It is possible to establish a double-hole arrangement that forms a common jet with an anti-kidney vortex pair;
2. As a result, the double-jet keeps wall contact and cooling air is also distributed in a lateral direction;
3. High values of adiabatic film-cooling effectiveness are reached; and
4. The holes have a cylindrical shape and, therefore, are easier to manufacture than shaped holes.

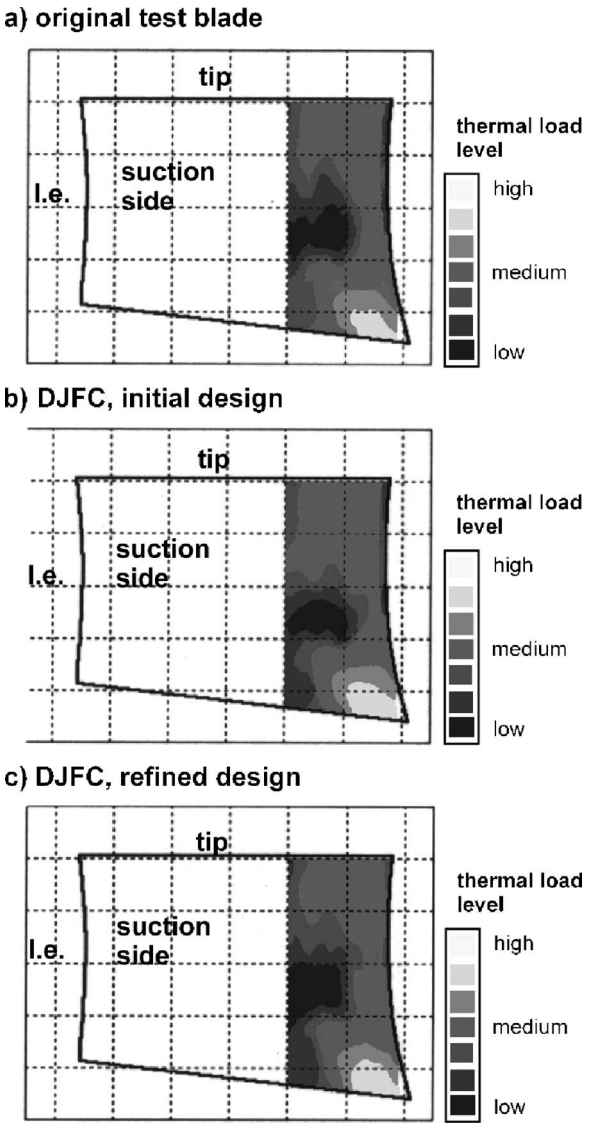

Fig. 10 (*a*), (*b*), (*c*) Pyrometer measurements for test blades with different cooling designs

Furthermore, the DJFC application for a test blade of the L20A gas turbine from KHI has been investigated. It has been found that the DJFC could be included to the current design of a test blade. The test blade has been tested successfully by KHI under realistic gas turbine operating conditions. The DJFC has been able to replace a row of shaped holes on the suction side of the blade without negative effects on the thermal load level.

Nomenclature

c = velocity (m/s)
D = hole diameter (mm)
l = hole length (mm)
M = local blowing ratio (-)
Ma = Mach number (-)
p = pressure (N/m^2)
T = temperature (K)
x = streamwise coordinate (mm)
y = perpendicular coordinate (mm)
z = lateral coordinate (mm)
Ω_i = vortex structures (-)
α_{res}, β_b = ejection angles (deg)
γ_s, γ_r = ejection angles (deg)

η_f = adiabatic film effectiveness (-)
ρ = density kg/m^3

Subscripts

a, ad = adiabatic
c = cooling condition
g = hot gas
0 = stagnation condition
r = recovery
w = wall
1 = inlet (main duct)
2 = outlet

Abbreviation

DJFC = double-jet film cooling

References

[1] Bergeles, G., Gosman, A. D., and Launder, A. D., 1976, "The Prediction of Three-dimensional Discrete-hole Cooling Processes," J. Heat Transfer, **98**, pp. 379–386.
[2] Leylek, J. H., and Zerkle, R. D., 1994, "Discrete-Jet Film Cooling: A Comparison of Computational Results with Experiments," ASME J. Turbomach., **116**, pp. 358–368.
[3] Walters, D. K., and Leylek, J. H., 2000, "A Detailed Analysis of Film-Cooling Physics Part I: Streamwise Injection with Cylindrical Holes," ASME J. Turbomach., **122**, pp. 102–112.
[4] Hall, J. E., Topp, D. A., and Delaney, R. A., 1994, "Aerodymamic/Heat Transfer Analysis of Discrete Site Film-cooled Turbine Airfoils," AIAA Paper No. 94–3070.
[5] Bohn, D., and Kusterer, K., 1999, "Blowing Ratio Influence on Jet Mixing Flow Phenomena at the Leading Edge," AIAA Paper No. 99–0670.
[6] Lee, S. W., Kim, Y. B., and Lee, J. S., 1995, "Flow Characteristics and Aerodynamic Losses of Film-cooling Jets with Compound Angle Orientations," ASME Paper No. 95-GT-38.
[7] McGovern, K. T., and Leylek, J. H., 2000, "A Detailed Analysis of Film Cooling Physics Part II. Compound-Angle Injection with Cylindrical Holes," ASME J. Turbomach., **122**, pp. 113–121.
[8] Baier, R.-D., Broichhausen, K.-D., Koschel, W., and Parvizinia, M., 1997, "Numerical and Experimental Study on the Influence of Angle Orientations on the Behaviour of Discrete Film Cooling Holes on Turbine Bladings," Proceedings International Symposium on Airbreathing Engines, ISABE Paper No. 97–7109, Chattanooga, TN, Sept. 7–12, 1997.
[9] York, D. Y., and Leylek, J. H., 2002, "Leading-Edge Film-Cooling Physics: Part I—Adiabatic Effectiveness," ASME Paper No. GT-2002-30166.
[10] York, D. Y. and Leylek, J. H., 2002, "Leading-Edge Film-Cooling Physics: Part II—Heat Transfer Coefficient," ASME Paper No. GT-2002-30167.
[11] Goldstein, R. J., and Jin, P., 2000, "Film Cooling Downstream of a Row of Discrete Holes with Compound Angle," ASME Paper No. 2000-GT-248.
[12] Bohn, D., and Kusterer, K., 2000, "Aerothermal Investigations of Mixing Flow Phenomena in Case of Radially Inclined Ejection Holes at the Leading Edge," ASME J. Turbomach., **122**, pp. 334–339.
[13] Ardey, S., 1998, "3D-Messung des Strömungsfeldes um die filmgekühlte Vorderkante einer Referenzschaufel," Ph.D. thesis, University of the Armed Forces, Munich, Germany (in German).
[14] Goldstein, R. J., Eckert, E. R. G., and Burggraf, F., 1974, "Effects of Hole Geometry and Density on Three-Dimensional Film Cooling," Int. J. Heat Mass Transfer, **17**, pp. 595–607.
[15] Gritsch, M., Schulz, A., and Wittig, S., 1998, "Adiabatic Wall Measurements of Film-Cooling Holes with Expanded Exits," ASME J. Turbomach., **120**, pp. 568–574.
[16] Lutum, E., von Wolfersdorf, J., Semmler, K., Dittmar, J., and Weigand, B., 2001, "An Experimental Investigation of Film Cooling on a Convex Surface Subjected to Favourable Pressure Gradient Flow," Int. J. Heat Mass Transfer, **45**, pp. 939–951.
[17] Yuen, C. H. N., Martinez-Botas, R. F., and Whitelaw, J. H., 2001, "Film Cooling Effectiveness Downstream of Compound and Fan-shaped Holes," ASME Paper No. 2001-GT-0131.
[18] Saumweber, C., and Schulz, A., 2003, "Interaction of Film Cooling Rows: Effects of Hole Geometry and Row Spacing on the Cooling Performance Downstream of the Second Row of Holes," ASME Paper No. GT-2003-38195.
[19] Bohn, D., Ren, J., and Kusterer, K., 2003, "Conjugate Heat Transfer Analysis for Film Cooling Configurations with Different Hole Geometries," ASME Paper No. GT-2003-38369.
[20] Martin, C. A., and Thole, K. A., 1997, "A CFD Benchmark Study: Leading Edge Film-cooling with Compound Angle Injection," ASME Paper No. 97-GT-297.
[21] Martelli, F., Adami, P., and Belardini, E., 2001, "Numerical Investigation of Heat Transfer and Film Cooling for Gas Turbine Application," Proceedings International Symposium on Airbreathing Engines, ISABE Paper No. 2001-1102, Bangalore, India, Sept. 2–7, 2001.
[22] Bohn, D., Becker, V., Kusterer, K., Fottner, L., and Ardey, S., 2000, "Three-Dimensional Flow Analysis of Turbine Blade Cascades with Leading Edge Ejection," J. Propul. Power, **16**, pp. 49–56.
[23] Heidmann, J. D., Rigby, D. L., and Ameri, A. A., 2000, "A Three-Dimensional Coupled Internal/External Simulation of a Film-cooled Turbine Vane," ASME J. Turbomach., **122**, pp. 348–359.
[24] Vogel, D. T., 1998, "Numerical Investigation of the Influence of Specific Vortex Generation on the Mixing Process of Film Cooling Jets," ASME Paper No. 98-GT-210.
[25] Haven, B. A., Yamagata, D. K., Kurosaka, M., Yamawaki, S., and Maya, T., 1997, "Anti-Kidney Pair of Vortices in Shaped Holes and their Influence on Film Cooling Effectiveness," ASME Paper No. 97-GT-45.
[26] Japanese Patent Application No. 332530, "Double Jet Film Cooling Structure," 2005.
[27] Bohn, D., Krüger, U., and Kusterer, K., 2001, "Conjugate Heat Transfer: An Advanced Computational Method for the Cooling Design of Modern Gas Turbine Blades and Vanes," *Heat Transfer in Gas Turbines*, B. Sundén and M. Faghri, eds., WIT Press, Southampton, UK, pp. 58–108.
[28] Baldwin, B. S., and Lomax, H., 1978, "Thin Layer Approximation and Algebraic Model for Separated Turbulent Flows," AIAA Paper No. 78–257.

Transport of Particulates in an Internal Cooling Ribbed Duct

Anant Shah

Danesh K. Tafti

High Performance Computational Fluids, Thermal Sciences and Engineering Lab, Mechanical Engineering Department, Virginia Polytechnic Institute and State University, Blacksburg, VA 24061

A ribbed square duct ($P/e=10$, $e/D_h=0.10$) subjected to sand ingestion is studied using large-eddy simulations (LES). Particle sizes of 10 μm, 50 μm, *and* 100 μm *with nondimensional response times (normalized by friction velocity and hydraulic diameter) of 0.06875, 1.71875, and 6.875, respectively are considered. The calculations are performed for a nominal bulk Reynolds number of 20,000 under fully-developed conditions. Distributions of impingement density, impingement velocities and angles, together with fractional energy transfer are presented for each surface. It is found that about 40% of the total number of* 10 micron *particles are concentrated in the vicinity (within 0.05 D_h) of the duct surfaces, compared to 25–30% of the 50 and* 100 micron *particles. The* 10 micron *particles are more sensitive to the primary and secondary flow velocities than the larger particles. While the* 10 micron *particles exhibit high energy transfer to the surface near the rib side-wall junction and immediately upstream of the rib, the larger particles exhibit more uniform distributions. The largest fraction of incoming particulate energy is transferred to the front face of the rib and is between one to two orders of magnitude larger than the other surfaces. As particle size increases, substantial particle energy is also transferred to the back face of the rib by particles bouncing off the front face and carrying enough momentum to impinge on the back face of the preceding rib.* [DOI: 10.1115/1.2720509]

1 Introduction

Gas turbines for military applications, when operating in harsh environments like deserts often encounter unexpected operation faults that lead to reduced time on wing per engine, which simultaneously decreases the mission readiness and increases the maintenance costs for the Air Force [1]. Some of the major factors responsible for the performance deterioration of these turbines are ingestion of debris during take off and landing, distorted intake flows, and hot gas ingestion [2]. The focus of this paper is on ingestion of debris, specifically sand. The primary issues of concern are deposition and erosion (DE) by sand particles. The components most likely to experience erosion and deposition are the compressor and turbine sections that are exposed to high temperatures and high stream velocities. In addition, regions where air flows through curved passages and where secondary flows dominate are prone to DE. One such region of interest is the internal cooling duct of the gas turbine blade. The coolant air flowing in these ducts is bled from individual compressor stages and is used to provide cooling to the turbine blade. Previous studies [1–6] have shown sand laden air has been responsible for eroding the compressor blades to a limit where the gas turbine cannot deliver adequate output due to stall of the compressor system. Experiments by Schneider et al. [7] have shown that even with a filter upstream of the turbine these particles reach the internal air cooling system of the turbine and are responsible for blocking the film cooling holes thus reducing the film cooling effectiveness. Prior to reaching the film cooling holes, this mixture flows through serpentine internal cooling passages to provide convective cooling to the blade, and is then directed to the film cooling holes for surface cooling.

During this passage these particles may:

- Melt or break into smaller particles and get deposited on the internal cooling duct walls thereby increasing the blade temperature by inhibiting heat transfer from the blade surface to the coolant air.
- Remove material by impinging on the surfaces which simultaneously reduces the blade life due to local overheating [8].

This paper focuses on the latter, i.e., impingement of sand particles. In order to calculate the material removed from a surface, empirical correlations relating the material properties of the surface with the impact velocity and angles are needed. The primary purpose of our study is to map the impact velocity and angles for the given particle sizes, which when combined with empirical correlations can give a measure of the amount of material removed from the surface during a given operation time of the gas turbine. No heat transfer is considered in this investigation, which precludes the study of deposition. However, the observed preferential concentration of particles can give some indication of the regions most prone to deposition.

2 Objective

The objective of the current study is to understand the particle transport in an internal cooling duct. Of particular interest are the following:

1. How do particles of different sizes (10 μm, 50 μm, and 100 μm) impinge on the duct walls and ribs? What is the average impingement velocity and angle of the particles hitting the walls?
2. Which are the areas most prone to erosion and deposition due to prolonged operation of the gas turbine in deserts?

The study uses large eddy simulation (LES) as a theoretical tool for simulating the particle dynamics. LES, by accurately representing the unsteady nature of the flow and resolving the relevant turbulent eddies leaves little uncertainty in modeling the trajectory of the particles. The particles in turn are treated in a Lagrangian frame with a dynamical equation describing the relevant forces acting on them.

Contributed by the International Gas Turbine Institute of ASME for publication in the JOURNAL OF TURBOMACHINERY. Manuscript received August 2, 2006; final manuscript received August 4, 2006. Review conducted by David Wisler. Paper presented at the ASME Turbo Expo 2006: Land, Sea and Air (GT2006), May 8–11, 2006, Barcelona, Spain, paper No. GT2006-91284.

3 Methodology

3.1 Carrier Phase. Large-eddy simulations are performed with the code GenIDLEST. The fluid field equations are discretized with a conservative finite-volume formulation using a second-order central difference scheme on a nonstaggered grid topology. The Cartesian velocities and pressure are calculated and stored at the cell center, whereas contravariant fluxes are stored and calculated at the cell faces. The subgrid stresses are modeled using the Dynamic Smagorinksy Model (DSM) [9]. A projection method is used to integrate the discretized continuity and momentum equations in time. The temporal advancement is performed in two steps, a predictor step, which calculates an intermediate velocity field, and a corrector step, which calculates the updated velocity at the new time step by satisfying discrete continuity. Details about the method can be found in [10], and application to ribbed duct flow in [11].

3.2 Dispersed Phase. The dispersed phase is solved by following the trajectories of individual particles in a Lagrangian frame of reference. A Lagrangian particle tracking module was developed [12] for this purpose which interfaced with the flow solver in a general parallel-unstructured-multiblock framework. The position of a particle is described by the following set of ODE's:

$$\frac{d\mathbf{x}_p}{dt} = \mathbf{u}_p \tag{1}$$

$$m_p \frac{d\mathbf{u}_p}{dt} = \sum \mathbf{F}_p \tag{2}$$

Here,

$$\text{Here,} \quad \sum \mathbf{F}_p = \mathbf{F}_{\text{drag}} + \mathbf{F}_{\text{body}} + \mathbf{F}_{\text{lift}} + \mathbf{F}_{\text{collision}} + \mathbf{F}_{\text{Brownian}} + \mathbf{F}_{\text{thermophoresis}} + \mathbf{F}_{\text{other}} \tag{3}$$

Here, Stokes drag is the force exerted on the particle due to the relative velocity between the fluid and the particle and acts in a direction opposing the relative flow. The body force consists of the gravitational force. Saffman's lift force is caused by the shear of the surrounding fluid which results in a nonuniform pressure distribution around the particle. Force exerted due to inter particle collisions is represented by the fourth term in Eq. (3). Brownian and thermophoresis forces are important in the study of submicron particles, and are a result of random molecular motion and forces induced due to temperature gradients, respectively. Other forces include the Basset force, added mass, buoyancy force, and force due to acceleration of the fluid surrounding the particle. The effect of these forces is usually small and is often neglected in studies involving particle transport.

The particle equation of motion used for the present study is based on the following assumptions:

- The particles are rigid spheres and that they are considered as points located at the center of the sphere. This assumption induces some inaccuracy for particles sizes which are greater than the near-wall grid spacing. But, considering previous studies [13,14] we found that it is the best approximation for calculating particle drag.
- The particle density is substantially larger than the fluid density. Elgobashi and Truesdell [15] showed that for particles with $(\rho_p/\rho_f \gg 1)$, the only significant forces are the Stokes drag and gravitational forces,
- The contribution of lift force to particle motion is small and can be neglected. Wang et al. [16] have shown that neglecting the lift force results in a slight decrease in the deposition rate.
- Due to low volume fraction of the particles, interparticle collisions are negligible.
- Particles do not affect the fluid turbulence. Experiments by Kulick et al. [17], and Kaftori et al. [18] have shown that for low volume fractions the turbulence modifications are negligible. Also, in the near-wall region where the particle concentration may be locally large, the turbulence intensities are modified by a very small amount and can be neglected [19].
- For the particle sizes considered in the present study, subgrid-scales have a negligible effect on particle trajectories. Wang and Squires [20] investigated the effect of subgrid scale fluctuations on the trajectory of particles in a vertical turbulent channel flow for bulk Reynolds number up to 79,400. They found that the difference in results obtained with and without the added fluctuating velocities was negligible and that they compared well with the DNS results of McLaughlin [21]. Yeh and Lei [22] performed LES calculations using the Smagorinsky subgrid-scale model to study particle motion in homogeneous isotropic turbulence. They found that the particle motion is governed by the large scales and obtained good agreement with experimental data. Armenio et al. [23] in their study on the effect of the subgrid scales on the particle motion concluded that particles with finite inertia are less sensitive to the subgird scale fluctuations and that for small filter sizes the difference in statistics obtained with a filtered field and with a DNS field are very small. Considering previous studies, the effect of subgrid scale fluctuations on the particle motion is neglected. The filter size chosen for the current study resolves the turbulent scales well below the inertial range as shown in Tafti [11].
- Lastly, in order to avoid additional complexity, the effect of material roughness is not considered while bouncing the particles from the wall. Sommerfeld [24] has shown that in a wall bounded channel flow the effect of surface roughness was pronounced for large particles because they tend to maintain their motion after colliding with one wall and hence may end up colliding with the opposite wall of the channel. Small particles act as tracer particles by closely following the fluid which makes them less affected by surface roughness.

Invoking the above assumptions, the particle equation of motion reduces to

$$\frac{du_i^p}{dt} = -\frac{\rho_f}{\rho_p}\frac{3}{4}\frac{C_D}{d_p}|\mathbf{u}-\mathbf{v}|(u_i^p - v_i^f) \tag{4}$$

The value for the drag coefficient $C_D = (24/\mathrm{Re}_p)(1+0.15\,\mathrm{Re}_p^{0.687})$ was used from Clift et al. [25]. The particle Reynolds number is given by $|\mathbf{u}-\mathbf{v}|d_p/\nu$. Nondimensionalizing Eq. (4) by u_τ and D_h and using "+" for nondimensional variables the particle equation of motion becomes

$$\frac{du_i^{p+}}{dt^+} = -\frac{1}{\tau_p^+}(1+0.15\,\mathrm{Re}_p^{0.687})(u_i^{p+} - v_i^{f+}) \tag{5}$$

where, τ_p is the particle response time given by

$$\tau_p = \frac{d_p^2 S}{18\nu} \quad S = \frac{\rho_p}{\rho_f} \quad u_i^{p+} = \frac{u_i^p}{u_\tau} \quad v_i^{f+} = \frac{v_i^f}{u_\tau} \quad \tau_p^+ = \frac{\tau_p}{D_h/u_\tau} = \frac{\tau_p}{\tau_f} = \mathrm{St}_p$$

The ratio τ_p/τ_f is the Stokes number for a given particle and it gives an estimate as to how quickly a particle responds to the flow structure [26]. For Stokes numbers much less than unity, the particle responds almost instantaneously to the carrier phase and hence at a given instant in time, the particle and fluid velocities are nearly identical. The converse is true for Stokes number much greater than unity. In this case, the particle carries its own inertia and takes a long time to adjust to external conditions. Between these two extremes are particles that respond to some of the structures. Hence for the same flow, particles with different Stokes

Table 1 Channel and carrier phase properties used in the calculation

u_τ	0.294 m/s
δ	0.009 m
ν	1.47×10^{-5} m^2/s

number exhibit different dynamics [27].

The following steps are taken to advance the particle location [12]:

- Locate the particle in computational space by using a stencil walk search algorithm.
- Find the fluid velocity at the particle location at time step $n\Delta t$ using a second-order Lagrange polynomial.
- Use Eq. (5) to calculate particle velocity at $(n+1)\Delta t$ using a third-order accurate Adams-Bashforth scheme.
- Use Eq. (1) to calculate the particle location at $(n+1)\Delta t$ using a third-order accurate Adams-Bashforth scheme.

4 Turbulent Channel Flow at $Re_\tau=180$

To validate the code, turbulent channel flow simulations at $Re_\tau=180$, based on friction velocity (u_τ) and channel half-width (δ) were carried out on a grid consisting of $64\times64\times64$ cells in the streamwise, wall-normal, and spanwise directions, respectively. It was assumed that particle concentration was low enough so as to allow the use of one way coupling, i.e., the carrier phase was not affected by the presence of the particles. The accuracy of the model was assessed by comparing the computed particle statistics with available data [14] for 70 μm copper, 50 μm glass, and 28 μm Lycopodium particles with Stokes numbers 4.5, 0.65, and 0.048, respectively. Tables 1 and 2 describe the properties used for the calculation at $Re_\tau=180$ [28].

4.1 Simulation Overview

- First, the turbulent flow field was integrated to reach a statistically stationary state.
- 250,000 particles were then randomly distributed throughout the channel with an initial velocity same as the local fluid velocity.
- Particle motion was governed by Eq. (4) with gravity ($g^+ = g\delta/u_\tau^2$) acting in the streamwise direction. Particles were time advanced until they became independent of the initial conditions.
- Elastic collisions were assumed for the particles hitting the wall. A particle was assumed to hit the wall when its center was one radius away from the wall. Periodic conditions were applied on the particles leaving from the streamwise and spanwise directions. These particles were reintroduced in the domain at the corresponding location with the same exit velocity.
- Particle statistics were accumulated by following the trajectories of 250,000 particles. Wang and Squires [14] showed that this sample size gives a smooth representation of the particle statistics.

4.2 Results. Figure 1 compares the mean streamwise velocity

Table 2 Particle properties for a turbulent channel flow at $Re_\tau=180$ (Wang and Squires [14])

	Lycopodium	Glass	Copper
d_p in μm	28	50	70
ρ_p in kg/m^3	610	2500	8800
$\tau_p u_\tau/\delta$	0.048	0.650	4.500
T_d in s	$0.5\delta/u_\tau$	$2.5\delta/u_\tau$	$6.0\delta/u_\tau$

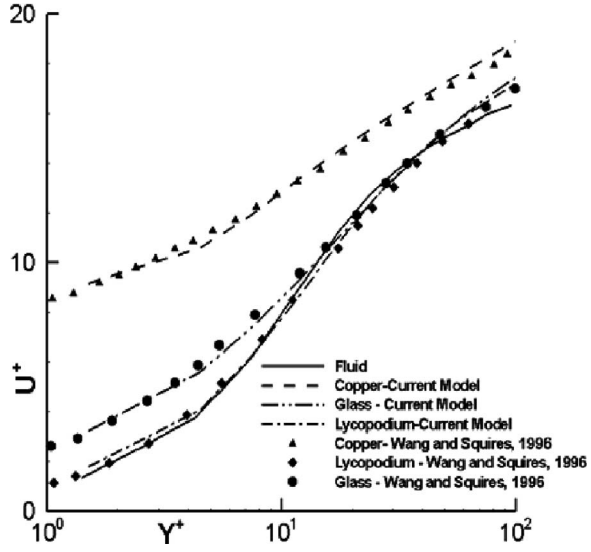

Fig. 1 Comparison of mean streamwise velocity predicted by the current model with particle statistics by Wang and Squires [14]. Particles compared: 70 μm copper, 50 μm glass, and 28 μm Lycopodium.

in wall coordinates of the particles predicted by the model with the LES results of Wang and Squires [14]. The lighter Lycopodium particles follow the carrier phase and hence their velocity distribution is nearly identical to the fluid velocity distribution. On the other hand the heavier copper particles have a much higher velocity than the fluid throughout the channel because the copper particles transported from the outer regions of the channel carry high velocity and retain a significant fraction of their streamwise momentum after colliding with the walls. Glass particles exhibit behavior patterns between the two extremes. In all cases good agreement was found with the calculations of Wang and Squires [14].

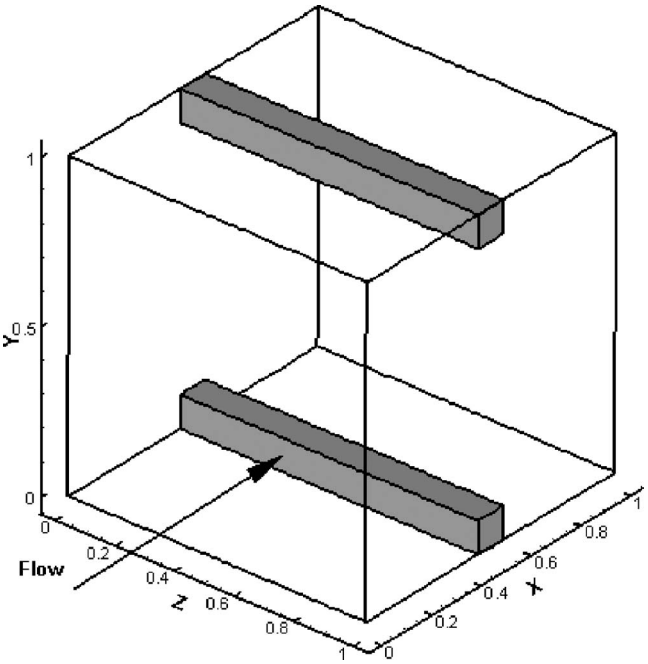

Fig. 2 Computational domain nondimensionalized by the hydraulic diameter (D_h) [11]

Table 3 Flow and geometrical parameters used in the calculation

u_τ	56.05 m/s
u_b	168.15 m/s
D_h	0.01 m
ν	8.49×10^{-5} m^2/s

Table 4 Properties of the carrier phase

Carrier phase-air	
Temperature	800 K
Pressure	2.0265 MPa
Density	8.8 kg/m^3

5 Internal Cooling Ribbed Duct

5.1 Choice of Particle Sizes. Van der Walt and Nurick [29] conducted experiments on a dust filtered helicopter turbine engine and concluded that only particles with diameter less than 100 μm are ingested into the engine while the others were filtered out. In addition, they observed that all particles below 100 μm can be considered sparse and that interparticle collisions can be neglected. This again reconfirms our previous assumption of one-way coupling. Also, Jensen et al. [30] in their study of deposition in a land based turbine observed that particle sizes between 0 and 80 microns are ingested into the engine. Based on this data, three particle sizes are studied: 10 μm, 50 μm, and 100 μm.

5.2 Computational Details. Large-eddy simulations at $\mathrm{Re}_\tau=6660$, based on friction velocity (u_τ) and hydraulic diameter (D_h) are carried out on a grid consisting of $128\times128\times128$ cells in the streamwise, wall-normal, and spanwise directions, respectively [11]. The computational domain normalized by the hydraulic diameter is shown in Fig. 2. A square rib ($e/D_h=0.1$ and $P/e=10$) is placed on two sides of the duct. Tables 3–5 describe the flow and geometrical parameters and the particle properties used in the calculations. Under these conditions, the three particle sizes have Stokes numbers ranging from 0.07 to 6.9.

5.3 Simulation Overview

- Once a statistical stationary state for the carrier phase is established, 268,800 particles are distributed uniformly in the computational domain. The particles are allowed to evolve for a minimum of seven nondimensional time units which corresponds to between 103 particle time constants for the 10 μm particles, 4.1 time constants for 50 μm particles, and 1 time constant for 100 μm particles.[1] During integration, the number of particles in the calculation domain remain constant. Particles leaving the domain at the periodic boundary are reintroduced into the domain at the exit velocity at the equivalent location.
- A particle is said to impinge at a given location when its center is one radius away from the wall. Elastic collisions are assumed, although in reality some particle energy will be imparted to the wall.
- When a particle impinged at a given location its impingement velocity, which is the magnitude of its velocity vector and the angle it made with the surface were calculated. Particle statistics were accumulated for an additional seven nondimensional time units. At the end of the simulation, an average impact velocity and angle is calculated at all impingement locations on the surfaces.

5.4 Results and Discussion. Before describing the results, it is important to clarify that the number of particles impinging on the walls of the duct are reported for a finite time, which in this case is seven nondimensional time units or 1.3 ms. To put this time in perspective, a typical gas turbine service cycle is 10,000–25,000 h. Although the whole domain (Fig. 2) was considered for the calculation, owing to the symmetry along the Y and Z directions, the average particle statistics are only presented for a quadrant. This quadruples the statistical sample size. All calculations utilize 32 processors (dual 2.3 GHz Xserve G5) and each nondimensional time unit with the dispersed phase consumes about 12–16 h of wall clock time. All results are nondimensionalized by the hydraulic diameter of the duct, D_h, and the bulk flow velocity u_b.

5.4.1 Mean Flow Features. Figure 3(a) shows the mean streamline pattern at the center of the duct ($z=0.5$). The mean flow is characterized by a leading edge eddy at the rib-wall junction, a counter-rotating eddy in the rib wake, the main recirculation region and the recirculation region on top of the rib. In the vicinity of the smooth walls ($z=0.0$) the flow field becomes strongly three-dimensional with mean cross flow velocities (w_b) approaching 30% of the mean streamwise velocity (u_b). Figure 3(b) shows contours of w_b in a plane $z=0.05$ in the vicinity of the smooth wall. Strong localized cross flow components are found to occur. Of particular interest is the high lateral velocity moving towards and impinging on the smooth wall within the confines of the shear layer at the leading edge of the rib. All the mean features of the flow are in fact time averages of highly unsteady events, which are dominated by unsteady coherent vortices. For example, the eddy at the front of the rib is the manifestation of unsteady spanwise vortices which continuosly form and dissipate in this region. The high lateral velocities at the junction between the rib and the smooth wall is also a manifestation of highly unsteady vortices which form in this region. These unsteady structures have a large impact on the 10 micron particle distributions as will be shown later.

5.4.2 Instantaneous Particle Distributions. Figure 4 shows the time evolution of the instantaneous distribution of sand particles within $0.05D_h$ of duct surfaces, respectively, for 10, 50, and 100 micron sizes. The following observations are made:

- In all cases, a development time of seven nondimensional time units is sufficient for the particles to reach a near asymptotic distribution.
- Up to 40% of the 10 micron particles are near the surfaces of the duct compared to only 25–30% of the larger particles.
- The smaller 10 micron particles which closely follow the flow are found to accumulate at the center of the side-walls (not shown). In comparison, the 50 and 100 micron particles are more homogeneously distributed in the duct. This can be attributed to the fact that particles with Stokes number closer to Kolmogorov scales exhibit stronger effects of preferential concentration [31]. In addition, previous studies [32,33] in wall-bounded flows show that particles tend to accumulate in regions of low streamwise velocity.

Table 5 Particle properties used in the calculation

Dispersed phase-sand			
d_p in μm	10	50	100
ρ_p in kg/m^3	1650	1650	1650
$\tau_p u_\tau/D_h$	0.06875	1.71875	6.8750
$\tau_p u_b/D_h$	0.20625	5.15625	20.6250

[1]Earlier studies were done with a development time of 23.5 nondimensional time units. No difference was found in the measured particle statistics with the shorter development time.

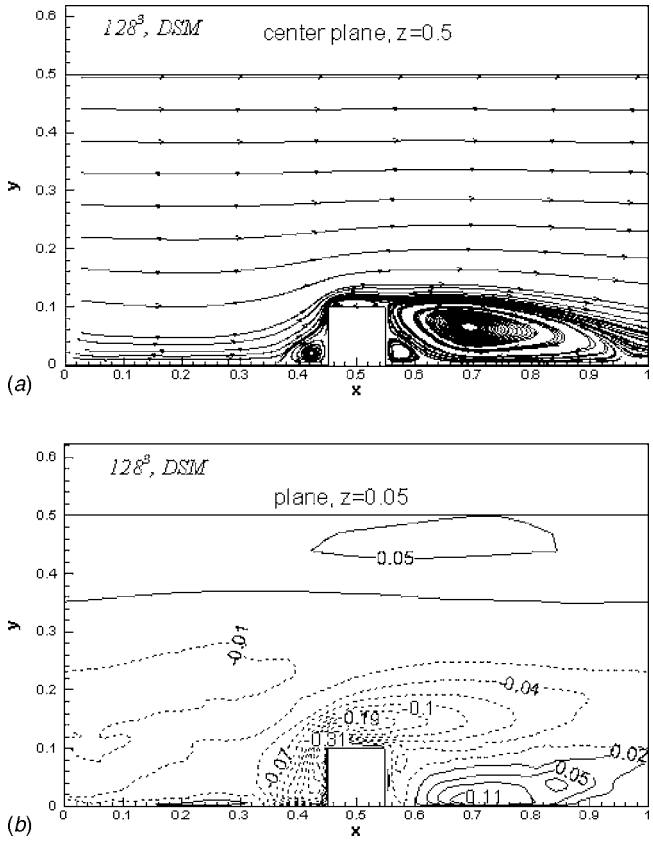

Fig. 3 (*a*) Mean streamline distribution in the *z*-symmetry plane. Reattachment occurs at 4.1*e* downstream of rib. The leading edge eddy extends between 0.8 and 0.9*e* upstream of rib. (*b*) Mean lateral or spanwise flow velocity (w_b) in the vicinity of the smooth wall. Taken from [11].

- Another clear trend with particle size is the distribution in the vicinity of the ribbed wall. The number of 10 μm particles near the ribbed wall is much less than that present for the larger particle sizes. This can be attributed to the presence of the separated shear layer on the rib and the resulting large separation zone behind the rib (Fig. 3(*a*)). Very few of the 10 micron particles infiltrate into the separation zone because they are prone to follow the fluid streamlines. On the other hand, the larger particles because of their inertia, infiltrate into the separation zone and exhibit a larger concentration near the ribbed wall.

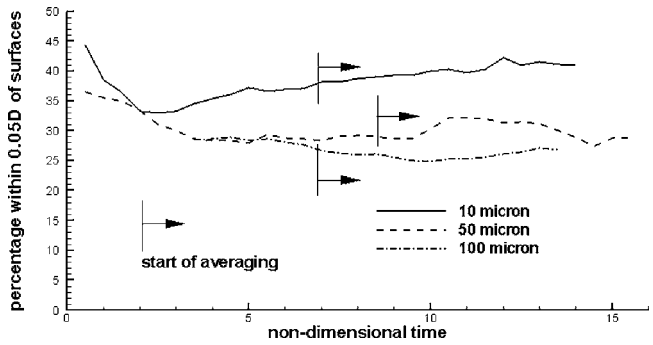

Fig. 4 Time evolution of particle distribution near duct surfaces

5.4.3 Characteristics of Time-Averaged Particle Impingement. Three quantities are presented for each surface:

- The total number of particles impinging in 1.3 ms milliseconds out of a total population of $N_{\text{tot}}=268{,}800$ particles.
- The average magnitude of impingement velocity.
- The average impingement angle with respect to the surface.

The three quantities are combined to define the fraction of energy of incoming particulates which can be potentially transferred to the surface of the duct. In order to estimate this quantity, an equivalent particle mass flow rate is calculated and is given by

$$\dot{m}_p = (N_{\text{tot}} \cdot m_p)/(P/u_b) \tag{6}$$

which assumes that the mean particle velocity is the same as the bulk flow velocity. Hence the total flow of particulate energy per unit time is given by

$$\dot{E}_{p_{\text{tot}}} = 1/2\dot{m}_p u_b^2 \tag{7}$$

In a given time period, a measure of the rate of energy which can be potentially transferred to the surface due to particle impingement is given by

$$\dot{E}_{p_{\text{impinge}}} = 1/2 \cdot (N_{\text{impinge}} \cdot m_p/\Delta t) \cdot (u_{p_{\text{impinge}}} \sin\theta)^2 \tag{8}$$

where N_{impinge} is the number of particles that impinge at a given location, $u_{p_{\text{impinge}}}$ and θ is the impingement velocity magnitude and angle, respectively. Equation (8) assumes that the kinetic energy of the normal velocity component is completely transferred to the surface. It is evaluated by summing the quantity $(u_{p_{\text{impinge}}} \sin\theta)^2$ over all particle impingements (N_{impinge}) during the averaging period of seven nondimensional time units.

The fraction of incoming particle energy transferred to the surface is then given by

$$\psi = \dot{E}_{p_{\text{impinge}}}/\dot{E}_{p_{\text{tot}}} \tag{9}$$

Hence if the mass loading of particulates is known with the mean flow velocity, Eq. (9) can be used to estimate the potential energy transfer to surfaces. The fractional energy transfer to the surface can be used to qualitatively estimate the potential areas of deposition and erosion at the duct surfaces by assuming that to first-order, both erosion and deposition are dependent on the energy transferred by the normal velocity component to the surface.[2]

It is noted that ψ is a fraction of incoming energy and although ψ may be smaller for 50 and 100 microns, the total incoming energy is larger for the larger particles. For example, a 100 micron particle has 100 times more energy than a 10 micron particle traveling at the same velocity.

5.4.4 Smooth Side Wall. Flow near the smooth wall is characterized by a streamwise velocity and a spanwise cross-flow which varies in sign and magnitude as shown in Fig. 3(*b*) in the vicinity of the rib-wall junction. Figures 5(*a*)–5(*c*) shows the number of particles colliding with the smooth wall in seven dimensionless time units or 1.3 ms for half the duct. A careful investigation of the plots reveal that in the region above the rib within the confines of the shear layer where the flow accelerates, the number of particles colliding with the smooth wall decreases with an increase in the particle Stokes number. Also, in the region behind the rib in its wake, where secondary fluid motion is away from the wall (Fig. 3(*b*)), the number of particles impinging on the smooth wall increases with an increase in the particle response time. The smaller 10 micron particles which closely follow the fluid motion respond to the outward velocity and hence cause little impingement as compared to the inertial 50 and 100 micron particles. These particles which have more inertia and respond slowly to the flow

[2]This is a reasonably good approximation for erosion of ductile materials.

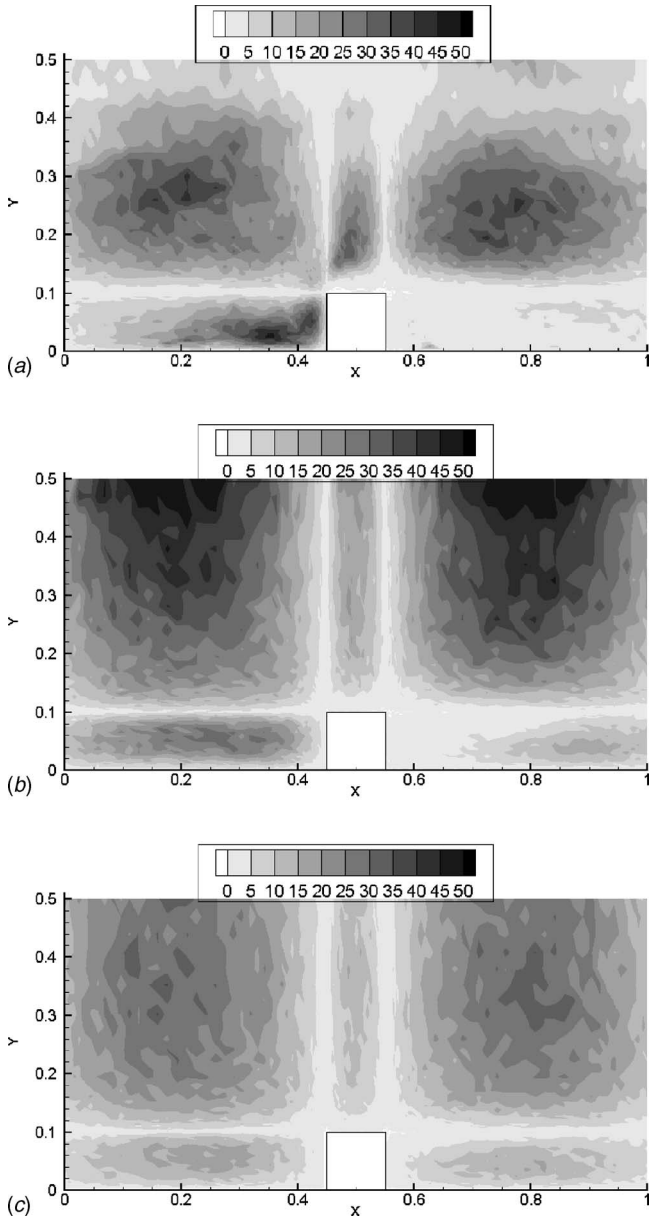

Fig. 5 Number of particles impinging on the side wall in 1.3 ms: (*a*) 10 μm; (*b*) 50 μm; (*c*) 100 μm

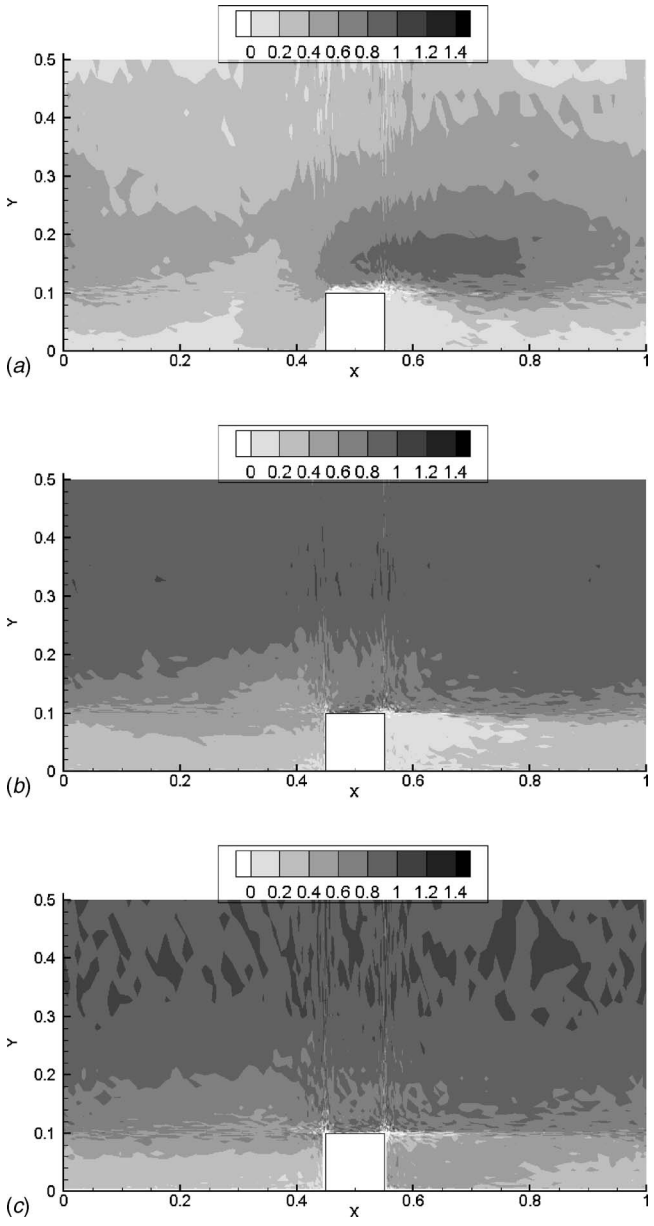

Fig. 6 Impact velocity on the side wall: (*a*) 10 μm; (*b*) 50 μm; (*c*) 100 μm

continue on their trajectories and impinge on the smooth wall. Overall, the impingement density is highest for the 50 micron particles at the center of the duct.

Figures 6(*a*)–6(*c*) show the impingement velocity, respectively, for 10, 50, and 100 micron particles. The following observations are made:

- Near the center of the duct, the 10 micron particles impinge at smaller velocities as compared to a uniform impingement velocity of the 50 and 100 micron particles. The higher impact velocities of the 50 and 100 micron particles indicate that they carry more momentum than the smaller particles.
- In the shear layer above the rib, the velocity distribution of the 10 micron particles correlates with the secondary flow in Fig. 3(*b*), whereas the larger particles have no preferential impingement velocities in this region. In the rib wake, consistent with the observation in Figs. 5(*a*)–5(*c*), impingement velocities increase steadily as the particle size increases because the smaller particles are forced away from the wall by the secondary flow velocities.

The average angles at which these particles impact the smooth wall are shown in Figs. 7(*a*)–7(*c*). It can be observed that in the high impingement regions at the center of the duct, particles have a very shallow angle (<5 deg) indicating that streamwise motion of the fluid dominates the particle trajectories and that they move nearly parallel to the smooth wall. In comparison, particles impinge at an angle between 40 deg and 50 deg on the smooth-wall in front and behind the rib ($0<y/D_h<0.1$) for the 10 and 50 micron particles. This observation coupled with the high impingement density in front of the rib indicates that particles get trapped in the instantaneous vortices which form in this region and impinge on the smooth wall. Figure 8 plots the fraction $\psi \times 10^6$ which consolidates the data in Figs. 5–7 and gives a qualitative measure of the potential for erosion and deposition at the side wall of the duct. For the 10 micron particles, ψ has the largest values in the region of secondary flow impingement in the vicinity

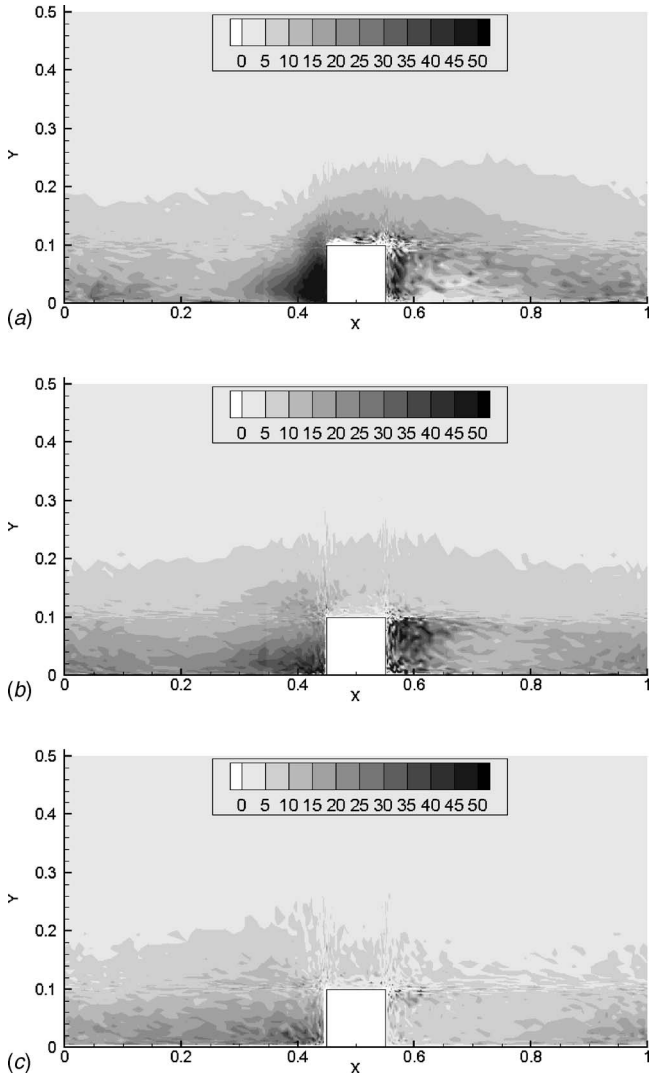

Fig. 7 Impact angle on the side wall: (*a*) 10 μm; (*b*) 50 μm; (*c*) 100 μm

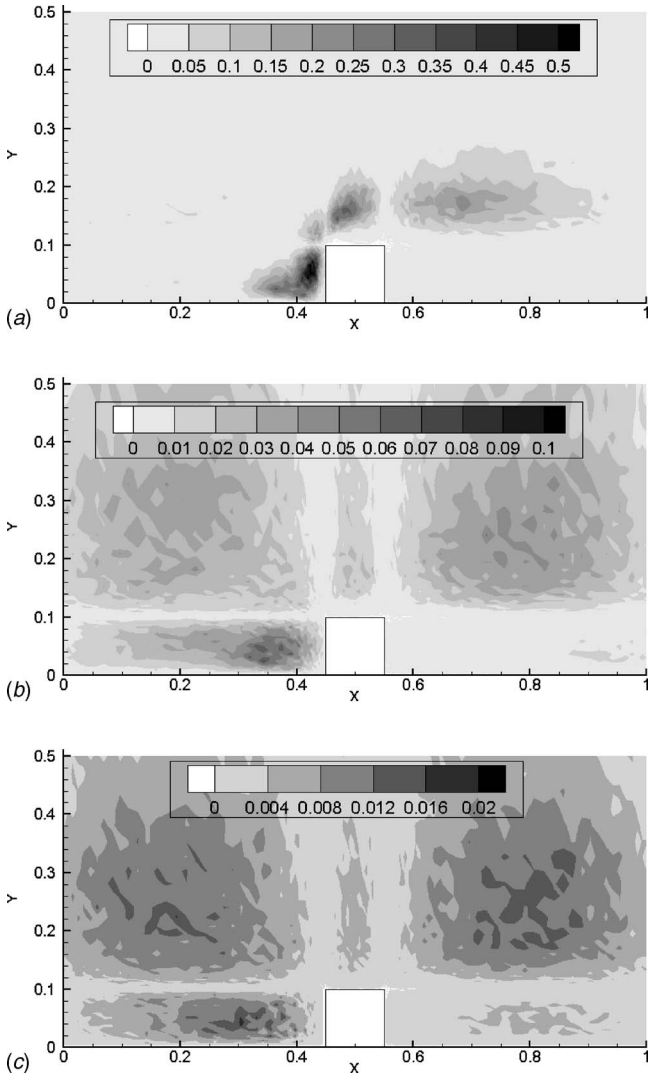

Fig. 8 Fractional energy transfer to side wall ($\psi\times10^6$): (*a*) 10 μm; (*b*) 50 μm; (*c*) 100 μm

of the rib. As the particles get bigger, ψ has a much broader coverage but with lower values. Interestingly, the 100 micron particles transfer the lowest fraction of incoming energy to the surface.

5.4.5 Ribbed Wall. Figures 9(*a*)–9(*c*) shows the number of particles colliding with the ribbed wall for half the duct from the side wall to the centerline. It can be found that the 50 and 100 micron particles exhibit a more uniform impingement pattern as compared to a more selective impingement by the 10 micron particles. The 10 micron particles exhibit the highest impingement near the upstream base of the rib, indicating that the smaller particles are entrained into the instantaneous vortical structures which form in this region. It is observed that the 50 micron particles show a larger impingement density than the 100 micron particles. While the 10 micron particles do not impinge in the recirculating region behind the rib (Fig. 3(*a*)), both the 50 and 100 micron particles infiltrate into the recirculation region. Figures 10(*a*)–10(*c*) show the average impingement velocity of the particles on the ribbed wall. The 10 and 50 micron particles impinge at low velocities in the recirculating region, but with higher velocities after the flow reattaches to the surface. In comparison, the 100 micron particles impinge at fairly uniform and somewhat higher velocities across the full rib pitch. Figures 11(*a*)–11(*c*) show the angles at which these particles impinge on the wall. In all cases, impingement angles vary anywhere from 5 to 40 deg, with generally low impingement angles immediately behind the rib. Both 10 and 50 micron particles exhibit similar patterns of impingement angles, with one notable exception. The 10 micron particles impinge at large angles immediately upstream of the rib and supports the observation that particles get entrained in the unsteady junction vortices (Fig. 3(*a*)). The 100 micron particles impinge at much shallower angles to the surface.

The fraction of incoming energy transferred to the ribbed wall is of the same order of magnitude as the side wall. Figures 12(*a*)–12(*c*) plot $\psi\times10^6$ for the three particle sizes. There is a gradual decrease in the magnitude of ψ as the particle size increases. Once again, the 10 micron particles show localized high fractions immediately upstream of the rib, which is dominated by energetic eddies in which the particles are entrained. Conversely, the 50 and 100 micron particles exhibit a broader and more uniform albeit lower fractional energy transfer to the ribbed wall.

5.4.6 Ribs. Figures 13(*a*)–13(*c*) show the number of particles impinging on the front surface of half the rib. From all the other surfaces, the front of the rib has by far the largest amount of impingement. The impingement density is highest for 50 micron particles. While the impingement density increases towards the center of the duct, the impingement velocity (Fig. 14) and im-

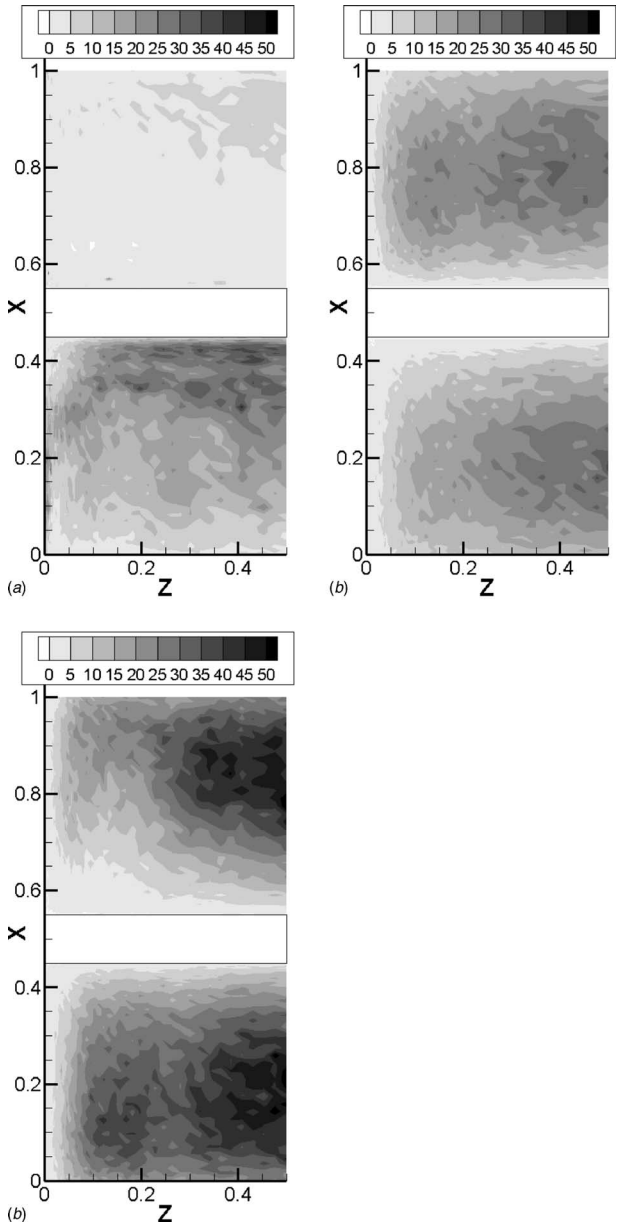

Fig. 9 Number of particles impinging on the ribbed wall in 1.3 ms: (*a*) 10 μm; (*b*) 50 μm; (c) 100 μm

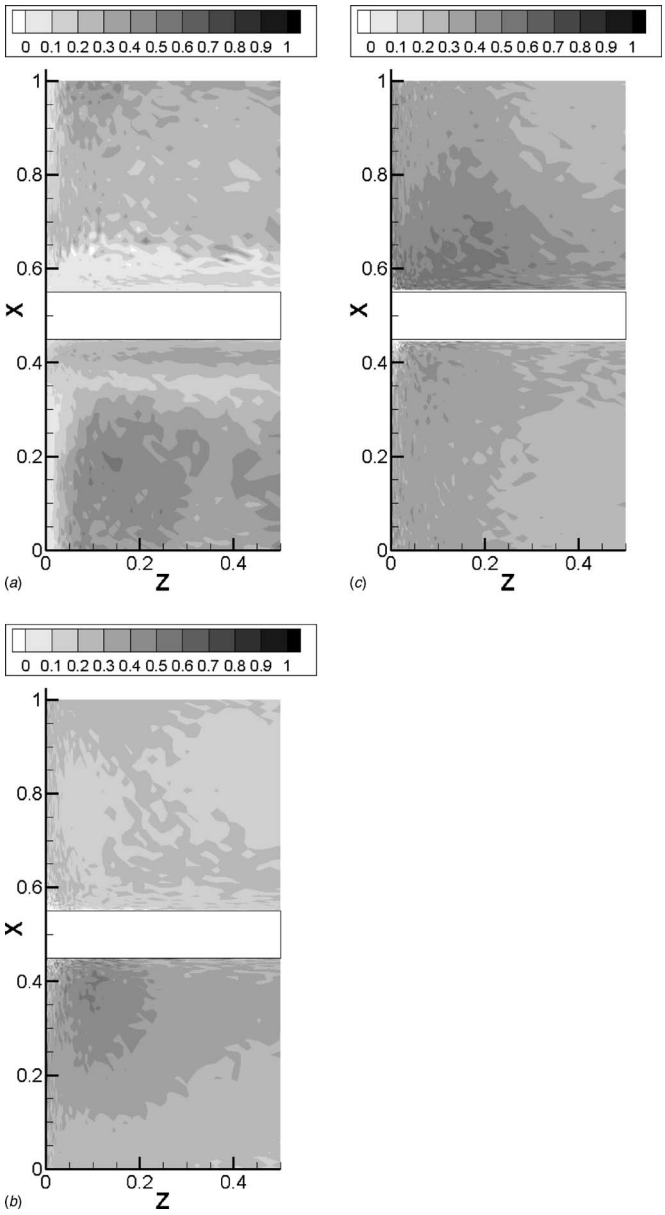

Fig. 10 Average impingement velocities at the ribbed wall: (*a*) 10 μm; (*b*) 50 μm; (*c*) 100 μm

pingement angle (Fig. 15) are highest closes to the side wall at the top edge of the rib. The impingement angle steadily increases with particle size ranging from 30 to 60 deg for 10 micron particles to 70–90 for the 100 micron particles, indicating a more direct head-on impact as the particle size increases. The increasing trend is also reflected in the impingement velocities between the 10 micron and the larger particles, where unlike the angles, the velocities do not change substantially between the 50 and 100 micron particles. Overall, the front of the rib is most susceptible to erosion and deposition as indicated by the distribution of $\psi \times 10^6$ shown in Figs. 16(*a*)–16(*c*). The magnitude of ψ is approximately one to two orders of magnitude larger than that on the ribbed and side wall. It is observed once again that the 50 micron particles show a larger region of higher fractional energy transfer to the rib surface than the 100 micron particles.

While the fractional energy transfer to the top of the rib is negligible compared to the other surfaces, surprisingly, the back of the rib is not exempt from particle impact. Particle impingement on the back of the rib is shown in Figs. 17(*a*)–17(*c*). It is observed that whereas the particle impingement density is small for the 10 micron particles, it steadily increases to higher values with broader coverage as the particle size increases to 50 and 100 micron. By following individual particle trajectories, it was established that the larger particles bouncing off the front face of the rib had enough momentum to move against the flow and impinge on the back of the preceding rib. This is reflected in the impingement velocities (Fig. 18), and impingement angles (Fig. 19) which also increase as the particle size increases, consistent with the observation that larger particles carry more momentum. Figures 20(*a*)–20(*c*) show the fraction of energy that is transferred to the back surface of the rib. The fraction increases as the particle size increases and exhibits values of the same order as the front of the rib for the 100 micron particles. For both the 50 and 100 micron particles, the calculated energy transfer is higher than that on the side and ribbed wall.

6 Summary and Conclusions

LES calculations are performed for a bulk Reynolds number of 20,000 to study particle transport in an internal cooling duct with

Fig. 11 Average impingement angles at the bottom wall: (*a*) 10 μm; (*b*) 50 μm; (*c*) 100 μm

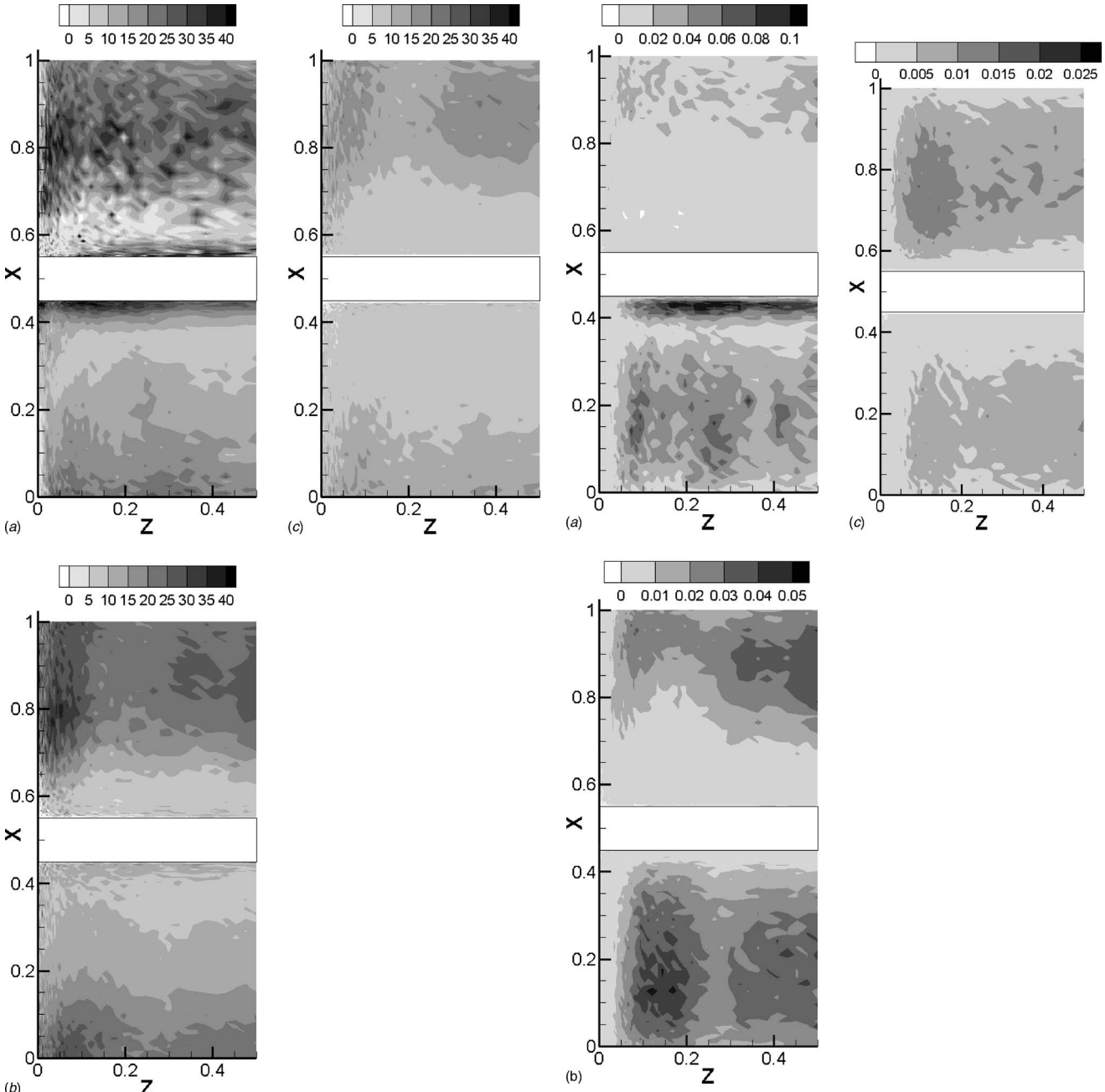

Fig. 12 Fractional energy transfer to the ribbed wall ($\psi \times 10^6$): (*a*) 10 μm; (*b*) 50 μm; (*c*) 100 μm

normal ribs. Particle sizes of 10, 50, and 100 micron with nondimensional response times, respectively, 0.06875, 1.71875, and 6.875 are considered, which are fairly typical of sand and dust ingestion. The particle motion was governed by drag forces. Due to low volume fraction of the particles, one way coupling was assumed. Particles were time advanced for seven dimensionless time units to become independent of their initial locations. Particle statistics were gathered for seven dimensionless time units or 1.3 ms.

Statistics comprised of the number of particles impinging at a given location, and their average impact velocity and angle, and fraction of particle energy which can potentially be transferred to the duct surfaces are presented for each surface. It is found that after an initial development time about 40% of the total number of 10 micron particles are concentrated in the vicinity (within 0.05 D_h) of the duct surfaces compared to 25–30% of the 50 and 100 micron particles. The 10 micron particles are more prone to follow the primary and secondary velocity field. At the side walls, the 10 micron particles exhibit a high potential of energy transfer in the region of secondary flow impingement. The larger particles are more prone to energy transfer in the area between the ribs and towards the center of the duct. At the ribbed walls, the 10 micron particles exhibit high energy transfers just upstream of the rib in the region where junction eddies exist, and downstream of reattachment. The 50 and 100 micron particles, on the other hand tend to a more uniform energy transfer. The front face of the rib is by far the most susceptible to energy transfer by impingement for all particle sizes, followed by the back face of rib. The primary energy transfer mechanism to the back face is from particles bouncing off the front face and carrying enough momentum to impinge on the back face of the preceding rib.

The results presented in this work can be readily extended to other materials and particle sizes if the nondimensional Stokes number falls within the range studied. The current model can be used to estimate duct surfaces which are potentially vulnerable to erosion and deposition. However, for more detailed modeling of these phenomena, additional particle surface interaction models specific to the material properties need to be incorporated.

Acknowledgment

The authors acknowledge the use of the Terascale Computing Facility System-X at Virginia Tech for these calculations.

Nomenclature

C_D = drag coefficient
D_h = hydraulic diameter of the duct
e = rib height
$\mathbf{F}_p$ = force acting on the particle
m_p = mass of the particle
P = rib pitch
Re_p = particle Reynolds number
St_p = particle Stokes number
T_d = development time; time taken by the particles to be independent of their initial location
u_b = mean bulk velocity
u_i^p = particle velocity in the i direction
$\mathbf{u}_p$ = particle velocity at time t
u_τ = friction velocity
v_i^f = fluid velocity in the i direction
$\mathbf{x}_p$ = particle position at time t
δ = channel half-width
τ_f = time scale of the flow
ψ = fraction of incoming particle energy transferred to the surface

References

[1] Scala, S. M., Konrad, M., and Mason, R. B., 2003, "Predicting the Performance of a Gas Turbine Undergoing Compressor Blade Erosion," 39th AIAA/ASME/SAE/ASEE Joint Propulsion Conference and Exhibit, Huntsville, AL, July 20–23, Paper No. AIAA 2003-5259.
[2] Hathaway, M. D., Chen, J., and Webster, R., 2003, "Time Accurate Unsteady Simulation of the Stall Inception Process in the Compression System of a US Army Helicopter Gas Turbine Engine," DoD HPCMP User's Group Conference (UGC), Bellevuew, Washington, June 9–13.
[3] Tabakoff, W., and Hamed, A., 1984, "Installed Engine Performance in Dust-Laden Atmosphere," AIAA/AHS/ASEE Aircraft Design Systems and Operations Meeting, San Diego, CA, October 31–November 2, Paper No. AIAA-84-2488.
[4] Tabakoff, W., Lakshminarasimha, A. N., and Pasin, M., 1989, "Simulation of Compressor Performance Deterioration Due to Erosion," 34th International Gas Turbine and Aeroengine Congress and Exhibition, Toronto, Canada, June 4–8.
[5] Tabakoff, W., 1986, "Compressor Erosion and Performance Deterioration," AIAA/ASME 4th Joint Fluid Mechanics, Plasma Dynamics and Laser Conference, Atlanta, GA, May 12–14.
[6] Balan, C., and Tabakoff, W., 1983, "A Method of Predicting the Performance Deterioration of a Compressor Cascade Due to Sand Erosion," AIAA 21st Aerospace Sciences Meeting, Reno, Nevada, January 10–13, Paper No. AIAA-83-0178.
[7] Schneider, O., Dohmen, H. J., Benra, F.-K., and Brillert, D., 2003, "Investigations of Dust Separation in the Internal Cooling Air System of Gas Turbines," ASME Paper No. GT2003-38293.
[8] Han, J. C., Dutta, S., and Ekkad, V., 2000, *Gas Turbine Heat Transfer and Cooling Technology*, Taylor and Francis, New York.
[9] Germano, M., Piomelli, U., Moin, P., and Cabot, W. H., 1991, "A Dynamic Subgrid-Scale Eddy Viscosity Model," Phys. Fluids A, **3**, pp. 1760–1765.
[10] Tafti, D. K., 2001, "Genidlest—a Scalable Parallel Computational Tool for Simulating Complex Turbulent Flows," *Proceedings of the ASME Fluids Engineering Division, FED-Vol. 256*, ASME, New York.
[11] Tafti, D. K., 2005, "Evaluating the Role of Subgrid Stress Modeling in a Ribbed Duct for the Internal Cooling of Turbine Blades," Int. J. Heat Fluid Flow, **26**, pp. 92–104.
[12] Shah, A., 2005, "Development and Application of Dispersed Two Phase Capability in a General Multi-Block Navier-Stokes Solver," thesis, Virginia Polytechnic Institute and State University, Blacksburg, VA.
[13] Pan, Y., and Banerjee, S., 1996, "Numerical Simulation of Particle Interactions With Wall Turbulence," Phys. Fluids, **8**(10), pp. 2733–2755.
[14] Wang, Q., and Squires, K. D., 1996, "Large Eddy Simulation of Particle-Laden Turbulent Channel Flow," Phys. Fluids, **8**(5), pp. 1207–1223.
[15] Elgobashi, S., and Truesdell, G. C., 1992, "Direct Simulation of Particle Dispersion in Decaying Isotropic Turbulence," J. Fluid Mech., **242**, p. 655–700.
[16] Wang, Q., Squires, K. D., Chen, M., and McLaughlin, J. B., 1997, "On the Role of the Lift Force in Turbulence Simulations of Particle Deposition," Int. J. Multiphase Flow, **23**(4), pp. 749–763.
[17] Kulick, J. D., Fessler, J. R., and Eaton, J. K., 1994, "Particle Response and Turbulence Modification in Fully Developed Channel Flow," J. Fluid Mech., **277**, pp. 109–134.
[18] Kaftori, D., Hetsroni, G., and Banerjee, S., 1995, "Particle Behavior in the Turbulent Boundary Layer. I. Motion, Deposition, and Entrainment," Phys. Fluids, **7**, pp. 1095–1106.
[19] Marchioli, C., and Soldati, A., 2002, "Mechanisms for Particle Transfer and Segregation in a Turbulent Boundary Layer," J. Fluid Mech., **468**, pp. 283–315.
[20] Wang, Q., and Squires, K. D., 1996, "Large Eddy Simulation of Particle Deposition in a Vertical Turbulent Channel Flow," Int. J. Multiphase Flow, **22**(4), pp. 667–683.
[21] McLaughlin, J. B., 1989, "Aerosol Particle Deposition in Numerically Simulated Channel Flow," Phys. Fluids A, **1**(7), pp. 1211–1244.
[22] Yeh, F., and Lei, U., 1991, "On the Motion of Small Particles in a Homogeneous Isotropic Turbulent Flow," Phys. Fluids A, **3**(11), pp. 2571–2586.
[23] Armenio, V., Piomelli, U., and Fiorotto, V., 1999, "Effect of the Subgrid Scales on Particle Motion," Phys. Fluids, **11**(10), pp. 3030–3042.
[24] Sommerfeld, M., 1992, "Modeling of Particle-Wall Collisions in Confined Gas-Particle Flows," Int. J. Multiphase Flow, **18**(6), pp. 905–926.
[25] Clift, R., Grace, J. R., and Weber, M. E., 1978, *Bubbles, Drops and Particles*, Academic, New York.
[26] Crowe, C. T., Gore, R. A., and Troutt, T. R., 2003, "Particle Dispersion by Coherent Structures in Free Shear Flows," Part. Sci. Technol., **3**, pp. 149–158.
[27] Fessler, J. R., Kulick, J. D., and Eaton, J. K., 1994, "Preferential Concentration of Heavy Particles in a Turbulent Channel Flow," Phys. Fluids, **6**(11), pp. 3742–3749.
[28] Fukagata, K., Zahrai, S., and Bark, F. H., 1997, "Large Eddy Simulation of Particle Motion in a Turbulent Channel Flow," *Proceedings of the ASME Fluids Engineering Division Summer Meeting*, June 22–26, FEDSM97-3591, ASME, New York.
[29] Van der Walt, J. P., and Nurick, A., 1995, "Erosion of Dust-Filtered Helicopter Turbine Engines Part I: Basic Theoretical Considerations," J. Aircr., **32**(1), pp. 106–111.
[30] Jensen, J. W., Squire, S. W., Bons, J. P., and Fletcher, T. H., 2004, "Simulated Land-Based Turbine Deposits Generated in an Accelerated Deposition Facility," ASME Paper No. GT2004-53324.
[31] Wang, L.-P., and Maxey, M. R., 1993, "Settling Velocity and Concentration Distribution of Heavy Particles in Homogeneous Isotropic Turbulence," J. Fluid Mech., **256**, pp. 27–68.
[32] Pedinotti, S., Mariotti, G., and Banerjee, S., 1992, "Direct Numerical Simulation of Particle Behaviour in the Wall Region of Turbulent Flows in Horizontal Channels," Int. J. Multiphase Flow, **18**(6), pp. 927–941.
[33] Rouson, D. W. I., and Eaton, J. K., 1997, "Direct Numerical Simulation of Particles Interacting with a Turbulent Channel Flow," *Proceedings of the 7th Workshop on Two-Phase Flow Predictions*, M. Sommerfeld, ed., Erlangen, Germany.

High-Pressure Pocket Damper Seals: Leakage Rates and Cavity Pressures

Ahmed M. Gamal
Turbomachinery Laboratory, Mechanical Engineering Department, Texas A&M University, College Station, TX 77843
e-mail: ahmedmg@tamu.edu

Bugra H. Ertas
Vibration/Dynamics Laboratory, Physical Sciences Department, General Electric Global Research, Niskayuna, NY 12309
e-mail: ertas@research.ge.com

John M. Vance
Turbomachinery Laboratory, Mechanical Engineering Department, Texas A&M University, College Station, TX 77843
e-mail: jvance@tamu.edu

The turbomachinery component of interest in this paper, the pocket damper seal, has the dual purpose of limiting leakage and providing an additional source of damping at the seal location. The rotordynamic coefficients of these seals (primarily the direct stiffness and damping) are highly dependent on the leakage rates through the seals and the pressures in the seals' cavities. This paper presents both numerical predictions and experimentally obtained results for the leakage and the cavity pressures of pocket damper seals operating at high pressures. The seals were tested with air, at pressures up to 1000 psi (6.92 MPa), as the working fluid. Earlier flow-prediction models were modified and used to obtain theoretical reference values for both mass flow rates and pressures. Leakage and static pressure measurements on straight-through and diverging-clearance configurations of eight-bladed and twelve-bladed seals were used for code validation and for calculation of seal discharge coefficients. Higher than expected leakage rates were measured in the case of the twelve-bladed seal, while the leakage rates for the eight-bladed seals were predicted with reasonable accuracy. Differences in the axial pitch lengths of the cavities and the blade profiles of the seals are used to explain the discrepancy in the case of the twelve-bladed seal. The analysis code used also predicted the static cavity pressures reasonably well. Tests conducted on a six-bladed pocket damper seal to further investigate the effect of blade profile supported the results of the eight-bladed and twelve-bladed seal tests and matched theoretical predictions with satisfactory accuracy. [DOI: 10.1115/1.2720871]

Keywords: pocket damper seal, leakage, cavity pressure, rotordynamics, turbomachinery

1 Introduction

With increasing demand for higher rates of productivity, turbomachines are being designed to run faster, operate more efficiently, and last longer. The result is a need to reach an optimum balance between a turbomachine's leakage characteristics and its rotordynamic performance while dealing with ever-tightening clearances between rotor and stator.

Annular gas seals are essential to the successful operation of a turbomachine in that they limit the leakage across regions of unequal pressure. Labyrinth seals have been invaluable in this respect due to their desirable leakage prevention characteristics and their noncontacting nature, which allows rotor speeds to be increased considerably. These seals do, however, have certain undesirable rotordynamic characteristics, mainly related to instability. In addition, they offer only limited damping of rotor vibrations, leaving the bearing locations as the only feasible location to add significant damping.

The pocket damper seal (PDS), developed in 1991 at Texas A&M University, does not exhibit the labyrinth seal's instability problems, and at the same time allows the application of a considerable amount of damping at the seal location. The PDS (also known as the TAMSEAL®) has since shown in both tests and field applications that it can significantly lower rotor vibration amplitudes. These seals can, for example, be used in place of the labyrinth seals currently employed in compressors.

A schematic of a ten-bladed PDS is shown in Fig. 1. The seal is made up of a series of blades dividing the seal into active and inactive cavities and a series of circumferential partition walls, dividing the active cavities into pockets. The active cavities normally have a longer pitch length and are diverging (the blade-to-journal clearance area at the cavity inlet is smaller than that at the exit) while the inactive plenums are usually converging. More detailed descriptions of the features of a PDS are given by Vance and Shultz [1], Childs and Vance [2], and Gamal [3]. These sources, along with Laos [4], also discuss the rotordynamic behavior of pocket damper seals and present comparisons of the leakage characteristics of these seals with those of other annular gas seals, such as honeycomb and labyrinth seals. The comparisons show that the PDS exhibits comparable and, in some instances (especially for short seal lengths), superior leakage-reduction capacities [4].

Although the rotordynamic characteristics of pocket damper seals can affect the reliability of a turbomachine and are therefore worthy of study, leakage reduction remains an important purpose of the seals. Developing an accurate model for the prediction of the mass flow rate through the seal is therefore an essential first step in its design. Furthermore, the stiffness and damping of a pocket damper seal are highly dependent on the mass flow rate, making it vital that the flow model offers an accurate prediction of the leakage before attempting to predict seal rotordynamic coefficients.

2 Analytical Model

In order to calculate the mass flow rate through a PDS, a static model in which the journal does not vibrate [5,3] is assumed. A simplified two-bladed seal model is shown in Fig. 2. For the static case in which $x(t)=0$, the following steady-state condition for the flow rate across each blade applies,

$$\dot{m}_1 = \dot{m}_2 = \dot{m}_3 = \cdots = \dot{m}_n = \dot{m} \tag{1}$$

Contributed by the International Gas Turbine Institute of ASME for publication in the JOURNAL OF TURBOMACHINERY. Manuscript received August 26, 2006; final manuscript received September 3, 2006. Review conducted by David Wisler. Paper presented at the ASME Turbo Expo 2006: Land, Sea and Air (GT2006), May 8–11, 2006, Barcelona, Spain. Paper No. GT2006-90858.

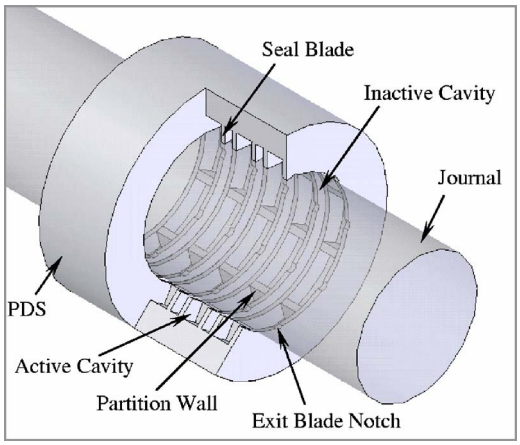

Fig. 1 Ten-bladed pocket damper seal (sectioned view)

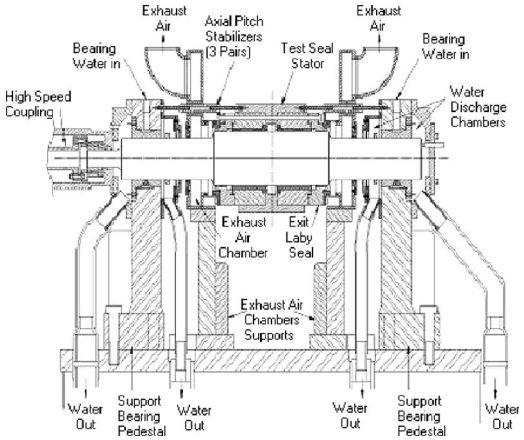

Fig. 3 Annular gas seal test-rig schematic

Assuming that the fluid passing through the seal is a perfect gas and that the process is isentropic, the mass flow-rate for the unchoked flow condition is given by the St. Venant equation, a modified form of which is given by Eq. (2). In the case of choked flow across a blade, the flow-rate becomes independent of the downstream pressure and is given by Eq. (3), in which $\beta=0.5283$ for air.

$$\dot{m}_i = C_d \frac{P_i A_i}{\sqrt{\gamma R T_i}} \sqrt{\frac{2\gamma^2}{\gamma-1}\left[\left(\frac{P_{i+1}}{P_i}\right)^{2/\gamma} - \left(\frac{P_{i+1}}{P_i}\right)^{(\gamma+1)/\gamma}\right]} \quad (2)$$

$$\dot{m}_i = \frac{\beta P_i A_i}{\sqrt{\gamma R T}} \quad (3)$$

The St. Venant equation is intended for use in the case of flow through an orifice of a round cross section, and it is therefore to be expected that the flow rate predicted by this equation would not match the flow rate through the annular sections formed by the seal blades and the journal. Shultz [5] used discharge coefficients to compensate for this disparity between the actual configuration and the configuration for which the St. Venant equation was intended. In the modified expression for the flow-rate (Eq. (2)), the numerical value of the discharge coefficient C_d differs, depending on whether the equation is being written for the inlet blade or the exit blade of an active cavity. This model was used as the basis for a code [3] developed by the authors as a simulation and design tool that evaluates the leakage, pressure, and rotordynamic characteristics of pocket damper seals.

It is should be noted that the terms "static pressure," and "dynamic pressure," as used in this paper, refer to the constant and time-varying cavity pressures, respectively. This terminology is different from the fluid dynamics definitions of static, dynamic, and stagnation pressures, which can be either steady or unsteady.

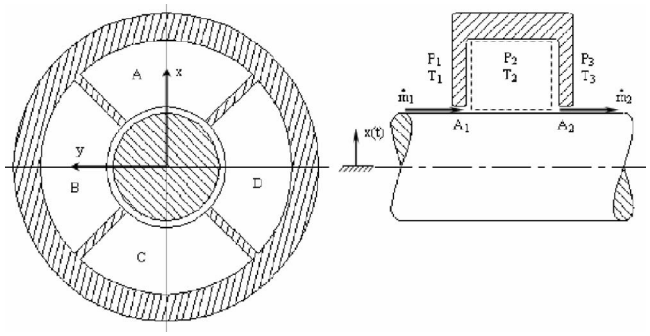

Fig. 2 Two-bladed flow-rate model

3 Test-Rig and Testing Procedure

The facility used to test the seals was initially built to test hydrostatic bearings at the Turbomachinery Laboratory at Texas A&M University and has since been modified to test annular gas seals. A high-pressure pipeline from a wind tunnel provides air at pressures of up to 2500 psi (17.3 MPa). A schematic of the test facility is shown in Fig. 3, and more detailed descriptions of the test rig are given by Childs and Hale [6], Picardo [7], and Gamal [3]. In addition to the leakage and static pressure tests that are the subject of this paper, the test rig and test seals described here were used to determine the rotordynamic coefficients of pocket damper seals at high pressures, as described by Gamal [3] and Ertas [8].

The rig consists of a rotor connected by a coupling to a gearbox with the test seals mounted in a stator assembly around the rotor. The rotor was spun at speeds of 10,200 rpm, 15,200 rpm, and 20,200 rpm. The stator is connected to two Zonic® shakers. The rotor possesses a fundamental natural frequency that is significantly higher than the test frequency range and is mounted on hydrostatic bearings that have high stiffness. Two air-buffer seals utilizing shop air at 110 psi (0.76 MPa) prevent leakage of the bearing water.

Air enters the assembly through the center of the stator and moves axially outward through two sets of identical seals. The pressure drop across the seals can be controlled by varying the inlet pressure and by opening or closing a back-pressure valve, which modifies the seal's exit pressure. The same test rig is also used to test hole pattern and labyrinth seals. A photograph of the test rig with the stator assembly installed is shown in Fig. 4.

The stator assembly consists of five components: a brass stator, two steel pocket damper seals, and two aluminum labyrinth seals. The stator holds the seals in place and provides a method of connection to the shakers and the pressure, temperature, and vibration sensors. The labyrinth seals at either end of the stator control the pressure drop across the test seals by regulating the back pressure. With the back pressure valve fully open, there should be almost no flow across the labyrinth seals, and the PDS exit pressure will be on the order of 150 Psi (1.03 MPa) for an inlet pressure of 1000 Psi (6.92 MPa). With the valve fully closed, the back-pressure is maintained by the labyrinth seals.

Initially, two seal types were tested; a twelve-bladed seal and an eight-bladed seal (Fig. 5). Both seals were first tested with a 1:1 clearance ratio and then had their exit blades notched to provide an effective 1:2 clearance ratio for the twelve-bladed seal and an effective 1:1.5 clearance ratio for the eight-bladed seal. These notches serve to provide the desired overall positive direct damping by creating an effective diverging clearance in the active cavi-

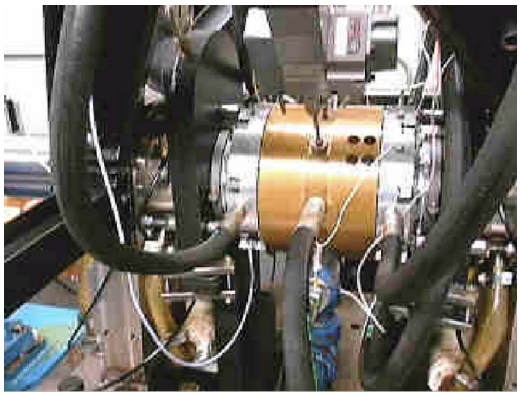

Fig. 4 Assembled test rig

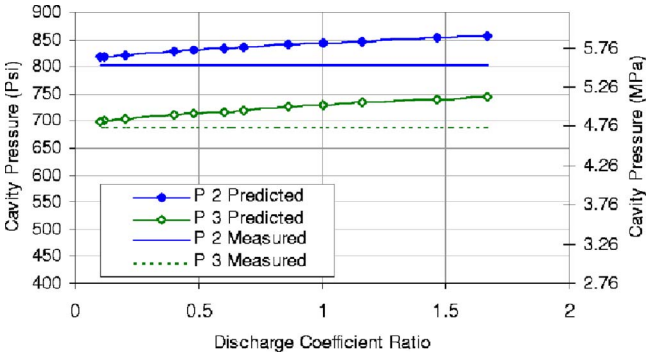

Fig. 7 Effect of discharge coefficient ratio on static cavity pressures

ties (as in hole-pattern and honeycomb seals, a diverging clearance in a PDS also generally results in positive damping). For each test, two of the same types of seals are placed back to back in the stator so as to minimize the resulting axial thrust.

The static cavity pressure measurements were made in the second and third active cavities of both configurations of the eight-bladed seal using Kulite™ XT-190M pressure transducers. The pressure probe holes can be seen on the eight-bladed seal of Fig. 5.

In the case of the twelve-bladed seal, the inlet blades for each active cavity are beveled on the upstream side and the exit blades for each active cavity are beveled on the downstream side. The major dimensions of the diverging configurations of the two seals are listed in the Appendix. Solid models of the diverging configurations of the test seals (including the six-bladed seal that was tested later) are shown in Fig. 6.

Once the test seals were installed in the stator assembly and assembled onto the test rig described above, the procedure followed during testing and the method employed for data acquisition were identical to those used by Marquette et al. [9]. The leakage through the seals was measured as described by Picardo [7].

Fig. 5 Twelve-bladed (left) and eight-bladed (right) pocket damper seals

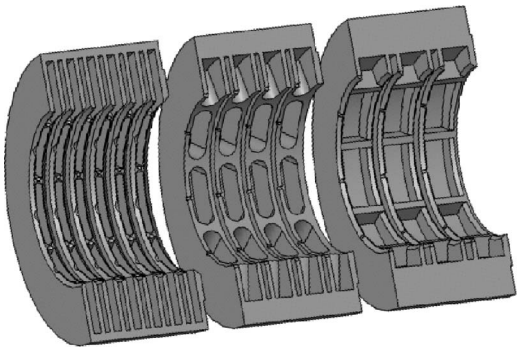

Fig. 6 Half-section models of the diverging twelve-bladed (left), eight-bladed (center), and six-bladed (right) seals

4 Results

Shultz [5] determined that the discharge coefficients that best matched his experimental data were 1.1 for the inlet blade and 0.95 for the exit blade. As will be seen, however, for the test results presented in this paper, these coefficients significantly overpredicted the leakage through the eight-bladed seal, underpredicted the leakage through the twelve-bladed seal, and underpredicted the static cavity pressures.

4.1 Discharge Coefficients. Trial runs of the damper seal code revealed that the static cavity pressures are affected by the ratio of the discharge coefficients and not by their absolute magnitudes. Figure 7 represents static pressures in the second and third active cavities of the diverging eight-bladed PDS with inlet and exit pressures of 1007 psi and 539 psi (6.92 MPa and 3.72 MPa), respectively.

Figure 7 shows that the predicted static pressure values match experimental results more closely as the ratio of inlet-to-exit discharge coefficients decreases. The seal leakage predicted by Eq. (2), however, depends on the absolute magnitudes of the discharge coefficients. As a result, using a discharge coefficient ratio close to zero may closely match pressure readings, but it would severely underpredict the mass flowrate through the seal. There are two different combinations of discharge coefficients that will result in the same mass flow-rate prediction. Of these, the combination that yields an improved static pressure prediction—the one with the smaller inlet to exit discharge coefficient ratio—should be selected.

These numerical results support the need to use different discharge coefficient values for the inlet and exit blades of each seal so as to more accurately match the cavity pressure data as well as the leakage rates. The data presented in this paper were used to

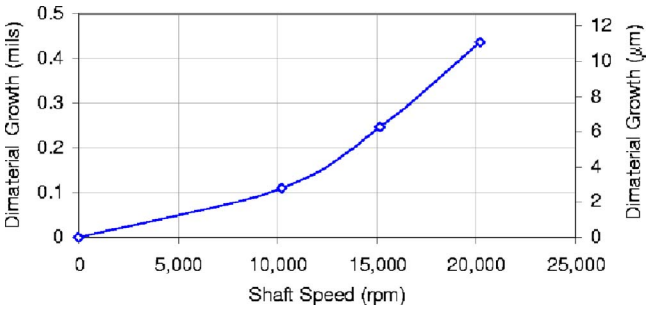

Fig. 8 Rotor growth at high speeds

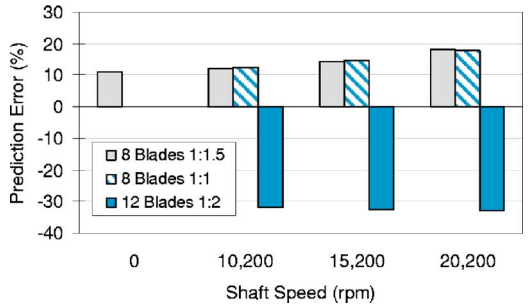

Fig. 9 Average leakage error (discharge coefficients 1.1 inlet and 0.95 exit)

obtain new discharge coefficients that more accurately match leakage measurements and that have a ratio that results in acceptably accurate static cavity pressure measurements.

4.2 Rotor Growth. Initial analysis of the leakage data showed that there is a significant reduction in leakage as the speed of the rotor increases. At high rotational speeds, the centrifugal forces acting on the material of the rotor increase and cause the rotor to expand. The increase in rotor radius is given by Eq. (4) [10].

$$\Delta R = \frac{\delta \omega^2}{4gE}(3+\upsilon)R_S^3 \tag{4}$$

Since the seal clearances are only a few thousands of an inch wide, even a small radial expansion of the rotor is significant. Figure 8 shows the increase in diameter of the 4.5 in (114.3 mm) test rotor, calculated using Eq. (4), as the rotational speed is increased. At the highest rotor speed (20,200 rpm), the inlet blade radial clearances of the test seal are reduced by ~5%. The importance of taking rotor growth into consideration is made apparent by the leakage results presented below.

4.3 Leakage Results. Leakage measurements were made on all three of the test seal configurations described earlier. The diverging twelve-bladed seal and the straight-through eight-bladed seal were each tested with three different pressure drops. The diverging eight-bladed seal was tested with only two pressure drops. Because of its more negative stiffness, this last seal could not be maintained in a centered position on the very low-stiffness test rig with the largest pressure drop. For each pressure drop, the seals were tested with rotor speeds of 10,200 rpm, 15,200 rpm, and 20,200 rpm (the diverging eight-bladed seal was also tested at zero rotor speed).

For a given seal, the inlet pressure and pressure drop were slightly different for each of these speeds, with a maximum deviation of about 30 psi (0.67 MPa). The results, therefore, would more accurately be presented in the form of separate plots for each speed and each pressure drop. This is the way in which the leakage data for the straight-through eight-bladed seal are presented. A complete summary of the exact test conditions and the mass flow-rate results for all three seal configurations can be found in the Appendix. The average test pressures are summarized in Table 1. For the diverging eight-bladed and twelve-bladed seals, these average pressures are used and the results are presented on a single plot for each seal.

A comparison of code predictions with experimental data (Fig. 9) shows that using the original discharge coefficients that Shultz [5] had used for lower-pressure seals would lead to significant prediction errors (seals are labeled by number of blades and clearance ratio). The prediction error in Fig. 9 is the average of the errors for the different pressure drops across the seal for each rotor speed. These data take into consideration rotor growth with speed.

Table 1 Average pressure conditions for leakage tests

Seal	Test ΔP	P_{in} (psi)	P_{in} (MPa)	P_{exit} (psi)	P_{exit} (MPa)	ΔP (psi)	ΔP (MPa)
Diverging twelve-bladed	Low	992	6.84	713	4.92	279	1.92
	Inter.	1009	6.96	458	3.16	551	3.80
	High	1017	7.01	226	1.56	791	5.46
Diverging eight-bladed	Low	723	4.99	441	3.04	282	1.94
	High	941	6.49	572	3.94	369	2.54
Straight-through eight-bladed	Low	1027	7.08	525	3.62	502	3.46
	Inter.	1024	7.06	336	2.32	688	4.74
	High	1024	7.06	129	0.89	895	6.17

Since the original coefficients overpredict the leakage through the eight-bladed seal and underpredict the leakage through the twelve-bladed seal, it is clear that the discharge coefficients that best match the leakage data will be different for each seal. It should be noted that there are significant differences between the blade geometries of the twelve-bladed and eight-bladed seals. Generally, the amount of leakage through a PDS will increase if the seal's clearances are increased and will decrease if the number of blades in the seal is increased. Although the twelve-bladed seal contained a higher number of blades, it also had a smaller clearance ratio (1:2) and, therefore, larger exit clearances, than the eight-bladed seal (1:1.5). Each of these two opposing factors should have at least partially countered the effect of the other, suggesting that yet another factor was also responsible for the significantly higher leakage through the twelve-bladed seal. Furthermore, the prediction code showed that even with the higher clearance ratio, the twelve-bladed seal should still have been more effective than the eight-bladed seal in terms of leakage reduction. The effect of the difference in blade-tip geometry is examined in detail below in the case of two identical six-bladed seals, thus eliminating other variables from the analysis, and is used to explain this unexpectedly high leakage rate.

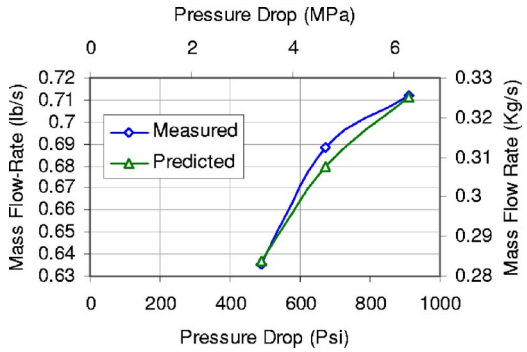

Fig. 10 10,200 rpm leakage (eight blades, CR=1:1, $C_{d_{in}}$ =0.866, $C_{d_{exit}}$=0.922)

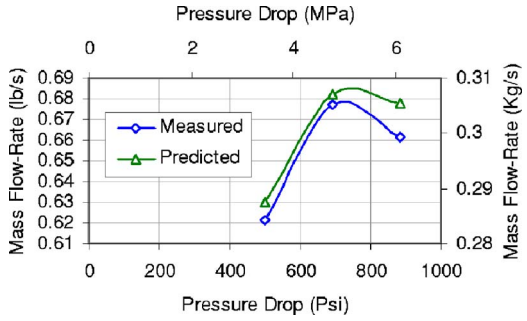

Fig. 11 15,200 rpm leakage (eight blades, CR=1:1, $C_{d_{in}}$=0.866, $C_{d_{exit}}$=0.922)

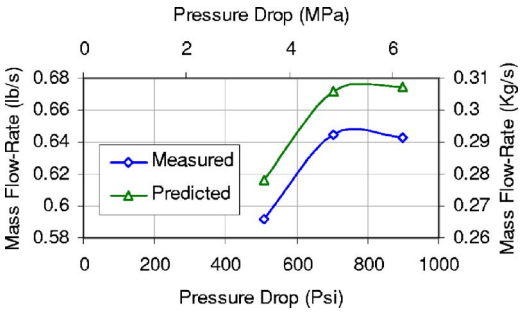

Fig. 12 20,200 rpm leakage (eight blades, CR=1:1, $C_{d_{in}}$ =0.866, $C_{d_{exit}}$=0.922)

4.3.1 Straight-Through Eight-Bladed Seal. The leakage and static pressure data for the straight-through eight-bladed seal were best matched with an inlet discharge coefficient of 0.866 and an exit coefficient of 0.922. Figures 10–12 compare the measured leakage for this seal with the predicted values using the damper seal code with these coefficients.

Even though rotor growth was taken into consideration, the damper seal code overpredicts the leakage by a larger amount as the rotor speed increases. The slight drop in flow rate in the *predicted* curve of Fig. 15 is due to the inlet pressure for the third data point being lower than that for the second data point. The code predicts that for the same inlet pressure, the flow rate will increase with increasing pressure drop. This does not, however, explain why the third *measured* data points on the plots for both 15,200 rpm and 20,200 rpm show a lower flow rate than the previous points. For these two pressure drops, the damper seal code predicts choked flow through the last blade of the seal. Theoretically, the flow rate would increase with increasing pressure drop and would asymptotically approach a maximum value corresponding to the choked flow condition. This does not, however,

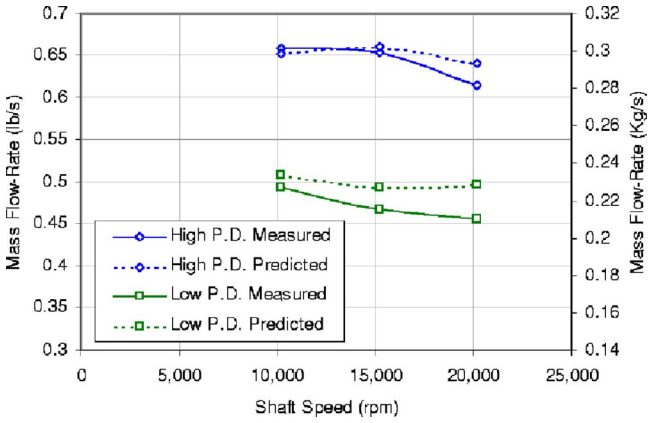

Fig. 13 Measured versus predicted leakage (eight blades, CR =1:1.5, $C_{d_{in}}$=0.866, $C_{d_{exit}}$=1.118)

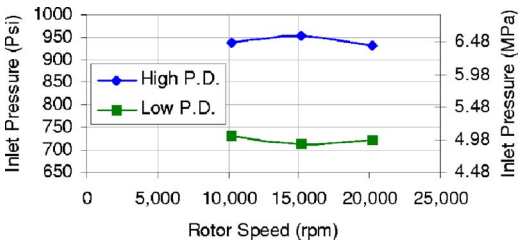

Fig. 14 Leakage test inlet pressures (eight blades, CR=1:1.5)

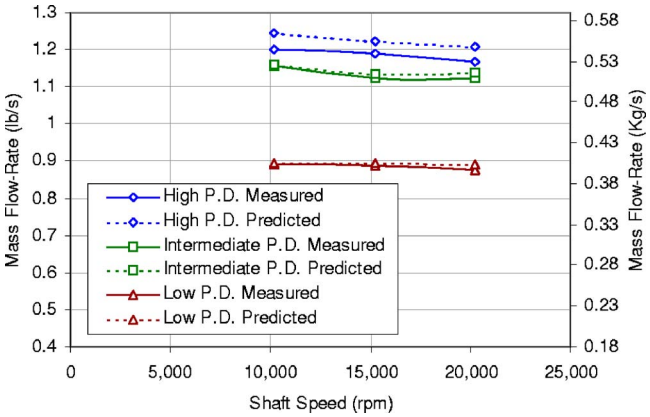

Fig. 15 Measured versus predicted leakage (twelve blades, CR =1:2, $C_{d_{in}}$=1.517, $C_{d_{exit}}$=1.658)

match the experimental data, which show a drop in flow rate after the flow theoretically becomes choked.

4.3.2 Diverging Eight-Bladed Seal. The inlet and exit discharge coefficients that best matched the leakage data for the 1:1.5 clearance ratio eight-bladed seal are 0.866 and 1.118, respectively. Since the only difference between this seal and the straight-through eight-bladed seal is the inclusion of notches in the exit blades, the same inlet blade coefficient was used for both seals. The exit blade coefficient was increased to match the data. It should be noted that the increased flow area due to the notches is already accounted for in the damper seal code in the form of the exit clearance. The exit blade discharge coefficient merely, as mentioned above, accounts for the difference between the actual flow area and the flow area for which the code's equations were intended.

The mass flow rates through the diverging eight-bladed seal are shown in Fig. 13 for two average pressure drops and three rotor speeds. As can be expected, the measured leakage through the seal decreases with increasing rotor speed for both pressure drops. The high ΔP predicted curve shows a slight increase in leakage at 15,200 rpm over 10,200 rpm. Likewise, the low ΔP curve shows a slight increase in the leakage at 20,200 rpm over 15,200 rpm. These increases can be explained by the fact that the inlet pressures for both these cases were slightly higher than the inlet pressures for the previous points (Fig. 14). These minor inconsistencies in the inlet pressures are apparently large enough to slightly offset the downward trend in leakage with increasing rotor speed.

4.3.3 Diverging 12-Bladed Seal. The discharge coefficients that best matched the experimental results for the diverging

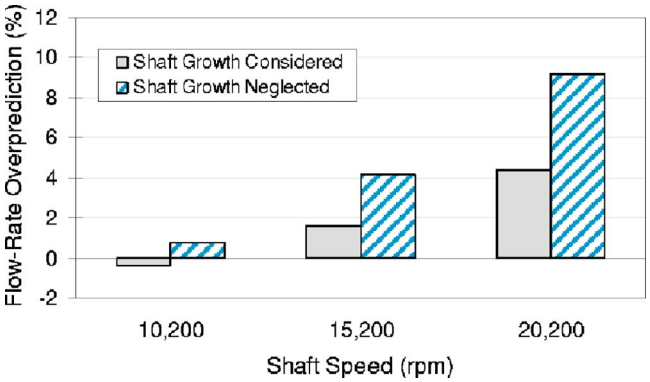

Fig. 16 Leakage overprediction (eight blades, CR=1:1, $C_{d_{in}}$ =0.866, $C_{d_{exit}}$=0.922)

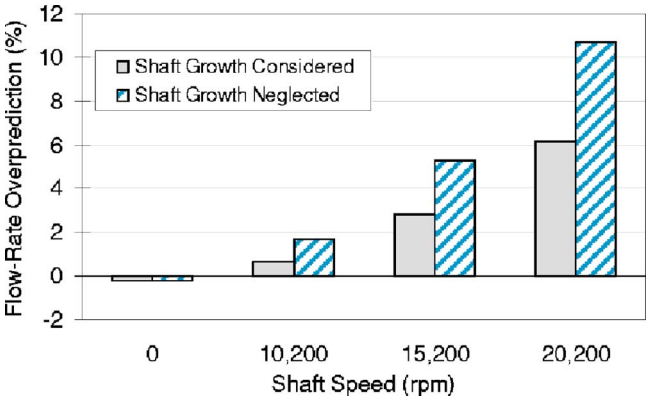

Fig. 17 Leakage over-prediction (eight blades, CR=1:1.5, $C_{d_{in}}$=0.866, $C_{d_{exit}}$=1.118)

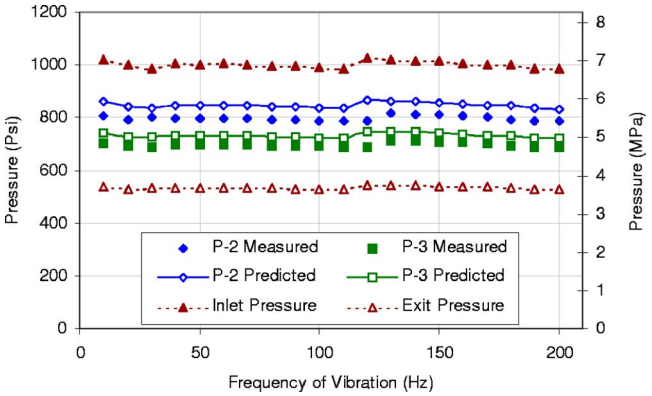

Fig. 19 Static cavity pressures (eight blades, CR=1:1)

twelve-bladed seal are 1.517 for the inlet blades and 1.658 for the exit blades. These values (which are much higher than those obtained for the eight-bladed seals) and the corresponding higher leakage rates can, at least in part, be attributed to the blade geometry of the twelve-bladed seal. Leakage data are presented here only for the diverging configuration of the twelve-bladed seal, but two different sets of data were taken for the seal during two separate rig assemblies. The results of these two sets of tests are almost identical. The predicted and measured results for this seal with three different rotor speeds and three pressure drops are presented in Fig. 15.

Once again, the expected drop in leakage with increasing rotor speed can be seen. The damper seal code predicts that for the high ΔP case, the flow through the last two constrictions of this seal is choked. The marked increase in the overprediction of the seal's leakage for the high ΔP condition could be due to choked flow in that case.

4.4 Prediction Errors. As was mentioned above, the amount by which the damper seal code overpredicted the leakage through a seal was found to increase as the rotor speed increased, even when rotor growth was taken into account. The average percentage overpredictions of the flow rate with and without rotor growth included are shown for each of the three test seals in Figs. 16–18.

These figures show that while rotor growth accounts for a portion of the overprediction of flow rate, there is some other phenomenon, perhaps related to increased circumferential velocity in the flow, which becomes more pronounced at higher speeds. If this is indeed the case, the circumferential partition walls of the pocket damper seal, which reduce circumferential flow markedly, prevent this phenomenon from becoming significant enough to reduce the usefulness of the prediction model.

The error in predicting the leakage through the two configurations of the eight-bladed seal followed a general trend: the overprediction became more pronounced as either the rotor speed or the pressure drop across the seal increased. The overprediction of leakage through the diverging twelve-bladed seal was also observed to increase with increasing rotor speed, but decreased as the pressure drop across the seal rose. Since the discharge coefficients were altered so that the predicted leakage matched the measured leakage, it could be argued that coefficients could be chosen so that the high-pressure drop data are matched more closely and the flow rates for lower-pressure drops are underpredicted.

4.5 Static Pressure Results. The discharge coefficients for all three test configurations were chosen so that the inlet to exit coefficient ratio is <1. This was done to improve the prediction of the static cavity pressures for the eight-bladed seal configurations (cavity pressure measurements were not made on the twelve-bladed seal). Figure 19. shows the results for the static pressures in the second and third active cavities of the straight-through eight-bladed seal, while Fig. 20. shows the same data for the diverging eight-bladed seal.

The static pressure data were taken in conjunction with dynamic pressure measurements [3,8] taken every 10 Hz from 10 Hz to 200 Hz. The frequency of vibration was not expected to impact the static cavity pressures (an assumption that was supported by the results), and the 20 test frequencies can be thought of as 20 independent static pressure test cases.

During the tests, the inlet pressure was kept as close to 1000 psi (6.92 MPa) as possible and was raised whenever it dropped below this value. The inlet pressure was raised immediately before the 40 Hz, 60 Hz, and 120 Hz readings for the straight-through seal

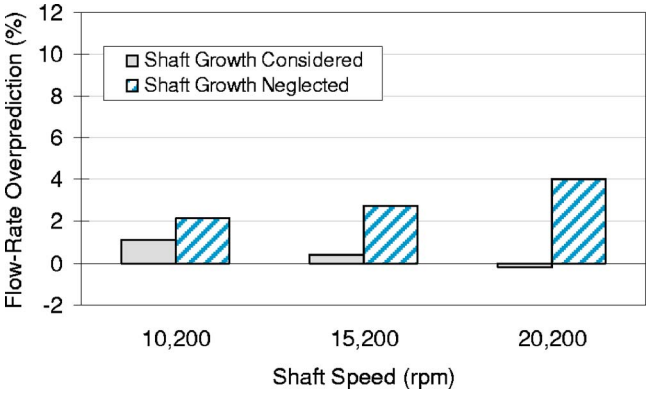

Fig. 18 Leakage overprediction (twelve blades, CR=1:2, $C_{d_{in}}$=1.517, $C_{d_{exit}}$=1.658)

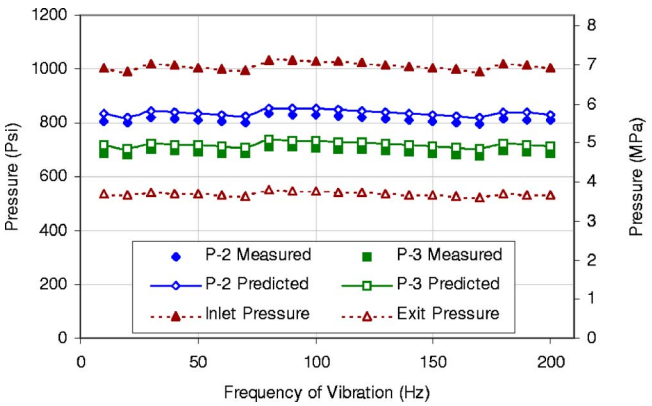

Fig. 20 Static cavity pressures (eight blades, CR=1:1.5)

Table 2 Discharge coefficient summary

Seal	Inlet C_d	Exit C_D
Straight-through eight-bladed	0.866	0.922
Diverging eight-bladed	0.866	1.118
Diverging twelve-bladed	1.517	1.658

and immediately before the 30 Hz, 80 Hz, and 180 Hz readings for the diverging seal. The slight deviations in cavity pressures from a constant value are due to these changes in the inlet pressure and not due to a dependency on frequency.

In the case of the straight-through seal, the code overpredicts the second active cavity pressure by an average of 49.9 psi (0.344 MPa) or ~6.3% and overpredicts the third active cavity pressure by an average of 36.7 psi (0.253 MPa) or 5.3%. Since the discharge coefficient ratio (Cd_{in}:Cd_{exit}) is smaller for the diverging seal, it was expected that the static pressure data for this seal would be better matched than that for the straight-through seal. This is indeed the case, and the average overpredictions of the second and third active cavity pressures in the diverging seal are only 23.3 psi (0.161 MPa) or 2.9% and 23.1 psi (0.159 MPa) or 3.3%, respectively. Table 2 summarizes the discharge coefficients found to best match the experimental leakage and static pressure results for the three seal configurations.

4.6 Six-Bladed Seal Tests: Blade Profile Effects. As was discussed in detail in a previous section, the tests by Gamal [3] showed that, contrary to theoretical predictions, the leakage through the twelve-bladed PDS was higher than that through the eight-bladed PDS for the same pressure ratio. It was theorized that the differences in blade profile and cavity pitch length were the main contributing factors to this surprising result. However, additional differences between the two seals, including differences in cavity depths and clearance ratios, complicated comparison of the results.

Ertas [8] avoided such complications by testing a six-bladed PDS first with rectangular-profiled blades, then with bevels machined into the downstream sides of the blades. Using the same seal ensured that all other factors remained constant for the two sets of tests. The major dimensions of this seal are presented in the Appendix. Figure 21 shows Ertas's two downstream-beveled six-bladed seals installed in the stator test assembly, and Fig. 22 shows the results of the leakage tests on the two configurations of this seal with a pressure drop of 400 psi (2.77 MPa).

The results of this comparison showed that for different rotor speeds, the leakage through the seal with beveled blades was 15–20% higher than that through the flat-tipped seal. This result supports the earlier results obtained from the tests on the eight-bladed and twelve-bladed seals. As was done with the eight-bladed seal configurations, the leakage values were used in conjunction with the static cavity pressures to determine the inlet and exit discharge coefficients for each six-bladed seal configuration. The inlet and exit discharge coefficients for the six-bladed seals were determined to be 0.71 and 0.78, respectively, for the rectangular configuration and 0.965 and 1.2, respectively, for the downstream-beveled configuration.

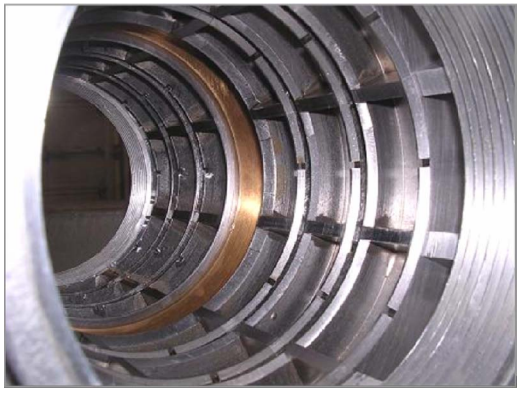

Fig. 21 Beveled six-bladed seals

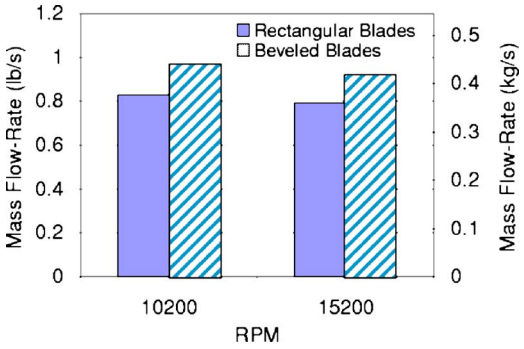

Fig. 22 Leakage through six-bladed PDS configurations

5 Discussion

The seal tests described in this paper differ from previous tests not only in that they were conducted at considerably higher pressures, but also in the significant geometric differences between the test seals and previously tested seals. Furthermore, there were differences between the eight-bladed and twelve-bladed seals that no doubt, contributed to the need for different discharge coefficients for each seal configuration.

Close-up views of the blades and partition walls of the diverging eight-bladed and twelve-bladed seals are shown in Fig. 23. The first difference between the two seals is the shape of the notch. The analysis presented here did not take notch effects (which were examined by Kannan [11]) into account and, instead, used the difference in area to calculate an enlarged equivalent exit clearance between seal and rotor, which was then used in the

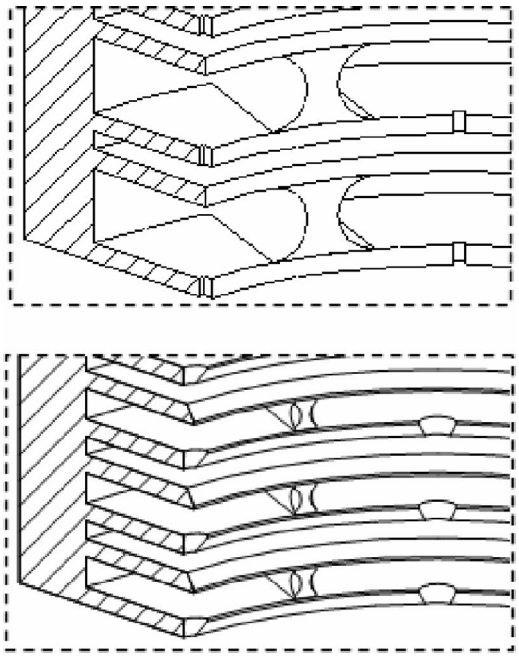

Fig. 23 Blade geometry for diverging eight-bladed (upper) and twelve-bladed (lower) seals

Table 3 Major dimensions of test seals

Seal	Twelve-bladed seal		Eight-bladed seal		Six-bladed seal	
	(in)	(mm)	(in)	(mm)	(in)	(mm)
Length	3.375	85.73	3.375	85.73	3.375	85.73
Inner diameter	4.51	114.55	4.51	114.55	4.51	114.55
Radial inlet clearance	0.005	0.13	0.005	0.13	0.005	0.13
Radial exit clearance	0.010	0.25	0.0075	0.19	0.010	0.25
Pocket depth	1.40	35.56	1.00	25.40	0.56	14.22
Number of pockets	8		8		8	
Wall thickness	0.15	3.81	0.20	5.08	0.20	5.08
Blade thickness	0.125	3.18	0.125	3.18	0.125	3.18
Active cavity length	0.208	5.29	0.500	12.70	0.742	18.85
Inactive cavity length	0.125	3.18	0.125	3.18	0.200	5.08

modified St. Venant equation to calculate the mass flow rate through the seal. Based on Kannan's [11] work and based on the fact that all the diverging seals that were tested had notches rather than higher clearance exit blades, it can be assumed that for the sake of the comparisons described in this paper, ignoring notch effects would not have a significant impact on the results.

The main remaining geometric features that influence the leakage and discharge coefficients are the shape of the blade tips and the cavity pitch of the twelve-bladed seal. The relatively high discharge coefficients for this seal may be due to increased leakage across the forward and backward beveled blades and the axially shorter cavities of this seal.

The differences between the discharge coefficients obtained for the test seals and those used by Shultz [5] are probably due, in part, to such geometric differences, but are also influenced by the difference in test pressures. Wittig et al. [12] present numerical predictions for the discharge coefficients of labyrinth seals that show their dependence on the ratio of pressures across the seals.

The importance of taking shaft growth into consideration in labyrinth seal applications is cited by Waschka et al. [13], who also discuss the speed dependency of the discharge coefficients due to rotational effects. Although such effects can be expected to have less importance in a PDS with its partition walls, this does go some way in explaining the error in predicting mass flow rates at higher speeds.

6 Conclusions

The following points summarize the topics covered in this paper and the results that were presented:

Table 4 Leakage data for eight-bladed seal (pressure in pounds per square inch and mass flow rates in pounds per second)

Seal	rpm	P_{in}	P_{exit}	ΔP	Measured flow	Flow 1	Flow 2	Flow 3
1:1 Clearance ratio	10,200	1046	135	912	0.7120	0.8004	0.7112	0.7192
	10,200	1013	342	671	0.6882	0.7674	0.6798	0.6874
	10,200	1030	539	491	0.6357	0.7202	0.6370	0.6442
	15,200	1011	126	885	0.6611	0.7630	0.6780	0.6951
	15,200	1029	338	691	0.6768	0.7704	0.6825	0.6998
	15,200	1028	530	498	0.6212	0.7124	0.6301	0.6460
	20,200	1025	126	899	0.6427	0.7586	0.6741	0.7048
	20,200	1031	328	703	0.6443	0.7585	0.6722	0.7028
	20,200	1014	505	509	0.5921	0.6964	0.6160	0.6441
1:1.5 Clearance ratio	0	1009	599	410	0.7275	0.8069	0.7252	0.7252
	0	1012	601	411	0.7341	0.8092	0.7272	0.7272
	0	1027	615	412	0.7319	0.8177	0.7349	0.7349
	0	1016	604	412	0.7385	0.8119	0.7297	0.7297
	0	1027	613	414	0.7297	0.8190	0.7363	0.7363
	10,200	939	582	357	0.6592	0.7263	0.6527	0.6596
	10,200	731	454	277	0.4938	0.5647	0.5075	0.5129
	15,200	953	581	372	0.6548	0.7350	0.6600	0.6757
	15,200	714	436	278	0.4674	0.5502	0.4941	0.5057
	20,200	930	553	377	0.6151	0.7142	0.6407	0.6679
	20,200	723	432	291	0.4564	0.5539	0.4969	0.5180

Table 5 Leakage data for 12-bladed seal (pressure in pounds per square inch and mass flow rates in pounds per second)

Seal	rpm	P_{in}	P_{exit}	ΔP	Measured flow	Flow 1	Flow 2	Flow 3
1:1 Clearance ratio	10,200	1018	229	789	1.1993	0.8392	1.2442	1.2572
	10,200	1011	464	547	1.1552	0.7789	1.1598	1.1718
	10,200	987	713	273	0.8907	0.6005	0.8957	0.9049
	15,200	1014	226	789	1.1883	0.8256	1.2234	1.2524
	15,200	999	454	545	1.1243	0.7619	1.1341	1.1605
	15,200	993	715	279	0.8885	0.5989	0.8928	0.9135
	20,200	1019	224	795	1.1684	0.8153	1.2072	1.2587
	20,200	1018	457	561	1.1221	0.765	1.1381	1.1858
	20,200	997	710	288	0.8752	0.5976	0.8904	0.9275
1:2 Clearance ratio	10,200	1018	238	781	1.1995	0.8385	1.2436	1.2566
	10,200	1010	494	516	1.1498	0.7655	1.1402	1.152
	10,200	1023	744	278	0.9372	0.618	0.9217	0.9312
	15,200	1011	236	776	1.1924	0.8224	1.2192	1.248
	15,200	1006	491	515	1.1443	0.7536	1.122	1.1481
	15,200	1019	742	277	0.9339	0.6072	0.9053	0.9263
	20,200	1016	237	779	1.1988	0.8119	1.203	1.2542
	20,200	999	488	511	1.1369	0.7352	1.094	1.1398
	20,200	1014	738	276	0.9302	0.5941	0.8853	0.9222

- The correlation between measured and predicted values of the cavity pressures was improved by selecting discharge coefficients such that the ratio of the inlet to the exit coefficient was as low as possible.
- Whereas the ratio of these coefficients was found to affect the static pressure predictions, the actual values of the coefficients determine the amount of leakage through the seal. Therefore, in order to avoid significantly underpredicting the leakage, there is a lower limit to the discharge coefficient ratio. The coefficients selected were those that offered the best match between theoretical and measured values for both the static pressures and the leakage data.
- The comparatively high values of the discharge coefficients selected for the diverging twelve-blade seal are, at least partially, attributable to increased leakage due to the beveled blade profile of that seal.
- Taking rotor growth into account resulted in more accurate leakage predictions, but the error in prediction increased with increasing shaft speeds due to rotational effects.
- Tests on the six-bladed seal configurations confirmed that machining a downstream bevel into the blades of a pocket damper seal increases the leakage through the seal, suggesting that using flat-tipped blades would result in better PDS designs.

Further examination of the effects of seal geometry on the mass flow rate would provide better understanding of the factors that led to the need for the discharge coefficient values used for each test seal. Investigation of the accuracy of other leakage prediction models may also result in better understanding of the leakage and pressure characteristics of pocket damper seals. Such investigations are currently underway at the Turbomachinery Laboratory at Texas A&M University at the time of the writing of this paper.

Acknowledgment

The research presented in this paper was conducted at Texas A&M University's Turbomachinery Laboratory and was funded by the TAMSEAL® Consortium. The direction and assistance of Dr. Fouad Zeidan, of Bearings Plus Inc., was greatly appreciated. The test facility used was made available by Dr. Dara Childs.

Nomenclature

A_i = flow area for the ith construction (L^2)
C_d = discharge coefficient (-)
CR = exit to inlet blade clearance ratio (-)
E = modulus of elasticity for shaft material (F/L^2)
g = acceleration due to gravity (L/t^2)
$\dot{m}_i$ = mass flow rate through the ith constriction (M/t)
n = number of seal blades (-)
PD = pressure drop across the seal (F/L^2)
P_{in} = pressure upstream of the seal (F/L^2)
P_{exit} = pressure downstream of the seal (F/L^2)
P_i = pressure in the ith cavity (F/L^2)
PR = ratio of inlet to exit pressures (-)
ΔP = difference between inlet and exit pressures (F/L^2)
R = gas constant (FL/(MT))
R_S = shaft radius (L)
ΔR = increase in shaft radius (L)
rpm = revolutions per minute (1/t)
T_i = temperature in the ith cavity (T)
t = time (t)
x = journal displacement (L)
γ = specific heat ratio (-)
δ = weight per unit volume of shaft material (F/L^3)
ν = Poisson's ratio for shaft material (-)
ρ = gas density (M/L^3)
ω = rotor speed (1/t)

Appendix

Tables 4 and 5 contain additional data referred to in the body of this paper. This consists of the major dimensions of the test seals and the detailed leakage data that were used to determine the discharge coefficients. Table 3 lists the major dimensions of the diverging configurations of the test seals.

Table 4 lists all data for the leakage tests carried out on both the straight-through and diverging eight-bladed seals. The modified inlet and exit discharge coefficients were 0.866 and 0.922, respectively, for the straight-through seal and 0.866 and 1.118, respectively, for the diverging seal. Table 4 shows the flow rates for three cases: Using the original discharge coefficients (1.1 for $C_{d_{\text{in}}}$ and 0.95 for $C_{d_{\text{exit}}}$) with rotor growth considered (flow 1), using the modified discharge coefficients with rotor growth considered (flow 2), and using the modified discharge coefficients with rotor growth neglected (flow 3).

Table 5 lists all data for the leakage tests carried out on the diverging twelve-bladed seal (two sets of data). The modified inlet and exit discharge coefficients for this seal were 1.517 and 1.658, respectively. Table 5 shows the flow rates for three cases: using the original discharge coefficients (1.1 for $C_{d_{\text{in}}}$ and 0.95 for $C_{d_{\text{exit}}}$) with rotor growth considered (flow 1), using the modified discharge coefficients with rotor growth considered (flow 2), and using the modified discharge coefficients with rotor growth neglected (flow 3).

References

[1] Vance, J. M., and Shultz, R. R., 1993, "New Damper Seal for Turbomachinery," *Proc. of 14th Vibration and Noise Conference, Vibration of Rotating Systems*, ASME, New York, Vol. 60, pp. 139–148.
[2] Childs, D. W., and Vance, J. M., 1997, "Annular Gas Seals and Rotordynamics of Compressors and Turbines," *Proc. of 26th Turbomachinery Symposium*, Texas A&M University, College Station, TX, pp. 201–220.
[3] Gamal, A. M., 2003, "Analytical and Experimental Evaluation of the Leakage and Stiffness Characteristics of High Pressure Pocket Damper Seals," M.S. thesis, Mechanical Engineering Department, Texas A&M University, College Station, TX.
[4] Laos, H. E., 1999, "Rotordynamic Effects of Pocket Damper Seals," Ph.D. dissertation, Mechanical Engineering Department, Texas A&M University, College Station, TX.
[5] Shultz, R. R., 1996, "Analytical and Experimental Investigation of a Labyrinth Seal Test Rig and Damper Seals for Turbomachinery," M.S. thesis, Mechanical Engineering Department, Texas A&M University, College Station, TX.
[6] Childs, D. W., and Hale, K., 1994, "A Test Apparatus and Facility to Identify the Rotordynamic Coefficients of High-Speed Hydrostatic Bearings," ASME J. Tribol., **116**, pp. 337–344.
[7] Picardo, A. M., 2003, "High Pressure Testing of See-Through Labyrinth Seals," M.S. thesis, Mechanical Engineering Department, Texas A&M University, College Station, TX.
[8] Ertas, B. H., 2005, "Rotordynamic Force Coefficients of Pocket Damper Seals," Ph.D. dissertation, Mechanical Engineering Department, Texas A&M University, College Station, TX.
[9] Marquette, O. R., Childs, D. W., and San Andres, L., 1997, "Eccentricity Effects on the Rotordynamic Coefficients of Plain Annular Seals: Theory Versus Experiment," J. Tribol., **119**, pp. 443–448.
[10] Young, W. C., 1989, *Roark's Formulas for Stress and Strain*, 6th ed., McGraw-Hill, New York.
[11] Kannan, B. S., 2003, "Development and Validation of an Analytical Model for the Notched Pocket Damper Seal," M.S. thesis, Mechanical Engineering Department, Texas A&M University, College Station, TX.
[12] Wittig, S., Schelling, U., Kim, S., and Jacobsen, K., 1987, "Numerical Predictions and Measurements of Discharge Coefficients in Labyrinth Seals," ASME Paper No. 87-GT-188.
[13] Waschka, W., Wittig, S., and Kim, S., 1992, "Influence of High Rotational Speeds on the Heat Transfer and Discharge Coefficients in Labyrinth Seals," ASME J. Turbomach., **114**(2), pp. 462–468.

T. Verstraete
e-mail: verstraete@vki.ac.be

Z. Alsalihi
e-mail: alsalihi@vki.ac.be

R. A. Van den Braembussche
e-mail: vdb@vki.ac.be

von Kármán Institute for fluid Dynamics,
Waterloose steenweg, 72,
1640, Sint-Genesius-Rode, Belgium

Numerical Study of the Heat Transfer in Micro Gas Turbines

This paper presents a numerical investigation of the heat transfer inside a micro gas turbine and its impact on the performance. The large temperature difference between turbine and compressor in combination with the small dimensions results in a high heat transfer causing a drop in efficiency of both components. Present study aims to quantify this heat transfer and to reveal the different mechanisms that contribute to it. A conjugate heat transfer solver has been developed for this purpose. It combines a three-dimensional (3D) conduction calculation inside the rotor and the stator with a 3D flow calculation in the radial compressor, turbine and gap between stator and rotor. The results for micro gas turbines of different size and shape and different material characteristics are presented and the impact on performance is evaluated. [DOI: 10.1115/1.2720874]

Introduction

The last decade has seen a lot of research effort being oriented toward the development of micro gas turbines. Their potential for high power and energy density makes them well suited to replace batteries in mobile applications. However, new problems arise when downscaling large turbomachines. They are related to machining, materials and the high heat transfer resulting from the high-temperature differences over small distances. The latter one is the main topic of the investigation presented in the present paper.

Conduction in the solid is normally not an important issue in turbomachines except when cooling is applied to high-temperature turbines. Most computational fluid dynamics (CFD) predictions assume adiabatic conditions at the solid boundaries. However, this is no longer acceptable in micro gas turbines due to the heat conduction in the solid. Gong et al. [1] claim that the performance penalty associated with the heat flux from the turbine to the compressor is a primary performance-limiting factor for micro gas turbines. Isomura et al. [2] indicate a drop of compressor efficiency ranging from 10% at 500 K wall temperature to 30% at 1000 K. Similar values are provided by Sirakov et al. [3]. Some authors [4] assume a high constant temperature in both rotor and stator. None of them provides a clear picture of the temperature distribution in the solids and its dependence on geometry.

A better knowledge of the material temperature is also important since it influences corrosion, creep, and maximum allowable stress. Furthermore, the temperature distribution in the solid is also needed to predict the thermal stresses and deformations of the individual components.

The present paper intends to provide accurate values of the temperature in the solids by means of a conjugate heat transfer calculation (CHT). The model includes the heat transfer in the turbine and compressor rotor, the shaft, the stator, and shrouds. It also calculates the diabatic flow in the radial compressor and turbine, including the leakage flow in the gap between the stator and rotor. It is used to predict the flow and heat transfer in complete gasturbines of different size and material.

Numerical Method

There are two main approaches to the conjugate heat transfer problem in turbomachinery [5–11]. One is by an extension of the CFD code to the solid region, where only the energy equation is solved. This method is mostly used and referred to in the literature as the conjugate method [7,10,11]. The main advantage is that only one code is needed for the whole domain. However, modifications of the CFD code and grid generator are required.

The other approach is a coupling of two codes: a nonadiabatic Navier-Stokes (NS) solver for the flow in the fluid domain and a finite element analysis (FEA) for the heat conduction in the solid. Continuity of temperature and heat flux at the common boundaries is obtained by an iterative adjustment of the boundary conditions. The advantage of the coupled approach is that one can use standard NS and FEA solvers and grid generators. Those codes have been extensively verified, and their limitations and capabilities are well known. A FEA calculation is anyway needed for stress and vibration analysis. These have been the main arguments for using the coupled method in present analysis.

Disadvantages of the coupled method are the noncoinciding grids at the common boundary, requiring an interpolation to pass boundary conditions from one grid to the other and the need for an iterative procedure.

The nonadiabatic flow is calculated by means of TRAF3D [12]. This full 3D compressible Navier-Stokes solver uses a multistage Runge-Kutta time integration and central differencing with artificial dissipation applied to finite volumes. Convergence is accelerated by multigrid interpolation and implicit residual smoothing. The overall accuracy is second order at convergence. All calculations are done with the Baldwin-Lomax algebraic eddy-viscosity turbulence model. Despite its simplicity and low computational effort, good agreement with experiments is obtained for conjugate heat transfer as long as the flow is not separated [13]. The steady-state heat transfer computation in the solid domain is predicted by the commercial FEA code SAMCEF [14], using quadratic tetrahedral elements.

Coupled Method. The coupled method uses an iterative approach to obtain the same temperature and heat flux distribution at the boundaries that are common to the NS and FEA calculation domain. Fluid and solid conduction computations alternate with exchange of boundary conditions in one of the following ways.

In a first method [9], the wall temperature distribution is imposed to the fluid solver and the heat flux distribution predicted by the fluid computation is imposed as a boundary condition to the solid conduction solver. This, in turn, predicts an updated temperature distribution at the fluid solver solid boundaries. This loop is repeated until convergence i.e. when the temperature and heat flux are continuous between both domains.

Alternatively, one can also impose the heat flux distribution as a boundary condition for the fluid computation and the resulting wall temperature to the solid conduction solver. The updated heat flux is then returned as a boundary condition to the fluid solver.

Contributed by the International Gas Turbine Institute of ASME for publication in the JOURNAL OF TURBOMACHINERY. Manuscript received June 20, 2006; final manuscript received October 11, 2006. Review conducted by David Wisler. Paper presented at the ASME Turbo Expo 2006: Land, Sea and Air (GT2006), May 8–11, 2006, Barcelona, Spain. Paper No. GT2006-90161.

This method has been successfully applied by Heidmann et al. [6].

The main disadvantages of previous methods are a slow convergence and a risk of stability problems in areas of high-temperature gradient. A third method [8,9,15] uses the wall heat transfer equation (1) to update the boundary conditions

$$q_W = h(T_W - T_{fl}) \tag{1}$$

It starts again with an initial temperature distribution T_w at the solid boundary of the flow solver. The results of the NS computation are used to estimate the heat transfer coefficient h and fluid temperature T_{fl}. Substituting them in (1) provides an implicit relation between T_w and q_w that can be used as a boundary condition for the solid conduction computation. The advantage of using (1) as boundary condition is an automatic adjustment of q_w as a function of the new T_w. The latter one is then returned to the fluid solver, and the loop is repeated until convergence.

The remaining problem is the definition of h and T_{fl} from the NS solution. They also need to satisfy Eq. (1) in which T_w is the imposed boundary condition and q_w is the solution of the fluid solver. However, there is only one equation for two unknowns. One possibility is to make an extra fluid flow calculation with a different wall temperature [9] or even an adiabatic one [8]. Substituting the two solutions of q_w in (1) and assuming that h and T_{fl} remain unchanged provides Eq. (2) to define h

$$h = \frac{q^f_{W1} - q^f_{W2}}{T^f_{W1} - T^f_{W2}} \tag{2}$$

T_{fl} can then be calculated by Eq. (1) in function of the imposed T_w and corresponding q_w. The difficulty is to ensure a positive value of h on the entire solid wall because negative values would make the conduction problem ill-posed [8]. They are likely to occur in regions where the heat flux is changing sign.

A simpler and more stable approach is by imposing a constant positive value of h. This is allowed because the value of h only influences the convergence rate. The following shows that it does not affect the final result.

The boundary conditions at iteration n are

$$q^{fn}_W = h(T^{fn}_W - T^n_{fl}) \tag{3}$$

$$q^{sn}_W = h(T^{sn}_W - T^n_{fl}) \tag{4}$$

$$T^{fn+1}_W = T^{sn}_W \tag{5}$$

Equation (3) is used to compute, for a fixed value of h, the value of T_{fl} in function of the value T_w and q_w defined by the fluid computation. Equation (4) is the boundary condition for the conduction calculation in the solid. This results in a new T_w and q_w on the solid wall. Equation (5) defines the boundary condition for the next iteration of the fluid computation. Subtracting (4) from (3) gives

$$q^{fn}_W - q^{sn}_W = h(T^{fn}_W - T^{sn}_W) \tag{6}$$

and substituting (5) results in

$$q^{fn}_W - q^{sn}_W = h(T^{fn}_W - T^{fn+1}_W) \tag{7}$$

This means that if $|T^{fn}_W - T^{fn+1}_W| \to 0$ also $|q^{fn}_W - q^{sn}_W| \to 0$ and $|T^{fn}_W - T^{sn}_W| \to 0$.

Hence, the value of h has no effect on the solution once the continuity of temperature and heat flux between both domains is satisfied. It affects only the convergence history as can be seen from (7). A smaller value of h results in a larger change of the wall temperature between two successive iterations. This leads to a faster convergence but, as confirmed by the numerical experience, also leads to a less stable calculation. The choice of h is a trade off between computational time and stability. A value of 3000 $Wm^{-2}K^{-1}$ has been used for all the computations.

The fluid computations between two successive solid calculations are not continued until full convergence. They are stopped after 100 pseudo time steps to update the wall temperature by a solid conduction calculation. The choice of the number of NS iterations per solid-fluid iteration is driven by a minimization of the total CPU time. The number of pseudo-time steps should be high enough to obtain a modified boundary condition for the FEA code. Full convergence of NS computations is useless as long as the boundary conditions are not correct. Convergence is obtained when q_w and T_w do not change anymore. The initial guess of the wall temperature at the common boundary can be a uniform temperature or the local fluid temperature of an adiabatic NS computation.

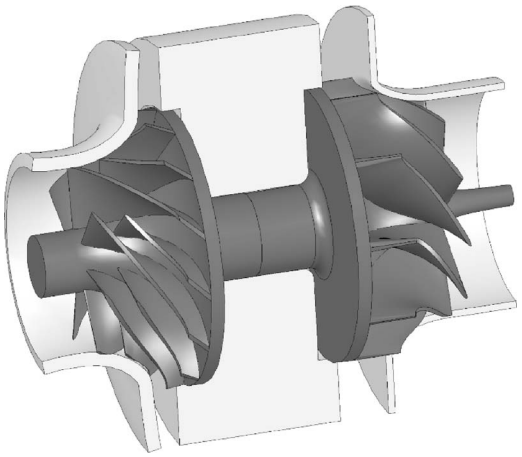

Fig. 1 Micro gas turbine layout

Interpolation Between Grids. Since the appropriate grid generators for both domains are different, the grid points at the common boundaries will not coincide. A NS solver needs small cells at boundaries where the velocity gradients are large. A FEA requires a finer grid distribution in areas of high curvature. Furthermore, the NS solver defines the temperature in the cell center, whereas in the FEA the temperature is stored at the vertices of the elements. Hence, two different interpolations are necessary on the common wall. The T_{fl}, defined in the center of the NS cells, needs to be transferred to the cell center of the FEA where the boundary condition (Eq. (1)) is applied. On the other hand, the temperature at the FEA vertices needs to be transferred to the cell center of the CFD cells. A distance-weighted interpolation based on Shapard's method [16] is used in both cases.

Geometry

The influence of size on heat transfer has been investigated by analyzing three micro gas turbines of different sizes. Each one is an exact geometrical scaling of the baseline geometry, schematically shown in Fig. 1. The main dimensions are listed in Table 1.

Both rotor and stator are made of Kersit. This ceramic material has been selected for its low density and for conserving its high strength at high temperatures. This is needed because the small size of the components does not allow cooling. The thermal conductivity is 28 W/(m K). This is comparable to Ni-based high-

Table 1 Dimensions of different geometries

	geo1	geo2	geo3
Comp. and turb. diameter (mm)	10	20	40
Length shaft (mm)	5	10	20
Diameter shaft (mm)	3	6	12
Blade clearance (mm)	0.075	0.15	0.30
rpm (krpm)	1000	500	250
cavity width (mm)	0.2	0.4	0.8
shaft clearance (mm)	0.1	0.2	0.4

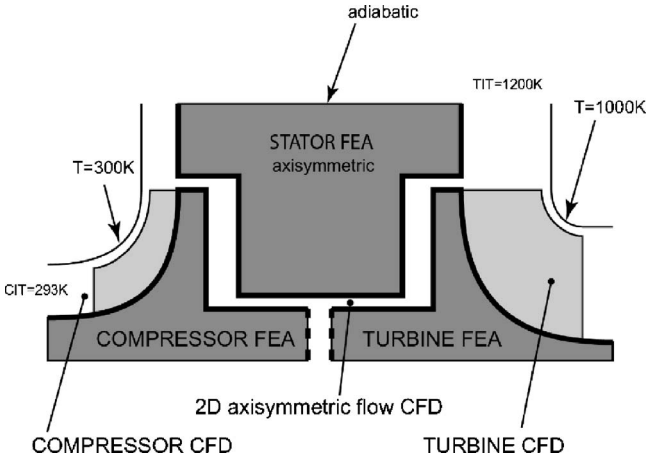

Fig. 2 Computational domains

temperature alloys (~20 W/(m K)). It is lower than steel (~50 W/(m K)) and higher then stainless steel (~15 W/(m K)). No temperature dependencies are implemented.

The cavities between the impellers and the stator are dimensioned for minimum friction losses [17]. The clearance between shaft and stator simulates the flow resistance of the air bearings. Thermal dilatation and machining tolerances justify the rather large clearance between the impellers and nonrotating shrouds.

The three-dimensional (3D) radial compressor has seven full blades and seven splitters with 40 deg trailing-edge lean. The axial inlet flow is at 293 K and 100 kPa. The parallel vaneless diffuser has a radius ratio of 1.5.

The 3D radial turbine has ten blades with radial leading edge and 60 deg trailing-edge blade angle at shroud. The vaneless nozzle inlet flow angle is 72.5 deg at radius ratio 1.5. The inlet total temperature and pressure are respectively 1200 K and 300 kPa.

Computational Details

The computational domains are schematically shown on Fig. 2. NS computations are made for the compressor, turbine, and leakage flow between rotor and stator. Three FEA calculations are required: two for the solid compressor and turbine and one for the stator. Some simplifications have been implemented in order to obtain accurate results in a reasonable amount of CPU time.

Only conduction and convection are taken into account. Radiation is neglected since differences in surface temperatures are small. It has been calculated that the heat transfer due to radiation in the entire turbine of geo 2 is <1 W.

An axisymmetric temperature distribution is assumed in the stator. It constitutes a time-averaged boundary condition for the rotating components. Hence, the stator can be analyzed with a two-dimensional (2D) axisymmetric model.

Adiabatic boundary conditions are imposed at the stator outer wall. This means that all the heat entering the stator from the turbine side is delivered to the compressor and clearance gap.

It is further assumed that the compressor and turbine shroud temperature are mainly defined by external conditions. The compressor shroud temperature is fixed at 300 K, which is close to the ambient temperature at compressor inlet. The proximity of the combustion chamber justifies a turbine shroud temperature of 1000 K.

One can assume that the flow in the cavities and shaft clearance will be axisymmetric and can be analyzed with a 2D grid. The inlet temperature and pressure are equal to the compressor rotor exit values. The exit pressure for the leakage flow is equal to the turbine inlet pressure. The inlet and outlet conditions for the leakage flow are updated only after the first iteration of the conjugate heat transfer calculation and remain constant for the rest of the computation. The 2D grid of the leakage flow inlet section has been axially extended to create a realistic inlet flow velocity profile. However, the heat transfer is calculated only starting from the rim of the compressor disk.

Only one periodic part of the compressor and turbine is analyzed imposing periodic boundary conditions in both solid and fluid calculations. The NS calculations of the compressor and turbine interact with the FEA computations for rotor and stator. The value of wall temperature and T_{fl} are passed between both grids by a regular interpolation as explained previously. The surfaces where the NS and FEA exchange boundary conditions are marked with a thick line in Fig. 2. The boundary conditions for the 2D stator and clearance gap calculations are the circumferentially averaged values of the 3D impeller flow. For the 2D-3D interaction (for example, leakage flow CFD turbine FEA), first a circumferential averaging of the 3D results is made. It is followed by a 2D grid interpolation. The uniform temperature on the shrouds and the 2D stator- and clearance gap calculation results are time-averaged boundary conditions for the 3D calculations.

The difference in periodicity between the turbine ($2\pi/10$) and the compressor ($2\pi/7$) requires a separate FEA for both components. Continuity of temperature and heat flux at the common boundary, marked with a thick dashed line on Fig. 2, is obtained by an iterative update of the temperature. After each FEA analysis, the heat flux at the interface is compared, taking into account the difference in cross section. Any difference between them will give rise to a modified temperature on the interface defined by

$$T_{\text{new}} = T_{\text{old}} + C(q_w^{\text{comp}} + q_w^{\text{turb}}) \tag{8}$$

Positive values of q_w correspond to heat fluxes leaving the solid. C in formula (8) is a positive value fixed at 1×10^{-5} K m^2/W for all computations. More heat leaving the turbine than going in the compressor will lead to an increase of the interface temperature. The turbine heat flux will decrease and more heat will enter the compressor. Higher values of C favor convergence but decrease stability.

The compressor NS grid contains 840,000 cells; the FEA grid has 180,000 elements and 275,000 nodes. The turbine NS grid contains 590,000 cells. The FEA model has also 180,000 elements. The 2D FEA grid for the stator has 20,000 elements, and the leakage flow is modeled on a 2D grid with 10,000 axisymmetric cells.

Calculations are run in parallel on three CPUs. One is dedicated to the compressor, one to the turbine, and the third one calculates the gap flow and stator heat transfer. Each CPU switches between a NS and FEA calculation for one part of the model. A typical convergence history of the temperatures L^∞ residuals ($|T^{sn+1} - T^{sn}|_{\max}$) is plotted in Fig. 3. Convergence of the entire model is obtained after ~20 solid-fluid iterations.

Results

CHT computations have been performed on six different test cases. The first three are the three scaled geometries defined in Table 1. A fourth one is a modified version of geo2 and attempts to reduce the heat conduction by a modification of the stator geometry. The fifth one investigates the influence of the material characteristics on the heat transfer, and a last one evaluates the possible impact of the shroud boundary conditions.

Figure 4 presents a schematic view on the geometry and defines some of the contributions to the heat flux between the turbine and the compressor. The main results obtained in the six calculations are listed in Table 2. A and I present the total heat flux on the shroud, including, respectively, the diffuser and nozzle.

Figures 5 and 6 show the temperature field in the solids for the smallest and largest geometry. A more detailed view on the compressor and turbine rotor of geo2 is shown in Figs. 7 and 8. Comparison between Figs. 5 and 6 makes clear that the compressor

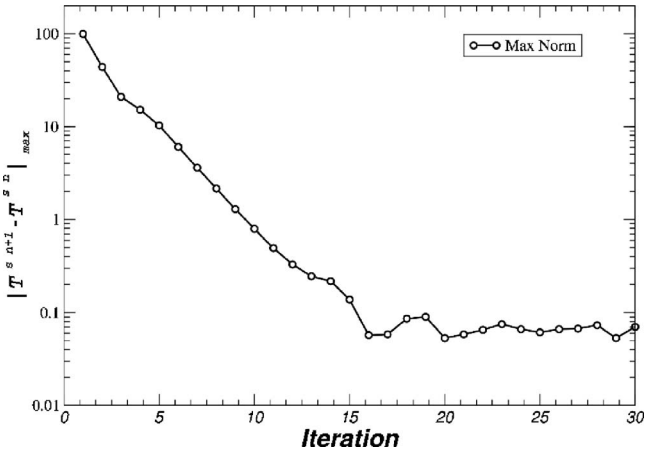

Fig. 3 Convergence history of L^∞

and turbine surface temperatures become more uniform with downscaling. However, nonuniformities exist even for very small gasturbines.

One observes a non-negligible temperature difference between the blade tip and hub. This is most pronounced for the turbine blades that act as long cooling vanes. The hot turbine shroud heats up the nearby fluid and the blade tips. This is responsible for the large radial temperature gradient near the trailing edge. The total fluid cooling by the turbine (row H in Table 2) for geo2 is the sum of 58 W by blade cooling and 27 W by hub surface cooling. The 14 compressor blades transmit 35 W to the flow while the hub contributes with 41 W. This gives a total of 76 W (row B in Table 2).

The heat transfer in the micro gas turbine can be divided into two main parts: the heat trough the impeller shaft and the heat trough the stator. Each part will be discussed in detail in the next sections.

Impeller Heat Transfer. A large temperature difference is observed between the compressor and turbine impeller. In spite of this, only a small amount of heat from turbine to compressor is predicted. This heat transfer can also be divided into two

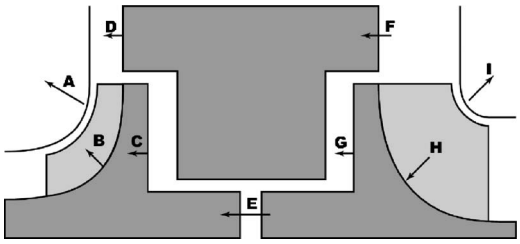

Fig. 4 Heat transfer in the micro gas turbine

Table 2 Heat (in watts) in all geometries

	geo1	geo2	geo3	geo2 mod. stat.	geo2 steel	geo2 adiab. shroud
A	84	217	490	217	223	0
B	30	76	213	65	97	76
C	12	35	116	26	37	35
D	50	140	382	56	160	134
E	12	25	44	25	46	25
F	72	208	655	128	231	206
G	10	46	169	53	44	46
H	26	85	257	96	103	86
I	28	95	462	86	91	0

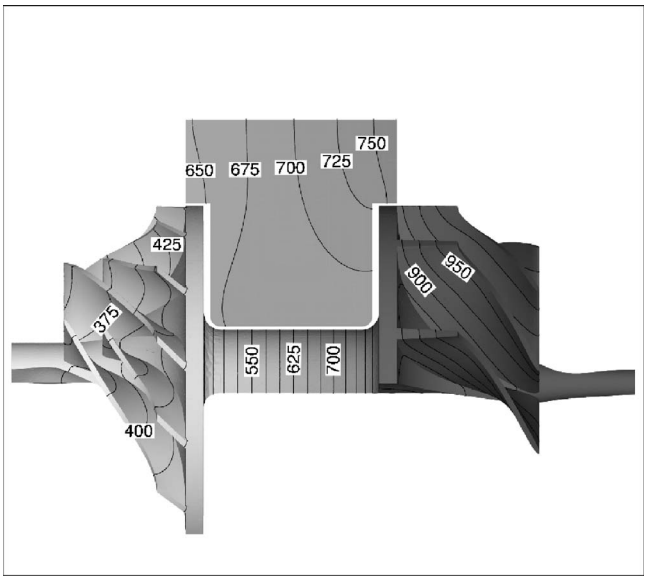

Fig. 5 Temperature distribution (in degrees Kelvin) in geo1. The interval between the isolines is 25 K.

contributions.

A first one is the heat transfer trough the shaft (arrow E in Fig. 4). The shaft thermal resistance, defined by $(\pi d^2 \lambda)/l$, equals 0.079 W/K in geo2. This explains why a 316 K temperature difference is needed to pass 25 W through the shaft of 10 mm length. Only a small amount of heat is leaving the shaft to enter the leakage flow.

The second contribution is passing trough the back of the compressor and turbine disks (arrows C and G in Fig. 4). It is influenced by the thermal resistance of the stator and the flow in the gap. The thermal resistance of the stator is much smaller than the one of the rotor because of a much bigger cross section. The main resistance for the second heat flux thus results from the flow in the cavity.

The pressure difference between the compressor exit and turbine inlet results in a leakage flow from compressor to turbine. This flow acts like a coolant taking away heat from the stator and

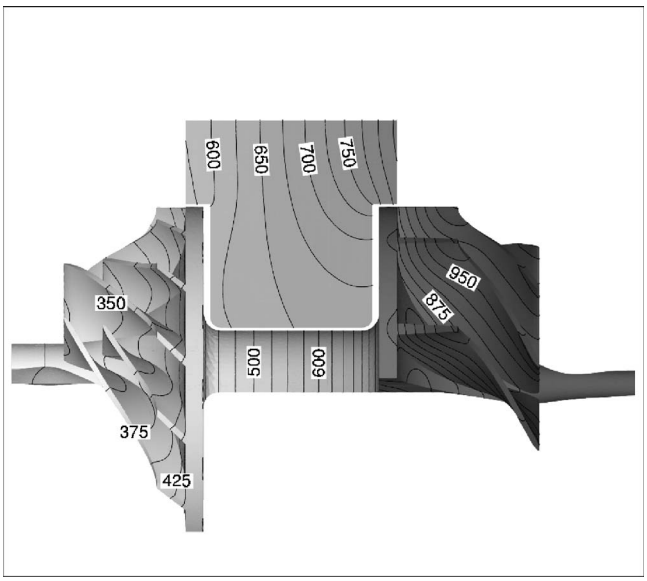

Fig. 6 Temperature distribution (in degrees Kelvin) in geo3. The interval in between the isolines is 25 K.

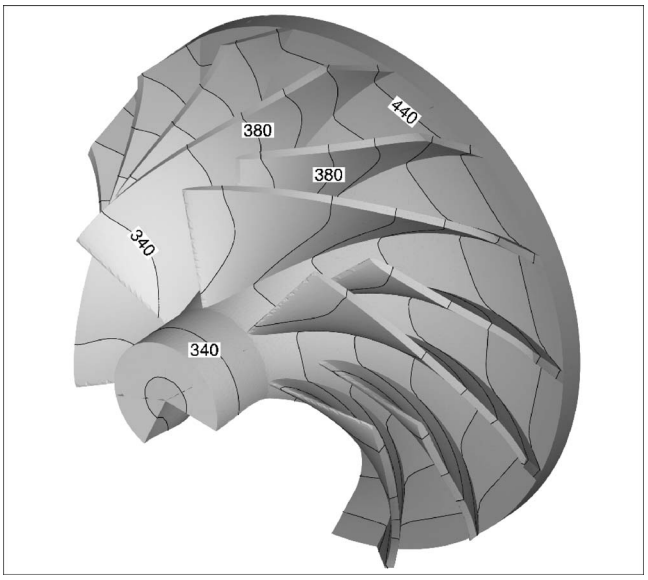

Fig. 7 Temperature distribution (in degrees Kelvin) in compressor of geo2. The interval in between the isolines is 20 K.

turbine rotor. The flow pattern in the cavities behind the compressor and turbine are visualized in Fig. 9 together with the total temperature distribution. The flow is centrifuged outwards near the impeller and driven inward near the stator by the radial pressure gradient. This recirculation not only enhances the heating by disk friction losses but also favors the heat transfer in the cavity. Note that the computed flow in the cavity is a 3D flow, but only the projection of the velocity on the meridional plane is shown in Fig. 9.

The flow in the compressor cavity is heated by the stator wall and disk friction. A considerable amount of the heat is transmitted to the impeller through the compressor disk. The flow in the turbine cavity is heated on the disk side, but not much heat is transmitted to the stator since the stator and fluid have almost the same temperature.

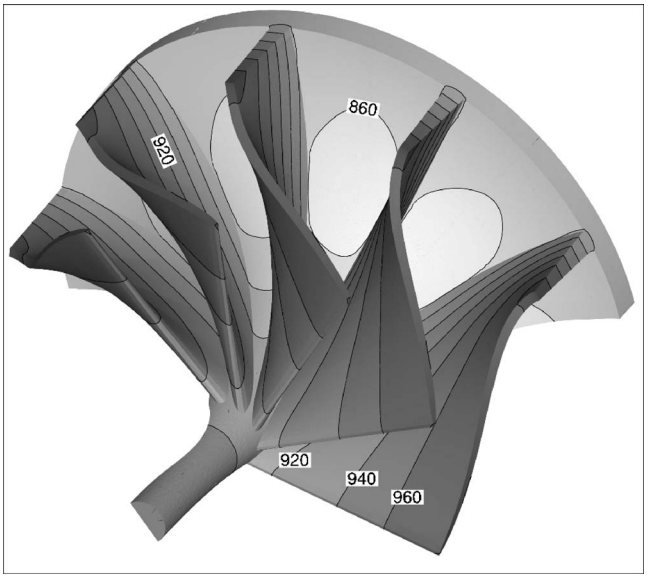

Fig. 8 Temperature distribution (in degrees Kelvin) in turbine of geo2. The interval in between the isolines is 20 K.

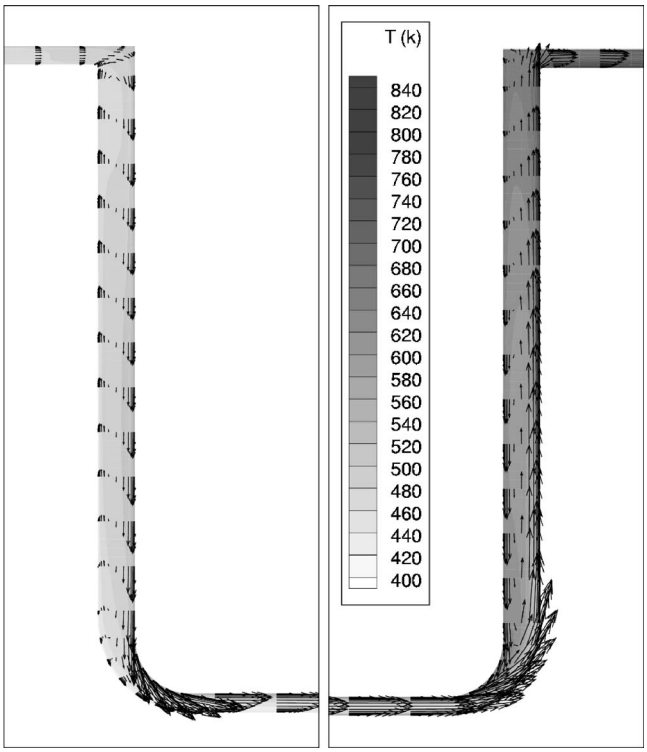

Fig. 9 Total temperature (in degrees Kelvin) and flow field in the compressor (left) and turbine (right) cavity

Scale Effect. The influence of size on the impeller heat transfer can be investigated by comparing the first three columns of Table 2. A simple analytical model can be derived by splitting the heat transfer into the two contributions mentioned previously. The heat transfer in the shaft is proportional to the cross section and decreases with shaft length. Hence, this part of the heat transfer changes linearly with the scale factor D_2. The disk friction heating is proportional to the $D_2^2U_2^3$ [17]. Aerodynamic scaling requires a constant U_2 so that the heat production by disk friction scales with D_2^2. Also the heating by the stator is proportional to the surface ($\sim D_2^2$). The total heat flux between turbine and compressor impeller can then be written as

$$Q = C_1 D_2 + C_2 D_2^2 \tag{9}$$

Substituting the numerical results of the geo1 and geo2 in this expression allows defining the coefficients C_1 and C_2. Using this relation to predict the heat flux for the geo3 impeller results in 216 W, which is very close to the Navier-Stokes and finite element analysis prediction of 213 W. This simple analytical model allows extrapolation of present results to smaller and larger geometries. It also makes clear that the heat transfer is not scaling only with $\sim D_2^2$.

The influence of the gas turbine dimensions on compressor power and efficiency is listed in Table 3. Note that, in order to compare the heat transfer, power, and efficiency, the three geometries need to work at corresponding operating points. Hence, the mass flow in the three cases is fixed respectively at 5.375, 21.5, and 86 g/s, proportional to the square of the diameters ($\sim D_2^2$). The same scaling applies to the compressor and turbine shaft power (P), as they also change with mass flow. Q is the heat added to the fluid by the hub, blades, and shroud, and changes according to Eq. (9). Hence, the heat transfer to power ratio Q/P increases with downscaling.

Performance is compared to that of an adiabatic computation. This allows the distinction between the change in efficiency due to Reynolds number and heat transfer. The difference between both

Table 3 Compressor power and efficiency

	geo1	geo2	geo3
$P(W)$	900	3 570	14 250
$Q(W)$	11.6	34.4	124
Q/P	1.28%	0.96%	0.87%
η_{t-t}	72.6	74.4	75.8
Adiabatic			
$P_{ad}(W)$	894	3 505	14 047
$\eta_{t-t,ad}$	74.3	75.1	76.5
$\Delta\eta_{ad}$	1.7	0.7	0.7

computations is a measure for the drop in performance due to the heat transfer and is listed in the last row of Table 3. The increase of Q/P is responsible for the drop in efficiency when downscaling.

The turbine power, heat flux, and efficiencies are listed in Table 4. Increasing the size from geo2 to geo3 has almost no impact on efficiency. The gain in efficiency, which can be expected from the increasing Reynolds number, is almost completely annihilated by a larger fluid cooling on the constant temperature shroud ($\sim D_2^2$).

Influence of Shroud Boundary Condition. An additional computation of geo2 with adiabatic wall conditions at both compressor and turbine shroud has been performed. Results are listed in Table 2 (column 6) and allow evaluation of the impact of the constant wall temperature condition imposed at the shrouds. Comparison of the data of geo2 and geo2 adiabatic shroud indicates almost no change in internal heat transfer (rows B to H). But the absence of cooling at the compressor shroud results in a net fluid heating of 76 W instead of 34 W previously. This results in a drop in efficiency from 74.4% to 71.2%. The impact is smaller at the turbine where the cooling at hub and shroud (137 W) is replaced by hub cooling only (86 W).

Comparison With 2D Machines. Manufacturing techniques may limit the impeller to 2D geometries for ultra small micro gas turbines [1–4]. This results in a decrease of mass flows and power typically of the order of 4. The Q/P ratio increases by the same ratio, resulting in a proportional impact on efficiency. Hence, the drop in efficiency for a 2D 10 mm diam impeller would therefore be ~8%, which is still lower than previously assumed [1–3,18].

Stator Heat Transfer. The stator shows a rather linear temperature variation from the turbine to the compressor side (Figs. 5 and 6). The heat exchange in the stator, between the turbine nozzle and compressor diffuser, is much larger than between the impellers. It increases the combustion chamber inlet temperature and decreases the temperature at the inlet of the turbine impeller. The heat transfer in the stator between the turbine nozzle and the diffuser acts like a badly placed recuperator. It is heating up the flow after compression but cools it down before the expansion takes place, leaving less energy available to extract in the turbine. This heat transfer is not affecting the efficiency of compressor or turbine since no more work is added to the fluid during the heating. However, the power output of the micro gas turbine decreases at constant combustion temperature. The effect is also increasing with decreased size. In the absence of a recuperator, it could easily be compensated by increasing the combustion chamber outlet temperature proportional to the increase of inlet temperature.

These temperature changes unfavorably affect the effectiveness of the recuperator. The turbine outlet temperature being lower and the compressor outlet temperature being higher, the heat transfer in the recuperator will decrease. The corresponding increase of gas turbine outlet temperature results in a lower cycle efficiency.

Table 4 Turbine power and efficiency

	geo1	geo2	geo3
$P(W)$	1 079	4 492	18,377
$Q(W)$	−43	−137	−424
η_{t-t}	88.3	88.9	89.2

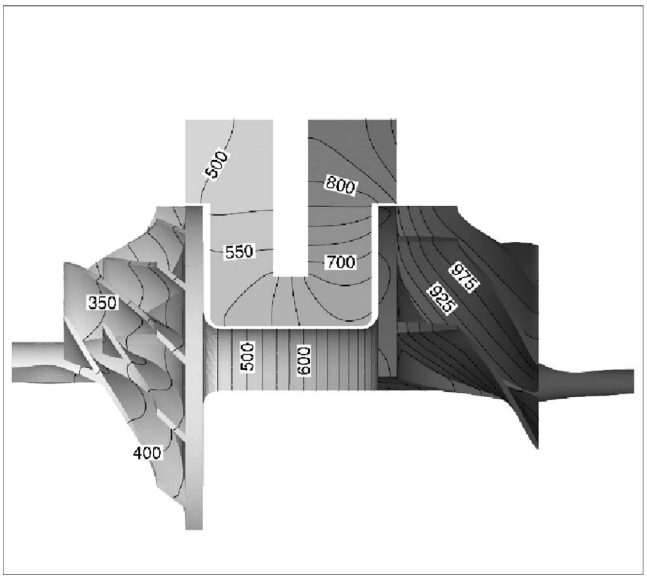

Fig. 10 geo2 with a modified stator geometry. A 2 mm gap is inserted in the middle of the stator. The interval in between the isolines is 25 K.

Modified Stator Geometry. Figure 10 shows the temperature distribution for geo2 with modified stator geometry. A gap of 2 mm width is inserted into the stator. Adiabatic boundary conditions are applied to the gap walls, assuming that a good insulator is placed inside the gap.

The gap results in a reduced heat transfer inside the stator. The heat flux in the nozzle drops from 208 W to 128 W, the heat given to the diffuser drops from 140 W to 56 W (Table 2). Another benefit of the stator modification is a decrease in temperature on the stator side of the compressor cavity. The heat transfer to the compressor impeller drops from 76 W to 65 W. On the other hand, the turbine sinks more heat since the turbine inlet temperature is higher. That part of the heat transfer increases from 85 W to 96 W. Almost all the additional heat contributes to an increase of heat flux by the leakage flow from 77 W to 102 W. Both the turbine and stator contribute to this. The leakage flow becomes a more efficient coolant for the turbine impeller.

Change of Solid Material. Changing the material of the micro gas turbine has more impact on the rotor heat transfer than on the stator. The temperature distribution for geo2 made in steel (conductivity 50 W/(m K)) is shown in Fig. 11. The higher conductivity results in an increase of the shaft heat transfer (arrow E in Fig. 4) from 25 W to 46 W. The heat transfer through the compressor and turbine cavities remains almost constant. Table 2 shows a small increase from 35 W to 37 W for the compressor (arrow C in Fig. 4) and a similar drop from 46 W to 44 W for the turbine (arrow G). This is explained by the fact that the heat transfer through the stator is mainly defined by disk friction and the thermal resistance of the cavity flow. Combining both changes in heat transfer results in a small increase of the total heat transfer with a negligible impact on performance.

The heat transfer in the stator increases slightly. The heat added

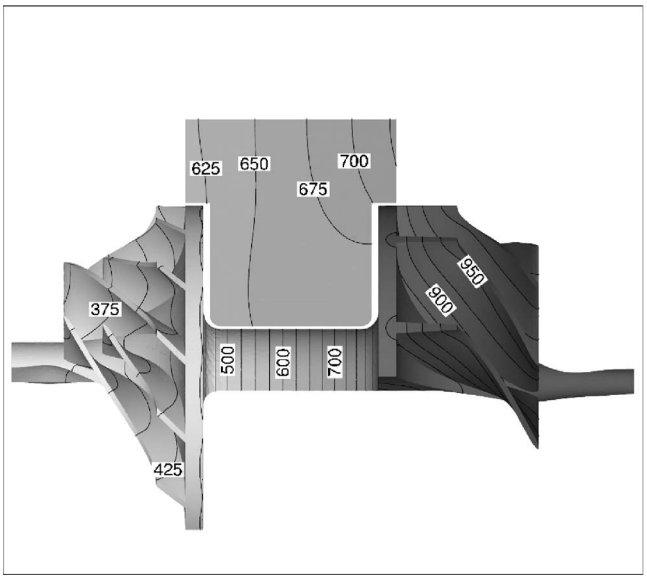

Fig. 11 geo2 made of steel. The interval in between the isolines is 25 K.

to the flow in the compressor diffuser (arrow D) increases from 140 W to 160 W, the cooling in the turbine nozzle (arrow F) increases from 208 W to 231 W.

Conclusions

A conjugate heat transfer solver has been developed and applied to micro gas turbines of different sizes, shapes, and materials.

The three main contributions to the internal heat transfer have been evaluated.

- The heat transfer in the shaft increases linearly with the scale factor. It depends on the material characteristics and can easily be predicted by a one-dimensional analytical approach.
- The heat transfer in the cavities varies with the square of the scale factor and is mainly defined by the conductivity of the fluid.
- The heat transfer on the large surfaces of diffuser and nozzle is the main contribution and can be substantially reduced by a simple modification of the stator geometry. This heat transfer depends on both solid and fluid conduction properties with more weight to the fluid conduction.

Shroud boundary conditions have a direct influence on the compressor and turbine performance and should be defined with care. It turned out that the compressor wall temperature is lower and the turbine temperature is higher than what was assumed in previous studies. It results in a smaller impact of the internal heat transfer on the overall gas turbine performance.

Acknowledgment

This research is sponsored by the IWT, the Institute for the Promotion of Innovation by Science and Technology in Flanders, Belgium, Project No. SBO 030288 "PowerMEMS."

Nomenclature

C = constants
d = shaft diameter
D_2 = scale factor
h = heat transfer coefficient
l = shaft length
P = power
q = flux
Q = total amount of heat transfer
T = temperature
η = polytropic efficiency
λ = conductivity of solid material (W/m^oK)

Subscripts

fl = in the flow
W = at the wall

Superscripts

comp = in the compressor
f = from the fluid solver
n = iteration number n
s = from the solid solver
turb = in the turbine

References

[1] Gong, Y., Sirakov, B. T., Epstein, A. H., and Tan, C. S., 2004, "Aerothermodynamics of Micro-Turbomachinery," ASME Paper No. GT2004-53877.
[2] Isomura, K., Murayama, M., and Kawakubo, 2001, "Feasibility Study of a Gas Turbine at Micro Scale," ASME Paper No. 2001-GT-101.
[3] Sirakov, B. T., Gong, Y., Epstein, A. H., and Tan, C. S., 2004, "Design and Characterization of Micro-Compressor Impellers," ASME Paper No. GT2004-53332.
[4] Onishi, T., Burguburu, S., Dessornes, O., and Ribaud, Y., 2005, "Numerical Design and Study of a MEMS-Based Micro Turbine," ASME Paper No. GT2005-68168.
[5] Bohn, D., Bonhoff, B., and Schonenborn, H., 1995, "Combined Aerodynamic and Thermal Analysis of a Turbine Nozzle Guide Vane," IGTC Paper No. 95-108.
[6] Heidmann, J. D., Kassab, A. J., Divo, E. A., Rodriguez, F., and Steinthorsson, E., 2003, "Conjugate Heat Transfer Effects on a Realistic Film-Cooled Turbine Vane," ASME Paper No. GT2003-38553.
[7] Han, Z.-X., Dennis, B. H., and Dulikravich, G. S., 2000, "Simultaneous Prediction of External Flow-Field and Temperature in Internally Cooled 3-D Turbine Blade Material," ASME Paper No. 2000-GT-253.
[8] Montenay, A., Paté, L., and Duboué, J., 2000, "Conjugate Heat Transfer Analysis of an Engine Internal Cavity," ASME Paper No. 2000-GT-282.
[9] Verdicchio, J. A., Chew, J. W., and Hills, N. J., 2001, "Coupled Fluid/Solid Heat Transfer Computation for Turbine Discs," ASME Paper No. 2001-GT-0205.
[10] York, W. D., and Leylek, J. H., 2003, "Three-Dimensional Conjugate Heat Transfer Simulation of An Internally-Cooled Gas Turbine Vane," ASME Paper No. GT2003-38551.
[11] Bohn, D., Heuer, T., and Kusterer, K., 2003, "Conjugate Flow and Heat Transfer Investigation of a Turbo Gharger—Part I: Numerical Results," ASME Paper No. GT2003-38445.
[12] Arnone, A., 1994, "Viscous Analysis of Three-Dimensional Rotor Flow Using a Multigrid Method," ASME J. Turbomach., **116**, pp. 435–445.
[13] Grag, V. K., 2002, "Heat Transfer Research on Gas Turbine Airfoils at NASA GRC," Int. J. Heat Fluid Flow, **23**, pp. 109–136.
[14] SAMCEF FEA code by Samtech Group, www.samcef.com
[15] Lassaux, G., Daux, S., and Descamps, L., 2004, "Conjugate Heat Transfer Analysis of a Tri-Dimensional Turbine Blade Internal Cavity," 24th ICAS.
[16] Shepard, D., 1968, "A Two-Dimensional Interpolation Function for Irregularly Spaced Data," *Proc. 23rd ACM National Conference*, ACM, New York, pp. 517–524.
[17] Daily, J. W., and Nece, R. E., 1960, "Chamber Dimension Effects on Reduced Flow and Frictional Resistance of Enclosed Rotating Disks," ASME J. Basic Eng., **82**(1), pp. 217–232.
[18] Van den Braembussche, R. A., Alsalihi, Z., and Verstraete, T., 2004, "Heat and Power Balance in Micro Gasturbine Rotors," *Proc. of POWERMEMS*, Kyoto, Japan, pp. 84–87.

High-Frequency Effects in the Aspirating Probe

S. J. Payne

A. J. W. Moxon

Department of Engineering Science,
University of Oxford,
Oxford OX1 3PJ,
United Kingdom

The aspirating probe has recently been successfully used to measure entropy within a turbomachine; however, it was found that its sensitivity to total pressure and total temperature fluctuations was significantly altered at high frequencies. If the aspirating probe is to be used to measure unsteady flow fields accurately, these high-frequency effects must be better understood. The analysis of this behavior presented here shows that there are three effects that must be considered: the frequency response of the hot wires, the presence of Mach number fluctuations inside the probe, and the change in heat transfer from the hot wires at high frequencies. A theoretical analysis of the first effect has provided a correction factor that can be used for any hot wire, dependent solely on the baseline heat transfer ratio, the overheat ratio, and the time constant of the hot wires. The second and third effects have been examined numerically, since no theoretical solution is known to exist. The Mach number fluctuations are found to be well predicted by a simple one-dimensional solver and to show a variation of ±2.4% in Mach number at the hot-wire plane for the geometry and flow field considered here. The variation in heat transfer with frequency is found to be negligible at high overheat ratios, but significant at overheat ratios below ~0.4. Coefficients that determine how the measured total pressure and total temperature depend on the actual total pressure, total temperature, and Mach number have been derived, and these show significant variation with the values of the two overheat ratios. Using synthetic data, based on previous experimental data, the effects on the probe measurement accuracy are analyzed. This shows that the amplitudes of total pressure and total temperature are reduced. At widely spaced overheat ratios, the amplitudes are reduced by similar amounts, but at smaller spacing the reductions become dissimilar, resulting in highly erroneous entropy/R measurements. High-frequency effects thus have a significant effect on the performance of the aspirating probe and should be carefully considered when using it in a highly unsteady flow field. [DOI: 10.1115/1.2720872]

1 Introduction

The flow fields found in turbomachines are highly complex and unsteady, due to the interaction between adjacent blade rows. Experimental data are still highly prized in interpreting the flow fields and thus improving our understanding of interaction processes, as well as for validating CFD codes. However, the mechanisms that govern loss, and hence determine efficiency, are still far from being fully understood, and their impact on the efficiency of individual blade stages has only received limited attention. Since "the only rational measure of loss in an adiabatic machine is entropy creation" [1], any attempts to understand loss mechanisms require the measurement of entropy.

However, the only current accurate means of measuring entropy is the aspirating probe, originally proposed by [2]. Although thin-film heat transfer gages are an alternative method of measuring total temperature at high frequencies [3], the aspirating probe remains the only means of simultaneously measuring total pressure and total temperature both spatially and temporally. This is crucial in obtaining the necessary measurement accuracy, as was shown in [4]. The other advantages associated with the aspirating probe include a high-frequency response, good spatial resolution, small sensitivity to flow angle, and a reduction in the effects of probe blockage. Other authors have used the aspirating probe in turbomachines, including [5,6], although an extra semiconductor probe was required to give more accurate results. This extra probe was shown by [7] to be unnecessary if care was taken in the design and calibration of the aspirating probe: the authors also presented stationary measurements of total pressure and total temperature, as did [8], who calculated the local isentropic efficiency. Similarly, [9] used the aspirating probe in the facility at VKI behind a turbine stage at higher rotational speeds. Most recently, measurements of unsteady entropy in a model of a high-pressure turbine stage operated at engine-representative conditions have been presented (Fig. 1) [4,10]. These measurements enabled the quantification of the different loss mechanisms on the stage efficiency to be performed for the first time.

The aspirating probe essentially consists of two hot wires placed upstream of an orifice (Fig. 2). By maintaining a low pressure downstream of the orifice, it remains choked and the probe "sucks" in the flow passing toward it. By calculating the mass flow for a given total pressure, total temperature, and Mach number, the mass flow at the choked orifice and the hot-wire plane can be equated in the steady state to give

$$(\rho u)_w = \sqrt{\frac{\gamma}{R}}\frac{p_o}{\sqrt{T_o}}\frac{A^*}{A_w}\left(\frac{2}{\gamma+1}\right)^{(\gamma+1)/2(\gamma-1)} \tag{1}$$

The Reynolds number at the hot-wire plane is thus dependent solely on the total pressure and total temperature. The steady-state Mach number is fixed by the area ratio

$$M_w\left(1+\frac{\gamma-1}{2}M_w^2\right)^{[(\gamma+1)/2(\gamma-1)]} = \frac{A^*}{A_w}\left(\frac{\gamma+1}{2}\right)^{[(\gamma+1)/2(\gamma-1)]} \tag{2}$$

For a hot wire used with constant temperature anemometry (CTA) in a constant Mach number flow, the Nusselt number is solely dependent on the Reynolds number (see, for example, [11]). When placed inside the aspirating probe, hot wires can thus be used to measure the Reynolds number, using the general relationship between Nusselt number and Reynolds number for a given Mach number [12]

Contributed by the Turbomachinery Division of ASME for publication in the JOURNAL OF TURBOMACHINERY. Manuscript received May 16, 2005; final manuscript received October 9, 2006. Review conducted by Wing Ng.

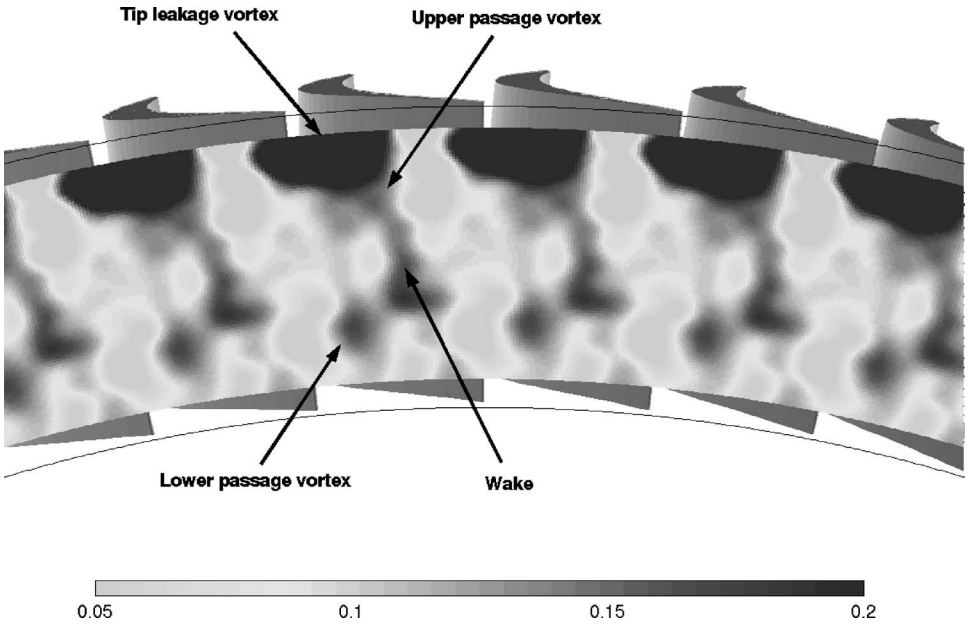

Fig. 1 Experimental entropy/R contour plot at 30% vane position (from [4])

$$\mathrm{Nu} = A + B\mathrm{Re}^n \tag{3}$$

When combined with the standard hot-wire equation, this gives the aspirating probe calibration equation

$$E^2 = \left[C\left(\frac{p_o}{\sqrt{T_o}} \right)^n + D \right](T_m - \eta T_o) \tag{4}$$

where the recovery factor η is the ratio of recovery temperature to total temperature and C, D, and n are constants. These constants are all found by calibration, despite η being a known function of Mach number, to give the greatest accuracy. Two hot wires are thus required to measure both total pressure and total temperature. Although the wire temperatures should be far apart to give a high level of measurement accuracy, there is a lower limit due to the need for a high bandwidth and an upper limit due to the melting temperature of the wire.

However, it was shown in [10], that there are significant high frequency effects present in the aspirating probe that affect its performance at high frequencies relative to a steady state calibration. The rotor blades rotate at ~10,000 rpm in the experiments by [10], which require the aspirating probe to measure flow phenomena at a fundamental frequency of 10 kHz, given that there are 60 rotor blades. Since multiple harmonics will also need to be measured, the device must have a bandwidth of several multiples of this frequency. Given the nature of operation of the aspirating probe, there are three possible causes of variations at these frequencies from the steady-state behavior. The first is the frequency response of the hot wires, which may respond differently at different frequencies. The second is the fluctuations in Mach number within the aspirating probe, due to the compressibility of the flow.

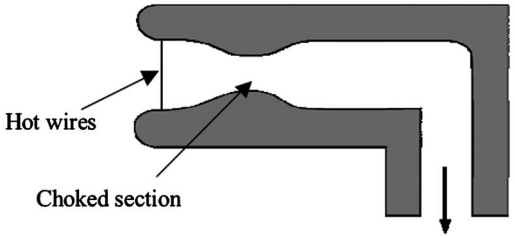

Fig. 2 Aspirating probe

The third is the variations in heat transfer from the hot wire to the flow at high frequencies. These will each be examined, in turn, before being combined to analyze the complete frequency response of the aspirating probe in detail.

2 Hot Wire Frequency Response

A number of authors have examined the frequency response of a hot wire. Reference [13] examined the effects of fluctuations in the flow temperature on the wire temperature distribution. However, no fluctuations in heat transfer coefficient or current were considered, and the overall wire resistance was not kept constant. Reference [14] defined a fluctuation ratio as the ratio of heat transfer at high frequencies, when the conduction fluctuations drop to zero, to that at steady-state conditions. Although the mean wire temperature was kept constant, the results are only applicable for low overheat ratios and no general solution is given, although two distinct break frequencies were found. Reference [15] performed a more detailed analysis, which was confirmed well by experimental results up to the maximum experimental frequency of 800 Hz. In this case, as with [14], the dependent parameters are not clearly expressed and the physical background is not clear.

The most recent attempt to compensate for high-frequency effects experimentally used a step change in flow temperature [9]. A series of first-order differential equations was developed and used to compensate for conduction effects at all frequencies. This has the advantages of being experimentally derived and applicable to any hot wire; however, neither the derivation nor the application of this procedure is described clearly. A complete theoretical analysis of the frequency response of a hot wire is thus presented here for completeness. This provides compensation factors for any hot wire at any frequency, clearly outlining the physical basis for the solution. The details of the derivation are outlined in the Appendix, with only the final results being presented here.

The solution is based on the general hot-wire equation [13], with radial variations in wire temperature and the radiation heat transfer assumed to be negligible. These were shown by [10] to be valid assumptions for typical flow conditions and wire properties. By assuming sinusoidal fluctuations with time, a reasonable assumption since the flow field observed in turbomachines is highly periodic, both the steady-state and time varying equations can be solved for wire temperature over wire length to give a transfer function style relationship of the form

$$Z_I = G_a Z_a + G_h Z_h \tag{5}$$

The fractional change in wire current Z_I is related solely to the fractional changes in flow temperature Z_a and heat transfer coefficient Z_h through nondimensional transfer functions G_a and G_h, respectively. Note that the fractional changes in current are directly equivalent to those in voltage, since the wire resistance is kept constant in constant temperature anemometry up to a bandwidth of many tens of kilohertz. The transfer functions can be expressed in nondimensional form as a function of a number of other nondimensional quantities and frequency

$$G_a(\omega') = -\frac{1}{2\tau}\frac{(\xi_1-1)^2\omega'\left\{F(1+\omega') + \left(\frac{\xi_{11}-1}{\xi_1-1}\right)[(\xi_1-1)+\xi_1 a]\right\}}{\xi_1\{(1+\omega')a(\xi_1-\xi_{11}) + \omega'(\xi_{11}-1)[(\xi_1-1)+\xi_1 a]\}} \tag{6}$$

$$G_h(\omega') = \frac{1}{2}\frac{[(\xi_1-1)+\xi_1 a][(\xi_1-\xi_{11}) + \omega'\xi_{11}(\xi-1)]}{\xi_1\{(1+\omega')a(\xi_1-\xi_{11}) + \omega'(\xi_{11}-1)[(\xi_1-1)+\xi_1 a]\}} \tag{7}$$

Making use of the simplifications detailed in the Appendix, these transfer functions can be shown to be completely characterized by two forms of the overheat ratio, a and τ,

$$a = \alpha(T_m - \bar{T}_a) \tag{8}$$

$$\tau = \frac{(T_m - \bar{T}_a)}{\bar{T}_a} \tag{9}$$

the ratio of heat transfer by conduction to convection χ,

$$\chi = \frac{d}{2l}\sqrt{\frac{k_w}{k\mathrm{Nu}}} \tag{10}$$

the frequency response of the supports, $F(j\omega)$, and the nondimensional frequency,

$$\omega' = j\omega\frac{\bar{K}_1}{\bar{\beta}_1} \tag{11}$$

The parameter $\bar{K}_1/\bar{\beta}_1$ represents the attenuation frequency of heat waves along the wire and can be considered as the time constant of the wire.

Note that ξ_1 is calculated iteratively from the overheat ratio and the heat transfer ratio

$$\xi_1 = \frac{1}{\chi}\sqrt{\frac{(\xi_1-1)}{(\xi_1-1)+\xi_1 a}} \tag{12}$$

In addition,

$$\xi_{11} = \xi_1\sqrt{1+\omega'} \tag{13}$$

The frequency response of the wire supports is not well characterised, but a first-order low-pass filter is usually assumed, with a time constant of $\sim$1 s [13,14]. Since this is so much lower than the frequencies of interest, this is adopted here; its precise value is unimportant since complete attenuation has occurred by the frequencies of interest.

The absolute values of the coefficients G_a and G_h are not of primary interest. What is more important is their deviation with frequency from the steady-state values. By allowing the frequency to tend to zero, Eqs. (6) and (7) reduce to

$$G_{a,ss} = -\frac{1}{\tau}\frac{(\xi_1-1)^2(1+a)}{2(\xi_1-1)^2 + \xi_1 a(2\xi_1-3)} \tag{14}$$

$$G_{h,ss} = \frac{1}{2}\frac{((\xi_1-1)+\xi_1 a)(2\xi_1-3)}{2(\xi_1-1)^2 + \xi_1 a(2\xi_1-3)} \tag{15}$$

As χ tends to zero, as for an infinitely long wire, these tend toward $-1/2\tau$ and $1/2$, respectively, as expected. The changes in coefficients with frequency relative to the steady-state values are thus,

$$\frac{G_a(\omega')}{G_{a,ss}} = \frac{1}{2}\frac{[2(\xi_1-1)^2 + \xi_1 a(2\xi_1-3)]\omega'\left[F(1+\omega') + \left(\frac{\xi_{11}-1}{\xi_1-1}\right)[(\xi_1-1)+\xi_1 a]\right]}{\xi_1(1+a)\{(1+\omega')a(\xi_1-\xi_{11}) + \omega'(\xi_{11}-1)[(\xi_1-1)+\xi_1 a]\}} \tag{16}$$

$$\frac{G_h(\omega')}{G_{h,ss}} = \frac{[2(\xi_1-1)^2 + \xi_1 a(2\xi_1-3)][(\xi_1-\xi_{11}) + \omega'\xi_{11}(\xi-1)]}{\xi_1(2\xi_1-3)\{(1+\omega')a(\xi_1-\xi_{11}) + \omega'(\xi_{11}-1)[(\xi_1-1)+\xi_1 a]\}} \tag{17}$$

Note that τ is removed from the equations; these ratios are thus solely dependent on the heat transfer ratio χ, the overheat ratio a, and the time constant of the wires, $\bar{K}_1/\bar{\beta}_1$.

The flow conditions studied by [4] were a total pressure of 3.25 bar, a total temperature of 297 K, Mach number of 0.45 with a hot-wire diameter and length of 5 μm and 1.2 mm, respectively. This gives a heat transfer ratio χ=0.139. The time constant of the wire was set to be 1.29 ms. The values of the transfer functions in Eqs. (16) and (17) with frequency for varying overheat ratios are thus shown in Fig. 3. There are two break frequencies, one due to the attenuation of heat transfer to the supports, and the other due to the attenuation of heat waves along the wire. The first only affects the sensitivity to temperature fluctuations and occurs at $\sim$1 Hz, but the second affects both sensitivities. Although it starts to occur at $\sim$10 kHz, its effects last until $\sim$1 MHz. The phase errors are negligible. For a given hot wire in a given flow field, the frequency response can thus be predicted for any overheat ratio. Note that the deviation from steady state behavior is smallest at high values of the overheat ratio.

3 Mach Number Fluctuations

The calibration of the aspirating probe assumes that the mass flow through the flow is constant at all positions along the probe. This then results in constant Mach number at the hot-wire plane (Eq. (2)), one of the key factors governing the probe's behavior. Although this is clearly true in the steady state, it is possible that compressibility effects influence the probe's behavior at high frequencies. Since the Nusselt number for a heated wire is dependent on both Reynolds number and Mach number [11], if the Mach number fluctuates within the probe at high frequencies, use of the steady-state calibration will introduce an error into the prediction of Reynolds number.

To examine the likely impact of Mach number fluctuations on

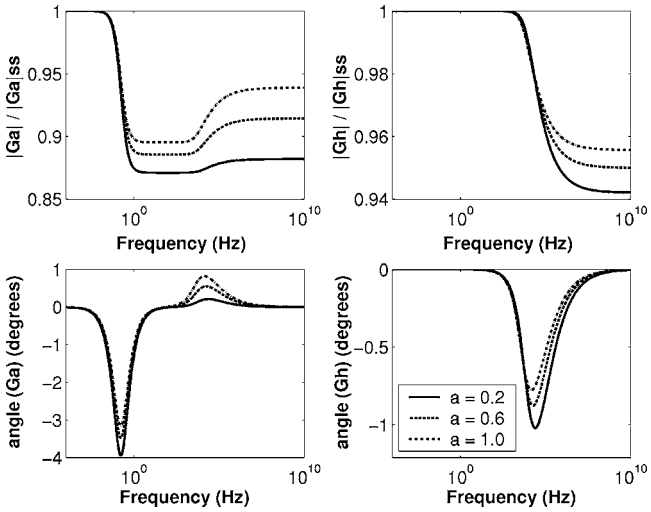

Fig. 3 Variation in sensitivity coefficients with frequency (*f*) and overheat ratio (*a*)

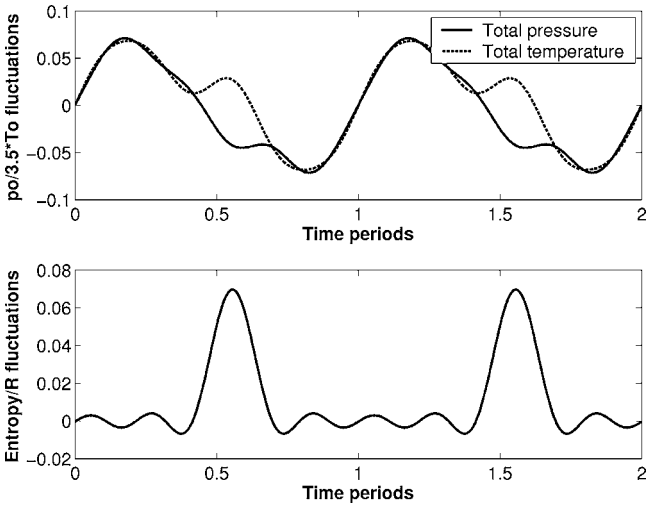

Fig. 4 Inlet boundary conditions for convergent-divergent nozzle: total pressure, total temperature, and entropy/R

heat transfer, we use the correlation by [16], which is an exhaustive tabulation of experimental data in the ranges $0.02<\mathrm{Re}<1000$ and $M>0.2$. Given that our typical Reynolds and Mach number values are approximately 150 and 0.45, this is a valid correlation. Since the correlation is not analytically tractable for differentiation, a numerical differentiation was used about the operating point, yielding

$$\frac{\mathrm{Nu}'/\overline{\mathrm{Nu}}}{M'/\bar{M}} = -0.175 \tag{18}$$

i.e., a 1% change in Mach number results in a −0.175% change in Nusselt number. Fluctuations in Mach number thus cause a significant change in Nusselt number; the corresponding sensitivity to Reynolds number is 0.515%, which is only a factor of 3 greater.

However, we also need to estimate the magnitude of the Mach number fluctuations inside the aspirating probe. Two methods were used to predict these fluctuations in Mach number. The first is based on the one-dimensional equations governing flow in an axisymmetric duct, the second a full three-dimensional computational fluid dynamics (CFD) solution of the flow inside the probe. We present results from both simulations for comparison.

3.1 One-Dimensional Flow Solution. The equations governing flow in a one-dimensional duct of changing cross-sectional area are given by [17]

$$\frac{\partial}{\partial t}\begin{pmatrix} u \\ \rho \\ p \end{pmatrix} = \begin{pmatrix} -\frac{1}{\rho}\frac{\partial p}{\partial x} - u\frac{\partial u}{\partial x} \\ -\rho\frac{\partial u}{\partial x} - u\frac{\partial \rho}{\partial x} - \rho u\frac{1}{A}\frac{\partial A}{\partial x} \\ -\gamma p\frac{\partial u}{\partial x} - u\frac{\partial p}{\partial x} - \gamma p u\frac{1}{A}\frac{\partial A}{\partial x} \end{pmatrix} \tag{19}$$

Reference [18] shows that these equations, without the change in area terms, can be arranged into conservation form

$$\frac{\partial}{\partial t}\begin{pmatrix} \rho \\ \rho u \\ E \end{pmatrix} + \frac{\partial}{\partial x}\begin{pmatrix} \rho u \\ \rho u^2 + p \\ (E+p)u \end{pmatrix} = 0 \tag{20}$$

where $E=p/(\gamma-1)+(1/2)\rho u^2$. We thus rearranged Eq. (19) in a similar manner, but retaining the area variation terms to give

$$\frac{\partial}{\partial t}\begin{pmatrix} \rho \\ \rho u \\ E \end{pmatrix} + \frac{\partial}{\partial x}\begin{pmatrix} \rho u \\ \rho u^2 + p \\ (E+p)u \end{pmatrix} = -\begin{bmatrix} \rho u \\ \rho u^2 \\ (E+p)u \end{bmatrix}\frac{1}{A}\frac{\partial A}{\partial x} \tag{21}$$

This can be solved using standard numerical techniques, since it is of the form

$$\frac{\partial U}{\partial t} + \frac{\partial F(U)}{\partial x} = S(U) \tag{22}$$

where

$$U = \begin{pmatrix} \rho \\ \rho u \\ E \end{pmatrix} \tag{23}$$

Equation (22) was solved numerically using the two-step Lax-Wendroff method [19], where the grid is assumed uniform in space and time with increments Δx and Δt, respectively. The approximate solution after m length and n time steps is denoted by U_m^n. The method then proceeds using the updated equation

$$U_m^{(n+1)} = U_m^n - \frac{\Delta t}{\Delta x}[F(U_{m+1/2}^{n+1/2}) - F(U_{m-1/2}^{n+1/2})] + \frac{\Delta t}{2}[S(U_{m+1/2}^{n+1/2}) + S(U_{m-1/2}^{n+1/2})] \tag{24}$$

where

$$U_j^{n+1/2} = \frac{U_{j+1/2}^n + U_{j-1/2}^n}{2} - \frac{\Delta t}{2\Delta x}[-F(U_{j+1/2}^n) + F(U_{j-1/2}^n)] + \frac{\Delta t}{4}[S(U_{j+1/2}^n) + S(U_{j-1/2}^n)] \tag{25}$$

for $j=m+1/2$ and $j=m-1/2$. The probe was modeled as a convergent-divergent nozzle, with a radial profile given by

$$r(x) = 0.051[\tanh(-5x+2.5) + \tanh(5x-7.5)] + 0.6007 \tag{26}$$

where the hot-wire plane is assumed to be at 0 mm and the throat at 1 mm. The inlet is defined to be at −0.3 mm. All these dimensions correspond to the aspirating probe used by [4] and are typical of values used by other authors. At the inlet, the total pressure and total temperature are assumed to vary as shown in Fig. 4 and the Mach number is assumed constant at 0.454. These are derived from the experimental results presented in [4] and simulate the flow field seen by a stationary probe behind a high-pressure tur-

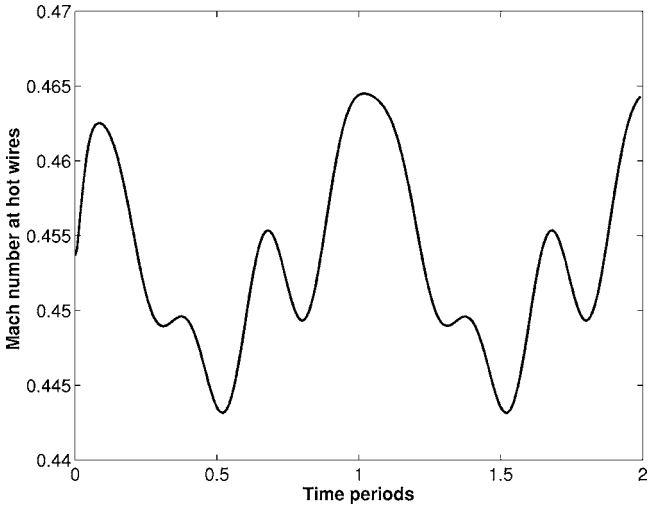

Fig. 5 Mach number fluctuations

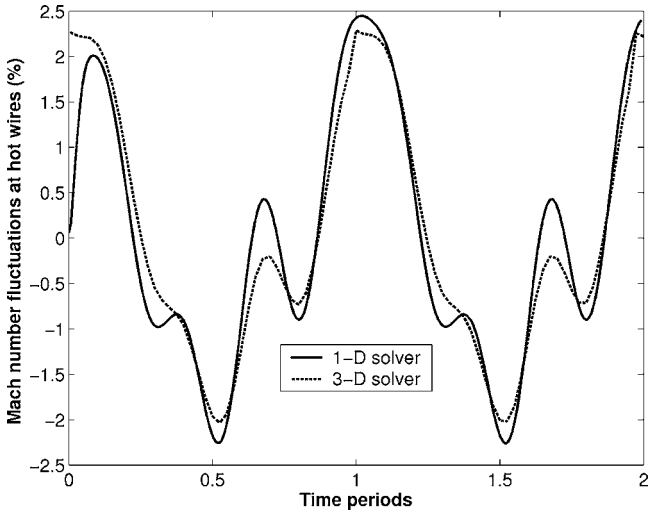

Fig. 6 Normalized Mach number fluctuations at the hot-wire plane for both the one-dimensional and three-dimensional flow solutions

bine rotor blade at midheight. These synthetic data are used to give realistic traces for the likely flow fields measured by the aspirating probe. Clearly, the analysis presented here could be used for any inlet flow field. The fundamental frequency of oscillations is assumed here at 10 kHz, since this is close to the value found in the experimental facility used by [4]. The outlet boundary was allowed to go supersonic.

The Mach number fluctuations at the hot wire plane, 0.3 mm downstream from the inlet, shown in Fig. 5, have amplitude 0.022, with a mean level of ~0.454. This is a variation of ±2.4%. Whether this has a significant effect on the measurement of entropy will be examined later, once the CFD solution has been presented.

3.2 Three-Dimensional Flow Solution. The one-dimensional flow solution presented above obviously neglects a number of aspects of the flow field, which might prove to be important. In particular, the boundary layers are not considered. A three-dimensional flow solution was thus generated to test the accuracy of the one-dimensional solution in predicting fluctuations in Mach number inside the probe.

The commercial package FLUENT v. 6.1 was used to simulate the flow field within the probe. Given the nature of the flow field, a simple laminar model was used: a Reynolds-averaged turbulence model was also used for comparison, but yielded almost identical results. Since the turbulence model increased computation time by approximately an order of magnitude, it was decided to use the laminar flow model. This also removed any unwanted entropy generation from turbulence in the flow, enabling us to examine the Mach number fluctuations alone. As for the one-dimensional solution, only the convergent-divergent nozzle was considered, to enable direct comparisons to be made. The radial profile, Eq. (26), was used over a distance of −0.3–2 mm, and the internal part of the probe meshed three times with increasing fineness. This was done to check the grid independence of the solution and to examine whether the boundary layer comprised a significant proportion of the cross-sectional area. Finally, a mesh with 34,900 tetrahedral elements was chosen, with a total volume of 1.91 mm^3, giving an average element length of order 5 μm. The boundary layer at the throat is found to be ~50 μm in thickness, which is close to the 45 μm predicted by boundary layer theory. The boundary conditions were as for the one-dimensional solution.

The flow field inside the probe was examined to determine the position at which the Mach number equals one. It was found that at 10 kHz this position fluctuated very slightly, with amplitude 8 μm. Because of the fluctuations in total pressure and total temperature, local variations in the flow field pass through the probe, influencing the local Mach number. The fractional variation in Mach number along the probe decreases as the flow approaches the throat, fluctuations at the point of minimum area being possible by this small oscillation in the position of the throat.

The resulting normalized fluctuations in Mach number at the hot-wire plane are shown in Fig. 6, in comparison to those calculated from the one-dimensional solution. There is very good agreement between the two plots, indicating that the assumption of one-dimensional flow is a good one. The effects of frequency on the flow field can thus be examined using the one-dimensional solver. The nondimensional frequency considered in the example here is of order 0.1. The same fluctuating flow field was used to simulate the Mach number variations at the hot-wire plane in this particular probe geometry for a range of nondimensional frequencies, by stretching the same flow field over a different time period. As expected, the fluctuations in Mach number are found to increase monotonically with nondimensional frequency, from ±0.26% at 1 kHz to ±2.4% at 10 kHz and ±7.0% at 100 kHz. The typical blade passing frequency in a turbomachinery test environment is in the range of 1–10 kHz [6–8]; thus, the expected fluctuations in Mach number are of the order of ±1%. However, if the test facility is operated close to 1 kHz, the fluctuations will be much smaller than if operated close to 10 kHz.

3.3 Effects of Mach Number Fluctuations. The effects of Mach number fluctuations on the measured total pressure and total temperature can be calculated using small-signal analysis. By linearizing Eq. (4) using a Taylor series expansion about the baseline conditions, and assuming that $D=0$, the fluctuations in hot wire voltage can be related to fluctuations in total pressure and total temperature

$$\frac{E_i'}{\bar{E}_i} = S_{p,i}\left(\frac{p_o'}{\bar{p}_o}\right) + S_{T,i}\left(\frac{T_o'}{\bar{T}_o}\right) \tag{27}$$

where $S_{p,i}=n_i/2$ and $S_{T,i}=-n_i/4-1/2\tau_i$ for $i=1,2$. By inverting the equations, expressions for total pressure and total temperature can be found as functions of the wire voltages

$$\left(\frac{p_o'}{\bar{p}_o}\right)_{\text{derived}} = \frac{\tau_1(2+n_2\tau_2)}{n_1\tau_1 - n_2\tau_2}\frac{E_1'}{\bar{E}_1} + \frac{\tau_2(2+n_1\tau_1)}{n_2\tau_2 - n_1\tau_1}\frac{E_2'}{\bar{E}_2} \tag{28}$$

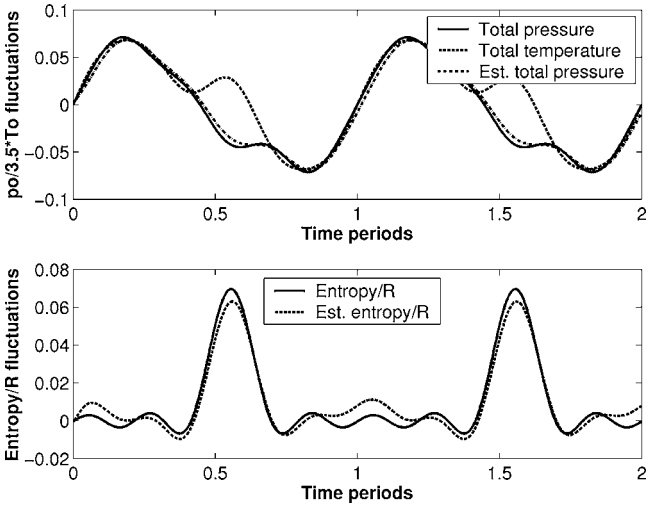

Fig. 7 Total pressure, total temperature, and entropy/R fluctuations, both true and derived, neglecting Mach number fluctuations

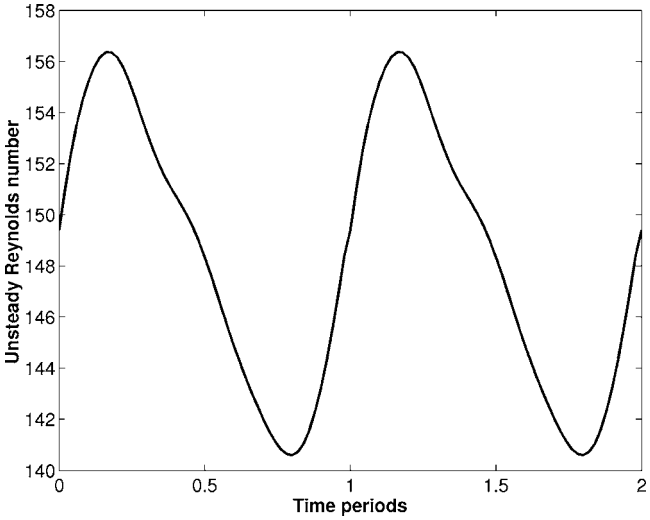

Fig. 8 Fluctuations in Reynolds number used to simulate heat transfer variations

$$\left(\frac{T_o'}{\bar{T}_o}\right)_{\text{derived}} = \frac{2n_2\tau_1\tau_2}{n_1\tau_1 - n_2\tau_2}\frac{E_1'}{\bar{E}_1} + \frac{2n_1\tau_1\tau_2}{n_2\tau_2 - n_1\tau_1}\frac{E_2'}{\bar{E}_2} \tag{29}$$

However, under dynamic conditions, the hot wire voltages are also sensitive to changes in Mach number

$$\left(\frac{E_i'}{\bar{E}_i}\right)_{\text{true}} = S_{p,i}\left(\frac{p_o'}{\bar{p}_o}\right)_{\text{true}} + S_{T,i}\left(\frac{T_o'}{\bar{T}_o}\right)_{\text{true}} + S_M\left(\frac{M'}{\bar{M}}\right)_{\text{true}} \tag{30}$$

where the sensitivity to Mach number is half the value from Eq. (18). If Eqs. (28) and (29) are still used to invert the solution, then the derived total pressure and total temperature are found to be

$$\left(\frac{p_o'}{\bar{p}_o}\right)_{\text{derived}} = \left(\frac{p_o'}{\bar{p}_o}\right)_{\text{true}} + \frac{2}{n}\mathrm{S_M}\left(\frac{M'}{\bar{M}}\right)_{\text{true}} \tag{31}$$

$$\left(\frac{T_o'}{\bar{T}_o}\right)_{\text{derived}} = \left(\frac{T_o'}{\bar{T}_o}\right)_{\text{true}} \tag{32}$$

where, for simplicity, it is assumed that $n_1=n_2=n$. Note that there is no error in total temperature, but that the total pressure is reduced by the presence of Mach number fluctuations. This is because both wires are equally sensitive to fluctuations in both total pressure and Mach number, but not so to changes in total temperature. The latter can be calculated accurately even in the presence of Mach number fluctuations, whereas the first two cannot be separated. This will have an effect on the accuracy of entropy measurements. The entropy/R calculated from the entry conditions is compared to that calculated using Eqs. (31) and (32) in Fig. 7, together with the total pressure and total temperature. Note that total temperature fluctuations are scaled by a factor of 3.5 so that entropy is calculated as the difference between the scaled total temperature and the total pressure traces. The estimated total pressure trace is only slightly different from the actual value, but the peak value of entropy/R is reduced from 0.07 to 0.063, $\sim$10%, if Mach number fluctuations are neglected in this flow field. This is likely to have a noticeable impact on the estimate of the stage efficiency.

4 Heat Transfer Fluctuations

Having considered the frequency response of the hot wire and the fluctuations in the flow field inside the probe, the only remaining potential source of high-frequency behavior is the heat transfer from the hot wire to the probe. We investigated this numerically, since we were unable to find any experimental data at sufficiently high frequencies. Analytical solutions were ruled out due to the nature of the flow, in particular, the separation at the back of the wire. Since it has been shown that the thickness of the probe internal boundary layer is very small in comparison to the probe diameter, a two-dimensional model is used to simulate heat transfer around a heated circle in cross-flow. Since the heat transfer is strongly dependent on the surface temperature, a range of wire temperatures were examined. Fluctuations in Reynolds number were then used to examine the resultant fluctuations in Nusselt number.

The commercial package FLUENT v.6.1 was again used, as in Sec. 3, with a mesh containing 14,358 triangular elements. The same assumptions about the flow field were used, and the inlet conditions for this part of the flow field were taken from the three-dimensional solution for flow inside the probe, thus linking the two models together. Based on these earlier results, the Reynolds number at the hot-wire plane was found to fluctuate between approximately 141 and 156. To examine the effects of fluctuations in Reynolds number at high frequencies, three numerical simulations were run at each wire temperature (Fig. 8). The first simulated the unsteady flow with Reynolds number varying between these limits at the relevant frequency. The second and third were steady-state simulations at the maximum and minimum values of Reynolds number. This enables the effects of high-frequency oscillations in the flow to be calculated relative to the steady-state calibration, which is, of course, determined experimentally for any given probe. These simulations were run for a range of wire temperatures, in steps of 50 K from 350 K to 600 K. It should be emphasized that it is only the relative difference between Nusselt number at steady state and at a given frequency that is of interest here.

The resulting fluctuations in Nusselt number for the different overheat ratios (Fig. 9) map well onto each other at higher values of the overheat ratio. However, this changes at lower overheat ratios, with the amplitude increasing for overheat ratios below $\sim$0.3. At low overheat ratios, the maximum Nusselt number no longer occurs at the point of maximum Reynolds number, but is very slightly delayed. However, this is a small effect, being $<$0.1 time periods at the lowest overheat ratio considered. Since this makes very little difference to the accuracy of the measurements made using the aspirating probe, we do not consider it further.

The resulting comparison between the maximum and minimum Nusselt numbers in the steady-state and the dynamic conditions (Fig. 10) shows that, at high overheat ratios, there is no variation in the heat transfer with frequency. However, at very low overheat

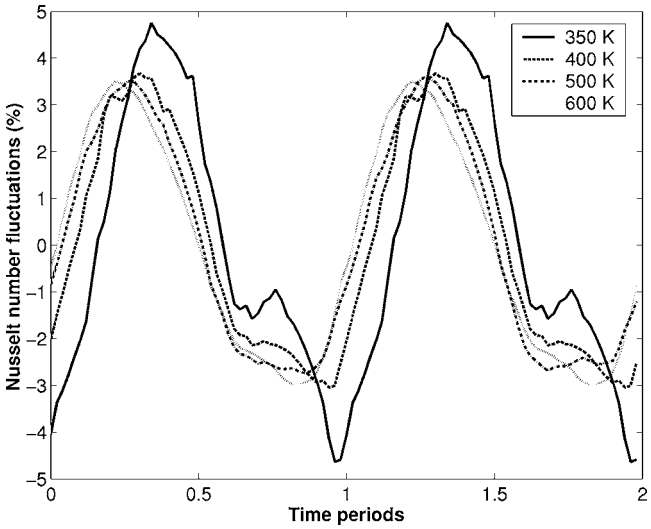

Fig. 9 Fluctuations in Nusselt number as a function of overheat ratio

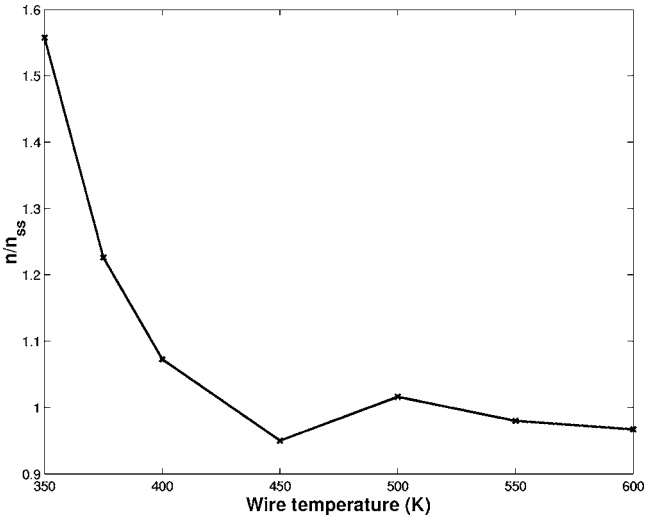

Fig. 11 Variation in sensitivity to Reynolds number due to Nusselt number fluctuations at high frequencies with overheat ratio

ratios, there is significant deviation from the steady state at high frequencies. The sensitivity of Nusselt number to fluctuations in Reynolds numbers is thus dependent on the overheat ratio. The mean level of Nusselt number decreases with increased overheat ratio, but is consistently larger than the values predicted from the Dewey [16] correlation (5.22 and 5.51 for Reynolds numbers of 140.6 and 156.4, respectively, at a Mach number of 0.44). The correlation of Collis and Williams [12] gives a much larger value for Nusselt number (5.98 and 6.32 for the same Reynolds numbers as above), but Mach number is not considered there, which makes comparisons more difficult. Since there appears to be no correlation that provides for a complete relationship of Nusselt number as a function of Reynolds number, Mach number, and overheat ratio, it is difficult to make direct comparisons to the literature. In addition, to the best of the authors' knowledge, there is no available data on unsteady Nusselt number at the frequencies considered here. Since we are only comparing the CFD predictions at high frequency to those at steady state, the absolute value of the steady-state Nusselt number is not crucial to the results presented here. It should be noted that Reynolds number, Mach number, and overheat ratio all fluctuate under the conditions analyzed here, since these were taken from the one-dimensional solution for fluctuating flow presented in Sec. 4. The individual components of the fluctuations in Nusselt number due to Mach number, Reynolds number, or overheat ratio have not been considered here, since only a single case is considered. However, the analysis presented here could be applied to any other probe and flow field.

The physical causes of this change in Nusselt number at low overheat ratios are not investigated here for two reasons. The first is that only a particular flow field is explored and we do not wish to draw conclusions about the general high-frequency behavior without considering the phenomenon in more detail. It would be of great interest, however, to investigate this high-frequency behavior in more detail. The second, more relevant, reason is that the effect is only seen at very low overheat ratios, which are not used in practice for other reasons. This effect is thus of more academic than practical interest.

A sensitivity coefficient correction factor can be calculated that is dependent on overheat ratio (Fig. 11). Since we are only examining the effects of Reynolds number fluctuations on Nusselt number, this essentially scales the value of n, from Eq. (3). This correction factor is close to unity for high overheat ratios, small variations about this value arising from insignificant numerical differences, rising as the overheat ratio drops. However, this correction factor can often be neglected since, although the two hot wires in the aspirating probe are normally operated with as large an overheat ratio difference as possible, in practice the very low overheat ratios are not often used for practical reasons.

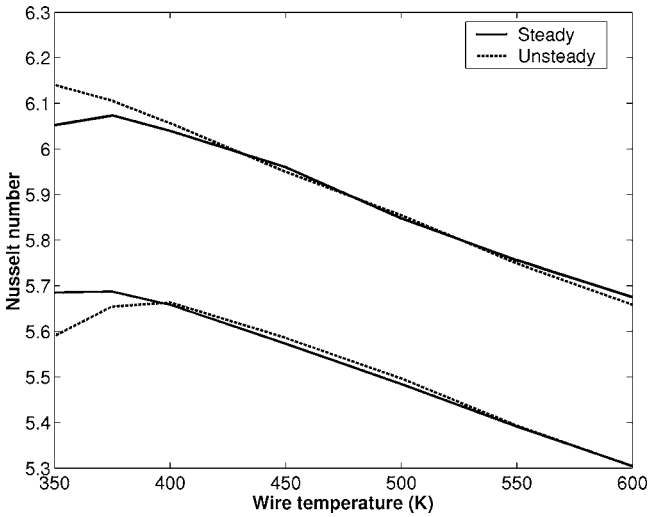

Fig. 10 Comparison of unsteady Nusselt numbers at the point of maximum and minimum Reynolds numbers with steady-state Nusselt numbers at the same Reynolds numbers

5 Complete Frequency Response of Aspirating Probe

The three previous sections have examined the three high-frequency effects present in the aspirating probe: hot-wire frequency response, Mach number fluctuations, and heat transfer frequency response. For simplicity, for the last two only the conditions relevant to a particular probe and flow field have been considered; however, the analysis could be performed for any probe and flow field using the approach set out here.

We thus now combine all the results presented earlier to examine the total effect of the high-frequency effects on the aspirating probe and, particularly, its measurement of total pressure, total temperature, and hence, entropy. For small fluctuations about the mean values, the voltage sensitivity to total pressure, total temperature, and Mach number fluctuations is given by Eq. (30).

However, the sensitivity coefficients at high frequencies are different from those found by a steady-state calibration

$$n_i' = f_c(\tau_i) f_N(\tau_i) n \tag{33}$$

$$\tau_i' = f_T(\tau_i)\tau_i \tag{34}$$

where $f_N(\tau_i)$ is the correction factor from Nusselt number fluctuation effects and $f_c(\tau_i)$ and $f_T(\tau_i)$ are the correction factors from conduction effects. As earlier, the steady-state calibration can be used to invert the hot-wire voltage signals to yield derived total pressure, total temperature, and entropy fluctuations based on the true values

$$\left(\frac{p_o'}{\bar{p}_o}\right)_{\text{derived}} = C_{pp}\left(\frac{p_o'}{\bar{p}_o}\right)_{\text{true}} + C_{pT}\left(\frac{T_o'}{\bar{T}_o}\right)_{\text{true}} + C_{pM}\left(\frac{M'}{\bar{M}}\right)_{\text{true}} \tag{35}$$

$$\left(\frac{T_o'}{\bar{T}_o}\right)_{\text{derived}} = C_{TT}\left(\frac{T_o'}{\bar{T}_o}\right)_{\text{true}} + C_{Tp}\left(\frac{p_o'}{\bar{p}_o}\right)_{\text{true}} \tag{36}$$

where the coefficients C describe the relative contributions from each term and are given by

$$C_{pp} = \frac{1}{2(\tau_1 - \tau_2)}[\tau_1(2 + n\tau_2) f_c(\tau_1) f_N(\tau_1) - \tau_2(2 + n\tau_1) f_c(\tau_2) f_N(\tau_2)] \tag{37}$$

$$C_{pT} = \frac{1}{2n(\tau_1 - \tau_2)}\left[\left(\frac{f_c(\tau_2) f_N(\tau_2) n}{2} + \frac{1}{f_T(\tau_2)\tau_2}\right)\tau_2(2 + n\tau_1) - \left(\frac{f_c(\tau_1) f_N(\tau_1) n}{2} + \frac{1}{f_T(\tau_1)\tau_1}\right)\tau_1(2 + n\tau_2)\right] \tag{38}$$

$$C_M = \frac{2}{n} S_M \tag{39}$$

$$C_{Tp} = \frac{n\tau_1\tau_2}{(\tau_1 - \tau_2)}[f_c(\tau_1) f_N(\tau_1) - f_c(\tau_2) f_N(\tau_2)] \tag{40}$$

$$C_{TT} = \frac{\tau_1\tau_2}{(\tau_1 - \tau_2)}\left[\left(\frac{f_c(\tau_2) f_N(\tau_2) n}{2} + \frac{1}{f_T(\tau_2)\tau_2}\right) - \left(\frac{f_c(\tau_1) f_N(\tau_1) n}{2} + \frac{1}{f_T(\tau_1)\tau_1}\right)\right] \tag{41}$$

where it is assumed that in the steady state, $n_1 = n_2 = n$, for simplicity. Note that if the correction factors are all unity, then $C_{pp} = C_{TT} = 1$ and $C_{pT} = C_{Tp} = 0$ and, apart from Mach number fluctuations, the total pressure and total temperature are found exactly by the steady-state calibration. The variation in the coefficients as the lower overheat ratio varies, the higher value being set at 1, is shown in Fig. 12. Note that the coefficients are significantly different from the ideal values. The correction factors must thus be carefully considered when using the aspirating probe. In particular, C_{pp} increases toward 1 as the second overheat ratio increases, whereas C_{TT} decreases from 1 rapidly as the second overheat ratio increases. C_{pT} becomes smaller as the second overheat ratio increases, while C_{Tp} crosses from negative to positive. Choosing an optimal overheat ratio is thus not a simple matter, since some coefficients tend toward their ideal values as the overheat ratio increases, whereas others diverge. To examine the effects of these coefficients on the measurement of total pressure and total temperature, we now use the synthetic data for total pressure and total temperature presented earlier.

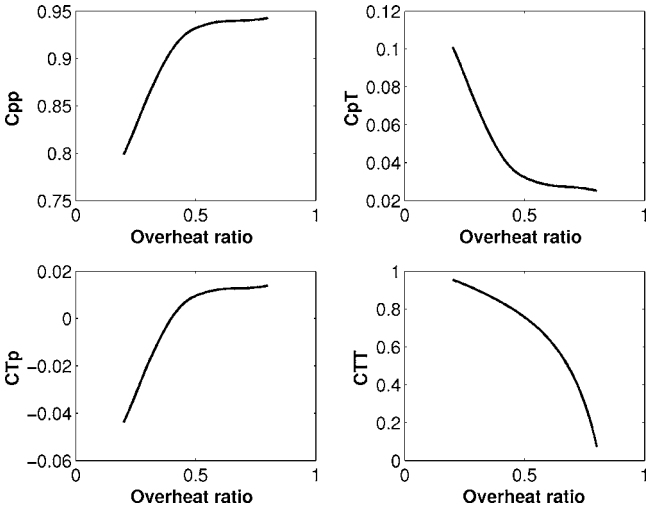

Fig. 12 Variation in correction coefficients with second overheat ratio for first wire at unity overheat ratio

6 Discussion

The changes in total pressure and total temperature from the actual values are shown in Fig. 13, together with the change in entropy, for overheat ratios of 0.2 and 1.0. For the first case, the amplitudes of total pressure and total temperature drop by 21% and 20%, respectively. The change in entropy is thus relatively small over most of the time period. In the region where there is a peak in entropy/R, the value drops from 0.070 to 0.059, however. Although the peak is still clearly seen, there is a 15% reduction in this peak value, which will be highly misleading in attempting to quantify the loss associated with this peak.

Figure 14 shows the corresponding plots for overheat ratios of 0.5 and 1.0. For this case, where the overheat ratios are closer (0.5 and 1.0), there is a smaller drop in total pressure amplitude (10%) than for the first case, but a similar drop in total temperature amplitude (21%). The dependence of derived total temperature on actual total temperature is found to reduce significantly as the lower overheat ratio is increased. The entropy/R peak value falls from 0.070 to 0.052, a drop of 25%. This is a much more significant drop and would introduce a significant error into any attempts to quantify loss. If the second overheat ratio is increased further,

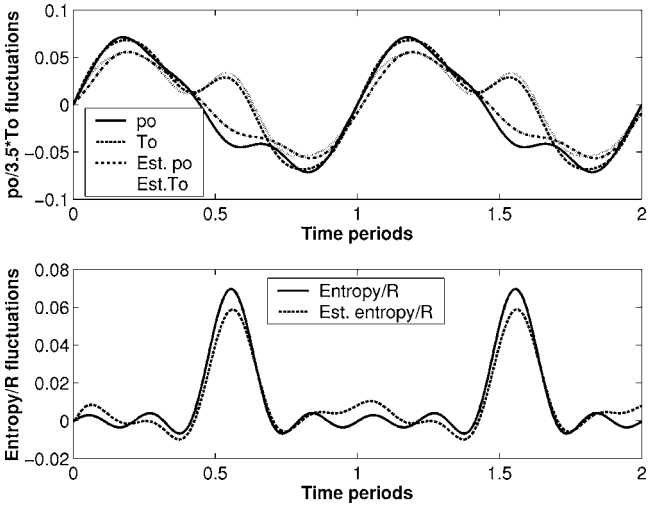

Fig. 13 Total pressure, total temperature and entropy/R fluctuations, both true and derived, neglecting high-frequency behavior, for overheat ratios 0.2 and 1.0

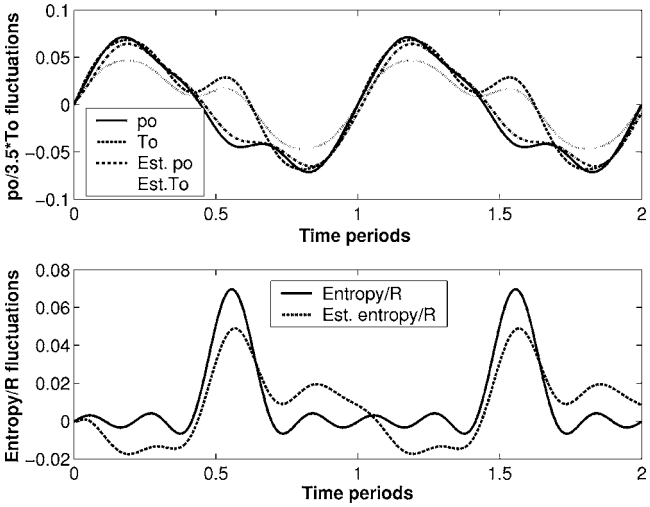

Fig. 14 Total pressure, total temperature, and entropy/R fluctuations, both true and derived, neglecting high-frequency behavior, for overheat ratios 0.5 and 1.0

the errors rapidly become much larger, due to C_{TT} decreasing. If overheat ratios of 0.8 and 1.0 are chosen, for example, the estimate of total temperature drops by 88%, total pressure dropping by 10%, resulting in an estimated entropy/R trace that is completely different from the true value.

The amplitudes of total pressure and total temperature are consistently reduced. However, as the lower overheat ratio is increased, the reductions become dissimilar. This dissimilarity has a disastrous effect on the accuracy of entropy measurements: if the lower overheat ratio is increased significantly above 0.5 the predicted entropy plot is completely different from the actual trace. These results mean that the use of the aspirating probe to measure total pressure and total temperature must be undertaken with caution and the high-frequency effects must be considered carefully if the experimental data are not to be highly inaccurate. In addition, the overheat ratios must be chosen carefully: too small a difference results in highly erroneous measurements if the high-frequency effects are not taken into account. Although we have only examined the behavior of the aspirating probe for one particular set of flow conditions and probe dimensions, as used by [4], the analysis above should be performed for any choice of probe geometry and flow conditions when using the aspirating probe in highly unsteady flow. The steady-state calibration can then be corrected for these high-frequency effects to ensure that the experimental measurements are accurate.

Nomenclature

c = specific heat capacity
d = diameter
h = heat transfer coefficient
k = thermal conductivity
n = constant
p = pressure
r = radius
s = specific entropy
t = time
u = velocity
x = distance
A = area, constant
B = constant
C = constant
D = constant
E = voltage
G = coefficient
I = current
M = Mach number
Nu = Nusselt number
R = gas constant
Re = Reynolds number
T = temperature
Z = coefficient
γ = ratio of specific heats
α = coefficient of resistance
η = recovery factor
ρ = density, resistivity
ω = frequency

Subscripts

a = flow temperature
h = heat transfer coefficient
m = mean
o = total conditions
ref = reference
w = wire
I = current

Superscripts

$-$ = mean
$*$ = choked
$'$ = fluctuating component

Appendix

The solution is based on the general hot-wire equation [13]

$$K_1\frac{\partial T_w}{\partial t} = \frac{\partial^2 T_w}{\partial x^2} - \beta_1 T_w + K_2 T_a - K_3 \tag{A1}$$

where

$$K_1 = \frac{\rho_w c_w}{k_w} \tag{A2}$$

$$\beta_1 = \frac{h\pi d}{k_w A} - \frac{\alpha I^2 \rho_{\text{ref}}}{k_w A^2} \tag{A3}$$

$$K_2 = \frac{h\pi d}{k_w A} \tag{A4}$$

$$K_3 = \frac{I^2 \rho_{\text{ref}}}{k_w A^2}(\alpha T_{\text{ref}} - 1) \tag{A5}$$

The wire temperature is a function of both the distance along the wire and time. The two main assumptions made in the hot-wire equation are that the radial variations in wire temperature and the radiation heat transfer are negligible. These were shown by [10] to be valid assumptions for typical flow conditions and wire properties.

It is then assumed that the time-varying parameters show sinusoidal fluctuations with time: the general hot-wire equation separates into steady-state and time-varying components:

$$\frac{\partial^2 \bar{T}_w}{\partial x^2} - \bar{\beta}_1 \bar{T}_w = \bar{K}_3 - \bar{K}_2 \bar{T}_a \tag{A6}$$

$$T_w'[\bar{\beta}_1 + j\omega\bar{K}_1] - \frac{\partial (T_w')^2}{\partial x^2} = \bar{K}_2 T_a' + [\bar{T}_a - \bar{T}_w]\frac{\pi d}{k_w A}h' + \left[\frac{2\alpha\bar{I}\rho_{\text{ref}}}{k_w A^2}\bar{T}_w - \frac{2\bar{I}\rho_{\text{ref}}}{k_w A^2}(\alpha T_{\text{ref}} - 1)\right]I' \tag{A7}$$

where the overbar is used to denote steady-state conditions and the prime the fluctuating components of the heat transfer coefficient, flow, and wire temperatures. The steady-state equation can

be directly solved to give the well-known tanh solution for wire temperature [11]. The time-varying equation is solved in a similar manner and, using the fact that the net change in wire temperature over its length remains constant at all times, and that the supports have a frequency response $F(j\omega)$, gives a relationship of the form

$$\frac{I'}{\bar{I}} = G_a \frac{T_a'}{\bar{T}_a} + G_h \frac{h'}{\bar{h}} \tag{A8}$$

where

$$G_a(\omega') = -\frac{1}{2\tau}\frac{(\xi_1-1)^2\omega'\left\{F(1+\omega') + \left(\frac{\xi_{11}-1}{\xi_1-1}\right)[(\xi_1-1)+\xi_1 a]\right\}}{\xi_1\{(1+\omega')a(\xi_1-\xi_{11}) + \omega'(\xi_{11}-1)[(\xi_1-1)+\xi_1 a]\}} \tag{A9}$$

$$G_h(\omega') = \frac{1}{2}\frac{[(\xi_1-1)+\xi_1 a][(\xi_1-\xi_{11}) + \omega'\xi_{11}(\xi-1)]}{\xi_1\{(1+\omega')a(\xi_1-\xi_{11}) + \omega'(\xi_{11}-1)[(\xi_1-1)+\xi_1 a]\}} \tag{A10}$$

The relevant nondimensional quantities are

$$\omega' = j\omega\frac{\bar{K}_1}{\bar{\beta}_1} \tag{A11}$$

$$\xi_1 = \sqrt{\bar{\beta}_1} l \coth(\sqrt{\bar{\beta}_1} l) \tag{A12}$$

$$\xi_{11} = \sqrt{\bar{\beta}_{11}} l \coth(\sqrt{\bar{\beta}_{11}} l) \tag{A13}$$

$$\bar{\beta}_{11} = \bar{\beta}_1(1+\omega') \tag{A14}$$

$$a = \alpha(T_m - \bar{T}_a) \tag{A15}$$

$$\tau = \frac{(T_m - \bar{T}_a)}{\bar{T}_a} \tag{A16}$$

For simplicity, it is assumed that the reference temperature T_{ref}, is the same as the mean flow temperature $\bar{T}_a$; this is possible since the reference temperature is simply a datum point. If it is then assumed that the Biot number is larger than ~ 3, ξ_1 can be found from the overheat ratio if the ratio of heat transfer by conduction to heat transfer by convection is known, (Eq. (10)). This yields a relationship

$$\xi_1 = \frac{1}{\chi}\sqrt{\frac{(\xi_1-1)}{(\xi_1-1)+\xi_1 a}} \tag{A17}$$

which allows ξ_1 to be found iteratively once the overheat and heat transfer ratios are known. Equation (A13) can also be simplified to give

$$\xi_{11} = \xi_1\sqrt{1+\omega'}. \tag{A18}$$

References

[1] Denton, J. D., 1993, "Loss Mechanisms in Turbomachines," ASME J. Turbomach., **115**, pp. 621–656.

[2] Ng, W. F., and Epstein, A. H., 1983, "High-Frequency Temperature and Pressure Probe for Unsteady Compressible Flows," Rev. Sci. Instrum., **54**, pp. 1678–1683.

[3] Buttsworth, D. R., Jones, T. V., and Chana, K. S., 1998, "Unsteady Total Temperature Measurements Downstream of a High Pressure Turbine," ASME J. Turbomach., **120**, pp. 760–767.

[4] Payne, S. J., Ainsworth, R. W., Miller, R. J., Moss, R. W., and Harvey, N. W., 2003, "Unsteady Loss in a High Pressure Turbine Stage," Int. J. Heat Fluid Flow, **24**, pp. 698–708.

[5] Ng, W. F., and Epstein, A. H., 1985, "Unsteady Losses in Transonic Compressors," ASME J. Eng. Gas Turbines Power, **107**, pp. 345–353.

[6] Alday, J., Osborne, D. J., Morris, B., Ng, W., and Gertz, J., 1993, "Flow Randomness and Tip Losses in Transonic Rotors," ASME Paper No. 93-GT-189.

[7] Van Zante, D. E., Suder, K. L., Strazisar, A. J., and Okiishi, T. H., 1995, "An Improved Aspirating Probe for Total-Temperature and Total-pressure Measurements in Compressor Flows," ASME J. Turbomach., **117**, pp. 642–649.

[8] Suryavamshi, N., Lakshminarayana, B., and Prato, J., 1996, "Aspirating Probe Measurements of the Unsteady Total Temperature Field Downstream of an Embedded Stator in a Multistage Axial Flow Compressor," ASME Paper No. 96-GT-543.

[9] Brouckaert, J. F., 1998, "Experience With a Double-Hot-Wire Aspirating Probe in a Transonic Turbine Stage," *Proc. of 14th Symposium on Measuring Techniques for Transonic and Supersonic Flows in Cascades in Turbomachinery*, Limerick.

[10] Payne, S. J., 2001, "Unsteady Loss in a High Pressure Turbine Stage," D. Phil. thesis, University of Oxford.

[11] Bruun, H. H., 1995, *Hot-Wire Anemometry: Principles and Signal Analysis*, Oxford University Press, London.

[12] Collis, D. C., and Williams, M. J., 1959, "Two-Dimensional Convection From Heated Wires at Low Reynolds Numbers," J. Fluid Mech., **6**, pp. 357–389.

[13] Højstrup, J., Rasmussen, K., and Larsen, S. E., 1976, "Dynamic Calibration of Temperature Wires in Still Air," DISA Inf., **20**, pp. 22–30.

[14] Freymuth, P., 1979, "Engineering Estimate of Heat Conduction Loss in Constant Temperature Thermal Sensors," TSI Q., **V**(3), pp. 3–9.

[15] Parantheon, P., Lecordier, J. C., and Petit, C., 1983, "Dynamic Sensitivity of the Constant-temperature Hot-Sire Anemometer to Temperature Fluctuations," TSI Q., **9**, pp. 3–8.

[16] Dewey, C. F., 1965, "A Correlation of Convective Heat Transfer and Recovery Temperature Data or Cylinders in Compressible Flow," Int. J. Heat Mass Transfer, **8**, pp. 245–252.

[17] Shapiro, A. H., 1957, *The Dynamics and Thermodynamics of Compressible Fluid Flow*, Wiley, New York, Vol. 2.

[18] LeVeque, R. J., 2002, *Finite Volume Methods for Hyperbolic Problems*, Cambridge University Press, Cambridge, England.

[19] LeVeque, R. J., 1992, *Numerical Methods for Conservation Laws*, Birkhauser, Boston.